Synthesis and functionality of boron-, nitrogen- and oxygen-doped shaped carbon-based nanomaterials and titania nanocomposites in electrochemical capacitors

by

Edwin Tonderai Mombeshora

Submitted in fulfilment of the academic requirements of

Doctor of Philosophy

in Science

School of Chemistry and Physics

College of Agriculture, Engineering and Science

University of KwaZulu-Natal

Durban

South Africa

July 2017

Abstract

Energy is a global fundamental sector and major concerns are inclusive of; making renewable power economical, reliable and accessible to all, maintain and improve power quality, voltage and frequency, amongst others. There is need for development of intelligent energy storage systems (ESS) that maximise and provides durable storage of electrical power generated. This is a suitable approach towards reducing gas emissions, lowering electricity bills, meet power needs at any time and for lowering excess power fluctuations. Much advancement is required on ESS to shift their optimum working regions towards preferred limits with both high justifiable power and energy. Advancement of ESS need to be sought through developing effective electrode materials. Shaped carbon nanomaterials (SCNMs) are suitable for ESS in the Smart Grids with potential better cost effective and scalable standards. The investigation of related physicochemical properties of SCNMs, modification of nano-structural parameters and development of appropriate strategies that would enhance their functionality in ESS is key in this regard.

In this study, various ESS were reviewed with more focus on development of electrochemical capacitors (ECs) with a bias towards the use of SCNMs as electrodes. The work was aimed at understanding the influence of reagent ratio in the physicochemical properties of N-doped multiwalled carbon nanotubes (N-MWCNTs) and graphene oxide (GO). Also, it focused on modifying the functionality of MWCNTs, N-MWCNTs and reduced graphene oxide (RGO) in ECs *via* introduction and control of heteroatoms such as nitrogen and its functional moieties or introduction of oxygen-containing groups. Thirdly, the work investigated the effect of composite synthesis on the performances of individual components *via* control of wt.% ratios. Characterisation techniques used include transmission and scanning electron microscopies, atomic force microscopy, textural characteristics, thermogravimetric analysis, elemental analysis, cyclic voltammetry, electrochemical impedance spectroscopy, X-ray photoelectron spectroscopy, X-ray diffraction, ultraviolet-visible spectrophotometry, Raman and Fourier transform infra-red spectroscopies.

N-MWCNTs were synthesized from *N,N'*-dimethyl formamide and acetonitrile as sp^3 and *sp* hybridized nitrogen sources, respectively, as materials for ECs. The combination of ferrocene carboxaldehyde, *N,N'*-dimethyl formamide and acetonitrile in N-MWCNTs synthesis was a novel approach. Mixing the sp^3 and *sp* sources in 1:3 ratio enhanced nitrogen content to 9.38%

from that of both sp^3 (5.87%) and *sp* (3.49%). The physical properties such as number of concentric shells were tailored by varying synthesis temperature. Pyrrolic N-doping was achieved as the main constituent of nitrogen moieties.

Furthermore, GO was synthesized as a preliminary step for further N-doping. The effect of graphite: Na_2NO_4 reagent ratio in the synthesis of GO was studied to elucidate the influence of the initial step in GO synthesis, *via* modified Hummer's method, and to develop novel strategies towards controllable products. The physicochemical properties such as content of oxygen-containing groups on GO and the surface areas were increased from 0% and 2 $m^2\ g^{-1}$ to 30% and 188 $m^2\ g^{-1}$, respectively, by increasing the proportion of Na_2NO_4 in reagents. The manipulation of the initial step was a novel means of tailoring the associated physicochemical properties of GO.

Also, this study determined, for the first time, the most effective group one sulfate electrolyte at fixed concentrations. This aided the selection of the electrolyte used in the application of the SCNMs in this thesis. Oxygen moieties were introduced, by ultra-sonic waterbath treatment, onto MWCNT surfaces using various reagents namely; HCl, HNO_3, H_2O_2 and HNO_3/ HCl solutions. The study highlighted how the various reagents, commonly used to purify MWCNTs after synthesis, modify associated physicochemical properties and alter charge storage characteristics. Oxygen-containing groups increased capacitance of pristine MWCNTs and introduced pseudo charge storage mechanism *via* oxygen functionalities. HNO_3 treated MWCNTs had a 77- and 2.5-fold upgrading from pristine using Li_2SO_4 and Na_2SO_4, respectively, whilst HNO_3/ HCl was the best, 5 times better, in K_2SO_4. The oxygen-modified MWCNTs performance was highest and of best quality in Na_2SO_4.

The effectiveness of common GO reductants, namely; ascorbic acid, hydrazine hydrate and sodium borohydride were practically investigated. This was done to select a reductant for the current work. This study also provided a viable novel chemical tuning approach for nitrogen moieties and content as well as to introduce boron, with sodium borohydride. Thirdly, under this particular study, the effect of heteroatoms, boron and nitrogen, as well as nitrogen moieties on physicochemical characteristics of RGO was also explored. Hydrazine hydrate was the most effective reductant and was associated with highest surface area and N-content of 390.55 $m^2\ g^{-1}$ and 4.07 at.%, respectively. The nitrogen groups of RGO reduced by means of ascorbic acid, hydrazine hydrate and pristine were pyrrolic, pyridinic and sp^3 N-C, respectively. N-doped RGO, particularly pyrrolic moieties, were 76-fold better than B-doped. A further

thermal reduction, of RGO from hydrazine hydrate, increased surface area from c.a. 391 to c.a. 600 $m^2 g^{-1}$ at 750 ℃.

The effect of oxygen-containing groups was then investigated in composites of titania with GO, RGO and cellulose reduced graphene oxide (CRG). The wt.% ratios of titania were varied; i.e., 5, 10, 20 and 40%. Based on earlier deductions in this thesis, reductant chosen was hydrazine hydrate. Titania enabled better exfoliation of GO but at higher wt.%, it culminated in larger agglomerates which in turn increased diffusion path-length. RGOTi at 5 wt.% titania increased surface area from 136.89 to 434.24 $m^2 g^{-1}$. The study generally showed that capacitance was better at lower wt.% titania in RGOTi and that cellulose surface area increase was outweighed by associated insulating effect. The present data infers that the impact of oxygen moieties on capacitance of SCNMs was subject to specific structures; MWCNTs, GO and RGO. Capacitance of titania and GO were improved by composite synthesis.

Graphenated N-MWCNTs were targeted, as a means, to lessen agglomeration, without the use of surfactants, and to generate *3-D* scaffolds for better electrical conductivity channels. Also, better physicochemical characteristics for higher capacitance were obtained *via* sol-gel than CVD method. The ratios of sp^3- and *sp*-hybridized nitrogen in reagent mixtures, in this thesis, was effectively used to tune the composition of pyrrolic nitrogen moieties. Pyrrolic composition of N-MWCNTs was uniquely aimed because studies of typical moieties on RGO deduced pyrrolic to be better than pyridinic groups. The increase of pyrrolic nitrogen composition; 35, 45 and 60%, culminated in capacitance deterioration. Composite synthesis reduced Warbug length and amplified associated capacitance.

The physicochemical properties of RGO, GO, MWCNTs and N-MWCNTs were positively tuned from reagent ratios, conditions and composite syntheses. The conjectured strategies could modulate their overall capacitance *via* manipulation of heteroatom content and functional groups, amongst others listed herein. Several traits that linked physicochemical properties and capacitance were successfully elucidated. This affirms the hypothesized potential of SCNMs in ESS through understanding and control of both nano-structural parameters and physicochemical properties.

Preface

The research contained in this thesis was completed by the candidate while based in the discipline of Chemistry, School of Chemistry and Physics of the College of Agriculture, Engineering and Science, University of KwaZulu-Natal, Westville Campus, South Africa, from July 2014 to March 2017, under the supervision of Prof Vincent O. Nyamori, Prof Patrick G. Ndungu and Dr. A. L. Leigh Jarvis.

The contents represent original work by the candidate and have not otherwise been submitted in any form to another tertiary institution and, except where the work of others is acknowledged in the text, the results reported are due to investigations by the candidate.

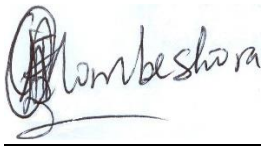

Signed: Edwin T. Mombeshora

Student number: 212561878

July 2017

Declaration 1 - plagiarism

I, Edwin Tonderai Mombeshora, declare that:

1. The research reported in this thesis, except where otherwise indicated, is my original research.

2. This thesis has not been submitted for any degree or examination at any other university.

3. This thesis does not contain other persons' data, pictures, graphs or other information, unless specifically acknowledged as being sourced from other persons.

4. This thesis does not contain other persons' writing, unless specifically acknowledged as being sourced from other researchers. Where other written sources have been quoted, then:
    a. Their words have been re-written, but the general information attributed to them has been referenced.
    b. Where their exact words have been used, then their writing has been placed in italics and inside quotation marks, and referenced.

5. This thesis does not contain text, graphics or tables copied and pasted from the internet, unless specifically acknowledged, and the source being detailed in the thesis and in the References sections.

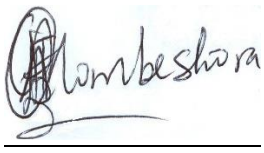

Signed: Edwin T. Mombeshora

July 2017

Declaration 2 - publications and conference contributions

Details of contribution to publications that form part and/or include research presented in this thesis (includes manuscripts in preparation, *in press* and published articles. The details of the contributions of each author to the experimental work and writing of each publication is specified).

Publications

Publication 1

Mombeshora ET, Nyamori VO. A review on the use of carbon nanostructured materials in electrochemical capacitors. *International Journal of Energy Research* 2015; **39**:1955-1988.

Contributions: I planned and wrote the review paper. Prof Nyamori, as my main-supervisor, provided general guidance and proofread the manuscript.

Publication 2

Mombeshora ET, Doyle BP, Carleschi E, Ndungu PG, Jarvis ALL, Nyamori VO. Some perspectives on nitrogen-doped carbon nanotube synthesis from acetonitrile and *N,N'*-dimethylformamide mixtures. *Journal of Materials Chemistry and Phyisics* 2017; **199**:435-453.

Contributions: I designed the experiments, synthesised the nitrogen-doped carbon nanotubes, characterised, analysed the data and wrote the manuscript. Prof Nyamori, Prof Ndungu and Dr Jarvis are my supervisors who provided guidance and proofread the manuscript. Drs Doyle and Carleschi carried out the X-ray photoelectron spectroscopy analysis.

Publication 3

Mombeshora ET, Ndungu PG, Nyamori VO. Effect of graphite/ sodium nitrate ratio and reaction time on physicochemical properties of graphene oxide. *New Carbon Materials* 2017; **32**:174-187.

Contributions: I conceptualise, designed and conducted synthesis of the graphene oxide, and wrote the paper. Prof Nyamori and Prof Ndungu are my supervisors who provided general guidance and proofread the manuscript.

Publication 4

Mombeshora ET, Ndungu PG, Jarvis ALL, Nyamori VO. Oxygen-modified multiwalled carbon nanotubes: physicochemical properties and capacitor functionality. *International Journal of Energy Research* 2017; **41**:1182-1201.

Contributions: I designed the experiments, collected and analysed the data, and wrote the paper. Prof Nyamori, Prof Ndungu and Dr Jarvis are my supervisors who provided guidance and proofread the manuscript.

Publication 5

Mombeshora ET, Ndungu PG, Nyamori VO. The physicochemical properties and capacitive functionality of pyrrolic- and pyridinic-nitrogen, and boron-doped reduced graphene oxide. *Electrochimica Acta*. Manuscript in press.

Contributions: I designed the experiment, collected and analysed the data, and wrote the paper**.** Prof Nyamori and Prof Ndungu are my supervisors who provided guidance and proofread the paper.

Publication 6

Mombeshora ET, Nyamori VO. Physicochemical characterisation of graphene oxide and reduced graphene oxide composites for electrochemical capacitors. *Journal of Materials Science: Materials in Electronics* 2017; **28**:18715-18734.

Contributions: I synthesised and characterised the composites, carried-out electrochemical characterisation experiments, data collection and analysis, and wrote the paper**.** Prof Nyamori is my main supervisor who gave guidance and proofread the manuscript.

Publication 7

Mombeshora ET, Ndungu PG, Jarvis ALL, Nyamori VO. Nitrogen-doped carbon nanotube- and reduced graphene oxide- titania nanocomposites: Synthesis and application in charge storage. Manuscript in preparation.

Contributions: I designed the experiments, synthesised and characterised the nitrogen-doped carbon nanotube composites, performed electrochemical characterisation, data collection and analysis, and wrote the paper. Prof Nyamori, Prof Ndungu and Dr Jarvis are my supervisors who gave guidance and proofread the manuscript.

Signed: Edwin T. Mombeshora

Student number: 212561878

July 2017

Conference contributions

1. Poster presentation: Green chemistry approach towards sustainable energy, at 2nd International Symposium and Workshop of the Global Green Chemistry Centres (G2C2) at Two Oceans Aquarium, Cape Town, South Africa (August 2014).
2. Oral presentation: Nano-structural parameters and functionality of MWCNT-titania nanocomposites in energy conversion systems, at Annual Renewable Sustainable Postgraduate Symposium held at University of Fort Hare, Alice campus, South Africa (September 2016).
3. Oral presentation: Some perspectives on nitrogen-doped carbon nanotubes synthesis, at University of KwaZulu-Natal College of Agriculture Engineering and Science Postgraduate Research Day, Shepstone Building, Howard College Campus, South Africa (November 2016).
4. Oral presentation: Carbon-based energy materials, at Eco-Design of Printable Photovoltaics – the Building of an African Infrastructure Meeting held in Durban, Durban Manor Hotel, South Africa (January 2017).
5. Poster presentation: Oxygen-functionalised carbon nanotubes for supercapacitors, at SACI Inorganic 2017 held in Hermanus, Arabella hotel and Spa, Western Cape, South Africa (June 2017).
6. Poster presentation: Oxygen-functionalised carbon nanotubes for supercapacitors, at 28th International Conference on Diamond and Carbon Materials to be held in Gothia Towers hotel, Gothenburg, Sweden (September 2017).

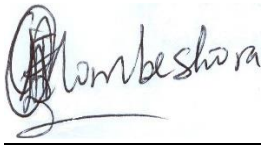

Signed: Edwin T. Mombeshora

Student number: 212561878

July 2017

Acknowledgements

Foremost, I would like to exalt and glorify the God, Almighty, profoundly for his grace and providence throughout my life journey. This thesis is a life testimony to me and I am greatly humbled by His mercies!

Secondly, I would like to direct my sincere gratitude to my main supervisor Prof V.O. Nyamori for his unceasing and timeous support throughout my PhD studentship, for his advises, guidance and motivation. I could not have imagined having a better advisor and mentor not only for my PhD study but also for my MSc. I would also like to express the deepest appreciation to my core-supervisor Prof P.G. Ndungu, for his attitude and convincingly conveying a spirit of adventure with regards to doctoral research. Without his valuable support, it would not be possible to conduct this research. In addition, a thank you to Dr A.L.L. Jarvis, my second core-supervisor, and whose enthusiasm for the "capacitors" had lasting effect. I generally, thank all my supervisors for providing me an opportunity to join their research groups, from whom I acquired acquaintance with fruitful research facts, and for access to their laboratories and research facilities, their unwavering commitment to my progress and for their forthright and pragmatic critique.

Besides my supervisors, I would like to thank the rest of the academic staff, who attended our group meetings particularly Prof B.S. Martincigh, Dr B.O. Owaga and Dr B. Varadwaj, for their insightful comments and encouragement, but also for the hard questions which incented me to widen my research from various perspectives. I am also indebted to Prof R.H. Simoyi for his dependable support and assistance.

My perpetual cheerleader, late sister Taona Mombeshora: I miss our interesting and teasing chats, and our general moments of laughter. I am also grateful to my siblings and mother (Mrs F Mombeshora nee Musonza), who have always been pillars of moral and emotional support throughout my life. Special appreciation goes to Dr S. Mombeshora, Ms N. Mombeshora, Tawanda Mombeshora, Edgar Mombeshora and Elton Mombeshora for their love, prayers encouragement, realizing the potential in me and their financial support towards cultivation of my dreams and aspirations. I am also grateful to my other family members and friends who have supported me along the lengthy road.

A very special gratitude goes out to India Brazil South Africa Nanotechnology Initiative (IBSA) and UKZN Nanotechnology Platform for partially funding the work. A special thank you also goes to the technical and administration staff; Renee Naidoo, Crescencia Nkosi, Mpho

Sehoto, Clementine Dhlamini, Gregory Moodley, Unathi Bongoza, Vashti Reddy, Anita Naidoo, Nundkumar Miller, Philip Christopher, Vishal Bharuth, Dr Veresha Dukhi, Dr. Philani Mashazi, Dr Bryan Doyle and Dr Emanuela Carleschi. It was a fantastic opportunity to get technical support of my research work with facilities within your expertise. What a conducive milieu to work!

And finally, last but by no means least, also to everyone in the Nanochemistry/Physical Chemistry/Materials Research groups, it was a great pleasure stimulating discussions, sharing laboratory space and equipment with all of you during my doctoral studies. My sincere thanks go to Ms Mugadza, for overwhelming support throughout my career and writing phase of this thesis. She has been my motivation and inspiration for advancing my knowledge and career forward.

Thanks for all your encouragements!

Dedication

This thesis is dedicated to the memory of Mr Easwell Mombeshora. Although he was my inspiration to pursue my doctoral degree, he was unable to see my graduation. This is for him.

I also dedicate this thesis to the love of my life, mum, my siblings, uncle Solo and aunt Naume with modesty, gratefulness and love, for the sacrifices and support throughout the long road to quality knowledge.

List of abbreviations

Full meaning	Abbreviation
Asymmetrical electrochemical capacitors	AES
Atomic force microscopy	AFM
Brunauer–Emmett–Teller	BET
Carbon nanofibers	CNFs
Carbon nano-onions	CNOs
Carbon nanorods	CNRs
Carbon nanotubes	CNTs
Cauliflower-fungus graphene	CFG
Chemical vapour deposition	CVD
Cyclic voltammetry	CV
Density functional theory	DFT
Electrochemical double layer capacitors	EDLCs
Double-walled carbon nanotubes	DWCNTs
Electrochemical capacitors	ECs
Electrochemical impedance spectroscopy	EIS
Energy dispersive X-ray spectroscopy	EDX
Energy storage systems	ESSs
Equivalent series resistance	ESR
Face-centred cubic	FCC

Graphenated carbon nanotubes	G-CNTs
Graphene	G
Graphene oxide	GO
High resolution transmission electron microscopy	HRTEM
Imaginary impedance	Z_{im}
Metal oxide	MO
Microwave plasma enhanced chemical vapor deposition	MPECVD
Multiwalled carbon nanotubes	MWCNTs
Nitrogen-doped carbon nano-onions	N-CNO
Nitrogen-doped carbon nanotubes	N-CNTs
One dimensional	1D
Real impedance	Z_{re}
Reduced graphene oxide	RGO
Saturated calomel electrode	SCE
Scanning electron microscopy	SEM
Scanning transmission electron microscopy	STEM
Single-walled carbon nanotubes	SWCNTs
Specific capacitance	C_s
Thermal gravimetric analysis	TGA
Three dimensional	3D

Transmission electron microscopy	TEM
Two dimensional	2D
X-ray diffraction spectroscopy	XRD
X-ray photoelectron spectroscopy	XPS

Table of contents

Chapter One

Introduction

1.1. Energy storage systems

Currently, there is immense pressure on traditional electrical energy storage systems (ESS) [1.1]. The reasons for this include the increasing demand for energy from both industries and households, global climate change effects due to use of finite fossils fuels and the rising dependence on renewable energy resources. Hence, there is need for the development of new, cost-effective, reliable, long-lasting and environmentally friendly ESS with quick energy delivery as a support to ever-rising energy applications. ESS are structures in power networks that are used to convert electrical energy to different forms, from the available source, that can be stored and converted back to electricity upon need [1.1-1.3]. The historical background of ESS dates back as early as the 20th century. Here power stations could be shut down overnight and lead acid batteries would supply energy directly into the small but established electrical grids [1.2]. The ESS arena still needs to be furnished with adequate information with regards to the economy of utility scale [1.1] and therefore more research is needed. ESS are essential network components in terms of their influence on consumption and cost of power, and find use in network power quality and management [1.3,1.4]. This amongst other reasons has kept ESS amongst vital components of a growing industrial economy. By the year 2012, over 400 energy storage projects had been established around the world [1.5].

Several attributes of ESS, and their potential to enhance existing life spans of electric power generation plants have spearheaded focus on them. This is attained when excess power generated is stored and this means plants will not be overworked. Additionally, other advantages of ESS include prevention of costly plant upgrades and ability to lower fuel consumption on vehicles powered by petrol. They act as buffers to effectively integrate energy resources into the network and can damp electrical fluctuations or faults in the power grids [1.6]. Integration of ESS is a practical way of improving on sustainability for both non-renewable and renewable resources such as hydroelectric, tidal, geothermal, wind and solar energy sources [1.2,1.7-1.10]. For instance, solar energy, a clean renewable resource, is a current public utility for both homes and companies. The drawbacks of solar energy include

lack of available cheap and efficient storage systems, and this in turn hinders transition towards newer and 'greener' energy generation systems [1.4,1.8,1.11]. Electricity can be produced during low demand times and at low generation costs. Intermittent energy sources are then released during peak demand and therefore, ESS are important [1.2,1.5,1.6]. In an extreme situation, one would consider, is that without the use of storage devices energy must be used immediately when it is produced [1.12]. This is far from reality since energy demands vary hourly, daily, seasonally, regionally and also maximum demand only lasts a few hours [1.5,1.11].

In light of all this, energy storage becomes the core for the development of smart grids and utilisation of renewable energy [1.1,1.5]. There is need to invest in ESS such as the renewable energy grid infrastructures and capacitors in order to match the global levels of market competition from other established systems, such as the batteries, [1.8] and to boost energy security [1.1]. This is because lack of energy storage devices leads to inefficient, overdesigned, shortfalls in energy transmission and distribution, and expensive plant maintenance [1.2,1.11]. ESS therefore, allows independence of electrical power from its supply and self-generation upon need, load monitoring, peak power and standby reserve [1.1,1.8]. Effective ESS has potential transform several industrial companies; such as those that deals with turbines, cars and consumer electronics; and to meet other energy needs such as relieving power congestion. In this way, affordable energy storage bridges the gap between production and demand *via* enhancement efficiency, quality and stability of electrical networks [1.1]. Capacitors are normally short duration devices. Technologies or devices such as ESS can be categorised based on the methodology utilised *i.e.*, mechanical or electrical [1.1-1.3,1.13].

1.1.1. Mechanical storage energy system

Some of the major mechanical energy storage systems include the fly wheel [1.4], pumped-hydro energy [1.14] and compressed air [1.5].

1.1.1.1. Compressed air energy

The technique was invented in the year 1978 and it works in a similar way as conventional turbines [1.15]. In a typical system (Fig. 1.1.), air is compressed using off-peak electrical power and is stored in large reservoirs such as hard rock cavern, salt cavern and depleted gas

fields [1.6]. Such systems can produce large amounts of energy on demand [1.6]. Major parts (Fig. 1.1) include motor/generator which alternatively engages either the compressor or turbine train *via* use of clutches [1.16]. The compressor has two main stages with an intercooler system that reduces the moisture content of the incoming air. The turbine train is made up of both high and low-pressure turbines. The compressed air is stored in a container or cavity [1.2]. The system works in a similar way as gas-based turbine generators but decouples the compression and expansion cycles into separate processes. Energy is stored in the form of gas elastic potential energy. This method has efficiencies in the range 40-50%, energy density of 10-30 Wh kg^{-1} and power density of 1000 W kg^{-1} [1.16].

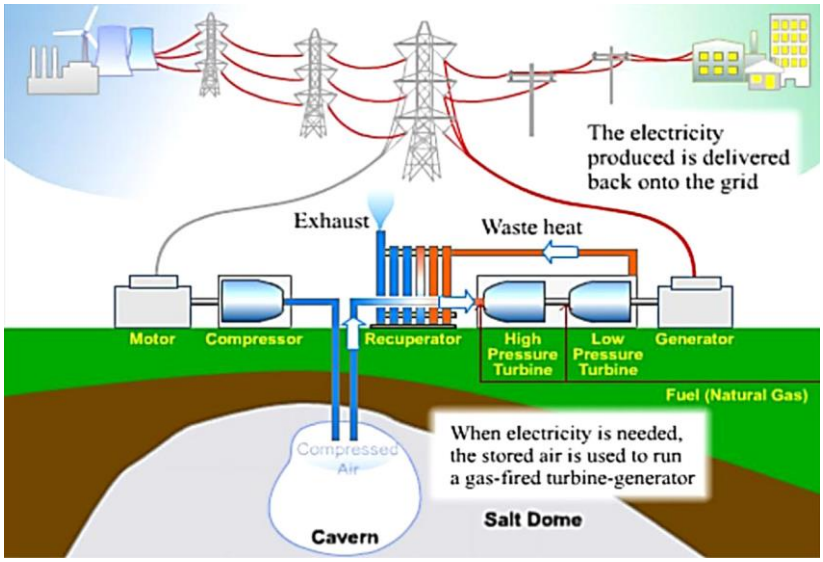

Fig. 1.1. Compressed air energy storage system [1.4].

Aspects that favour use of compressed air energy storage (CAES) include the fact that they produce three times more electrical power than traditional turbines and, involve faster reactions that makes it suitable for high energy supply and demand. CAES systems as a choice of energy storage suffers from drawbacks such as, small amount of gases used to heat air produce carbon dioxide that is then released into the atmosphere, energy losses as dissipated heat of compression, dependence on geological formations and the system is often coupled with other energy sources, hence associated with high costs [1.15].

1.1.1.2. Pumped-hydro energy

The first pumped-hydro energy storage system was built in the year 1929 [1.2]. Since then, to 2005, more than 200 pumped-hydro energy systems (PHS) have been recorded around the globe. ESKOM, South African electricity public utility company, has one typical system in the Drakensberg. Underground PHS have been built from flooded mine shafts and other cavities. The PHS offers the largest energy storage capacity, a large storage period and high efficiency [1.2]. Some of the reported performance parameters include an efficiency between 65-80% and energy density of 0.3 Wh kg^{-1} [1.16]. The technique stores energy by pumping water to an uphill reservoir. When there is a demand for electrical power, water is allowed to flow downhill driving generators in the process [1.4,1.17]. Amount of energy stored is proportional to the height difference between two reservoirs and volume of water stored [1.2]. The major problems associated with this method include large capital cost, high dependency on local topography and availability of rain [1.14,1.15]. Also, this method has a direct negative impact to the surroundings since it damages natural environment. Additionally, special attention need to be directed towards evaporation and conversion losses to maintain storage capacity.

1.1.1.3. Flywheel

Flywheel method was introduced in the 1950s and it makes use of the fly wheel design (Fig. 1.2) [1.1,1.9]. Energy is stored by accelerating the rotor using a motor which maintains the energy system at very high speeds with the help of inertia [1.2,1.4,1.11]. This way electrical energy is converted to mechanical energy for storage [1.17]. Energy is stored in angular momentum of a spinning mass [1.2] of a motor. The motor also acts as an electricity generator from the wheel's rotational energy. Hence, total energy is a function of power rating of the motor, size and speed of the rotor [1.18].

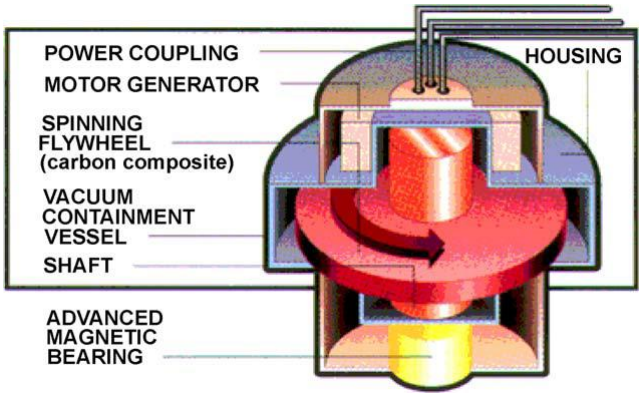

Fig. 1.2. Illustration of the main parts of a flywheel [1.11].

A flywheel typically has an energy density in the range 5-30 Wh kg^{-1} and power density of 1000 W kg^{-1} [1.16]. The flywheel is often associated with low maintenance costs, long life cycles (10^5-10^7), long operational life, high power efficiency of about 95%, environmental pleasantness and wide operating temperatures [1.1,1.2,1.4,1.16]. Negative traits of this method include idling losses due to friction and magnetic force and has problems associated with lubrication life. Other disadvantages are allied high capital costs ($1000 - 5000 per kW h) and high discharge rates (55 - 100% per day) [1.19].

1.1.2. Electrical energy storage systems

The most popular examples of electrical energy storage systems are superconducting magnetic energy storage devices (SMES), supercapacitors and batteries. The following subsections present insights on some of common types of batteries.

1.1.2.1. Batteries

Batteries are the most common and oldest electrical energy storage devices [1.2,1.7,1.13,1.20]. A battery is made up of stacked cells in which chemical reactions convert stored chemical energy into electrical energy [1.2,1.7,1.20]. A battery typically consists of a positive electrode (anode), negative electrode (cathode) and a paste/solid electrolyte [1.2]. In this scheme, potential is built up between the terminals during the discharge process. This allows electrons to flow in the system *via* an external circuit [1.2,1.4,1.17]. A battery can be viewed as an

energy device with an efficiency of between 60-95% [1.2,1.20,1.21]. Given voltage (V) and charge (Q), useable energy (E) in a battery can be calculated by the equation (1).

$$E = VQ. \qquad (1)$$

Voltage in such structures depends on active materials and is closer to the open circuit voltage of the respective material [1.20]. For a given time (t), and current (I), Q is given by equation (2).

$$Q = It \qquad (2)$$

Some of the common battery types are briefly discussed in the following sub-sections.

1.1.2.1.1. Lead acid battery

Lead acid batteries are the first commercially successful batteries to store electrical energy. Lead acid batteries were invented in 1859 and are the most developed rechargeable battery [1.2]. They constitutes more than 90% of the commercial batteries [1.13] available on the market and are widely used in consumer electronics. They consist of metallic lead anode, sponge lead oxide cathode and aqueous sulfuric acid electrolyte [1.4,1.7]. The two electrodes are separated by a micro-porous material. They have an efficiency between 70-80%, limited life cycles (approximately 2500), energy density of 20-35 Wh kg^{-1} and power density of 25 W kg^{-1} [1.16,1.22]. The main benefits of this particular type include; low cost [1.13], simple production steps and relatively quick electrochemical reaction kinetics. They are highly criticized because they use lead, a heavy metal, which is toxic and hazardous to the environment. They characteristically perform poorly at low temperatures.

1.1.2.1.2. Nickel battery

It is a secondary battery type (rechargeable many times before discarding) that consist of nickel hydroxide as a positive electrode [1.4]. The most common examples of this type include Ni-Cd and NiMH. The Ni-Cd is nearly 114 years old [1.2]. They have a typical efficiency between 60-90%, energy density of 40-60 Wh kg^{-1} and power density in the range 140-180 W kg^{-1} [1.16]. This type is made up of NiOH anode, CdOH cathode, a separator and an alkaline electrolyte [1.3]. They have low maintenance requirements, higher energy density, usually 50-75 Wh kg^{-1} and low cycle life of about 200-2500 [1.2,1.3,1.11]. They are associated with an

expensive manufacturing process and cadmium is a toxic heavy metal with associated disposal and environmental problems [1.13].

1.1.2.1.3. Sodium sulfide battery

Sodium sulfide battery is an advanced secondary form that was pioneered by Tokyo electric power co-operation in 1983. It comprises of molten sodium as negative electrode, sulfide as positive electrode and solid beta alumina ceramic as the electrolyte as well as, electrode separator [1.2,4,7]. The electrolyte only allows positive electrons to pass through and combine with sulfur to form sodium polysulfide [1.7].

Sodium sulfide batteries have found numerous applications in large scale energy storage systems. This is due to high energy densities of 120 Wh kg^{-1}, high efficiency of charge/discharge (70%) and zero maintenance [1.16]. They have a cycle life of approximately 2500 cycles [1.2]. Main setbacks of this type include its requirement for sulfur to be kept in molten state at a temperature of approximately 300 ^{o}C [1.13]. This means the system partially reduces its performance since it uses the battery's own energy to heat the source. Also, the system must be protected from reacting with the atmosphere. This is because pure Na metal explodes in air and has high corrosion possibilities in insulators. Corrosion enhances battery conductivity and ultimately increase self-discharge rate.

1.1.2.1.4. Lithium battery

The first lithium battery was produced by Sony © in 1990 but was first proposed in the 1960s [1.2]. This type is a primary battery made up of lithium and lithium compound as cathodes. The anode comprises of graphitic carbon and the electrolyte is lithium salt dissolved in organic carbonates [1.2,1.7]. Upon charging lithium cathode forms lithium ions which migrate to anode and are intercalated [1.23], the process is reversed on discharging.

Their efficiency is within the range of 70-85%, energy density of 100-200 Wh kg^{-1} and power density of 360 W kg^{-1} [1.16]. Its main positive qualities include light weight, high safety levels, low self-discharge effects, less memory effects, higher abundance and low cost of cathode material [1.4,1.18]. Hence, this attribute makes them suitable for mobile applications. However, such batteries require special packaging and internal overcharge protection circuit which ultimately leads to high overall costs.

1.1.2.1.5. Metal-air battery

They comprise of high density metal such as zinc that release electrons when oxidised as an anode [1.2,1.7]. Their cathodes are commonly made up of porous carbon structures or metal mesh covered with an appropriate catalyst. They utilise ionic liquids as electrolytes [1.7]. Also, they are the most compact and potentially cheapest batteries currently on the market [1.4]. Their main weakness is that the electrical recharging involved is very complicated and leads to it being inefficient [1.2].

1.1.2.1.6. Flow battery

A flow battery converts chemical energy directly into electricity *via* chemical reactions (Fig. 1.3) [1.4]. The system uses externally stored electro-active material in two tanks of electrolysis [1.3]. The power is produced by a reversible electrochemical reaction between the two electrolytes. The size of tanks and amount of electrolyte determines energy density [1.2,1.7]. This specific type can supply energy continuously for up to 10 hours at a higher rate. This type of battery is associated with several advantages. The advantages include; high stability and durability, high safety since electrodes are separated from reactive parts of the systems and high tolerance to over-charging [1.4]. However, flow batteries are a complicated system, that require pumps, sensors, good flow and power management.

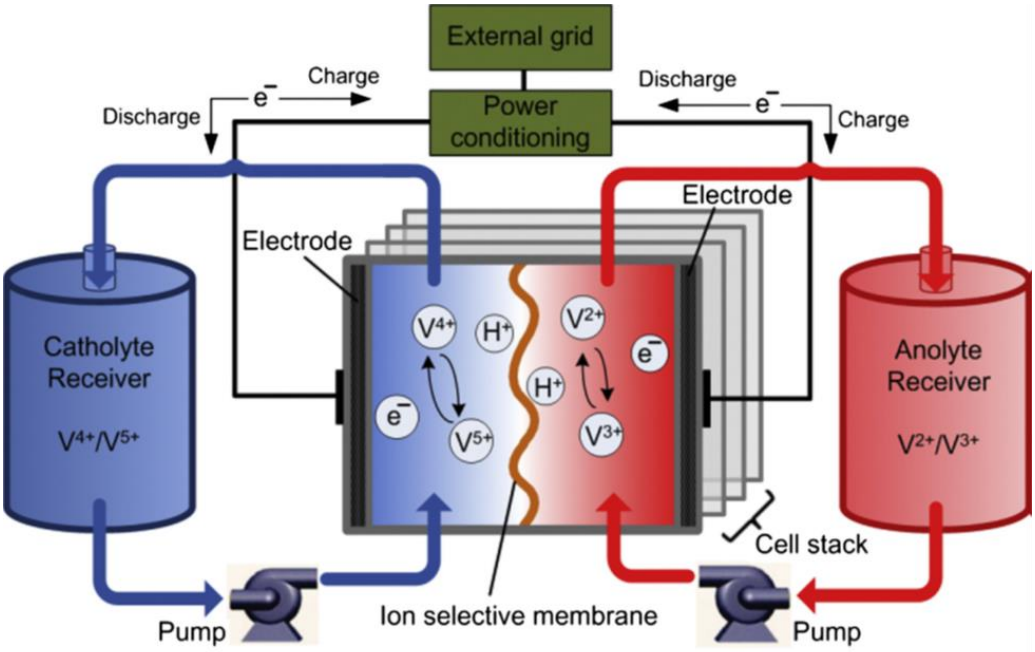

Fig. 1.3. Typical example of a flow battery (Vanadium redox flow battery) [1.3].

1.1.2.2. Superconducting magnetic energy storage

The superconducting magnetic energy storage system make use of a magnetic field to store energy, which would have been cryogenically cooled to a temperature below its superconducting critical temperature (Fig. 1.4) [1.2,1.4,1.8,1.17]. Once the energy is stored the current remains intact, due to the superconductive phase, as long as the system is maintained under refrigeration [1.3,1.8]. There are no moving parts in the SMES. It is suitable for short term energy bursts with a very fast responses rate i.e. during a power fluctuation and have long cycle life [1.1]. However, SMESs are associated with high costs ($1000 - 10 000 per Kw) [1.19]. This is largely due to the cryogenic operating temperatures utilised in the system. The other challenge, related to their use, is environmental considerations due to involvement of strong magnetic fields [1.1].

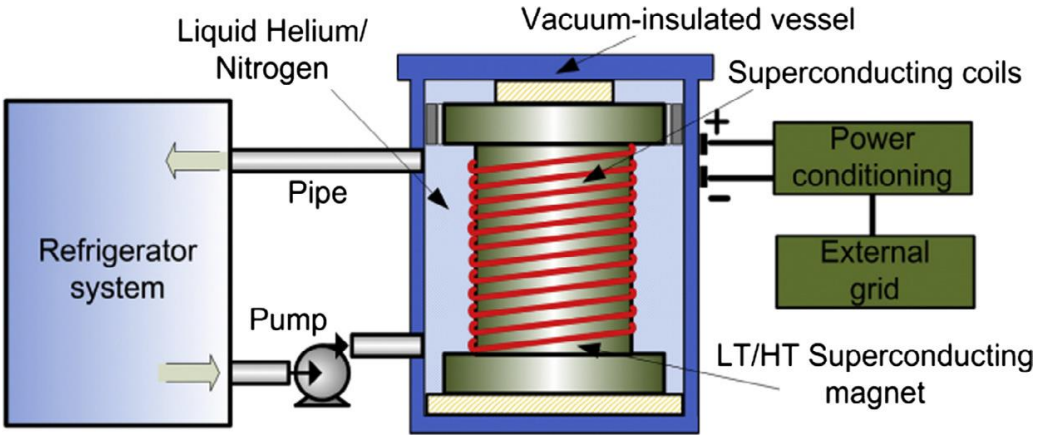

Fig. 1.4. Typical example of SME systems [1.3].

1.1.3. Electrochemical capacitors

Electrochemical capacitors (ECs) are a promising alternative to rechargeable batteries, especially, where high power delivery and/or fast energy harvesting capabilities are required [1.20,1.24,1.25]. The EC technology has perceived substantial growth over the years with associated sales reaching a hundred million dollars per year. This was triggered by the need for better quality of power and other emerging energy management/conservation restrictions. ECs will be further discussed in greater detail in Chapter two. One of the most common challenges related to ECs is their low energy density and this is a current research focus [1.1]. Material development is one of the important active research areas towards EC development. Material development has potential to increase EC grid applications. Additionally, one of the key ways to increase specific capacitance (C_s) is the development of porous and nano-sized electrode materials that facilitates attainment of various attributes, such as shortening of the diffusion path-length of electrolytes [1.24]. In this regard, the following sections presents background information about materials that can be utilised in ECs.

1.1.3.1. Transition metal oxide-based materials for electrochemical capacitors

Various nano-sized metal oxides (MOs), as electrode materials, have been explored for ECs. This include amorphous ruthenium oxide [1.26], iron oxide [1.27], cobalt oxide, nickel oxide [1.28] and manganese oxides (MnO_x) [1.29]. The most theoretically promising MO in capacitors is MnO_x. The MnO_x nanoparticles are suitable for ECs because of their high

abundance, wide electrochemical window, rich redox chemistry, low cost, high theoretical specific capacitance C_s of 1370 F g^{-1} and good environmental compatibility [1.29-1.33]. The electrodes fabricated using MnO_x can function well in neutral aqueous electrolytes [1.34]. However, due to lower conductivity of MnO_x, between 10^{-5} and 10^{-6} S cm^{-1}, and low ionic conductivity [1.29,1.32], measured C_s is often lower than the theoretical expected value. Major challenges in this regard remains controllable, efficient and reproducible deposition of MnO_x onto conductive frameworks [1.29]. Textural characteristics, weight percentage, distribution and crystal forms of MnO_x affect ultimate EC performance. For these reasons, several other materials and nanocomposites morphologies have been investigated to improve the EC performance. For instance, Ni and Co oxides have been reported to be the most alkaline electrolyte corrosion resistant transition metals. They form protective oxide/hydroxide layers on their surfaces. The main reason for using NiO as pseudocapacitor electrode is its superior redox behaviour and high capacitance even though it is kinetically unfavourable for fast e^-/ion transport [1.28].

Titania, on the other hand, is a widely-investigated semiconductor MO material. This is due to its non-toxicity, chemical inertness, photo-stability characteristics, long term thermodynamic stability and cheap production costs [1.35,1.36]. However, titania is particularly more common in the photo-catalysis and light harvesting arenas [1.37]. For example, Rathee *et al.* [1.38] deposited TiO_2 onto Si using a sol-gel. They concluded that TiO_2 was suitable for sustainable energy due to high incident photon to electron conversion efficiency. They also observed that their fabrication technique influenced electrical properties due to reactions between TiO_2 and Si substrate. Despite the presented scenario, titania is also scarcely reported as an electrode material for EC applications. Wu *et al.* [1.39] expounds on TiO/NiO core/shell nanorod arrays as EC working electrodes in a three electrode cell. Their counter electrode, electrolyte and reference electrode were Pt foil, 2 M KOH and Hg/HgO, respectively. They experimentally encountered redox peaks similar to the findings by Wu *et al.* [1.40]. Specifically, in their work they reported that TiO_2 on carbon cloth offers negligible peaks compared to Ni in KOH. TiO/NiO core/shell showed better peak currents than NiO nanoflake array. Such results inferred better electrochemical activity in TiO/NiO core/shell. Also, TiO/NiO core array /shell nanorod gave a smaller polarisation during charge-discharge processes of 611 F g^{-1} at 40 g^{-1} and 500 F g^{-1} at 40 g^{-1}, relative to 338 F g^{-1} and 210 F g^{-1}, respectively, for NiO nano flakes arrays. Such observations imply that C_s decreased with increase in current density. The TiO/NiO core array /shell nanorod was also observed to have

better retention time than NiO. After 5000 cycles at 2 A g^{-1}, retention was 89% and 75% of the initial capacitance for the former and latter, respectively. In their work, they point out that core/shell nano-array configuration leads to large surface area, easier electrolyte penetration and more contact area between electrolyte and active material. This ultimately enhanced e^-/ion transport and their direct growth method eliminated resistance from binders. In the similar work reported by Hsieh *et al.* [1.41], TiO_2 increased C_s from 76.5 to 176.5 F g^{-1} at 0.2 A g^{-1}. They attributed their observations to a higher hydrophilic surface fraction available for EDLC electrolyte and the pseudo capacitance behaviour introduced by TiO_2 crystals. In the current work, a further study that involves titania, as EC electrode, in composites with shaped carbon nanomaterials is presented.

1.1.3.2. Shaped carbon-based materials for electrochemical capacitors

Numerous carbon-based materials have been discovered over the years. They have shown potential applications as electrode materials in ECs. The sp^2-hybridisation of carbon facilitates the occurrence of numerous shapes [1.42]. Kroto *et al.* [1.43] discovered the first shaped carbon nanomaterial (SCNM), C_{60} molecules (Fig. 1.5a) whilst, in 1991, Iijima reported the first tubular nanostructured nanomaterial, multiwalled carbon nanotubes (MWCNTs) (Fig. 1.5b) [1.44,1.45]. Additionally, the first report on synthesis of single walled carbon nanotubes (SWCNTs) was in 1993 [1.46]. Whilst the first report of a successful isolation of graphene was in 2004 (Fig. 1.5c) [1.47].

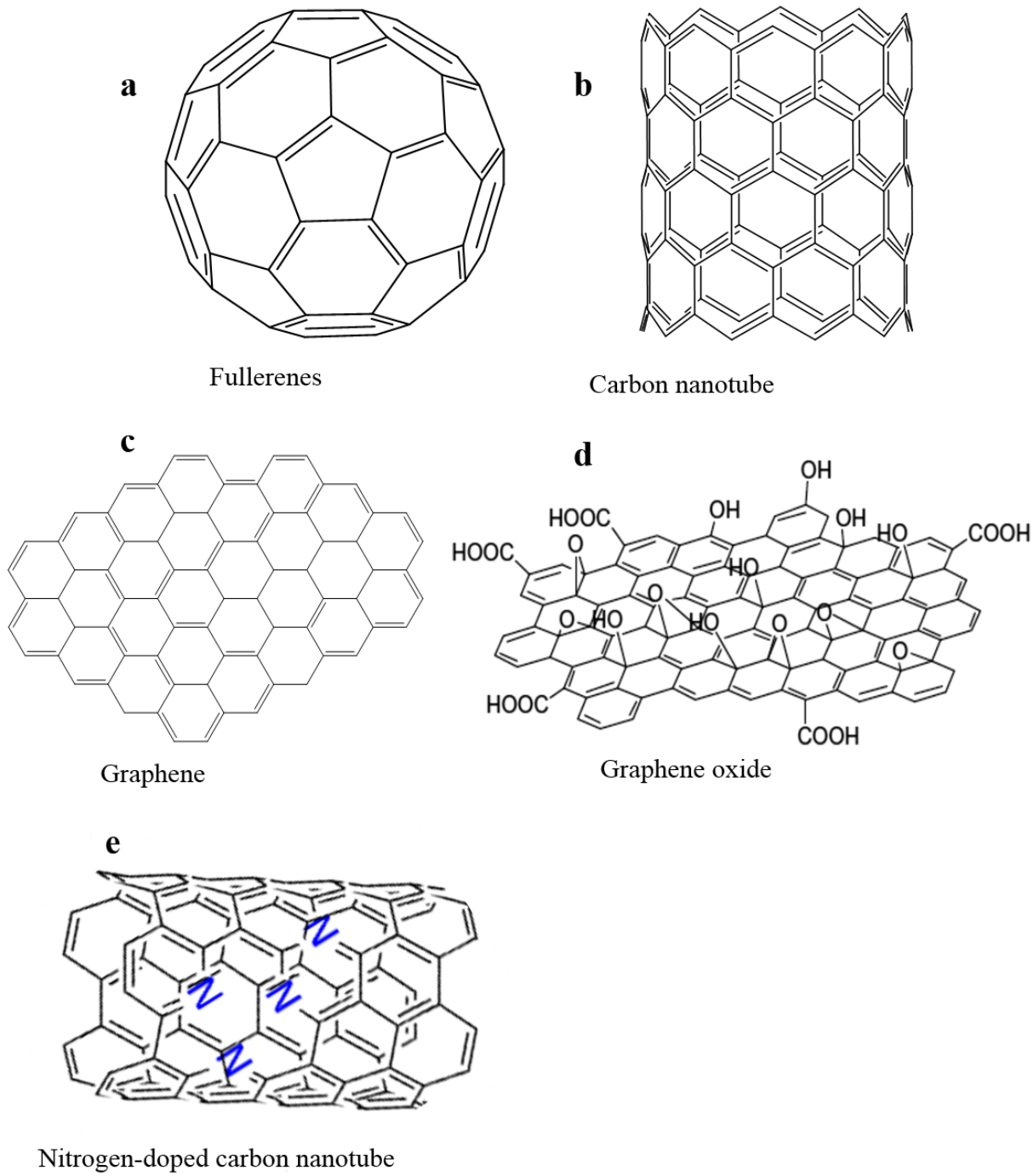

Fig. 1.5. Examples of shaped carbon nanomaterials [1.48].

1.1.3.2.1 Graphene

Graphene (G) is associated with fewer health-related hazards than other carbon allotropes [1.49]. The development of sheets of different structure, functionality and sheet sizes is of extraordinary interest to several researchers [1.50]. This is due to the numerous associated

potential applications. Current synthetic methods produce defects such as structural imperfections and chemical impurities randomly distributed within the graphitic framework [1.51]. Use of different starting materials, oxidation methods and reduction processes widen possible materials that can be obtained. In such endeavours, there is a need to control defects and locally induced chemical alterations [1.52]. G can be conveniently synthesised in bulk at low cost [1.53]. The preparation methods include chemical vapour deposition (CVD), solvent thermal reaction, chemical routes from CNTs, exfoliation of graphite through ultra-sonication, graphite intercalation compounds and graphite oxide, and thermal desorption of Si from SiC and even 'scotch tape' [1.50,1.52,1.54].

Physical exfoliation, such as micromechanical cleavage [1.55] ('scotch tape'), is the most preferred in scenarios were the graphene structure and electronic properties need to be preserved [1.56]. However, the procedure produces graphene sheets (GS) of different sizes, shapes, thickness and leds to low GS yields [1.55]. The chemical approach *via* graphene oxide (GO, Fig. 1.5d), as the initial stage, is a common synthesis method. Practically, it is almost impossible to synthesise G chemically but reduced graphene oxide (RGO) can be produced *via* synthesis of GO. GO is a non-stoichiometric graphitic carbon material in which the lamellar structure is conserved [1.57]. GO synthesis as a preliminary step to RGO synthesis can be achieved by thermal exfoliation, Brodie's method and Hummer's as well as several modified Hummer's methods [1.50,1.55,1.58].

In fact, GO was first reported by Brodie in 1859 [1.59]. The synthesis steps were time consuming and involved vigorous reaction kinetics such as explosion of potassium chlorate. The Brodie's approach involved several treatments of Ceylon graphite using potassium chlorate and fuming nitric acid. Later, Hummer's method, which was relatively safer, was reported. In the Hummer's way, H_2SO_4, $NaNO_3$, graphite flakes and $KMnO_4$ were mixed sequentially followed by slow addition of deionised water (DI) [1.58,1.59].

The thermal reduction approach has several attributes relative to chemical synthesis. These are inclusive of simplicity, ease to perform due to the involvement of simultaneous exfoliation and reduction of graphite oxide [1.50]. Major challenges common to the thermal methods of GS synthesis include large scale production and effective defect control. Oxidation and reduction of G is one of the most effective ways for economical mass production [1.50,1.54]. Yield and size of GS can be controlled by varying crystal structure of parent material and or/graphite exfoliation conditions.

G, amongst other graphitic materials, can also be synthesized from graphite *via* ultra-sonication in organic solvents such N-methyl-2-pyrolidene and dimethyl formamide (DMF). According to Quintana *et al.* [1.52], ultra-sound waves break the basal structure and produce graphitic carbon fragments of variable sizes and such structures are latter intercalated by solvent molecules. Similar views were shared by Dhakate *et al.* [1.51]. They highlighted that, typical reactions are more ideal in solvents with surface tensions in the range 40-50 mJ m^{-2} to avoid enthalpic cost of mixing. According to their report a balance is required because harsh ultra-sonication treatments increase both G yield per mL and defect intensity, and shortens sheet sizes. In their work, they also reported that addition of ferrocene carboxaldehyde to G may result in formation of both graphenated carbon nanotubes and larger GS layers. Graphene nano-ribbons can be synthesised from unzipping of CNTs and depending on the intensity of the procedure, a mixture of starting and product may be obtained [1.60-1.62]. Unzipping of CNTs increases their effective surface area [1.63].

In the CVD method, direct growth of GS on metal substrates has potential to lower contact resistance on current collectors. It also reduces inter-particle resistance, thus ultimately increases power density of electronic devices such as ECs [1.64]. There is a current debate on possibility of epoxy and hydroxyl moieties at the basal plane of GS, and the carboxyl groups at either defect edges or framework in the GO structure. The type and amount of such functionalities can be varied by modifying preparation methods [1.50]. Additionally, mesoporous molecular sieves are preferred in graphene synthesis because of their large surface area, pore volume, narrow pore size distribution and easy surface functionalization. Atchudan *et al.* [1.65] used Si-MCM-41 enhanced through isomorphous substitution of Si with a transition metal. In their work, transition metal stabilised catalytic sites. Hence, pore sizes were tunable and also growth of graphene balls (GBs) depended on metal particles, catalytic template nature and reaction temperature [1.65].

1.3.2.2. Multiwalled carbon nanotubes

Multiwalled carbon nanotubes can be synthesised by several methods such as laser ablation [1.66], arch discharge [1.67], sol-gel [1.68] and chemical vapour deposition (CVD) [1.69] methods. The CVD method can easily be scaled to industrial quantities and offers better morphology control [1.70]. MWCNTs, due to their *1-D* character and their associated electronic structure, have extraordinary electrical properties. Electrical resistance in MWCNTs

occurs when an electron collides with defects in the graphitic structure, i.e. any deflection of an electron from its normal path [1.42,1.71]. Defects in MWCNTs include impurity atoms (doped-MWCNTs, Fig. 1.5e) or an atom vibrating about its position in the graphitic structure but electrons inside MWCNTs are not easily impeded. This is because of their smaller diameters and the higher aspect ratios [1.42]. Additionally, in *1-D* materials electrons can only travel either forward or backwards. This infers minimum chances of back scattering, hence, MWCNTs are associated with low electrical resistance. MWCNTs have a Young's modulus of 1.4 TPa [1.42]. This is facilitated by the carbon-carbon sp^2 bonding and their thermal conductivity is general twice as that of diamond [1.68].

1.3.2.3. Surface modifications of carbon nano-materials

Functionalization with organic and inorganic materials offers an alternative way of controlling electronic properties of SCNMs [1.52]. Additionally, SCNMs can be modified by both non-covalent and covalent bonding of moieties. The most common covalent approach is through treatment of MWCNTs by means of oxidative reagents. Oxidizing reagents, such as acid, often used to purify MWCNTs often leaves high oxygen-containing groups on their surfaces, hence, introduces new functionality on the MWCNTs [1.72]. Similarly, the degree of GO oxidation can influence physicochemical properties such as conductivity [1.73] and hydrophilic properties. This often lead to better intercalation chemistry [1.57]. The negatively charged oxygen-containing groups enable chemical integration of metal ions such as titania *via* electrostatic adsorption [1.36,1.74]. Also, radicals, nitrenes, carbenes and arynes can be used to functionalise G *via* free radical reaction, CH insertion or cycloaddition. High energy barriers associated with inter-layer conjugation and interlayer van der Waals forces, makes modification of a flat, rigid G structure a challenge [1.75]. This lowers the GS capacitive capability [1.76].

Whereas, in molecular level mixing, carbon nanostructures can act as nucleation sites for metal reduction to form metal oxide (MO) SCNMs suspension [1.70]. Thereby facilitating coating of SCNMs by a MO, hence, promotes a homogeneous distribution. A non-covalent attachment *via* use of surfactants is a possible way for SCNM modifications that preserves their integrity [1.72]. In this regard, G is soluble in a limited number of solvents such as N-methylpyrolidine and 1,2-dichlorobenzene. Surfactants and polymers are appropriate enhancers of solubility.

On the contrary, mechanical integration, *via* ways such as ball-milling of metal powders and GO, is a better approach to achieve the required dispersion [1.74]. However, they introduce relatively larger amounts of defects which are often detrimental to their suitability in several applications. On the other hand, in colloidal mixing, SCNMs are dispersed with an ultrasonic waterbath, homogeniser, magnetic stirrer or a combination of the strategies. Dispersion in this regard is influenced by both surface area available on the SCNM surface and the solvent used [1.70]. This means variations in this respect can be utilised to alter physicochemical characteristics. Additionally, reaction conditions, such as time spent on the ultrasonic bath influences overall properties, could affect the defect intensity of the graphitic material.

1.1.3.3. Composite-based materials

Composite synthesis of SCNMs provide strategies to tailor properties by varying simple variables [1.49,1.70] such as weight percentage (wt.%) ratios of reagents and synthesis conditions, amongst others. Composites that involve ceramic formations are often an option where inertness at high temperatures and high mechanical strength are requirements whilst metal matrices are common where nanostructures are tailored to influence physicochemical properties [1.49,1.70]. The ultimate application is a very important consideration when designing composite synthesis. For instance, a ceramic nature will be detrimental in cases where transfer properties are required.

The advantages of SCNMs composites synthesis are numerous. This has been a useful material development strategy, particularly in catalysis and energy conversion systems [1.70]. For example, synthesis of MWCNTs composites has led their better suitability in industrial scale, high throughput manufacturing of lightweight, flexible electronic and energy harvesting devices at low costs [1.72]. Also, MWCNT, by virtue of high thermal conductivity, have been utilised in composites manufactured for thermal management [1.42]. Additionally, MWCNTs are used as reinforcement agent in polymer composites because of their elasticity, tensile strength and large specific surface area [1.47,1.70]. In addition, they are principally useful where low weight and low temperature is a requirement. Another reported useful utilisation of composites is tailoring of polymer conductivity by varying MWCNTs wt.% [1.42].

In comparison, the G advantages over MWCNTs include high surface area per gram, unique electronic properties, high transparency, flexible structure and less tendency to twist [1.49,1.73,1.74]. Therefore, culminates in better dispersion in matrices i.e. more suitable for

composite formation. Active research areas that involve G-based materials in composites include control of G sheets on matrices, reinforcement and functionalisation with other surface moieties and understanding interfacial chemical interactions [1.47,1.49]. The inclusion of G/polymer and G/MO nanocomposites have been reported but the G/MO nanocomposites are still at infancy stage [1.47].

Much focus has been given to metal oxide-shaped carbon nanomaterials (MO-SCNMs) composites but the dissimilar results, common in literature [1.70], have generated a lot of gaps in understanding the physicochemical properties of the several composites reported. Hence, there is still need for new insights with regards to aforementioned materials, particularly for EC applications. The G/MO nanocomposites has potential to meet high strength, stiffness and light weight as ideal components of machinery such as batteries and capacitors [1.74]. Most reported composites that involves titania are extensively focused on inhibition of electron/hole recombination [1.37,1.77]. Also, much has been done on composite synthesis of titania/SCNMs for photo-catalysis [1.78,1.79] and other applications. There is relatively little attention on their functionality in energy storage devices. The nano-metal oxides (MO) can be incorporated in various nanostructured morphologies of carbon nanomaterials to enhance capacitive characteristics. Uniform distribution of MO on SCNMs needs to be critically considered in classical nanocomposites. Furthermore, a wide range of combinations of MO and SCNMs differences culminates in varied capacitance behaviour.

1.1.3.4. Electrolytes

Two main classes of electrolytes can be utilised in ECs, namely, non-aqueous/organic and aqueous. Examples of aqueous electrolytes include acids such as sulfuric acid or alkalis such as lithium sulfate and potassium hydroxide [1.11]. The K^+ ions have the smallest hydrated ionic radius (0.33 nm) and highest ionic radius (72.2 cm^2 Ω^{-1} mol^{-1}). Lithium ion-based electrolytes are common in both batteries and ECs [1.80]. Neutral aqueous electrolytes have low cost, are safe, environmentally friendly, and are also associated with high ionic conductivity [1.10,1.33]. Hence, neutral aqueous electrolytes are favourable in large scale commercial production, i.e. in terms of cost and environmental perspectives. Aqueous electrolytes have higher ionic conductivity, i.e., up to 1 S cm^{-1}, low decomposition voltage (approximately 1.23 V) and low electrical resistance [1.17,1.20,1.80-1.82]. Their low voltage

window results in low energy density [1.10]. In aqueous acid electrolyte solutions, fundamental charge storage process is proton insertion [1.17].

Electrochemically active electrolytes containing transition metals such as Fe^{2+}/Fe^{3+}, VO^{+}/VO^{2+} and Cu^{2+}/Cu^{0} have been reported [1.83]. Recently, ionic liquids such as 1-butyl-1-methyl pyrrolidium dicyanamide have been reported to enhance operating voltage of ECs [1.84,1.85]. Choices of solvents for typical electrolytes depend on the ability to dissociates, solvate and form highly concentrated thermodynamically stable ionic salts. Additionally, low viscosity, high ionic conductivity, low melting point, high decomposition temperature and negligible vapour pressure of ionic liquids is of equal importance [1.85].

Advantages of aqueous over non-aqueous electrolytes include low costs and, less stringent purification and drying process requirements. On the other hand, aqueous electrolytes have low thermal stability and ion conductivity, have large dependency on humidity [1.86]. Examples of non-aqueous electrolytes include triethylmethylammonium tetrafluoroborate, propylene carbonate or acetonitrile with dissolved quaternary alkyl ammonium salts [1.11,1.81,1.87]. Also, solid state ECs can be fabricated using organic electrolytes such as PVA-H_3PO_4 [1.86]. Cell voltage for organic electrolytes is approximately 3-3.5 V [1.11,1.20]. Polymer gel electrolytes, such as PMMA-EC-PC-$TEACLO_4$ and PEO-$LiClO_4$-EC-THF, can be used but low capacitance values have been so far reported [1.80]. Organic electrolytes have high achievable voltages and cell voltage is limited by water content of electrolyte [1.17]. Their specific resistance is 20 times higher than the aqueous electrolytes and this reduce maximum obtainable power. However, reduced power outputs are compensated by use of higher voltage [1.17].

Based on the aforementioned background, this thesis investigated the use GO, RGO, MWCNTs and their composites with titania and nanocellulose as electrodes of ECs. This comprehended an investigation and tailoring of physicochemical properties of nanomaterials and linking them to their functionality in ECs. The modification of the typical carbon nanomaterials with oxygen and nitrogen was also investigated. In this regard, the influence of both moieties and content on EC performances were also studied. In summary, the thesis aims, and objectives are as started in section 2.

1.2. Research aim and objectives

The aim of the presented study was to provide insights in the development of carbon nanostructured-based materials by reagent ratio tailoring, understanding and establishing crucial nano-structural parameters together with other related physicochemical properties towards better modulation of electrochemical capacitance.

To achieve the aim, the following objectives were set:

- Synthesis and physicochemical characterisation of N-MWCNTs.
- Synthesis and physicochemical characterisation of GO.
- Functionalisation of graphene- and MWCNT-based materials with different surface moieties and the understanding associated interfacial chemical interactions.
- Establishing how nano-structural parameters and transformations influences ultimate EC characteristics.
- Investigating functionality and effects of group one sulfate cationic sizes as aqueous electrolytes in EC functionality.
- Investigating the influence of combining either graphene oxide or reduced graphene oxide with other abundant functional materials to obtain composites, which can be used in the fabrication EC devices.
- Tailoring of physicochemical properties of GO, RGO, MWCNTs and N-MWCNTs by varying wt.% ratios of reagents and reaction conditions towards better functionality in ECs.

1.3. Theses outline

This thesis focuses on the synthesis of SCNMs, particularly MWCNTs and RGO, as suitable electrode materials for ECs. It also investigated the influence of boron- and nitrogen-doping, oxygen modifications and synthesis of composites on the EC functionality. The thesis starts with an introduction to the research in chapter one (Introduction) and concludes with chapter nine (Conclusions and future works). Chapters two to chapter eight consisted of a series of separate publications/manuscripts that adopted the referencing style, figures and table formats, and the general presentation style that fits styles of specific journal were the work was published, submitted or intended for submission. **Chapter one** introduces the work by setting a general background for the various findings communicated within the thesis. Also, it defines

the scope of the work presented and states the research aim, objectives and outline of the current work.

In **Chapter two** (paper one), the use of carbon nanostructured materials in energy storage devices was reviewed. Also, a comparative discussion of ECs against other energy storage devices such as batteries and fuel cells are also presented. The paper also elucidated possible protocols to enhance the suitability of carbon nanostructured materials in ECs.

Chapter three (paper 2) evaluated the influence of sp^3 to *sp*, dimethyl formamide to acetonitrile, reagent ratios in the synthesis and physicochemical properties of nitrogen-doped carbon nanotubes (N-CNTs). This chapter also explains the possibilities of tailoring doping type, content and other physicochemical properties of N-CNTs by varying the sp^3 to *sp* reagent ratios. Furthermore, the paper compares N-CNTs from sp^3- and *sp*-hybridized N sources, as well as temperature effects to the products.

Chapter four (paper 3) focused on the synthesis of graphene oxide (GO). The core focus was to optimize graphite to sodium nitrate ratio and the reaction time. The paper also aimed at attaining a better understanding of the influence of oxygen functionalities on the overall physicochemical properties of GO.

Chapter five (paper 4) reported the influence of oxygen moieties, attached on MWCNTs, and their associated physicochemical properties on ECs. The specific objectives in this chapter include investigating the influence of HNO_3, HCl, H_2O_2 and HCl/HNO_3 in the treatment of MWCNTs on both physicochemical properties and EC performance. It also presented a study of functionality of group one sulfates, namely, Li_2SO_4, Na_2SO_4 and K_2SO_4 as electrolytes of the aforementioned materials. Additionally, the paper links the physicochemical properties to EC energy storage capabilities.

In **Chapter six** (paper 5), chemical transformations associated with the use of ascorbic acid, hydrazine hydrate and sodium borohydride to reduce GO are reported. In addition, the paper presents a study of the influence of B- and N-doping of RGO as well as sp^3 N-C, pyrrolic- and pyridinic-N-doping of RGO on both physicochemical properties and charge storage suitability.

The aims of **Chapter seven** (paper 6) was on the synthesis and physicochemical comparison of GO/titania (GOTi), RGO/titania (RGOTi) and cellulose/RGO (CRGTi). The chapter focused on possibilities of tailoring properties of titania, GO and RGO towards charge storage applications *via* composite synthesis. Chapter seven also presents a study of the influence of Ti wt.% on the aforementioned composites on EC performance.

The focus of **Chapter eight** (paper 7), was on the synthesis of graphenated N-MWNTs, N-MWCNT/titania and graphenated N-MWCNTs/titania composites for EC applications. The designed aforementioned composites were investigated as possible material development strategy for EC applications.

Finally, **Chapter nine** presented the overall summary of the thesis by tying together the major findings of each chapter. The main conclusions were also linked to the specific aim and objectives of each chapter as well as to future works emanating from the reported deductions.

References

1.1. Amiryar M, Pullen K. A review of flywheel energy storage system technologies and their applications. *Applied Sciences* 2017; **7**(3):286.

1.2. Chen H, Cong TN, Yang W, Tan C, Li Y, Ding Y. Progress in electrical energy storage system: A critical review. *Progress in Natural Science* 2009; **19**(3):291-312.

1.3. Luo X, Wang J, Dooner M, Clarke J. Overview of current development in electrical energy storage technologies and the application potential in power system operation. *Applied Energy* 2015; **137**:511-536.

1.4. Mahlia TMI, Saktisahdan TJ, Jannifar A, Hasan MH, Matseelar HSC. A review of available methods and development on energy storage; technology update. *Renewable and Sustainable Energy Reviews* 2014; **33**:532-545.

1.5. Liu W, Liu L, Zhou L, Huang J, Zhang Y, Xu G, Yang Y. Analysis and optimization of a compressed air energy storage-combined cycle system. *Entropy* 2014; **16**:3103-3120.

1.6. Safaei H, Keith DW, Hugo RJ. Compressed air energy storage (CAES) with compressors distributed at heat loads to enable waste heat utilization. *Applied Energy* 2013; **103**:165-179.

1.7. Divya KC, Østergaard J. Battery energy storage technology for power systems-An overview. *Electric Power Systems Research* 2009; **79**(4):511-520.

1.8. Cotterman T. Energy storage technolgies: transforming America's intelligent electrical infrastructure. *Wise Intern* 2013:19-24.

1.9. Sebastián R, Peña-Alzola R. Control and simulation of a flywheel energy storage for a wind diesel power system. *International Journal of Electrical Power and Energy Systems* 2015; **64**:1049-1056.

1.10. Zhang Y, Yuan C, Ye K, Jiang X, Yin J, Wang G, Cao D. An aqueous capacitor battery hybrid device based on Na-ion insertion-deinsertion in l-MnO_2 positive electrode. *Electrochimica Acta* 2014; **148**:237-243.

1.11. Hadjipaschalis I, Poullikkas A, Efthimiou V. Overview of current and future energy storage technologies for electric power applications. *Renewable and Sustainable Energy Reviews* 2009; **13**:1513-1522.

1.12. Amin M, Stringer J. The Electric Power Grid: Today and Tomorrow. *Harnessing Materials for Energy* 2008; **33**:399-407.

1.13. Antonucci PL, Antonucci V. Electrochemical energy storage. 2011 [cited 2016 10 October]; Available from: http://www.intechopen.com/books/energy-storage-in-the-emerging-era-of-smart-grids/electrochemical-energystorage

1.14. Arántegui RL. Pumped-hydro energy storage: potential for transformation from single dams Netherlands: European Union. *JRC scientific and technical report* 2011; 1-50.

1.15. Kim Y-M, Lee J-H, Kim S-J, Favrat D. Potential and evolution of compressed air energy storage: energy and exergy analyses. *Entropy* 2012; **14**:1501-1521.

1.16. Vazquez S, Lukic SM, Galvan E, Franquelo LG, Carrasco JM. Energy Storage Systems for Transport and Grid Applications. *IEEE Transactions on industrial electronics* 2010; **57**(12):3881-3895.

1.17. Ko¨tz R, Carlen M. Principles and applications of electrochemical capacitors. *Electrochimica Acta* 2000; **45**:2483-2498.

1.18. Ren G, Ma G, Cong N. Review of electrical energy storage system for vehicular applications. *Renewable and Sustainable Energy Reviews* 2015; **41**:225-236.

1.19. Beaudin M, Zareipour H, Schellenberglabe A, Rosehart W. Energy storage for mitigating the variability of renewable electricity sources: An updated review. *Energy for Sustainable Development* 2010; **14**:302-314.

1.20. Burke A. Ultracapacitors: why, how, and where is the technology. *Journal of Power Sources* 2000; **91**:37-50.

1.21. Shukla AK, Banerjee A, Ravikumar MK, Jalajakshi A. Electrochemical capacitors: Technical challenges and prognosis for future markets. *Electrochimica Acta* 2012; **84**:165-173.

1.22. Zakeri B, Syri S. Electrical energy storage systems: A comparative life cycle cost analysis. *Renewable and Sustainable Energy Reviews* 2015; **42**:569-596.

1.23. McMeeking RM, Purkayastha R. The role of solid mechanics in electrochemical energy systems such as lithium-ion batteries. *Procedia IUTAM* 2014; **10**:294-306.

1.24. Wang Y, Song Y, Xia Y. Electrochemical capacitors: mechanism, materials, systems, characterization and applications. *Chemical Society Reviews* 2016; **45**:5925-5950.

1.25. Wang C, Zhou E, He W, Deng X, Huang J, Ding M, Wei X, Liu X, Xu X. $NiCo_2O_4$-based supercapacitor nanomaterials. *Nanomaterials (Basel)* 2017; **7**(2):1-23.

1.26. Naoi K, Simon P. New materials and new configurations for advanced electrochemical capacitors. *The Electrochemical Society* 2008; **17**(1):34-37.

1.27. Li Y, Kang L, Bai G, Li P, Deng J, Liu X, Yang Y, Gao F, Liang W. Solvothermal synthesis of Fe_2O_3 loaded activated carbon as electrode materials for high-performance electrochemical capacitors. *Electrochimica Acta* 2014; **134**:67-75.

1.28. Wu JB, Guo RQ, Huang XH, Lin Y. Construction of self-supported porous TiO_2/NiO core/shell nanorod arrays for electrochemical capacitor application. *Journal of Power Sources* 2013; **243**:317-322.

1.29. Shen J, Liu A, Tu Y, Wang H, Jiang R, Ouyang J, Chen Y. Asymmetric deposition of manganese oxide in single walled carbon nanotube films as electrodes for flexible high frequency response electrochemical capacitors. *Electrochimica Acta* 2012; **78**:122-132.

1.30. Deng L, Hao Z, Wang J, Zhu G, Kang L, Liu Z-H, Yang Z, Wang Z. Preparation and capacitance of graphene/multiwall carbon nanotubes/MnO_2 hybrid material for high-performance asymmetrical electrochemical capacitor. *Electrochimica Acta* 2013; **89**:191-198.

1.31. Li S-M, Wang Y-S, Yang S-Y, Liu C-H, Chang K-H, Tien H-W, Wen N-T, Ma C-CM, Hu C-C. Electrochemical deposition of nanostructured manganese oxide on hierarchically porous graphene-carbon nanotube structure for ultrahigh-performance electrochemical capacitors. *Journal of Power Sources* 2013; **225**:347-355.

1.32. Li S, Wen J, Mo X, Long H, Wang H, Wang J, Fang G. Three-dimensional MnO_2 nanowire/ZnO nanorod arrays hybrid nanostructure for high-performance and flexible supercapacitor electrode. *Journal of Power Sources* 2014; **256**:206-211.

1.33. Chen L, Li H, Yoshitake H, Qi L, Gu N, Wang H. Low-temperature performance of aqueous electrochemical capacitors based on manganese oxides. *Electrochimica Acta* 2015; **157**:333-344.

1.34. Li S, Wang C-A. Design and synthesis of hierarchically porous MnO_2/carbon hybrids for high performance electrochemical capacitors. *Journal of Colloid and Interface Science* 2015; **438**:61-67.

1.35. Thien GSH, Omar FS, Blya NISA, Chiu WS, Lim HN, Yousefi R, Sheini F-J, Huang NM. Improved synthesis of reduced graphene oxide-titanium dioxide composite with highly exposed{001}facets and its photoelectrochemical response. *International Journal of Photoenergy* 2014; **2014**:1-9.

1.36. Tan L-L, Ong W-J, Chai S-P, Mohamed AR. Reduced graphene oxide-TiO_2 nanocomposite as a promising visible-light-active photocatalyst for the conversion of carbon dioxide. *Nanoscale Research Letters* 2013; **8**(465):1-9.

1.37. Perera SD, Mariano RG, Vu K, Nour N, Seitz O, Chabal Y, Balkus KJ. Hydrothermal synthesis of graphene-TiO_2 nanotube composites with enhanced photocatalytic activity. *ACS Catalysis* 2012; **2**(6):949-956.

1.38. Rathee D, Kumar M, Arya SK. Deposition of nanocrystalline thin TiO_2 films for MOS capacitors using sol-gel spin method with Pt and Al top electrodes. *Solid-State Electronics* 2012; **76**:71-76.

1.39. Wu JB, Guo RQ, Huang XH, Lin Y. Construction of self-supported porous TiO_2/NiO core/shell nanorod arrays for electrochemical capacitor application. *Journal of Power Sources* 2013; **243**:317-322.

1.40. Wu M-S, Chan D-S, Lin K-H, Jow J-J. A simple route to electrophoretic deposition of transition metal-coated nickel oxide films for electrochemical capacitors. *Materials Chemistry and Physics* 2011; **130**(3):1239-1245.

1.41. Hsieh C-T, Chen Y-C, Chen Y-F, Huq MM, Chen P-Y, Jang B-S. Microwave synthesis of titania-coated carbon nanotube composites for electrochemical capacitors. *Journal of Power Sources* 2014; **269**:526-533.

1.42. Khare R, Bose S. Carbon nanotube based composites- A review. *Journal of Minerals and Materials Characterization and Engineering* 2005; **4**(1):31-46.

1.43. Ginsberg J. The discovery of fullerenes. In: Program NHCL, ed. *American Chemical Society* 2010.

1.44. Gebhardt P, Eder D. A short introduction on carbon nanotubes; **1**:1-22.

1.45. Iijima S. Synthesis of carbon nanotubes. *Nature* 1991; **354**:56-58

1.46. Iijima S, Ichihashi T. Single-shell carbon nanotubes of 1-nm diameter. *Nature* 1993; **363**:603-604.

1.47. Hu Z, Tong G, Lin D, Chen C, Guo H, Xu J, Zhou L. Graphene-reinforced metal matrix nanocomposites - a review. *Materials Science and Technology* 2016; **32**(9):930-953.

1.48. Mombeshora ET, Nyamori VO. A review on the use of carbon nanostructured materials in electrochemical capacitors. *International Journal of Energy Research* 2015; **39**(15):1955-1980.

1.49. Kumar HGP, Xavior MA. Graphene reinforced metal matrix composite (GRMMC): A review. *Procedia Engineering* 2014; **97**:1033-1040.

1.50. Botas C, Álvarez P, Blanco P, Granda M, Blanco C, Santamaría R, Romasanta LJ, Verdejo R, López-Manchado MA, Menéndez R. Graphene materials with different structures prepared from the same graphite by the Hummers and Brodie methods. *Carbon* 2013; **65**:156-164.

1.51. Dhakate SR, Chauhan N, Sharma S, Tawale J, Singh S, Sahare PD. An approach to produce single and double layer graphene from re-exfoliation of expanded graphite. *Carbon* 2011; **49**:1946-1954.

1.52. Quintana M, Vazquez E, Prato M. Organic functionalization of graphene in dispersions. *Accounts of Chemical Research* 2013; **46**(1):138-148

1.53. Zhou Z, Wu X-F. High-performance porous electrodes for pseudosupercapacitors based on graphene-beaded carbon nanofibers surface-coated with nanostructured conducting polymers. *Journal of Power Sources* 2014; **262**:44-49.

1.54. Fan Z, Yan J, Zhi L, Zhang Q, Wei T, Feng J, Zhang M, Qian W, Wei F. A three-dimensional carbon nanotube/graphene sandwich and its application as electrode in supercapacitors. *Advanced Materials* 2010; **22**:3723-3728.

1.55. Hai-Ping H, Jun-Jie Z. Preparation of novel carbon-based nanomaterial of graphene and its applications electrochemistry. *Chinese Journal of Analytical Chemistry* 2011; **39**(7):963-971.

1.56. Liu W-W, Chai S-P, Mohamed AR, Hashim U. Synthesis and characterization of graphene and carbon nanotubes: A review on the past and recent developments. *Journal of Industrial and Engineering Chemistry* 2014; **20**(4):1171-1185.

1.57. Zhang Q, He Y, Chen X, Hu D, Li L, Yin T, Ji LL. Structure and photocatalytic properties of TiO_2-Graphene Oxide intercalated composite. *Chinese Science Bulletin* 2011; **56**(3):331-339.

1.58. Wu T-T, Ting J-M. Preparation and characteristics of graphene oxide and its thin films. *Surface and Coatings Technology* 2013; **231**:487-491.

1.59. Hummers W, Offeman R. Preparation of Graphitic Oxide. *National lead company* 1958:1339.

1.60. Mohammadi S, Kolahdouz Z, Darbari S, Mohajerzadeh S, Masoumi N. Graphene formation by unzipping carbon nanotubes using a sequential plasma assisted processing. *Carbon* 2013; **52**:451-463.

1.61. Dhakate SR, Chauhan N, Sharma S, Mathur RB. The production of multi-layer graphene nanoribbons from thermally reduced unzipped multi-walled carbon nanotubes. *Carbon* 2011; **49**:4170-4178.

1.62. Terrones M, Botello-Méndez AR, Campos-Delgado J, López-Urías F, Vega-Cantú YI, Rodríguez-Macías FJ, Elías AL, Mu˜noz-Sandoval E, Cano-Márquez AG, Charlier J-C, Terrones H. Graphene and graphite nanoribbons: Morphology, properties, synthesis, defects and applications. *Nano Today* 2010; **5**:351-372.

1.63. He L, Xia G, Sun J, Zhao Q, Song R, Ma Z. Unzipped multiwalled carbon nanotubes-incorporated poly(vinylidene fluoride) nanocomposites with enhanced interface and piezoelectric b phase. *Journal of Colloid and Interface Science* 2013; **393**:97-103.

1.64. Brown B, Swain B, Hiltwine J, Brooks DB, Zhou Z. Carbon nanosheet buckypaper: A graphene-carbon nanotube hybrid material for enhanced supercapacitor performance. *Journal of Power Sources* 2014; **272**:979-986.

1.65. Atchudan R, Pandurangan A, Joo J. Synthesis of multilayer graphene balls on mesoporous Co-MCM-41 molecular sieves by chemical vapour deposition method. *Microporous and Mesoporous Materials* 2013; **175**:161–169.

1.66. Chrzanowska J, Hoffman J, Małolepszy A, Mazurkiewicz M, Kowalewski TA, Szymanski Z, Stobinski L. Synthesis of carbon nanotubes by the laser ablation method: Effect of laser wavelength. *Physica Status Solidi (b)* 2015; **252**(8):1860-1867.

1.67. Sharma R, Sharma AK, Sharma V, Harkin-Jones E. Synthesis of carbon nanotubes by arc-discharge and chemical vapor deposition method with analysis of its morphology, dispersion and functionalization characteristics. *Cogent Engineering* 2015; **2**(1):1-10.

1.68. Kang Z, Gu L. Sol-gel synthesis of multi-walled carbon nanotubes reinforced alumina-silica fibers. *Journal of Macromolecular Science B* 2011; **50**:1402-1412.

1.69. Zhao Q, Xu Z, Hu Y, Ding F, Zhang J. Chemical vapor deposition synthesis of near-zigzag single-walled carbon nanotubes with stable tube-catalyst interface. *Science Advances* 2016; **2**:1-7.

1.70. Suárez S, Reinert L, Mücklich F. Carbon nanotube (CNT)-reinforced metal matrix bulk composites: manufacturing and evaluation: *InTech Open*; 2016.

1.71. Pandolfo AG, Hollenkamp AF. Carbon properties and their role in supercapacitors. *Journal of Power Sources:* 2006; **157**(1):11-27.

1.72. Hosseini T, Kouklin N. Carbon nanotube-polymer composites: device properties and photovoltaic applications: *InTech Open*; 2016.

1.73. Chen C, Cai W, Long M, Zhou B, Wu Y, Wu D, et al. Synthesis of visible-light responsive graphene oxide/TiO_2 composites with p/n heterojunction. *ACS Nano* 2010; **4**(11):6425-6432.

1.74. Chen Y, Zhang X, Liu E, He C, Shi C, Li J, Nash P, Zhao N. Fabrication of in-situ grown graphene reinforced Cu matrix composites. *Scientific Reports* 2016; **6**:1-9.

1.75. Sun Z, James DK, Tour JM. Graphene chemistry: Synthesis and manipulation. *Physical Chemistry Letters* 2011; **2**:2425-2432.

1.76. Srivastava RK, Xingjue W, Kumar V, Srivastava A, Singh VN. Synthesis of benzimidazole-grafted graphene oxide/multi-walled carbon nanotubes composite for supercapacitance application. *Journal of Alloys and Compounds* 2014; **612**:343-348.

1.77. Mombeshora ET, Simoyi R, Nyamori VO, Ndungu PG. Multiwalled carbon nanotube-titania nanocomposites: Understanding nano-structural parameters and functionality in dye-sensitized solar cells. *South African Journal of Chemistry* 2015; **68**:153-164.

1.78. Nguyen BH, Nguyen VH, Vu DL. Photocatalytic composites based on titania nanoparticles and carbon nanomaterials. *Advances in Natural Sciences: Nanoscience and Nanotechnology* 2015; **6**(3):1-13.

1.79. Zhou K, Zhu Y, Yang X, Jiang X, Li C. Preparation of graphene-TiO_2 composites with enhanced photocatalytic activity. *New Journal of Chemistry* 2011; **35**(2):353-359.

1.80. Lekakou C, Moudam O, Markoulidis F, Andrews T, Watts JF, Reed GT. Carbon-based fibrous edlc capacitors and supercapacitors. *Journal of Nanotechnology* 2011; **2011**:1-7.

1.81. Pandolfo AG, Hollenkamp AF. Carbon properties and their role in supercapacitors. *Journal of Power Sources* 2006; **157**:11-27.

1.82. Deng L, Zhang G, Kang L, Lei Z, Liu C, Liu Z-H. Graphene/VO_2 hybrid material for high performance electrochemical capacitor. *Electrochimica Acta* 2013; **112**:448-457.

1.83. Tian Y, Xue R, Zhou X, Liu Z, Huang L. Double layer capacitor based on active carbon and its improved capacitive properties using redox additive electrolyte of anthraquinonedisulphonate. *Electrochimica Acta* 2015; **152**:135-139.

1.84. Hu C, Qu W, Rajagopalan R, Randall C. Factors influencing high voltage performance of coconut char derived carbon based electrical double layer capacitor made using acetonitrile and propylene carbonate based electrolytes. *Journal of Power Sources* 2014; **272**:90-99.

1.85. Romann T, Oll O, Pikma P, Kirsimäe K, Lust E. 4–10 V capacitors with graphene-based electrodes and ionic liquid electrolyte. *Journal of Power Sources* 2015; **280**:606-611.

1.86. Shimamoto K, Tadanaga K, Tatsumisago M. All-solid-state electrochemical capacitors using MnO_2/carbon nanotube composite electrode. *Electrochimica Acta* 2013; **109**:651-655.

1.87. Al-zubaidi A, Inoue T, Matsushita T, Ishii Y, Hashimoto T, Kawasaki S. Cyclic voltammogram profile of single-walled carbon nanotube electric double-layer capacitor electrode reveals dumbbell shape. *Journal of Physical Chemistry C* 2012; **116**:7681-7686.

Chapter Two

International Journal of Energy Research

INTERNATIONAL JOURNAL OF ENERGY RESEARCH
Int. J. Energy Res. 2015; **39**:1955–1980
Published online 1 October 2015 in Wiley Online Library (wileyonlinelibrary.com). DOI: 10.1002/er.3423

REVIEW PAPER

A review on the use of carbon nanostructured materials in electrochemical capacitors

Edwin T. Mombeshora and Vincent O. Nyamori*,†

School of Chemistry and Physics, University of KwaZulu-Natal, Westville Campus, Private Bag X54001, Durban 4000, South Africa

SUMMARY

Sustainable and renewable energy resources, as well as energy storage systems (ESSs), are amongst the current and critical global requirements. A comparative discussion on batteries, fuel cells and electrochemical capacitors (ECs) is presented. The mechanisms involved in various classes of ECs are also elaborated. Additionally, a historical background highlighting some of the major steps associated with EC development over the years is discussed in this review. In particular, carbon nanostructured materials have high potential in the development of ESSs, and hence this review presents an insight on the current ESSs with a strong bias towards these materials as ECs. The current status of carbon nanomaterials, such as carbon nanotubes, nanofibers, nano-onions, nanorods, fullerenes and graphene nanosheets, in ECs is reviewed. The associated effects of nanostructural parameters, such as pore sizes and specific electro-active areas, amongst others, in terms of energy storage capabilities are also discussed. Typical physicochemical characterisation techniques, which enrich understanding of their characteristics, are also reviewed. The discussion views set platforms for a variety of unique carbon nanomaterial designs with high prospective specific capacitance. Key porosity tailoring protocols, such as chemical activation, introduction of heteroatoms in carbon nanostructures and template synthesis methods, are also reviewed. The effects of other device components, such as electrolyte ion size and solvent system, electrode design and use of binders, to the overall capability of EC, are also discussed.

A review on the use of carbon nanostructured materials in electrochemical capacitors

Edwin T. Mombeshora and Vincent O. Nyamori*

School of Chemistry and Physics, University of KwaZulu-Natal, Westville Campus, Private Bag X54001, Durban, 4000, South Africa

Graphical abstract

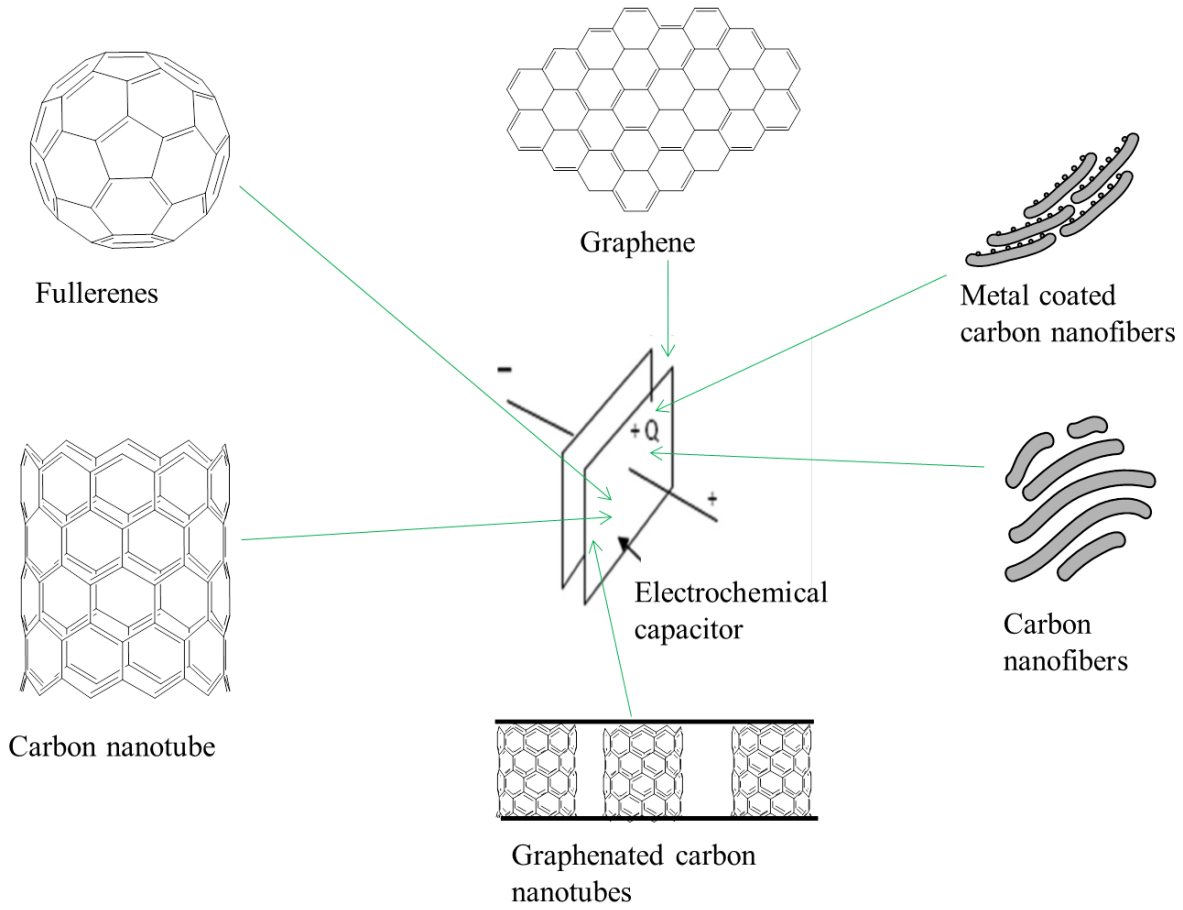

Summary

Sustainable and renewable energy resources, as well as energy storage systems (ESS), are amongst the current and critical global requirements. A comparative discussion on batteries, fuel cells and electrochemical capacitors (ECs) is presented. The mechanisms involved in various classes of ECs are also elaborated. Additionally, a historical background highlighting some of the major steps associated with EC development over the years is discussed in this review. In particular, carbon nanostructured materials have high potential in the development of ESS and hence this review presents an insight on the current ESS with a strong bias towards these materials as ECs. The current status of carbon nanomaterials, such as carbon nanotubes, nanofibers, nano-onions, nanorods, fullerenes and graphene nanosheets, in ECs is reviewed. The associated effects of nanostructural parameters, such as pore sizes and specific electro-active areas, amongst others, in terms of energy storage capabilities are also discussed. Typical physicochemical characterisation techniques, that enrich understanding of their characteristics, are also reviewed. The discussion views set platforms for a variety of unique carbon nanomaterial designs with high prospective specific capacitance. Key porosity tailoring protocols, such as chemical activation, introduction of heteroatoms in carbon nanostructures and template synthesis methods, are also reviewed. The effects other device components, such as electrolyte ion size and solvent system, electrode design and use of binders, to the overall capability of EC, are also discussed.

KEYWORDS: Electrochemical capacitor; Carbon; Nanomaterial; Energy storage; Supercapacitor

Correspondence

* Vincent O. Nyamori, School of Chemistry and Physics, University of KwaZulu-Natal, Westville Campus, Private Bag X54001, Durban, 4000, South Africa

Tel.: +27-31 2608256; Fax +27-31 260 3091

Email: nyamori@ukzn.ac.za

2.1. Introduction

Energy, and its sustainability, that can save and lower the associated costs, are closely linked to its storage phenomenon. Also, there are concerns on how to scale up energy resources and energy storage to meet the growing demand [2.1]. The energy demand has been projected to increase by 65% before 2040 [2.2,2.3]. Among other key players, the digitisation of global societies doesn't favour or lessen the severe strain on the energy grids [2.4]. However, efforts are being made to decentralise energy generation facilities, alleviate environmental problems, minimize energy shortages and to lower the high cost of building new plants through innovative technologies [2.2,2.5-2.7]. Amongst the urgent global requirements are sustainable, renewable and alternative energy sources, as well as energy storage systems [2.8,2.9]. The storage of energy being wasted in industrial, commercial and domestic processes [2.10] is a collective global obligation. Most importantly, minimising energy loss, amongst other aspects in the energy grid, can positively impact on the world's sustainability [2.3]. To improve the overall stability and reliability of power systems, advanced storage technologies are particularly required, especially in developing countries where less sophisticated means of energy generation is the norm [2.11]. Dependable power systems have positive effects on the world economy through ways that include reduction of costs needed to improve on the transmission and distribution of energy capacity. There are two main classes of energy storage systems (ESS), i.e. mechanical and electrical. Examples of mechanical energy storage systems include compressed air [2.5], pumped hydro-energy [2.12] and the flywheel [2.10].

In the case of electrical energy, it can be stored by various methods and Figure 2.1 displays common approaches in a Ragone plot. The figure relates the power and energy density of a device, which in turn provides the energy available for a constant power load [2.13]. The areas in a typical Ragone plot are a rough guideline of the representative energy storage and conversion devices in terms of their specific energy and power outputs [2.14,2.15].

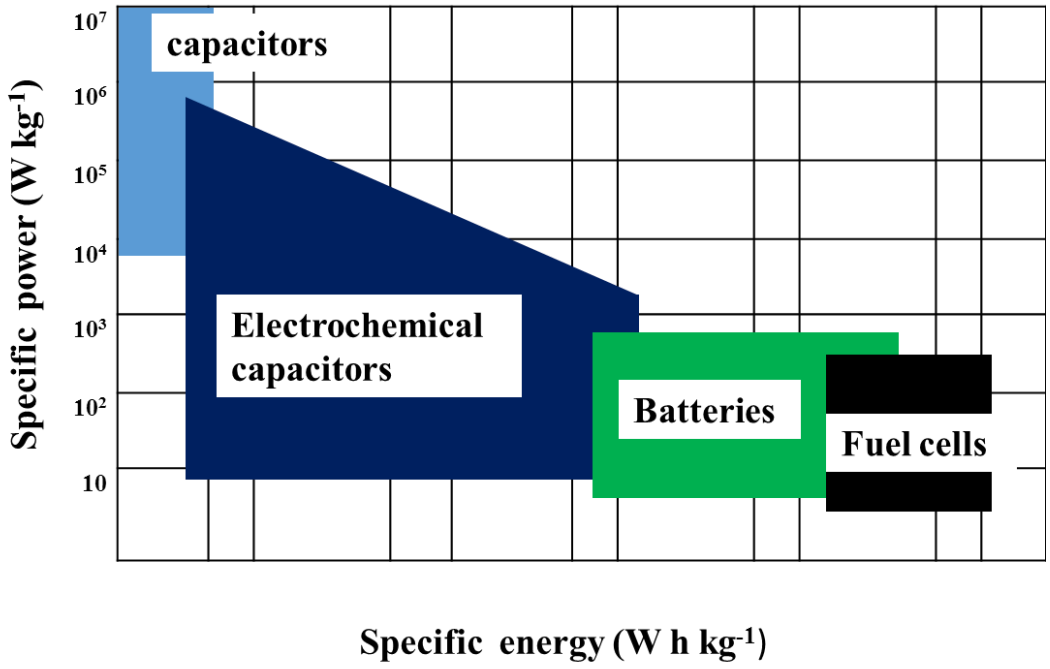

Figure 2.1. Ragone plot sketch for various energy storage and conversion system in the literature.

In general, energy often decreases as a function of power in capacitors [2.13]. In the case of electrochemical capacitors (ECs), a class of supercapacitors, their development trend so far is to either have a high-power output or high energy storage capacity. Usually, before disposal, ECs are understood to give an almost zero waste emission [2.16]. Hence, through a Ragone plot (Figure 2.1), much attention is currently being given to ECs in order to shift their optimum working regions towards preferred limits with both high power and energy being justified. Therefore, new technologies for electrical energy storage, such as nanotechnology, must be sought in the development of ECs.

In case of nanotechnology, a vast range of resources are available for enabling the engineering of functional systems at the molecular scale [2.17,2.18], which in turn serve as a potential approach towards eliminating the current global concerns in the energy sector. Even though there is an over-emphasis on economic gain, with no consideration of the dark side of nanotechnology [2.19], it still provides new approaches to generate, store and exchange energy. Since conventional physicochemical properties of bulk materials may be altered at the nano-scale, it is therefore feasible to tailor their characteristics [2.20,2.21] for a beneficial cause. For instance, a material that is normally an insulator can be electrically conductive at the nano-scale [2.22]. For example, carbon nanostructured materials in this context can be tailor-made

to enhance functionalities for various energy applications [2.23]. The basis of unique comportment in nanotechnology are size and shape [2.24], textural characteristics [2.25], surface energy and surface chemistry [2.26] of the synthesised carbon nanostructured materials. A good example are the 1D carbon nanostructured materials which are promising potential transport carriers and charge collection components [2.22]. They provide high conductivity, short ion diffusion pathways and excellent interfacial integrity [2.27].

The focus of this review is on how carbon nanostructured materials can be tailored towards the high-power density required of supercapacitors and how conductivity enhancement of these typical materials can be achieved. The role of their pore size distribution in charge storage is also illustrated. The influence of other factors such as binders and carbon nanomaterial packing in the performance of ECs is also highlighted in this review. This sets the consideration of crucial parameters in ECs in one platform. The review also provides an insight into the general energy storage phenomena, particularly concerning ECs. The potential of various shaped carbon nanostructured materials in designing unique and effective EC devices is also elaborated. The basis of altering their morphology as a way of tailoring other physicochemical properties such as electro-active area and conductive pathways towards better performances is also expounded.

2.2. Supercapacitors

Capacitors are inactive electrical constituents that comprise of two conducting plates disconnected with a dielectric material (Figure 2.2a). They form part of our everyday lives and their common applications include television satellite receivers, television channel setting, car audio systems, taxi meters, process controllers, cameras and mobile phones, among others [2.14]. Hence, companies, such as Panasonic, Maxwell, ELIT, US Army and Siemens Matsushita, are investing in capacitors (Figure 2.2b) [2.14,2.28-2.30]. Capacitors store electrostatic charges, a form of electrical energy, in the Helmholtz layer with distribution of equal and opposite charges on each plate [2.1,2.14,2.29]. The plates are the terminals of the ECs and their performance is influenced by electro-active surface area and the separation between electrode charge and electrolyte charge [2.1]. The energy storage mechanism in ECs is a physical process devoid of chemical changes. Therefore, stored energy is released upon connecting a capacitor to an external circuit and the process is reversible on charging.

Supercapacitors are associated with some self-discharge caused by various transfer mechanisms or some device imperfections. One disadvantage associated with EC designs, among others, is the need to critically consider mass balance to avoid masking the performance of one of the components, i.e. charge balance [2.31,2.32]. Also, performance is influenced by design parameters such as the thickness of the ultimate electrode.

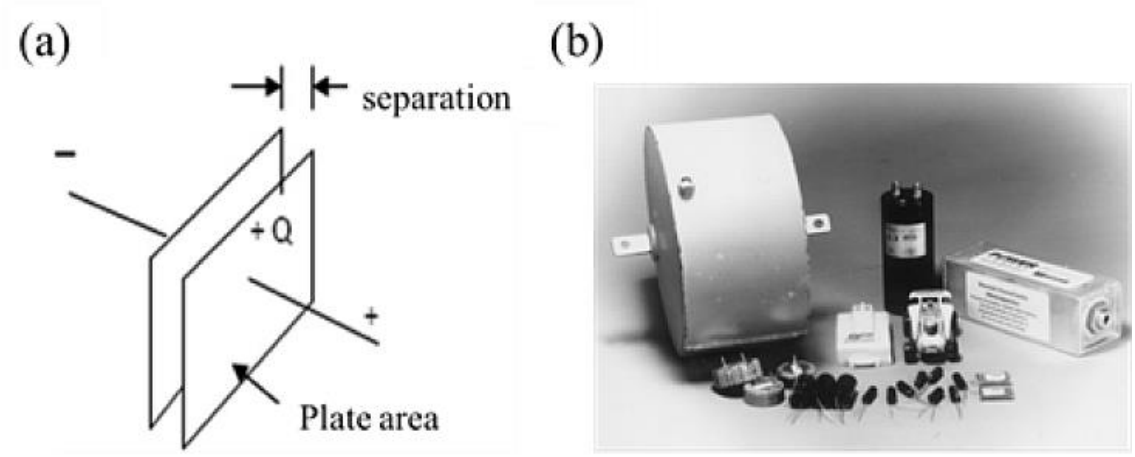

Figure 2.2. (a) A schematic diagram showing a typical capacitor [2.28] and (b) images of commercially available capacitors [2.14].

In reality there exists an inverse relationship between energy and power [2.33], i.e. a higher rate of releasing energy implies a higher power, and this is associated with smaller energy capacity [2.28]. There is need for balance between these two phenomena of ECs and, therefore, capacitors are an interesting area of research.

The dielectric medium, an electrolyte in ECs, determines the permittivity and therefore influences or is affected by the electric field [2.14]. In simple terms, it is the quantity of electric flux generated per unit charge and high amount implies low electrical flux. Hence, the capacity of a material to polarise in response to the inside field influences its permittivity. The maximum charge storage in this context is determined by the breakdown characteristics of the dielectric medium [2.29]. Furthermore, in case of carbon nanostructured material-based ECs, the voltage window is subject to the electrolyte solvent [2.34]. This is signal emphasises the importance of dielectric materials, i.e. electrolytes in capacitors. The energy generation

processes occurring at the electrolyte/electrode interphase of supercapacitors are similar, though the mechanisms are different, to those of fuel cells and batteries [2.35,2.36].

Batteries have numerous applications and this is due to a variety of reasons, such as lower cost per unit charge [2.37], more established markets with commercial availability [2.7], and the ability to store enormous energy quantities in comparatively lesser weight and volume units [2.1]. Anticipated energy and power outputs are obtainable by connecting batteries in series or parallel [2.11]. However, batteries have several disadvantages relative to supercapacitors and these include the use of toxic heavy metals, limited charge/discharge abilities and small power densities [2.1,2.38,2.39]. Supercapacitors are preferred to batteries where high power is needed because they release energy at faster rates [2.1]. Also, short shelf and cycle life are common problems associated with battery use [2.5,2.39]. These shortcomings have become globally acceptable due to lack of competitive alternatives. However, the fast growing and competitive markets, compels scientists and engineers in industry, as well as in academia, to search for alternatives that can enhance battery capacity amongst other aspects [2.40].

The average life span of conventional capacitors is about five years and they have a 60-70% cycle efficiency [2.41]. Supercapacitors have several pluses over other energy storage systems, especially fuel cells and batteries, such as high safety levels, absence of rotating parts and cooling requirements, large modularity in terms of voltage and capacitance, less chances of discharging on their own, high recyclability, low production cost and no service requirements [2.14]. Supercapacitors undergo reversible charge storage processes, have better power density, longer life cycles, lower internal resistance and a broader range of working temperatures compared to batteries (10^6 W dm^{-3}) [2.14,2.42-2.46]. Supercapacitors undergo self-discharge over a period of time and this lowers their voltage in a similar manner to batteries but, unlike batteries, without degrading, and thus they retain their maximum capacitance [2.29]. The uppermost power density of supercapacitors can be 100-fold more than the power output of batteries [2.1]. Compared with fuel cells, supercapacitors have a higher efficiency of recovery of 85-98% than the 25-85% of fuel cells [2.5]. Disadvantages of fuel cells over supercapacitors include lower power density per volume, lower durability, and shortened cell-life due to pulse strains and impurities associated with the gas stream [2.35]. Fuel cells have a reduced dynamic response due to the involvement of air compression at the cathode [2.47] and, hence, often require supercapacitors to achieve maximum power outputs [2.39]. They are still behind both batteries and supercapacitors in terms of market development [2.35]. Unlike fuel

cells, supercapacitors do not involve expensive catalysts, hence they have lower capital costs [2.5,2.35]. However, although fuel cells utilise more toxic and corrosive electrolytes than supercapacitors, they exist in several forms and are therefore suitable for more applications.

The major forms of electrical capacitors are electrochemical, electrolytic and electrostatic [2.33], and these are discussed in the following sections. A pair of conductors disjointed by a dielectric material [2.14] constitute electrostatic capacitors and energy is stored in the form of separated electrical charges [2.1]. Common dielectric media of electrostatic capacitors include air and mica. Electrostatic capacitors have a charge time of approximately 10^{-9} s and store the lowest energy relative to the other two. Hence, more ideas and research inputs are still required in this regard.

Electrolytic capacitors are made -up of a narrower and greater dielectric constant material built on a robust metal [2.14,2.48]. Their response time is approximately 10^{-4} s and have ten-fold better energy storage than electrostatic capacitors. This makes them commercially preferred to electrostatic capacitors and they can be applied in small electronic devices [2.49]. However, the interest of this review is towards ECs often referred to as supercapacitors in literature [2.50].

2.3. Electrochemical capacitors

Traditional capacitors regularly found in electronic circuits cannot meet energy volumes and mass available for storage and use, hence there is a need for efficient ECs [2.29]. The ECs, also recognized as ultracapacitors or supercapacitors, are among the potential energy storage system (ESS) [2.1,2.15,2.51]. These terms will be used interchangeably in this article.

ECs are electrochemical ESS that can accumulate and discharge energy rapidly [2.15,2.33,2.37,2.52]. Reasons for their high energy conversion capabilities include their small distances of electrode/electrolyte interface charge separation as well as the large amount of charge on the electrode surface [2.53]. In terms of voltage per cell, three generations of ECs can be derived [2.54]. The first generation, based on aqueous electrolytes and symmetric designs, achieved cell voltages of about 1.2 V whilst second and third generations, based on organic electrolytes and asymmetric designs, had about 2.7 and 3.8 V/cell, respectively. ECs were first reported around the 1950s with capacitances of fractional Farads [2.55]. By then, in the early 1950s, no strategy had been developed to increase the energy density of ECs [2.56].

Around 1977, SOHIO designed ECs with several Farads of capacitance [2.55,2.57]. During that time and until the 1990s, some incremental performances were recorded. In the 1990s, ECs became more popular and they were prevalent in hybrid electric vehicles [2.14,2.47]. For example, Alexander Ivanov was able to achieve a maximum energy of 1.8 MJ in the ECs designed for electric vehicles in 1993 [2.55]. A typical illustration of how ECs developed over the years is provided by reviewing the Gold Cap capacitors produced by Panasonic (Figure 2.3).

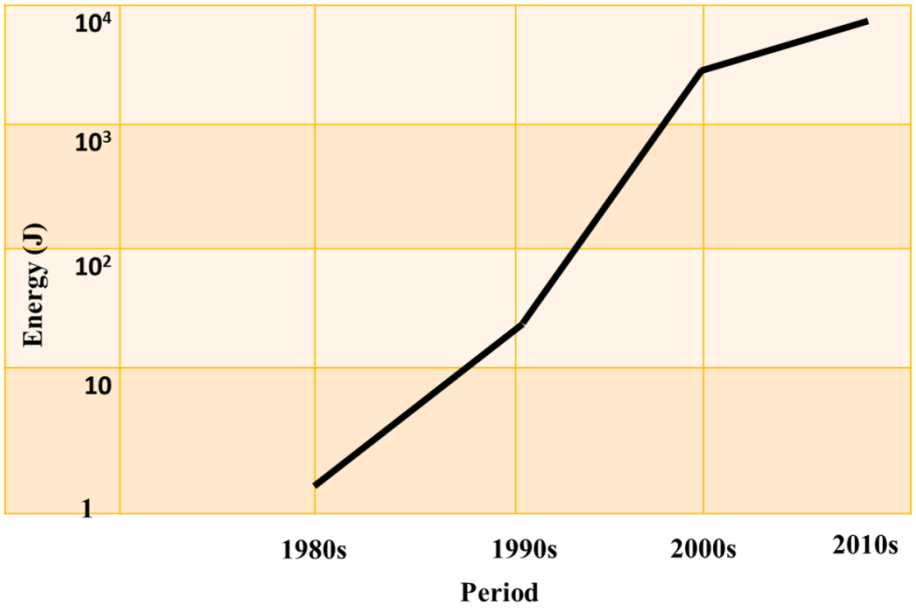

Year	US$/Farad	US$/Kj
1996	0.75	283.55
1998	0.4	151.23
2000	0.1	32
2002	0.023	7.51
2006	0.01	2.85
2010	0.005	1.28

Figure 2.3. The trend in development of energy and energy prices of electrochemical capacitors over the years [2.55,2.58].

The energy density of ECs improved significantly between the 1990s and 2000s but recently the development has been slower (Figure 2.3). The rapid development of ECs between this period also matched the rapid decrease in cost of energy during that period (Figure 2.3 insert) [2.58]. By 2008, the energy density of ECs had reached 4.5 W h kg^{-1} [2.59] and the current record is 50-70 W h kg^{-1} [2.32]. At least by 2010, ECs with capacitances in the range 1000-5000 Farads were commercially accessible from various companies such as Maxwell, Panasonic and Ness [2.37,2.47]. The life cycle of ECs is in the range of 10^6 cycles and response time is approximately 1 s [2.28], this is too fast for most applications [2.50]. Usually ECs have high rates of charge and discharge [2.60]. The energy densities of both batteries and ECs

depend on time of discharge, i.e. rated power, but ECs have shorter charging durations [2.44,2.61]. The energy density and the capacitive performances of ECs are 10^5 times better than conventional capacitors but they require a larger accessible surface area [2.32,2.62]. Moreover, ECs have higher efficiencies (95%) than batteries [2.63]. Their power density can be as high as 10 kW kg^{-1} [2.41]. Hence, they have attracted great attention where high power is a necessity [2.64]. The energy densities of ECs (< 50 W h kg^{-1} [2.63]) are higher than those of electrolytic capacitors [2.65]. Batteries and fuel cells have higher energy storage capacity than ECs, i.e. 30-200 W h kg^{-1} and 300-1000 W h kg^{-1}, respectively [2.28, 2.66]. The energy density of ECs is in the range of 3-5 W h kg^{-1} and power density of 300-500 W kg^{-1} [2.29]. This is because supercapacitors characteristically have lower working voltages, from 1 to 3.5 V per cell. Cell voltage influences their specific energy and power outputs. Therefore, developing ECs with a wider voltage window will be an advantageous step.

To counteract that, ultracapacitors are often connected in series to match the battery outputs. Activated carbon-based electrodes are currently the main components of commercial ECs. This is attributable to their high micro porosity as well as associated low costs [2.67], however, they typically have low specific capacitance (C_s) and energy density. In light of this, it is clear that ECs have a bridging role in terms of power and energy between the old-style capacitors and fuel cells/batteries [2.14,2.15,2.42,2.68,2.69]. The goal is the achievement of several common commercial products on the market but there are a couple of setbacks towards such a milestone.

For instance, faster graphene-based supercapacitors have only achieved voltages in the range 0.8-2.4 V, yet modern electronic devices such as USB chargers and mobile phones use capacitors in the 4 - 10 V range. Supercapacitors only constitute 4% of the $ 18 billion annual global market [2.50]. Challenges in commercialisation of supercapacitors include lack of cost competitiveness and estimated costs of $ 20 000 per kW h compared with other energy storage methods and also because of their low energy densities [2.29,2.41,2.70]. Despite all these challenges, ultracapacitors have found numerous applications in electric vehicles, large-scale power systems, hybrid power-driven vehicles, memory back-ups and energy management systems [2.5,2.14,2.28,2.29]. Attributes of supercapacitors in the representative applications include low maintenance requirements, fast charge propagation activities and exceptional cyclic performance, high specific capacitance, and are associated with high power densities during charge/discharge activities [2.45,2.69]. This makes them superior to conventional

capacitors and their market is projected to reach $ 15 billion in 2015 [2.28]. The main attention in ECs seems to include development of high cell voltage, high power delivery and long cycle stability [2.28,2.68]. High cell voltage implies high energy density. The current focus area in this field is enhancing energy density whilst maintaining high power densities and long cycle lives of ECs [2.71]. These are key areas that can positively influence power and energy densities for grid power storage.

2.3.1. Classification of supercapacitors

The complete assembled device, i.e. the electrode materials and electrolytes, influences the EC capacitive properties. Charges accumulate within the electrolyte at solid electrodes and the double layer thickness depends on the ion size and concentration, i.e. the former two determine the quantity of ions adsorbed in a given area [2.14,2.72]. The nature of the electrode material determines the capacitive behaviour of ECs [2.43,2.46,2.69]. A wide range of materials based on carbon nanostructured materials, conducting polymers and transition metal oxides, such as Ti, Mo, Mn, Ni, Ir, Co, Fe and V, have been used to fabricate various types of ECs [2.28]. They can be categorised according to a wider range of criteria such as electrode material, cell design and electrolyte [2.14]. Aqueous, non-aqueous or solid state are the three classes arising on the basis of the electrolyte system [2.73]. ECs are commonly classified into two categories, i.e. as pseudocapacitors and electrochemical double layer capacitors (EDLCs), subject to both the charge storage mechanism and material technology exploited in the fabrication of electrodes [2.10,2.46,2.74] (Figure 2.4) [2.8,2.43,2.66,2.75,2.76].

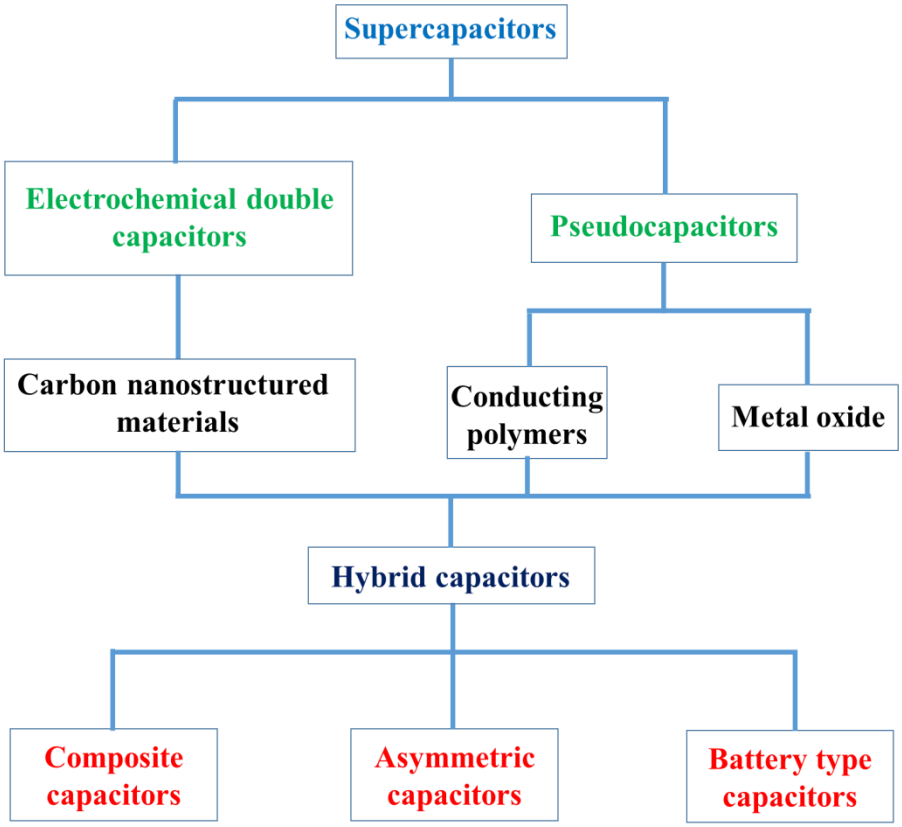

Figure 2.4. Types of ultra-capacitors.

2.3.1.1. Electrochemical double layer capacitors

The double layer concept was developed by von Helmholtz in the 1900s and General Electric pioneered the EDLCs in 1957 (Figure 2.5) [2.1,2.15,2.30]. Interest in EDLCs is particularly growing because of the drive towards 'greener' environments and sustainable energy systems. An EDLC based on nano-structured carbons can be fabricated by using two carbon electrodes with high surface areas that are immersed in an appropriate electrolyte [2.34]. The separator must be permeable to ions; charge separation occurs over a small inter-phase space between the electrolyte and electrode. Unlike batteries, EDLCs are independent of chemical phase changes and heterogeneous charge transfers [2.77].

In EDLCs, charging of the double layer at the electrolyte-electrode interface forms the basis of the technique (Figure 2.5) [2.30,2.37]. They operate through a non-Faradaic process [2.37,2.75,2.78] which involves no chemical or compositional changes due to the absence of electron transfer activities [2.30]. Additionally, the thickness of the dielectric in a solid state

capacitor is often higher than that in the Helmholtz layer in carbon nanostructured material-based capacitors, i.e. 0.5 – 1 nm [2.14,2.79]. Hence, EDLCs normally have rapid response and reversible interfaces with respect to changes in electrode potentials. Energy is stored electrostatically as opposite electric charges, i.e. through a charge separation mechanism (Figure 2.5) [2.37,2.75,2.77,2.80]. Electrolyte ions are reversibly adsorbed into the micropores of the electrode material [2.29,2.69]. The basic requirements for quick formation of a double layer in such capacitors are porosity and accessible surface area [2.29]. The ion movement, associated with the double layer formation in the pores, from the electrode *via* the electrolyte to the counter electrode, is facilitated by a diffusion process [2.1,2.29]. Some authors view EDLCs as substitutes for dielectric capacitors [2.12]. ECs have a higher energy density by virtue of their quick response, high ion mobility in electrolytes and inverse proportionality relationship with double layer thickness, but they usually have a low power density [2.78,2.81, 2.82].

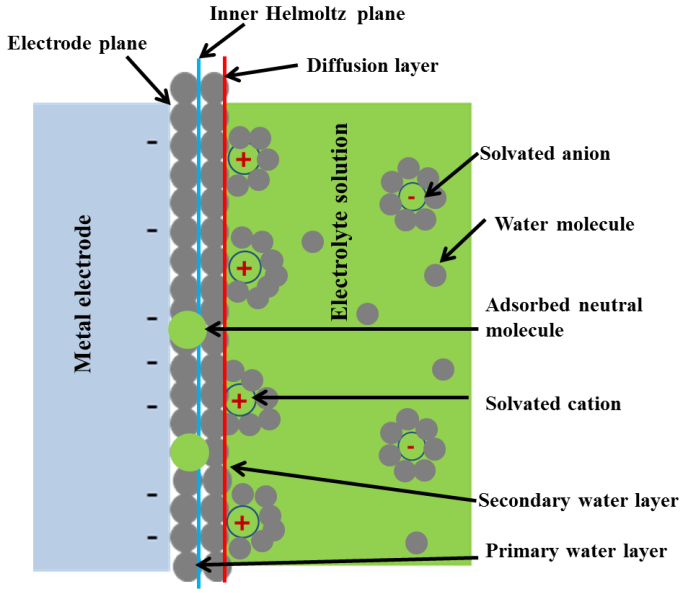

Figure 2.5. Representation of an EDLC illustration of Helmholtz layer.

Carbon nanostructured material-based EDLCs are highly conductive, porous, associated with low costs and ease of processability, and are electrochemically stable [2.75,2.83]. Related energy storage capability is restricted by the electrostatic nature of the finite electrical charge separation at the interface, but they store more energy per unit volume/mass [2.76]. Use of

carbon nanostructures in this regard is affected by oxidation during recycling and ageing, but can exceed 500 000 cycles [2.37,2.76,2.77]. This aspect will be reviewed in later sections.

2.3.1.2. Pseudocapacitors

Contrary to EDLCs, pseudo/redox capacitors utilize both double layer charge and Faradaic reactions [2.43]. Redox capacitors are battery-like in behaviour but are non-electrostatic in nature and transfer charge electrochemically [2.1,2.37,2.44,2.80]. Charge is transported near the exterior or in bulk region close to the electrode surface [2.29]. The proposed mechanism involves space charge density increase and attraction of protons [2.84]. They are based on electrode charge storage mechanisms and require highly reversible surface redox processes between electrode-electrolyte interfaces or through intercalation of ions [2.37,2.75,2.80,2.85]. Their performances are governed by ion kinetics and electrode electron transport as well as the electrode-electrolyte interface [2.86]. The electrolyte ions participate in three main processes at the working electrode of a pseudocapacitor, i.e. electrosorption, redox reactions and intercalation [2.29,2.30]. Their intercalation is a bulk process largely dependent on electrode porosity whilst the other two are surface activities with a high dependency on surface area.

Pseudocapacitors have a high energy storage potential due to the associated specific capacitance (C_s), high power density, low self-discharge, safe operation, high cycling stability and fast charge/discharge capability [2.28,2.75,2.76]. Hence, their applications include aeroplanes, subway trains, power electronics and smart grids. Conversely, pseudocapacitors have low porosity, low mechanical strength and conduct electricity poorly.

The active electrodes of pseudocapacitors are mostly either transition metal oxides or based on conducting polymers [2.30,2.52]. The capability of carbon nanostructured materials in supercapacitors can be enhanced by the use of transition metal-based oxides and conducting polymers such as polyaniline and polythiophene [2.46]. Pseudocapacitors fabricated from transition metal oxides have high energy density and large charge transfer reaction characteristics; this is due to variable oxidation-state structures. For example, noble metal oxide-based capacitors of approximately 700 F g^{-1} have been reported [2.28]. Conducting RuO_2 and IrO_2 were the most preferred in ECs and have found use in space charge and military applications [2.14]. However, cost and economic reasons, such as 90% of the cost being linked

to the electrode material, point to the necessity of exploring other alternatives. Also, other options, that can offer decent electrical conductivity with sufficient surface area and high capability to participate in Faradaic EC reactions, are required for energy storage in distinctive devices [2.28].

Carbon nanostructured materials such as carbon nanotubes (CNTs) and graphene (G), enhance the charge transfer efficiency of pseudocapacitors [2.76]. If functionalised, the acidic oxide surfaces serve as adsorption sites for polar molecules and hence improve wettability and hydrophilicity. Consequently, the acid-base nature of carbon nanomaterials enhances the pseudocapacitive behaviour. Thus, modifying the surface chemistry and porous nanostructure of carbon materials, particularly man-made carbon nanostructured materials, is necessary especially for generating better functionality at high scan speeds and durability for continuous short and long pulse power intervals. The characteristics of the earlier two mentioned classes of capacitors can be combined into one device (Figure 2.4) to make a new class, hybrid electrochemical capacitors.

2.3.1.3. Hybrid electrochemical capacitors

Composites of carbon nanostructured materials and other nanomaterials combine EDLC and pseudocapacitance features in hybrid electrochemical devices [2.10,2.30,2.85]. Each ESS method and EC, in particular, has their own strengths, limitations and operational characteristics [2.6]. Andrew Burke's [2.29] view is that separating energy and power requirements *via* peak power supply with the use of a capacitor charged periodically using an energy storage unit could be a reasonable approach to sustainable energy. Hence, combinations of ECs with either fuel cells or batteries produce advanced hybrid power systems [2.7,2.87]. Various designs of hybrid EC devices bridging the gap between batteries, fuel cells and EDLCs have been reported. The design of their device is an example of an internal series hybrid capacitor since the two electrodes function with different mechanisms [2.88]. Likewise, the components of hybrid capacitors can have mechanisms of both pseudocapacitors and EDLCs [2.29].

Hybrid electrochemical devices rely on Faradaic charge transfer processes of surface atoms and non-Faradaic processes [2.28,2.30]. Examples of such capacitors, according to their

electrode configurations, include nano-hybrids, battery-like and asymmetrical ECs (AECs) [2.30] (Figure 2.4). An AEC is a combination of an EDLC and a battery in order to improve cycleability and energy density [2.66,2.70]. They have two different active materials combined to make one device. The transition metal electrode relies on reversible redox Faradaic processes whereas the counter carbon-based electrode is influenced by reversible surface adsorption/desorption activities occurring *via* non-Faradaic mechanisms. Advantages of AECs over EDLCs include their slower self-discharge rate and this arises from the lithium revocable redox reactions. Hence, amongst other reasons, commercial automobile companies such as Honda, Nissan, Chrysler and General Motors have become increasingly interested in typical hybrid systems [2.64].

2.3.2. Carbon nanostructured electrodes

In addition to the drive towards enhancing capacitance through novel designs, the development of affordable environmentally friendly materials is also a priority [2.89]. Oxides of transition metals, conducting polymers and porous carbon nanostructured materials are the common EC materials reported [2.42]. Porous activated carbon currently dominates the market, since it possesses large surface areas and ultimately large energy densities but its narrow pores and low electronic conductivity limits its applicability due to slow ion diffusion [2.65]. The highest C_s for nano-porous activated carbon reported so far is 240 F g^{-1} [2.33].

2.3.2.1. General background on carbon

Carbon is a flexible group 14 element and is capable of forming a wide range of architectures at the nano level [2.90]. Several reasons influence nanostructured carbon as the material of choice in energy storage applications. For example, these include well established fabrication methods, tuneable pore sizes, high porosity, large surface areas (between 1 and over 2000 m^2 g^{-1}), ability to be an intercalation host, corrosion resistance, high thermal and chemical stability, low mass, compatibility with other materials, desirable architectures and good electronic conductivity [2.37,2.66,2.69-2.71,2.75,2.85,2.91]. Ordered allotropes of carbon have received much attention in the electronics field. Their micro-texture, dimensions and variable degrees

of hybridisation in the respective carbon nanostructured material play a role in their electronic properties as EDLCs [2.92,2.93]. Diamond (sp^3 hybridised) and graphite (sp^2 hybridised) are examples of natural allotropes while carbyne (sp hybridised) and fullerenes (distorted sp^2) are synthetic [2.37]. The sp^2 hybridised carbon materials have found the greatest application in electronics. The delocalised π-bonds in the carbon sp^2 hybrids render electron availability as charge carriers. Furthermore, the capacitive behaviour of carbonaceous nanomaterials is structure-dependent [2.94]. For example, flake- or sheet-like nanostructures are highly accessible to the electrolyte cations, hence they have increased charge transfer even though they have low specific surface areas [2.95]. In most cases internal surfaces of nanostructured carbons are inactive in double layer formation. Various forms of carbon nanostructured materials such as carbon nanofibers, nanorods, G nanosheets and CNTs, amongst others, have been reported as electrodes in EDLCs [2.16,2.28,2.46,2.53,2.90,2.95] (Figure 2.6). For instance, CNTs and G are common materials used in enhancing electrode surface accessibility to electrolytes [2.44].

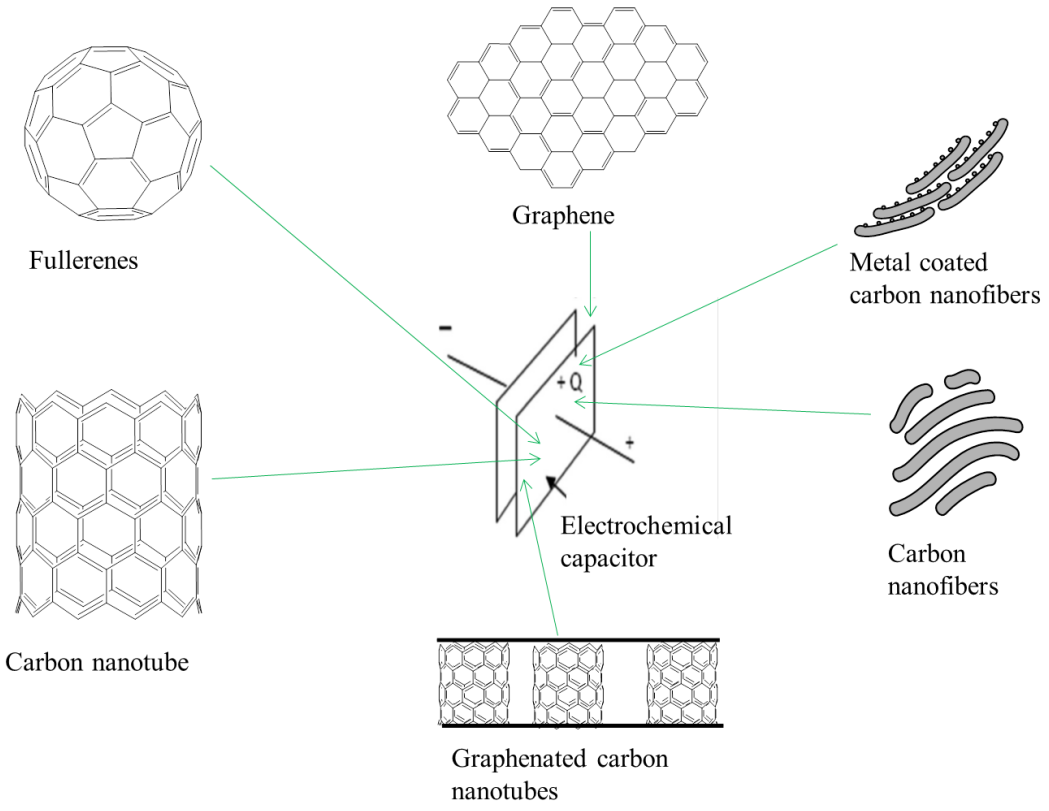

Figure 2.6. Typical shaped carbon nanomaterials for ECs.

While heat treatment has been reported as a way of improving structural order and conductivity, this practise reduces the surface areas of the carbon nanostructured materials. Egashira *et al.'*s [2.12] stance on this aspect is that porous carbon nanostructured materials are usually less graphitic and have low electronic conductivity. Their work also mentions that the graphitic structure has a larger double layer capacitance per surface area than basal carbons. They argued that amorphous carbon exposes a larger number of edges on its surface and also that larger surface roughness gives a higher C_s and their views were validated by the work of Chen *et al.* [2.96].

Preparation methods also affect electrochemical performance of carbon nanostructured materials [2.97]. Most of the carbon nanostructured materials for EDLCs are produced mainly through either an electro-spinning or chemical vapour deposition (CVD) carbonization process [2.79]. In such processes, carbon precursors go through pyrolysis, elimination of volatile materials, followed by condensation reactions at high temperatures, culminating in the localised graphitic unit formation. Carbon sources for synthetic carbon nanostructured materials are mainly biomass, polymers and hydrocarbons [2.98]. Microwave irradiation as a synthesis approach reduces the reaction time, prevents side-reactions, and facilitates yield and reproducibility of specific synthesis protocols [2.69]. The best method for carbon nanostructured material production is catalytic deposition [2.99]. Acetylene is one of the best carbon sources utilized in the syntheses of graphitic nanomaterials. The main reasons are its greater activity and the smaller carbon atom ratio of its molecule compared with most hydrocarbons. High carbon content increases the surface area and conductivity of capacitance electrodes [2.76]. Porous carbonaceous structures increase the effective contact area between the electrode surface and electrolyte ions, ultimately giving better electrochemical performances [2.78]. G is one of the carbonaceous materials reported to have a high surface area and is therefore appropriate as an electrode material in ECs.

2.3.2.2. Graphene

The name graphene (G) is derived from graphite and alkene [2.100] and G is a form of graphite with less than ten layers of six-membered carbon species in a honeycombed network [2.101-

2.103]. Applications of G range from flexible electronics to functional nano-devices and G is so far the best carbon nanostructured material-based electrode for ECs [2.85,2.104,2.105]. Types of G include monolayer, plane sheet, mesh and ribbons [2.101,2.106,2.107] and there are two generations of G, i.e. first (2D) and second (3D) [2.32]. Focus on G began in earnest in 2004 with publications on G increasing exponentially since 2005 [2.80]. G nanosheets are now regarded as the next generation electrode, this is principally due to their theoretical superior conductivity and surface area [2.8]. The high surface area of G nanosheets comes from interconnected open channels between layers, not pores [2.72, 2.108]. Electrons move unimpeded at higher speeds throughout the lattice in G than in ordinary metals [2.100]. The conductivity, specific surface area, thermal conductivity and intrinsic mobility of G are approximately 2000 S cm^{-1}, 3100 m^2 g^{-1}, 3000 W m^{-1} K^{-1} and 200 000 cm^2 V^{-1} s^{-1}, respectively [2.32,2.102,2.109-2.111].

Traditionally, G is regarded as the mother of conjugated carbon nanomaterials and is the thinnest known material [2.30,2.92,2.105,2.112]. It resembles polycyclic aromatic hydrocarbons and benzene. G is made up of sp^2 carbon atoms and its π-electrons are delocalised throughout the 2D network [2.103,2.105,2.109]. However, the role of monatomic thick G and the 2D honeycomb network of sp^2-hybridised carbons is still not fully understood [2.113,2.114]. G is chemically inert, and this is a setback to its manipulation. Its chemistry can be viewed to involve breaking and formation of conjugated sp^2 C-C bonds. Oxidation of G enhances the hydrophilic character and enhances agglomeration and precipitation [2.115]. G easily agglomerates due to van der Waals forces arising from $\pi - \pi$ stacking interactions between sheets. This makes fabrication of a porous electrode a difficult task [2.30], especially in the G first generation, due to limited accessibility of internal pores by electrolyte ions [2.32]. The stacking order and coupling between layers determines the electronic properties. The actual capacitive performance of G-based nanocomposites is often lower than anticipated due to aggregation of G sheets [2.116]. Theoretical studies of G postulate high C_s values of 550 F g^{-1} if restacking problems are eliminated [2.32, 2.60].

Since G has a zero band gap, the properties of G such as band gap opening and conductivity can be enhanced through covalent modification [2.106]. In principle, G modification is possible at the edges and surface planes, altering the energetic characteristics in the process. The zigzag edges are more reactive than arm chair but in practice G nanosheets have a mixture of configurations [2.105]. This makes altering chemical functionalities a difficult task.

Controlling the configuration length of a delocalised carbon lattice *via* covalent functionalization influences band gap tunability [2.101,2.106]. Band gap and type of charge carriers are important in the semiconductor industry. Substitution of carbon with heteroatoms is a possible way of altering charge carrier types.

G has found numerous applications in EDLCs mainly as a substrate for nanomaterials, such as carbon, and this gives them better functionalities. For instance, Haiyang *et al.* [2.74] recently reported G nanosheets synthesised at low temperatures of 100 and 400 ºC, with the G nanosheets at the latter temperatures achieving the best C_s of 212 F g^{-1}. The work on G nanosheets by Nasbi *et al*. [2.72] achieved low current responses due to low mobility of OH^- ions and the large K^+ ionic radius in the electrolyte. Their low surface G nanosheets achieved a C_s of 3.62 F g^{-1} in 3 mol L^{-1} NaCl electrolyte at a scan speed of 5 mV s^{-1}.

Recently, a cauliflower-fungus graphene (CFG) with a mesoporous 3D structure, surface area of 462 m^2 g^{-1} and rectangular cyclic voltammetry (CV) at 50 mV s^{-1}, achieved a C_s of 103 F g^{-1} [2.32]. This value was greater than 92.4 F g^{-1}, the theoretical value, and also their energy density was 15.6 W h kg^{-1}. They attributed these findings to the creation of fast 3D channels and hierarchical mesoporous structure for electrolyte ion mobility synthesized from CO_2 *via* a one-step exothermic reaction.

Du *et al.* [2.53] also reported good charge propagation on oxidised G nanosheets (GO) with narrow mesopores of 4 nm and redox peaks from oxygen functionalities. They also reported that disordered G nanosheets with many edges in the electrode store more energy with increase in scan rate. Also, 3D GO, G functionalised with oxygen moieties, achieved a C_s of 352 F g^{-1} at a sweep rate of 5 mV s^{-1} [2.117]. A composite of G/CeO_2/carbon black in electrodes with a narrow deep morphology was reported to increase charge storage but reduced current response [2.95]. This in turn increased the specific surface area, Faradaic reactions and charge storage capabilities, but reduced the current response and power delivery capabilities. The same researchers were able to achieve a C_s of 11.84 F g^{-1} at 10 mV s^{-1} in their recent report based on G nanosheets modified with zirconium dioxide [2.27].

In another study by Battumur *et al.* [2.62], an optimum mass of 5% of multiwalled carbon nanotubes (MWCNTs) in 1% G nanosheets and Co_3O_4 nanocomposites provided additional nano-channels for flow of charge and electrolyte penetration. This therefore improved charge storage in their typical G nanosheet materials by reducing diffusion and the migration length

of the electrolyte ions. Higher loadings of G nanosheets were reported to hinder formation of a 3D network for an effective conductive system. G can also add conductivity to nanoparticles [2.42,2.80,2.85]. Additionally, electron injection from G into oxides increases the concentration of holes in G and may improve the conductivity of the entire hybrid material. Corrugations in G nanosheets can achieve a 10-fold enhancement of electron transfer rates relative to the basal graphitic plane [2.82] but G has limited capability to store charge in aqueous electrolytes [2.85].

Cobalt-based composites, such as Co_3O_4/GO nanosheet, and $Co(OH)_2$/GO nanosheet are also reported to have high capacitance values and a capacitance retention of 85-95% after 1000 cycles with 6 mol L^{-1} KOH [2.85]. Such observations were attributed to both the Co^{2+}/Co^{3+} system in CoO_4/CoOOH and Co^{3+}/Co^{4+} in the CoOOH/CoO_2 phase change. The Co_3O_4 form is preferred in capacitors because of the low costs involved in using it, environmental friendliness, and favourable microstructure and morphology [2.62]. Ramakrishnan *et al.* [2.85] are of the opinion that a uniform distribution of metal oxide (MO) in nano-carbon based capacitor architectures is still a common challenge to most reported work.

Anosori *et al.* [2.80] designed a hybrid structure consisting of Nb_2O_5 nanoparticles with sizes between 10 and 20 nm deposited on a 3D graphene aerogel. Their design reduced the diffusion limitation of electrolyte ions moving through the electrode and increased electrode conductivity. They attributed their findings to the orthorhombic structure of niobium oxide which offers a 2D transport pathway for fast Li^+ (cation from electrolyte) intercalation. Their stance was that thin films and microelectrodes perform better in supercapacitors.

In the report by Deng *et al.* [2.42], a G/V_2O_2 composite was prepared by a single-step hydrothermal technique. A nickel foam current collector, Pt counter electrode and SCE reference electrode were used with the scan speed applied at 5 mV s^{-1}, whilst 3 mg was the mass load. They observed a deviation from the classic rectangular CV curve with a high profile and no redox peaks, this inferred high C_s values. In explaining their findings, they referred to the ability of the star fruit-like V_2O_2 structure to shorten the path length and this increased the contact area between V_2O_2 and G. Hence, ion accessibility in pores was improved and according to their interpretation, typical structures that shorten electrolyte diffusion length during charge/discharge improve electrochemical utilization of nanoparticles. After 1000 cycles their capacitance retention for G, VO_2 and G/VO_2 was 99%, 47% and 65%, respectively. They proposed that the star fruit-like G/VO_2 conversion to hollow hemispheres during

galvanostatic charge/discharge as a manifestation of poor cycle stability. They ascribed it to oxidation of V^{4+} to V^{5+}. In their work, they also pointed out the C_s lowering effect of the electrode high charge transfer resistance.

2.3.2.3. Carbon nanotubes

CNTs are a hollow tubular form of carbon nanostructured materials and they can be classified according to the number of tubular layers as single-walled carbon nanotubes (SWCNTs), double-walled carbon nanotubes (DWCNTs) and multiwalled carbon nanotubes (MWCNTs). The CNT morphology and purity influences C_s, and the metal residue from the synthesis catalyst also affects the electrochemistry of CNTs [2.112]. On the other hand, the low reactivity of basal planes on the walls of CNTs limits their energy density [2.65]. CNTs can be used as electrodes in both aqueous and non-aqueous electrolytes [2.37,2.78]. Preparation of CNTs as electrode materials falls into two main categories. Firstly, as-grown CNT arrays, such as vertically aligned, and, secondly, as designed patterns, such as CNT bundles [2.45]. As-grown arrays make use of 1D material in shaping the electrode morphology. This method is straightforward and well-suited for thin film technology of integrated circuits. Whereas in a typical designed pattern, CNTs are grown on a substrate then disbursed in liquids and then remoulded on current collectors. In this approach CNTs act as raw materials that provide more accessible interfaces for charging and discharging. The list of possible nanocomposite designs with other constituents in this respect is endless.

CNTs are good potential electrodes because of the high fraction of surface area accessible to electrolytes in EDLCs [2.69]. The mesopores in CNT electrodes are interconnected and therefore allow a continuous distribution of charge on the available surface [2.30]. The high aspect ratio of CNTs increases the effective surface area, chemical stability of electrodes and electrical conductivity [2.78]. CNTs can form electrically conductive networks that are suitable for energy storage capabilities [2.81]. CNTs generally have a lower equivalent series resistance (ESR) than activated carbon [2.30]. Furthermore, their ESR can be lowered by growing CNTs directly on current collectors. Additionally, CNTs reduce current path-length and hence enhance capacitance [2.79].

In theory, SWCNTs have a larger surface area than MWCNTs. The conductivity of SWCNTs depends on structural parameters such as chirality; hence, they can be metallic or semiconducting [2.1]. Metallic conductivity is of the order 10^4 S cm^{-1} [2.1]. Therefore, SWCNTs have a classical C_s of 180 F g^{-1} whilst that of MWCNTs is between 4 and 137 F g^{-1} [2.15]. CNTs have been widely applied as an additive rather than being the main component [2.45] of EC devices. Lekakou *et al.* [2.81] used aligned CNT electrodes perpendicularly to the current collector and reported a power rating of 1.5 kW kg^{-1}. They pointed out that a typical C_s of CNTs is from 15 to 80 F g^{-1} [2.37]. Oxidative treatments of CNTs have been reported to increase their capacitive behaviour. In another parallel study, Chang *et al.* [2.78] coated CNT/carbon cloth with nanostructured NiO in making an electrode. They justified choosing carbon cloth by its flexibility, low mass, corrosion resistance and conductive nature in addition to its strong adhesion to CNTs. The electrolyte was 1 mol L^{-1} KOH, with a Pt counter electrode and a Ag/AgCl reference electrode in saturated KCl. All the electrodes fabricated with carbon cloth, CNT/carbon cloth and NiO/CNT/carbon cloth had a nearly rectangular CV curve and a high charge storage at 50 mV s^{-1} was attained. The C_s order was carbon cloth < CNT/carbon cloth < NiO/CNT/carbon cloth and they explained their observations as being due to the Ni^{2+}/Ni^{3+} Faradaic reaction.

Wu *et al.* [2.118] used CNTs decorated with titania nanorods and in their view, a long oleic acid chain in a sol-gel synthesis improved the compatibility between titanium sols and pristine CNTs, as well as acting as a guide to titania growth on the CNT surface. Their work was an indication that almost complete coverage of the CNT surface with titania nanorods is suitable for EC electrodes.

Jiang *et al*. [2.119] reported on a cellulose woven fabric as a textile electrode template for CNT-MnO_2 composites with complex surface morphology that comprised of several functional groups such as the hydroxyl groups. They reported a C_s of 247 F g^{-1} for their CNT/activated cellulose textile/MnO_2 nanostructure. They proposed dispersion enhancement due to H-bonding with acid-treated CNTs to be the main factor of their results.

2.3.2.4. Graphenated carbon nanotubes

A composite of graphene nanosheets and CNTs can be referred to as graphenated CNTs (G-CNT). G-CNTs can also be produced *via* a microwave plasma enhanced chemical vapor deposition method (MPECVD) as perpendicularly oriented foliates on CNT sidewalls [2.120,2.121]. The important benefit in such composites is the combined high CNT surface area and the high density edges of G [2.120]. The edges from G provide high charge density and reactivity. Understanding the relationship between electrochemical characteristics and nanostructures of typical hybrid carbon material-based electrodes is a fundamental aspect in this regard [2.121]. For example, Henry *et al.* [2.121] reported that G-CNTs had faster electron transfer kinetics than CNTs, this is important in the charge/discharge rate of capacitors. Electro-polymerisation technology can be used to coat a dielectric monolayer onto G-CNTs composites in order to enhance charge storage [2.50]

Yan *et al.* [2.122] grew CNTs on G sheets by using porous nickel mesh and iron catalysts. Fan *et al.* [2.115] synthesised CNTs on G sheets. They reported that CNTs between G sheets lack uniformity due to poor wettability between the catalyst and G. According to their description, this caused aggregation and coalescence of catalyst particulates on G during sintering. Some of the key physiochemical attributes pointed out in their materials include improved surface area arising from effective CNT intercalation and distribution between G layers. Their view was that increased surface area provided diffusion pathways that facilitate rapid electrolyte transport. The CNT dimensions in their report were less than 100 nm in length, 5-7 nm internal diameter (ID) and 7-12 nm outer diameter (OD). Upon use of KOH and H_2SO_4 as electrolytes, at 10 mV s^{-1}, a negligible cathodic peak was observed and this means the reaction was irreversible and the pseudocapacitance behaviour was two times amplified with respect to G. The C_s attained in 6 mol L^{-1} KOH electrolyte was 385 F g^{-1}. Raising the scan rate increased the current response in their study and this implied a good rate capability. They concluded that their material was electrochemically stable since their ECs were still at about 20% of their original capacitance after 2000 cycles.

Romann *et al.* [2.50] reported the generation of meso-macroporous electrodes with large surface areas from a rigid connection in the carbon backbone of G and CNTs. This prevents electrical isolation during dielectric formation. G-CNTs in their work displayed best capacitive performances due to high electrical conductivities and compactness. They also stressed that

thin G-based capacitors have higher energy densities than current commercial capacitors on the market.

In the work reported by Deng *et al.* [2.68], G, CNTs and G/CNT electrodes in 1 mol L^{-1} Na_2SO_4 showed a rectangular CV curve shape with no Faradaic reactions between -0.1 and 0 V [2.68]. They reported a large CV curve area from G/CNT electrodes to infer higher C_s. In the range 0 to 1.1 V against a SCE the electrodes showed a rectangular CV curve shape with a mirror image feature and they interpreted it to be an ideal capacitance character. Addition of MnO_2 to G/CNT increased the C_s and changes were noted when the sweep rate was altered from 5 to 200 mV s^{-1}. In their work they provided evidence of the thermodynamic relationship between the oxygen evolution reaction and the positive potential acquired by an electrode material.

Li *et al.* [2.8] synthesised a hierarchically nanostructured porous *a*-MnO_x, 2D G nanosheets and ID MWCNT composites. G sheets were chemically functionalised prior to MWCNT insertion *via* a solution assembly process. They reported *a*-MnO_x grown on the G-MWCNT framework through a potentio-dynamic deposition with a flowery nanostructured morphology decorated with slim petals of approximately 5-8 nm. In their work, the CNT role was to act as a spacer and their optimum loading was 10 mass % in terms of surface area. This corroborated the views of several researchers [2.15,2.60]. They reported that the resulting structure was highly porous, had a large surface area and had good wetting properties. In their electrochemical characterisation, G-CNT, *a*-MnO_x/G-CNT and *a*-MnO_x all gave a nearly rectangular shaped CV curve at 5 mV s^{-1}. The current density response was higher for *a*-MnO_x/G-CNT than for *a*-MnO_x. Also, G-CNT exhibited a better rate capability at high scan speeds of 200 mV s^{-1}. On the contrary, *a*-MnO_x resulted in a skewed CV curve. They attributed their observations to the higher electrical conductivity and active utilization of Mn in the resulting hierarchical nanostructured composite. The C_s for *a*-MnO_x/G-CNT was 535 F g^{-1}, 140 F g^{-1} for G-CNT and 233 F g^{-1} for *a*-MnO_x. According to their research, such an observation was due to excellent electron transport passage in G-CNT nanostructures and better electrolyte permeation *via* Na^+ and H^+ intercalation. They also concluded that residual oxygen functionalities on G-CNT led to better redox kinetics. The G-CNT had a capacitance retention of 29% whilst that for *a*-MnO_x/G-CNT was 38% and that for *a*-MnO_x was 70% at 200 mV s^{-1}.

2.3.2.5. Carbon nanofibers

Carbon nanofibers (CNFs) have been extensively studied with respect to EDLCs because of their good chemical stability, low resistivity and remarkable conductivity, but exhibit a low C_s due to low surface area [2.123]. CNFs are significantly cheaper to produce and are better electrical conductors than other carbon nanostructured materials such as CNTs [2.79,2.124]. The method of preparation and the particular CNF type influence their ultimate performance. Some of the reported types of CNFs include fishbone, platelet, ribbon, stacked cap carbon and thickened [2.125]. CNFs have a high surface-to-mass ratio of 462 $m^2\ g^{-1}$, excellent physicochemical stability and have an electrical conductivity of 10^2 S cm^{-1} [2.46]. Hence, fibrous carbon nanostructured materials, by virtue of good electrical conductivity, are preferred for high power density output and large surface area for high energy density [2.81]. CNFs are widely used in EDLCs as electrodes and their associated C_s is closely related to their porosity [2.126]. Additionally, CNFs have exteriors made up of many edges and such characteristics give them a wider range of pore size distribution culminating in large surface area and capacitance [2.64]. Their conductivity increases with increase in accessible surface area or micropore volume and this in turn enhances capacitance. Some researchers have synthesised CNF-based materials that incorporate heteroatoms in order to enhance functionalities such as surface wettability. Moreover, there is no consensus in the literature on the specific class of oxygen groups on CNF surfaces that are involved in pseudo-Faradaic redox reactions.

Also, incorporating CNFs in nanostructured networks provides efficient electron transport networks. An *et al.* [2.46] synthesised surface modified RuO_2-CNF composites by using electro-spinning and acid treatment in sequence. They recorded an increased performance of surface modified RuO_2-CNF with a C_s of 224.6 F g^{-1} when the current density was 0.2 A g^{-1}, 80% capacitance retention, energy density in the 26.9 – 21.5 W h kg^{-1} range and a cycling stability of 3000 cycles. They emphasized that the high surface oxygen-containing group content and well distributed RuO_2 were the chief reasons for better performances. Saleem *et al.* [2.79] designed a one chip decoupling capacitor based on vertically aligned CNFs and from their study they reported a slight decrease in both C_s and resistance but the decrease in resistance was larger. In the opinion of Sliwak *et al.* [2.126], encapsulated metal is not accessible to the electrolyte and their pristine CNFs gave a rectangular CV curve. They also point out that CO_2 evolving moieties such as anhydrides, lactonic and carboxylic acids do not contribute to capacitance, and that surface oxygen functionalities on CNFs enhance

capacitance. Graphenated CNFs have also been applied in EDLCs [2.109]. Lekakou *et al.* [2.81] challenge the view that adding pseudo capacitance to fibrous nano-carbon electrodes is advantageous since they may reduce the lifetimes of capacitors.

Wang *et al.* [2.127] reported a 5.6 times enhancement of CNF/MnO_2 to 517 F g^{-1} at a scan speed of 5 mV s^{-1} upon CNT inclusion in a CNT/CNF/MnO_2 nanocomposite. They also achieved a 25% capacitance drop after 1000 cycles with accompanying rectangular CV curves at 200 mV s^{-1}. They attributed their results to the hierarchical nanostructure and high surface area of their materials. Ma *et al.* [2.128] designed a binder-free CNF/G-based EC device with a conductivity of 7.7 S cm^{-1} and they recorded an energy storage of 112 F cm^{-3} at 0.5 A g^{-1} as the current density.

2.3.2.6. Fullerenes

According to Ginsberg [2.129] fullerenes were discovered in the 1980s. Fullerenes have both a conducting and a semiconducting electrical character, are strong and tough [2.3]. Fullerene-based EDLC electrodes are scarce in the open literature but a single C_{60} molecule has capacity to store charge by virtue of its hollow structure [2.94]. In reality it is almost impossible for electrolyte to penetrate the inside of fullerene, C_{60}, because it is non-porous [2.94]. Hence, only the outer surfaces participate in EDLCs. Egashira *et al*. [2.12] used a heat treatment procedure at 900 ℃ to improve the porosity uniformity of fullerene soot. This in turn positively impacted EC behaviour to 58 F g^{-1}. Winkler *et al.* [2.130] loaded Pd on C_{60} to make nanocomposite polymers and reported the allowance of polymer swelling and ion transfer by the structure. They also emphasised C_s dependence on electrolyte and solvent, i.e. 295 F g^{-1} for tetra(methyl)ammonium ion- and 375 F g^{-1} for Cs^+ ion-containing electrolytes.

2.3.2.7. Carbon nano-onions

Carbon nano-onions (CNOs) are spherical nanoparticles that consist of hollow concentric shells of sp^2 bonded graphitic carbons [2.131-2.134]. They are associated with moderate capacitance in the 20 - 50 F g^{-1} range for both aqueous and organic electrolytes [2.82,2.132]. CNOs can maintain capacitive character at high scan rates, i.e. up to 200 mV s^{-1}. The outer shell of CNOs

is easily accessible [2.133] to electrolyte ions. However, CNOs are associated with some setbacks when used as the main electrode material, such as high cost related to their precursors, high temperatures during synthesis and moderate EC performances [2.132]. CNOs are potential enhancers of capacitance as additives to electrode materials due to their small sizes of 5 - 10 nm and surface areas of about 500 m^2 g^{-1} [2.131,2.134]. This allows better dispersion on supercapacitor electrodes and the double layer establishment is on the external planes of the oxohedral structure of carbons, not pores. A closed graphitic surface of minimal defects after vacuum annealing has been reported to be beneficial for fast charging and discharging [2.131]. This enables the suitability of ionic liquid and organic electrolytes at temperature of –50 ºC and –40 ºC, respectively. McDonoug *et al*. [2.131] studied the effects of temperature on capacitive performance of CNOs and observed redox peaks at low synthesis temperature upon using slow scan rates but the peaks disappeared at higher scan rates. They accounted for their results by the fact that high synthesis temperatures remove impurities and improve nano-structural order. The research efforts by Gao *et al.* [2.133] were able to make the inner shells accessible to electrolytes by introducing porosity to outer shells. They managed to achieve more than two-fold C_s and energy density through 6 mol L^{-1} KOH activation. Also, Gu *et al.* [2.135] doubled the C_s upon oxidation of CNOs.

2.3.2.8. Carbon nanorods

Carbon nanorods (CNRs) [2.85] can also be applied as electrode materials of ECs. CNRs are mostly used as additives to MO capacitors [2.136]. Ramakrishnan *et al.* [2.85] synthesised CNR/Co nanocomposites by the electro-spinning method. According to their report, the role of Co was to improve the conductivity of CNRs, Ag/AgCl was the reference electrode, Pt was the counter electrode and electrochemical characterisations were carried out in N_2 saturated 0.5 mol L^{-1} H_2SO_4 solution. In their study, face-centred cubic (FCC) Co nanoparticle sizes were between 20-100 nm and an increase in mass % increased the microporosity and mesoporosity as well as surface area of the nanocomposites. They reported that diffusion restriction culminated in pseudo capacitance behaviour and high conductivity values. Additionally, 10 mass % was the Co percolation threshold in CNRs. Their electrode material had high structural integrity properties as evidenced by absence of Co redox reactions in the CV curve. The C_s decreased with increase in scan rate, i.e. 2-100 mV s^{-1}. CNR-based nanomaterials reported by Sun *et al.* [2.137] displayed a weak current response but the discharge times were still

comparable to those of α-NiS/CNR nanocomposites. The CNRs enhanced the ultimate conductivity of the nanocomposites. The C_s of CNRs directly deposited on G nanosheets was studied with respect to temperature in 1 mol L^{-1} KOH [2.138]. At 60 ºC, the C_s was 830 F g^{-1} and this was attributable to accelerated changes on the electrode surface, i.e. irreversible capacitive activities. From their study they concluded that a combination of G nanosheets and CNRs is associated with low internal resistance and better contact than the individual components. They also noted replacement of N atoms in CNRs with electrolyte O atoms. In a similar study, carbon nanowires exhibited a C_s of 200 F g^{-1} at a charge density of 1 A g^{-1} with good rate capability when high scan rates were applied [2.139].

2.3.2.9. Other forms of carbon nanostructures

Apart from the aforementioned forms of carbon nanostructured materials, there are other types such as carbon nanosheets [2.140,2.141] and carbon yolk shell nanospheres [2.89]. Yolk shell carbon nanospheres, with sizes of 190 nm, shell breadth of 21 nm and yolk sizes of 60 nm with hierarchical nano-porous structures for ECs were reported recently [2.142]. They exhibited an associated C_s of 159 F g^{-1} at a scan rate 10 mV s^{-1}. Li *et al.* [2.89] reported C_s of 583 F g^{-1} at a current density of 1 A g^{-1} in 0.1 mol L^{-1} Na_2SO_4 electrolyte by synthesising a MnO_2/carbon yolk shell structure and MnO_2 hollow spheres.

Carbon nanosheets, prepared from orange peels, have been used as supports for MnO_2 nano-rods [2.140]. This material achieved a high C_s of 656 F g^{-1} and retained over 80% capacitance after 5000 cycles. The physicochemical properties of nanostructured morphologies of nano-sized carbon materials ultimately influence EC performance. Also, combinations of nano-structural variations from both MO and carbon materials in nanocomposites is a worthwhile avenue. Hence, tailoring nanomaterial properties towards high energy storage capabilities without sacrificing power density is crucial [2.143].

2.3.3. Material characterisation techniques

The ultimate performance of carbon-based nanomaterial depends on their physicochemical properties, which are commonly influenced by the various synthetic routes [2.37,2.66]. Carbon

nanomaterials with similar porosity and surface areas might not have similar physicochemical properties, and therefore, ultimately have varied resistivity amongst other electronic properties. Relating the area of porous carbon nanostructures directly to the surface area is an oversimplification. The BET surface area accessed by adsorption of nitrogen molecules may not be available to the electrolyte ions. Also, application of the BET equation gives the total surface area including some surfaces not participating in electrochemical processes [2.37,2.144], and is thus a limitation of this method. Density functional theory (DFT) calculations are more advanced than the BET model but the basis of DFT calculations is simple pore shapes, different from the micropore structure of carbon nanomaterials. Computer modelling and subsequent calculations have the potential to provide a superior understanding of the link between ion adsorption characteristics and EC performances, but in reality carbon nanostructures are too complex for simulations since most models involve numerous assumptions [2.58].

Morphology, surface chemistry and conditions of capacitance measurements influence accessibility of the pores of carbon nanostructured materials [2.37]. Therefore, several other techniques can be employed in physicochemical characterisation of carbon-based nanomaterials and key examples are given. Energy dispersive X-ray spectroscopy (EDX) is used to identify metal catalyst residues or the presence of metal in carbon nanocomposites [2.124]. Scanning transmission electron microscopy (STEM) element mapping is used to investigate the distribution and presence of metal catalyst residues remaining from the synthesis of carbon nanostructured materials [2.8]. Nanomaterial structure and d-spacing can be studied by means of X-ray diffraction (XRD) and atomic force microscopy (AFM) while film thickness can be deduced from ellipsometry [2.145].

2.3.4. Electrochemical characterisation

X-ray photoelectron spectroscopy (XPS) (Figure 2.7a) is applicable in the determination of surface electronic states of nanostructured carbon-based electrode materials [2.42,2.124]. Additionally, the four probe technique can be employed in measuring electrical conductivity [2.62] of carbon nanostructured materials. Ion adsorption sites on carbon nanomaterials can be identified by means of neutron scattering [2.58]. Methods of EC characterisation are not yet fully standardised [2.146] and studies have shown that the two electrode cell is more similar

to the physical configuration. Capacitance and charge transfer mechanisms can be understood by the use of CV (Figure 2.7b). Traditionally, this is done *via* the use of a three electrode scheme made up of a working, counter and reference electrode immersed in relevant electrolytes [2.33]. From this technique, the specific capacitance can be evaluated. A common interpretation, though not always the case in literature, is the direct relationship between decreases in scan rate with increase in capacitance. The electrochemical measurements done by CV are extraordinarily sensitive but the technique does not give an insight on the structural changes associated with redox processes in electrodes [2.40], and such details are vital in material design for ECs. Constant power and current tests are usually involved in evaluating ECs [2.59]; the former allows the determination of energy storage characteristics. The charge/discharge behaviour of electrodes can be studied by a chronopotentiometry method [2.33] (Figure 2.7c) and the technique involves varying the current density while voltage is the dependable variable. Typically, charging curves are almost identical to discharging curves with a slight variation from the initial. This technique is a simple and quick method of determining the capacitance of ECs and it is similar to electrochemical impedance spectroscopy (EIS) at frequencies above 0.1 Hz [2.147]. EIS (Figure 2.7d) is a technique used to measure and analyse the resistance at various interfaces on the device [2.8,2.45,2.62]. This way specific capacitance can be ultimately evaluated [2.33]. Nyquist plots of imaginary impedance (Z_{im}) and real impedance (Z_{re}) obtained by using a frequency range from high to low are useful in this area. A plot through a 45° phase angle resembles the Warburg impedance which implies a high resistance to ion diffusion [2.8,2.33]. Common inference in literature has been that a decrease in Faradaic resistance entails an increase in power density. Self-discharge can be tested by fully charging an EC, followed by disconnection of the terminals, and the voltage is determined across the capacitor plates with a dc voltammeter.

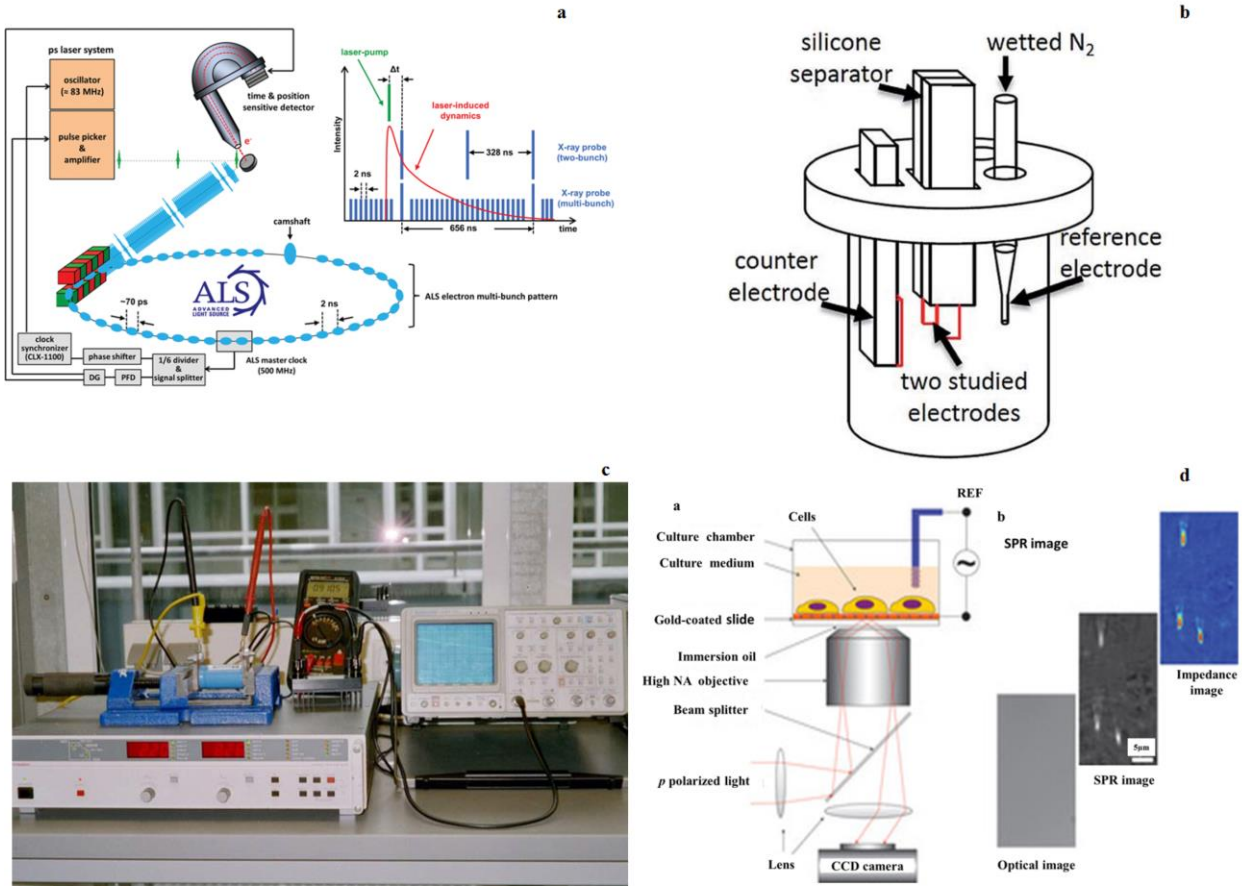

Figure 2.7. Key techniques namely (a) XPS [2.149], (b) CV [2.150], (c) chronopotentiometry [2.148] and (d) EIS [2.151] for ECs.

2.4. Tailoring nanomaterial properties towards high supercapacitance

Some theoretical aspects and possible routes of enhancing supercapacitance of carbon nanostructured materials are discussed in this section.

2.4.1. Theoretical basis

Physical adsorption of solvated ions takes place along the electrode surface [2.28,2.85]. If the peak current is directly proportional to the square root of sweep rate then a diffusion-controlled non-surface adsorption process is involved [2.82]. Large quantities of charge accumulate on

the available exterior area of electrodes. Each electrode-electrolyte inter-phase represents a capacitor and therefore, the whole cell is essentially two capacitors in series.

Therefore, by use of equation (1) [2.37], the overall cell capacitance, C can be determined,

$$\frac{1}{C} = \frac{1}{C_1} + \frac{1}{C_2} \qquad (1)$$

Hence, the double layer capacitance, C_{dl}, of each electrode with dielectric constant, ε, often referred to as relative permittivity, area, A, and thickness, *t*, is given by equation (2) [2.37]:

$$C_{dl} = \frac{\varepsilon A}{4\pi t} \qquad (2)$$

Also, capacitance, C, can be expressed as in equation (3):

$$C = \frac{\varepsilon \varepsilon_0 A}{d} \qquad (3)$$

where d is the distance between the electrode surface and ions in the electrolyte, ε is the relative permittivity, ε_0 is the permittivity in a vacuum and A is the external area of the electrode accessible to the ions [2.44]. Consequently, if *t* is the film thickness then the relative permittivity is given by equation (4) [2.145]:

$$\varepsilon = \frac{Ct}{\varepsilon_0 A} \qquad (4)$$

Assuming that ΔV is a voltage window in volts and *i* is the discharge current density in A g^{-1} functional in a period (Δt), then the specific capacitance (C_s) in F g^{-1} is given by equation (5) [2.43,2.78,2.85,2.86]:

$$C_s = \frac{i\Delta \mathrm{t}}{\mathrm{m}\Delta \mathrm{V}} \qquad (5)$$

Since *i*Δt is voltammetry charge that means dividing the integral area of non-symmetrical CV curves by scan speed is more accurate [2.96]. Columbic efficiency (η) is the ratio of discharging time (t_D) to charging time (t_C) as shown by equation (6) [2.33]:

$$\eta = \frac{t_D}{t_C} \times 100\% \qquad (6)$$

Increasing the energy density requires increasing either the capacitance or the voltage window. The energy density (E_d) in W h kg^{-1} can be calculated by use of equation (7) [2.9,2.68,2.76]:

$$E_d = \frac{1}{2} C_s V^2 \qquad (7)$$

and also if m is mass in mg at that juncture then C_s is given by equation (8) [2.42,2.76]:

$$C_s = \frac{I}{-\left(\frac{\Delta E}{\Delta t}\right) m} \qquad (8)$$

with power density (P) in kW kg^{-1} then power is expressed in equation (9) as [2.42,2.76]:

$$P = \frac{E}{t} \qquad (9)$$

Connected capacitors will have an equivalent resistance associated with them. Sources of ESR take account of:

- Electrical impedance of the fabricated working electrode in terms of shape and form.
- Electrode/current collector interfacial impedance and the degree of cleanliness are important in this regard.
- Ionic resistance since they move in minute pores.
- Ionic impedance through the separator during diffusion.
- Electrolyte resistance to conduct an electric current.

This implies device architectures, as well as type of electrode material, are crucial components of ECs that need careful designing. In addition, connecting N capacitors of capacitance (C) with a cell resistance (R), then the total capacitance (C) is given by equation (10) [2.81]:

$$\mathrm{C} = \frac{C}{N} \qquad (10)$$

In such a set-up, the overall resistance comes from individual cells. A better contact in typical devices plays a critical role in nullifying high resistance problems. Compaction pressure used in electrode preparation reduces resistivity through contact improvements and reduction of path length. Thin films also reduce equivalent series resistance in this regard. However, excessive adherence may reduce the electrolyte concentration below desirable thresholds in the pores. This means material packaging on electrodes will affect the overall charge stored no matter how good the nature of the carbon nanomaterial. The charge (Q) stored by each capacitor is given by equation (11) [2.77]:

$$Q = CV \qquad (11)$$

2.4.2. Porosity of carbon nanostructured materials for electrodes

General prerequisites for a good electrode material include suitable pore size ranges of numerous nm, ease of fabrication and high electrical conductivity [2.12,2.48,2.49,2.64]. High C_s with respect to electrical conductivity can be achieved through designing of devices with appropriate electron conductive pathways [2.148]. High electrode electronic conductivity plays a role in distribution and collection of electron current [2.29].

Various aspects related to typical carbon nanostructured materials such as defect intensity, dimensions with respect to chirality, surface functional groups and metal impurities can influence electron transfer kinetics in a complicated way [2.149]. Imperfections, carbon orientation and phases in nanostructured carbons can act as sites of electron transfer. A large crystalline structured material with large d-spacing would be expected to have high charge accumulation abilities [2.94,2.143]. In EDLCs, high active electrode surface areas, typically greater than 1500 $m^2\ g^{-1}$, and tiny distances between charges theoretically implies high capacitance values [2.37]. Most of the literature seems to reach a consensus on the argument that the BET surface area is not directly related to the electrochemically effective surface area [2.12]. A high surface area limits the volumetric capacitance [2.150]. In addition, C_s is not always proportional to the BET surface area because not all micropores, i.e. < 2 nm, are available for electrolyte permeation. This is mainly because of either sealed narrow pores or bottle neck pores [2.72,2.151]. In practice, studies that involved simultaneous increase in pore size and specific surface area were not able to raise C_s [2.58]. Therefore, with most carbon

nanostructured materials containing pores that cannot be reached by the electrolyte ions [2.29], the selection of a suitable carbon nanostructured materials depends mainly on either the required performance or electrolyte choice [2.28]. This is mainly because intercalation of electrolyte ions tends to be amongst the main factors that drive capacitive behaviour.

Electrolyte ion penetration into carbon nanomaterial pores depends on structural parameters, surface properties and pore size distribution [2.37]. Uniform pore size of electrode materials has been associated with clear EC behaviour [2.12]. Additionally, porous carbon nanostructured materials for use in EDLCs are the most studied due to their availability and low price, amongst other reasons [2.150]. Porous nano-based structural designs facilitate rapid ion/electron transfer and offer an enhanced active surface [2.86]. Electrolyte ion penetration into carbon nanomaterial pores, especially for organic electrolytes, is subject to ion sieving effects and size, which eventually has an effect on capacitance [2.37,2.58]. Pores sizes < 0.5 nm were reported to be unavailable to hydrated ions [2.56]. A nanoporous carbon with a large portion of pore volume and pore sizes ranging between 1-5 nm is more appropriate [2.29]. Capacitance can be optimised by use of pores which are twice the size of solvated ions [2.59]. Additionally, charge can also be stored in pores with sizes smaller than those of solvated ions and this is facilitated with the distortion of the ion solvation shell [2.58,2.152,2.153]. Solvation shell distortion depends on both the electrolyte ion and solvent [2.58]. Since intercalation is also significant in carbon nanostructures [2.58], this means electrolyte ions approach the surface of nanostructured carbons more closely [2.59]. Carbon nanomaterials with pore diameters less than 1 nm typically have discharge currents of less than 100 mA cm^{-1} especially upon use of organic electrolytes [2.29]. Large diameters, on the other hand, have current densities typically of not more than 500 mA cm^{-1} with minimum capacitance loss. Furthermore, increasing porosity of the nanostructured carbon may be associated with a decrease in electro-conductivity due to non-compatible conductive pathways [2.150]. Appropriate pore sizes are important in quick ion diffusion and mass transfer [2.154].

Mesopores (2 - 50 nm) of nanocarbon materials participate in transportation of electrolyte ion to micropores [2.142], i.e. act as transport channels [2.133], and this way they mainly affect rate capability of ECs [2.156]. This means wider mesopores favour electrolyte ion diffusion [2.37] and high rate capability. On the other hand, the function of micropores in charge storage is to house electrolyte ions [2.142]. The micropores enhance surface area [2.150], surface to volume ratio of carbon nanostructures and they also play a crucial role in the ion selectivity

during the double layer formation [2.37]. In addition, pores large enough to house electrolyte ions are preferred for high electro-sorption efficiency. From the above views, it means the contributions of mesopores and micropores towards enhanced charge storage of ECs are interlinked. In fact, there have been reports on the high effectiveness of micropores in double layer formation whilst mesopores increase accessibility of micropores to electrolytes [2.37,2.133,2.142,2.150,2.155]. It is also important to emphasize that charges stored in pores of a given nano-carbon based electrode have an upper limit [2.23]. Excessive existence of micropores limits electrolyte ions transportation towards the electrode, thus causing ohmic resistance [2.150]. Micropores tend to decrease C_s when the electrolyte cationic sizes are large [2.156]. In fact, adsorption/desorption becomes a surface process since cations cannot fit into the small micropores [2.37] whilst macropores (> 50 nm) allow ion buffering [2.142], i.e. act as transport paths [2.37]. Based on the aforementioned views, different pore sizes have different roles in charge storage. In designing nanostructured carbons, the electrolyte ion solvation energy, electrolyte solvent system, electrolyte ion size and carbon nanomaterial pore sizes need to be matched towards high capacitance [2.59,2.152]. A mismatch will render some pores of carbon nanomaterials inaccessible to the electrolyte and this means poor utilisation of the electrolyte ions in forming the double layer [2.152]. Also, with the need to optimise pore sizes for the operational mode and electrolyte in terms of ion size and mobility [2.132,2.143], the implication is that the subject of pore sizes in ECs is a critical area that still requires focussed studies.

Several approaches can be carried out to tailor the porosity of electrode nanomaterials in order to enhance their capacitance. For example, carbonate and hydroxide co-precipitation approach to nanomaterial based electrodes have higher surface areas with suitable pore size distribution [2.66]. This is advantageous in that it increases the self-discharge stability and lowers current leakages. Such compensations imply high energy storage capacity. The characteristics of ECs, especially those derived from the nanostructure of the carbon material, highly depend on the concentration of defects, average pore sizes, pore shapes and distribution [2.58,2.59]. The norm is that a narrow pore size distribution is preferred to those broadly distributed because the relative increase in surface area is better and this means energy storage capabilities can easily be controlled [2.157]. Hence, nanotechnology enables fabrication of novel carbon nanomaterials, nano-structures and nano-devices with tailored properties for EDLCs [2.18]. In fact, from the electrode point of view, energy storage and power delivery rate of nano-structural carbons can be enhanced by tuning their porosity to match the electrolyte ion size

[2.71,2.75,2.143,2.151]. For example, in a recent study, pores were tailored from microporosity (0.6 nm) to mesoporosity (40 nm) by varying the thickness of silica on yolk shell carbon nano-spheres [2.142].

In addition, nanostructured carbon nanomaterial can be tailored to be pseudocapacitive by the introduction of heteroatoms, such as nitrogen and phosphorus [2.23,2.97,2.123,2.155,2.158,2.159], oxygen-containing surface moieties including carboxyl and hydroxyl groups [2.91], and the use of redox materials such as MO and polymers. The pseudo-capacitive character is associated with charge/mass transfer between the electrode material and electrolyte ions [2.150]. Heteroatoms modify the electron donor-acceptor properties of carbon nanostructures [2.159]. Oxygen-containing moieties are naturally acidic and therefore induce electron acceptor features to the nanomaterials of carbon but they bring detrimental outcomes in organic electrolytes [2.159]. For example, Gu *et al*. [2.135] reported undesirable interactions between the electrolyte and CNO surface functionalities. The diminishing consequences were noticeable and highly undesirable current leakages with respect to solvent used. This is due to associated high surface activities culminating in irreversible reactions between oxygen and electrolyte ions [2.150]. Hence, oxygen-containing groups can be sites of electrolyte decomposition and reduce the overall cycle stability of the device especially at high scan rates [2.53]. Surface functionalities also enhance the wettability of carbon nanostructures [2.46]. Wettability is increased due to an increase in the quantity of hydrophilic polar regions on the working electrode surface [2.123]. High capability for charge accumulation at the interface depends on availability and wettability of ideal pore dimensions. The amount and nature of functionalisation of the carbon nano-forms, in this view, can be tailored to suit a particular electrolyte in EDLCs [2.97].

2.4.3. Carbon nanomaterial activation

One key example of tuning porosity in carbon nanostructures is by physical or chemical activation, which enriches pore networks [2.160]. Activation of carbon nanostructures *via* traditional methods has limited pore size control, however, with the development of template synthesis methods, better control capabilities have been achieved, i.e. in the 2-10 nm range [2.59] . Examples of physical activation include O_2, CO_2 and steam whereas the chemical approach is inclusive of KOH, HNO_3, H_2SO_4 and $ZnCl_2$. Chemical activation results in high

yields, reduced time, high surface area and large pore volume even though it is associated with some disadvantages. For instance, in KOH activation, special attention needs to be given to the amount used as well as the activation temperature [2.71,2.161]. Jäckel *et al*. [2.132] activated CNOs with 6 mol L^{-1} KOH and achieved 100% surface area enhancement with a corresponding 200% C_s increase.

Electrochemical oxidation of carbon nanostructures is also a possible way of enhancing capacitance [2.134]. This is due to the increased electrode surface area from opening and breaking of graphitic units in layers as well as the creation of a Faradaic current from reactions of chemical moieties located at the edges.

Additionally, introduction of electro-active metallic particles in nanostructured carbon materials can positively modify the pore size distribution [2.64]. The MO nanoparticles are useful in supercapacitors and variable oxidation states of transition metals contribute to their characteristic fast redox reactions at the surface of active nanomaterials in supercapacitors [2.8,2.78]. Hence, there are more articles on MO-based supercapacitors than there are on nano-carbons [2.33]. This means the performance of carbon nanostructures still needs special attention and MOs can be useful for their advancement. Nano-structuring of the capacitor carbon electrode material increases charge storage efficiency, electrical energy and electrode stability against induced swelling from ion uptake. However, in some cases heteroatoms can facilitate degradation of supercapacitors upon cycling [2.97].

Another important electrode material related parameter in storing energy and homogenization of an electric field is the relative permittivity. Reducing dielectric loss and maintaining the relative permittivity of a system is preferred. This can be achieved through ways like varying electron densities around the carbon nanostructured materials in the electrode active material. Changing transition metals used in coating carbon surfaces is a possible way of attaining this goal. In this view, creating sophisticated surface morphologies and utilisation of Faradaic materials are possible ways of enhancing energy density [2.44,2.71]. Nitrogen-doping is a possible way of changing the electronic structure of nanostructured carbon materials.

2.4.4. Nitrogen-doping of carbon nanostructured materials

Nitrogen is the best n-type dopant of carbon nanomaterials [2.162], because it has a similar size to carbon, and its inclusion in the carbon lattice is related to two main roles as far as ECs are concerned. Firstly, nitrogen atoms act as electron donors in the framework since each atom has five outermost shell electrons and this shifts the Fermi level towards the valence band in the nanostructured carbon [2.84]. Secondly, they introduce nitrogen and oxygen functionalities resulting in an altered charge storage mechanism [2.163,2.164]. However, nitrogen-containing moieties from N-doping [2.98] may introduce instability during recycling [2.123]. Nonetheless and by and large, N-doping in nanostructured carbon has shown improvement in C_s of supercapacitors [2.21]. This is due to their corresponding tailored physicochemical properties [2.113] such as increased wettability [2.159], mass transfer efficiency [2.123], electron transfer rate [2.150, 2.158], enhanced electron donor capability [2.151], stability and pseudo capacitance [2.97], as well as decrease in ESR [2.23]. Literature suggests that nitrogen-rich carbon nanostructured materials synthesised at high temperatures results in pyrrolic, pyridinic, quaternary and pyridinic-nitrogen oxides [2.113,2.158]. Pyridinic and pyrrolic nitrogen have unpaired p electrons that are available for the aromatic π-system and neighbouring species. Hence, they are more electro-catalytically active than quaternary sites. Furthermore, low carbonisation temperature with a nitrogen-containing precursor can preserve high nitrogen content [2.123]. In N-doped carbon nanomaterials, pseudocapacitance is due to functionalities with negative charges found at the boundaries of the graphitic network such as the pyridinic and pyrrolic arrangements [2.97,2.158].

The work reported by Hulicova-Jurcakov *et al.* [2.150] demonstrated that surface area and porosity of nitrogen-enriched carbon materials are not the only crucial parameters for high performance electrode materials. They also highlighted the effectiveness of ultra-micropores, i.e. < 0.7 nm in charge electro-sorption processes but such pores are not detected by nitrogen in textural analysis. This is probably part of the reason why BET surface area tends to be independent of capacitive character of N-doped carbon nanostructured materials. This observation corroborated with the conclusions by Yun *et al.* [2.155] in which they observed an increase in both micro-porosity and C_s upon N-doping but with no significant increase in BET surface area. The work recently reported by Yen *et al.* [2.113] on pyridinic N-doping in epitaxial G nanowalls with a 3D architecture reached a C_s of 991.6 F g^{-1}. Song *et al.* [2.151] developed a hierarchical N-doped carbon with micropores pierced on mesoporous walls. Their

unique structure was typically of high surface area of 1344 cm^2 g^{-1}, mesopore sizes of 4.6 nm and micropores sizes of 0.7, 097 and 1.61 nm drilled walls. Their electrodes displayed rectangular CV curves and C_s of 325 F g^{-1} in 1 mol L^{-1} H_2SO_4 as well as a broadened redox peak due to 7.51% N_2 content.

Nitrogen has been reported to reduce oxygen content in N-doped G synthesised *via* a NH_3-assisted hydrothermal technique [2.165]. In that report, 7.2% nitrogen content and a supreme C_s of 144.6 F g^{-1} was attained. In addition, Chen *et al.* [2.67] similarly reported N-doped phenolic resin-based carbon with a high C_s of 216 F g^{-1} at 0.1 A g^{-1} current density, and 10000 cycle stability. Their explanation was related to the mesopore channels and interconnections enhancing C_s. Chen *at al.* [2.108] recorded a C_s of 139 and 100 F g^{-1} at current densities of 3 and 6 A g^{-1}, respectively. The C_s enhancement was explained by the adsorption/desorption improvement due to positive N^+ introduced in their G nanosheets from *p*-phenylene diamine by electrophoretic deposition. In the report by Yuanyun *et al.* [2.160] novel 3D N-doped hierarchical porous carbon/G synthesised from beer yeast cells and graphite oxide attained a conductivity of 3096 S m^{-1}, a surface area of 3108.7 m^2 g^{-1} and C_s of 318 F g^{-1} at 1 A g^{-1} in tetraethylammonium tetrafluoroborate electrolyte. The direct proportionality between sweep rate and topmost currents noted by Hou *et al.* [2.141] by using N-doped G nanosheets was attributed to a capacitive process independent of diffusion and mesoporosity. They reported 239 F g^{-1} as C_s when the current density was 0.5 A g^{-1}.

Salinas-Torres *et al.* [2.97] reported nitrogen-containing nanostructures synthesised from carbonisation of polyaniline (PANI)-containing activated CNF that were comparable to commercial activated carbon-based supercapacitors with better capacitance retention than pristine CNF. Ordered nitrogen-doped mesoporous CNF arrays with hierarchical structure synthesized *via* a hard templating technique coupled with a surfactant-oriented self-assembly was reported to achieve a C_s of 264 F g^{-1} [2.123]. The associated capacitance retention was 86%, over 10000 cycle stability in 1 mol L^{-1} H_2SO_4, a pore volume of 2.35 cm^3 g^{-1}, surface area of 1030 m^2 g^{-1} and 6.7% nitrogen content. Similarly, a novel electro-spinning synthesis approach to porous N-doped CNF from polyacrylonitrile (PAN)-based solution was reported to achieve 5.4% doping, 94.6% capacitance retention after 2000 cycles and a C_s of 302 F g^{-1} in 6 mol L^{-1} KOH and at a current density of 0.2 A g^{-1} [2.67].

The role of particular nitrogen functional groups in supercapacitors is still to be fully understood [2.113,2.162]. Theoretical studies suggest that lactams and imides contain

electrochemically active nitrogen groups [2.150]. Imides and amines bonded onto the nano-carbon structures do not affect electron donor characteristics. Presently, there have been suggestions that quaternary nitrogen and oxidised nitrogen do not participate in pseudocapacitance [2.97] but earlier reports by authors such as Hulicova-Jurcakova *et al.* [2.158] suggested that they enhance capacitance. Some researchers have opted for the route of depositing nitrogen-containing groups on the surface rather than on the bulk *via* polymers such as polypyrrole [2.159]. Coating carbon with nitrogen enhances both surface chemistry and electrode impedance due to diffusivity and surface charge resistance. For instance, Lota *et al.* [2.93] enhanced cycleability and electrical conductivity of carbon materials by synthesizing CNT-polypyrrole based composites. Polypyrrole provides a flexible skeleton adaptable to any form of mechanical stress. In their work they reported good cycle stability, 99.6% efficiency and an increase in C_s upon addition of CNTs to polypyrrole. They also highlighted the influence of carbon nanomaterial type, dimensions and ratio in typical nanocomposites on charge storage of EDLCs. From the work of Liu *et al.* [2.134], the N-CNO capacitance reliance on scan rate was noted. They attributed such outcomes to high electrical conductivity of the mesoporous structure that allows fast contact of electrolyte ions to the electrode surface and their admittance into inner pores, and insignificant contact impedance of the N-CNO framework. They also observed a decrease in C_s due to resistance introduced by N-CNO edge locations with oxygen functionalities. Negative effects associated with coating nanostructured carbon surfaces include the blocking of the pores by the polymer, swelling and shrinking of the polymer culminating in a decrease in cycle stability [2.159].

Relative to N-doping, B-doping induces more defects in the carbon framework through the induction of an uneven charge distribution facilitating charge transfer between neighbouring carbon atoms [2.110]. This enhances electrochemical properties. Also, unlike in N-doping, the oxygen content in synthetic carbon nanostructures increases upon B-doping [2.110,2.163]. Niu *et al.* [2.110] reported a C_s of 172.5 F g^{-1} at a current density of 0.5 A g^{-1}, cycle strength of 96.5% after 5000 cycles and 80% capacitance increase upon B-doping of G.

2.4.5. Binders

Bonding of carbon nanomaterials to the current collector is one of the major problems accompanying their use [2.29] in supercapacitors. Mechanically strong and electrically

conductive electrode materials with stable structures are vital for repeatability of electrochemical results. A good contact implies reduced internal resistance. The ECs contain only small amounts of active material [2.45] and usually require a binder material to improve contact with the current collector. Use of small amounts of non-conductive polymers (5 - 10 mass%) as binders in nanocomposites can be prolific in terms of obtaining a stable matrix [2.32,2.37]. Polymer binders help attach electrode material to the substrate [2.43]. Small amounts and good distribution will minimise chances of compromising conductivity of carbon nanomaterial-based electrodes [2.166]. Metal binders can enhance electronic properties of capacitors as well. The hydrophilic nature of the surface strongly enhances electrolyte penetration into the pores of the material. Hence, a tight contact between electrode material and current collector will be achieved. It is also important to use a suitable current collector for the electrolyte system and the voltage range, i.e. non-corroding [2.37,2.75].

2.4.6. Ideal EDLC behavior

The ideal behaviour of EDLC electrodes is a rectangular shape in the CV curve [2.75,2.77,2.150]. This means the sign of the current is reversed instantaneously when the voltage sweep is reversed. This suggests great reversibility and less Ohmic loss, i.e. high conductivity [2.64]. A delay in potential during reversing the potential sweep means there will be a kinetically slow electron transfer reaction during charging of a pseudocapacitor. Most carbon nanomaterials become less capacitive and more resistive at scan rates above 20 mV s^{-1}, i.e. deviation from square CV curve [2.131]. The decrease in C_s with increase in scan rate is linked to poor electrical conductivity [2.51]. A non-rectangular CV form is mostly attributed to the contribution of electrode species pseudocapacitance character [2.62]. Other sources of deviations from rectangular CV include low conductivity, low mechanical strength, limited access of the electrolyte into the material pores and irreversible charge transfer [2.93]. Additionally, a two electrode cell better imitates EC performance of a real capacitor but ideally ECs must supply equal amounts of energy despite operational conditions [2.150]. This makes the study of capacitance retention at high current loads a significant practise.

2.4.7. Electrolytes

Electrolytes are also important in the performance and functioning of EDLCs. It is crucial to choose an appropriate electrolyte system that suits the pore sizes of the synthetic carbon electrode material [2.12]. Interfacial chemistry between nanostructured carbon-based electrodes and electrolytes still requires more focussed studies. The voltage window is restricted by the electrolyte decomposition temperature at elevated potentials [2.44,2.50,2.68]. The importance of electrolyte temperature on carbon-based nanomaterials for EDLCs was recently mentioned in the work reported by Chen *et al*. [2.73]. They observed a decline in C_s upon drop of electrolyte temperature and attributed this effect to increase in charge transfer resistance. If EDLCs are to be suitable for colder regions of the world then temperature needs to be critically considered in the development of carbon nanomaterial-based devices. Ion mobility and electrochemical stability, i.e. potential range of usage, are vital in this regard [2.81]. Electrolyte concentration should be large enough relative to available area [2.14]. If electrostatic interactions are operative in EDLCs then surface charges and pH of the electrolyte should impact charge storage [2.149].

2.5. Conclusion

A combination of factors associated with electrode design, fabrication methods, electrolyte ion dimensions, solvent characteristics and physicochemical properties of carbon nanostructured materials influence the ultimate efficiencies of ECs. Several carbon nanostructured materials have high potential in the design of unique ECs with decent electrochemical capacitance capability. Chemical activation, template synthesis methods and N-doping are promising ways of tailoring physicochemical properties of carbon nanostructured materials for EC applications. In addition, architectures and morphologies that create good electron transport pathways, lower equivalent series resistance, enhance electro-active area and porosity of the carbon nanostructured material enriches their suitability in ECs.

Carbon nanomaterial/substrate adhesion is influential to long cycle stability. A critical consideration of nanostructured carbon material use in ECs is a lucrative approach in enhancing their energy densities and this ultimately lowers the associated costs of the technology. This goes a long way in their wide application in industry and their commercialisation.

Acknowledgements

Edwin Tonderai Mombeshora thanks the India, Brazil and South Africa (IBSA) Nanotechnology Initiative for the award of a study bursary. The authors wish to extend their sincere gratitude to the University of KwaZulu-Natal (UKZN), UKZN Nanochemistry Research group and National Research Foundation (NRF). We are also thankful to Prof Tony Ford and Prof Bice Martincigh for their critical comments and for proofreading the manuscript.

References

2.1. Du C, Pan N. Carbon nanotube-based supercapacitors. *Nanotechnology Law and business* 2007; **4**:569-676.

2.2. Bortolini M, Gamberi M, Graziani A. Technical and economic design of photovoltaic and battery energy storage system. *Energy Conversion and Management.* 2014; **86**:81-92.

2.3. Amin M, Stringer J. The electric power grid: Today and tomorrow. *Harnessing Materials for Energy* 2008; **33**:399-407.

2.4. Cotterman T. Energy storage technolgies: transforming America's intelligent electrical infrastructure. *Wise Intern* 2013:19-24.

2.5. Mahlia TMI, Saktisahdan TJ, Jannifar A, Hasan MH, Matseelar HSC. A review of available methods and development on energy storage; technology update. *Renewable and Sustainable Energy Reviews* 2014; **33**:532-545.

2.6. Ren G, Ma G, Cong N. Review of electrical energy storage system for vehicular applications. *Renewable and Sustainable Energy Reviews* 2015; **41**:225-236.

2.7. Antonucci PL, Antonucci V. Electrochemical Energy Storage. 2011 [cited 2014 10 October]; Available from: http://www.intechopen.com/books/energy-storage-in-the-emerging-era-of-smart-grids/electrochemical-energystorage

2.8. Li S-M, Wang Y-S, Yang S-Y, Liu C-H, Chang K-H, Tien H-W, Niann-Tsyr W,

Chen-Chi M. MaChi-Chang H. Electrochemical deposition of nanostructured manganese oxide on hierarchically porous graphene–carbon nanotube structure for ultrahigh-performance electrochemical capacitors. *Journal of Power Sources* 2013; **225**:347-355.

2.9. Kim M, Hwang Y, Kim J. Super-capacitive performance depending on different crystal structures of MnO_2 in graphene/MnO_2 composites for supercapacitors. *Journal of Materials Science* 2013; **8**:7652-7663.

2.10. Hadjipaschalis I, Poullikkas A, Efthimiou V. Overview of current and future energy storage technologies for electric power applications. *Renewable and Sustainable Energy Reviews* 2009; **13**:1513–1522.

2.11. Divya KC, Østergaard J. Battery energy storage technology for power systems—An overview. *Electric Power Systems Research* 2009; **79**:511-520.

2.12. Egashira M, Okada S, Korai Y, Yamaki J-I, Mochida I. Toluene-insoluble fraction of fullerene-soot as the electrode of a double-layer capacitor. *Journal of Power Sources* 2005; **148**:116–120.

2.13. Christen T, Carlen MW. Theory of Ragone plots. *Journal of Power Sources* 2000; **91**:210–216.

2.14. Ko¨tz R, Carlen M. Principles and applications of electrochemical capacitors. *Electrochimica Acta* 2000; **45**:2483–2498.

2.15. Li J, Cheng X, Shashurin A, Keidar M. Review of electrochemical capacitors based on carbon nanotubes and graphene. *Graphene* 2012; **1**:1-13.

2.16. Liang M, Luo B, Zhi L. Application of graphene and graphene-based materials in clean energy-related devices. *International Journal of Energy Research* 2009; **33**:1161-1170.

2.17. Mansoori A. Advances in atomic and molecular nanotechnology. *UN-APCTT Tech Monitor* 2002:53-59.

2.18. Rossi M, Cubadda F, Dini L, Terranova ML, Aureli F, Sorbo A, Passeri D. Scientific basis of nanotechnology, implications for the food sector and future trends. *Trends in Food Science and Technology* 2014:1-22.

2.19. Foley RW, Wiek A. Scenarios of nanotechnology innovation vis-à-vis sustainability challenges. *Futures* 2014; **64**:1-14.

2.20. Kreyling WG, Semmler-Behnke M, Chaudhry Q. A complementary definition of nanomaterial. *Nano Today* 2010; **5**:165-168.

2.21. Hussain S, Amade R, Jover E, Bertran E. Nitrogen plasma functionalization of carbon nanotubes for supercapacitor applications. *Journal of Materials Science* 2013; **48**:7620-7628.

2.22. Hwang SK, Lee JM, Kim S, Park JS, Park H, Ahn CW, Lee KJ, Lee T, Kim SO. *Nano Letters* 2012; **12**:2217-2221

2.23. Zhou J, Li N, Gao F, Zhao Y, Hou L, Xu Z. Vertically-aligned BCN nanotube arrays with superior performance in electrochemical capacitors. *Scientific reports* 2014; **4**:1-6.

2.24. He X, Shi H. Size and shape effects on magnetic properties of Ni nanoparticles. *Particuology* 2012; **10**:497-502.

2.25. Oltulu M, Şahin R. Pore structure analysis of hardened cement mortars containing silica fume and different nano-powders. *Construction and Building Materials* 2014; **53**:658-64.

2.26. Wang J, Huang Z, Duan H, Yu S, Feng X, Wang G, Zhang W, Wang T. Surface stress effect in mechanics of nanostructured materials. *Acta Mechanica Solida Sinica* 2011; **24**:52-82.

2.27. Nasibi M, Shishesaz MR, Sarpoushi MR, Borhani MR, Ahmad Z. Fabrication of a novel graphene nano-sheet electrode embedded with nano-particles of zirconium dioxide for electrochemical capacitors: Ions-redeposition on the surface of nanoporous electrode. *Materials Science in Semiconductor Processing* 2015; **30**:625-630.

2.28. Shukla AK, Banerjee A, Ravikumar MK, Jalajakshi A. Electrochemical capacitors: Technical challenges and prognosis for future markets. *Electrochimica Acta* 2012; **84**:165-173.

2.29. Burke A. Ultracapacitors: why, how, and where is the technology. *Journal of Power Sources* 2000; **91**:37–50.

2.30. Kiamahalleh MV, Zein SHS. Multiwalled carbon nanotubes based nanocomposites for supercapacitors: A review of electrode materials. NANO: *Brief Reports and Reviews* 2012; **7**:1-27.

2.31. Dsoke S, Fuchs B, Gucciardi E, Wohlfahrt-Mehrens M. The importance of the electrode mass ratio in a Li-ion capacitor based on activated carbon and $Li_4Ti_5O_{12}$. *Journal of Power Sources* 2015; **282**:385-393.

2.32. Chang L, Wei W, Sun K, Hu YH. 3D flower-structured graphene from CO_2 for supercapacitors with ultrahigh areal capacitance at high current density. *Journal of Materials Chemistry A* 2015; **3**:10183-7.

2.33. Chen S-M, Ramachandran R, Mani V, Saraswathi R. Recent advancements in electrode materials for the high performance electrochemical supercapacitors: A review. *International Journal of Electrochemical Science* 2014; **9**:4072-4085

2.34. Hu C, Qu W, Rajagopalan R, Randall C. Factors influencing high voltage performance of coconut char derived carbon based electrical double layer capacitor made using

acetonitrile and propylene carbonate based electrolytes. *Journal of Power Sources* 2014; **272**:90-99

2.35. Winter M, Brodd RJ. What Are batteries, fuel cells, and supercapacitors? *Chemical Reviews* 2004; **104**: 4245-4269.

2.36. Scherson DA, Palencsár A. Batteries and electrochemical capacitors. *The Electrochemical Society Interface* 2006:17-22.

2.37. Pandolfo AG, Hollenkamp AF. Carbon properties and their role in supercapacitors. *Journal of Materials Science* 2006; **157**:11-27.

2.38. Chen H, Cong TN, Yang W, Tan C, Li Y, Ding Y. Progress in electrical energy storage system: A critical review. *Progress in Natural Science* 2009; **19**:291-312.

2.39. Bujlo P, Pasciak G, Chmielowiec J, Sikora A. Experimental evaluation of supercapacitor-fuel cell hybrid power source for HY-IEL scooter. *Journal of Energy* 2013; **2013**:1-5.

2.40. Scherson DA, Palencsár A. Batteries and electrochemical capacitors. *The Electrochemical Society Interface* 2006:18-22.

2.41. Beaudin M, Zareipour H, Schellenberglabe A, Rosehart W. Energy storage for mitigating the variability of renewable electricity sources: An updated review. *Energy for Sustainable Development* 2010; **14**:302-314..

2.42. Deng L, Zhang G, Kang L, Lei Z, Liu C, Liu Z-H. Graphene/VO_2 hybrid material for high performance electrochemical capacitor. *Electrochimica Acta* 2013; **112**:448-457.

2.43. Wu M-S, Chan D-S, Lin K-H, Jow J-J. A simple route to electrophoretic deposition of transition metal-coated nickel oxide films for electrochemical capacitors. *Materials Chemistry and Physics* 2011; **130**:1239-45.

2.44. Leonard KC, Suyama WE, Anderson MA. Improvement of electrochemical capacitor electrodes using SiO_2 nanoparticles. *Electrochimica Acta* 2011; **56**:10137-10144.

2.45. Chen C-H, Tsai D-S, Chung W-H, Lee K-Y, Chen Y-M, Huang Y-S. Electrochemical capacitors of miniature size with patterned carbon nanotubes and cobalt hydroxide. *Journal of Power Sources* 2012; **205**:510-515.

2.46. An G-H, Ahn H-J. Surface modification of RuO_2 nanoparticles-carbon nanofiber composites for electrochemical capacitors. *Journal of Electroanalytical Chemistry* 2015; **744**:32-36.

2.47. Zhao H, Burke A. Fuel cell powered vehicles using supercapacitors: Device characteristics, control strategies, and simulation results. 2010 [cited 2015 23 July 2015]; 1-24.

2.48. Hong Z, Chunming L. Relationship between trace Mn and the pitting behavior of aluminum foil used for high voltage electrolytic capacitors. *Rare Metal Materials and Engineering* 2014; **43**:1031-1036.

2.49. Kim JW, Wada T, Kim SG, Kato H. Sub-micron porous niobium solid electrolytic capacitor prepared by dealloying in a metallic melt. *Materials Letters* 2014; **116**:223-226.

2.50. Romann T, Oll O, Pikma P, Kirsimäe K, Lust E. 4-10 V capacitors with graphene-based electrodes and ionic liquid electrolyte. *Journal of Power Sources* 2015; **280**:606-611.

2.51. Liu G-J, Fan L-Q, Yu F-D, Wu J-H, Liu L, Qiu Z-Y, et al. Facile one-step hydrothermal synthesis of reduced graphene oxide/Co_3O_4 composites for supercapacitors. *Journal of Materials Science* 2013; **48**:8463-8470.

2.52. Li S, Wen J, Mo X, Long H, Wang H, Wang J, et al. Three-dimensional MnO_2 nanowire/ZnO nanorod arrays hybrid nanostructure for high-performance and flexible supercapacitor electrode. *Journal of Power Sources* 2014; **256**:206-211.

2.53. Du X, Guo P, Song H, Chen X. Graphene nanosheets as electrode material for electric double-layer capacitors. *Electrochimica Acta* 2010; **55**:4812-4819.

2.54. Miller JR, Simon P. Fundamentals of electrochemical capacitor design and operation. *The Electrochemical Society Interface* 2008:31-32.

2.55. Miller J. A brief history of capacitors. *Batteries and Energy Storage Technology* 2007:61-78.

2.56. Simon P, Gogotsi Y. Materials for electrochemical capacitors. *Nature Materials* 2008; **7**:845-854

2.57. Pandolfo AG, Hollenkamp AF. Carbon properties and their role in supercapacitors. *Journal of Power Sources* 2006; **157**:11-27.

2.58. Gu W, Yushin G. Review of nanostructured carbon materials for electrochemical capacitor applications: advantages and limitations of activated carbon, carbide-derived carbon, zeolite-templated carbon, carbon aerogels, carbon nanotubes, onion-like carbon, and graphene. *Wires Energy Environmental* 2013:1-50.

2.59. Simon P, Burke A. Nanostructured carbons: double-layer capacitance and more. *The Electrochemical Society Interface* 2008:38-43.

2.60. Srivastava RK, Xingjue W, Kumar V, Srivastava A, Singh VN. Synthesis of benzimidazole-grafted graphene oxide/multi-walled carbon nanotubes composite for supercapacitance application. *Journal of Alloys and Compounds* 2014; **612**:343-348.

2.61. Li S-M, Wang Y-S, Yang S-Y, Liu C-H, Chang K-H, Tien H-W, Wen N-T, Ma C-C. MHu C-C. Electrochemical deposition of nanostructured manganese oxide on hierarchically porous grapheneecarbon nanotube structure for ultrahigh-performance electrochemical capacitors. *Journal of Power Sources* 2013; **225**:347-355.

2.62. Battumur T, Ambade SB, Ambade RB, Pokharel P, Lee DS, Han S-H, Lee W,

Lee S-H. Addition of multiwalled carbon nanotube and graphene nanosheet in cobalt oxide film for enhancement of capacitance in electrochemical capacitors. *Current Applied Physic*s 2013; **13**:196-204.

2.63. Vazquez S, Lukic SM, Galvan E, Franquelo LG, Carrasco JM. Energy storage systems for transport and grid applications. *IEEE Transactions on industrial electronics* 2010; **57**:3881-3895.

2.64. Gallegos AKC, Rinc´on ME. Carbon nanofiber and PEDOT-PSS bilayer systems as electrodes for symmetric and asymmetric electrochemical capacitor cells. *Journal of Power Sources* 2006; **162**:743–747.

2.65. Kim S-U, Lee K-H. Carbon nanofiber composites for the electrodes of electrochemical capacitors. *Chemical Physics Letters* 2004; **400**:253-257.

2.66. Yoon JH, Bang HJ, Prakash J, Sun YK. Comparative study of $Li[Ni_{1/3}Co_{1/3}Mn_{1/3}]O_2$ cathode material synthesized via different synthetic routes for asymmetric electrochemical capacitor applications. *Materials Chemistry and Physics* 2008; **110**:222-227.

2.67. Chen H, Zhou M, Wang Z, Zhao S, Guan S. Rich nitrogen-doped ordered mesoporous phenolic resin-based carbon for supercapacitors. *Electrochimica Acta* 2014; **148:**187-194.

2.68. Deng L, Hao Z, Wang J, Zhu G, Kang L, Liu Z-H, Yang Z, Wang Z. Preparation and capacitance of graphene/multiwall carbon nanotubes/MnO_2 hybrid material for high-performance asymmetrical electrochemical capacitor. *Electrochimica Acta* 2013; **89**:191-198.

2.69. Hsieh C-T, Chen Y-C, Chen Y-F, Huq MM, Chen P-Y, Jang B-S. Microwave synthesis of titania-coated carbon nanotube composites for electrochemical capacitors. *Journal of Power Sources* 2014; **269**:526-533.

2.70. Naoi K, Simon P. New materials and new configurations for advanced electrochemical capacitors. *The Electrochemical Society* 2008; **17**:34-37.

2.71. Sevilla M, Gu W, Falco C, Titirici MM, Fuertes AB, Yushin G. Hydrothermal synthesis of microalgae-derived microporous carbons for electrochemical capacitors. *Journal of Power Sources* 2014; **267**:26-32.

2.72. Nasibi M, Irankhah M, Sarpoushi MR, Golozar MA, Moshrefifar M, Shishesaz MR. Graphite nanosheets as an electrode material for electrochemical double layer capacitors. *Materials Science in Semiconductor Processing* 2014; **20**:49-54.

2.73. Chen L, Li H, Yoshitake H, Qi L, Gu N, Wang H. Low-temperature performance of aqueous electrochemical capacitors based on manganese oxides. *Electrochimica Acta* 2015; **157**:333-344.

2.74. Xian H, Peng T, Sun H, Wang J. Preparation of graphene nanosheets from microcrystalline graphite by low-temperature exfoliated method and their supercapacitive behavior. *Journal of Materials Science* 2015; **50**:4025-4033.

2.75. Njomo N, Waryo T, Masikini M, Ikpo CO, Mailu S, Tovide O, Ross N, Williams A, Matinise N, Sunday CE, Mayedwa N, Bakera PGL, Ozoemena KL, Iwuoh EI. Graphenated tantalum(IV) oxide and poly(4-styrene sulphonicacid)-doped polyaniline nanocomposite as cathode materialin an electrochemical capacitor. *Electrochimica Acta* 2014; **128**:226-237.

2.76. Li Y, Kang L, Bai G, Li P, Deng J, Liu X, Yang Y, Gao F, Liang W. Solvothermal synthesis of Fe_2O_3 loaded activated carbon as electrode materials for high-performance electrochemical capacitors. *Electrochimica Acta* 2014; **134**:67-75.

2.77. Al-zubaidi A, Inoue T, Matsushita T, Ishii Y, Hashimoto T, Kawasaki S. Cyclic voltammogram profile of single-walled carbon nanotube electric double-layer capacitor electrode reveals dumbbell shape. *Journal of Physical Chemistry C* 2012; **116**:7681-7686.

2.78. Chang H-Y, Chang H-C, Lee K-Y. Characteristics of NiO coating on carbon nanotubes for electric double layer capacitor application. *Vacuum* 2013; **87**:164-168.

2.79. Saleem AM, Göransson G, Desmaris V, Enoksson P. CMOS compatible on-chip decoupling capacitor based on vertically aligned carbon nanofibers. *Solid-State Electronics* 2015; **107**:15-19.

2.80. Anasori B, Beidaghi M, Gogotsi Y. Graphene-transition metal oxide hybrid materials Hybrid structures for energy storage. *Materials Today* 2014; **17**:253-425.

2.81. Lekakou C, Moudam O, Markoulidis F, Andrews T, Watts JF, Reed GT. Carbon-based fibrous EDLC capacitors and supercapacitors. *Journal of Nanotechnology* 2011:1-7.

2.82. Yang J, Gunasekaran S. Electrochemically reduced graphene oxide sheets for use in high performance supercapacitors. *Carbon* 2013; **51**:36-44.

2.83. Sharma RK, Zhai L. Multiwall carbon nanotube supported poly(3,4-ethylenedioxythiophene)/manganese oxide nano-composite electrode for super-capacitors. *Electrochimica Acta* 2009; **54**:7148–7155.

2.84. Wang DW, Li F, Yin LC, Lu X, Chen ZG, Gentle IR, Lu GQ, Cheng HM. Nitrogen-doped carbon monolith for alkaline supercapacitors and understanding nitrogen-induced redox transitions. *Chemistry* 2012; **18**:5345-535.

2.85. Ramakrishnan P, Shanmugam S. Electrochemical performance of carbon nanorods with embedded cobalt metal nanoparticles as an electrode material for electrochemical capacitors. *Electrochimica Acta* 2014; **125**:232-240.

2.86. Wu JB, Guo RQ, Huang XH, Lin Y. Construction of self-supported porous TiO_2/NiO core/shell nanorod arrays for electrochemical capacitor application. *Journal of Power Sources* 2013; **243**:317-322.

2.87. Zhang Y, Yuan C, Ye K, Jiang X, Yin J, Wang G, et al. An aqueous capacitor battery hybrid device based on Na-ion insertion-deinsertion in l-MnO_2 positive electrode. *Electrochimica Acta* 2014; **148**:237–243.

2.88. Satish R, Aravindan V, Ling WC, Madhavi S. Carbon-coated $Li_3V_2(PO_4)_3$ as insertion type electrode for lithium-ion hybrid electrochemical capacitors: An evaluation of anode and cathodic performance. *Journal of Power Sources* 2015; **281**:310-317.

2.89. Li S, Wang C-A. Design and synthesis of hierarchically porous MnO_2/carbon hybrids for high performance electrochemical capacitors. *Journal of Colloid and Interface Science* 2015; **438**:61-67.

2.90. Terrones M, Botello-Méndez AR, Campos-Delgado J, López-Urías F, Vega-Cantú YI, Rodríguez-Macías FJ, Elías AL, Mu˜noz-Sandoval E, Cano-Márquez AG, Charlier J-C, Terrones C. Graphene and graphite nanoribbons: Morphology, properties, synthesis, defects and applications. *Nano Today* 2010; **5**:351-372.

2.91. Tian Y, Xue R, Zhou X, Liu Z, Huang L. Double layer capacitor based on active carbon and its improved capacitive properties using redox additive electrolyte of anthraquinonedisulphonate. *Electrochimica Acta* 2015; **152**:135-139.

2.92. Haddon RC. Graphene - The mother of two-dimensional (2-D) materials. *Accounts of Chemical Research* 2013; **46**:2191–2192.

2.93. Lota K, Lota G, Sierczynska A, Acznik I. Carbon/polypyrrole composites for electrochemical capacitors. *Synthetic Metals* 2015; **203**:44-48.

2.94. Bae E, Kim ND, Kwak BK, Park J, Lee J, Kim Y, Choi K, Yi J. The effects of fullerene (C_{60}) crystal structure on its electrochemical capacitance. *Carbon* 2010; **48**:366-368.

2.95. Sarpoushi MR, Nasibi M, Shishesaz MR, Golozar MA, Riazi H. Graphite nanosheets/nanoporous carbon black/cerium oxide nanoparticles as an electrode material for electrochemical capacitors. *Synthetic Metals* 2015; **200**:117-122.

2.96. Chen W, Fan Z, Gu L, Bao X, Wang C. Enhanced capacitance of manganese oxide via confinement inside carbon nanotubes. *The Royal Society of Chemistry* 2010:S1-S7.

2.97. Salinas-Torres D, Shiraishi S, Morallón E, Cazorla-Amorós D. Improvement of carbon materials performance by nitrogen functional groups in electrochemical capacitors in organic electrolyte at severe conditions. *Carbon* 2015; **82**:205-213.

2.98. Fan X, Yu C, Yang J, Ling Z, Qiu J. Hydrothermal synthesis and activation of graphene-incorporated nitrogen-rich carbon composite for high-performance supercapacitors. *Carbon* 2014; **70**:130-141.

2.99. Atchudan R, Pandurangan A, Joo J. Synthesis of multilayer graphene balls on mesoporous Co-MCM-41 molecular sieves by chemical vapour deposition method. *Microporous and Mesoporous Materials* 2013; **175**:161-169.

2.100. Dhakate SR, Chauhan N, Sharma S, Tawale J, Singh S, Sahare PD, Mathur RB. An approach to produce single and double layer graphene from re-exfoliation of expanded graphite. *Carbon* 2011; **49**:1946–1954.

2.101. Sun Z, James DK, Tour JM. Graphene Chemistry: Synthesis and manipulation. *Physical Chemistry Letters* 2011; **2**:2425–2432.

2.102. Hai-Ping H, Jun-Jie2 Z. Preparation of novel carbon-based nanomaterial of graphene and its applications electrochemistry. *Chinese Journal of Analytical Chemistry* 2011; **39**:963-971.

2.103. Dhakate SR, Chauhan N, Sharma S, Mathur RB. The production of multi-layer graphene nanoribbons from thermally reduced unzipped multi-walled carbon nanotubes. *Carbon* 2011; **49**:4170-4178.

2.104. Fan Z, Jun Yan LZ, Zhang Q, Wei T, Jing Feng , Zhang M, Zhang M, Qian M, Wei F. A three-dimensional carbon nanotube/graphene sandwich and its application as electrode in supercapacitors. *Advanced Materials* 2010; **22**:3723-3728.

2.105. Quintana M, Vazquez E, Prato M. Organic functionalization of graphene in dispersions. *Accounts of Chemical Research* 2013; **46**:138-148.

2.106. Park J, Yan M. Covalent functionalization of graphene with reactive intermediates. *Accounts of Chemical Research* 2013; **46**:181-189.

2.107. Mohammadi S, Kolahdouz Z, Darbari S, Mohajerzadeh S, Masoumi N. Graphene formation by unzipping carbon nanotubes using a sequential plasma assisted processing. *Carbon* 2013; **52**:451-463.

2.108. Chen Y, Zhang X, Yu P, Ma Y. Electrophoretic deposition of graphene nanosheets on nickel foams for electrochemical capacitors. *Journal of Power Sources* 2010; **195**:3031-3035.

2.109. Zhou Z, Wu X-F. High-performance porous electrodes for pseudosupercapacitors based on graphene-beaded carbon nanofibers surface-coated with nanostructured conducting polymers. *Journal of Power Sources* 2014; **262**:44-49.

2.110. Niu L, Li Z, Hong W, Sun J, Wang Z, Ma L, Wang J, Yang S. Pyrolytic synthesis of boron-doped graphene and its application as electrode material for supercapacitors. *Electrochimica Acta* 2013; **108**:666-673.

2.111. Tu C-H, Wu C-H, Chen C-H, Li Y-C, Wang S-T, Chen Y-C, Lu C-H, Cai Y-J, Lin J-H, Liu, C-P. Direct growth of hollow carbon nanorods on porous graphenic carbon film without catalysts. *Carbon* 2015; **84**:272-279.

2.112. Liu W-W, Chai S-P, Mohamed AR, Hashim U. Synthesis and characterization of graphene and carbon nanotubes: A review on the past and recent developments. *Journal of Industrial and Engineering Chemistry* 2014; **20**:1171-1185.

2.113. Yen H-F, Horng Y-Y, Hu M-S, Yang W-H, Wen J-R, Ganguly A, Tai Y, Chen K-H Chen L-C. Vertically aligned epitaxial graphene nanowalls with dominated nitrogen doping for superior supercapacitors. *Carbon* 2015; **82**:124-134.

2.114. Cai X, Zhang Q, Wang S, Peng J, Zhang Y, Ma H, Li J, Zhai M. Surfactant-assisted synthesis of reduced graphene oxide/polyaniline composites by gamma irradiation for supercapacitors. *Journal of Materials Science*. 2014; **49**:5667-5675.

2.115. Fan Z, Yan J, Zhi L, Zhang Q, Wei T, Feng J, et al. A three-dimensional carbon nanotube/graphene sandwich and its application as electrode in supercapacitors. *Advanced Materials* 2010; 22:3723–3728.

2.116. Jiang R, Cui C, Ma H. Using graphene nanosheets as a conductive additive to enhance the capacitive performance of α-MnO_2. *Electrochimica Acta* 2013; **104**:198-207.

2.117. Li N, Tang S, Dai Y, Meng X. The synthesis of graphene oxide nanostructures for supercapacitors: a simple route. *Journal of Materials Science* 2014; **49**:2802-2809.

2.118. Wu C, Huang X, Wu X, Yu J, Xie L, Jiang P. TiO_2-nanorod decorated carbon nanotubes for high-permittivity and low-dielectric-loss polystyrene composites. *Composites Science and Technology* 2012; **72**:521-527.

2.119. Jiang Y, Ling X, Jiao Z, Li L, Ma Q, Wu M, Chu Y, Zhao B. Flexible of multiwalled carbon nanotubes/manganese dioxide nanoflake textiles for high-performance electrochemical capacitors. *Electrochimica Acta* 2015; **153**:246-253.

2.120. Parker CB, Raut AS, Brown B. Three-dimensional arrays of graphenated carbon nanotubes. *Materials Research Society* 2012; **27**:1046-1053.

2.121. Henry PA, Raut AS, Ubnoske SM, Parker CB, Glass JT. Enhanced electron transfer kinetics through hybrid graphene-carbon nanotube films. *Electrochemistry Communications* 2014; **48**:103-106.

2.122. Yan Z, Ma L, Zhu Y, Lahiri I, Hahm MG, Liu Z, Yang S, Xiang C, Lu W, Peng Z, Sun Z, Kittrell C, Lou J, Choi W, Ajayan PM, Tour JM. Three-dimensional metal graphene nanotube multifunctional hybrid materials. *American Chemical Society Nano* 2012.

2.123. Zhou D-D, Li W-Y, Dong X-L, Wang Y-G, Wang C-X, Xia Y-Y. A nitrogen-doped ordered mesoporous carbon nanofiber array for supercapacitors. *Journal of Materials Chemistry A* 2013; **1**:8488.

2.124. Krolow MZ, Hartwig CA, Link GC, Raubach CW, Pereira JSF, Picoloto RS, Gonçalves MRF, Carreño NLV, Mesko MF. Synthesis and characterisation of carbon nanocomposites. *NanoCarbon* 2011; **8**:33-45

2.125. Martin-Gullon I, Vera J, Conesa JA, Gonza´lez JL, Merino CS. Differences between carbon nanofibers produced using Fe and Ni catalysts in a floating catalyst reactor. *Carbon* 2006; **44**:1572–1580.

2.126. Śliwak A, Grzyb B, Ćwikła J, Gryglewicz G. Influence of wet oxidation of herringbone carbon nanofibers on the pseudocapacitance effect. *Carbon* 2013; **64**:324-333.

2.127. Wang T, Song D, Zhao H, Chen J, Zhao C, Chen L, Chen W, Zhou J, Xie E. Facilitated transport channels in carbon nanotube/carbon nanofiber hierarchical composites decorated with manganese dioxide for flexible supercapacitors. *Journal of Power Sources* 2015; **274**:709-717.

2.128. Ma C, Wang X, Ma Y, Sheng J, Li Y, Li S, Shi J. Carbon nanofiber/graphene composite paper for flexible supercapacitors with high volumetric capacitance. *Materials Letters* 2015; **145**:197-200.

2.129. Ginsberg J. The discovery of fullerenes. In: Program NHCL, ed. *American Chemical Society* 2010.

2.130. Winkler K, Grodzka E, D'Souza F, Balch AL. Two-component films of fullerene and palladium as materials for electrochemical capacitors. *Journal of The Electrochemical Society* 2007; **154**:K1-K10.

2.131. McDonough JK, Frolov AI, Presser V, Niu J, Miller CH, Ubieto T, Fedorov MV, Gogotsi Y. Influence of the structure of carbon onions on their electrochemical performance in supercapacitor electrodes. *Carbon* 2012; **50**:3298-3309.

2.132. Jäckel N, Weingarth D, Zeiger M, Aslan M, Grobelsek I, Presser V. Comparison of carbon onions and carbon blacks as conductive additives for carbon supercapacitors in organic electrolytes. *Journal of Power Sources* 2014; **272**:1122-1133.

2.133. Gao Y, Zhou YS, Qian M, He XN, Redepenning J, Goodman P, Li MH, Jiang L, Lu YF. Chemical activation of carbon nano-onions for high-rate supercapacitor electrodes. *Carbon* 2013; **51**:52-58.

2.134. Liu Y, Kim DY. Enhancement of capacitance by electrochemical oxidation of nanodiamond derived carbon nano-onions. *Electrochimica Acta* 2014; **139**:82-87.

2.135. Gu W, Peters N, Yushin G. Functionalized carbon onions, detonation nanodiamond and mesoporous carbon as cathodes in Li-ion electrochemical energy storage devices. *Carbon* 2013; **53**:292-301.

2.136. Lin Z, Yan X, Lang J, Wang R, Kong L-B. Adjusting electrode initial potential to obtain high-performance asymmetric supercapacitor based on porous vanadium pentoxide nanotubes and activated carbon nanorods. *Journal of Power Sources* 2015; **279**:358-364.

2.137. Sun C, Ma M, Yang J, Zhang Y, Chen P, Huang W, Dong X. Phase-controlled synthesis of alpha-NiS nanoparticles confined in carbon nanorods for high performance supercapacitors. *Scientific reports* 2014; **4**:7054.

2.138. Chang H-Y, Huang Y-J, Chang H-C, Su W-J, Shih Y-T, Chen JL, Honda S, Huang Y-S, Lee K-Y. Electrochemical characteristics of amorphous carbon nanorod synthesized by radio frequency magnetron sputtering. *Applied Surface Science* 2015; **326**:243-250.

2.139. Qin Z, Li ZJ, Yang BC. Synthesis of carbon nanowires as electrochemical electrode materials. *Materials Letters* 2012; **69**:55-58.

2.140. Sun K, Wang H, Peng H, Wu Y, Ma G, Lei Z. Manganese oxide nanorods supported on orange peel-based carbon nanosheets for high performance supercapacitors. *International Journal of Electrochemical Science* 2015; **10**:2000-2013.

2.141. Hou L, Lian L, Li D, Pang G, Li J, Zhang X, Xiong S, Yuan C. Mesoporous N-containing carbon nanosheets towards high-performance electrochemical capacitors. *Carbon* 2013; **64**:141-149.

2.142. Yang T, Zhou R, Wang DW, Jiang SP, Yamauchi Y, Qiao SZ, Qiao SZ, Monteiro MJ, Liu J. Hierarchical mesoporous yolk-shell structured carbonaceous nanospheres for high performance electrochemical capacitive energy storage. *Chemical Communications* 2015; **51**:2518-2521.

2.143. Chen R, Chen Y, Xu B, Zhang R, He Z, Wu F, Li L. How does lithium oxalyldifluoroborate enable the compatibility of ionic liquids and carbon-based capacitors? *Journal of Power Sources*. 2015; **276**:299-308.

2.144. Mombeshora ET, Simoyi R, Nyamori VO, Ndungu PG. Multiwalled carbon nanotube-titania nanocomposites: Understanding nano-structural parameters and functionality in dye-sensitized solar cells. *South African Journal of Chemistry* 2015; **68**:153-164.

2.145. Rathee D, Kumar M, Arya SK. Deposition of nanocrystalline thin TiO_2 films for MOS capacitors using sol–gel spin method with Pt and Al top electrodes. *Solid-State Electronics* 2012; **76**:71-76.

2.146. Stoller MD, Ruoff RS. Best practice methods for determining an electrode material's performance for ultracapacitors. *Energy and Environmental Science*. 2010; **3**:1294.

2.147. Kurzweil P, Frenzel B, Gallay R. Capacitance characterization methods and ageing behaviour of supercapacitors. Proceedings: The 15th International seminar on double Layer capacitors. Deerfield Beach, FL., U.S.A; p. 1-12.

2.148. Shimamoto K, Tadanaga K, Tatsumisago M. All-solid-state electrochemical capacitors using MnO_2/carbon nanotube composite electrode. *Electrochimica Acta* 2013; **109**:651-655.

2.149. Papakonstantinou P, Kern R, Robinson L, Murphy H, Irvine J, McAdams E, McLaughlin J, McNally T. Fundamental electrochemical properties of carbon nanotube electrodes. *Taylor and Francis* 2005; **13**:91–108.

2.150. Hulicova-Jurcakova D, Kodama M, Shiraishi S, Hatori H, Zhu ZH, Lu GQ. Nitrogen-enriched nonporous carbon electrodes with extraordinary supercapacitance. *Advanced Functional Materials* 2009; **19**:1800-1809.

2.151. Song Y, Hu S, Dong X, Wang Y, Wang C, Xia Y. A Nitrogen-doped hierarchical mesoporous/microporous carbon for supercapacitors. *Electrochimica Acta* 2014; **146**:485-494.

2.152. Li X, Wei B. Supercapacitors based on nanostructured carbon. *Nano Energy* 2013; **2**:159–173.

2.153. Wei L, GlebY. Nanostructured activated carbons from natural precursors for electrical double layer capacitors. *Nano Energy* 2012; **1**:552–565.

2.154. Ma X, Liu M, Gan L, Zhao Y, Chen L. Synthesis of micro- and mesoporous carbon spheres for supercapacitor electrode. *Journal of Solid State Electrochemistry* 2013; **17**:2293–2301.

2.155. Yun YS, Park HH, Jin H-J. Pseudocapacitive effects of N-doped carbon nanotube electrodes in supercapacitors. *Materials* 2012; **5**:1258-1266.

2.156. Wang L, Morishita T, Toyoda M, Inagaki M. Asymmetric electric double layer capacitors using carbon electrodes with different pore size distributions. *Electrochimica Acta* 2007; **53**:882-886.

2.157. Zhai Y, Dou Y, Zhao D, Fulvio PF, Richard T. Mayes, Dai S. Carbon materials for chemical capacitive energy storage. *Advanced Materials* 2011; **23**:4828–4850.

2.158. Hulicova-Jurcakova D, Seredych M, Lu GQ, Kodiweera NK, Stallworth PE, Greenbaum S, Bandosz TJ. Effect of surface phosphorus functionalities of activated carbons containing oxygen and nitrogen on electrochemical capacitance. *Carbon* 2009; **47**:1576-1584.

2.159. Candelaria SL, Garcia BB, Liu D, Cao G. Nitrogen modification of highly porous carbon for improved supercapacitor performance. *Journal of Materials Chemistry* 2012; **22**:9884.

2.160. Yuanyuan Y, Ruiyi L, Zaijun L, Junkang L, Zhiguo G, Guangli W. A facile self-template strategy to fabricate three-dimensional nitrogen-doped hierarchical porous carbon/graphene for conductive agent-free supercapacitors with excellent electrochemical performance. *Electrochimica Acta* 2014; **125**:330-337.

2.161. Wang G, Zhang J, Kuang S, Zhou J, Xing W, Zhuo S. Nitrogen-doped hierarchical porous carbon as an efficient electrode material for supercapacitors. *Electrochimica Acta* 2015; **153**:273-279.

2.162. Ray SC, Tetana ZN, Erasmus R, Mathur A, Coville NJ. Carbon spheres for energy applications: Raman and X-ray photoemission spectroscopy studies. *International Journal of Energy Research* 2014; **38**:444-451.

2.163. Li C, Zhao A, Xia W, Liang C, Muhler M. Quantitative Studies on the oxygen and nitrogen functionalization of carbon nanotubes performed in the gas phase. *The Journal of Physical Chemistry C* 2012;116(39):20930-6.

2.164. Maldonado S, Morin S, Stevenson KJ. Structure, composition, and chemical reactivity of carbon nanotubes by selective nitrogen doping. *Carbon* 2006;44(8):1429-37.

2.165. Jiang B, Tian C, Wang L, Sun L, Chen C, Nong X, Qiao Y, Fu H. Highly concentrated, stable nitrogen-doped graphene for supercapacitors: Simultaneous doping and reduction. *Applied Surface Science* 2012; **258**:3438-3443.

2.166. Brown B, Swain B, Hiltwine J, Brooks DB, Zhou Z. Carbon nanosheet buckypaper: A graphene-carbon nanotube hybrid material for enhanced supercapacitor performance. *Journal of Power Sources* 2014; **272**:979-986.

Appendix: Supporting information for Chapter 2

JOHN WILEY AND SONS LICENSE TERMS AND CONDITIONS

Nov 06, 2017

This Agreement between Mr. Edwin Mombeshora ("You") and John Wiley and Sons ("John Wiley and Sons") consists of your license details and the terms and conditions provided by John Wiley and Sons and Copyright Clearance Center.

License Number	4223031099744
License date	Nov 06, 2017
Licensed Content Publisher	John Wiley and Sons
Licensed Content Publication	International Journal of Energy Research
Licensed Content Title	A review on the use of carbon nanostructured materials in electrochemical capacitors
Licensed Content Author	Edwin T. Mombeshora,Vincent O. Nyamori
Licensed Content Date	Oct 1, 2015
Licensed Content Pages	26
Type of use	Dissertation/Thesis
Requestor type	Author of this Wiley article
Format	Print and electronic
Portion	Full article
Will you be translating?	No
Order reference number	Thesis ET Mombeshora
Title of your thesis / dissertation	Synthesis and functionality of boron-, nitrogen- and oxygen-doped shaped carbon-based nanomaterials and titania nanocomposites in electrochemical capacitors
Expected completion date	Nov 2017
Expected size (number of pages)	386
Requestor Location	Mr. Edwin Mombeshora School Of Chemistry and Physics University Of KwaZulu-Natal Westville campus, Private Bag X54001 Durban, KwaZulu-Natal 4000 South Africa Attn: Mr. Edwin Mombeshora

Chapter Three

Materials Chemistry and Physics 199 (2017) 485–493

Contents lists available at ScienceDirect

Materials Chemistry and Physics

journal homepage: www.elsevier.com/locate/matchemphys

Some perspectives on nitrogen-doped carbon nanotube synthesis from acetonitrile and *N,N′*-dimethylformamide mixtures

Edwin T. Mombeshora [a], A.L.Leigh Jarvis [b], Patrick G. Ndungu [c], Bryan P. Doyle [d], Emanuela Carleschi [d], Vincent O. Nyamori [a, *]

[a] School of Chemistry and Physics, University of KwaZulu-Natal, Westville Campus, Private Bag X54001, Durban, 4000, South Africa
[b] School of Electrical, Electronic and Computer Engineering, University of KwaZulu-Natal, King George V Avenue, Durban, 4014, South Africa
[c] Department of Applied Chemistry, University of Johannesburg, P.O. Box 17011, Doornfontein, Johannesburg, 2028, South Africa
[d] Department of Physics, University of Johannesburg, PO Box 524, Auckland Park, 2006, South Africa

HIGHLIGHTS

- Sp^3:*sp* reagent ratios were varied in N-doped carbon nanotubes (N-CNTs) synthesises.
- Varying sp^3:*sp* nitrogen sources ratio tailored N-CNT physicochemical properties.
- The sp^3:*sp* ratio of 1:3 had highest N-doping content of 9.38%.
- The major nitrogen moieties in the N-CNTs was pyrrolic.
- Highest yield of N-CNTs was obtained at 900 °C.

GRAPHICAL ABSTRACT

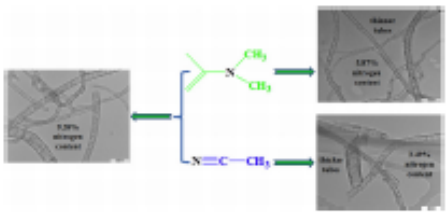

ARTICLE INFO

Article history:
Received 27 April 2017
Received in revised form
8 July 2017
Accepted 11 July 2017
Available online 12 July 2017

Keywords:
Nitrogen-doping
Carbon nanotubes
Nitrogen sources
N,N′-dimethyl formamide
Acetonitrile

ABSTRACT

This work reports on the influence of the ratio of sp^3 (*N,N′*-dimethylformamide, DMF) to *sp* (acetonitrile) hybridised nitrogen within the carbon source used in the synthesis of nitrogen-doped carbon nanotubes (N-CNTs) by means of the floating catalyst chemical vapour deposition method. The physicochemical properties of the N-CNTs were investigated by means of scanning and transmission electron microscopies, textural characteristics, powder X-ray diffraction, X-ray photoelectron spectroscopy, thermal gravimetric analysis and elemental analysis. When the two nitrogen sources were compared before mixing, it was found that sp^3 hybridised nitrogen in DMF was a more effective source for the incorporation of nitrogen atoms (5.87%) than *sp* hybridised nitrogen in acetonitrile (3.49%). The number of walls within the N-CNT synthesised from the sp^3 nitrogen source was tailored by changing the synthesis temperature. Overall, a 1:3 sp^3:*sp* ratio produced N-CNTs with the highest nitrogen content of 9.38% and a general abundance of pyrrolic nitrogen moieties within the samples. The best synthesis temperature in terms of nitrogen content and largest composition of N-CNTs with least residual iron was found to be 900 °C. Varying ratio of sp^3:*sp* hybridised nitrogen is suitable for tailoring the physicochemical properties of N-CNTs towards preferred applications.

Some perspectives on nitrogen-doped carbon nanotube synthesis from acetonitrile and *N,N*'-dimethylformamide mixtures

Edwin T. Mombeshora,[1] A. L. Leigh Jarvis,[2] Patrick G. Ndungu,[3] Bryan P. Doyle,[4] Emanuela Carleschi[4] and Vincent O. Nyamori[1] *

[1]School Chemistry and Physics, University of KwaZulu-Natal, Westville Campus, Private Bag X54001, Durban, 4000, South Africa

[2]School of Electrical, Electronic and Computer Engineering, University of KwaZulu-Natal, King George V Avenue, Durban, 4014, South Africa

[3]Department of Applied Chemistry, University of Johannesburg, P.O. Box 17011, Doornfontein, Johannesburg, 2028, South Africa

[4]Department of Physics, University of Johannesburg, PO Box 524, Auckland Park, 2006, South Africa

Graphical abstract

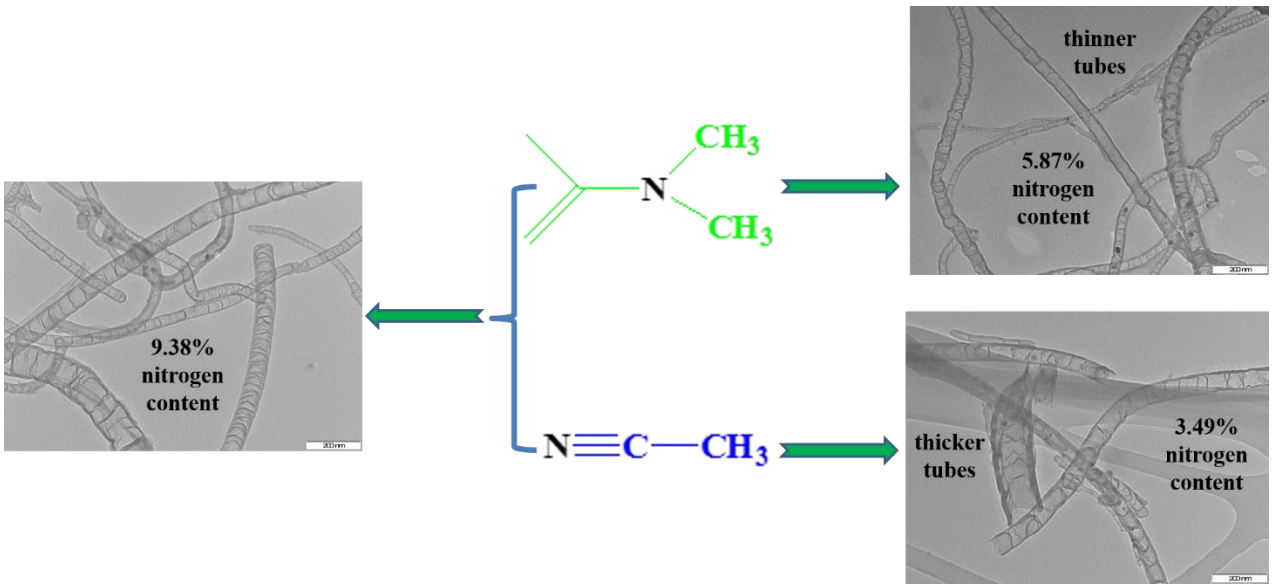

Abstract

This work reports on the influence of the ratio of sp^3 (*N,N'*-dimethyl formamide, DMF) to *sp* (acetonitrile) hybridised nitrogen within the carbon source used in the synthesis of nitrogen-doped carbon nanotubes (N-CNTs) by means of the floating catalyst chemical vapour deposition method. The physicochemical properties of the N-CNTs were investigated by means of scanning and transmission electron microscopies, textural characteristics, powder X-ray diffraction, X-ray photoelectron spectroscopy, thermal gravimetric analysis and elemental analysis. When the two nitrogen sources were compared before mixing, it was found that sp^3 hybridised nitrogen in DMF was a more effective source for the incorporation of nitrogen atoms (5.87%) than *sp* hybridised nitrogen in acetonitrile (3.49%). The number of walls within the N-CNT synthesised from the sp^3 nitrogen source was tailored by changing the synthesis temperature. Overall, a 1:3 sp^3:*sp* ratio produced N-CNTs with the highest nitrogen content of 9.38% and a general abundance of pyrrolic nitrogen moieties within the samples. The best synthesis temperature in terms of nitrogen content and largest composition of N-CNTs with least residual iron was found to be 900 °C. Varying ratio of sp^3:*sp* hybridised nitrogen is suitable for tailoring the physicochemical properties of N-CNTs towards preferred applications.

Keywords: nitrogen-doping, carbon nanotubes, nitrogen sources, *N,N'*-dimethyl formamide, acetonitrile

* Corresponding author*:* Vincent Nyamori, School of Chemistry and Physics, University of KwaZulu-Natal, Westville Campus, Private Bag X54001, Durban, 4000, South Africa

Email: nyamori@ukzn.ac.za Tel.: +27-31 2608256; Fax: +27-31 260 3091

3.1 Introduction

Carbon nanotubes (CNTs) can be synthesised by chemical vapour deposition method in scalable quantities [3.1,3.2]. CNTs are formed when both the carbon source and the catalysts are passed through a hot region of a suitable vessel in a temperature controlled furnace. Nitrogen-doped carbon nanotubes (N-CNTs) can be synthesised by either post or in situ doping [3.3]. In the in-situ synthesis of N-CNTs, the nitrogen source can either be part of the carbon source [3.3] or the catalyst [3.4]. As an example of the latter, Keru et al.,[3.5] synthesised N-

CNTs using (4-{[(pyridine-4-yl)methylidene]amino}phenyl)ferrocene that acted as both catalyst and nitrogen source [3.1]. On the other hand, Yadav et al., synthesised N-CNTs using acetonitrile, *N,N'*-dimethyl formamide (DMF), triethylamine, and hexamethylenetetramine as nitrogen sources [3.6].

Nitrogen gas is a suitable post-synthesis chemical vapour deposition N-doping strategy, but studies have shown that there is little incorporation of nitrogen in the graphitic frameworks [3.7-3.9]. NH_3 has been widely used in the preparation of N-CNTs [3.10] and is popularly reported in post-synthesis N-doping [3.11,3.12]. The final amount and functionalities of N-doping are of paramount importance for practical application in different fields [3.12]. Hence, different precursors and tuning strategies need to be explored to achieve better control of the above-mentioned attributes. The different approaches to N-CNTs production have resulted in differences in both nitrogen species and effects on carrier concentration with distinctive allied electronic structures, amongst other physicochemical properties [3.4,3.11]. Additionally, NH_3 mainly produces graphitic N-CNTs [3.12], whereas the current study is one of the approaches sought to produce higher composition of other nitrogen moieties, such as pyridinic and pyrrolic, using less toxic nitrogen sources, that also act as carbon sources, at relatively lower temperatures. Furthermore, according to theoretical studies [3.10], NH_3 doping effectiveness in the in-situ synthesis of N-CNTs is subject to 1) the pre-existing defects; 2) the ability to trap the -NH_2, -NH, -N active species, from NH_3 thermal decomposition, at appropriate locations; and 3) their associated dehydrogenation. This has been proved difficult to control and achieve. Hence, the current report utilises a different doping strategy in which different active species are involved as building blocks of the graphitic framework. Where NH_3 has been used in in-situ growth of N-CNTs, some of the common adversities have been poor uniformity and widely varied nitrogen content of lower levels. Zhu et al. [3.13] attributed these observations to the low NH_3 flow rate requirement in similar approaches.

Doping CNTs with nitrogen creates nitrogen rich centres such as pyridinic moieties that improve electrical properties (charge storage and oxygen reduction reactions, being two examples of those), and alters other physicochemical properties in devices that include fuel cells, organic solar cells and electrochemical capacitors [3.4,3.5,3.14-3.16]. The addition of a lone pair of electrons to the delocalised pi system enhances electronic properties [3.17,3.18]. Additionally, N ions in the N-CNTs create channels for electron transport [3.19]. The possibility of nitrogen inclusion in the graphitic network is due to the similar bond lengths of 1.38 Å and 1.34 Å for C=C and C=N, respectively. The shorter C=N bond length of N-CNTs,

relative to the C=C in pristine-CNTs, introduces defects in the carbon framework. Hence, N-CNTs typically display bamboo compartments by virtue of strain from the presence of nitrogen. This is explained theoretically through the mechanism that suggests the introduction of defects and pentagon rings in the graphitic network, [3.1,3.20] culminating in the formation of a positive curvature of the tube layers. Typically, nitrogen can be incorporated into the graphitic structure of N-CNTs as either pyridinic, pyloric, nitrogen oxide, cross-linked sp3, nitrile or quaternary [3.16,3.18,3.21-3.23].

Growth-limiting reactions are subject to composition of reagents in the hot zone of the furnace, amongst other factors [3.24]. Understanding of the N-doping process is key for better control of N-CNT properties [3.16]. Hence, nitrogen-doping is still a research focus towards better understanding of N-CNTs. This includes the study of the influence of numerous parameters such as effect of nitrogen source [3.17,3.20], synthesis temperature, reaction time, gas flow [3.15] and different catalysts. For example, Kim et al., [3.16] recently reported on the influence of dopant amount in nitrogen content and doping type. Also, Ombaka et al., [3.4] reported on the enhancement of nitrogen content of N-CNTs through the use of various oxygen containing moieties.

This study builds upon these earlier findings and explores the use of ferrocenecarboxaldehyde (Fc), an oxygen-containing organometallic compound, as the catalyst. The chemical nature of reactants controls species of products [3.25]. Additionally, small molecules have been reported to be suitable sources of carbon in synthesis of CNTs. Therefore, DMF and acetonitrile were chosen in this work. The use of DMF in the synthesis of N-CNTs has been done before, though not common. For instance Tang et al., [3.17] achieved a nitrogen doping level of 20 at.% using Fe_2O_3 /AlO_3 catalyst and ammonia in an aerosol assisted CVD method. The current work investigates influence of mixing ratios of reagents different from previously reported works. Furthermore, it specifically investigates the effect of mixing sp3-hybridised nitrogen in DMF and sp-hybridised nitrogen in acetonitrile and the physicochemical properties of the ultimate products. Additionally, DMF and acetonitrile were compared as both carbon and nitrogen sources in the synthesis of N-CNTs.

3.2. Experimental

The materials were synthesised with chemicals given in the subsequent sections and characterised as elaborated in the following subsections.

3.2.1 Chemical reagents

Acetonitrile (99.9%) was purchased from Merck, Germany while *N*,*N*'-dimethyl formamide (DMF) (99.8%) and ferrocene carboxaldehyde (98%) were procured from Sigma Aldrich.

3.2.2 Synthesis of N-CNTs

Synthesis of two series of N-CNTs at 900 °C was carried out by mixing DMF and acetonitrile, as both carbon and nitrogen sources, by means of the floating catalyst CVD method. The series was synthesised by firstly, varying the ratio of DMF (x) to a fixed mass of acetonitrile, which was generally referred to as DxA1 whilst the reverse was D1Ax. The DxA1 samples were named D0A1, D1A1, D2A1, D3A1, D4A1 and D5A1 for DMF:acetonitrile ratio of 0:1, 1:1, 2:1, 3:1, 4:1 and 5:1, respectively. D1Ax samples, with reverse ratios, were similarly named as D1A0, D1A1, D1A2, D1A3, D1A4 and D1A5, referring to DMF:acetonitrile ratio of 1:0, 1:1, 1:2, 1:3, 1:4 and 1:5. A similar notation based on the mol fractions of DMF and acetonitrile in the reagents is also presented in Table 3.S1 (supplementary information) for reference, otherwise the notation based on the mass ratios was used. Secondly, the influence of temperature on the products was also investigated by using the ratios that gave the highest level of nitrogen-doping, as determined by elemental analysis.

In general, the synthesis procedure used a quartz tube with length and inner diameter of 0.85 m and 0.027 m, respectively. The quartz tube was placed inside a tube furnace (model TSH12/50/610, Elite Thermal Systems Ltd) equipped with a main zone temperature controller (Eurotherm 2416). The purging and reducing gas used was 10% hydrogen in argon (v/v) at a flow rate of 100 mL min^{-1}. With the aid of a syringe pump (model NE 300, New Era Inc), a solution of 2.4 wt.% Fc catalyst and the carbon/nitrogen source were injected at a rate of 0.8 mL min^{-1} at the chosen synthesis temperature. The reaction temperature was held for 30 minutes during synthesis.

The products were collected from the hot zone of the furnace and typical yields were between 100-500 mg. 8-10 runs were done per sample. Products from various runs, using a specific ratio, were then mixed together to form an amalgamated sample. Samples were then characterized by scanning electron microscopy (SEM, JEOL JSM 6100) and transmission electron microscopy (TEM, JEOL TEM 1010). The image J software was used in the determinations of diameters to ascertain size distribution by counting at least 150 nanotubes. The TEM images used in this analysis were from several images taken from different sample areas. Thermogravimetric analysis (TGA, TA Instruments Q series^{TM} Thermal Analyser DSC/TGA Q600), Raman spectroscopy analysis (100 mW Delta Nu Advantage 532^{TM} spectrometer of 10 cm^{-1} resolution with a 2D CCD detector and grating lines were 1800 mm^{-1} with a laser source (Nd:YAG) at wavelength of 532 nm), Micromeritics TriStar II 3020 2.00 instrument at 77 K in N_2, LECO CHNS-932 elemental analyzer standardized with acetanilide and powder X-ray diffraction (PXRD, Rigaku MiniFlex 600) were also used to further characterise the samples. X-ray photoelectron spectroscopy (XPS) measurements were carried out at room temperature using a SPECS PHOIBOS 150 hemispherical electron energy analyser and a monochromatised Al source ($h\nu$ = 1487.1 eV). The overall energy resolution was approximately 0.7 eV. Due to surface charging a low energy flood gun was used. The binding energies were calibrated to the C1s core level which was arbitrarily set to 284.3 eV. Sample preparations for conductivity measurements were done by suspending N-CNTs in ethanol *via* ultrasound water treatment for 10 minutes. The mixture was then vacuum filtered through a Whatman filter paper. A consistent pressure was applied in making the bulky paper of all samples. The bulky paper was thereafter dried and analysed with a four-point probe. The Whatman filter paper, with no electrical conductivity, was used as control and the thickness was measured by means of a micrometer screw gauge. The N-CNTs film thickness was determined by subtracting thickness of filter paper from that of film and filter paper.

3.3. Results and discussion

Effects of both temperature variation and that of acetonitrile/*N,N'*-dimethyl formamide ratios on the physicochemical properties of N-CNTs are reported herein.

3.3.1 Effect of acetonitrile: *N,N'*-dimethyl formamide ratio

N-doping of CNTs creates defects that changes their physicochemical properties [3.1]. The influence of *sp*- (acetonitrile) and sp^3-hybridised (DMF) nitrogen source ratios, as both carbon and nitrogen sources, on the physicochemical properties of N-CNTs is discussed in this section.

3.3.1.1 Effects of varying acetonitrile ratio (*sp* hybridised nitrogen source)

D1A0 (DMF alone) consisted mainly of agglomerated 'spaghetti-like' N-CNTs (Fig. 3.1a) whilst D1A4 and D1A5 had noticeable amounts of amorphous carbon but D1A3 had a slight quantity (green circles in Fig. 3.1d-f). From the Fig. 3.1, it can be deduced that addition of acetonitrile increased the amount of amorphous carbon in the product. Additionally, the D1A1 N-CNTs were more aligned unlike the rest (green rectangle on Fig. 3.1b and supplementary information Fig. 3.S1). The Fe:C ratio (Table 3.S1 in supplementary material), decreased with addition of acetonitrile, and in the feedstock for D1Ax it was not responsible for increase in amorphous carbon in the product (Fig. 3.S1).

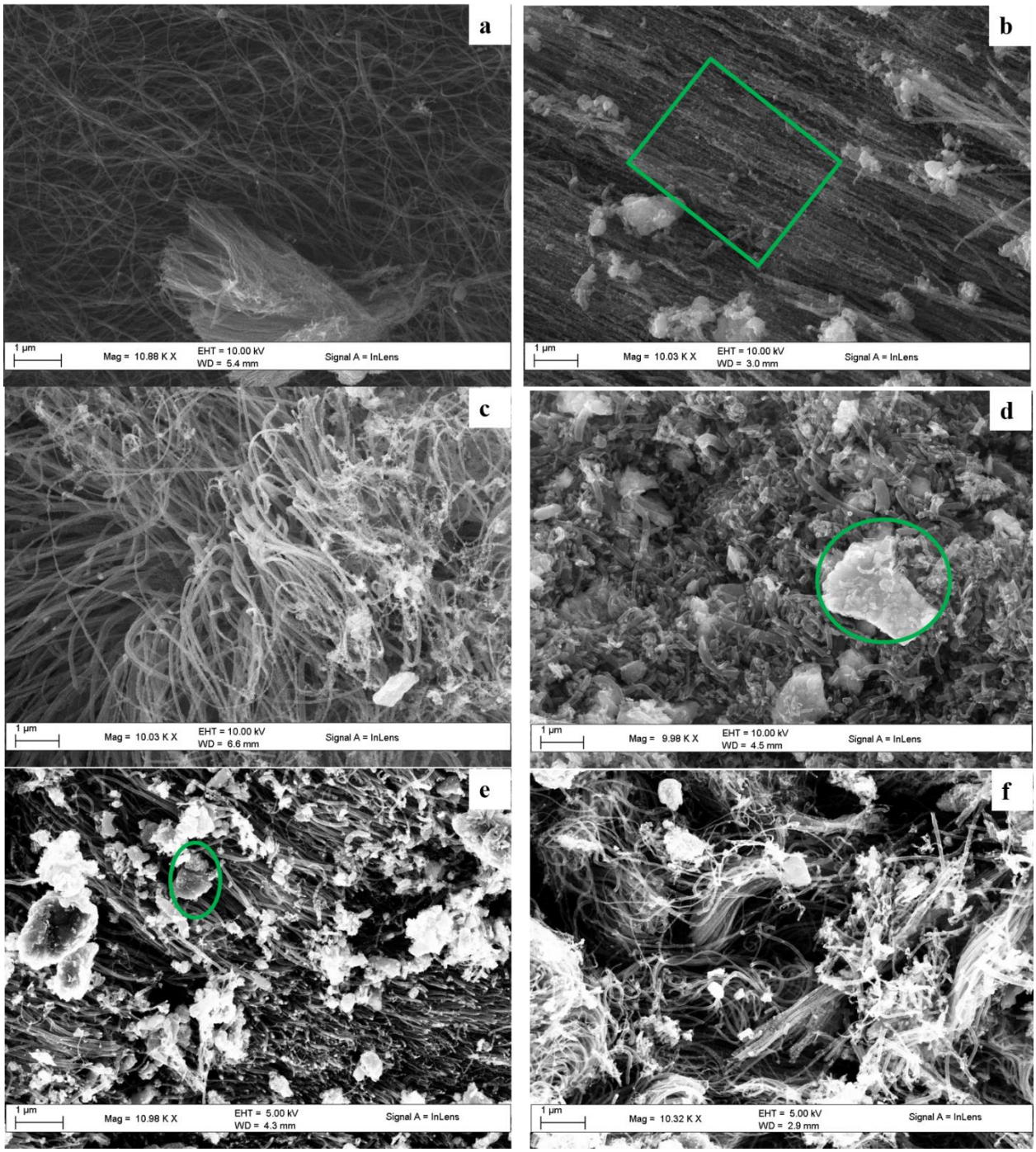

Fig. 3.1. The representative images for the D1Ax samples (a) D1A0, (b) D1A1, (c) D1A2, (d) D1A3, (e) D1A4 and (f) D1A5.

All samples displayed visible bamboo compartments (Fig. 3.2), a preliminary indicator of foreign atom doping and in this case nitrogen. The appearance of bamboo compartments is caused by incorporation of nitrogen in the graphitic structure culminating in a curvature graphitic layer. This correlates with several works reported on N-CNTs synthesised using iron-

based catalyst [3.15,3.26]. Iron metal residues, qualitatively determined by EDX and XPS, were noticeable on both tube walls and encapsulated inside N-CNTs (Fig. 3.2a and e-f). As the metal catalyst is deposited onto the N-CNT walls, it can be inferred that the injection rate does not match growth dynamics, i.e. the rate was too high and hence excess is deposited [3.15]. Considering that injection rate was the same in synthesis of all samples, the absence of iron residues on the D1A1, D1A2 and D1A3 N-CNT walls possibly points out on the changes in growth dynamics as a consequence of different ratios. The ratio of nitrogen sources influenced the product, for instance, D1A0 had some tubes with few bamboo compartments and the sizes of the compartments varied greatly (Fig. 3.2a). Addition of acetonitrile, in sample D1A1, produced N-CNTs with irregular shaped walls and fishbone-like shapes (Fig. 3.2b).

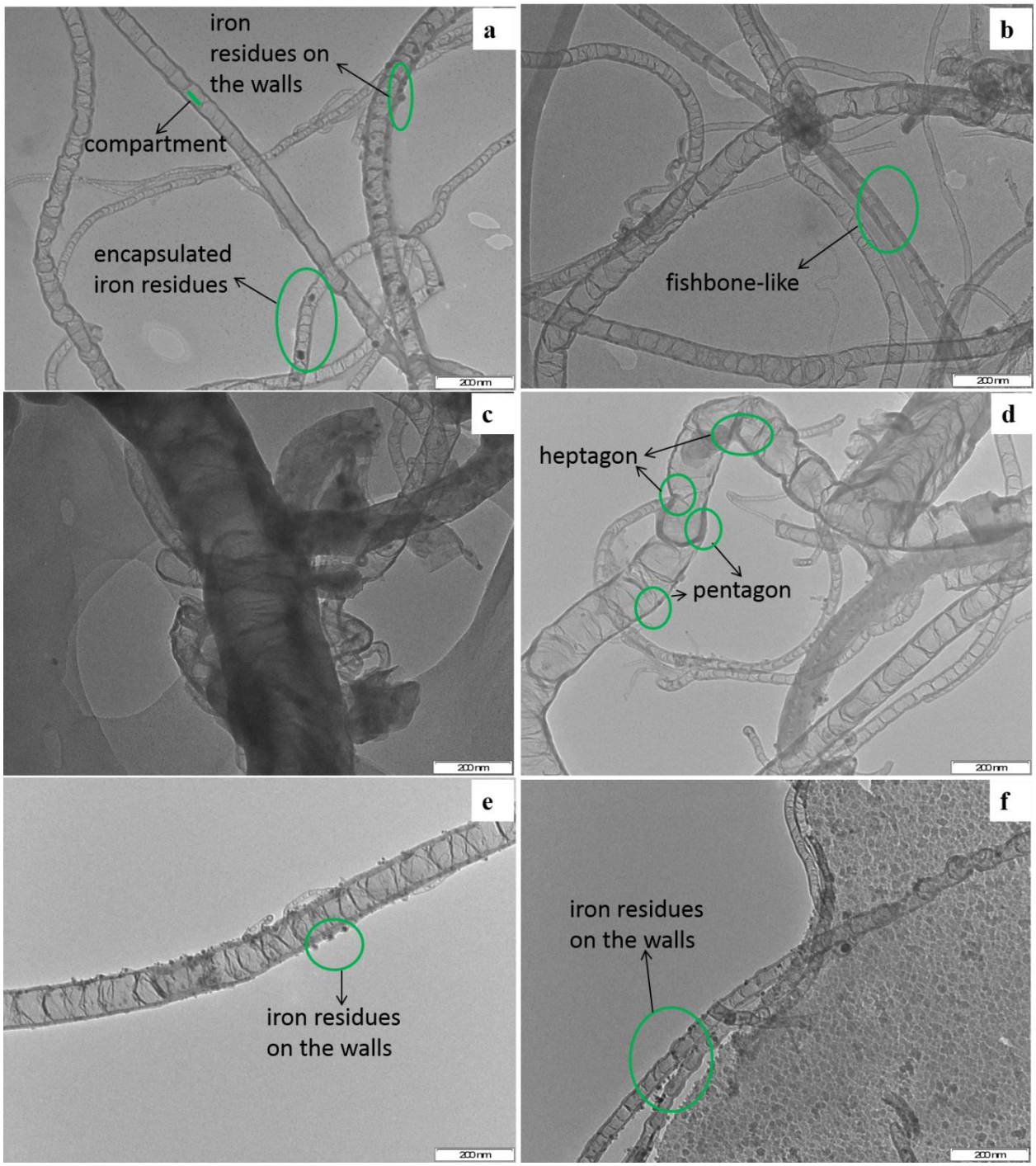

Fig. 3.2. Representative TEM images for the D1Ax samples (a) D1A0, (b) D1A1, (c) D1A2, (d) D1A3, (e) D1A4 and (f) D1A5.

The general observation in the D1Ax series was N-CNTs were bent and a possible explanation is the fact that radicals involved in the N-CNT growth are from sources with different hybridisation. Hence, pentagonal and heptagonal structures are formed [3.27,3.28] from the different associated reaction kinetics and this culminates in different growth dynamics. From

the dimensional analysis (Table 3.S2) the average wall thickness, obtained by subtracting average inner diameter (ID) from outer diameter (OD), increased from 9.3 nm (D1A0) to 40 nm in D1A1. The wall thickness thereafter decreased, although it was thicker than D1A0 in all samples, with increase in *sp* ratio except for sample D1A5. Whilst Thurakitseree *et al.*, [3.29] reported reduction of diameters of N-CNTs upon introduction of *sp*-hybridised-N to ethanol, the current study showed an opposite trait. In the current study, this is possibly due to the involvement of sp^3-hybridised-N source in the reagents for N-CNT synthesis culminating in active species different from the former.

All samples, as noticed from the SEM and TEM images, had high iron metal residues and this is a setback in applications were the metal interferes with functionality. There is a possibility of residual iron to be bound to nitrogen and therefore removal of the metal may result in reduction of nitrogen content [3.3]. However, the main reason of presenting the products as synthesised, before purification, in the current work was to get the traits of catalyst deactivation in the obtained N-CNTs. More studies will be done on the purified N-CNTs and physicochemical properties are also expected to change. The focus of the study was to elucidate how the mixing ratios of the two-small nitrogen/carbon sources with *sp* and sp^3 hybridised nitrogen, acetonitrile and DMF, influence the ultimate product as synthesised, without further purification. The thrust was to communicate the best ratio with respect to residual catalyst wt.%, nitrogen content and functionality, and overall physicochemical properties of the obtained products.

From thermogravimetric analysis, N-CNTs from D1A1 had the highest metal residues (70%) followed by D1A2 (38%) then D1A5 (32%) (Fig. 3.3a1 and b1). A plausible elucidation is that the N-CNT growth rate compete with catalyst deactivation [3.30] and hence, reagents mixtures (carbon sources) of the aforementioned samples facilitated high catalyst deactivation. On the other hand, D1A3 (84%), then D1A0 (82%) and D1A4 (79%) had the largest wt.% of N-CNTs. This means by controlling the ratios of reagents the composition of the product, particularly the wt.% of metal residues, can be altered. In addition, the occurrence of a sharpest derivative weight curve for D1A0 suggest the highest level of sample homogeneity and the almost flat curve for D1A1 means there was minimal carbonaceous material in the product (Fig. 3.3a2). Fig. 3b1-2 (green circle in Fig 3.3b2) shows that D1A4 and D1A5 had noticeable amount of amorphous carbon and D1A3 had a slight amount. The results corroborated SEM observations and a possible reason is that high ratio of *sp* hybridised nitrogen source results in formation of some radicals not favourable for N-CNT growth.

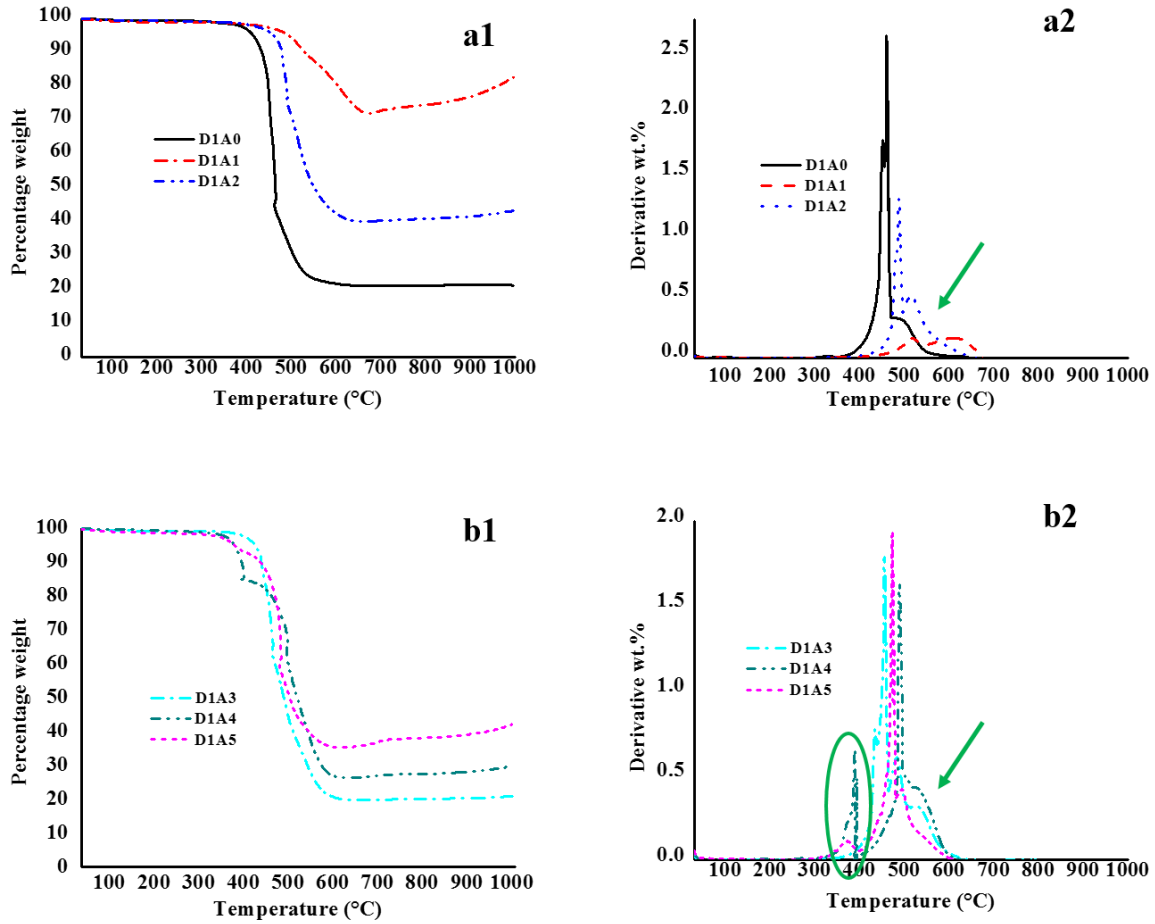

Fig. 3.3. Representative TGA (a1 and b1) thermograms and (a2 and b2) derivative weight curve for the D1Ax samples.

The N-CNTs decomposition range was between 450 and 700 °C (Fig. 3.3a2 and b2). The derivative weight curve shoulders above 550 °C in all samples (arrows in Fig. 3.3a2 and b2) and SEM images (Fig. 3.1), suggest the presence of either two different species of sp^2 hybridized carbon networks, carbon nanotubes and platelets, or existence of defective and non-defective sp^2 hexagonal structures. Several possibilities exist in this regard, such as either existence of doped and un-doped CNTs or the presence of various nitrogen functionalities. There was no clear trend on thermal stability but D1A1 was the most thermally stable mainly because of the limited exposure of the N-CNTs to air during decomposition due to high iron content. Again, the existence of N-CNTs with different levels of defects is a possible reason for lack of pronounced trend.

3.3.1.2 Effects of varying *N,N'*-dimethyl formamide (sp^3 hybridised nitrogen source) ratio

All the N-CNTs synthesized with varying ratios of DMF, DxA1 series, showed spaghetti-like morphologies with small quantities of amorphous carbon (Fig. 3.4a-f). The lumps of deposits on tubes were largest in D4A1 (green circle on Fig. 3.4e). In addition to bent N-CNTs (green arrows on Fig. 3.4), the DxA1 series had some coiled tubes, for instance D3A1 (green circle on Fig. 3.4d).

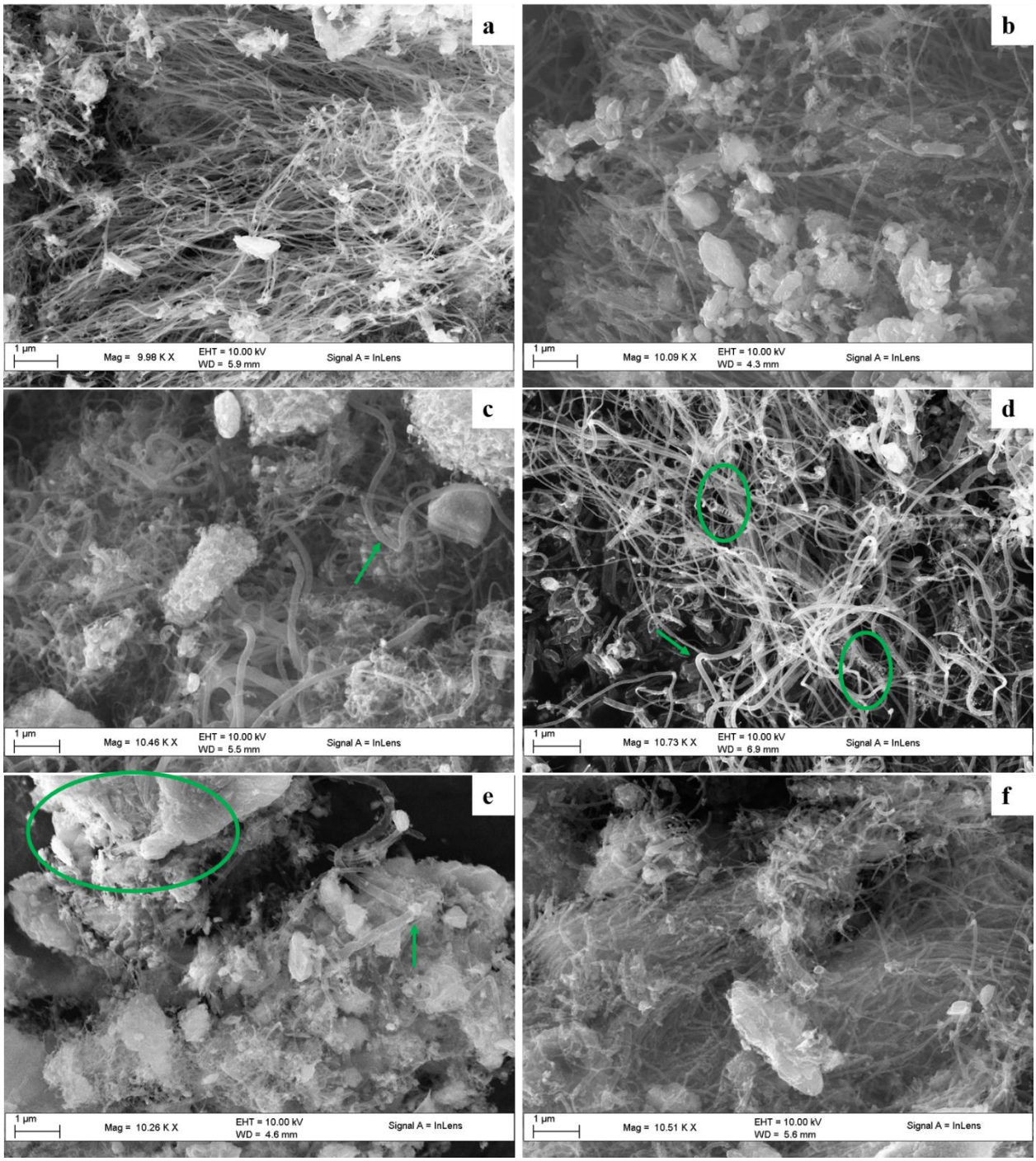

Fig. 3.4. The representative SEM images for the DxA1 samples (a) D0A1, (b) D1A1, (c) D2A1, (d) D3A1, (e) D4A1 and (f) D5A1.

Fig. 3.5 shows presence of bamboo compartments as well as a variety of N-CNT dimensions (Table 3.S2 in supplementary material) and the observed bent N-CNTs morphology corroborated with SEM images at all ratios. D3A1 displayed some rippled tube walls (Fig. 3.5d) and this can similarly be attributed to defects on the tube walls in the form of pentagons

and heptagons. Additionally, D1A1 and D5A1 had some tube with compartments that displayed wrinkled appearances on the walls (Fig. 3.5b and f). Encapsulated iron was also noticeable in some N-CNTs (Fig. 3.5e).

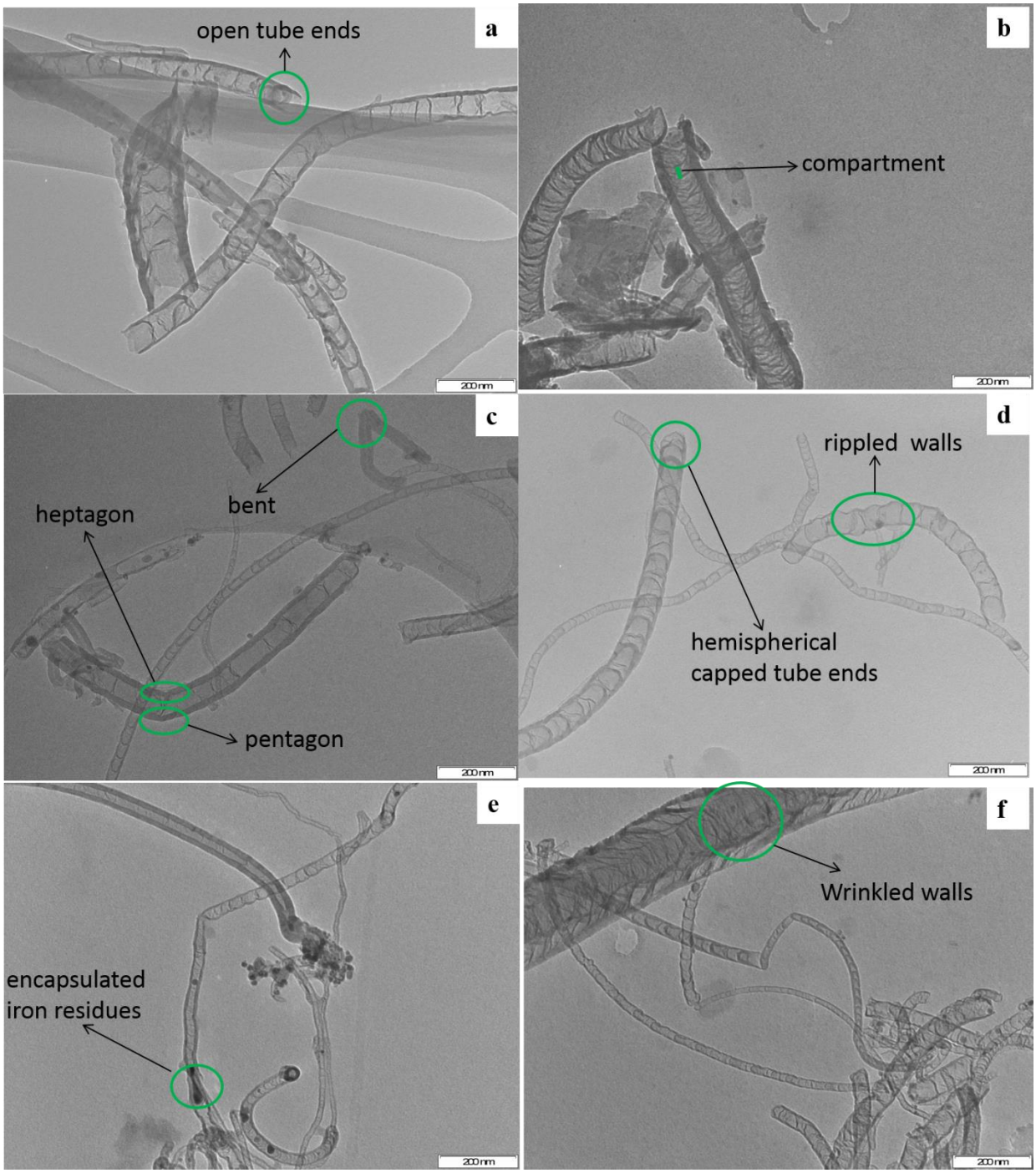

Fig. 3.5. The representative TEM images for the DxA1 samples (a) D0A1, (b) D1A1, (c) D2A1, (d) D3A1, (e) D4A1 and (f) D5A1.

Increase of sp^3:sp hybridised nitrogen source ratio, DMF:acetonitrile, in the DxA1 samples culminated in a decrease in average wall thickness from 95 nm in D0A1 to 40 nm in D1A1 and a decrease to approximately 11 nm then slightly increased (Table 3.S1 in supplementary information). All samples had high metal residues of 40, 70, 20, 29, 38 and 28% for D0A1 to D5A1, respectively (Fig 3.6 a1 and b2). Additionally, only D4A1 and D5A1 showed clear weight losses due to amorphous carbon (circle in Fig. 3.6b2). Samples D3A1, D4A1 and D5A1 displayed a slight kink at ca 500 °C (Fig. 3.6b1), within the main weight loss region, suggesting possibility of slight variations in thermal stability of N-CNTs as the ratio of DMF was raised in DxA1 samples. This can be attributable to different nitrogen species content, shapes and defect nature, amongst other factors, that arose from growth dynamics due to different composition of radicals in the reaction chamber. D2A1 had the largest N-CNTs wt.% (80%), the steepest thermogram (Fig. 3.6a) and the sharpest derivative weight curve (Fig. 3.6a2). These occurrences suggest that D2A1 was the most homogenous sample. Shoulders above 500 °C (arrows in Fig. 3.6a2 and b2), similar to that of D1Ax, were observed in the derivative curves of DxA1 and were attributed to the aforementioned reasons. The decomposition temperature range of DxA1 N-CNTs was 400-700 °C.

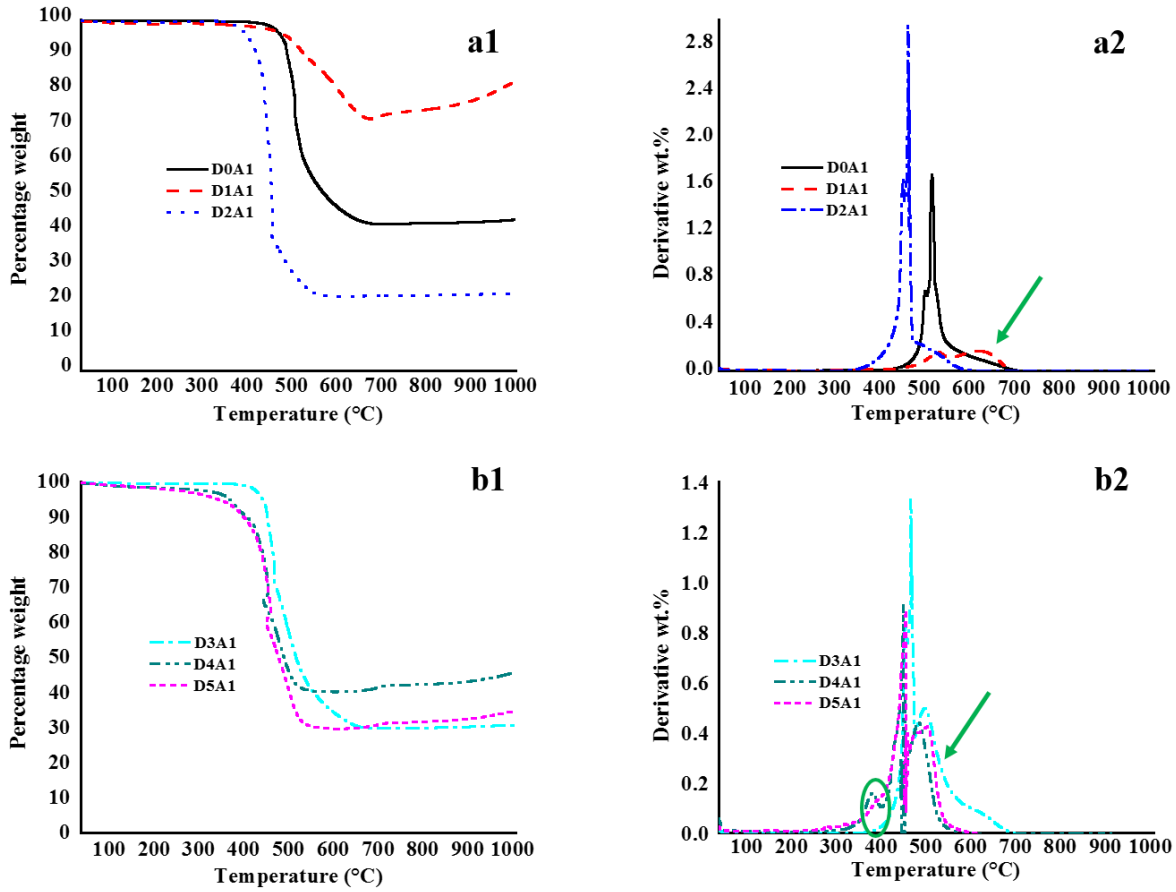

Fig. 3.6. Representative TGA (a1 and b1) thermograms and (a2 and b2) derivative weight curve for the DxA1 samples.

3.3.1.3 Comparative discussion

The elemental composition resulting in varying the aforementioned reagents is provided in the supplementary materials (Table 3.S1). The wt.% of carbon in the reagent were comparable with slight variations in both series and the results below show that despite being small carbon source molecules, the amount of carbon injected in the reaction chamber was sufficient for formation of CNTs. Ferrocenecarboxaldehyde (Fc), as catalyst, is also a source of carbon source but was applied as a constant parameter in this current work and hence the wt.% of Fe catalyst was also a constant but the above variations slightly changes the Fe:C, Fe:N, Fe:O and Fe:H ratios due to associated elemental variations (Table 3.S1). The variations in elemental compositions are negligible to be considered as the main contributors of the observed traits.

The ratios of DMF and acetonitrile (sp^3:*sp* nitrogen hybridisation) influence physicochemical properties such as thermal stability, elemental composition and morphology of N-CNTs. For instance, the number of N-CNT walls were approximated by the formula:

$$Number\ of\ walls\ = (\frac{OD-ID}{2\times 0.34}) + 1 \qquad \text{(Equation 1)}$$

The approximate number of walls decreased significantly with increase in ratio of DMF, in the DxA1, up to D2A1 then marginally increased thereafter (Table 3.S2 in supplementary information). The current work suggestively shows that the number of N-CNT walls formed from *sp* nitrogen source (acetonitrile) can be reduced by addition of sp^3 source (DMF) and *vice versa*.

Incorporation of nitrogen introduces some defects on N-CNT walls, manifesting in various forms such as rippled walls and bent structures, as seen on TEM images (Fig. 3.2 and 5). The study shows that synthesizing N-CNTs at 900 °C using DMF and acetonitrile may produce amorphous carbon depending on the reagent composition (Fig. 3.S1a-b). Both wt.% of oxygen atoms in the reagent mixture and amorphous carbon composition in the product for DxA1 was higher than D1Ax series (Fig. 3.S1 and Table 3.S1). This suggests that the cleaning effect of oxygen with respect to amorphous carbon [3.5] was minimal in the current work. Instead of reacting with amorphous carbon in the product and leaving reaction chamber as CO_x gases, a possible role of oxygen was the removal of the reactive hydrogen radicals [3.31]. This could have nullified the effect of oxygen in the reaction chamber because hydrogen was in excess from the carrier gas. Hence, insufficient oxygen available for the cleaning role led to appearance of amorphous carbon in the product. This was favourable because hydrogen radicals inhibit growth of sp^2 carbons for N-CNTs formation [3.31].

The N-CNTs from both series had a mixture of open and hemispherical capped tube ends. A possible reason for morphological variations with respect to mixing ratio in the samples is associated with the dynamics of radical diffusion and growth direction. The supplementary information (Fig. 3.S2-S3) show that OD sizes can be tailored by varying the ratios of sp^3:*sp* species in the reagent mixture. No correlation was observed between Fe:C ratio (reagent mixture) and the resulting N-CNT diameters and a possible explanation is that the associated ratios were too low to cause formation of large iron particles at 900 °C. D0A1 N-CNTs were more thermally stable and had more residual iron wt.% than D1A0 whilst it was the same case for D1A2 and D2A1, respectively. The samples D3A1 and D1A3 had similar thermal stabilities but the latter had a higher iron residue wt.%. D1A4 and D5A1 had less residual iron

than their counterparts. Again, the aforementioned variations in iron residues showed no correlation with differences between Fe:C ratios in reagents of the corresponding samples in the two series.

Molecular hydrogen reduces Fe^{2+} to Fe^0 and this favours formation of CNTs [3.19]. D1Ax samples and the product composition (Fig. 3.S1) indicates that D1A4 and D1A5 had higher amorphous carbon, despite the expected higher amount reduced catalyst in feedstock. A possible explanation is that the higher oxygen content in the reagents cancels out the reducing effect of hydrogen [3.32] and also removes the reactive hydrogen radicals [3.31]. In addition, there was low amount of oxygen content (Table 3.S1 in supplementary information) in the feedstock to sufficiently remove hydrogen radicals in D1A4 and D1A5. Hence, the radicals attack sp^2 carbons forming sp^3 carbons, hence, more amorphous carbon content was obtained.

Nyamori *et al.*, [3.32] reported on the influence of Fe:C ratios in the range 0 to 0.467 and recorded 30 wt.% of amorphous carbon in the product at Fe:C ratio of 0.016. The composition of amorphous carbon in the current study was considerably below and this was attributed to the significantly lower Fe:C ratios (Table 3.S1 and Fig. 3.S1 in supplementary information). Hence, the variations in Fe:C ratios were negligible to be considered as the main influence in this regard in the current work. The plausible differences introduced from the two sources, under study, was that DMF decompose to active species such as OHCN, CHO and CH_3 [3.17] whilst acetonitrile decomposes mostly into HCN and CH_3 [3.15]. The C-N bond-lengths in the original sources determine the nature of the active species [3.17]. The different sizes of the active species are associated with different radical diffusion kinetics, amongst other factors. Henceforth, another possible reason for the existence of amorphous carbon in N-CNT products at constant temperature is that the kinetics of the associated active species are dependent on the mixing ratio of DMF and acetonitrile (sp^3:sp). The general excellent N-CNT yield relative to amorphous carbon (Fig. 3.S1) can be attributed to high oxygen content in the reagents which was responsible for the reduction of reactive hydrogen radicals and the cleaning of the amorphous carbon. Another possibility is that different compositions of the active species (from the varied reagent ratios) are associated with different extents of dissolution in the catalysts and hence, also influences the yield composition [3.16]. The current work opens more room for the detailed determination of the mechanism involved.

The contribution of BET surface area from residual iron catalyst is negligible because the catalysts constitute a small proportion of the total surface [3.33]. Hence, the changes in surface area in the current work can only be significantly linked to the surface on the carbon materials.

Increasing the DMF to acetonitrile ratio in the DxA1 enhanced the BET surface area for N-CNTs from D0A1 up to D3A1 then decreased for samples D4A1 and D5A1 (Fig. 3.7a). Whereas in the D1Ax series, D1A0 had the highest surface area, higher than samples from both series, but it was noted that DxA1 series had larger surface areas when opposing ratios were compared, such as D2A1 and D1A2, were compared (Fig. 3.7b). The rationale behind the observed traits in the current work, that may possibly be deduced from the approximated number of tube walls (Table 3.S2 in supplementary information), is that smaller sizes culminated in higher surface areas. This concurs with the theoretical view that BET surface area is a function of the number walls in CNTs [3.28].

In general, the samples in the current work had small BET surface areas. A possible enlightenment is that there was less contribution from the inner surfaces of the tubes due to closed hemispherical caped ends in some MWCNTs (Fig. 3.2 and 5). Additionally, encapsulated metal as well as residues on the tube surface also reduces the MWCNT exterior available for appreciable nitrogen sorption. A possible way to enhance the textural properties, which was beyond the scope of the current work, is opening capped ends and purification of tubes by means of chemical treatment [3.28]. D0A1 and D5A1 had the least pore volumes but the rest were comparable (Fig. 3.7c). On the other hand, in the D1Ax, D1A0 had the highest and D1A4 had the least pore volumes (Fig. 3.7d). Except for D4A1 and D1A4, pores sizes in DxA1 series generally decreased from D0A1 to D5A1 (Fig. 3.7e) whereas for D1Ax series an almost constant value of 25 nm was noted (Fig. 3.7f).

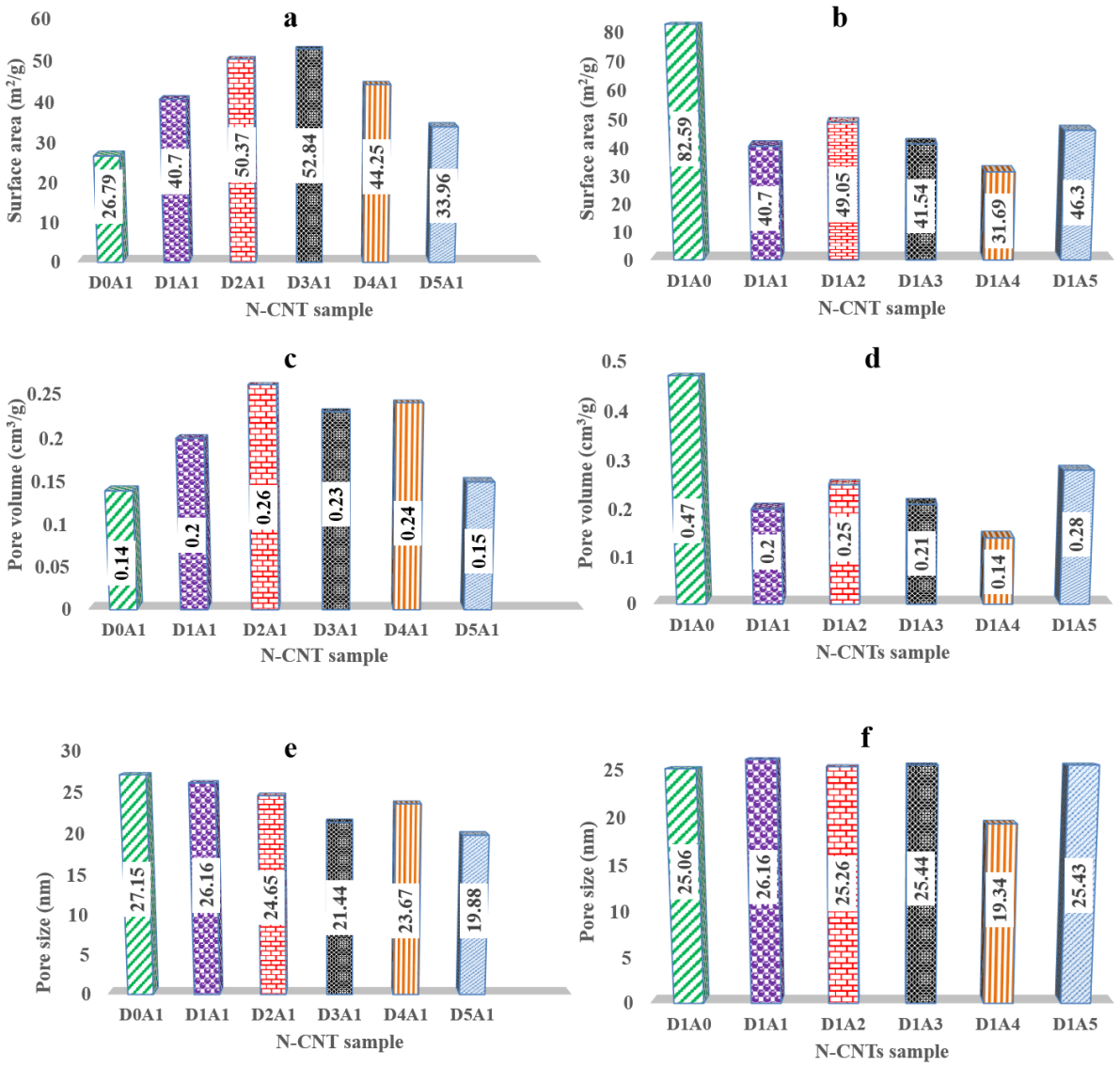

Fig. 3.7. Textural characteristics of samples synthesized at different ratios and constant temperature.

In the DxA1 series, nitrogen content initially increased with increase in DMF ratio, i.e. from D0A1 to D2A1 then decreased thereafter whereas no clear trend was perceived for the counter series but D1A3 and D1A0 had the highest nitrogen content of 9.38% and 5.87%, respectively (Table 3.1). Similar studies have been done by Kaushik *et al.*, [3.34] but they achieved lesser nitrogen content (5.5%) upon addition of 45% DMF as nitrogen source. The highest nitrogen content in D2A1 matched the smallest ID, OD and number of N-CNT walls in the DxA1 samples. This corroborates with deduction by Liu *et al.*, [3.15] in that incorporation of nitrogen reduces diameter of N-CNTs. This trait was not apparent in the D1Ax but the D1A0 (second

highest nitrogen content) had the smallest diameters and number of N-CNT walls. The most probable explanation of the lack of correlation in this regard is linked to the etching effect of oxygen on the tube walls contributing to the decrease of diameters. Additionally, the mismatch may infer the encapsulation of molecular nitrogen in the tubes [3.15]. This was supported by the XPS data (in the following sections).

The samples with high nitrogen content exhibited poorer thermal stabilities and this is due to the strain in the carbon framework upon introduction of nitrogen. Similar observations were reported by Nxumalo *et al*., [3.2] Additionally, from statistical analysis of D1Ax (Table 3.S2 in supplementary material), samples D1A0 and D1A3 had smallest average compartment sizes and this corroborated with their high nitrogen content. According to the elemental analysis data in Table 3.1, it is clear that sp^3 hybridised was better than *sp* hybridised nitrogen precursor in terms of higher level of nitrogen-doping of the products. A possible reason for high nitrogen incorporation in D1A0 relative to D0A1 is higher O:C ratio (in the reagent, Table 3.S1 in supplementary material). Additionally, the current work further showed a link between the higher nitrogen content in D1A0 (N-CNTs from DMF) and smaller OD, ID, number of N-CNT walls as well as compartment size than D0A1 (N-CNTs from acetonitrile). Basing on the molecular formulas of the precursor, $(CH_3)_2NCOH$ and CH_3CN, it may be deduced that the extra CH_3, H and O atom in DMF, culminating in structural differences, enhances the nitrogen incorporation in the N-CNTs. This may infer that $(CH_3)_2NCOH$ produced more C-N units in the reaction chamber than CH_3CN. The C-N units play a crucial role in the incorporation of nitrogen in the graphitic structure [3.15]. Ombaka *et al*., [3.4] reported on enhancement of nitrogen-doping content of N-CNTs by addition of oxygen in the reagent. Whilst the trends in O:C ratio (i.e. 1:2 and 2:1 ratio in reagent) was able to similarly account for the trends in nitrogen content for D1Ax and DxA1, respectively, however, this correlation could not account for tendencies at higher ratios of 1:3 and 3:1 and beyond. A probable reason is that the latter ratios introduces more radical influence as explained in earlier sections. In addition, Table 3.1 shows that a higher H atom wt.% in the carbon source does not necessarily imply higher hydrogen content in the product. Higher hydrogen content in the product could mean high amount of dangling bonds on N-CNTs walls.

Table 3.1: Elemental analysis and Raman I_D/I_G ratios of N-CNTs synthesised with varying reagent ratios at 900 °C

Sample	H	N	I_D/I_G
D0A1	0.06	3.49	2.03
D1A1	0.32	3.75	0.32
D2A1	0.12	4.11	1.61
D3A1	0.02	3.02	1.13
D4A1	0.08	1.89	1.50
D5A1	0.04	1.99	1.02
D1A0	0.07	5.87	1.27
D1A1	0.32	3.75	0.32
D1A2	0.07	3.19	0.80
D1A3	0.89	9.38	0.36
D1A4	0.17	3.30	0.32
D1A5	0.09	3.38	0.28

A representative Raman spectrum of the N-CNTs, showing the D- and the G-band located at 1350 and 1550 cm^{-1}, respectively, was given in the supplementary information (Fig. 3.S15). The given representative Raman spectrum is for D4A1 N-CNTs. Both D1A0 and D0A1 had the highest I_D/I_G ratios for D1Ax and DxA1 samples, respectively (Table 3.1). This infer higher defect nature in the aforementioned samples, but the current work suggests that mixing *sp* and sp^3 hybridised nitrogen sources reduced defects. Additionally, DxA1 samples were more defective than D1Ax (Table 3.1) and this infers that high sp^3-hybridised nitrogen in reagents, in DMF, increased the defects in the N-CNTs products. Whilst, high *sp*-hybridised nitrogen had an opposite effect. Also, no direct relationship was observed between I_D/I_G and nitrogen wt.% in N-CNTs.

PXRD shows that D1Ax N-CNTs were more crystalline than DxA1 and the most plausible reason is the lower defect nature, i.e. lower I_D/I_G ratios, in D1Ax N-CNT (Fig. 3.8 and Table 3.1). All samples showed peaks at two theta of 25°, 38°, 45°, 65°, 54°, 78° and 82° attributed to reflection of $C_{(002)}$ graphitic structure, Fe_3C, $C_{(101)}$, $C_{(006)}$, FeO, $C_{(110)}$ and Fe, respectively [3.4,3.35]. The presence of Fe_3C reflection suggests that it is the most predominant catalytic phase. The PXRD data substantiated the SEM, TEM and TGA residual metal in the product deductions. The peak at 25°, ascribed to graphitic structure, increased noticeably with increase in acetonitrile ratio in the D1Ax N-CNTs whereas in that of DxA1 peak intensification was negligible. This means, both Raman and PXRD spectroscopies, infers that D1Ax samples were more crystalline than DxA1 N-CNTs and that higher composition of *sp* source enhanced crystal quality of N-CNTs. This a clear indication of the influence of sp^3:*sp* ratios.

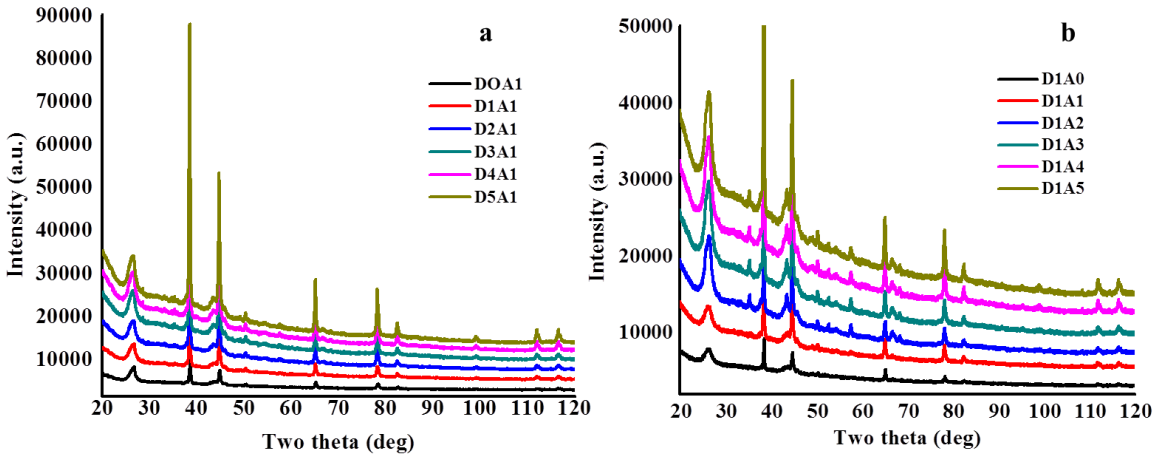

Fig. 3.8. The powder X-ray diffraction spectrums for (a) DxA1 and (b) D1Ax N-CNT samples.

The X-ray photoelectron spectroscopy analysis was done on representative samples, D1A0, D0A1, D1A3, D3A1 and D3A1, and the Fe2p peaks observed were accounted for as residual iron noticed in both TGA and PXRD. All the typical Fe peaks were of similar shapes and this infers they were in similar chemical states. This correlates well with the PXRD deductions. Additionally, the C1s peaks at 285 eV (Fig. 3.S14 in supplementary information) was assigned to the graphitic carbons in the N-CNTs. The slight peak at 288.5 eV in D3A1 can be attributed to oxygen-containing groups such as carbonyl moieties [3.36]. However, they are various components of C1s peaks that are not due to bonding configurations. These are principally the

energy-loss peaks, which are part of the photo-emission process. These are particularly strong in N-CNTs [3.37]. Hence, no further peak assignments for C1s moieties were done.

In addition, the peaks at 399 to 403 eV (Fig. 3.9) are due to various nitrogen species. The peaks at 398.2, 399.3, 400.6, 402.5 and 404.6 eV were attributed to pyridinic and carbonitrile molecules (N1), quaternary amine (N2), pyrrolic functionalities (N3), various nitrogen oxides (N4) whilst the fifth peak was accredited to either adsorbed or encapsulated nitrogen molecules within the graphitic framework (N5), respectively [3.38].

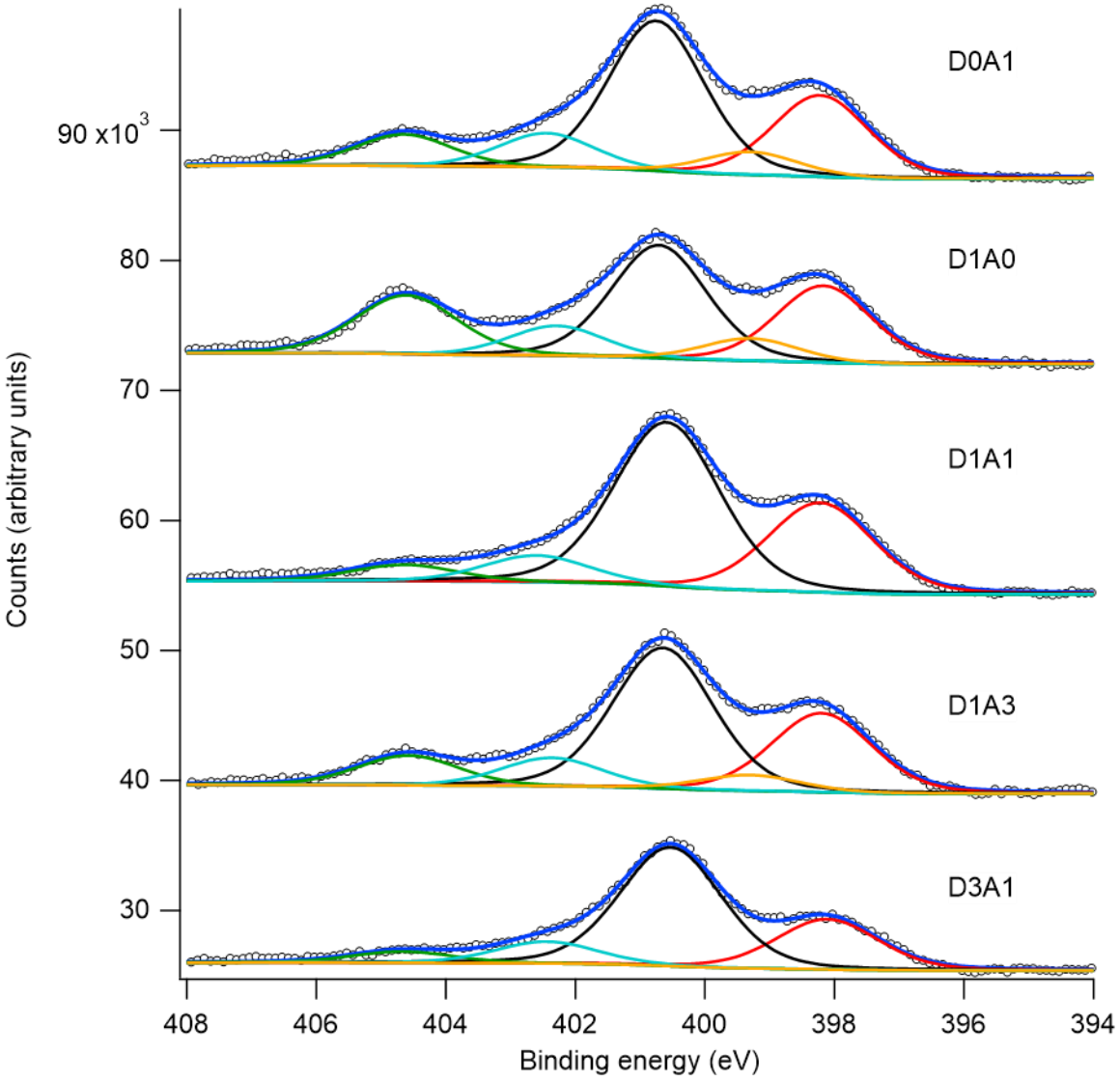

Fig. 3.9. The X-ray photoelectron spectroscopy spectra for representative N-CNT samples.

The spectra also show that the main N species was the N3 followed by the N1 and this agreed with the quantification in Fig. 3.10. The N3 functionality was the reason for the observed capped tube ends and the disordered and bent structures of N-CNTs (Fig. 3.1, 3.4-3.5) [3.21]. The representative N-CNTs samples show that varying reagent composition had no effect on the N4 (Fig. 3.10). From the current XPS data, D1A0 had higher N5 than D0A1 and this means the sp^3-hybridised nitrogen source, DMF, was a better source than *sp* source, acetonitrile. In addition, both *sp* and sp^3 sources had a similar composition of N1 and N2 but mixing the reagent slightly increased N1 whilst severely dropping the N2 species. This ties in well with the view that the composition of active species and associated kinetics influences the ultimate physicochemical properties.

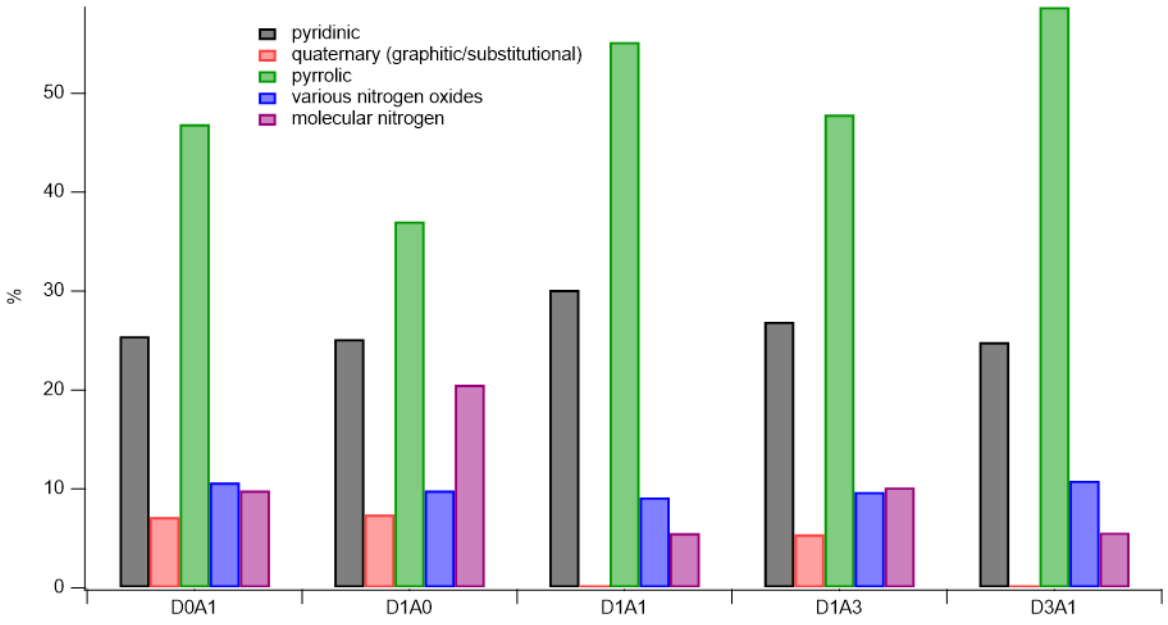

Fig. 3.10. The composition of the nitrogen species of the representative N-CNT samples.

In terms of the representative DxA1 N-CNTs, the trend for N3 species, upon increasing sp^3 source in reagent, was D0A1 < D1A1 < D3A1 but the effect was a decrease in both N2 and N5 moieties (Fig. 3.10). This is a manifestation of the ability to modify the nitrogen functionality using reagent composition. On the other hand, for D1Ax, both N1 and N3 reaches a plateau with D1A1 and decrease at D1A3 (Fig. 3.10).

States at the Fermi level means carriers can be excited into the conduction band, hence, the density of states at Fermi level is used as a gauge of metallicity [3.21]. All the representative N-CNTs, except D3A1, had similar metallicity (area enclosed by dotted rectangle in Fig. 3.11). The current data infers the D3A1 was less metallic than the rest of the N-CNTs and this can be rationalised by the oxygen-containing moieties ascribed in Fig. 3.S14 (Supplementary data), which introduce insulating effects.

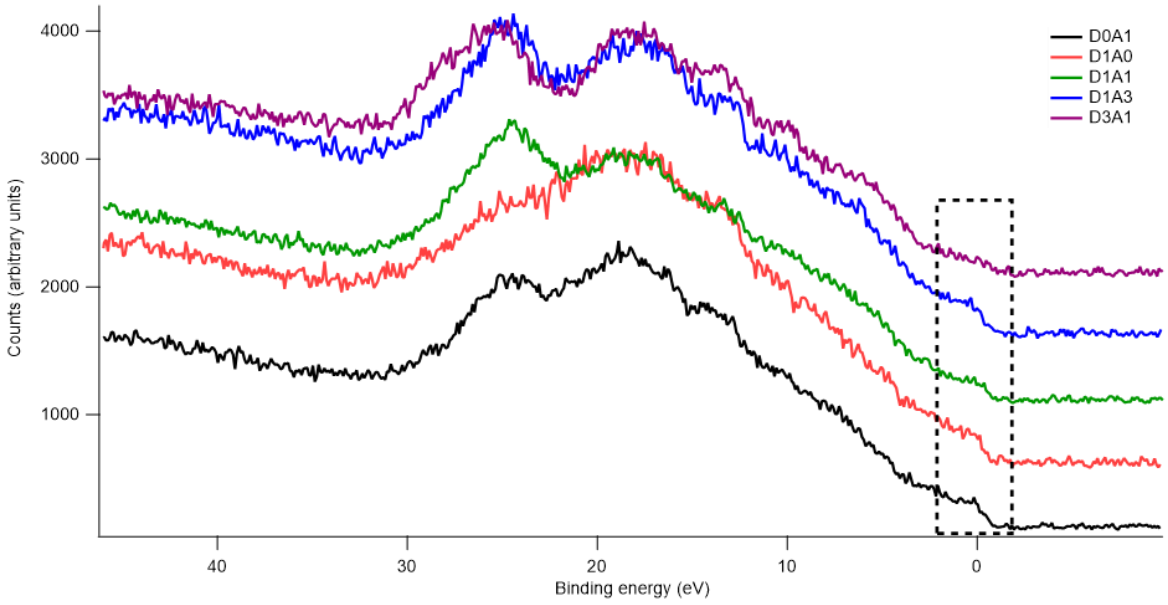

Fig. 3.11. Determination of metallicity of representative N-CNTs.

Conductivity measurements were done on selected samples, namely, D1A0, D0A1, D1A3 and D4A1. The rationale behind selection was that, D1A0 and D0A1 were samples synthesised from DMF (sp^3 source) and acetonitrile (sp source) as the only nitrogen sources, whilst D1A3 gave the highest nitrogen content. The D3A1 N-CNTs were non-conductive or conductivity values were below the detection limit, hence the data was not included in Fig. 3.12. The reason for poor conductivity was attributed to the poor metallicity as determined by the the density of states at the Fermi level (Fig. 3.11). The sample D4A1 had the least nitrogen content and hence, included for comparison with D1A3. A four-point probe was utilised in carrying out these measurements and the actual conductivity was calculated by use of the following equations:

$$\rho = \frac{\pi t}{In\ 2}\left(\frac{\Delta V}{I}\right) \qquad \text{(Equation 2)}$$

$$\sigma = \rho^{-1} \qquad \text{(Equation 3)}$$

Where, σ , t , ΔV , I is resistivity, conductivity, film thickness, change in voltage and measured current, respectively.

Electrical conductivity of N-CNTs is subjected to interactions amongst individual tubes, dimensions, purity, doping type and preparation method [3.4]. The data in Fig. 3.1a suggest that the D0A1 N-CNTs had the highest interactions and therefore the least internal resistance. The D1Ax generally had similar but lower conductivity values than DxA1 N-CNTs. This tend to suggest that high nitrogen content does not necessarily imply high electrical conductivity in the current work. A possible reason is likely linked to the composition of the pyrrolic nitrogen moieties, higher content was associated with better conductivity (Fig 3.10 and 3.12). No direct relationship between dimensions and conductivity was deduced and this is a clear indication that influence from either decrease in mean freepath of charge carriers or increase in Columbic repulsion between layers from decrease in OD [3.4,3.39] was negligible in the current work. Another general inference in the current work was the semiconducting behaviour of all N-CNT samples as exhibited by an increase in conductivity with increase in temperature. The semi conducting behaviour of N-CNTs can be explained theoretically *via* three models namely Mott variable range hopping, Efros-Shklovskii variable range hopping and Fluctuation induced tunnelling [3.40]. Mott variable range hopping view is that electrons traverse the material by hopping through different localised impurity states, Efros-Shklovskii variable range hopping suggest that that a Coulomb gap is formed as the density of states vanish at the Fermi level whilst in the Fluctuation induced tunnelling a material is modelled as a series of metallic regions with small barriers separating them. Similar observations have been reported in earlier studies [3.4,3.18,3.40]. A probable reason for a slight drop in conductivity of D0A1 at c.a. 330 K thermal desorption of nitrogen.

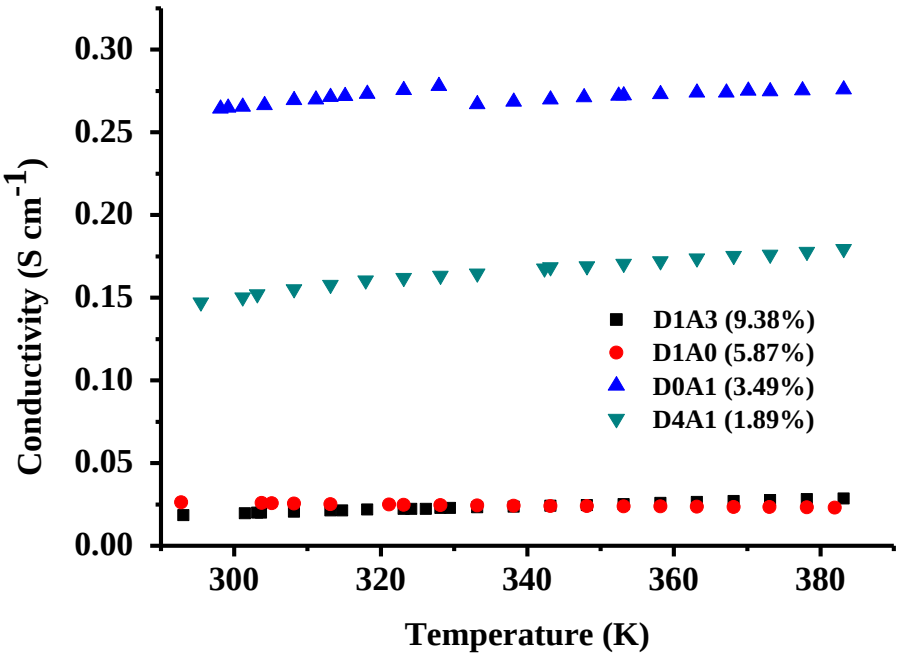

Fig. 3.12. Representative conductivity measurements of some selected N-CNTs samples.

The N-CNTs synthesised herein were tested for their potential application in charge storage, particularly, in electrochemical capacitors. Typically, the as-synthesised N-CNTs were purified to remove residual metal catalysts (Fig. 3.S16 in the supplementary information) and thereafter used as electrode materials for electrochemical capacitors (ECs). This means the associated physicochemical properties were altered during purification [3.41,3.42]. Hence, the scope of the current report was tuning associated physicochemical characteristics of N-CNTs using reagent compositions. The D0A1 N-CNTs were selected for the preliminary tests of the materials in ECs since they have the least internal resistance (Fig. 3.12). A representative cyclic voltammetry curve shown in Fig. 3.13 displays an enhanced current response and a more rectangular curve with increase in scan rate. This is an indication of an ideal capacitive behaviour and exhibition of physical adsorption/desorption of solvated electrolyte cations at higher scan rates [3.41,3.43]. Hence, this reflects their great potential as electrodes of ECs. Further studies will be done on D1A1 and D3A1 with higher N3 species, respectively, to investigate the associated effect on EC functionality.

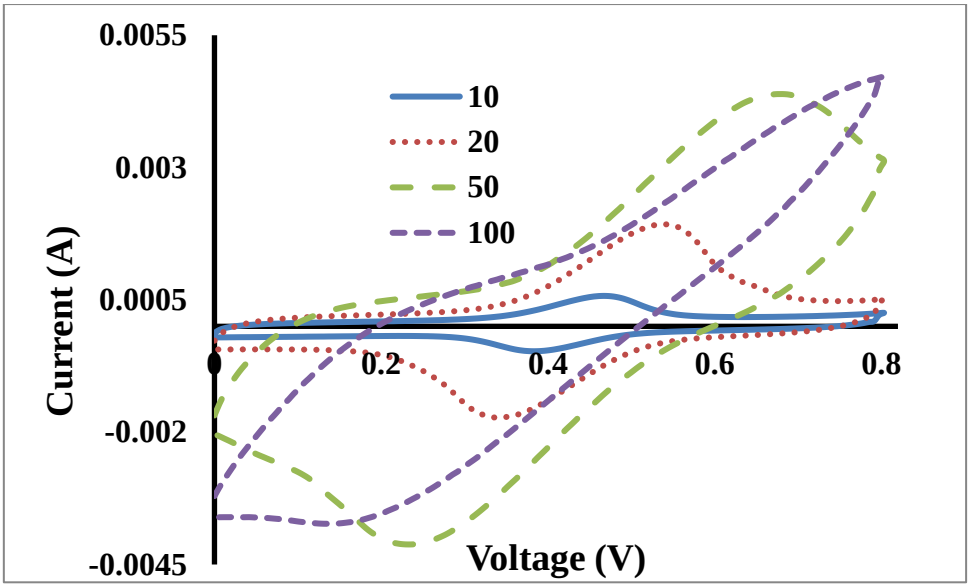

Fig. 3.13. The representative cyclic voltammetry curve for N-CNT samples, specifically for D0A1. The electrochemical characteristics were investigated at various scan rates of 10, 20, 50 and 100 mV s^{-1} in a three-electrode system.

3.3.2 Temperature effects on N-MWCNTs

The samples with the highest nitrogen content, i.e. D1A0 and D1A3, were used to investigate the optimum synthesis temperature and the outcomes are elaborated in the following sections.

3.3.2.1 Temperature effects on D1A0

Similar SEM images were obtained for D1A0 N-CNTs at different synthesis temperatures but products at 1000 °C had the largest number of N-CNT walls than the rest (Fig. 3.14 and Table 3.S3 in supplementary information). N-CNTs synthesised at 850 °C and 950 °C were debundled whilst those at 1000 °C were haphazardly oriented and slightly agglomerated. Similar observations at high temperatures were reported by van de Burgt *et al*., [3.24] and similarly the observations in the current work can be explained with the mechanism that refer to the carbon diffusion in the catalyst as the rate determining step. The mostly likely explanation is the differences in growth directions due to enhanced diffusion rate of active species towards the catalyst at higher synthesis temperatures.

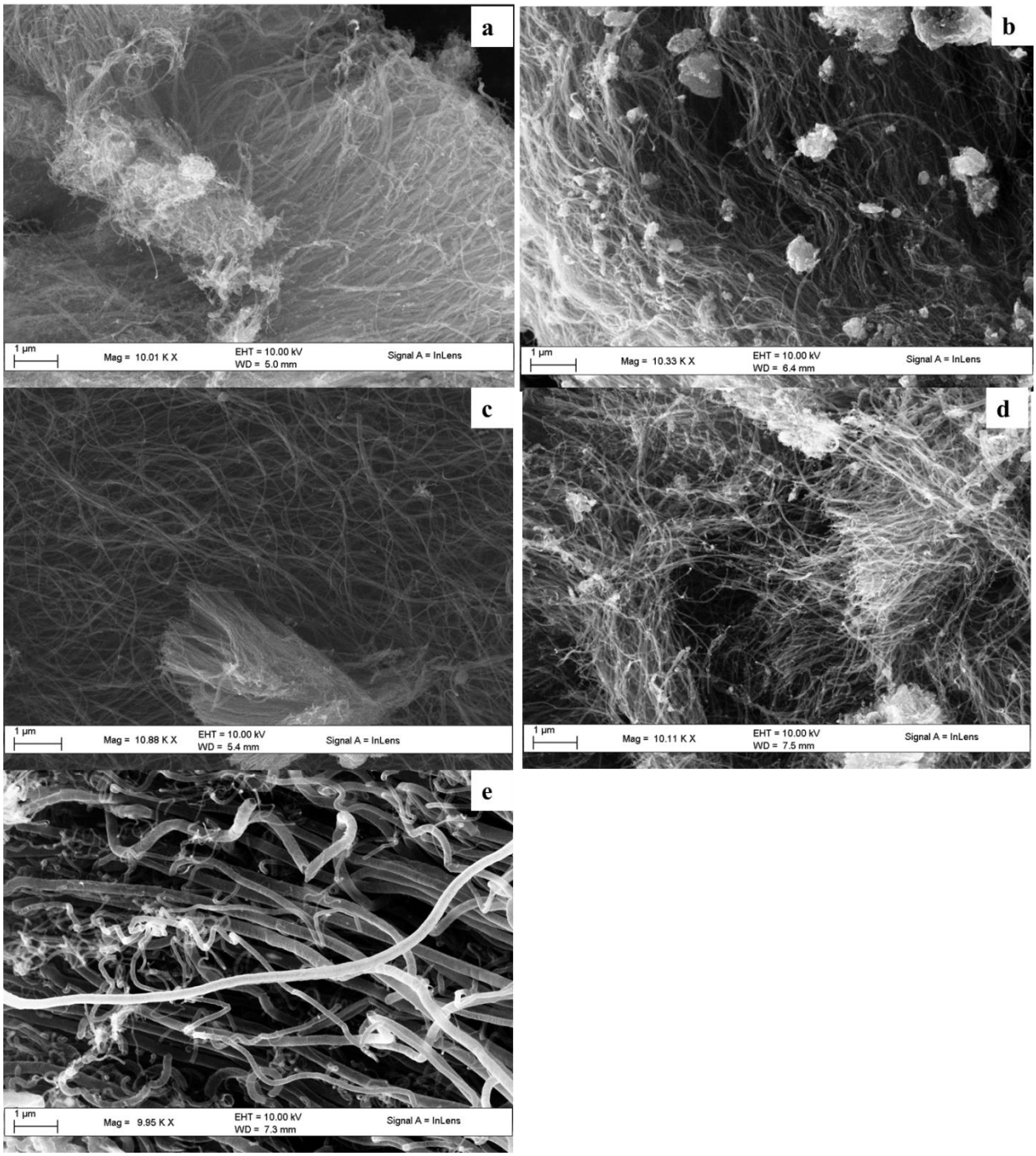

Fig. 3.14. The representative SEM images for the D1A0 samples (a) 800 °C, (b) 850 °C, (c) 900 °C, (d) 950 °C and (e) 1000 °C.

From Fig. 3.15, tubes of variable dimensional uniformity in terms of diameters and number of tube walls with respect to synthesis temperature (Fig. 3.S8-9 and Table 3.S3 in supplementary information). The number of N-CNT walls formed from synthesis from sp^3 source, DMF alone (D1A0), increased with increase in synthesis temperature from 800 °C to 1000 °C. This

conjectures that dimensions of the N-CNTs in the current work can be tailored by varying temperature of synthesis. This correlates with the view reported by van de Burgt *et al.*, [3.24] that high temperatures may lead to more efficient dissociation of carbon sources and thickening of the resulting tube walls. D1A0 at 850 °C showed some Y-shaped N-CNTs with nodes whilst at 900 °C coiled tubes were obtained (Fig. 3.15b-c). At 950 °C and 1000 °C, N-CNTs with irregular walls and thicker tubes were noticed on the later temperature of synthesis (Fig. 3.15d-e, Table 3.S2 and Fig. 3.S8 in supplementary information). A possible reason for the irregular wall thickness, bent structures and nodes on the N-CNT surfaces is the existence of pentagons and heptagons on their graphitic framework [3.28]. The average wall thickness increased as the synthesis temperature was raised from 800 °C to 1000 °C. This is instigated by higher catalyst sizes in the reaction vessel, due to agglomeration, at higher temperatures. A possible basis of this outcome is that at 800 °C, unlike at 1000 °C, the iron catalyst particles have minimal chances of agglomeration due to low kinetic energy.

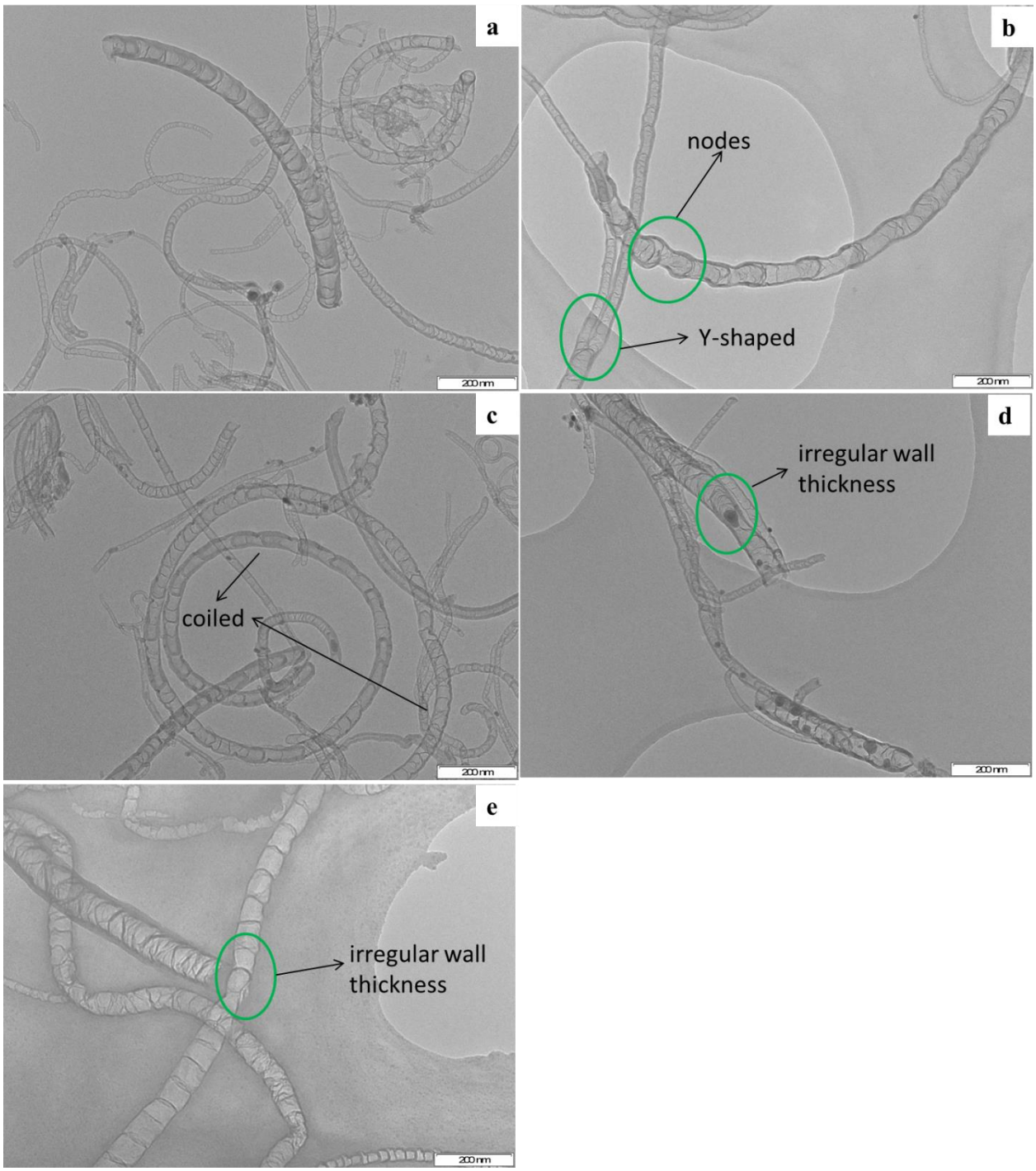

Fig. 3.15. The representative TEM images for the D1A0 samples (a) 800 °C, (b) 850 °C, (c) 900 °C, (d) 950 °C and (e) 1000 °C.

In terms of thermal stability, D1A0 synthesised at 850 °C had a slight weight loss at 150 °C due to water loss (Fig. 3.16a). Weight loss due to amorphous carbon was noticed at synthesis temperatures of 800, 850 and 950 °C (Fig. 3.16b). The slight kink on thermograms of samples synthesised at 950 °C and 1000 °C was attributed to various forms of defects on tube surface

such as irregular shaped and bend walls of N-CNTs as (Fig. 3.16a). The defects on the N-CNT walls are points of weakness in the graphitic framework, hence easily decompose [3.28]. The main weight loss, due to N-CNTs, was between 400 and 600 °C. Again, temperature at which N-CNTs were synthesised determined the residual iron content, at 800 °C, 950 °C and 1000 °C N-CNTs had similar quantities of iron but lower values were obtained at 850 °C and 900 °C (Fig. 3.16a). Similar observation of higher metal catalyst residue were obtained at high temperatures by Tang *et al*., [3.17] but unlike their report, lowest temperature in the current work also had higher wt.%. Whilst at high temperatures high growth rate reduced the catalyst life time [3.30], a plausible reason for higher metal residue at the lowest temperature, 800 °C, in the current work is linked to the low number of N-CNT walls (Table 3.S3 in supplementary material) and this culminates in higher carbon to iron ratio in the product. In addition, D1A0 produced predominantly N-CNTs in the products with respect to other shaped carbon materials (Fig 3.S1c in supplementary material). Therefore, in terms of residual iron catalyst and N-CNTs wt.% in the product, 900 °C was the best temperature of synthesis.

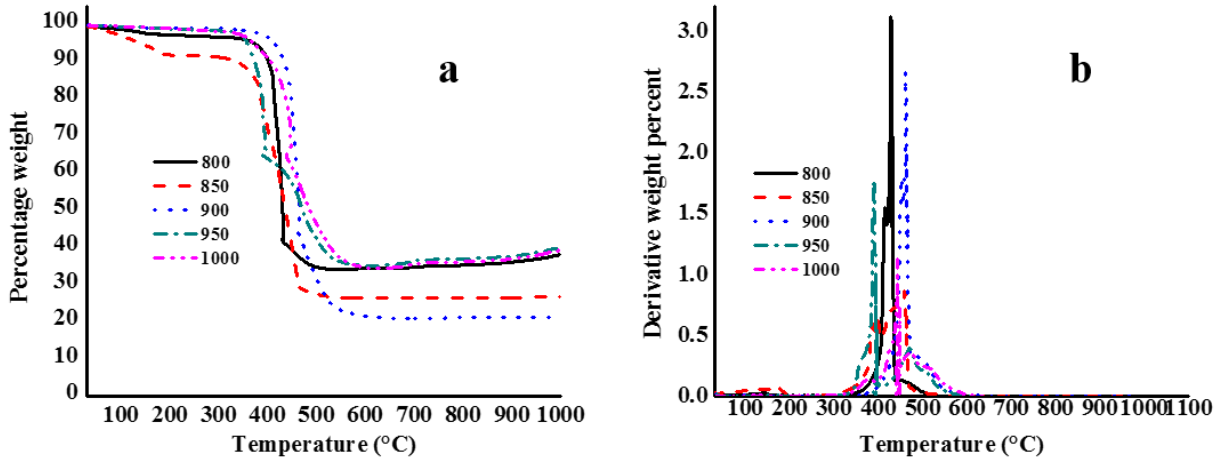

Fig. 3.16. Representative TGA (a) thermograms and (b) derivative weight curve for the D1A0 samples synthesised at different temperatures.

The products at 800 °C had a relatively remarkable BET surface area and BJH pore volume (Fig. 3.17a-b) and this corroborates with the smallest number N-CNT layers whilst 950 °C had the largest pore sizes (Fig. 3.17c). The textural characteristics data did not show a trend but it may be noted that synthesis temperature prompts changes.

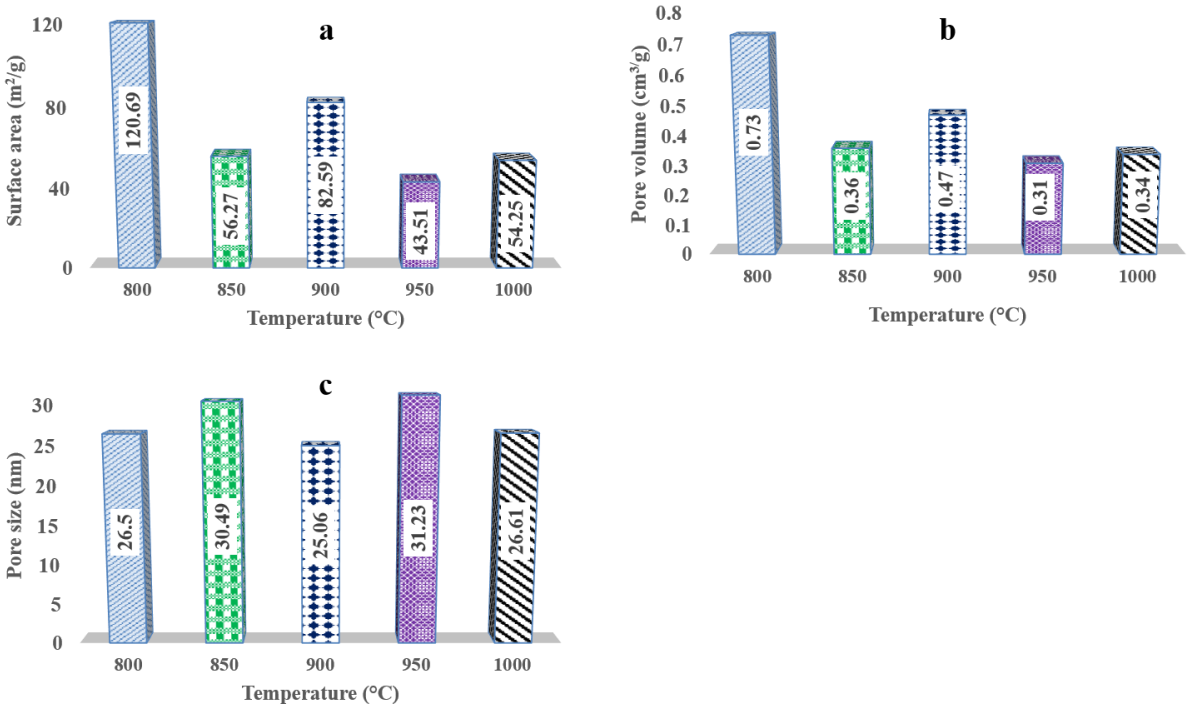

Fig. 3.17. Textural characteristics of D1A0 samples synthesized at different temperatures.

In the elemental quantification, hydrogen decreased with increase in synthesis temperature from 900 °C to 1000 °C (Table 3.2). A possible motive is that at higher temperatures, dangling bonds are minimal. The highest nitrogen content was achieved at 800 and 900 °C (Table 3.2) and these samples corresponded with smallest N-CNT diameters (Table 3.S3 and Fig. 3.S11-12 in supplementary material). The decrease in nitrogen content at 950 and 1000 °C corroborated the works of Yadav *et al*. [3.6] In addition, from the study, it is clear that DMF is a suitable carbon and nitrogen source for the synthesis of N-CNTs with between 2.5 and 6 % nitrogen depending on temperature of synthesis

Table 3.2: Elemental analysis and Raman spectroscopy data of D1A0

Sample	Temperature	H	N	I_D/I_G
D1A0	800	0.90	5.86	0.79
	850	1.15	4.88	0.19
	900	0.07	5.87	1.27
	950	0.04	2.98	1.13
	1000	0.00	2.47	1.19

Raman data (Table 3.2) suggest that lower temperatures of synthesis were associated with low defect concentrations in N-CNTs. Also, from critical examination of the data from TEM analysis (Table 3.S3 in supplementary information), elemental composition (Table 3.2) and textural characteristics (Fig. 3.17), it was eminent that high nitrogen doping using a sp^3 source induced a decrease in ID, OD and wall thickness and increase in BET surface area of N-CNTs.

3.3.2.2 Temperature effects on D1A3

A similar study on the influence of temperature was done with D1A3 samples and N-CNTs synthesised at lower temperatures tended to be more agglomerated (Fig. 3.18). Amorphous carbon was also present in the product synthesised at 800-950 °C (green circle in Fig. 3.18 and Fig. 3.S1d in supplementary information). At 800 °C and 850 °C haphazard N-CNTs were produced whilst at 900 °C bundled but aligned tubes were noticed (Fig. 3.18). Additionally, carbon spheres were also obtained at both 950 °C and 1000 °C (green rectangle in Fig. 3.18d).

This is because at high temperatures iron particles agglomerated due to high collision rates and therefore carbon sphere formation was facilitated [3.1].

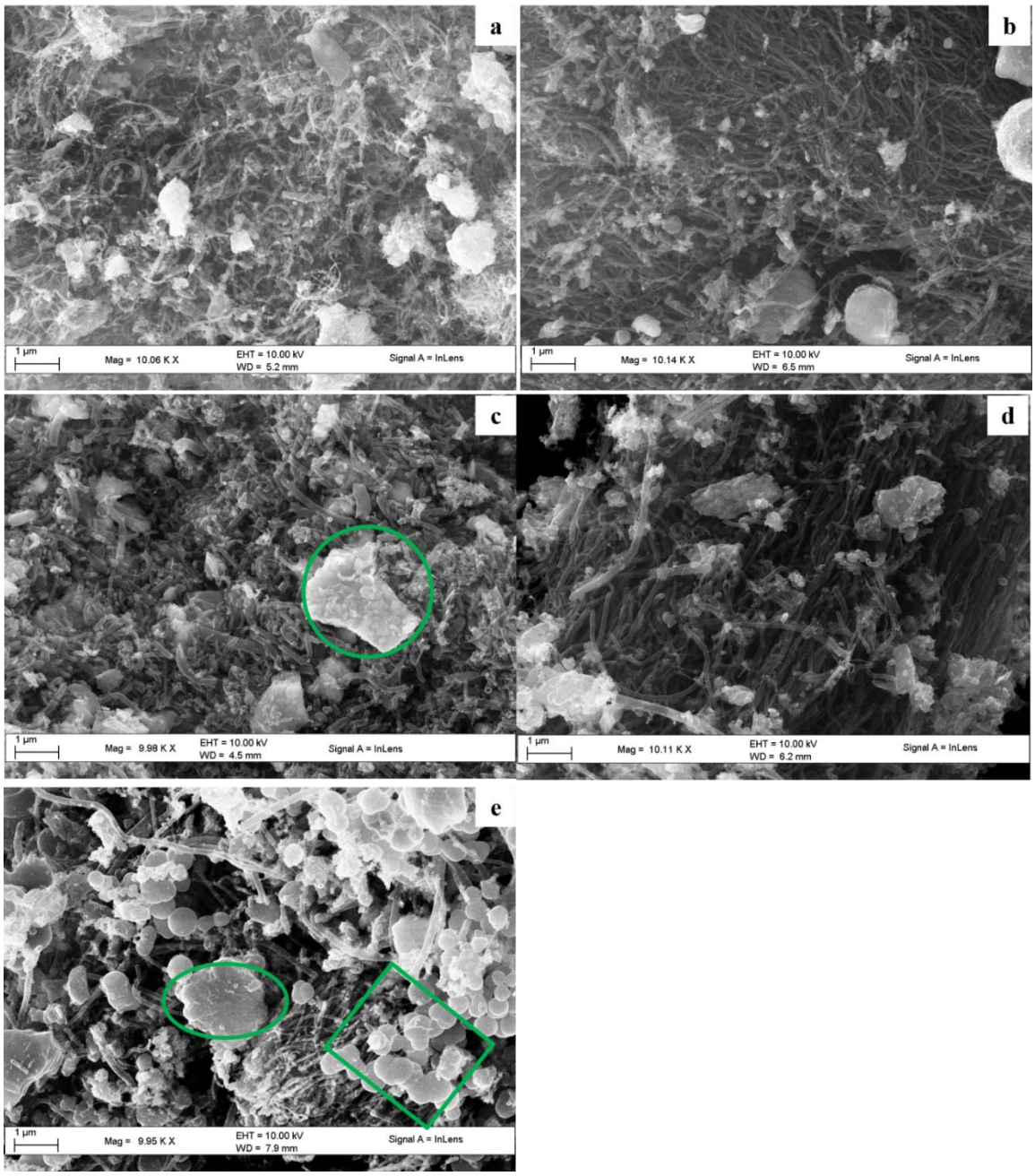

Fig. 3.18. The representative SEM images for the D1A3 samples (a) 800 °C, (b) 850 °C, (c) 900 °C, (d) 950 °C and (e) 1000 °C.

D1A3 synthesised at 800 °C had N-CNTs with lower intensities of bamboo compartments (Fig. 3.19a) and at 850 °C N-CNTs appeared to have wrinkled surfaces. At 900 °C defective tubes

walls were also observed whilst at 950 °C some Y shaped tubes were obtained (Fig. 3.19c-d). Defective walls at 900 °C were due to inclusion of heptagons and pentagons in the graphitic structures of N-CNTs.

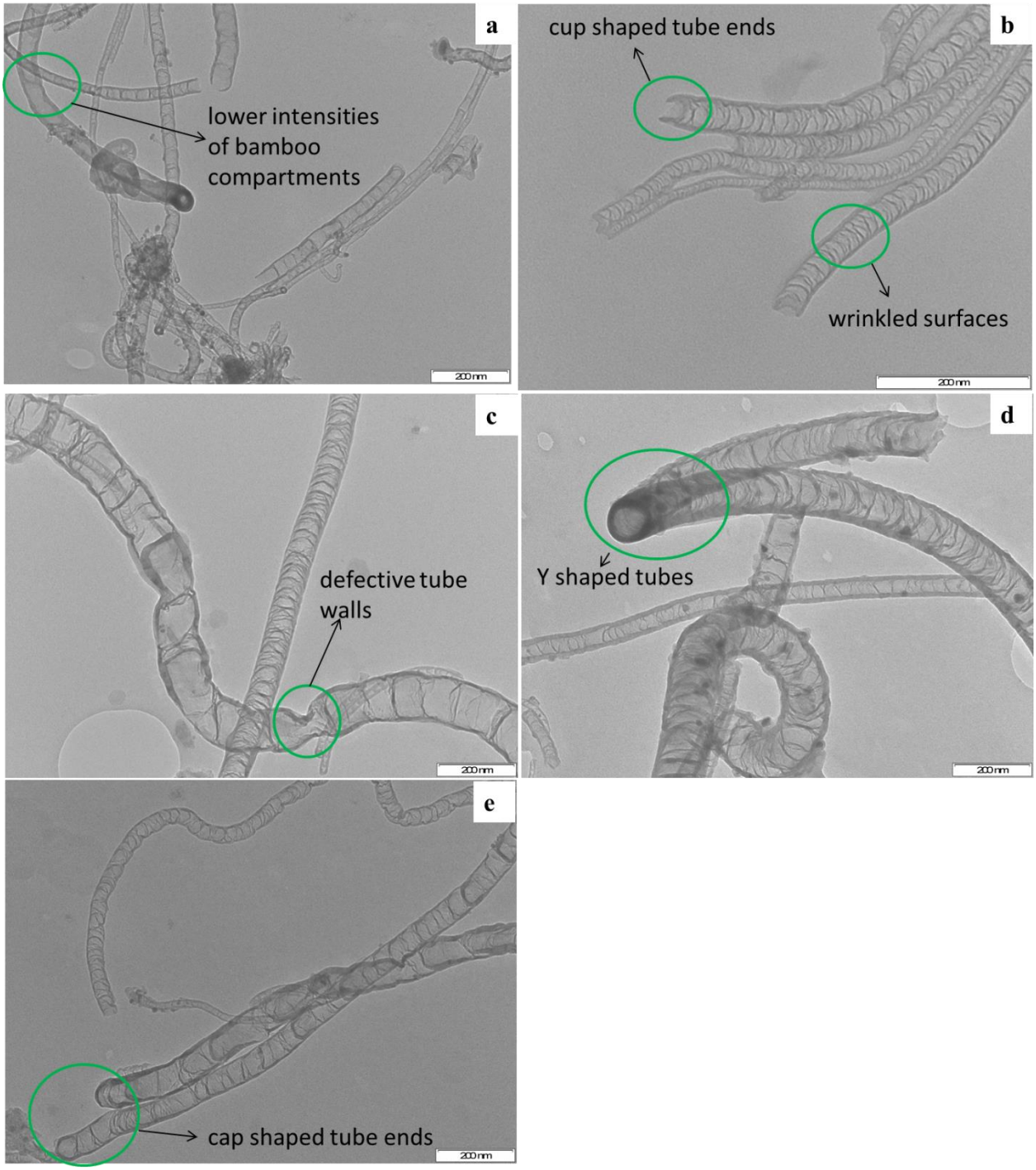

Fig. 3.19. The representative TEM images for the D1A3 samples (a) 800 °C, (b) 850 °C, (c) 900 °C, (d) 950 °C and (e) 1000 °C.

Temperature influenced morphology and dimensions, for instance synthesis at 850 °C produced cup shaped tube ends but at 1000 °C cap shaped tube ends were noticed. Additionally, OD, wall thickness and number of tube walls increased in the synthesis temperature range of 800-900 °C (Table 3.S2 in supplementary information). Beyond 900 °C, the number of N-CNT walls decreased. The different synthesis temperature produced different product composition and physical properties, and therefore decompose at different temperatures. Hence, different TGA profiles were obtained for the 5 samples shown in Fig. 20 a.

D1A3 samples at different synthesis temperatures had similar thermal stabilities (Fig. 3.20a), however, they had different residual iron wt. %. Residual iron wt.% decreases with increase in synthesis temperatures from 800 °C to 900 °C then increases at 950 °C (Fig. 3.20a). The reason for the decrease of iron residue wt.%., more inclined thermogram and a wider decomposition temperature for D1A3 sample synthesised at 1000 °C (Fig. 3.20) was attributed to formation of both carbon spheres and N-CNTs. The decomposition temperature region of the D1A3 N-CNTs was between 400 and 700 °C. This means beyond 700 °C all the carbonaceous material would have decomposed, and the catalyst residues are exposed to heat and oxygen. This led to formation of a metal oxides and hence, weight increased. Compared to D1A0, D1A3 samples decomposed over a wider range of temperature and had lower amounts of amorphous carbon (derivative weight curve on Fig. 3.20b). The composition of amorphous carbon decreased with increase in temperature and the parallel broadening of the derivative weight peak is an indication of decrease in sample homogeneity. This was attributed to the formation of both N-CNTs and carbon spheres at 1000 °C as well as increase in both OD and ID between 800 and 950 °C due catalyst agglomeration.

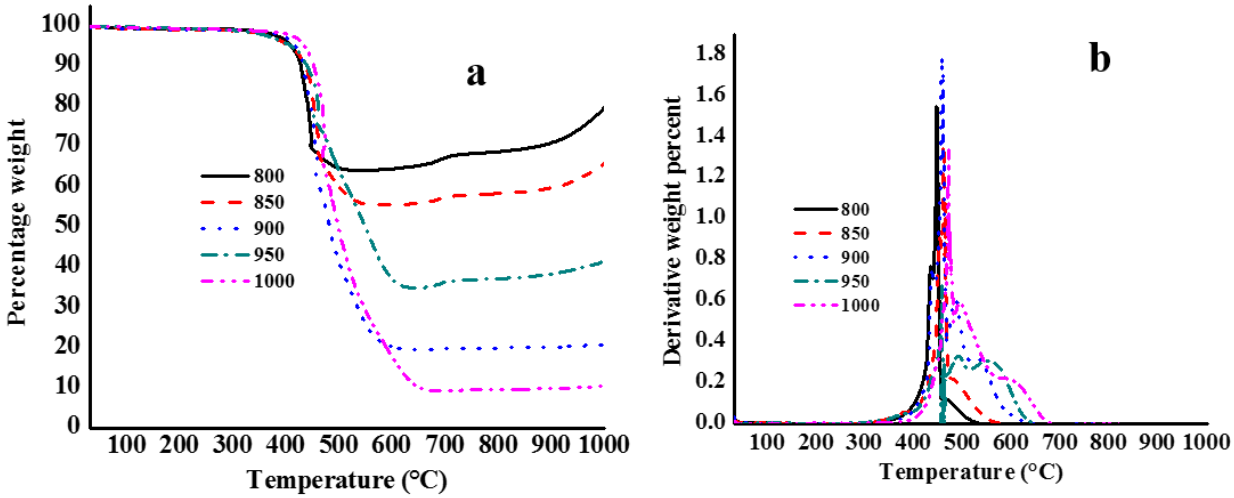

Fig. 3.20. Representative TGA (a) thermograms and (b) derivative weight curve for the D1A3 N-CNTs synthesised at different temperatures.

For D1A3, BET surface area decreased with increase in synthesis temperature (Fig. 3.21a). and no clear trend was noticeable on pore volume and size (Fig. 3.21b-c). A possibly reason for this trend is similarly linked to size variations. The lowest values of pore volume and sizes noticed at 1000 °C (Fig. 3.21b-c) were due to presence of carbon spheres. Hence, the presented data clearly shows mixing DMF with acetonitrile, 1:3 ratios, clearly allowed tailoring of BET surface area of the obtained products.

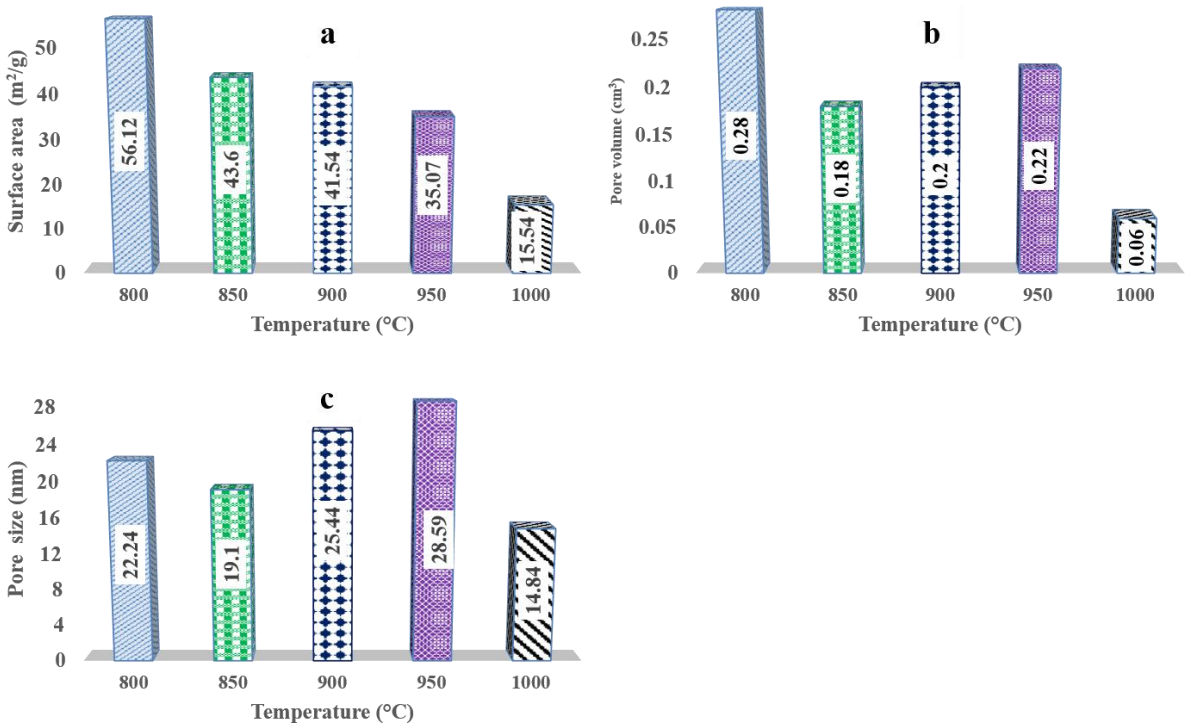

Fig. 3.21. Textural characteristics of D1A3 samples synthesized at different temperatures.

A possible source of hydrogen, determined by means of elemental analysis, in the products (Table 3.3) was the existence of dangling bonds. Nitrogen content increased from 800 °C to 900 °C then decreased at 950 °C and this an indication of temperature effect on nitrogen doping (Table 3.3). The decrease in nitrogen amount in the product in both D1A0 and D1A3 from 900°C to 950 °C corroborates with the report by Chazari *et al.*, [3.5] Unlike the optimum temperature of 850 °C reported by Keru *et al.*, [3.1] Ombaka *et al.*, [3.4] and Yadav *et al.*, [3.6] highest nitrogen content in the current work was achieved at 900 °C. This suggests the dynamics in the effect of nitrogen availability from source, influenced by nitrogen hybridisation in reagent, in addition to catalyst and growth temperature. Upsurge of nitrogen at 1000 °C can also be a result of the presence of carbon spheres. A critical analysis of the Table 3.2 - 3.3, unlike earlier reports [3.17,3.26], shows that nitrogen content does not necessarily decrease with increase in temperature. In addition, the two tables clearly indicate that at 900-1000°C D1A3 N-CNTs had higher nitrogen content composition unlike at 800-850 °C for D1A0. This means that enhancement of N-doping in N-CNTs is not obvious upon mixing sp^3 and *sp* nitrogen sources, DMF and acetonitrile, but is subject to the choice of synthesis temperature selected. A possible inference is the independence of N-doping to metal-

nitride pre-existence in the current work (low Fe:N ratios in Table 3.S1 supplementary information). Additionally, a further manifestation of induced differences in growth dynamics, it may be noted that the link between decrease in diameters, enhancement in BET surface area and increase N-doping levels was disrupted upon mixing *sp* and sp^3 sources in the current work.

Table 3.3: Elemental analysis and Raman spectroscopy data of D1A3

Sample	Temperature	H	N	I_D/I_G
D1A3	800	0.68	2.90	0.37
	850	0.12	3.40	0.44
	900	0.89	9.38	0.36
	950	0.05	3.69	0.76
	1000	0.35	4.16	0.33

Similarly, D1A3 was less defective than D1A0 at the temperatures under study despite the higher nitrogen content in D1A3 N-CNTs (Table 3.2-3.3) and this corroborates with the earlier deductions about lessening of defect concentration upon mixing reagents. Also, the peaks on the PXRD spectrum were similarly assigned as in Fig. 3.8. Upon comparing the graphitic peak at two theta of 25°, D1A3 N-CNTs were less crystalline than D1A0 at 900-1000 °C and this can be explained by the high nitrogen doping in D1A3 unlike at lower temperatures (Table 3.2 - 3.3). Whereas, an analysis of rest of the peaks showed an opposite trend probably due to the high defect nature in D1A0 than D1A3 N-CNTs. The general trend observed was increase in crystallinity of both Fe_3C and N-CNTs with increase in temperature for both D1A0 and D1A3 (Fig. 3.22).

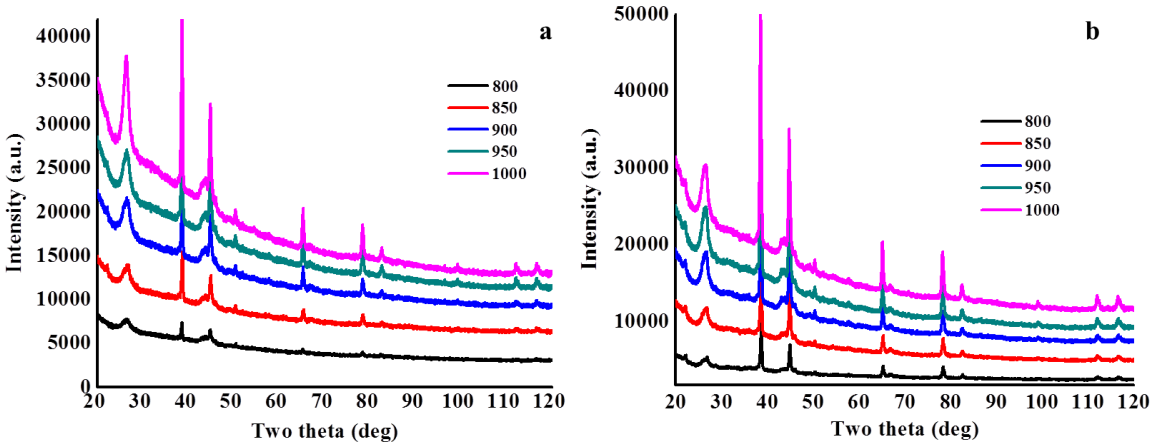

Fig. 3.22. The powder X-ray diffraction spectrums for (a) D1A0 and (b) D1A3 N-CNT samples synthesised at different temperatures.

The current results show several attributes when compared to most similar studies in literature; for instance, the nitrogen content was higher than most of the literature values obtained from analogous experimental set-ups [3.2,3.12,3.21]. The nitrogen content obtained was comparable to what Ombaka *et al.*, [3.38] obtained after introducing oxygen to acetonitrile. The selectivity towards formation of tubes rather than other shaped carbon nanomaterials (such as amorphous carbon, spheres and nano-rods, amongst others) was one of the key attributes of the current approach when compared to other works [3.1,3.2,3.4,3.8,3.18]. Also, it was a simpler strategy of tailoring physicochemical properties such as dimensions and chemical moieties, amongst others.

3.4. Conclusions

Varying the sp^3:*sp* hybridised nitrogen source ratio can be a manipulative step towards tailoring N-CNT growth dynamics and physicochemical properties. This can change several physicochemical properties such as inner and outer diameter, number tube walls, porosity and nitrogen content and moieties towards desired parameters. Increase in the ratio of acetonitrile (*sp* ratio) in the reagent solution increased wall thickness but reduced BET surface areas whereas higher DMF (sp^3 ratio) introduced coiling and wrinkling in some tubes. The sp^3 hybridised nitrogen containing hydrocarbon was a better source of nitrogen than sp. DMF gave N-CNTs with high values of pore volume and the associated inner diameters were enhanced

by increasing synthesis temperatures. Number of N-CNT walls from sp^3 nitrogen source, DMF, can be controlled by varying the synthesis temperature. Both synthesis temperature and *sp: sp*^{3} mixing ratio have an influence in the number of tube walls. The enhancement of N-doping in N-CNTs by mixing sp^3 and *sp* hybridised N sources is subject to synthesis temperature. The main N functionality in the N-CNTs reported herein was pyrrolic. N-CNTs synthesised at 900 °C from both *sp: sp*^{3} hybridised nitrogen source ratios of 1:0 and 1:3 had the lowest residual iron and highest N-CNTs composition. Therefore, according to the current work, DMF and acetonitrile in 1:3 ratio and 900 °C were the best synthesis conditions for N-CNTs.

Acknowledgements

The authors wish to thank the University of KwaZulu-Natal (UKZN) for the access to facilities used in this work. Edwin Tonderai Mombeshora is grateful to the UKZN Nanotechnology Platform for funding this work. The XPS analysis was supported by the National Research Foundation of South Africa (Grant Number 93205). Otherwise, this research did not receive any specific grant from funding agencies in the public, commercial, or not-for-profit sectors.

References

[3.1] G. Keru, P.G. Ndungu, V.O. Nyamori, Nitrogen-doped carbon nanotubes synthesised by pyrolysis of (4-{[(pyridine-4-yl)methylidene]amino}phenyl)ferrocene, Journal of Nanomaterials, 2013 (2013) 1-7.

[3.2] E.N. Nxumalo, V.O. Nyamori, N.J. Coville, CVD synthesis of nitrogen doped carbon nanotubes using ferrocene/aniline mixtures, Journal of Organometallic Chemistry, 693 (2008) 2942-2948.

[3.3] Y. Tang, S.C. Burkert, Y. Zhao, W.A. Saidi, A. Star, The effect of metal catalyst on the electrocatalytic activity of nitrogen-doped carbon nanotubes, The Journal of Physical Chemistry C, 117 (2013) 25213-25221.

[3.4] L.M. Ombaka, P.G. Ndungu, V.O. Nyamori, Tuning the nitrogen content and surface properties of nitrogen-doped carbon nanotubes synthesized using a nitrogen-containing ferrocenyl derivative and ethylbenzoate, Journal of Materials Science, 50 (2014) 1187-1200.

[3.5] K. Chizari, A. Vena, L. Laurentius, U. Sundararaj, The effect of temperature on the morphology and chemical surface properties of nitrogen-doped carbon nanotubes, Carbon, 68 (2014) 369-379.

[3.6] R.M. Yadav, J. Wu, R. Kochandra, L. Ma, C.S. Tiwary, L. Ge, G. Ye, R. Vajtai, J. Lou, P.M. Ajayan, Carbon nitrogen nanotubes as efficient bifunctional electrocatalysts for oxygen reduction and evolution reactions, ACS Applied Materials and Interfaces, 7 (2015) 11991-12000.

[3.7] Z. Zang, A. Nakamura, J. Temmyo, Nitrogen doping in cuprous oxide films synthesized by radical oxidation at low temperature, Materials Letters, 92 (2013) 188-191.

[3.8] M. Hafeez, L. Gan, H. Li, Y. Ma, T. Zhai, Chemical vapor deposition synthesis of ultrathin hexagonal rese2 flakes for anisotropic raman property and optoelectronic application, Advanced Materials, 28 (2016) 8296-8301.

[3.9] E.N. Nxumalo, N.J. Coville, Nitrogen doped carbon nanotubes from organometallic compounds: a review, Materials, 3 (2010) 2141-2171.

[3.10] W. Lv, K. Shi, L. Li, S. Shao, Nitrogen-doped multiwalled carbon nanotubes and their electrocatalysis towards oxidation of NO, Microchimica Acta, 170 (2010) 91-98.

[3.11] X.F. Li, K.Y. Lian, L. Liu, Y. Wu, Q. Qiu, J. Jiang, M. Deng, Y. Luo, Unraveling the formation mechanism of graphitic nitrogen-doping in thermally treated graphene with ammonia, Scientific Reports, 6 (2016) 23495.

[3.12] Q. Wei, X. Tong, G. Zhang, J. Qiao, Q. Gong, S. Sun, Nitrogen-doped carbon nanotube and graphene materials for oxygen reduction reactions, Catalysts, 5 (2015) 1574-1602.

[3.13] T. Susi, Z. Zhu, G. Ruiz-Soria, R. Arenal, P. Ayala, A.G. Nasibulin, H. Lin, H. Jiang, O. Stephan, T. Pichler, A. Loiseau, E.I. Kauppinen, Nitrogen-doped SWCNT synthesis using ammonia and carbon monoxide, Physica Status Solidi (b), 247 (2010) 2726-2729.

[3.14] E.T. Mombeshora, V.O. Nyamori, A review on the use of carbon nanostructured materials in electrochemical capacitors, International Journal of Energy Research, 39 (2015) 1955-1980.

[3.15] J. Liu, Y. Zhang, M.I. Ionescu, R. Li, X. Sun, Nitrogen-doped carbon nanotubes with tunable structure and high yield produced by ultrasonic spray pyrolysis, Applied Surface Science, 257 (2011) 7837-7844.

[3.16] C.-d. Kim, H.-R. Lee, H.T. Kim, Effect of NH_3 gas ratio on the formation of nitrogen-doped carbon nanotubes using thermal chemical vapor deposition, Materials Chemistry and Physics, 183 (2016) 315–319.

[3.17] C. Tang, Y. Bando, D. Golberg, F. Xu, Structure and nitrogen incorporation of carbon nanotubes synthesized by catalytic pyrolysis of dimethylformamide, Carbon, 42 (2004) 2625-2633.

[3.18] U. Ritter, N.G. Tsierkezos, Y.I. Prylutskyy, L.Y. Matzui, V.O. Gubanov, M.M. Bilyi, M.O. Davydenko, Structure–electrical resistivity relationship of N-doped multi-walled carbon nanotubes, Journal of Materials Science, 47 (2011) 2390-2395.

[3.19] H.T. Chung, P. Zelenay, A simple synthesis of nitrogen-doped carbon micro- and nanotubes, Chemical Communications (Camb), 51 (2015) 13546-13549.

[3.20] E.N. Nxumalo, P.J. Letsoalo, L.M. Cele, N.J. Coville, The influence of nitrogen sources on nitrogen doped multi-walled carbon nanotubes, Journal of Organometallic Chemistry, 695 (2010) 2596-2602.

[3.21] M. Arjmand, K. Chizari, B. Krause, P. Pötschke, U. Sundararaj, Effect of synthesis catalyst on structure of nitrogen-doped carbon nanotubes and electrical conductivity and electromagnetic interference shielding of their polymeric nanocomposite, Carbon, 98 (2016) 358–372.

[3.22] G. Ćirić-Marjanović, I. Pašti, S. Mentus, One-dimensional nitrogen-containing carbon nanostructures, Progress in Materials Science, 69 (2015) 61–182.

[3.23] S. Hussain, R. Amade, E. Jover, E. Bertran, Nitrogen plasma functionalization of carbon nanotubes for supercapacitor applications, Journal of Materials Science, 48 (2013) 7620-7628.

[3.24] Y. van de Burgt, Y. Bellouard, R. Mandamparambil, Kinetics of laser-assisted carbon nanotube growth, Physical Chemistry Chemical Physics, 16 (2014) 5162-5173.

[3.25] E.N. Nxumalo, V.P. Chabalala, V.O. Nyamori, M.J. Witcomb, N.J. Coville, Influence of methylimidazole isomers on ferrocene-catalysed nitrogen doped carbon nanotube synthesis, Journal of Organometallic Chemistry, 695 (2010) 1451-1457.

[3.26] S.V. Dommele, A. Romero-Izquirdo, R. Brydson, K.P.D. Jong, J.H. Bitter, Tuning nitrogen functionalities in catalytically grown nitrogen-containing carbon nanotubes, Carbon, 46 (2008) 138-148.

[3.27] A. Shaikjee, N.J. Coville, The role of the hydrocarbon source on the growth of carbon materials, Carbon, 50 (2012) 3376–3398.

[3.28] J.H. Lehman, M. Terrones, E. Mansfield, K.E. Hurst, V. Meunier, Evaluating the characteristics of multiwall carbon nanotubes, Carbon, 49 (2011) 2581-2602.

[3.29] T. Thurakitseree, C. Kramberger, P. Zhao, S. Aikawa, S. Harish, S. Chiashi, E. Einarsson, S. Maruyama, Diameter-controlled and nitrogen-doped vertically aligned single-walled carbon nanotubes, Carbon, 50 (2012) 2635-2640.

[3.30] G. Chen, R.C. Davis, H. Kimura, S. Sakurai, M. Yumura, D.N. Futaba, K. Hata, The relationship between the growth rate and the lifetime in carbon nanotube synthesis, Nanoscale, 7 (2015) 8873-8878.

[3.31] G. Zhang, D. Mann, L. Zhang, A. Javey, Y. Li, E. Yenilmez, Q. Wang, J.P. McVittie, Y. Nishi, J. Gibbons, H. Dai, Ultra-high-yield growth of vertical single-walled carbon nanotubes: Hidden roles of hydrogen and oxygen, Proceedings of the National Academy of Science USA, 102 (2005) 16141-16145.

[3.32] V.O. Nyamori, N.J. Coville, Effect of ferrocene/carbon ratio on the size and shape of carbon nanotubes and microspheres, Organometallics, 26 (2007) 4083–4085.

[3.33] F. Li, Y. Wang, D. Wang, F. Wei, Characterization of single-wall carbon nanotubes by N_2 adsorption, Carbon, 42 (2004) 2375-2383.

[3.34] K. Ghosh, M. Kumar, T. Maruyama, Y. Ando, Tailoring the field emission property of nitrogen-doped carbon nanotubes by controlling the graphitic/pyridinic substitution, Carbon, 48 (2010) 191-200.

[3.35] I. Stamatin, A. Morozan, A. Dumitru, V. Ciupina, G. Prodan, J. Niewolski, H. Figiel, The synthesis of multi-walled carbon nanotubes (MWNTs) by catalytic pyrolysis of the phenol-formaldehyde resins, Physica E: Low-dimensional Systems and Nanostructures, 37 (2007) 44-48.

[3.36] G. Zhou, C. Xu, W. Cheng, Q. Zhang, W. Nie, Effects of oxygen element and oxygen-containing functional groups on surface wettability of coal dust with various metamorphic degrees based on xps experiment, Journal of Analytical Methods in Chemistry, 2015 (2015) 467242.

[3.37] T. Susi, T. Pichler, P. Ayala, X-ray photoelectron spectroscopy of graphitic carbon nanomaterials doped with heteroatoms, Beilstein Journal of Nanotechnology, 6 (2015) 177-192.

[3.38] L.M. Ombaka, P.G. Ndungu, B. Omondi, J.D. McGettrick, M.L. Davies, V.O. Nyamori, A facile approach towards increasing the nitrogen-content in nitrogen-doped carbon nanotubes via halogenated catalysts, Journal of Solid State Chemistry, 235 (2016) 202-211.

[3.39] S. Latil, S. Roche, D. Mayou, J. Charlier, Mesoscopic transport in chemically doped carbon nanotubes Physical Review Letters, 92 (2004) 256805.

[3.40] W.P. Wright, V.D. Marsicano, J.M. Keartland, R.M. Erasmus, S.M.A. Dube, N.J. Coville, The electrical transport properties of nitrogen doped carbon microspheres, Materials Chemistry and Physics, 147 (2014) 908-914.

[3.41] E.T. Mombeshora, P.G. Ndungu, A.L.L. Jarvis, V.O. Nyamori, Oxygen-modified multiwalled carbon nanotubes: physicochemical properties and capacitor functionality, International Journal of Energy Research, (2017).

[43.2] I. Kruusenberg, N. Alexeyeva, K. Tammeveski, J. Kozlova, L. Matisen, V. Sammelselg, J. Solla-Gullón, J.M. Feliu, Effect of purification of carbon nanotubes on their electrocatalytic properties for oxygen reduction in acid solution, Carbon, 49 (2011) 4031-4039.

[3.43] Y. Tian, R. Xue, X. Zhou, Z. Liu, L. Huang, Double layer capacitor based on active carbon and its improved capacitive properties using redox additive electrolyte of anthraquinonedisulphonate, Electrochimica Acta, 152 (2015) 135-139.

Appendix: Supporting information for Chapter 3

Table 3.S1: Elemental composition in reagents

Mass ratios	Mol ratios	% in the reagent/catalyst mixture					Ratios in the catalyst/reagent mixture			
		C%	N%	O%	H%	Fe%	Fe:C ratio	Fe:N ratio	Fe:O ratio	O:C ratio
D1A0	**D1A0**	49.60	18.73	21.55	9.48	0.64	0.0128	0.00068	0.0295	0.4345
D1A1	**D0.36A0.64**	52.82	24.00	13.84	8.70	0.64	0.0121	0.00050	0.0460	0.2620
D1A2	**D0.21A0.78**	54.38	26.44	10.23	8.31	0.64	0.0117	0.00044	0.0622	0.1881
D1A3	**D0.16A0.84**	55.16	27.90	8.18	8.11	0.64	0.0115	0.00041	0.0778	0.1483
D1A4	**D0.12A0.87**	55.85	28.78	6.82	7.92	0.64	0.0114	0.00039	0.0934	0.1221
D1A5	**D0.1A0.90**	56.24	29.46	5.84	7.82	0.64	0.0113	0.00038	0.1090	0.1038
D0A1	**D0A1**	58.58	33.37	0.18	7.24	0.64	0.0109	0.00033	3.4800	0.0031
D1A1	**D0.36A0.64**	52.82	24.00	13.84	8.70	0.64	0.0121	0.00050	0.0460	0.2620
D2A1	**D0.53A0.47**	51.55	21.95	16.87	8.99	0.64	0.0123	0.00056	0.0377	0.3273
D3A1	**D0.63A0.37**	51.07	20.98	18.23	9.09	0.64	0.0125	0.00059	0.0349	0.3369
D4A1	**D0.69A0.31**	50.77	20.49	18.91	9.19	0.64	0.0125	0.00061	0.0337	0.3725
D5A1	**D0.74A0.26**	50.48	20.20	19.40	9.29	0.64	0.0126	0.00062	0.0328	0.3843

Table 3.S2: The average outer-diameter (OD), inner-diameter (ID) and compartment sizes

Sample	OD (nm)	ID (nm)	Thickness (nm)	Number of walls	Compartment size (nm)
D0A1	136.78	41.55	95.22	141	36.32
D1A1	115.07	74.93	40.14	60	45.47
D2A1	31.75	20.82	10.94	17	26.60
D3A1	51.40	39.40	12.00	19	25.05
D4A1	37.26	24.12	13.15	20	23.11
D5A1	51.95	37.64	14.31	22	29.13
D1A0	30.79	21.50	9.29	15	21.52
D1A1	115.07	74.93	40.14	60	45.47
D1A2	42.70	23.12	19.58	30	31.36
D1A3	55.71	36.43	19.28	29	29.78
D1A4	59.95	42.35	17.59	27	44.23
D1A5	47.05	28.84	18.20	28	32.25

Table 3.S3: The average OD, ID and compartment sizes for samples D1A0 and D1A3.

Sample	Temperature	OD (nm)	ID (nm)	Thickness (nm)	Number of walls	Compartment size (nm)
D1A0	800	23.29	14.29	9.00	13	20.54
	850	42.43	30.30	12.13	19	43.99
	900	31.18	17.75	13.43	21	20.80
	950	47.13	30.07	17.06	26	21.23
	1000	82.14	53.20	28.94	44	36.46
D1A3	800	34.85	21.81	13.03	20	30.99
	850	55.02	37.37	17.64	27	31.91
	900	55.71	36.43	19.27	29	29.78
	950	68.29	50.88	17.41	27	36.58
	1000	53.67	36.48	17.20	26	29.18

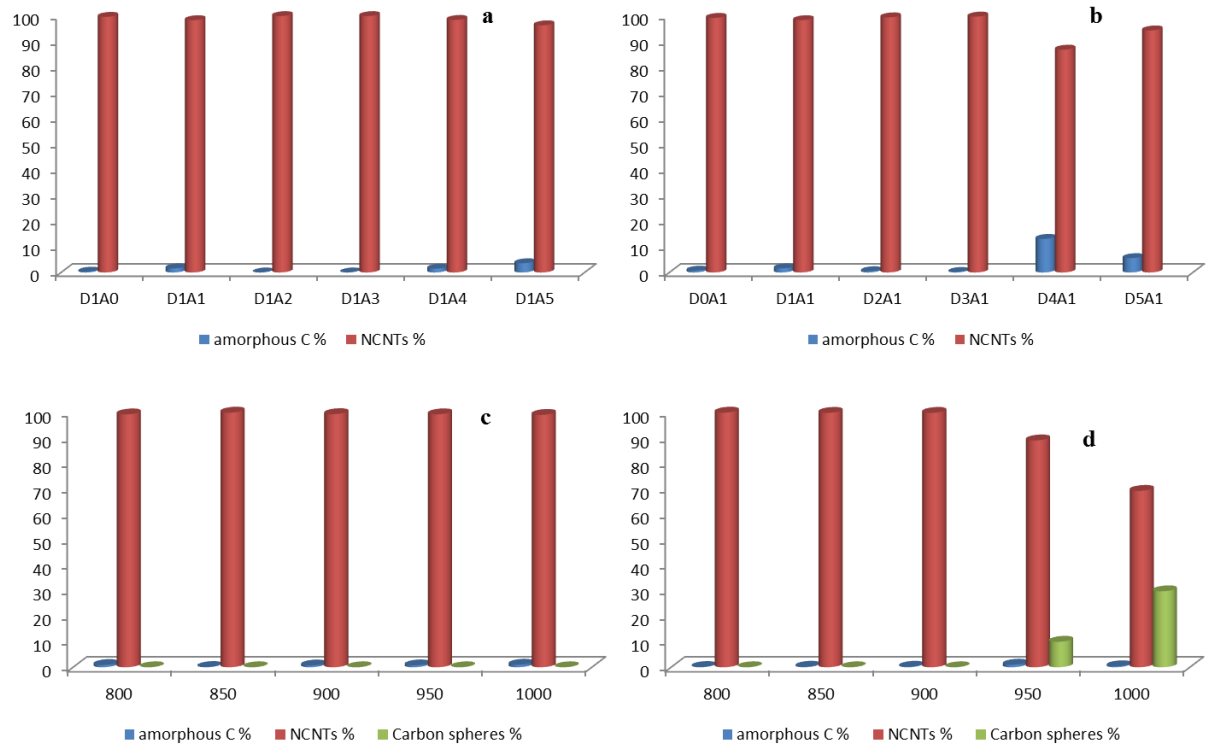

Fig. 3.S1. The distribution of products of (a) D1Ax, (b) DxA1, (c) D1A0 and (d) D1A3.

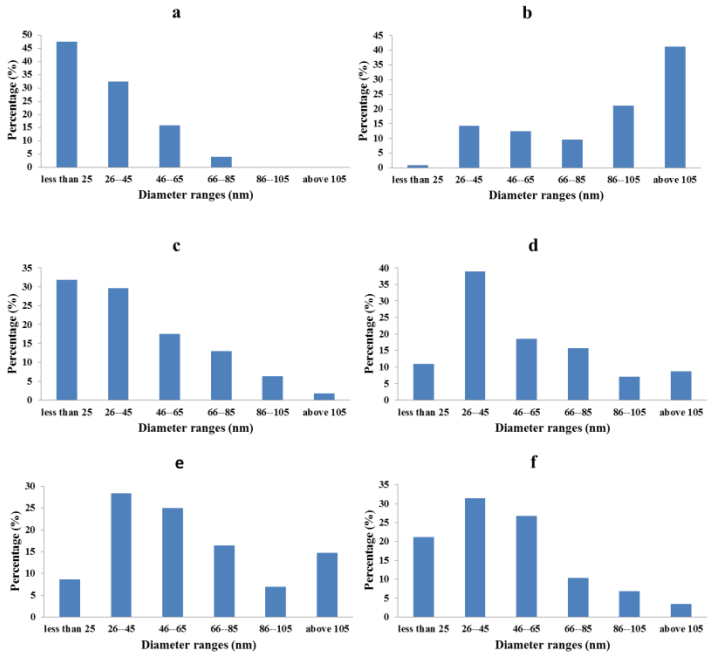

Fig. 3.S2. The representative OD for the D1Ax samples (a) D1A0, (b) D1A1, (c) D1A2, (d) D1A3, (e) D1A4 and (f) D1A5.

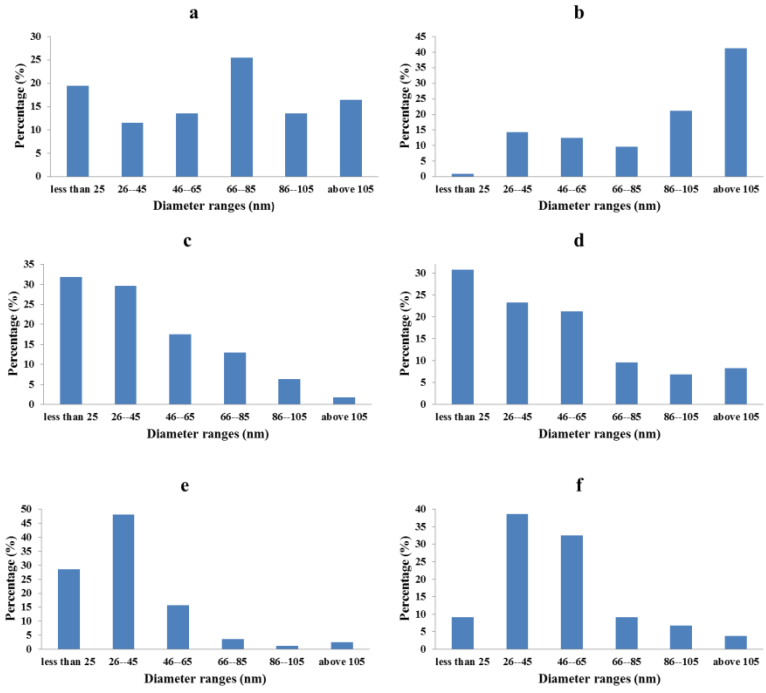

Fig. 3.S3. The representative OD for the DxA1 samples (a) D0A1, (b) D1A1, (c) D2A1, (d) D3A1, (e) D4A1 and (f) D5A1.

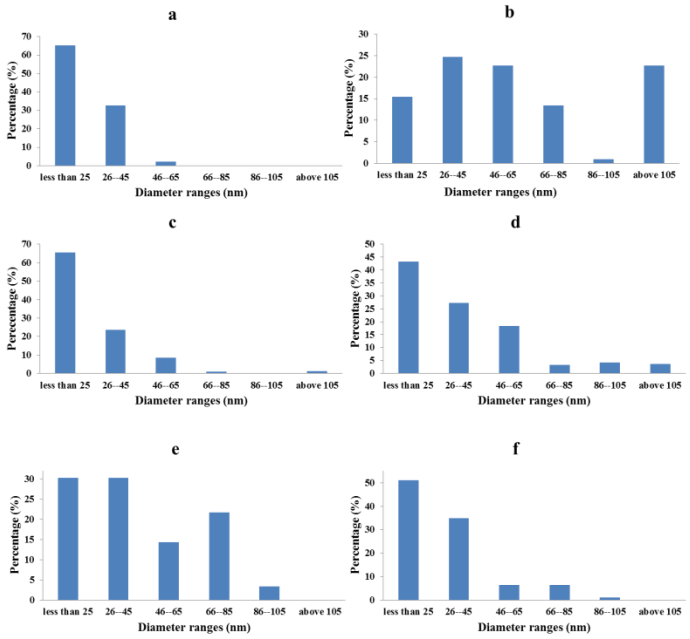

Fig. 3.S4. The representative ID for the D1Ax samples (a) D1A0, (b) D1A1, (c) D1A2, (d) D1A3, (e) D1A4 and (f) D1A5.

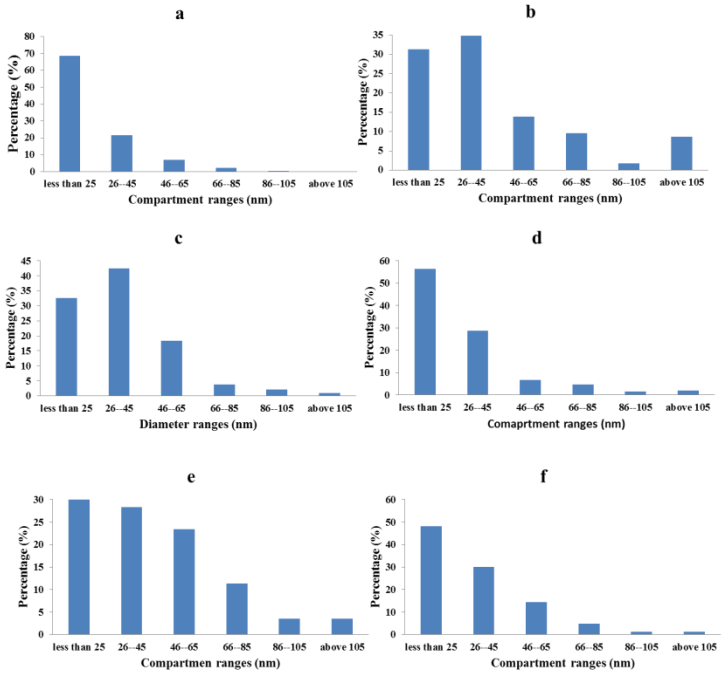

Fig. 3.S5. Compartment sizes for the D1Ax samples (a) D1A0, (b) D1A1, (c) D1A2, (d) D1A3, (e) D1A4 and (f) D1A5.

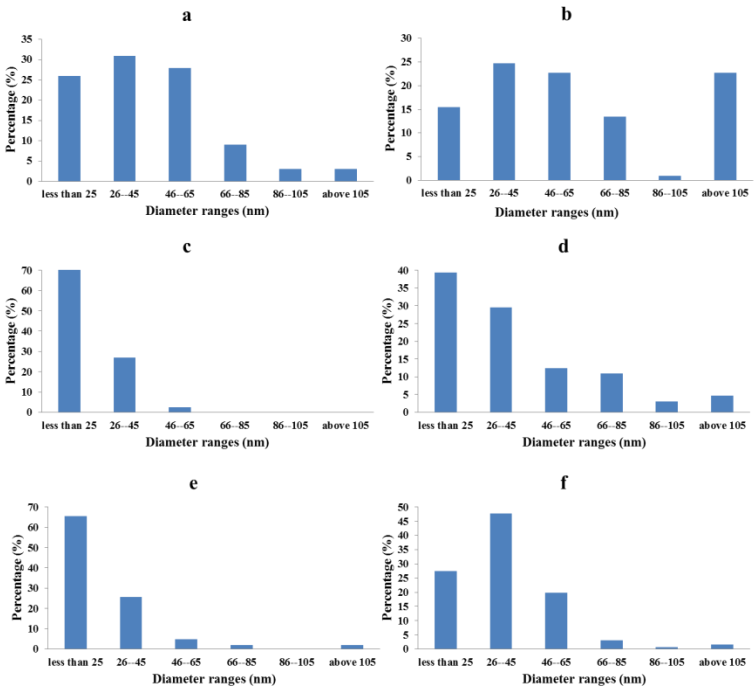

Fig. 3.S6. The representative ID for the DxA1 samples (a) D0A1, (b) D1A1, (c) D2A1, (d) D3A1, (e) D4A1 and (f) D5A1.

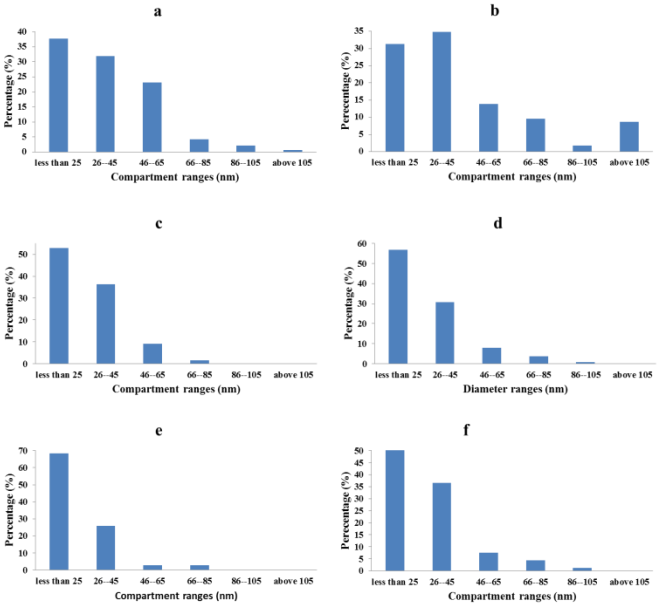

Fig. 3.S7. Compartment sizes for the DxA1 samples (a) D0A1, (b) D1A1, (c) D2A1, (d) D3A1, (e) D4A1 and (f) D5A1.

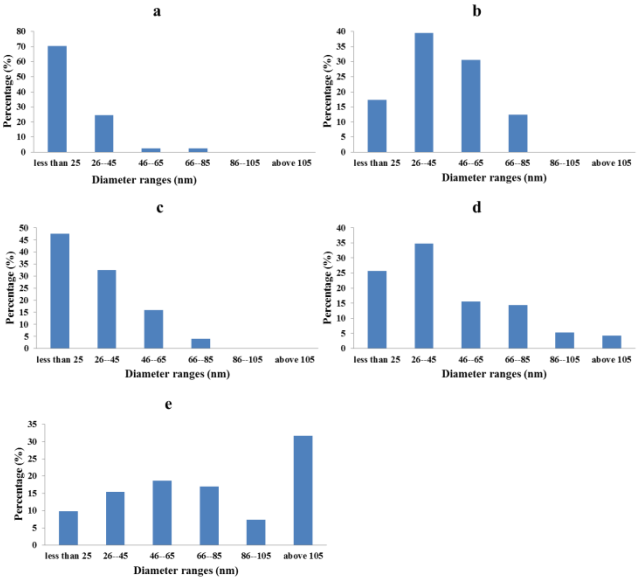

Fig. 3.S8. The OD for D1A0 samples synthesised at (a) 800 °C, (b) 850 °C, (c) 900 °C, (d) 950 °C and (e) 1000 °C.

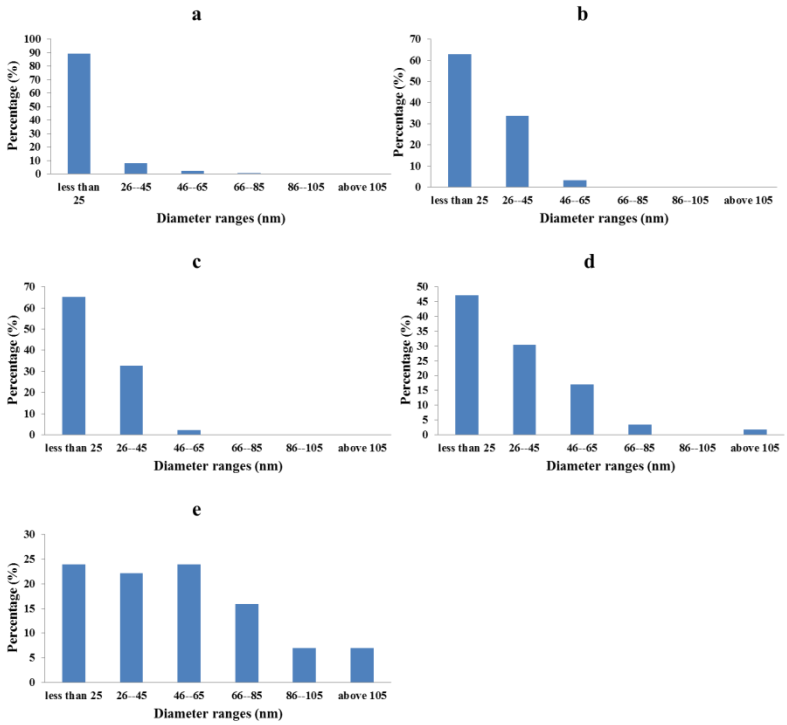

Fig. 3.S9. The ID for D1A0 samples synthesised at (a) 800 °C, (b) 850 °C, (c) 900 °C, (d) 950 °C and (e) 1000 °C.

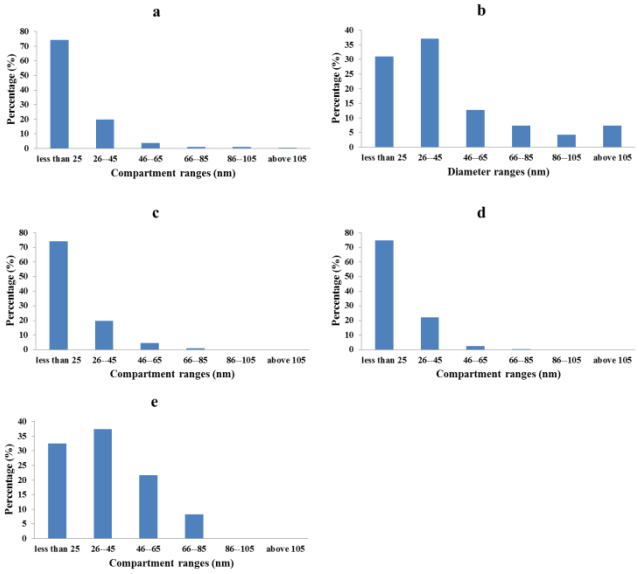

Fig. 3.S10. The compartment sizes for D1A0 samples synthesised at (a) 800 °C, (b) 850 °C, (c) 900 °C, (d) 950 °C and (e) 1000 °C.

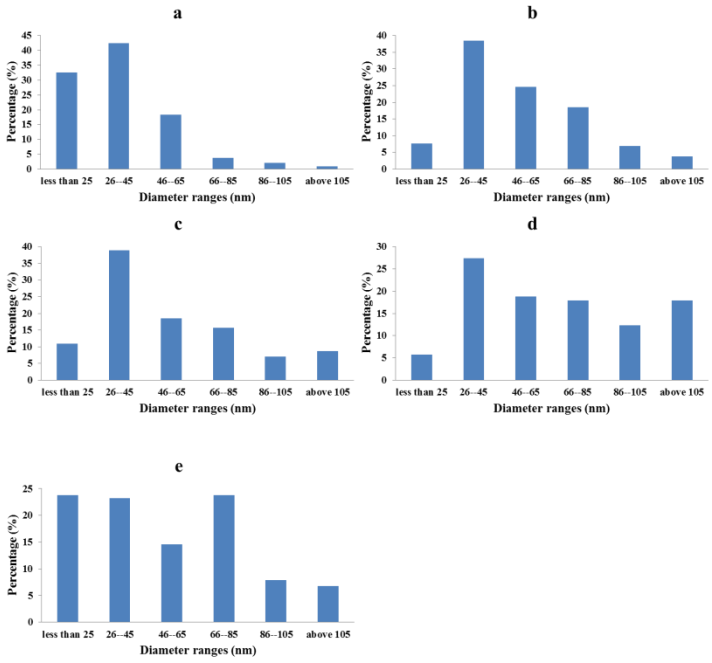

Fig. 3.S11. The OD for D1A3 samples synthesised at (a) 800 °C, (b) 850 °C, (c) 900 °C, (d) 950 °C and (e) 1000 °C.

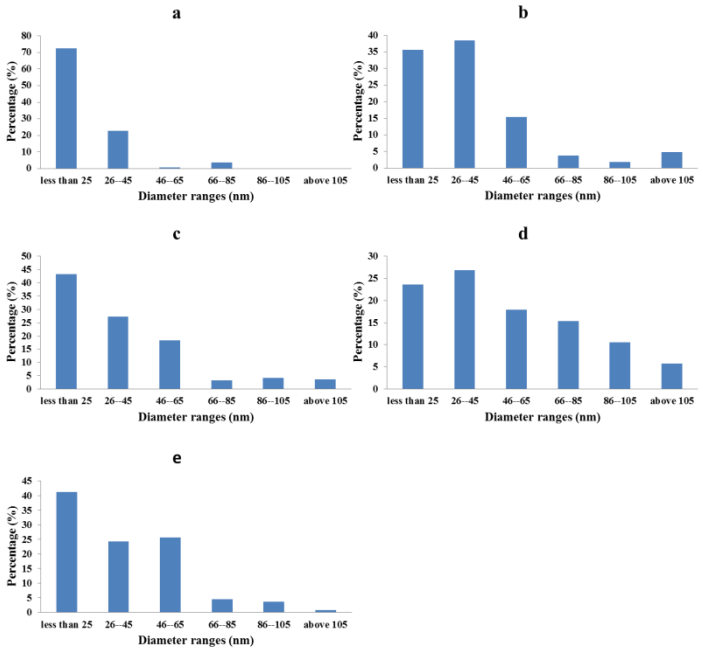

Fig. 3.S12. The ID for D1A3 samples synthesised at (a) 800 °C, (b) 850 °C, (c) 900 °C, (d) 950 °C and (e) 1000 °C.

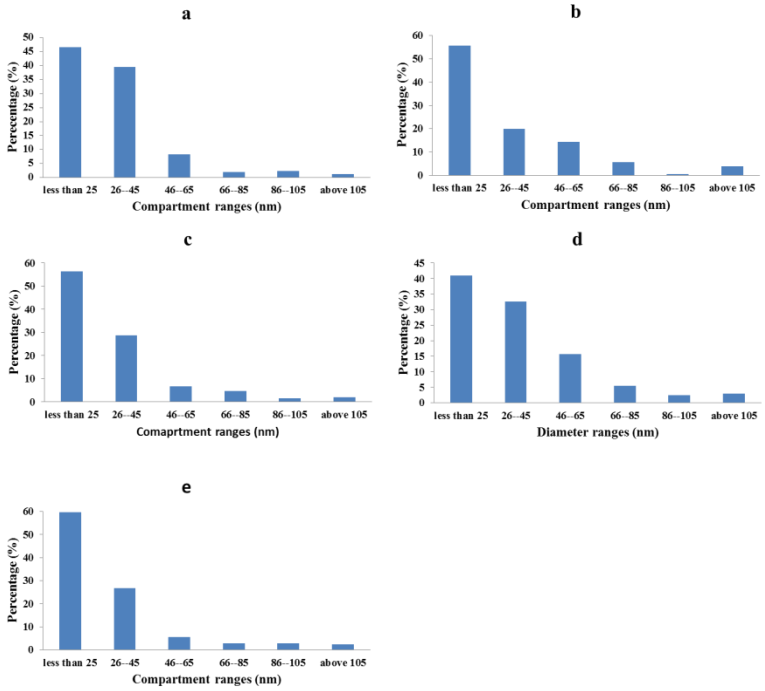

Fig. 3.S13. The compartment sizes for D1A3 samples synthesised at (a) 800 °C, (b) 850 °C, (c) 900 °C, (d) 950 °C and (e) 1000 °C.

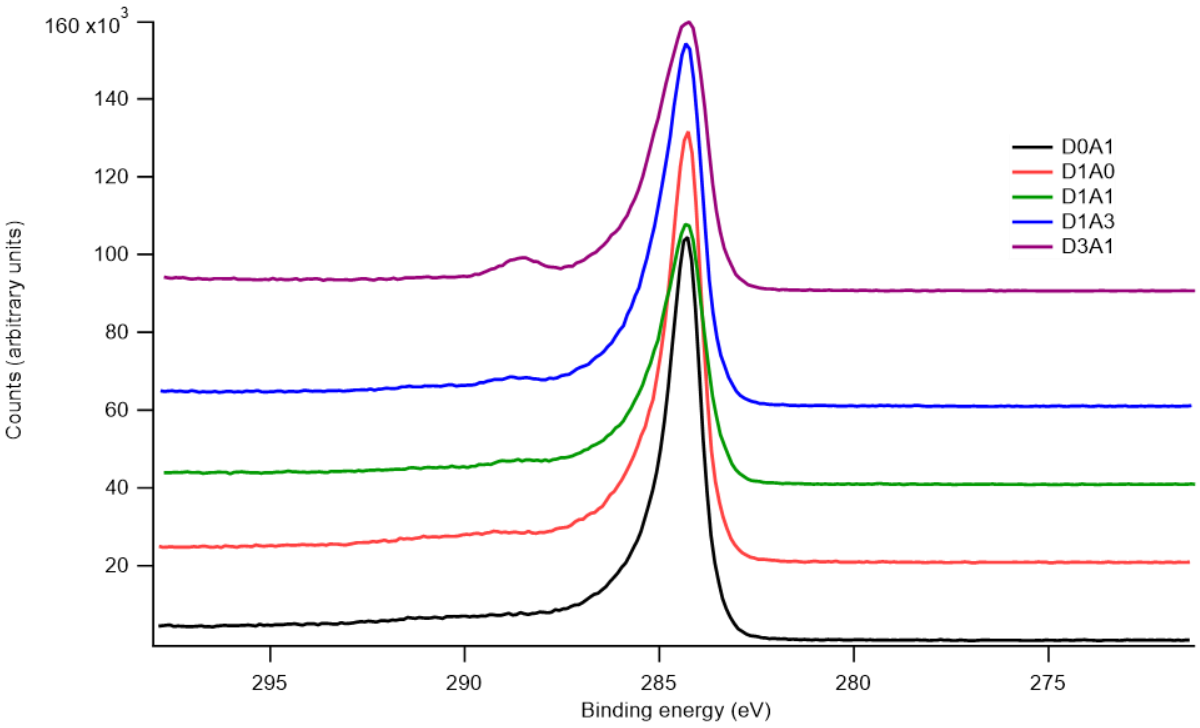

Fig. 3.S14. The C1s XPS spectra for representative N-CNT samples.

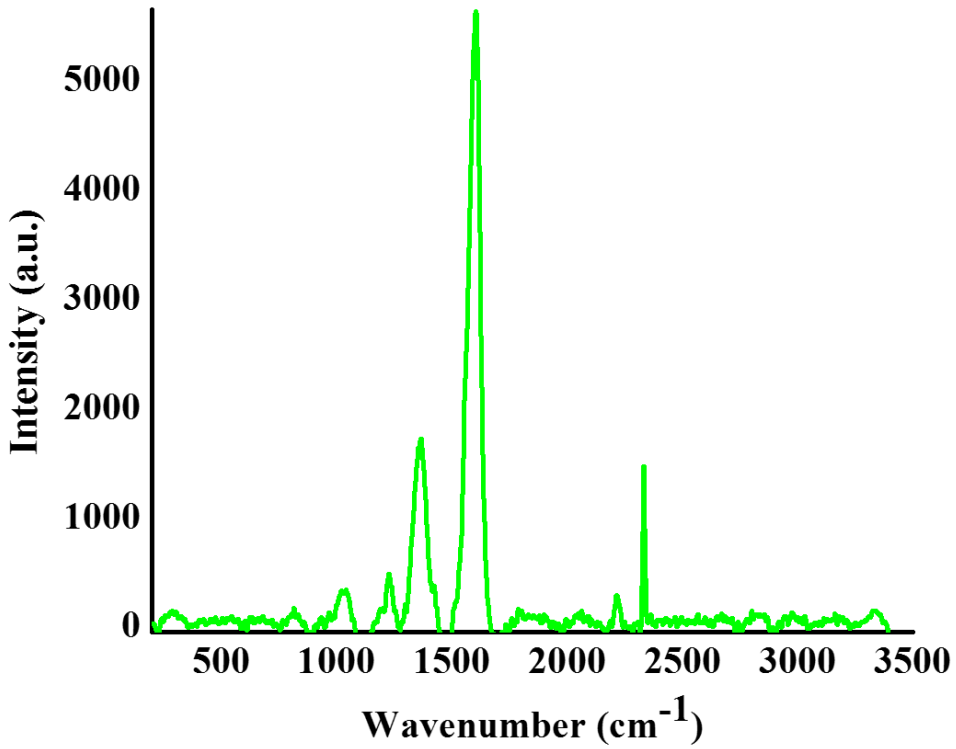

Fig. 3.S15. The Raman representative spectrum for N-CNT samples, D4A1 N-CNTs.

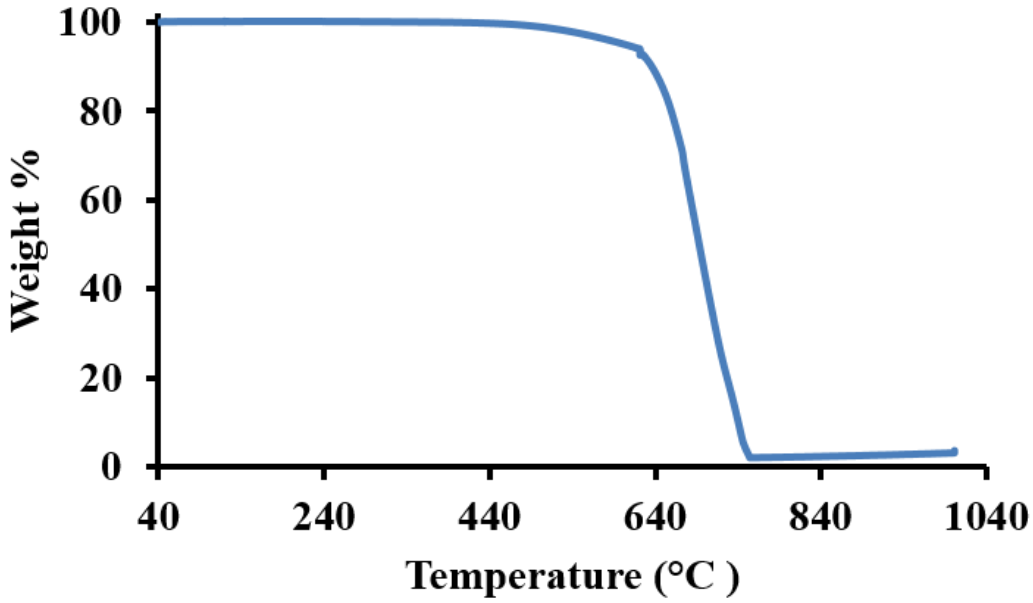

Fig. 3.S16. A representative thermogram of the purified N-CNT samples showing an almost zero residual catalyst mass.

Chapter Four

NEW CARBON MATERIALS
Volume 32, Issue 2, Apr 2017
Online English edition of the Chinese language journal

Available online at www.sciencedirect.com
ScienceDirect

Cite this article as: New Carbon Materials, 2017, 32(2): 174-187

RESEARCH PAPER

Effect of graphite/sodium nitrate ratio and reaction time on the physicochemical properties of graphene oxide

Edwin T. Mombeshora[1], Patrick G. Ndungu[2], Vincent O. Nyamori[1,*]

[1] School Chemistry and Physics, University of KwaZulu-Natal, Westville Campus, Private Bag X54001, Durban, 4000, South Africa;

[2] Department of Applied Chemistry, University of Johannesburg, P.O. Box 17011, Doornfontein, Johannesburg, 2028, South Africa

Abstract: Graphene oxide (GO) was synthesized by the reaction of graphite with sodium nitrate and the graphite/sodium nitrate mass ratio and the reaction time were varied in order to obtain the highest oxygen content. The GO was characterized by TEM, SEM, AFM, XRD, FT-IR, TGA, elemental analysis, and UV-vis and Raman spectroscopy. The effect of oxygen content on the physicochemical properties of GO was investigated. Results indicate that increasing the graphite to sodium nitrate ratio increases the oxygen content, BET surface area, pore volume and pore size but reduces the crystallite size of the GO samples. However, the oxygen content of GO is not directly related to the reaction time. Physicochemical properties such as d-spacing and defect density increase with increasing oxygen content while the thermal stability decreases. The physicochemical properties such as oxygen content, crystallinity, thermal stability and structure can be tailored by varying the graphite/sodium nitrate ratio and reaction time.

Key Words: Graphene oxide; Oxygen content; Reaction time; Carbon; Hummer's method

Effect of graphite/sodium nitrate ratio and reaction time on physicochemical properties of graphene oxide

Edwin T. Mombeshora,[1] Patrick G. Ndungu[2] and Vincent O. Nyamori[1] *

[1]School Chemistry and Physics, University of KwaZulu-Natal, Westville Campus, Private Bag X54001, Durban, 4000, South Africa

[2]Department of Applied Chemistry, University of Johannesburg, P.O. Box 17011, Doornfontein, Johannesburg, 2028, South Africa

Graphical abstract

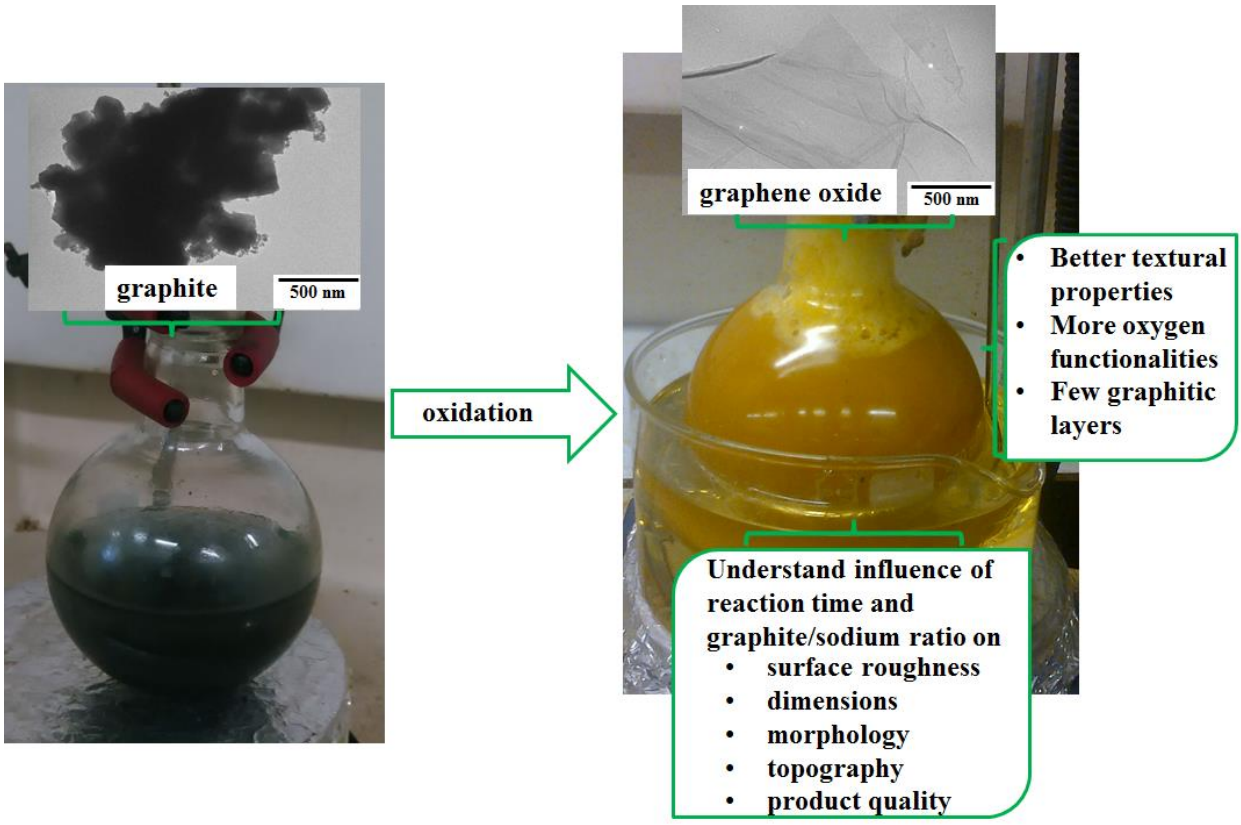

Abstract

Graphene oxide (GO) synthesis was done by varying graphite: sodium nitrate ratio and the reaction time. The study aimed at investigating the optimum graphite: sodium nitrate ratio and reaction time for obtaining the highest oxygen content in GO and it also explained the effect of oxygen content on physicochemical properties. GO was characterized by transmission electron microscopy, scanning electron microscopy, atomic force microscopy, powder X-ray diffraction, Raman spectroscopy, infra-red spectroscopy, thermogravimetric analysis, ultraviolet-visible spectrophotometry, and elemental analysis. Increasing sodium nitrate ratio amplified elemental oxygen content, BET surface area, pore volume and pore size but reduced crystallite sizes in the GO samples. Variation in reaction time did not show a clear trend in terms of oxygen amount. Physicochemical properties such as d-spacing and defect intensity increased whilst thermal stability decreased with increase in oxygen elemental properties. Varying graphite: sodium nitrate ratio and reaction time modifies physicochemical properties such as oxygen content, crystallinity, thermal stability and overall morphology.

Keywords: graphene oxide; oxygen content; reaction time; carbon; Hummer's method

* Corresponding author*:* Vincent Nyamori, School of Chemistry and Physics, University of KwaZulu-Natal, Westville Campus, Private Bag X54001, Durban, 4000, South Africa

Email: nyamori@ukzn.ac.za Tel.: +27-31 2608256; Fax: +27-31 260 3091

4.1 Introduction

Graphene is one of the thinnest known material and there have been numerous reports in the open literature since its discovery [4.1, 4.2]. The most explored aspect of graphene in these reports, even though some biomedical [4.3] and hydrogen storage [4.4] applications exist in literature, is electronic properties. Graphene has found numerous applications as both electron and hole transport layer in solar cells [4.5-4.13], as additives in batteries [4.14-4.16], components for field emission cathodes [4.17-4.19], transistors [4.20] and as electrochemical capacitors [4.2]. Single layers of graphene were initially made *via* mechanical separation of sheets [4.1]. However, availability of graphene oxide in solution has allowed functionalization, characterization and processing of graphene layers through numerous solution-based techniques [4.21]. This is facilitated by ionizability and hydrophilicity of most oxygen moieties on GO sheets [4.22].

The chemical route especially the modified Hummers methods are the most popularly utilized in graphene, a two-dimensional single atomic layer of sp^2 carbon atoms, synthesis [4.1,4.23-4.26]. The chemical route is easy, scalable and associated with reasonable costs [4.24,4.27-4.29]. The structural properties of graphene due to preparation routes *via* graphene oxide (GO) has attracted much attention due to their influence on quantum Hall effect, sensitivity, mechanical hardness, hydrophilicity, sheet size, defects and electrical conductivity amongst others [4.23,4.24,4.27,4.30,4.31]. For instance, even though GO from chemical oxidation is a suitable precursor of graphene, oxidation reduces conductivity but enhances exfoliation in water under ultrasonic treatment [4.24]. Additionally, in practice GO can only be partially reduced to form graphene-like sheets, i.e. only partial restoration of the conjugation system is achieved [4.25]. Therefore, it is critical to select suitable graphene synthesis parameters on the basis of intended application.

The main role of $NaNO_3$ in the Hummers methods is oxidizing effect [4.32], it aids H_2SO_4 and $KMnO_4$. Additionally, H_2O_2 also has an oxidizing effect *via* its decomposition to active oxygen atoms that oxidize graphite in the presence of H_2SO_4 [4.32]. Also, H_2O_2 reduces residual permanganate and manganese dioxide to a colourless manganese sulfate during the reaction. More research is still needed in understanding the synthesis routes for a number of reasons such as the exact GO structure elucidation [4.23,4.33] and the elimination of sodium nitrate because it generates toxic gases, NO_2 and N_2O_2. The main reason, amongst others, is the sample variation due to different synthesis parameters and therefore lack of standardized products [4.33]. This study brings out some insights towards controllable oxidation of graphite to GO. Also, a few studies have been dedicated to synthesis conditions. Similar studies were done on effect of oxidation time on graphite exfoliation using perchloric and nitric acids, and potassium chromate [4.29]. Wu and Ting [4.28] investigated the effect of sodium nitrate to potassium permanganate ratio using a fixed graphite amount on GO yield. They proposed that to form GO, Na^+ and NO_3^- are initially intercalated (equation 1) followed by reaction of expandable graphite with diamanganese heptoxide i.e. oxygen containing moieties from the $KMnO_4$ hydrolysis [4.33] (equation 3).

$$C_{(graphite)} + NaNO_3 \rightarrow C_{NaNO_3} \quad (1)$$

$$4\,KMnO_4 + 2H_2O \rightarrow 4KOH + 4MnO_2 + 3O_2 \quad (2)$$

$$C_{NaNO_3} + nO_2 \rightarrow \quad GO \quad (3)$$

This hints on the importance of the ratio of graphite to sodium nitrate in the synthesis of GO. This work highlights that the initial step in GO synthesis is affected by graphite to sodium nitrate ratio. Hence, the study elaborates the outcomes when either sodium nitrate or graphite mass was in excess as well as when it was the same. The influence of reaction duration on the physicochemical properties of GO is also explained.

4.2 Experimental

This section describes the materials, chemicals and other experimental parameters.

4.2.1 Materials

The procurement of graphite powder (< 150 µm, 99.99%) was from Sigma Aldrich, USA. $KMnO_4$ (99%) and $NaNO_3$ (99%) were both purchased from Associated Chemical Enterprise, South Africa. H_2SO_4 (98.37%, C.C. Imelmann Ltd, South Africa) was used as-received without dilution and H_2O_2 (30%, Merck ltd, South Africa) was diluted to the required concentrations in the respective methods as stated in the subsequent procedures. The product was washed with double deionized water (DI).

4.2.2 Method

In the general procedure, graphite was added to a round-bottomed flask with H_2SO_4 (98%, 12 mL) cooled in an ice water bath and stirred. After stirring for a few minutes, sodium nitrate was added to this mixture and allowed to further stir for 30 minutes. Thereafter, to the mixture, $KMnO_4$ (1.5 g) was slowly added while maintaining the temperature below 10 ℃. Afterwards, the reaction mixture was further stirred at room temperature for the required duration and DI (15 mL) was added slowly. The reaction temperature was raised to 98 ℃ and maintained for a specified time under stirring. H_2O_2 (30%, 50 mL) was added to the mixture prior to several cycles of washing using DI until the filtrate was at neutral pH. The samples were dried at 50 ℃ for 48 hours. The samples used to investigate effect of graphite: sodium nitrate ratios, i.e. 2:1, 1:1 and 1:2, were named as G2N1-$t_{12,24}$, G1N1-$t_{12,24}$ and G1N2-$t_{12,24}$, respectively. Where $t_{12,24}$ in this case means each sample was stirred for 12 hours at room temperature and 24 hours

at 98 ℃. Another series of samples with graphite: sodium nitrate ratios of 1:1 were synthesised and used to study the effect of reaction times. They were named as G1N1-$t_{3,3}$, G1N1-$t_{6,12}$, G1N1-$t_{12,12}$, G1N1-$t_{12,24}$, where the subscript t and the two sets of numbers refers to the reaction time at room temperature and at 98 ℃, respectively.

Similarly, samples G2N1-$t_{0,0.25}$ and G1N1-$t_{3,0}$ were synthesised as above, however with some slight variations, i.e. as for G1N1-$t_{3,0}$, the graphite: sodium nitrate ratio was 1:1 and the mixture was heated for 3 hours at 35 ℃. Thereafter, 3% H_2O_2 (150 mL) was added slowly followed by stirring for 30 minutes. This was done to investigate outcomes if reaction at room temperature in the previous series was changed to 35 ℃, a higher temperature without ramping temperature to 98 ℃. Whereas for G2N1-$t_{0,0.25}$, the graphite: sodium nitrate ratio was 2:1 and the temperature of the mixture was raised to 50 ℃. Thereafter, it was ramped to 98 ℃ and maintained at this temperature for 15 minutes. The reason for this case was to determine outcomes when reaction at room temperature in previous series was changed to 50°C, an intermediate temperature before reaction at 98°C for a short time of 15 minutes.

4.2.3 Materials characterization

Structures of the GO were examined with transmission electron microscopy (TEM, JEOL TEM 1010 transmission electron microscope) and scanning electron microscopy (SEM, JEOL JSM 6100 microscope). The GO sheet roughness was analysed in the tapping mode and in the micron level using as-synthesized sheets without use of a substrate using an atomic force microscopy (AFM, Bruker Inova). Images were captured and processed using Nano Drive software and Nanoscope analysis, respectively. The crystal structures of the GO samples were characterized by means of an X-ray diffractometer (Rigaku MiniFlex 600). The graphitic crystal quality was analyzed by Raman spectroscopy (100 mW Delta Nu Advantage 532^{TM} spectrometer of 10 cm^{-1} resolution with a 2D CCD detector and grating lines were 1800 mm^{-1} with a laser source (Nd:YAG) at wavelength of 532 nm). Thermal stability analyses were done with TGA thermal analyser (TA Instruments Q series^{TM} Thermal Analyser DSC/TGA (Q600) with TA instruments Universal Analysis 2000 software for data acquisition and analysis) from room temperature to 1000 ℃. Absorption characteristics were investigated with a Uv-Vis spectrometer (Perkin Elmer Lambda 35 double beam spectrometer with FL Winlab software) and infra-red transmission spectra were taken by Perkin Elmer spectrometer (Perkin Elmer spectrum 100 series with universal ATR accessory). Samples were prepared for textural

characterisation by degassing at 90 ^{0}C for one hour then at 200 ^{0}C for 10 hours. Nitrogen sorption analyses were done using a Micromeritics TRI STAR 3020V1.03(V1.03) instrument at 77 K in nitrogen. Elemental compositions determinations were done by use of LECO CHNS-932 elemental analyzer standardized with acetanilide.

4.3 Results and discussion

The samples were named according to the parameter under study and physicochemical properties of the materials synthesized were determined with PXRD, TGA, FT-IR, Uv-Vis, Raman, AFM, SEM and TEM.

4.3.1 Microscopic studies

The shape and morphology of GO was studied *via* TEM and SEM, respectively, whereas topography was done with AFM technique.

4.3.1.1 Transmission electron microscopy

TEM images show formation of transparent and wrinkled, paper-like materials, upon oxidative treatment of graphite at different ratios (Fig. 4.1). Such observations indicate graphite layer exfoliation and introduction of defects on the GO layers due to incorporation of oxygen atoms. All samples showed these traits regardless of reaction ratios of graphite and $NaNO_3$. Similar observations have been reported for typical GO synthesised by modified Hummer's methods [4.32]. On comparison, images in Fig. 4.1(b-d) showed different levels of transparency, and this is an indication of exfoliation. A possible explanation is that different ratios of graphite to $NaNO_3$ generated different levels of intercalated GO intermediate that facilitated different extents of exfoliation of layers upon release of oxygen molecules from the hydrolysis of $KMnO_4$.

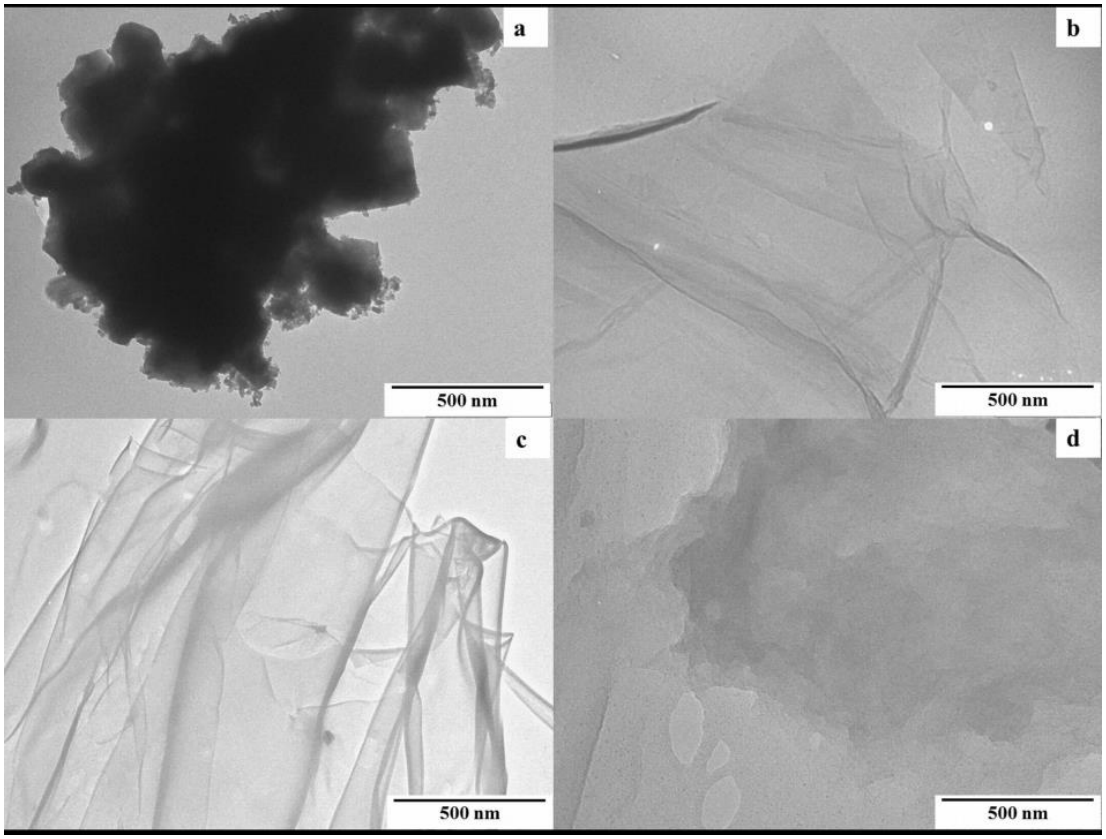

Fig. 4.1 TEM images for (a) graphite and GO samples from (b) G2N1-$t_{12,24}$, (c) G1N1-$t_{12,24}$ and (d) G1N2-$t_{12,24}$.

4.3.1.2 Scanning electron microscopy

SEM was used to further characterize the GO samples microscopically. Images of the samples obtained from SEM show different degrees of geometric wrinkling and rippling (Fig. 4.2). Such morphological variations are caused by nanoscale interlocking of GO nanosheets [4.34] shown in Fig 4.2b. On comparing starting material with the obtained products, SEM images clearly showed that the pristine graphite comprised of irregularly shaped flat platelet like structures with very little wrinkling or corrugation, typically observed with graphite unlike the GO samples. GO samples were arranged more intermittently edge to edge (Fig. 4.2 b-d). This is an indication of the effect of oxidative treatment on graphite morphology. Repulsive forces were generated between graphene layers as the increase in number of oxygen-containing groups [4.30] on the GO sheet were facilitated by the increase in ratio of $NaNO_3$ supplied for the initial step. Similar corrugation has been reported in material development towards better electron transport relative to basal graphite plane [4.34], their study inferred that once corrugated GO morphology is formed from graphite, superior electronic properties are attained. Hence,

the high $NaNO_3$: graphite ratios during GO synthesis can be used to tailor materials towards excellent electronic properties in this regard.

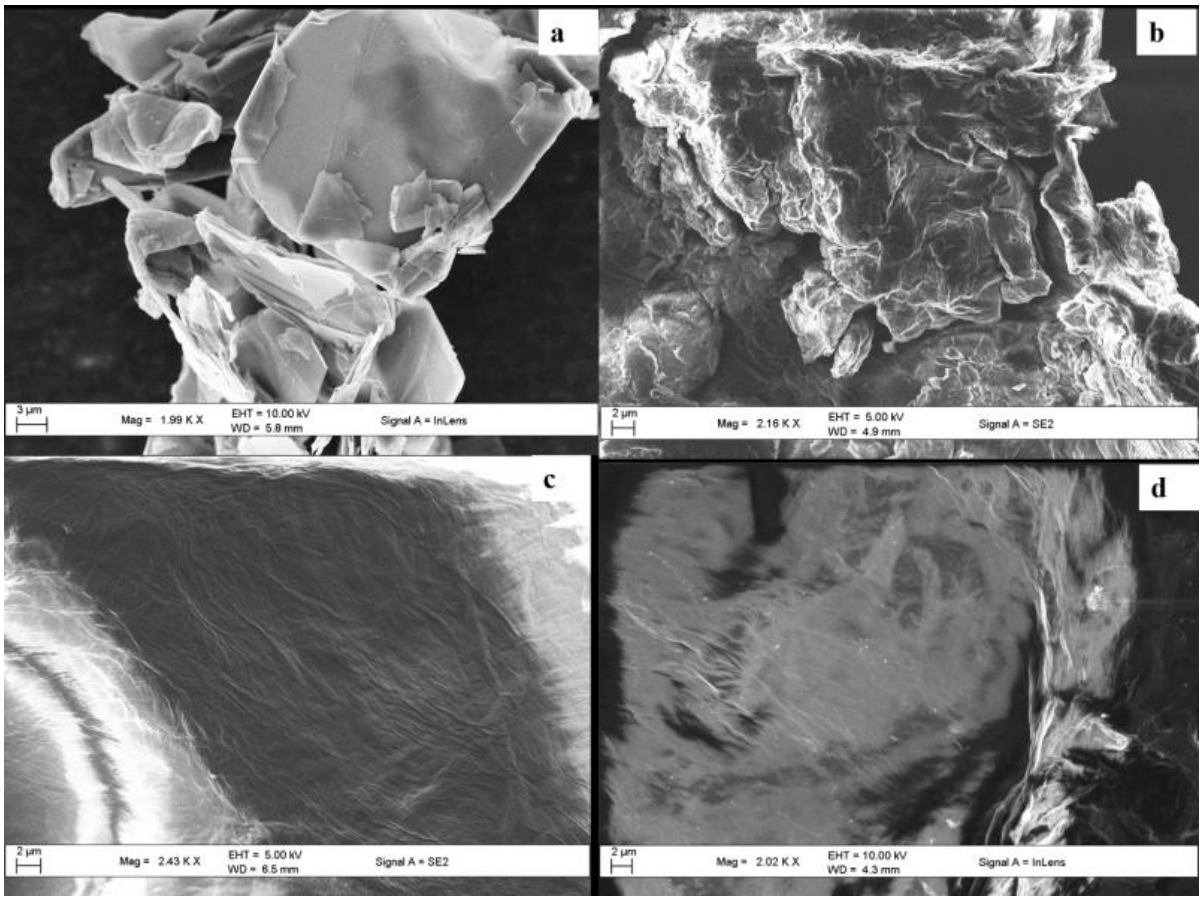

Fig. 4.2 SEM images for (a) graphite and SEM images of GO samples from (b) G2N1-$t_{12,24}$, (c) G1N1-$t_{12,24}$ and (d) G1N2-$t_{12,24}$.

Different graphite: sodium nitrate ratios culminated in different extends of agglomeration and was ranked as pristine graphite (Fig 4.2a) > G2N1-$t_{12,24}$ (Fig 4.2b) > G1N2-$t_{12,24}$ (Fig4. 2d) > G1N1-$t_{12,24}$ (Fig 4.2c). The contrast with Fig 4.2b and remanence of structure (some agglomeration between sheets) is indicative of less exfoliation, and agglomeration between sheets. The lower contrast with Fig 4.2c and Fig 4.2d, is that because of a greater amount of exfoliation, and greater amount of sheet like structures. This corroborates with the idea of creation of repulsive forces between GO sheets during synthesis.

4.3.1.3 Atomic force microscopy

The various wrinkling levels observed in the micron level, due to the different graphite: sodium nitrate ratios, culminated in different surface roughness (Fig. 4.3 a-d). This was attributed to the introduction of oxygen moieties onto the sheet inducing structural disorder. Such observations have been reported in literature by several authors [4.22,4.35]. The samples can be ranked in terms of roughness as G2N1-$t_{12,24}$ > G1N2-$t_{12,24}$ > graphite > G1N1-$t_{12,24}$ (Table 4.S1 in supplementary information). This inferred that matching mass ratios of graphite to sodium nitrate (1:1) reduces GO sheet roughness relative to pristine graphite whilst a mismatch enhances it. This can be explained with reference to the intercalation mechanism, an equal graphite: sodium nitrate mass ratio culminates in uniform Na^+ and NO_3^- intercalation between sheets, hence less sheet roughening.

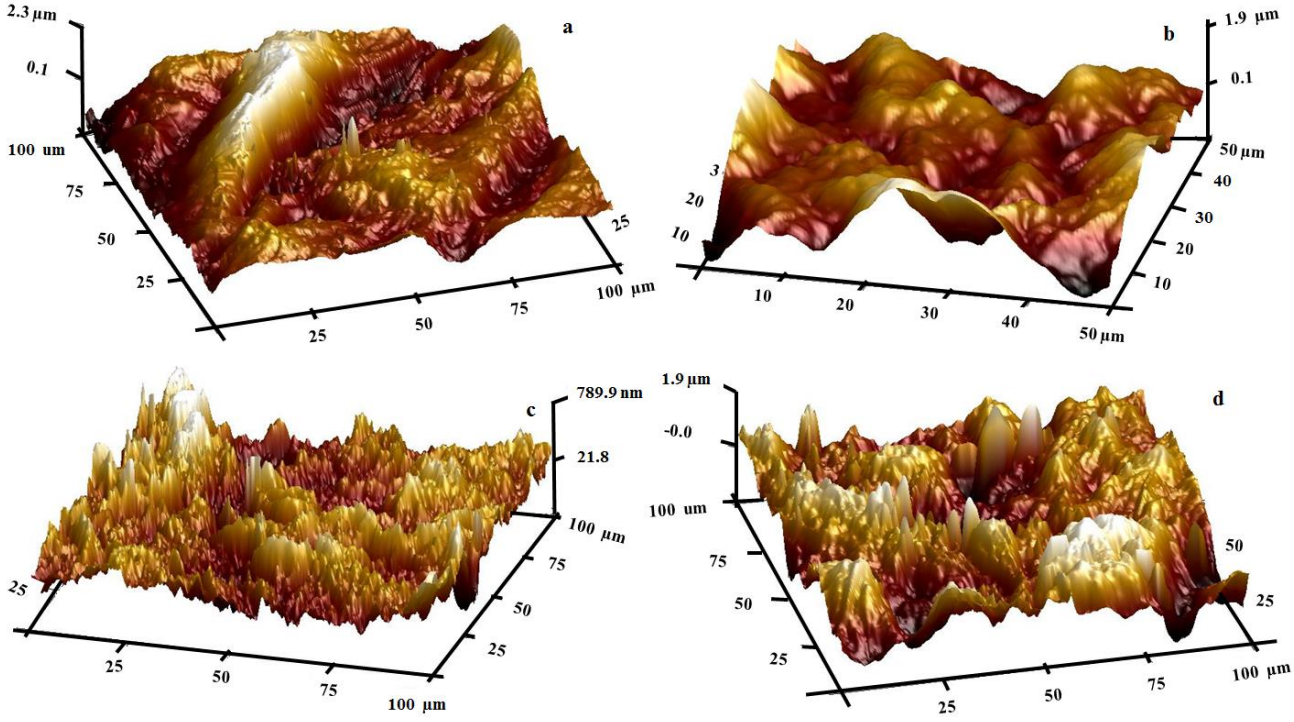

Fig. 4.3 The AFM images for (a) graphite and GO samples from (b) G2N1-$t_{12,24}$, (c) G1N1-$t_{12,24}$ and (d) G1N2-$t_{12,24}$.

Comparison of Fig. 4.3b-d, highlights G1N1-$t_{12,24}$ (1:1 graphite: sodium nitrate ratio) to have the most sharp-point projections whilst G2N1-$t_{12,24}$ (2:1 ratio) was the least. Quantification of surface roughness indicated the effects of reagent ratios, the G1N1-$t_{12,24}$ and G2N1-$t_{12,24}$

corroborated with lowest and highest values, respectively, for both root mean square roughness (Rq) and average roughness (Ra) measurements (Table 4.S1 in supplementary material).

4.3.2 Powder X-ray diffraction

The peak at 2θ of 30° was associated with a d-spacing of 0.34 nm and was assigned to 002 plane of graphite (Fig. 4.S1 and Table 4.1) [4.32,4.36]. The main peak for pristine graphite was at 2θ of 30° and other less prominent peaks at 25°, 50° and 63° (Fig. 4.S1a in supplementary material). Both G2N1-$t_{12,24}$ and G1N2-$t_{12,24}$ still had a peak at 2θ of 30° after the oxidation reaction (Fig. 4.S1b) and this means an initial mass ratio mismatch of graphite relative to $NaNO_3$ in the starting material resulted with some residual graphite. Only G1N1-$t_{12,24}$ had no peak at 2θ of 30° and this means only 1:1 graphite: sodium nitrate ratio resulted in completion of the reaction. The oxidative treatment resulted in the appearance of a new peak at 2θ of 13° (Fig. 4.S1b in supplementary material and Table 4.1). This peak was associated with a d-spacing of 0.80 nm and a 001 plane, it is attributed to increase in interlayer spacing along the c-axis due to oxygen functionalities from the oxidation process [4.23,4.27,4.32,4.36]. The peak is an indication of presence of GO in the product [4.32]. The increase in d-spacing is effected by repulsive forces between GO layers [4.37] and a possible explanation is the destruction of of H-bonding and $\pi - \pi$ interactions [4.38].

The d-spacing declined with a decrease in the ratio of graphite to sodium nitrate, i.e. 2:1, 1:1 and 1:2 in the starting material (indicated by data for G2N1-$t_{12,24}$, G1N1-$t_{12,24}$ and G1N2-$t_{12,24}$ in Table 4.1, respectively). As the ratio of graphite: sodium nitrate was varied from 2:1, 1:1 and 1:2 in the starting materials, the full width at half maxima (FWHM) of the peak at 2θ of 13° increased (Table 4.1). This is indicative of decrease in crystallite sizes as graphite: sodium nitrate ratio decreases. A possible inference is that a higher amount of Na^+ and NO_3^- initially intercalated reduces the crystallite sizes of the ultimate GO layers.

Table 4.1 Summary of Powder X-ray diffraction data for samples synthesised using different ratios of graphite: sodium nitrate.

Sample	2θ	d-spacing (nm)	FWHM (deg)
Graphite	30.92	0.34	0.22
G2N1-$t_{12,24}$	13.22	0.78	0.82
	30.58	0.34	0.93
G1N1-$t_{12,24}$	13.33	0.77	2.79
G1N2-$t_{12,24}$	13.61	0.76	3.35
	30.76	0.34	4.99

4.3.3 Textural characteristics

Textural characteristics studies of the GO samples indicate that the oxidation treatment of the graphite sheets significantly enhanced the BET surface area (Table 4.2). This is due to the contribution of the spaces between sheets as indicated by the increase in d-spacing (Table 4.S1 in supplementary material) due to enhanced repulsive forces between them. Additionally, the increase in BET surface area, BJH pore volume and pore sizes corroborated with decrease in crystallinity as inferred by the peak at 2θ of 13° (Fig 4.S1 in supplementary material and Table 4.2), i.e. G2N1-$t_{12,24}$ > G1N1-$t_{12,24}$ > G1N2-$t_{12,24}$. This is due to the decrease in crystallite sizes as deduced from PXRD analysis data as graphite: sodium nitrate ratio decreases.

Table 4.2 Textural characteristics of GO synthesized at different graphite: sodium nitrate ratio.

Sample	Surface area (m g^{-1})	Pore volume (cm^3 g^{-1})	Pore size (nm)
Graphite	2.32	0.010	14.87
G2N1-$t_{12,24}$	8.10	0.006	4.50
G1N1-$t_{12,24}$	185.43	0.260	6.36
G1N2-$t_{12,24}$	187.85	0.980	23.87

From the textural characteristics data (Table 4.2), it is clear that only graphite: sodium nitrate ratio of 1:2 enhances pore size of graphite. Porosity in GO samples culminates from voids between layers and this corroborates with earlier explanations in that higher sodium nitrate ratio enhances the cavities between layers.

4.3.4 Raman analysis

The common peaks often encountered in vibrational analyses of GO by the Raman spectroscopy are the G-, G'- and D-bands at 1580, 2700 and 1350 cm^{-1}, respectively [4.22,4.39,4.40]. Similarly, in the current work, Raman peaks were observed at the aforementioned peak positions. The D- and G'-bands were attributed to sp^3 bonding defects and second order Raman scattering, respectively. The G-band was associated with the tangential in-plane graphitic sp^2 hybridised carbons [4.40]. In the current work, a comparison of the effect of graphite: sodium nitrate ratio culminated in changes in the G-band (Fig. 4.4a), this peak was not observable in the starting material, i.e., graphite. The spectra in Fig. 4.4a showed that as the ratio of sodium nitrate was increased the width and intensity of the G-band also increased. The intensity of G-band is proportional to the number of GO layers [4.40]. Therefore, the sample ranking in terms of number of layers was G1N2-$t_{12,24}$ > G1N1-$t_{12,24}$ > G2N1-$t_{12,24}$ (Fig. 4.4a), hence it may be deduced that a higher ratio of $NaNO_3$ leads to poor exfoliation of layers.

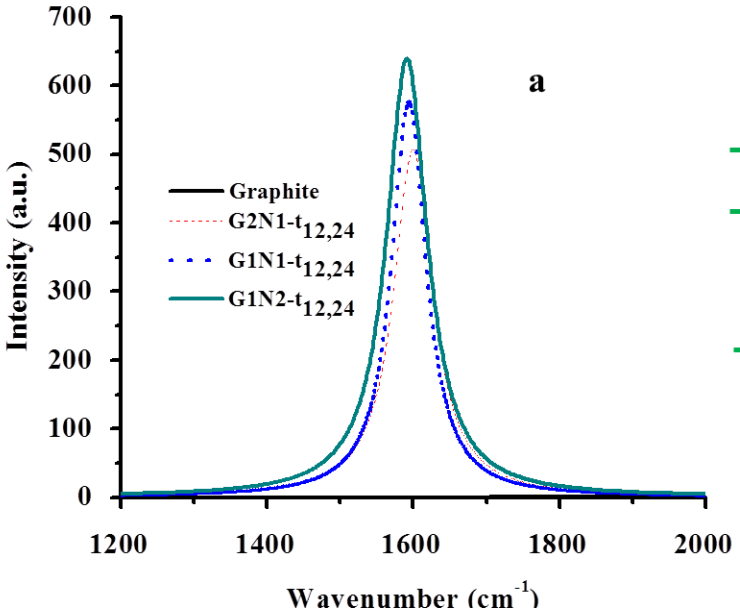

Sample	I_D/I_G
G2N1-$t_{12,24}$	0.26
G1N1-$t_{12,24}$	0.46
G1N2 -$t_{12,24}$	0.74

Fig. 4.4 (a) Raman spectroscopy G-band for graphite and GO at different mass ratios and (b) I_D/I_G ratios.

The slight shift in the G-band position observed in Fig. 4.4a showed that varying graphite: sodium nitrate ratios resulted in deviations in the distribution of oxygen-containing groups [4.27]. The ratio of the area under D- and G-bands (I_D/I_G) is often used as measure of the graphitic nature. In the current work, it is an indication of variation in both defects on the GO sheet and content of oxygen-containing moieties [4.37]. The order of the I_D/I_G ratio was G1N2-$t_{12,24}$ > G1N1-$t_{12,24}$ > G2N1-$t_{12,24}$ (insert in Fig. 4.4b). This clearly means I_D/I_G ratio was sensitive to proportion of the $NaNO_3$ in the reaction, i.e., the higher the amount of $NaNO_3$ the higher the defect density detected by Raman spectroscopy [4.41]. This corroborates with the decrease in crystallinity according to PXRD spectrum (Fig 4.S1b in supplementary material). This can be attributed to the development of an amorphous character on graphite sheet upon oxidation [4.22].

4.3.5 Thermal stability

A GO sample decomposed in several stages (Fig. 4.5a), the weight loss due to moisture and interstitial water was at ca. 100 ℃. The thermal stability of adsorbed water is influenced by interactions with oxygen-containing groups on GO surface [4.32,4.37]. Water strongly interact with GO *via* hydrogen bonding [4.33]. The loss at ca. 200 ℃ can be assigned to loss due to sp^3

hybridized carbons in the GO network, introduced by the oxidative treatment, i.e. carboxyl moieties [4.42]. The decline at ca. 450 ℃ and 800 ℃ (Fig. 4.6a), for GO and graphite samples, respectively, was due to sp^2 carbon atoms in the hexagonal structure. This implies that thermal decomposition temperature decreased after the oxidative reactions (Fig. 4.6b) and the reduction of thermal stability of GO relative to graphite corroborates with the findings by El-Khodary et al. [4.32] The decrease in decomposition temperature of hexagonal carbons relative to pristine graphite was due to various degrees of strains introduced onto the graphitic framework *via* the oxidative treatment.

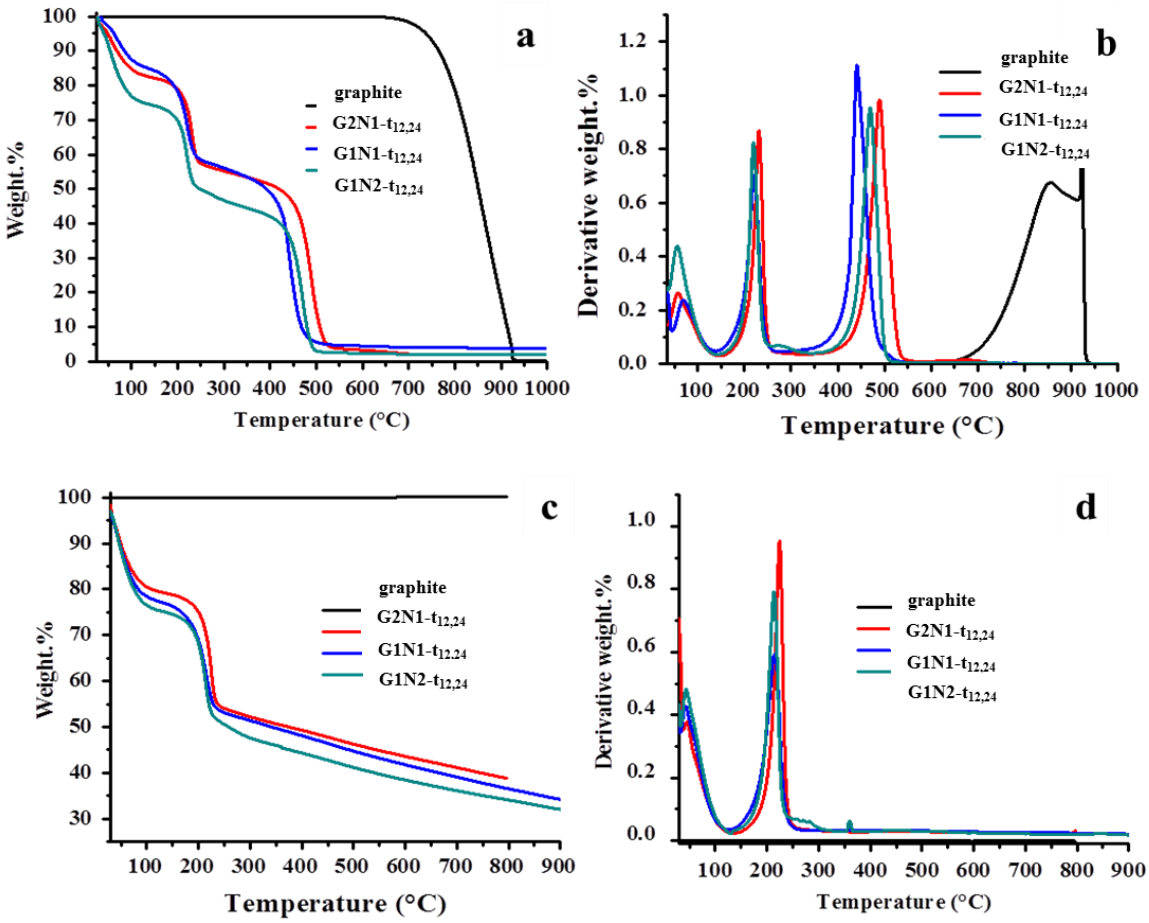

Fig. 4.5 Thermogravimetric analysis (a) thermogram and (b) derivative weight curve in oxygen, and under nitrogen (c) thermogram and (d) associated derivative weight curve.

No clear trend was observed in terms of thermal stability in air, for instance, below 450 ℃ G1N2-$t_{12,24}$ was the least thermally stable but was ranked second above that temperature (Fig. 4.5a). To further investigate the degree of oxidative treatments, thermal stability studies were done under nitrogen atmosphere (Fig. 4.5c and 4.5d). Similar trends were observed and the

loss between 150 and 300 ℃ implied the presence of oxygen-containing moieties in carbon networks, and particularly carboxylic acid groups [4.27,4.37]. The loss from 350 to 800 ℃ was assigned to decomposition of carbonyl groups formed on the graphite surface, i.e. more stable oxygen-containing functionalities [4.23,4.32]. A clear ranking in terms of oxygen moieties content in the product was obtained when TGA was performed under nitrogen, i.e. G1N2-$t_{12,24}$ > G1N1-$t_{12,24}$ > G2N1-$t_{12,24}$ (Fig. 4.5c and 4.5d). This infers that $NaNO_3$ enhances the oxidation reaction of graphite. The order of thermal stability was opposite to the content of oxygen functionalities; this means increase in oxygen content reduced thermal stability. Graphite had no weight loss in nitrogen and this means atleast 30% of oxygen-containing groups were introduced during the oxidation reactions (Fig. 4.5c). The thermogram also show that GO was composed of a variety of oxygen-containing moieties [4.24] and this is indicated by a weight loss of about 70% at 900 ℃. From the comparison of TGA curves under nitrogen, it is clear that the lower the graphite: sodium nitrate ratios the higher the amount of oxygen-containing groups in the sample.

4.3.6 Uv-Vis analysis

In Uv-Vis analyses, the peak at ca. 200 nm red shifted in all samples and the corresponding absorption intensity was stronger relative to pristine graphite (Fig. 4.6). This peak was assigned to $\pi \rightarrow \pi^*$ transition and this is associated with the transmission from C=C aromatic moieties [4.27,4.30,4.43]. This means oxidative treatment involved in GO synthesis did not severely interfere with the conjugation in the π system. The presence of the peak also suggests existence of more extensive oxygen-containing groups on GO surface that weakens van der Waals forces originally on graphite [4.27].

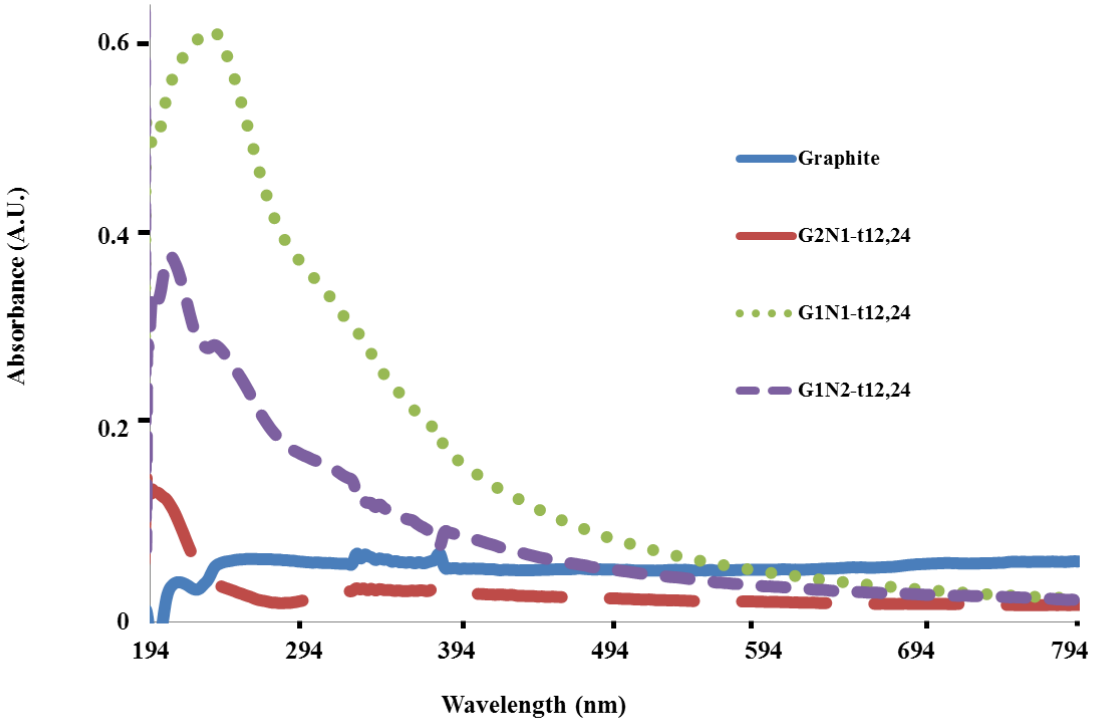

Fig. 4.6 The Uv-Vis samples at different mass ratios of reagents.

G1N1-$t_{12,24}$ and G1N2-$t_{12,24}$, especially the latter, had shoulder peaks at 308 and 235 nm, respectively. These peaks were assigned to $\pi \rightarrow \pi^*$ transition of C=O and COOH groups [4.27,4.43]. This means lower graphite: sodium nitrate ratio during GO synthesis tailors the graphite towards visible light absorption range *via* introduction of substantial content of oxygen-containing moieties.

4.3.7 IR analysis

From the ATR analyses, several new peaks appeared in the obtained products (Fig. 4.7). All samples had a broad peak at ca. 3500 cm^{-1} which is due to O-H (H-bonded) stretch vibration. The peak at ca. 2700 cm^{-1} due to overlap C-H stretching vibrations on graphite disappeared after oxidative treatment. Additionally, the peak at ca. 2300 cm^{-1} disappeared on the spectrum of G1N1-$t_{12,24}$. The peak at ca. 2000 cm^{-1}, due to C=C asymmetric stretch, was red-shifted on all GO samples (Fig. 4.7). Peaks at 1615 and 1720 cm^{-1} assigned to in plane C=C stretch (oxidised sp^2 C=C bonds in ring) and C=O stretch (COOH of carbonyl or carboxyl groups), respectively, appeared in all samples. Additionally, all oxidized samples exhibited a new peak

at ca. 1340 cm^{-1} due to O-H deformation (of the C-OH group). The ATR data clearly suggest the introduction of oxygen-containing moieties onto pristine graphite *via* chemical bonds.

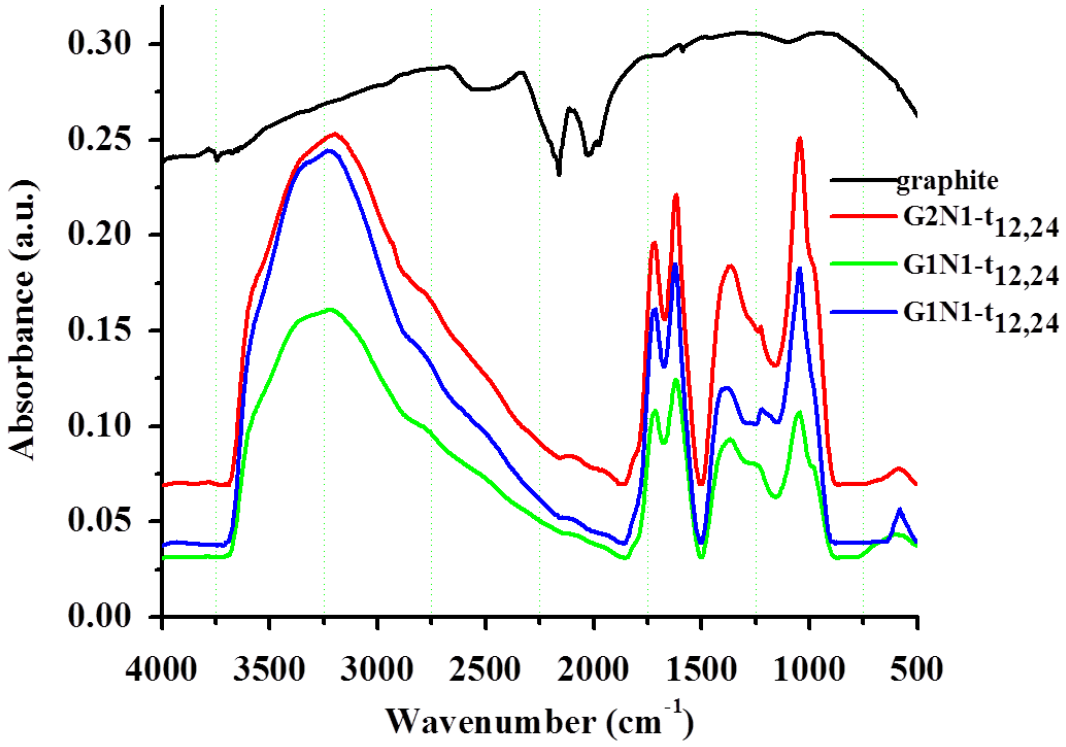

Fig. 4.7 ATR for GO samples synthesised from different graphite: sodium nitrate mass ratios.

All oxidatively treated samples had a peak at ca. 580 cm^{-1}, broadest for G1N1-$t_{12,24}$, from sulfur-containing moieties. This is the same position were diamond, sp^3 peak would appear, however, since the peak was absent in pristine graphite it means it came from oxidative treatments. This points out on possibility of sulfate groups bonding to O groups during H_2SO_4 treatment [4.27]. The absorption peak intensities for all the functional groups were in the following order G2N1-$t_{12,24}$ > G1N2-$t_{12,24}$ > G1N1-$t_{12,24}$ (Fig. 4.7).

4.3.8 Elemental analysis

Elemental analyses were carried out to determine H, N and O elemental composition in the products (Table 4.3). The H, N and O atoms were absent in the pristine graphite. This means

their presence after oxidative treatment is either directly or indirectly linked to synthesis steps. From elemental analyses data, it was apparent that 1:1 ratio had the highest N composition, i.e. G1N1-$t_{12,24}$. The presence of H atoms in all GO samples is attributed to presence of both hydroxyl groups and adsorbed water [4.33]; this agrees with weight loss at ca. 100 ℃ in TGA curves (Fig. 4.5). This means some of the oxygen atoms present in the samples was from the DI (water molecules). Only half of the percentage composition of H atoms in Table 4.3 minus H atoms due to hydroxyl groups is equivalent to the oxygen atom contribution from DI in each sample. This is because the ratio of H: O is 2:1 in DI, hence, a substantial amount of elemental oxygen was introduced onto the graphitic network of the samples.

Table 4.3 **Elemental analysis for GO samples.**

Sample name	H	N	O
Graphite	-	-	-
G2N1-$t_{12,24}$	1.46	0.13	27.60
G1N1-$t_{12,24}$	1.61	0.45	29.36
G1N2-$t_{12,24}$	1.45	0.19	30.18

From elemental analysis, the order elemental oxygen content was G1N2-$t_{12,24}$ > G1N1-$t_{12,24}$ > G2N1-$t_{12,24}$ (Table 4.3). This order verified the deductions from TGA in N_2 (Fig. 4.5c and d), and this means high $NaNO_3$ ratio culminated in high oxygen content in GO samples. High content of oxygen-containing functionalities agreed with increase in BET surface area, porosity, FWHM and decrease in d-spacing and crystallinity (data in Table 4.1 and 4.2). Additionally, the large number of layers and increase in defect intensity (G-band intensity and I_D/I_G data in Fig. 4.4) as well as decrease in thermal stability corroborate with high oxygen content. This means the ratio of sodium nitrate during GO synthesis modifies the associated physicochemical properties and hence avoiding the use of sodium nitrate brings out some variation in the ultimate product. Furthermore, the data from PXRD, TGA and elemental analysis techniques infers that high content of oxygen does not necessarily mean completion of reaction. The oxygen moieties have been reported to facilitate hydration and exfoliation of GO sheets in synthesis of graphene [4.30] but the current work suggest that their disruption of the π system reduces the crystal quality.

4.4 Variation of reaction time

From the earlier sections, it was deduced that the product from 1:1 graphite: sodium nitrate ratio had no residual graphite. Hence, the effect of reaction duration on the obtained GO products was studied mainly using this ratio. Reaction duration variations at both room temperatures and at 98 ℃, $t_{A,B}$, were investigated. The $t_{3,3}$ and $t_{12,12}$ were chosen to compare shorter and longer reaction times which were equal at both room temperature and at 98 ℃. Additionally, $t_{6,12}$ and $t_{12,24}$ were chosen to investigate the effect of reducing and increasing reaction time at room temperature and at 98 ℃, respectively. Whereas $t_{0,0.25}$ and $t_{3,3}$ were selected to further study the influence of even shorter reaction times relative to $t_{3,3}$ and to determine if a higher temperature instead of room temperature followed by no reaction or a shorter reaction at 98 ℃, respectively, would introduce substantial elemental oxygen in the samples.

4.4.1 Microscopic studies

Similarly, microscopic analyses were done with the AFM, SEM and TEM techniques.

4.4.1.1 Transmission electron microscopy

There was no clear relationship between reaction durations and exfoliation levels detectable from TEM. Longer reaction times, except for G2N1-$t_{0,0.25}$, led to small GO fragments as shown in Fig. 4.8. Since samples were prepared similarly for TEM analysis, it means prolonged stirring during GO synthesis break GO sheets into smaller fragments. The unusual observation on G2N1-$t_{0,0.25}$ is due to slight variations in the synthesis method (experimental section), i.e. a combination of variation in both reagent ratio, minimal reaction time and temperature.

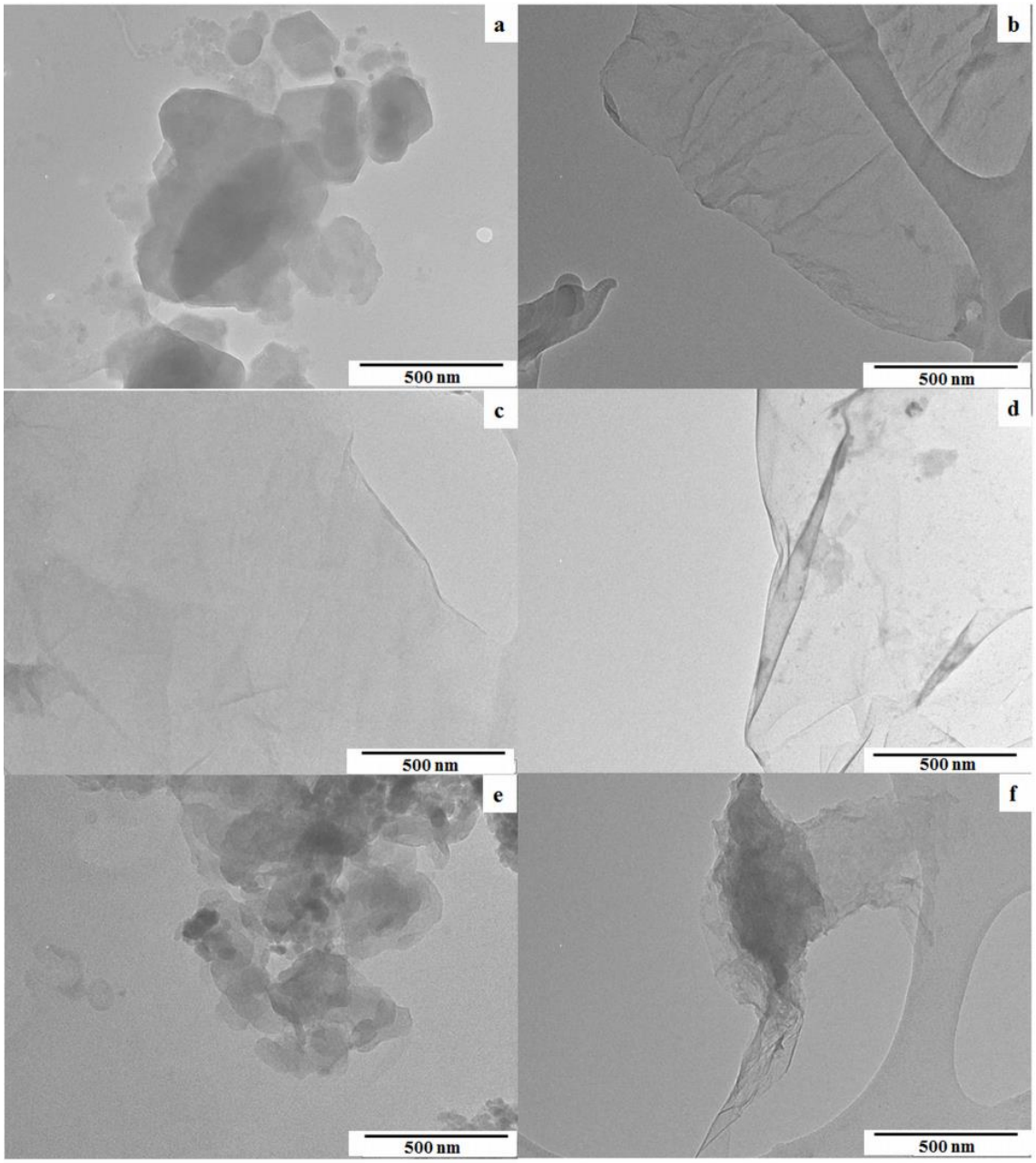

Fig. 4.8 TEM images for GO samples (a) G2N1-$t_{0,0.25}$, (b) G1N1-$t_{3,0}$, (c) G1N1-$t_{3,3}$, (d) G1N1-$t_{6,12}$, (e) G1N1-$t_{12,12}$ and (f) G1N1-$t_{12,24}$.

4.4.1.2 Scanning electron microscopy

Similar morphological observations were obtained from SEM analysis of GO samples synthesized by varying reaction durations, i.e. wrinkling and rippling of GO sheets (Fig. 4.S2). The synthesis conditions for G2N1-$t_{0,0.25}$ and G1N1-$t_{3,0}$, despite shorter reaction times, introduced significant wrinkling of GO sheets (Fig. 4.S2 a-b in supplementary material). The

morphology of the sample G1N1-$t_{3,3}$ was closer to that of pristine graphite and this can be explained by the introduction of fewer defects on the GO sheets due to the shorter reaction time (Fig. 4.2c and Fig. 4.S2 c-e in supplementary material).

4.4.1.3 Atomic force microscopy

Similarly, different surface topography culminated from varying reaction time at constant graphite: sodium nitrate ratio (Fig. 4.9 b-f). Comparison of GO relative to reaction times, from 3 to 24 hours, shows that the spike-like topography was generated as reaction time increased (Fig. 4.9 c-f). However, G1N1-$t_{3,0}$ exhibited the most spike-like projections and this can be attributed to the minor variations in the synthesis method. The roughening of the sheets is an indication of oxidation [4.22].

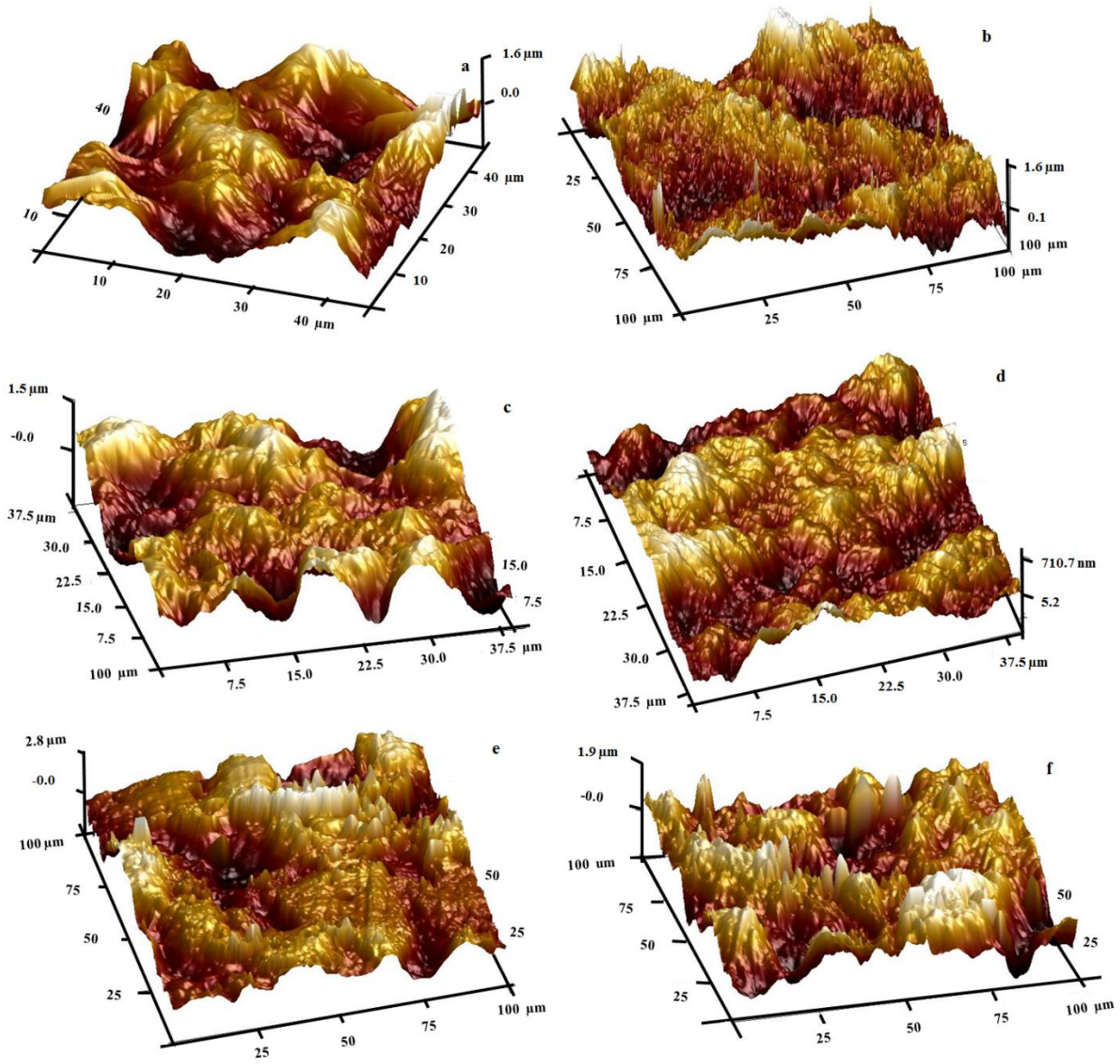

Fig. 4.9 The AFM images for GO samples (a) G2N1-$t_{0,0.25}$, (b) G1N1-$t_{3,0}$, (c) G1N1-$t_{3,3}$, (d) G1N1-$t_{6,12}$, (e) G1N1-$t_{12,12}$ and (f) G1N1-$t_{12,24}$.

In terms of reaction duration, 12 hours tends to be the threshold for highest Ra and Rq values, when samples G1N1-$t_{3,3}$, G1N1-$t_{6,12}$, G1N1-$t_{12,12}$ and G1N1-$t_{12,24}$ were compared (Table 4.S2 in supplementary material). Again, the samples with the most pronounced roughened sheet surfaces, i.e. G1N1-$t_{3,0}$ and G1N1-$t_{12,24}$ tend to be the least roughened.

4.4.2 Powder X-ray diffraction

The oxidative treatment resulted in the appearance of a new peak at 2θ of 13° and the corresponding peak for G1N1-$t_{3,0}$ was blue shifted from the rest (Fig. 4.S3b in supplementary material and Table 4.4). Only G1N1-$t_{3,0}$ and G1N1-$t_{12,24}$ did not show the peak at 2θ of 30° after oxidation (Fig. 4.S3b) and this infers reaction completion. Ranking in terms of residual graphite, as determined from Fig 4.S3, is G1N1-$t_{12,24}$ < G1N1-$t_{3,0}$ < G1N1-$t_{6,12}$ < G1N1-$t_{12,12}$ < G1N1-$t_{3,3}$ < G2N1-$t_{0,0.25}$. For G2N1-$t_{0,0.25}$, it means the synthesis conditions, i.e. the combination of reaction duration, temperature and graphite: sodium nitrate ratio did not introduce substantial number of oxygen-containing moieties on all the graphite sheets whereas for the rest of the samples it means 24 hours is the optimum reaction time at 98 ℃ (Table 4.4). Also, a possible explanation, amongst others, is that reaction at 98 ℃ for 15 minutes was not adequate reaction time in the current work. Additionally, the peak broadening at the 2θ of 30° on the GO is an indication of random packing of the sheets [4.30].

The d-spacing, with exception of G1N1-$t_{12,12}$ and G2N1-$t_{0,0.25}$, tend to upsurge with decrease in reaction durations (Table 4.4). This can be explained by the decrease in effective repulsion forces as the GO sheet size decreases, longer reaction duration exhibited smaller fragments in Fig 4.8. The order of FWHM was G2N1-$t_{0,0.25}$ < G1N1-$t_{3,3}$ < G1N1-$t_{3,0}$ < G1N1-$t_{6,12}$ < G1N1-$t_{12,12}$ < G1N1-$t_{12,24}$, hence, PXRD analyses for samples synthesised by varying only reaction duration showed correlation of increase in reaction time with increase in FWHM of the peak at 2θ of 13° (Table 4.4).

Table 4.4 Summary of powder X-ray diffraction data.

Sample	2θ	d-spacing (nm)	FWHM (deg)
Graphite	30.92	0.34	0.22
G2N1-$t_{0,0.25}$	12.71	0.81	0.94
	30.37	0.34	1.88
G1N1-$t_{3,0}$	11.79	0.87	1.23
G1N1-$t_{3,3}$	12.40	0.83	1.16
	30.02	0.35	0.98
G1N1-$t_{6,12}$	13.22	0.78	1.65
	29.78	0.35	5.43
G1N1-$t_{12,12}$	13.56	0.76	2.73
	30.88	0.34	1.32
G1N1-$t_{12,24}$	13.33	0.77	2.79

4.4.3 Raman analysis

Effect of varying reaction durations on the G-band of the synthesised GO did not give a clear trend but stirring at both room temperature and 98 ℃ for 3 hours resulted in the broadest peaks (Fig. 4.10a). The slight shift in the G-band position observed in Fig. 4.10a showed that varying reaction durations also culminated in deviations in the distribution of oxygen-containing groups [4.27].

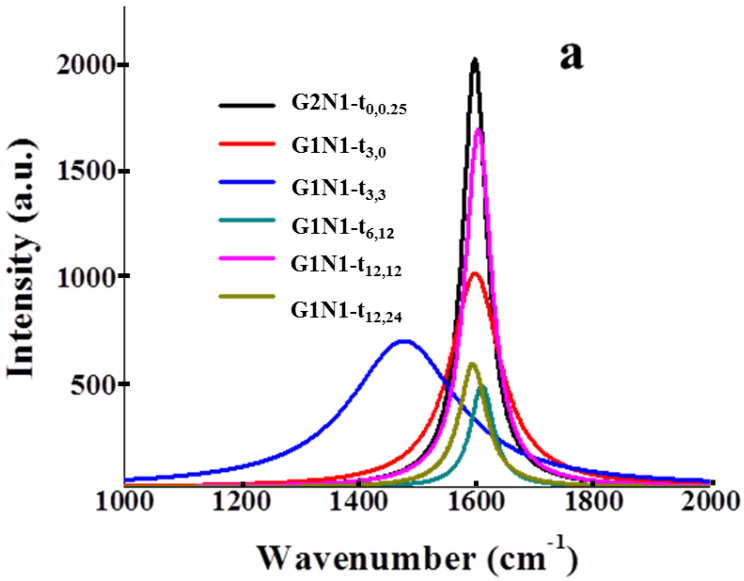

b

Sample	I_D/I_G
G2N1-$t_{0,0.25}$	0.79
G1N1-$t_{3,0}$	0.37
G1N1-$t_{3,3}$	-
G1N1-$t_{6,12}$	1.11
G1N1-$t_{12,12}$	0.56
G1N1-$t_{12,24}$	0.46

Fig. 4.10 Comparison of Raman spectroscopy (a) G-band and (b) I_D/I_G ratios for GO samples synthesised at different reaction durations.

The spectra suggest that the order of the number of sheets, i.e. the order of G-band intensity was G2N1-$t_{0,0.25}$ > G1N1-$t_{12,12}$ > G1N1-$t_{3,0}$ > G1N1-$t_{3,3}$ > G1N1-$t_{12,24}$ > G1N1-$t_{6,12}$. For samples with reaction time being the only variable, I_D/I_G ratio tends to decrease with increase in reaction time except for sample G1N1-$t_{3,3}$, which had no noticeable D-band, i.e. order was G1N1-$t_{6,12}$ > G1N1-$t_{12,12}$ > G1N1-$t_{12,24}$ (Fig. 4.10b). This trend is an indication of mainly increase in defects in the form of oxygen functionalities. Also, the D-band of G1N1-$t_{3,3}$ could have been obscured since the observed peak stretched over the wavenumbers for both D- and G-band peaks, i.e. peak overlap (Fig. 4.10a).

4.4.4 Thermal stability

All samples had loss of weight due to water, oxygen-containing groups and graphitic carbons. On comparison of G1N1-$t_{12,24}$ and G1N1-$t_{12,12}$, with different reaction times at 98 °C, it is noted that G1N1-$t_{12,24}$ with longer reaction duration had a larger ratio of both sp^2 and sp^3 carbons (Fig. 4.11a). It Was also noted that reducing the reaction time at room temperature increased the homogeneity of sp^2-hybridised carbons particularly in comparing G1N1-$t_{12,12}$ and G1N1-$t_{6,12}$. For G1N1-$t_{3,3}$ and G2N1-$t_{0,0.25}$, with an even shorter reaction duration, showed a further increase in sample homogeneity, i.e. less skewed thermograms (Fig. 4.11a).

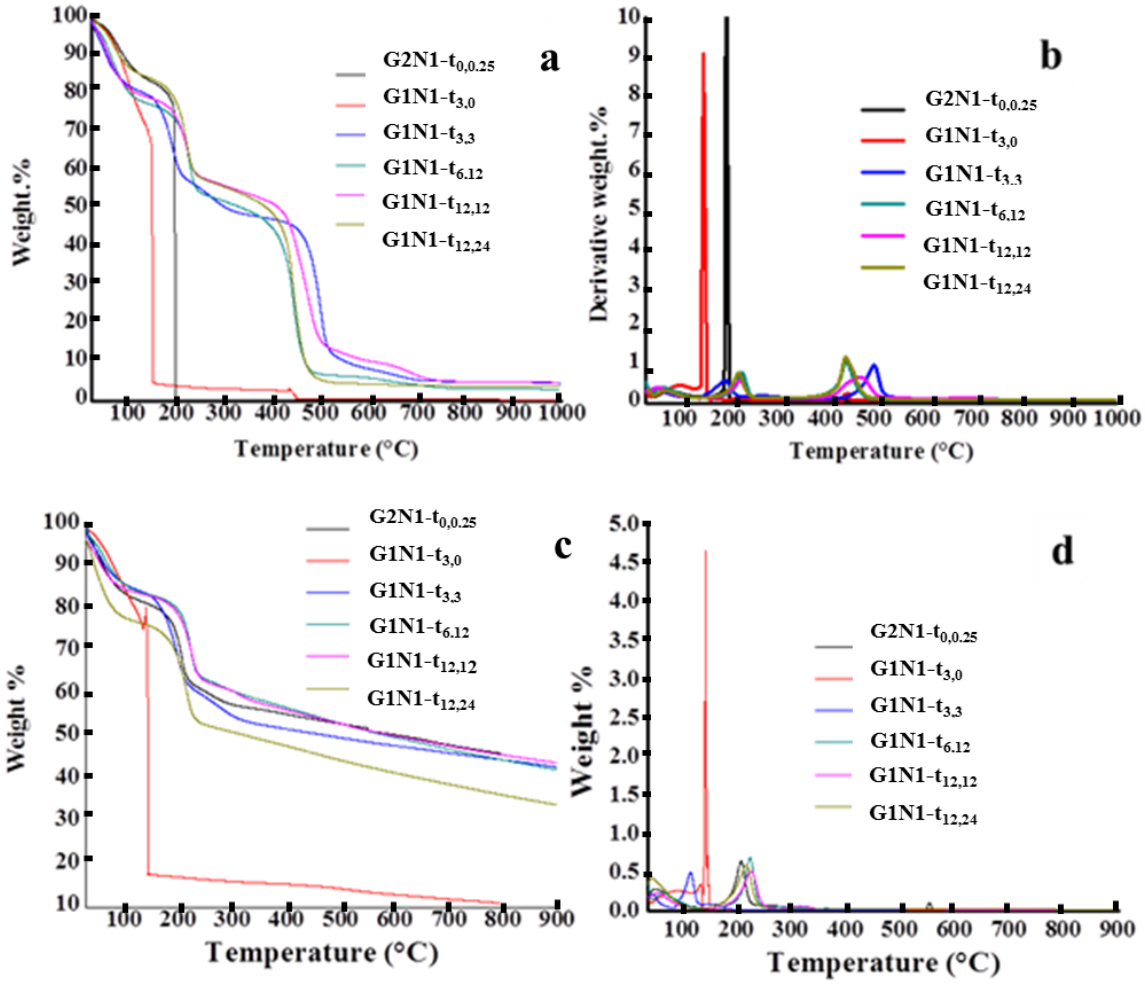

Fig. 4.11 Thermogravimetric analysis (a) in oxygen curve and (b) associated derivative weight curve, (c) in nitrogen and (d) associated derivative weight curve.

G1N1-$t_{3,0}$ was the least thermally stable followed by G2N1-$t_{0,0.25}$ (Fig. 4.14a). G2N1-$t_{0,0.25}$ had two decomposition stages whilst the rest of the samples had weight loss in three stages. G2N1-$t_{0,0.25}$ showed a sharp decrease in weight at ca. 200 ℃, no other weight loss was noticeable, and this suggest presence of homogenous amorphous species of carbons. All samples, except for G2N1-$t_{0,0.25}$, decreased in weight at ca. 450 ℃ and this decline was attributed to sp^2 carbon atoms in the GO hexagonal structure.

The thermogram in air tends to suggest introduction of high levels of sp^3 carbon atoms in the G1N1-$t_{3,3}$ and G2N1-$t_{0,0.25}$ (Fig. 4.11b), this could mean high content of oxygen moieties, and hence, an analysis under nitrogen atmosphere was carried out (Fig. 4.11 c-d). The thermal analyses in nitrogen suggest that G2N1-$t_{0,0.25}$ had the lowest amount of oxygen-containing

groups and this was attributed to the shortest reaction time in synthesizing GO in this sample. Again, the effect of combination of synthesis temperature and reaction time is highlighted by this observation. From the TGA (Fig. 4.11 c-d), though the order of the last three was almost the same or varied slightly, order of oxygen-containing groups derived is G1N1-$t_{3,0}$ > G1N1-$t_{12,24}$ > G1N1-$t_{3,3}$ > G1N1-$t_{6,12}$ > G1N1-$t_{12,12}$ > G2N1-$t_{0,0.25}$. This means substantial amount of elemental oxygen can also be introduced to graphite sheets at a temperature of 35℃.

4.4.5 Uv-Vis analysis

Similar observations were made on samples with varied oxidation durations (Fig. 4.S4 in supplementary material). Additionally, the corresponding peak at ca. 200 nm for G2N1-$t_{0,0.25}$ was broad and all samples had shoulder peaks at 311 nm. These peaks were attributed to the same functionalities as in earlier sections.

4.4.6 IR analysis

Functional groups similar to those elaborated in earlier sections were obtained. There was a slight peak at ca. 1226 cm^{-1} in all samples, especially for G2N1-$t_{0,0.25}$ and G1N1-$t_{3,0}$ (Fig. 4.S5 in supplementary material). This was from the skeletal in-plane C=C stretching vibrations in the graphitic domains. All GO samples had a peak at ca. 580 cm^{-1}, highly intense for G1N1-$t_{3,0}$. On varying reaction durations, the peak at ca. 2200 cm^{-1} disappeared in G1N1-$t_{12,24}$, but was still noticeable in all the GO samples (Fig. 4.S5 in supplementary material). This peak can be associated with graphite, the starting material. The order of peak intensities was G1N1-$t_{6,12}$ > G2N1-$t_{0,0.25}$ > G1N1-$t_{12,12}$ > G1N1-$t_{3,3}$ > G1N1-$t_{3,0}$ > G1N1-$t_{12,24}$.

4.4.7 Elemental analysis

Upon scrutinizing elemental analysis data for samples synthesised by varying reaction times, the ranking according to percentage amount of O atoms was G1N1-$t_{3,0}$ > G1N1-$t_{12,24}$ > G1N1-$t_{3,3}$ > G1N1-$t_{12,12}$ > G2N1-$t_{0,0.25}$ > G1N1-$t_{6,12}$. This order corroborated with the trend deduced from TGA in N_2 and the decrease in absorption intensities from IR analysis. Additionally, a possible deduction with reference to PXRD data and TEM analysis is that larger pieces of GO,

from shorter reaction durations, culminated in bigger gaps between layers. There was no clear relationship between increase in I_D/I_G ratio and oxygen content determined by elemental analyses (Table 4.5 and Fig. 4.10). In addition, the FWHM and peak intensity at 2θ of 13° tends to be influenced by reaction time rather than oxygen content.

Table 4.5 Elemental analysis for GO samples.

Sample	H	N	O
Graphite	-	-	-
G2N1-$t_{0,0.25}$	1.09	-	23.58
G1N1-$t_{3,0}$	1.87	-	30.10
G1N1-$t_{3,3}$	1.44	-	27.45
G1N1-$t_{6,12}$	0.61	1.07	18.53
G1N1-$t_{12,12}$	1.52	0.54	27.09
G1N1-$t_{12,24}$	1.61	0.45	29.36

If 25-30% oxygen intercalated in disordered cyclohexenyl carbon matrix is the basis of classifying samples as GO [4.32], therefore it implies that G2N1-$t_{0,0.25}$ and G1N1-$t_{6,12}$ are not forms of GO. Since a reaction at 35 ℃ introduced substantial amount of oxygen, this further supports earlier deductions that an initial reaction at 50 ℃, instead of room temperature followed by a reaction at 98 ℃ for 15 minutes was not adequate for reaction completion. From the angle of different reaction times, it was seen that shorter periods, i.e. G2N1-$t_{0,0.25}$, G1N1-$t_{3,0}$, G1N1-$t_{3,3}$ had no N atoms (Table 4.5). Additionally, G1N1-$t_{6,12}$ had the highest N atom percentage and thereafter N content decreased in samples, G1N1-$t_{12,12}$ and G1N1-$t_{12,24}$. This means reaction time enhanced N-doping up to a certain maximum threshold and thereafter decreased.

4.5 Conclusions

Fourier transform infra-red and Uv-Vis spectroscopies, and thermal stability analyses in nitrogen showed the presence of oxygen-containing groups. Oxidative treatment creates defects in the form of wrinkled paper-like morphology and reduced agglomeration of sheets by introducing repulsive forces between them. This culminates in increase of d-spacing from 0.34 to 0.80 nm. The ratio of graphite: sodium nitrate in the starting material, affect reaction completion. Graphene oxide samples, G1N1-$t_{3,0}$ (at graphite: sodium nitrate ratio of 1:1) and

G1N1-$t_{12,24}$ (at graphite: sodium nitrate ratio of 1:1 with longer reaction time) had no residual graphite. High sodium nitrate ratio in the starting material increased the oxygen content of GO whilst graphite: sodium nitrate mass ratio mismatch enhances sheet roughness. From thermal stability and elemental analyses, G1N2-$t_{12,24}$ and G1N1-$t_{3,0}$ had the highest number of oxygen-containing groups whilst G2N1-$t_{0,0.25}$ had the least amount. Additionally, high sodium nitrate ratio creates more defects on the GO sheets, but long reaction durations improved the crystal quality reduced sheet sizes. Samples, namely, G1N2-$t_{12,24}$, G1N1-$t_{3,0}$, G1N1-$t_{12,24}$, G2N1-$t_{12,24}$, G1N1-$t_{3,3}$ and G1N1-$t_{12,12}$ had enough amount of oxygen to be classified as GO. GO samples had lower thermal stability than graphite and also longer reaction times may introduce N in the GO samples. A short reaction time of 15 minutes did not introduce substantial amount of oxygen. The ratio of graphite: sodium nitrate in the starting material and reaction durations affect physicochemical properties such as number of oxygen-containing groups, crystal quality, absorption characteristics, thermal stability, topography, textural characteristics and overall morphology. Hence, the amount of Na^+ and NO_3^- ions intercalated in the initial step of GO synthesis and reaction duration are critical parameters that influences the overall quality of GO.

Acknowledgements

The authors wish to express their gratitude to Dr Bidita Varadwaj and Ms Kudzai Mugadza for their critical comments during the manuscript preparation. Edwin Tonderai Mombeshora thanks the University of KwaZulu-Natal Nanotechnology Platform for a study bursary. The authors wish to thank the National Research Foundation (NRF) for funding.

References

[4.1] Geim AK. Graphene: Status and prospects. Science. 2009, 324:1530-1534.

[4.2] Mombeshora ET, Nyamori VO. A review on the use of carbon nanostructured materials in electrochemical capacitors. International Journal of Energy Research. 2015, 39: 1955-1980.

[4.3] Chung C, Kim Y-K, Shin D, Ryoo S-R, Hong BH, Min D-H. Biomedical applications of graphene and graphene oxide. Accounts of Chemical Research. 2013, 46(10): 2211-2224.

[4.4] Tozzini V, Pellegrini V. Prospects for hydrogen storage in graphene. Phys Chem Chem Phys. 2013, 15(1): 80-89.

[4.5] Konios D, Kakavelakis G, Petridis C, Savva K, Stratakis E, Emmanuel Kymakis. Highly efficient organic photovoltaic devices utilizing work-function tuned graphene oxide derivatives as the anode and cathode charge extraction layers. Journal of Mateial Chemistry A. 2016, 4: 1612-1623.

[4.6] Kakavelakis G, Konios D, Stratakis E, Kymakis E. Enhancement of the efficiency and stability of organic photovoltaic devices via the addition of a lithium-neutralized graphene oxide electron-transporting layer. Chemistry of Materials. 2014, 26 (20): 5988-5993.

[4.7] Balis N, Konios D, Stratakis E, Kymakis E. Ternary organic solar cells with reduced graphene oxide–Sb_2S_3 hybrid nanosheets as the cascade material. ChemNanoMat. 2015, 1(5): 346-352.

[4.8] Sygletou M, Tzourmpakis P, Petridis C, Konios D, Fotakis C, Kymakis E, et al. Laser induced nucleation of plasmonic nanoparticles on two-dimensional nanosheets for organic photovoltaics. Journal of Material Chemistry A. 2016, 4: 1020-1027.

[4.9] Noori K, Konios D, Stylianakis MM, Kymakis E, Giustino F. Energy-level alignment and open-circuit voltage at graphene/polymer interfaces: theory and experiment. IOP Science. 2016, 3(1).

[4.10] Stylianakis MM, Konios D, Kakavelakis G, Charalambidis G, Stratakis E, Coutsolelos AG, et al. Efficient ternary organic photovoltaics incorporating a graphene-based

porphyrin molecule as a universal electron cascade material. Nanoscale. 2015, 7(42): 17827-17835.

[4.11] Chen X, Tang X-Z, Liang YN, Cheah JW, Hu P, Hu X. Controlled thermal functionalization for dispersion enhancement of multi-wall carbon nanotube in organic solvents. Journal of Material of Science. 2016, 51: 5625-5634.

[4.12] Agresti A, Pescetelli S, Cinà L, Konios D, Kakavelakis G, Kymakis E, et al. Efficiency and stability enhancement in perovskite solar cells by inserting lithium-neutralized graphene oxide as electron transporting layer. Advanced Functional Materials. 2016:n/a-n/a.

[4.13] Yang D, Zhou L, Chen L, Zhao B, Zhang J, Li C. Chemically modified graphene oxides as a hole transport layer in organic solar cells. Chem Commun (Camb). 2012, 48(65): 8078-8080.

[4.14] Hassoun J, Bonaccorso F, Agostini M, Angelucci M, Betti MG, Cingolani R, et al. An advanced lithium-ion battery based on a graphene anode and a lithium iron phosphate athode. Nano Letters. 2014, 14(8): 4901-4906.

[4.15] Chen R, Zhao T, Tian T, Cao S, Coxon PR, Xi K, et al. Graphene-wrapped sulfur/metal organic framework-derived microporous carbon composite for lithium sulfur batteries. APL Materials. 2014, 2(12): 124109.

[4.16] Sun J, Lee H-W, Pasta M, Yuan H, Zheng G, Sun Y, et al. A phosphorene–graphene hybrid material as a high-capacity anode for sodium-ion batteries. Nature Nanotechnology. 2015, 10:980-985.

[4.17] Viskadouros G, Konios D, Kymakis E, Stratakis E. Electron field emission from graphene oxide wrinkles. RSC Advances. 2016, 6: 2768-2773.

[4.18] Viskadouros G, Konios D, Kymakis E, Stratakis E. Direct laser writing of flexible graphene field emitters. Applied Physics Letters. 2014, 105: 203104.

[4.19] Novoselov KS, Geim AK, Morozov SV, Jiang D, Katsnelson MI, Grigorieva IV, et al. Two-dimensional gas of massless Dirac Fermions in graphene. Nature 2005, 438: 197-200

[4.20] Schwierz F. Graphene transistors. Nature Nanotechnology. 2010, 5(7): 487-496.

[4.21] Liu J, Xue Y, Gao Y, Yu D, Durstock M, Dai L. Hole and electron extraction layers based on graphene oxide derivatives for high-performance bulk heterojunction solar cells. Advanced Materials. 2012, 24(17): 2228-2233.

[4.22] Paredes JI, Villar-Rodil S, Solis-Fernandez P, Martinez-Alonso A, Tascon JM. Atomic force and scanning tunneling microscopy imaging of graphene nanosheets derived from graphite oxide. Langmuir. 2009; 25(10): 5957-5968.

[4.23] Marcano D C, Kosynkin D V, Berlin J M, et al. Improved synthesis of graphene oxide [J]. ACS Nano, 2013, 4(8): 4806-4814.

[4.24] Pei S, Cheng H-M. The reduction of graphene oxide. Carbon. 2012, 50(9): 3210-3228.

[4.25] Mo Y, Liu Q, Fan J, Shi P, Min Y, Xu Q. Heterocyclic aramid nanoparticle-assisted graphene exfoliation for fabrication of pristine graphene-based composite paper. Journal of Nanoparticle Research. 2015, 17(7).

[4.26] Yang Z-z, Zheng Q-b, Qiu H-x, Li J, Yang J-h. A simple method for the reduction of graphene oxide by sodium borohydride with $CaCl_2$ as a catalyst. New Carbon Materials. 2015, 30(1): 41-47.

[4.27] Botas C, Álvarez P, Blanco P, Granda M, Blanco C, Santamaría R, et al. Graphene materials with different structures prepared from the same graphite by the Hummers and Brodie methods. Carbon. 2013, 65(0): 156-164.

[4.28] Wu T-T, Ting J-M. Preparation and characteristics of graphene oxide and its thin films. Surface and Coatings Technology. 2013, 231(0): 487-491.

[4.29] Wojtoniszak M, Mijowska E. Controlled oxidation of graphite to graphene oxide with novel oxidants in a bulk scale. Journal of Nanoparticle Research. 2012, 14(11): 1248.

[4.30] Du X, Guo P, Song H, Chen X. Graphene nanosheets as electrode material for electric double-layer capacitors. Electrochimica Acta. 2010, 55(16): 4812-4819.

[4.31] Wang Q, Wang J, Lu C-x, Liu B-w, Zhang K, Li C-z. Influence of graphene oxide additions on the microstructure and mechanical strength of cement. New Carbon Materials. 2015, 30(4): 349-356.

[4.32] El-Khodary SA, El-Enany GM, El-Okr M, Ibrahim M. Preparation and characterization of microwave reduced graphite oxide for high-performance supercapacitors. Electrochimica Acta. 2014, 150: 269-278.

[4.33] Dreyer DR, Park S, Bielawski CW, Ruoff RS. The chemistry of graphene oxide. Chemical Society Reviews. 2010, 39(1): 228-240.

[4.34] Yang J, Gunasekaran S. Electrochemically reduced graphene oxide sheets for use in high performance supercapacitors. Carbon. 2013, 51: 36-44.

[4.35] Jeong H, Lee KM, Ahn YH, Lee S, Park JY. Non-Contact Local Conductance Mapping of Individual Graphene Oxide Sheets during the Reduction Process. J Phys Chem Lett. 2015;6(13):2629-35.

[4.36] Thema FT, Moloto MJ, Dikeo ED, Nyangiwe NN, Kotsedi L, Maaza M, et al. Synthesis and characterisation of graphene thin films by chemical reduction of exfoliated and intercalated graphite oxide. Journal of Chemistry. 2013: 1-6.

[4.37] Mohan VB, Brown R, Jayaraman K, Bhattacharyya D. Characterisation of reduced graphene oxide: Effects of reduction variables on electrical conductivity. Materials Science and Engineering: B. 2015: 193: 49-60.

[4.38] Hung W-S, Tsou C-H, De Guzman M, An Q-F, Liu Y-L, Zhang Y-M, et al. Cross-linking with diamine monomers to prepare composite graphene oxide-framework membranes with varyingd-spacing. Chemistry of Materials. 2014:26(9): 2983-2990.

[4.39] Terrones M, Botello-Méndez AR, Campos-Delgado J, López-Urías F, Vega-Cantú YI, Rodríguez-Macías FJ, et al. Graphene and graphite nanoribbons: Morphology, properties, synthesis, defects and applications. Nano Today 2010, 5: 351-372.

[4.40] Liu W-W, Chai S-P, Mohamed AR, Hashim U. Synthesis and characterization of graphene and carbon nanotubes: A review on the past and recent developments. Journal of Industrial and Engineering Chemistry. 2014, 20(4): 1171-1185.

[4.41] Zhu X, Ning G, Fan Z, Gao J, Xu C, Qian W, et al. One-step synthesis of a graphene-carbon nanotube hybrid decorated by magnetic nanoparticles. Carbon. 2012, 50: 2764-2771.

[4.42] Cai X, Zhang Q, Wang S, Peng J, Zhang Y, Ma H, et al. Surfactant-assisted synthesis of reduced graphene oxide/polyaniline composites by gamma irradiation for supercapacitors. Journal of Materials Science. 2014, 49(16): 5667-5675.

[4.43] Wang Z-M, Yoshizawa N, Kosuge K, Wang W, Ozin GA. Quiescent hydrothermal synthesis of reduced graphene oxide-periodic mesoporous silica sandwich nanocomposites with perpendicular mesochannel alignments. Adsorption. 2013, 20(2-3): 267-274.

Appendix: Supporting information for Chapter 4

Table 4.S1 The root mean and average surface roughness.

Sample	Rq (nm)	Ra (nm)
Graphite	642	487
G2N1-$t_{12,24}$	704	570
G1N1-$t_{12,24}$	243	193
G1N2-$t_{12,24}$	644	515

Table 4.S2 The root mean and average surface roughness.

Sample	Rq (nm)	Ra (nm)
Graphite	642	487
G2N1-$t_{0,0.25}$	832	683
G1N1-$t_{3,0}$	439	350
G1N1-$t_{3,3}$	447	350
G1N1-$t_{6,12}$	466	378
G1N1-$t_{12,12}$	812	644
G1N1-$t_{12,24}$	243	193

Table 4.S3 Summary of sample names and how they were synthesized.

Sample name	Mass ratio		Stirring time at room temperature/ hours	Stirring time at 98 ℃/hours
	graphite	$NaNO_3$		
G2N1-$t_{0,0.25}$	2	1	-	0.25
G1N1-$t_{3,0}$	1	1	3	-
G2N1-$t_{12,24}$	2	1	12	24
G1N1-$t_{12,24}$	1	1	12	24
G1N1-$t_{12,12}$	1	1	12	12
G1N1-$t_{6,12}$	1	1	6	12
G1N1-$t_{3,3}$	1	1	3	3
G1N2-$t_{12,24}$	1	2	12	24

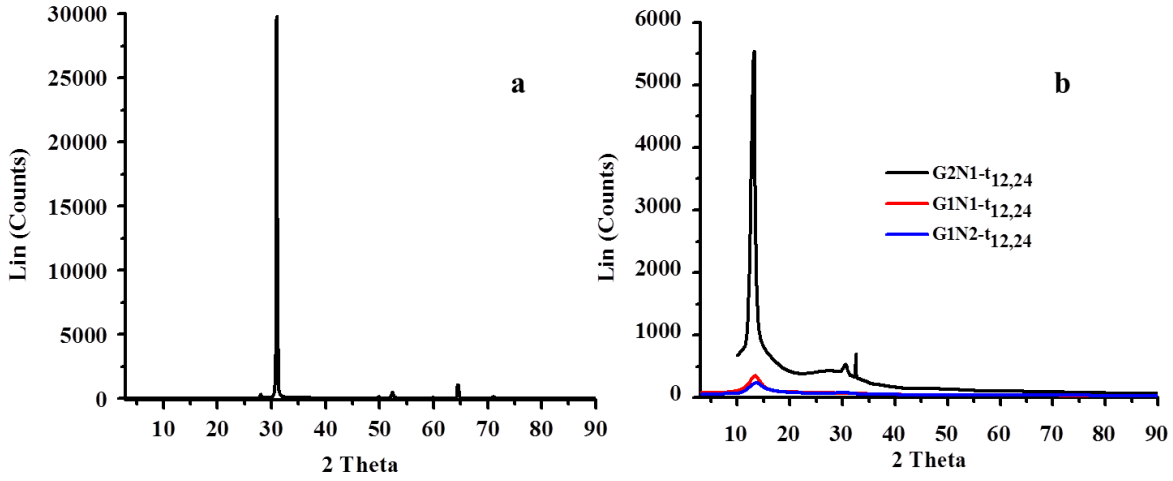

Fig. 4.S1 The powder X-ray diffractogram for pristine (a) graphite and (b) GO samples from (b) G2N1-$t_{12,24}$, G1N1-$t_{12,24}$ and G1N2-$t_{12,24}$.

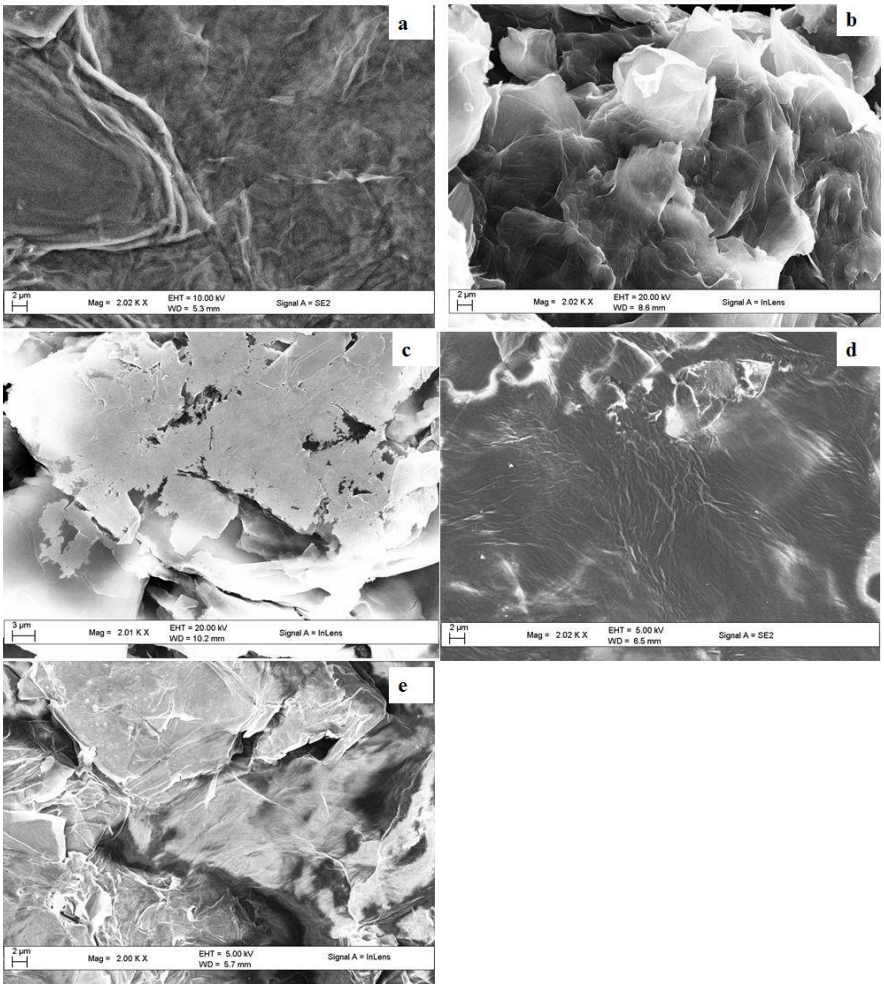

Fig. 4.S2 SEM images for GO samples (a) G2N1-$t_{0,0.25}$, (b) G1N1-$t_{3,0}$, (c) G1N1-$t_{3,3}$, (d) G1N1-$t_{6,12}$, and (e) G1N1-$t_{12,12}$

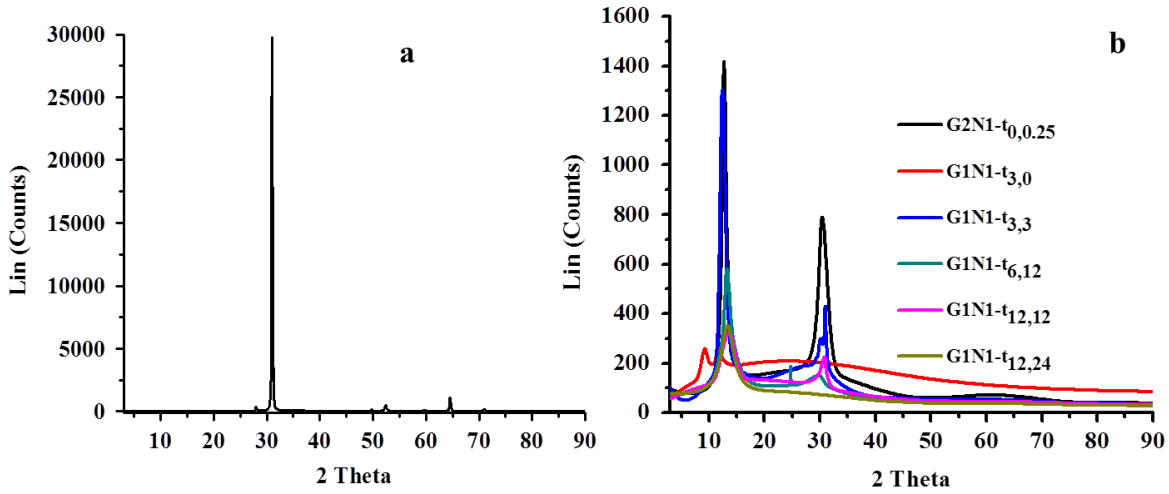

Fig. 4.S3 The powder X-ray diffractogram for (a) pristine graphite, GO samples (b) G2N1-$t_{0,0.25}$, (c) G1N1-$t_{3,0}$, (d) G1N1-$t_{3,3}$, (e) G1N1-$t_{6,12}$, (f) G1N1-$t_{12,12}$ and (g) G1N1-$t_{12,24}$.

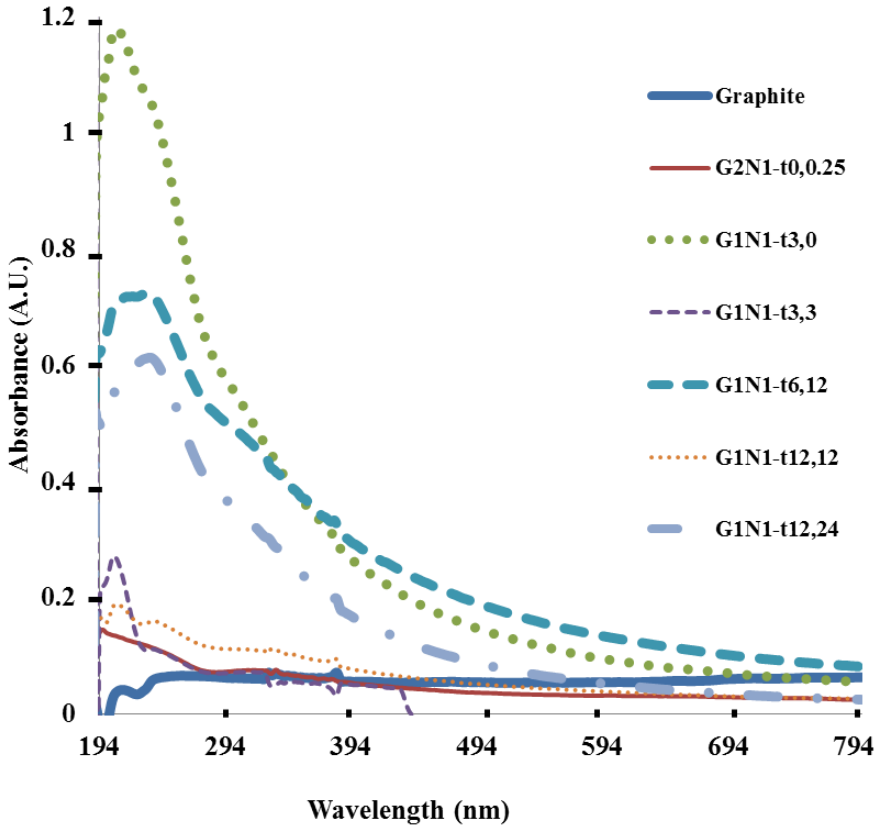

Fig. 4.S4 The Uv-Vis spectra of samples synthesised to investigate effect of different reaction times.

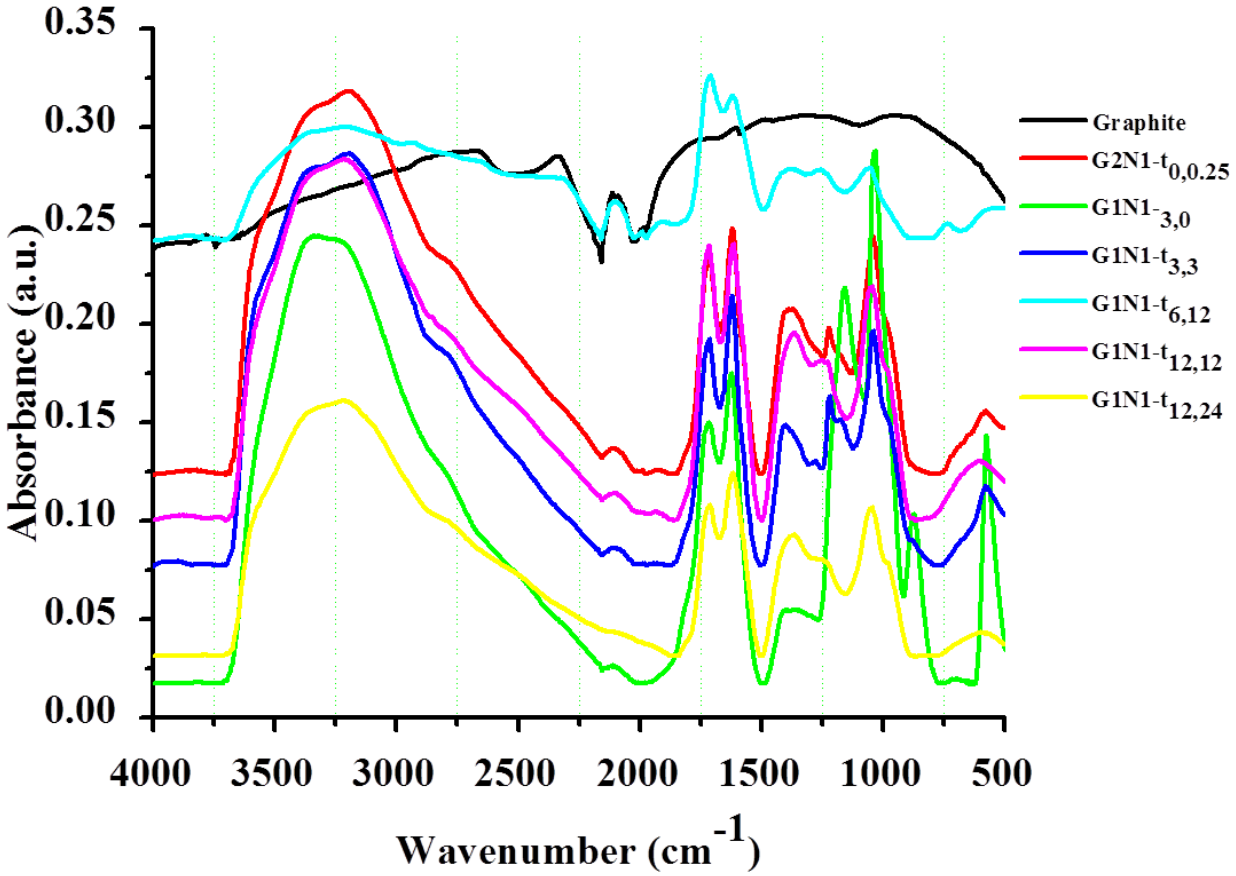

Fig. 4.S5 ATR for GO samples synthesised at varied reaction times.

Chapter Five

INTERNATIONAL JOURNAL OF
ENERGY RESEARCH

INTERNATIONAL JOURNAL OF ENERGY RESEARCH
Int. J. Energy Res. 2017; **41**:1182–1201
Published online 17 January 2017 in Wiley Online Library (wileyonlinelibrary.com). DOI: 10.1002/er.3702

Oxygen-modified multiwalled carbon nanotubes: physicochemical properties and capacitor functionality

Edwin T. Mombeshora[1], Patrick G. Ndungu[3], A. L. Leigh Jarvis[2] and Vincent O. Nyamori[1,*,†]

[1]School of Chemistry and Physics, University of KwaZulu-Natal, Westville Campus, Private Bag X54001, Durban, 4000, South Africa
[2]School of Electrical, Electronic and Computer Engineering, University of KwaZulu-Natal, King George V Avenue, Durban, 4014, South Africa
[3]Department of Applied Chemistry, University of Johannesburg, P.O. Box 17011, Doornfontein, Johannesburg, 2028, South Africa

SUMMARY

Multiwalled carbon nanotubes (MWCNTs) have found numerous applications in energy conversion systems. The current work focused on the introduction of oxygen moieties onto the walls of MWCNTs by five different reagents and investigating the associated physicochemical properties. Oxygen-containing groups were introduced onto MWCNTs using an ultrasound water-bath treatment with HNO_3, HCl, H_2O_2 or HCl/HNO_3 solution. Physicochemical properties were characterised by Fourier transform infrared spectroscopy, scanning electron microscopy, transmission electron microscopy, Raman, thermal gravimetric analysis, textural characteristics, cyclic voltammetry and electrochemical impedance spectroscopy. The study focus was mainly on linking the physicochemical properties of oxygen-functionalised MWCNTs and suitability in electrochemical capacitors using group one sulfates. From the Fourier transform infrared spectroscopy KBr pellet protocol, peaks at 3400, 2370 and 1170 cm^{-1} suggest oxygen-containing functionalities on MWCNTs. HNO_3 treatment introduced highest oxygen-containing moieties and achieved highest specific capacitance in Li_2SO_4 and Na_2SO_4 electrolytes of 36.200 F g^{-1} (77 times better than pristine) and 45.100 F g^{-1} (2.5 times enhancement), respectively. For K_2SO_4, it was 33.600 F g^{-1} (4.9 times better) with HNO_3/HCl-treated samples. Oxygen-functionalised MWCNTs displayed both pseudo and electrochemical double-layer mechanism of enhanced charge storage and cycle stability in group one sulfates electrolytes. The dominating charge storage mechanism was pseudo, and Na_2SO_4 was the best electrolyte amongst the three group one sulfates investigated. Copyright © 2017 John Wiley & Sons, Ltd.

KEY WORDS

nanostructures; electrochemical measurements; electrochemical properties; energy storage; surface properties; multiwalled carbon nanotubes; oxygen-containing

Oxygen-modified multiwalled carbon nanotubes: physicochemical properties and capacitor functionality

Edwin T. Mombeshora,[a] Patrick G. Ndungu,[c] A. L. Leigh Jarvis[b] and Vincent O. Nyamori[a] *

[a]School of Chemistry and Physics, University of KwaZulu-Natal, Westville Campus, Private Bag X54001, Durban, 4000, South Africa

[b]School of Electrical, Electronic and Computer Engineering, University of KwaZulu-Natal, King George V Avenue, Durban, 4014, South Africa

[c]Department of Applied Chemistry, University of Johannesburg, P.O. Box 17011, Doornfontein, Johannesburg, 2028, South Africa

Graphical abstract

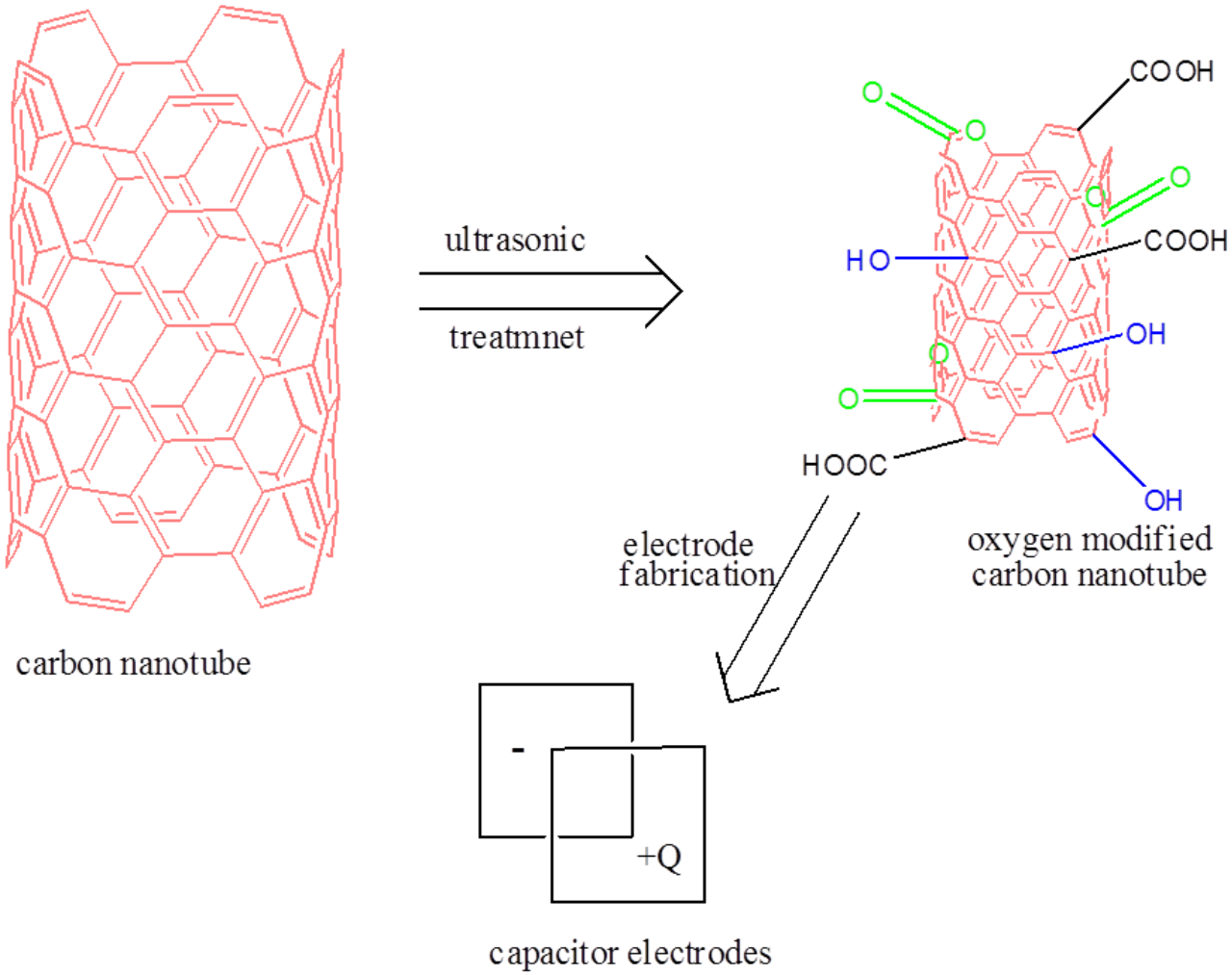

Summary

Multiwalled carbon nanotubes (MWCNTs) have found numerous applications in energy conversion systems. The current work focused on introduction of oxygen moieties onto the walls of MWCNTs by five different reagents and investigating the associated physicochemical properties. Oxygen-containing groups were introduced onto MWCNTs using an ultrasound water-bath treatment with HNO_3, HCl, H_2O_2 or HCl/HNO_3 solution. Physicochemical properties were characterised by Fourier transform infra-red spectroscopy, scanning electron microscopy, transmission electron microscopy, Raman, thermal gravimetric analysis, textural characteristics, cyclic voltammetry and electrochemical impedance spectroscopy. The study focus was mainly on linking the physicochemical properties of oxygen functionalised MWCNTs and suitability in electrochemical capacitors using group one sulfates. From the FTIR KBr pellet protocol, peaks at 3400, 2370 and 1170 cm^{-1} suggest oxygen-containing functionalities on MWCNTs. HNO_3 treatment introduced highest oxygen-containing moieties and achieved highest specific capacitance in Li_2SO_4 and Na_2SO_4 electrolytes of 36.200 F g^{-1} (77 times better than pristine) and 45.100 F g^{-1} (2.5 times enhancement), respectively. For K_2SO_4 it was 33.600 F g^{-1} (4.9 times better) with HNO_3/HCl treated samples. Oxygen functionalised MWCNTs displayed both pseudo and electrochemical double layer mechanism of enhanced charge storage and cycle stability in group one sulfates electrolytes. The dominating charge storage mechanism was pseudo and Na_2SO_4 was the best electrolyte amongst the three group one sulfates investigated.

KEYWORDS: nanostructures; electrochemical measurements; electrochemical properties; energy storage, surface properties; multiwalled carbon nanotubes; oxygen-containing.

* Corresponding author*:* Vincent Nyamori, School of Chemistry and Physics, University of KwaZulu-Natal, Westville Campus, Private Bag X54001, Durban, 4000, South Africa

Email: nyamori@ukzn.ac.za Tel.: +27-31 2608256; Fax: +27-31 260 3091

5.1. Introduction

Shaped carbon nanomaterials (SCNMs), such as carbon nanospheres, graphene, carbon nanofibers and carbon nanotubes (CNTs) have been shown to be suitable for various applications, such as catalyst supports, solar cells, fuel cells and electrochemical systems [5.1-5.5]. SCNMs are particularly suitable for use within electrochemical based energy conversion systems [5.6] due to their 3D nanoporous structure, stability in the potential range used, synergistic effects with included additives, and excellent electrical conductivity [5.7]. In addition, the effective surface area and any treatment that reduces the inherent agglomeration of these materials, also plays a key role on enhancing physicochemical properties and overall performance [5.8-5.11].

Electrochemical capacitors (ECs) are charge storage devices with relatively high-power densities and longer life cycles when compared to batteries [5.12,5.13]. ECs are classified according to the charge storage mechanisms as either electrochemical double layer capacitors (EDLCs) or pseudo capacitors [5.14]. EDLCs store charge through formation of a double layer at the interphase between the electrode and electrolyte [5.15,5.16]. On the other hand, pseudo capacitors are based on redox reactions of electro-active materials with several oxidation states [5.17].

Surface chemistry, such as oxygen-containing functionalities, plays a critical role in determining the suitability of a material for various applications [5.1,5.9,5.18]. Acid treatment of multiwalled carbon nanotubes (MWCNTs) is often undertaken prior to their use in ECs or any other application [5.18-5.20]. Acid treatment is done to remove metal catalyst residues, enhance hydrophilic character [5.10,5.15] and introduce oxygen containing moieties or other types of heteroatoms onto the surface of the nanotube [5.21]. Several reports within the open literature have highlighted how acid treatment on MWCNTs can add various chemical groups such as lactones, lactol, carbonyl, quinone and phenolic hydroxyl onto the nanotube surface, and such treatments can also be used as preliminary steps for further functionalization [5.22-5.25]. The current work accounts for the influence of these functionalities in electrochemical capacitors. The acidity of the different groups changes slightly, and is affected by the treatment duration, concentration of the acids used, the number of repeated treatment cycles and the use of sonication. Additionally, sonochemistry is associated with better dispersion, shortened reaction periods and ultimately reduces energy consumption [5.26]. In this regard, the current study, investigates the influence of ultrasonic treatment of MWCNTs in different reagents on

the ultimate functionality in EDLCs. Acid treatment can also result in physical changes to the nanotubes, and this can include opening of the tube ends, cutting or shortening of the MWCNTs, and surface damage or roughening of the nanotube walls. Since the electronic properties of MWCNTs are sensitive to physical and chemical properties such as length, diameter, doping, and alteration or introduction surface groups amongst other factors [5.18,5.21]. Hence, in this study, capacitive behaviour of acid treated MWCNTs in group one sulfates was investigated. The key objectives of the current work include comparing physicochemical properties of MWCNTs treated by means of ultrasonic waterbath in various reagents, linking the physicochemical properties of oxygen functionalised MWCNTs with charge storage capabilities, elucidation of the influence of oxygen-containing modifications and comparing performance of group one sulfates in electrochemical capacitors.

Studies have focused on experimental designs that used a combination of different acids and variations in the duration of the oxidation treatment on the MWCNTs [5.15]. The treated MWCNTs were annealed and then applied in manganese-based composites. The reaction conditions such as time and temperature were kept constant in this study. Additionally, Likodimos *et al.* [5.27] were able to vary the textural characteristics of the MWCNTs using different concentrations of HNO_3 along with hydrothermal treatment techniques. Pumera [5.28] treated CNTs in HNO_3 at 80 °C for 24 hours under reflux and reported enhanced capacitance due to a rugged surface and an increase in the porosity of double-walled carbon nanotubes (DWCNTs) and single walled-carbon nanotubes (SWCNTs). Huang *et al.* [5.29] studied the effect of concentrated nitric acid treated MWCNTs loading on activated carbon in ECs and reported a 15% enhancement at 10 wt.%. Wang *et al.* [5.30] reported on a threefold enhancement in the capacitance of MWCNTs after activating the material with KOH, and then treating the MWCNTS with H_2SO_4. Hu *et al.* [5.31] increased the capacitance of MWCNTs by 2.5 times, after treating the nanotubes with HNO_3. The improved capacitance was attributed to the enhancement of the accessible electrochemical surface area and the high density of functional groups on the surface of the MWCNTs. The results from the current work, show different traits in terms of the influence of textural characteristics on EDLC functionality, points out on major contributions from other physical-chemical properties. Understanding the physical-chemical characteristics of oxidative treated MWCNTs is a crucial step towards further modifications and their successful commercialisation in energy conversion or storage devices. Additionally, purification of MWCNTs with H_2O_2 is not well documented in literature [5.20]. In this paper we communicate on the suitability of oxygen functionalities introduced

by various reagents namely, HNO_3, HCl/HNO_3, HCl, and H_2O_2 relative to pristine MWCNTs as working electrodes in EDLCs. The associated physical-chemical properties such as thermal stability, vibrational modes and crystallinity, textural characteristics charge storage mechanism and ultimately the electrochemical capacitive performance were also thoroughly investigated and compared. Since the size of the ion in the electrolyte can influence capacitive performance [5.2], and the selection of an appropriate electrolyte is crucial in enhancing the rate capability of MWCNTs [5.32], three group one metal salts were compared in the current study. To the best of our knowledge, the performances of group one sulfates using MWCNTs and oxygen functionalised MWCNTs, with the aforementioned reagents, as electrode active materials in EDLCs are being evaluated for the first time.

5.2. Experimental

The experimental procedures are presented in the sub-sections that follow.

5.2.1. Initial treatment of MWCNTs

MWCNTs (8 - 15 nm OD, length 10 - 50 μ m, Ash >1.5 wt %, EC > 10^{-2} S/ cm, SKU number 030102) were purchased from Cheaptubes.com (MA, USA). HCl (32%) was purchased from C.c. Imelmann (South Africa) and HNO_3 (70%) was procured from Associated Chemical Enterprise (South Africa).

As received pristine MWCNTs (0.5 g) were added to (30 mL) of HNO_3, HCl, H_2O_2, or a mixture of HCl/HNO_3 (1:3, v/v) solution. The mixtures were then treated in an ultrasound water bath for a period of 4 hours. During sonication, the ultrasound water bath was allowed to rest for 15 minutes after every 1-hour interval and the average temperature was 50 °C. Thereafter, the samples were washed with deionised water (DI) and filtered until the filtrate was neutral in pH. The samples were dried overnight in an Economy Series oven (Model 220-224) at 120 °C and thereafter stored in a desiccator until when there were being characterized.

5.2.2. Instrumentation and sample preparation

For FTIR analysis, samples were prepared by mixing MWCNTs and KBr in the ratio 1:750 (m/m ratio) followed by grinding using quartz pestle and motor for 5 minutes. The mixture was then pelletized using a 25-ton ring press (00-25 model supplied by Research Industrial Company, England. The disk was analysed using a spectrum RXI, version 5.3, Perkin Elmer FTIR spectrometer. Transmission electron microscopy (TEM) was carried out by treating a typical sample in absolute ethanol for 5 minutes using an ultrasound water bath. Thereafter, either lacey or holey carbon grids were dipped in the dispersed sample/ethanol mixture and allowed to dry at room temperature. The analyses were done with a JEOL TEM 1010 transmission electron microscope. The images were taken at different magnifications on separate areas using Megaview 3 camera. Image J software was used to measure the diameters of at least 200 MWCNTs followed by plotting of histograms. For scanning electron microscopy (SEM), typical samples were stuck on aluminium stubs using double sided carbon tape and analysis were carried out with a JEOL JSM 6100 microscope. Thermogravimetric analyses were done using TA Instruments Q series^{TM} Thermal Analyser DSC/TGA (Q600) with a TA instruments Universal Analysis 2000 software for data acquisition and analysis. The gases used were oxygen and nitrogen, flow rate was 100 mL min^{-1}. The heating was from ambient temperatures to 1000 ^{0}C at 10 ^{0}C min^{-1}. Raman spectroscopy analysis was done with a 100 mW Delta Nu Advantage 532^{TM} spectrometer of 10 cm^{-1} resolution with a 2D CCD detector and grating lines were 1800 mm^{-1}. Excitation wavelength of the laser was 532 nm and integration time was 35 s. The graphitic (G-band) and disorder band (D-band) for several spots were fitted using a Lorenztian function, and the full analysis was done with the NuSpec software. Samples were prepared for textural characterisation by degassing at 90 ^{0}C for one hour then at 200 ^{0}C for 10 hours. Nitrogen sorption analyses were done using a Micrometrics TRI STAR 3020V1.03 (V1.03) instrument at 77 K in N_2.

5.2.3. Electrochemical characterisation

Typically, 10 mg of the sample was mixed with 100 µL of nafion exchange resin solution (20 wt.% solution in lower aliphatic alcohols/H_2O contains 34% water, Sigma Aldrich). The working electrode was prepared by casting the sample mixed with nafion onto a platinum electrode. The MWCNTs sample deposited on the platinum electrode (3 mm diameter) was

dried under room temperature conditions. Electrolytes, characteristically 1 M, were degassed with nitrogen for 5 minutes prior to cyclic voltammetry (CV) analysis. The electrolytes used were Li_2SO_4 (99%), Na_2SO_4 (97%), K_2SO_4 (99-100%) and were all purchased from Merck. CV was done using the three electrode 797 VA Computrace Metrohm CT798 application model with a 57970110 dosing processor (Metrohm, Switzerland). The prepared electrodes were scanned at 10, 25, 50, 100 and 200 mV s^{-1} in the potential range of 0 - 0.8 V. The specific capacitance, C_s was obtained using equation 1:

$$C_S = \frac{1}{2}\frac{\int idV}{msΔV} \qquad (1)$$

Where *m* is mass of active material, *s* is scan rate, *i* is the current and ΔV is the voltage window. The electrochemical impedance (EIS) analyses were done on the sample by using a CHI 600E work station (CHI Instruments, Inc, USA).

5.3. Results and discussion

This section presents the data and discussion from the physicochemical study of the acid treated MWCNTs.

5.3.1. Identification of chemical moieties on MWCNT surfaces

The oxidative treated MWCNTs samples were characterized using IR. Despite the well-known difficulties in using this technique to determine surface oxygen functionalities due to poor absorption intensities [5.1], an appearance of a new peak at ca. 2370 cm^{-1} was observed from all oxidative treatments (Figure 5.1). Whilst there is a possibility of trapping CO_2 from the atmosphere in the samples, culminating in the appearance of this peak, the samples were analysed in the same manner with pristine MWCNTs but the peak was not observed. Hence, this peak could be assigned to oxygen-containing functionalities associated with the OH moieties in H-bond-COOH introduced by the ultrasound treatment [5.18,5.33]. The proposed mechanism is that carboxylic acid and phenolic moieties comes from transformation of carbonyl or quinone groups initially formed from the sp^2 carbons [5.27,5.34]. Also, a peak at ca 1387 cm^{-1} was visible on spectra of all treated MWCNTs and this peak is attributed to CH_3 bending vibrations [5.35,5.36]. This shows the presence of defects in the form of oxygen-

containing groups. Furthermore, since the samples were prepared similarly for FTIR analysis, the amplified peaks at ca 1170 cm^{-1} for MWCNTs treated with HCl, H_2O_2 and HCl/HNO_3 suggest an increase in alcohols, lactones and ether groups manifesting as classical C-O stretching vibration in the C-O-C bonds [5.22,5.34,5.35,5.37]. In addition, these MWCNT samples exhibited a more intense peak at ca 2930 cm^{-1} assigned to symmetric stretching vibrations of CH_2 [5.22,5.35]. This demonstrates that the KBr pellet protocol was able to provide samples that could be analysed using FTIR spectroscopy, and detect the formation of defects on the tube walls.

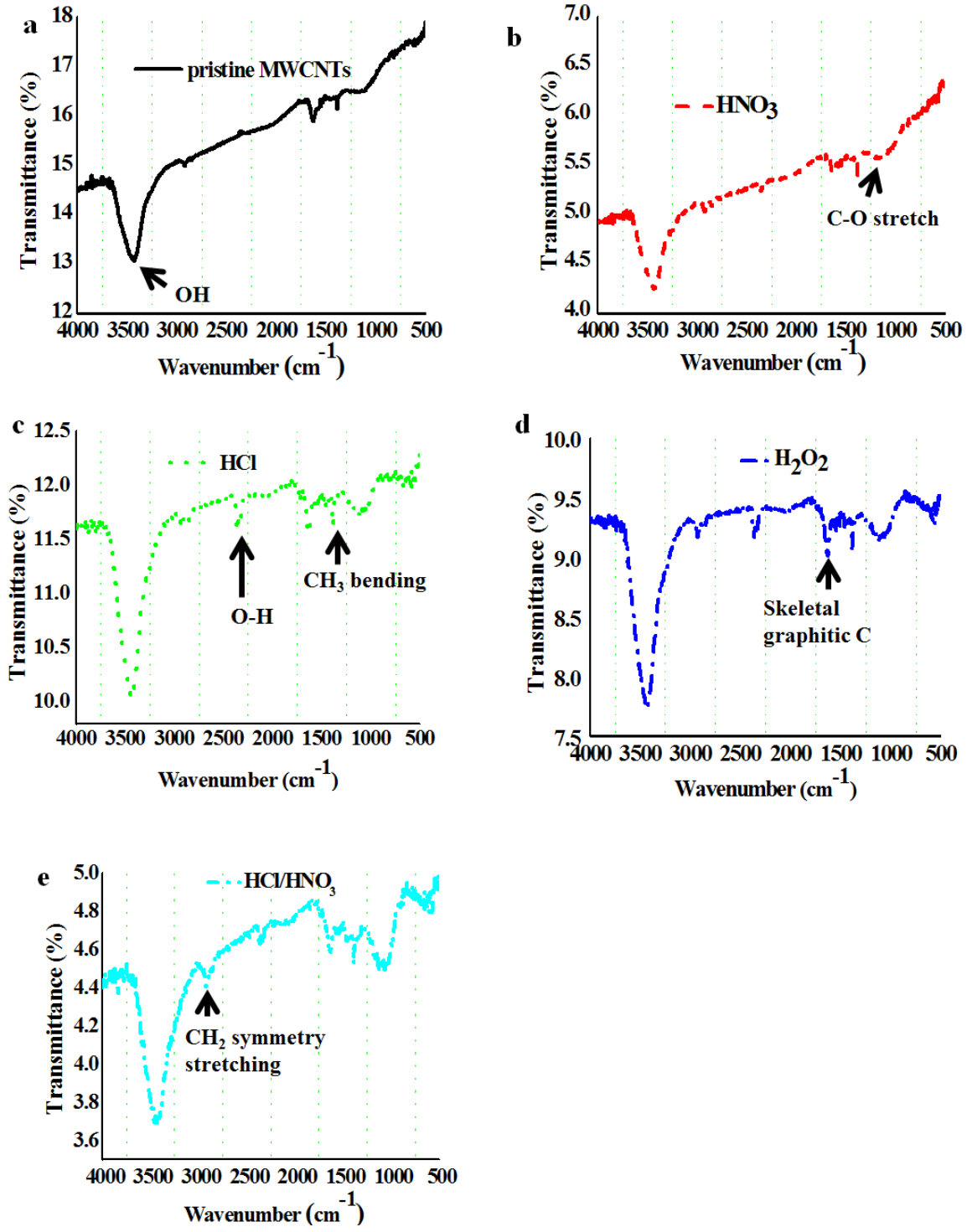

Figure 5.1. IR spectra for (a) pristine MWCNTs and after the first treatment step using (b) HNO_3, (c) HCl, (d) H_2O_2 and (e) HCl/ HNO_3.

Although there is possibility of water adsorption in the samples by the KBr, this was eliminated in the current work by preparing the pellets below sodium lamp and thereafter dried in an oven overnight and analysed from the oven. All the samples including pristine MWCNTs had peaks at ca. 3470 and 1650 cm^{-1} associated with absorbed hydroxyl molecules and skeletal graphitic vibration, respectively [5.22,5.25,5.35-5.38]. The TGA (Section 3.3) supported this deduction.

5.3.2. Morphology analysis

Pristine MWCNTs were typically tubular with traces of metal catalyst from synthesis, shown by an arrow in Figure 5.2a and EDX spectra (Figure 5.S1 in supplementary information). Such observations were scarcely noticeable on images from treated MWCNTs, hence treated samples had small amounts of metal residues. Nitric acid treatment was the most destructive, and this was inferred from the numerous thin walled MWCNTs observed within these samples (indicated by arrow in Figure 5.2b and 2f). In contrast, when comparing the pristine and HCl treated MWCNTs, there were fewer notable changes, but it was observed that the walls of the MWCNT were damaged. Whereas the HCl/HNO_3 resulted in similar differences when compared to the pristine sample, but the damage was not as extensive as HCl alone, and did seem to increase the surface roughness. This is because HCl attacks the tube walls [5.39] and hence a possible explanation based on the ODs determined from TEM images (Figure 5.2f) is that HCl/HNO_3 solution reduces the etching rate of HCl.

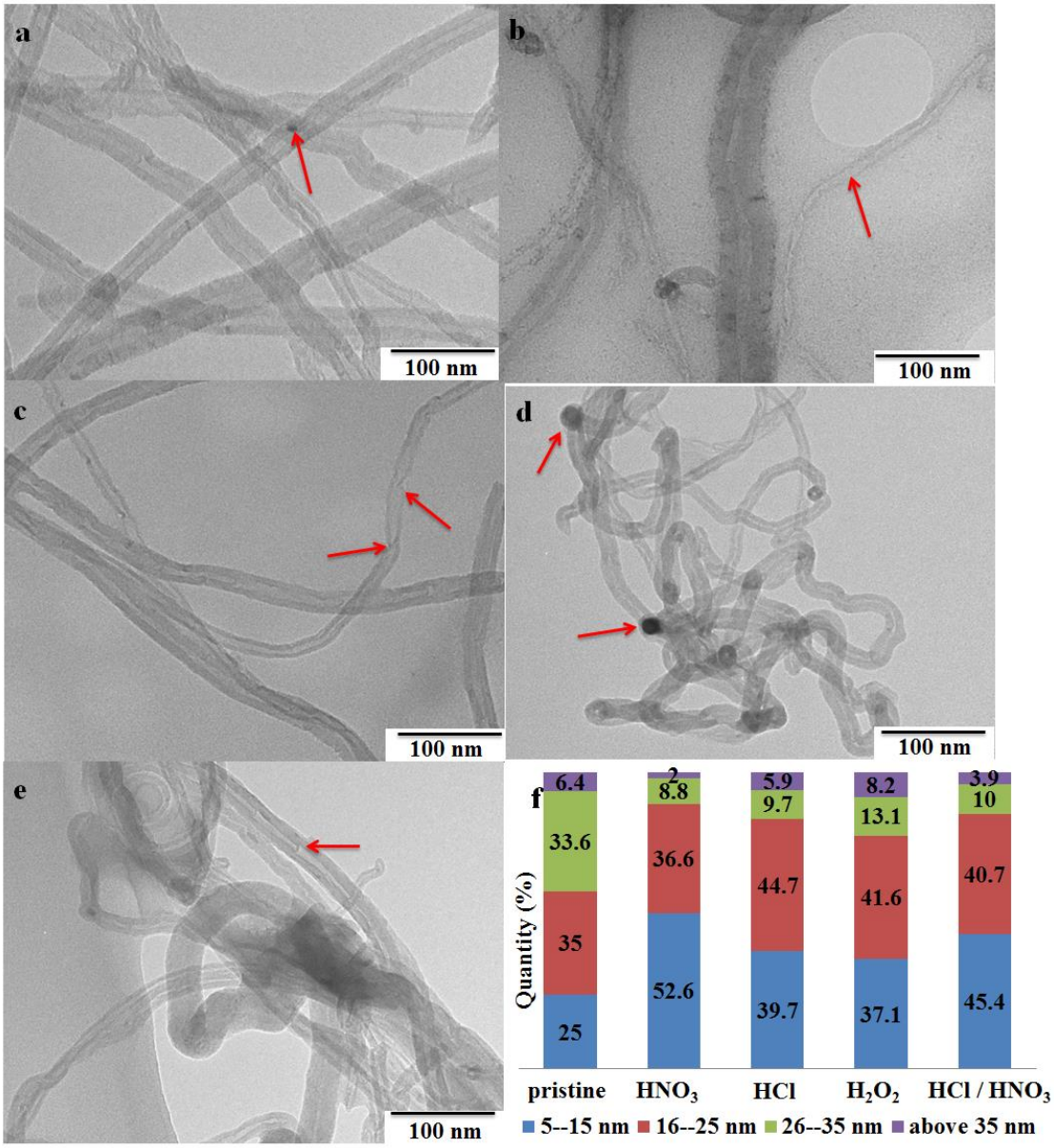

Figure 5.2. TEM images for (a) pristine MWCNTs and MWCNTs treated by (b) HNO_3, (c) HCl and (d) H_2O_2 (e) HCl/HNO_3 acids and (f) the outer diameter distribution of the pristine and treated MWCNTs.

At least 200 tubes were counted, and the data used to plot the histogram showing the distribution of outer diameter (OD) of pristine and treated MWCNTs. Pristine MWCNTs exhibited the highest ratio of MWCNTs with large OD (33.6% in the 26-35 nm range) and the least percentage of small OD (25% in the 4-15 nm). From Figure 5.2f, the order of treatment with highest ratio of small OD (4-15 nm) MWCNTs is HNO_3 (52.6%), HCl/HNO_3 (45.4%),

HCl (39.7%) then H_2O_2 (37.1%). For the interval 16 -25 nm, the order was HCl (44.7%), H_2O_2 (41.6%), HCl/HNO_3 (40.7%) and HNO_3 (36.6%), whilst H_2O_2 (13.3%) followed by HCl/HNO_3 (10%), HCl (9.7%) then HNO_3 (8.8%) was the trend for the 26-35 nm range. A similar trend was noticed above 36 nm, i.e. H_2O_2 (8.2%), HCl (5.9%), HCl/HNO_3 (3.9%), then HNO_3 (2%). This indicates the possibility that the treatments peeled off the outermost walls MWCNT. This further implies etching of sidewalls of MWCNTs as well as creation of carboxyl groups on sidewalls and MWCNT tips [5.18]. The decrease in OD is due to interaction of outermost walls with the solutions [5.1]. Hence, the derived order is a comparison of the oxidising effect of the reagents during an ultrasound water bath treatment of MWCNTs.

Bulky morphological analysis was done by use of SEM (Figure 5.3), all the samples were analysed using an accelerating voltage of 10 KV except for the H_2O_2 treated MWCNTs. The main reason for slightly reducing the accelerating voltage was to enhance image quality. The H_2O_2 treated MWCNTs was relatively associated with high charging effects, causing slight poor imaging at 10 KV, and this was due to its comparatively noticeable metal residues on the tube ends closer to the surface (Figure 5.2d). Additionally, since the samples were all prepared similarly for SEM analysis, the slightly lower surface area of H_2O_2 treated MWCNTs could have limited electron penetration culminating in relatively poor images at 10 KV [5.40].

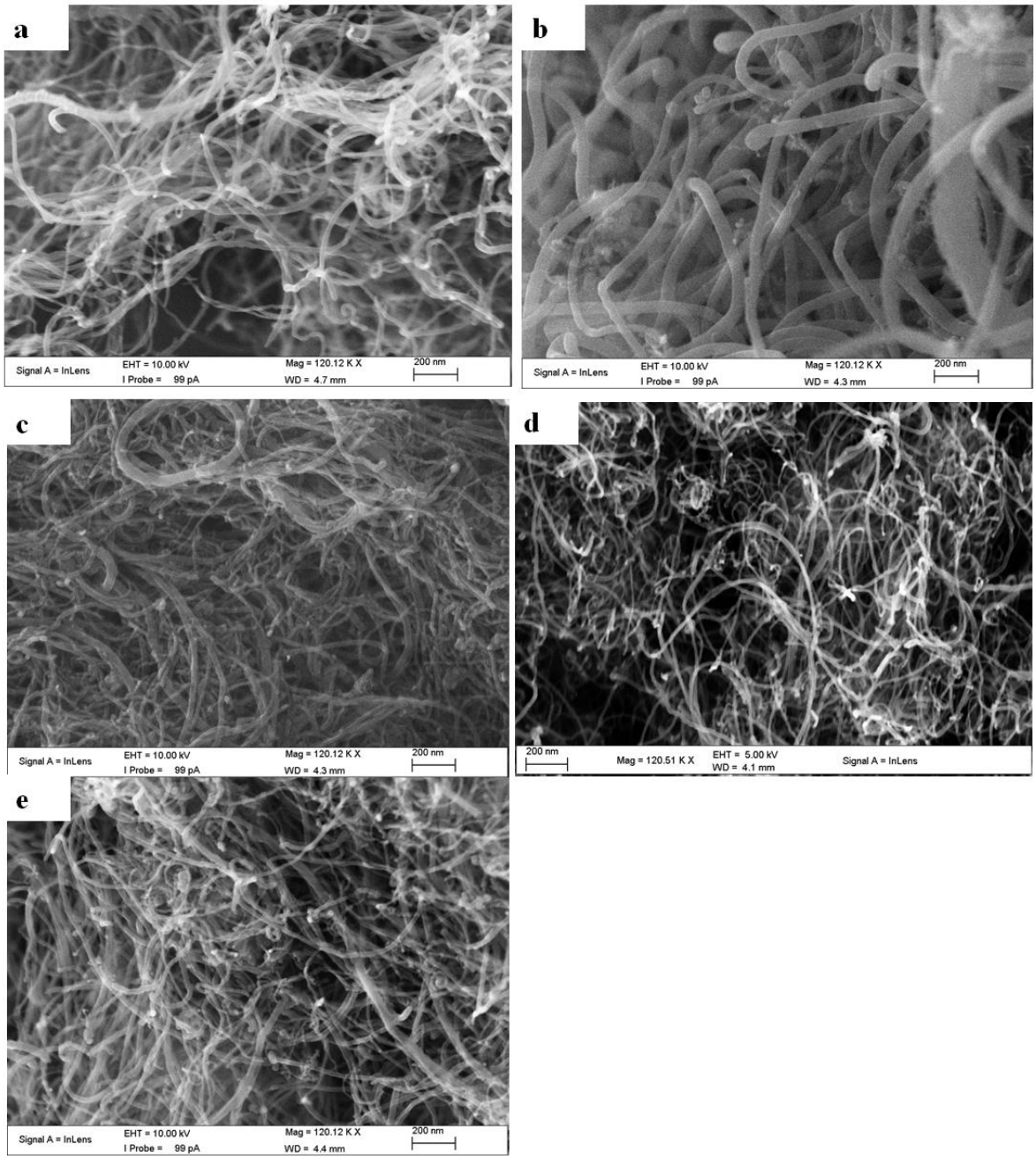

Figure 5.3. SEM micrographs of MWCNTs (a) pristine MWCNTs and MWCNTs treated by (b) HCl, (c) HNO_3 and (d) H_2O_2 (e) HCl/HNO_3 acid simultaneously.

From the SEM micrographs, the effects of water bath ultrasound treatment are not clear, i.e. no large morphological variations were noticeable (Figure 5.3). All the samples displayed a 'spaghetti-like' morphology, characteristic of MWCNTs. HCl treatment was expected to show the highest degree of MWCNT tube debundling [5.41].

5.3.3. Thermal stability analysis and quantification of oxygen-containing groups

Thermogravimetric analysis in air or pure oxygen can be used to estimate the purity and thermal stability of MWCNT samples [5.35]. From Figure 5.4, the pristine MWCNTs had a clear gain in mass at temperatures above 700 °C (inset in Figure 5.4a), and this mass gain is due to oxidation of the residual iron particles (FeO_x) from the synthesis of the CNTs. In addition, on visual inspection of the residues a reddish colour was observed, indicative of iron oxides, and similar observations have been reported in the literature by Osswald *et al.* [5.41]. The water bath ultrasound oxidative treatment reduced the metal catalyst residue in pristine MWCNTs, as seen with the difference in residues shown in the insert in Figure 5.4a. Similar results were reported by Motchelaho *et al.* [5.1]. The oxidative treatments resulted in different extents of metal catalyst removal. This corroborates with most chemical purification methods which are known for higher efficiencies in selectivity and faster rate kinetics [5.20]. The treatments with HNO_3 and HCl were the most effective in removing metal catalyst residual. H_2O_2 treatment with the most noticeable metal residues on the tube ends (Figure 5.2d), had the highest metal residues of all the treated samples. A possible explanation is linked to inefficiencies of H_2O_2 solutions in removal of residual catalyst materials at low pH [5.20].

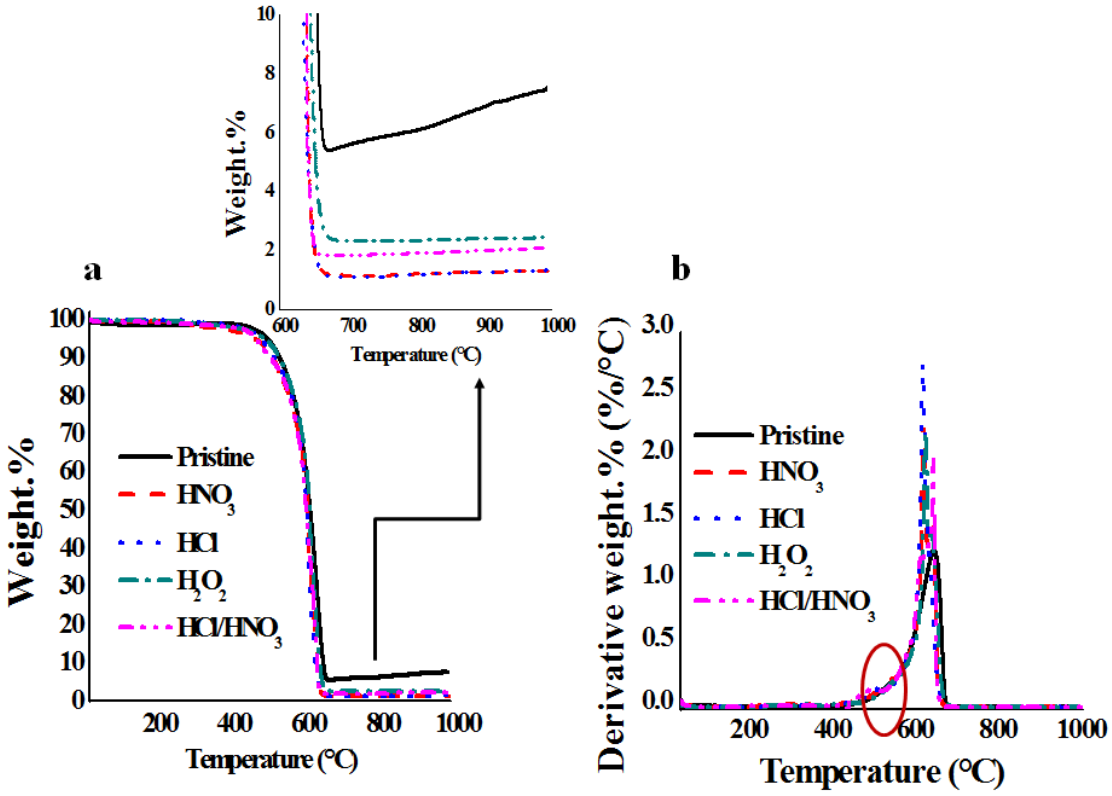

Figure 5.4. Thermogravimetric analysis of pristine and treated MWCNTs (a) thermogram and (b) derivative weight curve.

The temperatures of maximum thermal decomposition in air, deduced from derivative weight curve (Figure 5.4b), were 636, 634, 618, 614 and 612 °C for HCl/HNO_3 (1:3, v/v), pristine, H_2O_2, HNO_3 and HCl treated MWCNTs, respectively. The decrease in thermal stability upon treatment is often associated with attachment of oxygen-containing groups on MWCNT walls and destruction of the MWCNTs hexatomic structure [5.35]. The oxygen-containing groups identified by the FTIR include the COOH and COC moieties. These functionalities can be possibly associated with the slight humps at around 450 °C (indicated by circle in Figure 5.4b). Additionally, decrease in OD of MWCNTs, especially after HNO_3 treatment, could mean the most defective shells were removed leaving the most thermally stable inner layers. Also, the minimal surface roughness (Figure 5.2b) associated with HCl treatment is a possible reason for them being the more thermally stable than those from harsh treatments like HNO_3. This culminates in diverse reactivity of inner and outer layers of MWCNTs and hence, also contributes to the slight peaks at ca. 450 °C. Removal of metal catalyst led to a slight negative shift on the thermal decomposition temperature of H_2O_2, HNO_3 and HCl treated MWCNTs.

HCl/HNO_3 treated MWCNTs were the most thermally stable and the rest of the treatments induced a decrease in thermal stability (Figure 5.4b). The views by Osswald *et al.* [5.41] suggest that residual Fe catalyses thermal decomposition of MWCNTs. Their study implies increase of thermal stability upon reduction of residual Fe content and annealing MWCNTs. Their report corroborates with this work in that structural defects in the typical samples outweigh Fe decomposition catalytic effect. This work also highlights the possible effects of other factors such decrease in MWCNTs concentric shells, quantity of oxygen moieties and surface roughness on the overall thermal stability of MWCNTs.

The creation of local defects such as variations in curvature, bond-lengths and strains also cause decrease in oxidation temperature [5.41]. The first decrease in weight (indicated by a circle in Figure 5.4b) which occurred above 500 °C is assigned to functionalities on the MWCNTs surface [5.22,5.33]. Also, HCl/HNO_3 had the widest decomposition temperature range. An increase in carbon-containing defect intensity and decrease in thermal stability was observed in all samples except for H_2O_2 treated samples (Figure 5.6). Hence, it suggests that the decrease in thermal stability of the H_2O_2 treated samples, when compared with the pristine MWCNTs, is mainly due to carbon-free defects such as incorporation of oxygen in formation of lactone and phenolic groups (data on Table 5.1) on carbon framework.

The TGA profiles obtained under nitrogen atmosphere can be used to deduce oxygen-containing groups on the MWCNT surface [5.1,5.25,5.42]. The thermograms obtained under nitrogen are shown in Figure 5.5. The weight loss below 100 °C is due to water evaporating from the samples whilst the loss in the range 100 - 900 °C is attributed to loss from oxygen-containing groups (–COOH and CO groups), 150 - 400 °C is assigned to the decomposition of –COOH moieties on the MWCNTs surface, 400 - 500 °C from lactones and 650 - 700 °C for phenols [5.1,5.25].

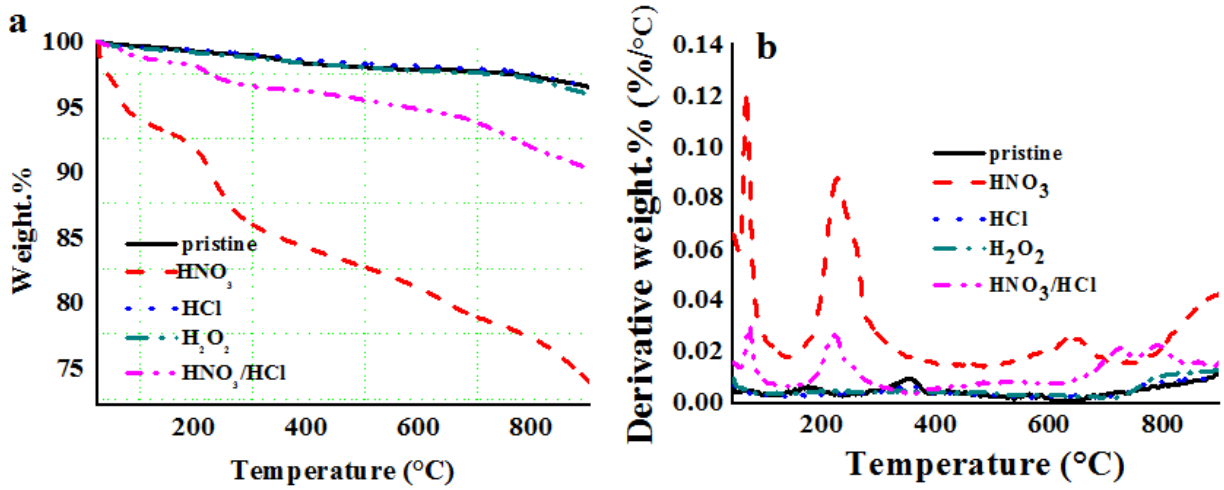

Figure 5.5. (a) Thermogravimetric profile under nitrogen atmosphere and (b) corresponding derivative weight curve.

The integrated area under the derivative weight curves correlates with thermal transitions due to loss of various oxygen-containing moieties (Table 5.S1 and 5.S2 in supplementary information). Table 5.1 shows the calculated weight losses attributed to water, CO_2 and CO from the weight loss curves recorded under nitrogen atmosphere. Since the samples were dried under the same conditions, the results show that the H_2O_2 and HCl treatments reduced the hygroscopic nature of the MWCNT walls whilst HNO_3/HCl raised it. This concurs with the view that OH groups identified by means of FTIR analysis was chiefly an effect of surface functionalities not KBr adsorption (Section 5.3.1).

Table 5.1. The determination of oxygen-containing groups on the MWCNTs surface.

Treatment	% weight loss due to					I_D/I_G	MWCNT 5 – 15 nm OD (%)
	water	Oxygen-containing groups	Carboxylic groups	Lactones	Phenols		
HNO_3	6.00	20.14	9.00	1.37	1.02	3.11	52.6
HNO_3/HCl	1.25	8.52	2.34	0.69	0.54	1.50	45.4
H_2O_2	0.59	3.49	0.97	0.27	0.09	0.86	37.1
HCl	0.50	2.95	0.88	0.37	0.09	2.00	39.7
pristine	0.45	3.15	1.15	0.28	0.09	1.60	25.0

Only the HNO_3 and HNO_3/HCl treatments significantly increased the amount of carboxylic acid, lactones, oxygen-containing and phenolic groups (Table 5.1) on the MWCNT walls. This is a possible explanation for their ultimate increased hygroscopic nature. H_2O_2 treatment slightly increased oxygen-containing groups whilst HCl only had a slight increase of lactones. The oxygen-containing moieties typically form at MWCNT defect sites and tube ends [5.42]. In terms of the acid treatments, the decrease in oxygen-containing groups in Table 5.1 (HNO_3, HNO_3/HCl, H_2O_2 then HCl), follows a similar trend with the measured outer diameters from the TEM analysis (Figure 5.2f; specifically, the 5-15 nm range, also provided in Table 5.1 for ease of reference). This means the strong oxidative reagents reduced the outer diameter and HCl treatment resulted in the lowest wt.% of oxygen containing groups. The less oxidative nature of HCl relative to HNO_3 agreed with the report by Datsyuk *et al.* [5.43]. The H_2O_2 and HCl treatments, unlike HNO_3 and HNO_3/HCl, had very little effect on the wt.% of phenolic groups on the MWCNTs walls. Based on the results in Table 5.1, HNO_3 is the most favourable treatment for increasing the wt.% of carboxylic, lactone and phenolic moieties on MWCNT tube walls.

5.3.4. Raman analysis on MWCNT

The key Raman peaks used in ascertaining the crystallinity of MWCNTs are the G-band, due to first order tangential in-plane vibrations, located at 1580 cm^{-1} and the defect induced D-band at 1350 cm^{-1}. The highest I_D/I_G ratio, the quotient of area under D-band by the G-band, was observed with the HNO_3 treated MWCNTs (Table 5.1) and this correlated with highest amount of the oxygen-containing groups as calculated from the TGA data (using nitrogen atmosphere).

There were no other noticeable forms of carbon such as amorphous carbon in the data from TEM, SEM and TGA techniques. Hence, an increase in D-band area observed was due to lattice distortion in MWCNTs geometry associated with binding of oxygen functional groups onto the tube walls [5.22,5.44,5.45]. This is in agreement with Table 5.1 data and the FTIR results which also showed the introduction of defects onto MWCNTs. The introduction of defects onto the sidewalls of MWCNT, due to acid treatment has been reported in the literature [5.18,5.41]. Samples treated with HCl were more crystalline than HNO_3 treated MWCNTs, and both treatments resulted in a larger I_D/I_G ratio when compared to the pristine MWCNTs (Table 5.1).

From this study, it was seen that the HNO_3/HCl mixture had a smaller effect on the crystallinity of the MWCNTs when compared with the individual acids. From the thermogravimetric analysis in nitrogen (Table 5.1), the HCl treatment of MWCNTs had less oxygen-containing groups than HCl/HNO_3 treated samples. Thus, these results show that HCl, in the HCl/HNO_3 solution, is a suitable additive for mitigating the HNO_3 defect intensity on MWCNT sidewalls with minimal compromise on carboxylic and lactone moieties content. There is no change in phenol groups between pristine and HCl treated MWCNTs, but moderate increase in lactones, and a decrease in COOH groups, so this means HCl does not introduce new defects onto the sidewalls of the MWCNTs. Instead, it simply attacks defects on the walls and the ends of the MWCNTs and this is probably the reason for slower peeling off of the walls which occurred since OD of 5-15 nm increased relative to pristine. Basically, the HCl treatment only attacked the pre-existing defects, does not add any new defects, unlike the HNO_3. The differences in ODs in the 5-15 nm range due to variation in etching rates corroborated with the Raman I_D/I_G ratios (Table 5.1). From TEM images, H_2O_2 treated MWCNTs were the least damaged and had more pronounced metal particles on tube ends relative to other treated MWCNTs samples (indicated by arrow on Figure 5.2d). Moreover, the metal residue wt.% in MWCNT samples treated with H_2O_2 was less than that in pristine MWCNTs (Figure 5.4). Also, H_2O_2 treatment of MWCNTs resulted in the least introduction of defects expressed as the smallest I_D/I_G ratio (Table 5.1). This means a typical H_2O_2 treatment play an effective role in removal of metal residues and also preserves and/or improves [5.41] the quality of the MWCNTs as evident from Raman spectroscopy, TGA and TEM analysis. From the IR analysis (Figure 5.1), it is seen that all treatments introduced carboxyl and lactone moieties amongst others. This means the variation in defect intensity is due to variation of content of functionalities and from deformation due to etching of the MWCNT tube walls as shown in Table 5.1.

5.3.5. Textural characteristics

There was no pronounced difference on sorption isotherms due to various treatments; all samples showed a type IV isotherm with H1 hysteresis loop. This means all the samples were meso-porous. A shift towards smaller pores sizes was observable on the Barrett-Joyner-Halenda (BJH) pore sizes distribution plot (Figure 5.6f) on the treated MWCNTs. Pristine MWCNTs had the highest ratio of larger pore sizes followed by HCl/HNO_3, H_2O_2, HNO_3 and eventually HCl treated MWCNTs.

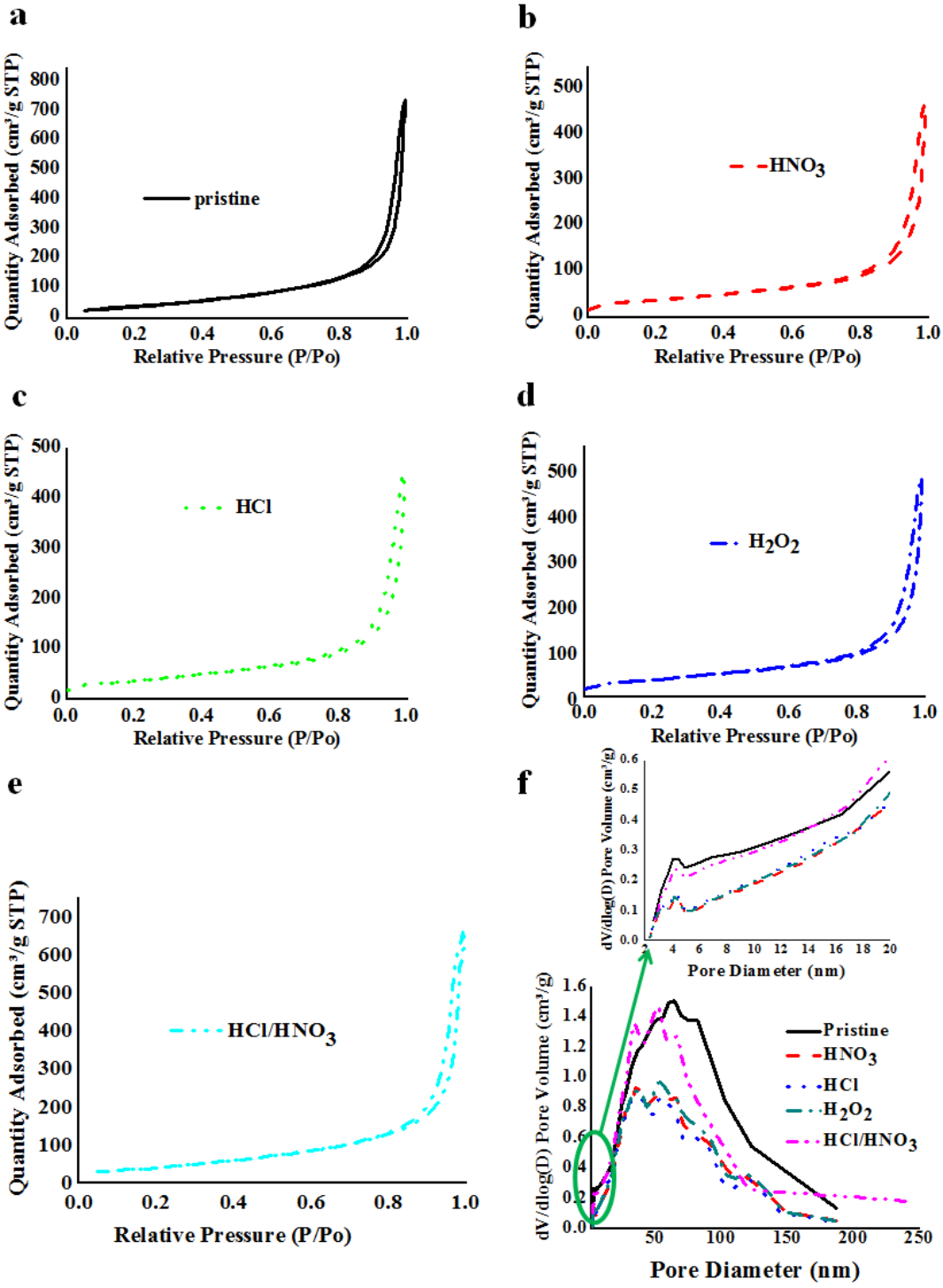

Figure 5.6. Nitrogen sorption isotherms for (a) pristine and treated MWCNTs with (b) HNO_3, (c) HCl, (d) H_2O_2 and (e) HCl/HNO_3 and (f) BJH pore size distribution.

The highest pore volume recorded for the MWCNTs samples oxidative treated with HCl/HNO_3 fits earlier reports [5.15] and the treatment with HNO_3 also enhanced porosity of MWCNTs (Table 5.2). This shows their ability to open tube ends culminating in enhancement of sorption surfaces. It is known that the attraction between the MWCNTs, and consequently their bundling, is reduced when treated with acids and not increased (i.e. their dispersibility in solvents increases) [5.46]. It is interesting to note that BET surface area of all treated MWCNTs in the current study were lower than that of pristine. The textural experiments were repeated two times, to verify the results in the current work, and the associated standard deviations show good precision and reproducibility (Table 5.2). The data can be explained with reference to the BET equation which accounts for the total surface area of MWCNTs from outer surface area, inner cavity and spaces between concentric rings. Therefore, even though smaller particle sizes are usually associated with large surface areas, the current study deductions are that decrease in tube sizes may possibly have been out-weighed by exfoliation of layers. Hence, the slight decrease in BET surface area on all oxidative treated MWCNTs relative to pristine can be linked to the decrease in the number of concentric layers; this is deduced indirectly *via* decrease in OD (Figure 5.2) whilst inner diameter (ID) was a constant. Also, the meso-pores are closely linked to the bundle free space between layers in MWCNTs [5.27]. Therefore, Figure 5.6f infers that oxidative treatments de-bundled the MWCNTs even though this was not clear from the SEM analysis (Figure 5.3). The pore size centres shifted slightly towards smaller values compared to the pristine MWCNTs (Figure 6f).

Table 5.2. The textural characteristics of the treated and pristine MWCNTs.

Treatment	BET area ± Std Dev (m^2g^{-1})	Pore volume± Std Dev (cm^3g^{-1})
HNO_3	139.93±1.30	0.86±0.30
HCl/HNO_3	142.26±0.15	0.95± 0.02
HCl	138.33±1.20	0.63±0.02
H_2O_2	136.17±1.17	0.63±0.06
pristine	149.49±0.30	0.77±0.22

5.3.6. Electrochemical characterization

The capacitive analyses were done using lithium sulfate, sodium sulfate and potassium sulfate electrolytes.

5.3.6.1. Lithium sulfate electrolyte

Absence of redox peaks, even though TGA (Figure 5.4) infers presence of small residual Fe after treatment, is a clear indication that metal particle levels inside the MWCNT tubes or encapsulated metal particles are not active in capacitive redox activities. This is in agreement with reports by Zhang *et al.* [5.7]. The ideal EDLC device should have current reversed instantly upon reversing voltage sweep, i.e., a rectangular CV. Only H_2O_2 and HNO_3 showed some substantial ELDC capacitive character at a scan rate of 10 mV s^{-1} (Figure 5.7a). The HNO_3 treated MWCNTs showed good EDLC capacitive property at scan rate of 10 and 25 mV s^{-1}. A possible explanation for the 'dumbbell-like' shape, exhibited by HNO_3 treatment at 10 and 25 mV s^{-1} as well as at 25 and 50 mV s^{-1} for HCl/HNO_3, is the contribution from either ion adsorption inside tubes or pseudo redox reactions from oxygen functionalities [5.16]. The observed steeper slope of the CV curves at switching potentials is attributed to either small ion diffusion resistance or kinetically faster redox reactions [5.11,5.47,5.48] introduced by the oxygen-containing groups on the surface of MWCNTs. The appearance of oval shaped CV curves with increase in scan rate is typical of increase in mass transfer resistance [5.11]. Also, typically EDLCs behaviour are usually interpreted based on textural properties [5.16], but in the current case, the oxygen functionalities are key, although this may have been reported previously in the literature, what is key here, is the importance on the type of oxygen moiety, i.e. the COOH plays a big role. At higher scan rates, i.e. 25, 50 and 100 mV s^{-1}, the HCl/HNO_3

treated MWCNTs exhibited better capacitive properties with the scan rate of 25 mV s^{-1} particularly having the best quality (Figure 5.7a, b and c).

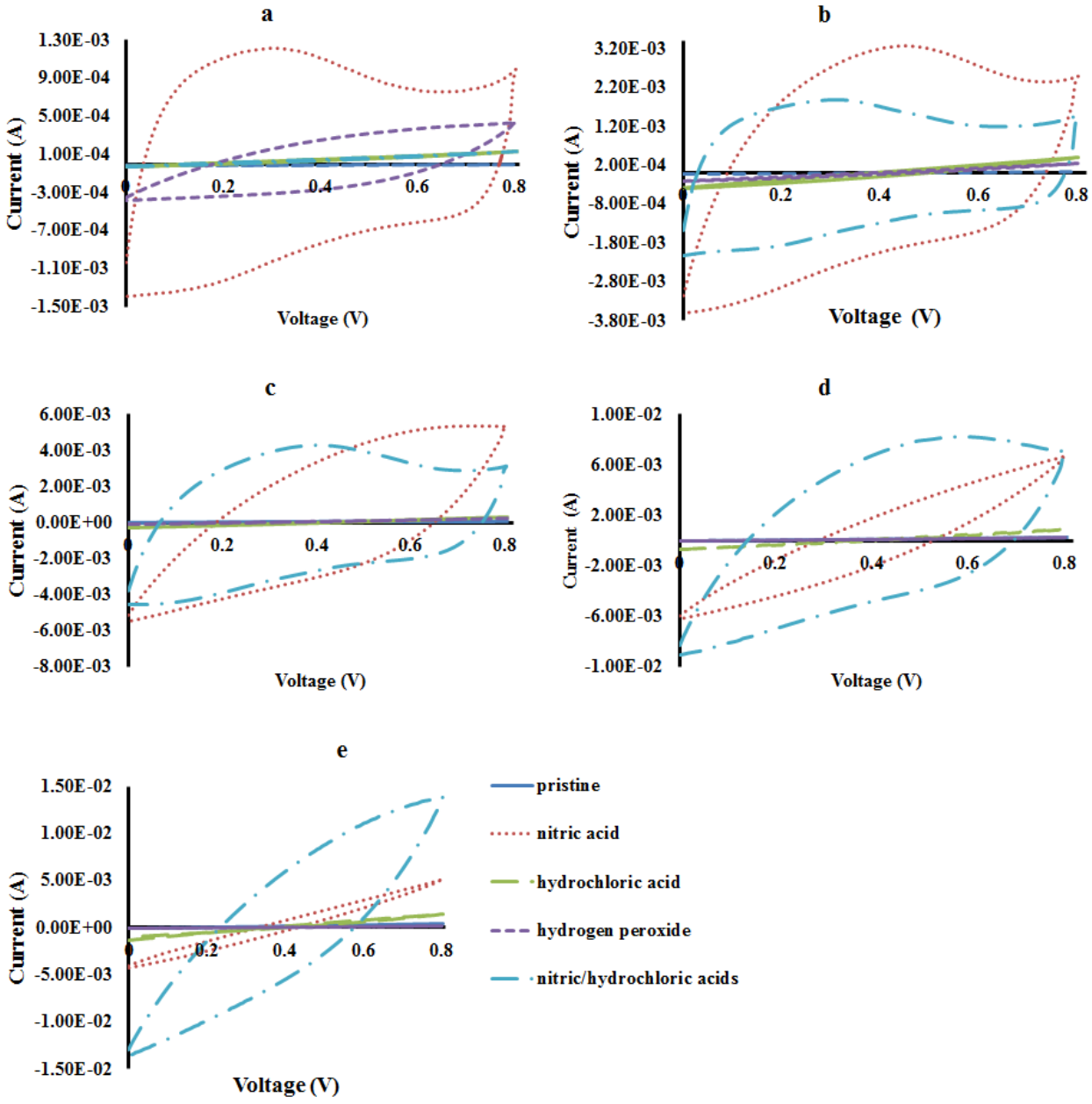

Figure 5.7. Cyclic voltammetry curves at scan rate of (a) 10, (b) 25, (c) 50, (d) 100 and (e) 200 mV s^{-1} using lithium sulfate as electrolyte.

All MWCNT treatments, except for HNO_3, displayed poor capacitive properties at higher scan rates in Li_2SO_4 electrolyte. Additionally, from the specific capacitance (C_s) values in Table 5.3, the order from the highest was HNO_3 (36.200 F g^{-1} at 25 mV s^{-1}), HCl/HNO_3 treated (23.700 F g^{-1} at 50 mV s^{-1}), H_2O_2 (9.599 F g^{-1} at 10 mV s^{-1}), HCl (3.190 F g^{-1} at 25 mV s^{-1}) and pristine (0.47 F g^{-1} at 100 mV s^{-1}). This highlighted the treatment effect on charge/discharge capability of MWCNTs and from the current results it shows that treatment improved charge storage capabilities.

Also, since BET surface area of treated MWCNTs decreased relative to pristine (Table 5.2), the deductions in this work could be that Li_2SO_4 electrolyte works better for MWCNTs with higher porosity and oxygen-containing functionalities. This could infer the pseudo capacitive charge storage as the main mechanism in Li_2SO_4 electrolyte. A relationship is expected between sizes of pores and Li^+ cations in an EDLC mechanism dominated electrode, however, the slight variation in pore sizes after MWCNT treatment limits a clear judgement.

The increased surface roughness [5.49] indicated by corresponding TEM image (Figure 5.2) for HNO_3 treated MWCNTs and their high I_D/I_G ratio (Table 5.1) also corroborates with their higher C_s. Contribution from high defect intensity acting as charge traps is a possibility but this trend was not noticed with respect to rest other samples. In short, all the treated samples performed quantitatively better than pristine MWCNTs. The results particularly show a relationship between the number of oxygen-containing groups and quantitative capacitance (similar trend in Table 5.1 for treated samples). This is could be validated by the effect of oxygen-containing groups on the electronic structure and surface activities of MWCNTs [5.18]. The hydrous layers in this case facilitate electron and proton transfer [5.50].

Table 5.3. Specific capacitance in F g^{-1} using lithium sulfate.

Sample	Scan rate (mV s^{-1})				
	10	**25**	**50**	**100**	**200**
pristine	0.026	0.178	0.429	0.470	0.333
HNO_3	33.821	36.200	26.350	13.400	4.613
HCl	2.045	3.190	1.195	1.543	1.263
H_2O_2	9.599	1.720	0.655	0.360	0.108
HNO_3/HCl	2.045	22.100	23.700	21.650	14.938

5.3.6.2. Sodium sulfate electrolyte

All the samples showed a quasi-rectangular and symmetrical cyclic voltammograms in Na_2SO_4 electrolyte at a scan rate of 10 mV s^{-1} and similar CV curves, except for HCl treated, were seen with 25 mV s^{-1} (Figure 5.8a and b). This is an indication of rapid current response to voltage reversal, minimal ion mass-transfer resistance and an excellent double layer capacitance at low scan rates [5.11,5.45,5.51,5.52]. This is a general notable difference between the capacitive characteristics of the samples in the current work when the group one cationic radius is changed from Li^+ to Na^+. At this scan rate MWCNT treatments involving HCl showed the highest C_s values (Table 5.4) whilst H_2O_2 had the best EDLC qualitative character (most rectangular curve).

Overall, H_2O_2 treated MWCNTs, after HNO_3 (C_s of 45.100 F g^{-1}), had the second highest C_s of 37.353 F g^{-1} followed by HNO_3/HCl (C_s of 31.136 F g^{-1}), HCl (C_s of 27.727 F g^{-1}) treated then pristine MWCNTs (C_s of 23.922 F g^{-1}). This trend was similar to that of Li_2SO_4 electrolyte in that the oxygen-containing moieties were the key influence. Additionally, larger ion results in slower diffusion, this is played out by the fact that the shape of the CV curve changes to oval/ellipsoidal at higher scan rates, so slower ion movement and slight differing textural characteristics with the different treatments occur.

Table 5.4. Specific capacitance in F g^{-1} using sodium sulfate.

Sample	Scan rate (mV s^{-1})				
	10	**25**	**50**	**100**	**200**
pristine	18.886	23.922	18.800	15.600	12.838
HNO_3	21.364	26.667	45.100	18.150	2.475
HCl	27.727	10.196	15.100	8.000	2.488
H_2O_2	26.364	37.353	21.050	3.025	9.300
HNO_3/HCl	31.136	7.657	1.860	0.116	2.213

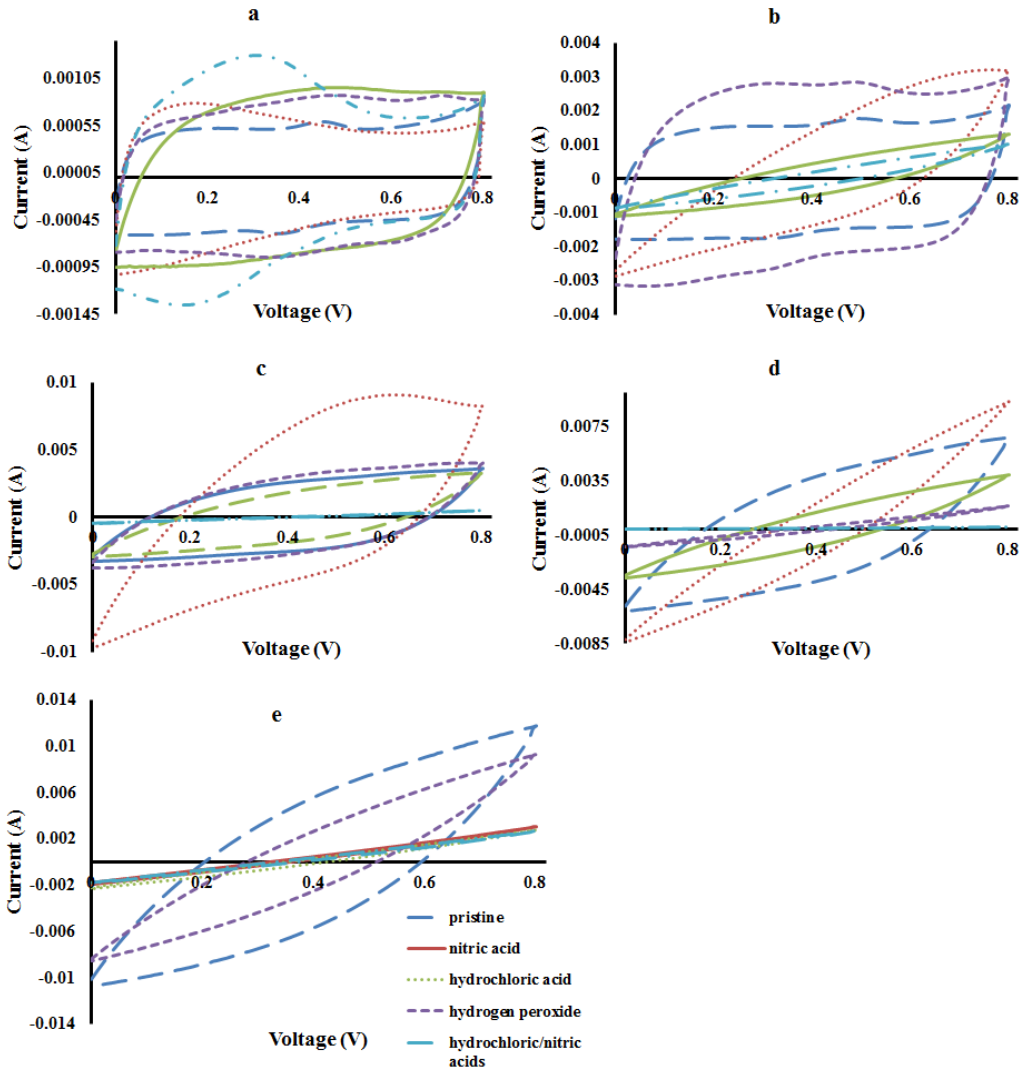

Figure 5.8. Cyclic voltammetry curves at scan rate of (**a**) 10, (**b**) 25, (**c**) 50, (**d**) 100 and (**e**) 200 mV s^{-1} using sodium sulfate as electrolyte.

Also, at scan rates of 10 and 25 mV s^{-1}, pristine MWCNTs showed a small redox peak at ca 0.45 V and this can be attributed to reversible oxygen evolution reactions [5.6,5.23]. At the scan rate of 25 mV s^{-1} (Figure 5.8b), H_2O_2 treated MWCNTs exhibited the best EDLCs characteristic followed by pristine MWCNTs. This can be attributed to low levels of oxygen-containing groups, reduced hydrophilic character and the least defective nature compared to the rest of the samples. The rest of the samples showed severely symmetrical distorted rectangles, i.e. deviation from EDLC character. According to this study, it is possible that pseudo charge storage mechanism, from oxygen-containing groups, was dominating and also that sodium sulfate required longer diffusion time in order to effectively form a double layer on all the samples [5.45]. The variations in ion mobility rates between Na^+ and Li^+ is related to their differences in size, i.e. larger Na^+ cation has a slower speed. This an interesting indicator of domination of physical properties, for MWCNTs treated in H_2O_2 opposed to oxygen moieties in the rest of the samples, such as opening of tube ends and pore size effects in relation to Na^+ cationic size [5.53] with sodium sulfates as electrolyte. At the scan rate of 50 mV s^{-1} (Figure 5.8c), all samples except HCl/HNO_3 treated sample exhibited symmetrical pseudo rectangular CVs. The pronounced shift of the cathodic peak to the right and that of the anodic peak to the left at scan rate of 25, 50 and 100 mV s^{-1} for HNO_3 treated MWCNTs is a clear indication of increase in internal resistance [5.51] and is common with open tubes [5.16]. It is noted that HNO_3 treated samples had the highest current response at a scan rate of 50 mV s^{-1} and that all treatments reduced current response at high scan rates. In a nutshell, the section 3.6.2 data similarly infers that treating MWCNTs quantitatively enhanced charge storage capabilities in Na_2SO_4 electrolyte.

5.3.6.3. Potassium sulfate electrolyte

Changing the electrolyte to K_2SO_4 resulted in outcomes different from those obtained using both Li_2SO_4 and Na_2SO_4 (Figure 5.9). At a scan rate of 10 mV s^{-1}, HCl/HNO_3 treated MWCNTs displayed the best capacitive performances (Figure 5.9a and Table 5.5). Additionally, HCl/HNO_3 treated MWCNTs displayed the highest current responses and had the highest C_s at all scan rates except at 200 mV s^{-1}. This is an indication of better electrochemical activities [5.54] of MWCNTs treated with HCl/HNO_3 solution. The HCl/HNO_3 treated MWCNTs performed better in K_2SO_4 than in Na_2SO_4 at scan rates of 25, 50 and 100 mV s^{-1}. Additionally, the associated 'dumbbell-like' shape indicates differences in ion

accessibility to the adsorption surfaces and pseudo character is attributed to oxygen moieties introduced by treatment.

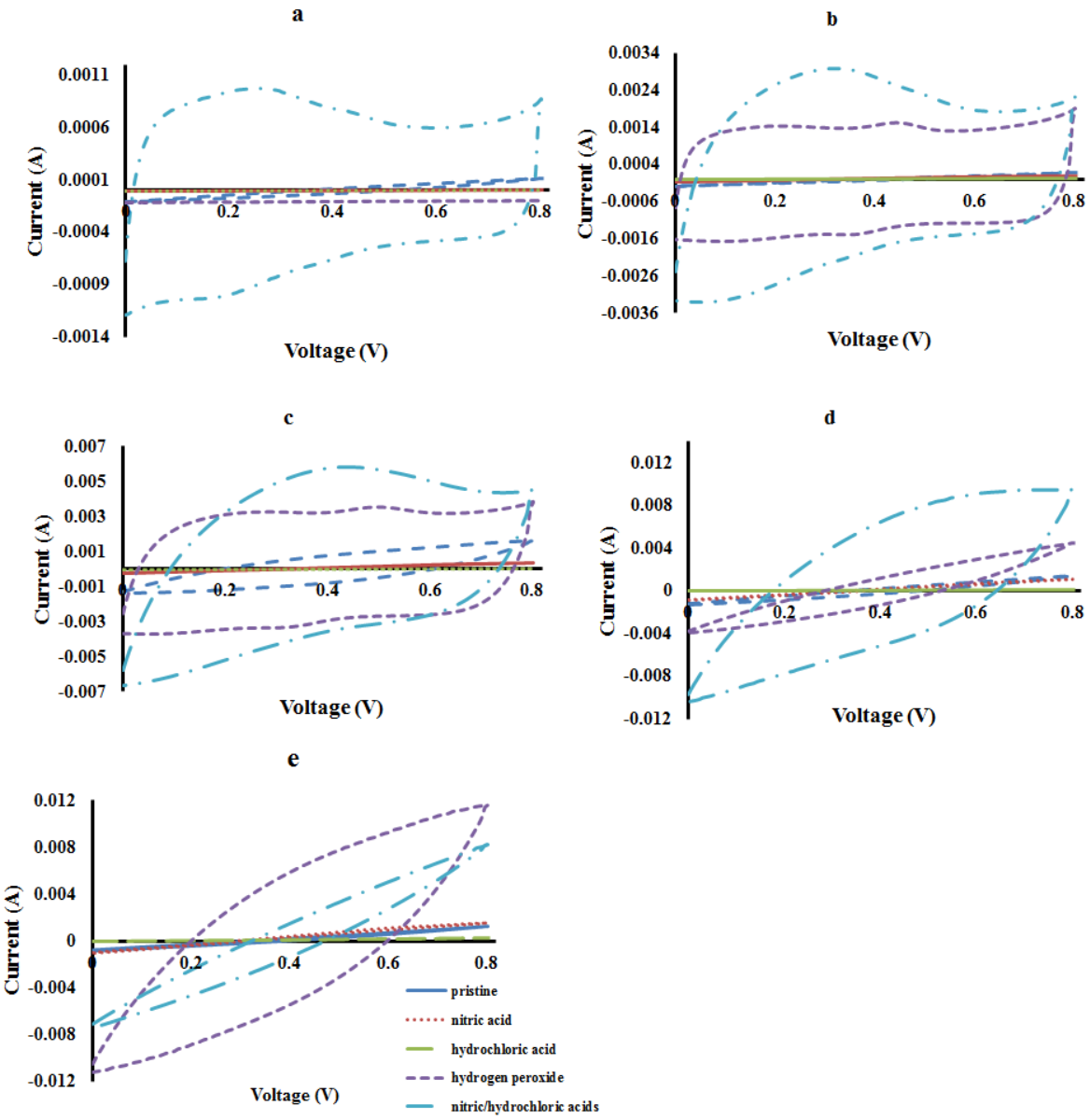

Figure 5.9. Cyclic voltammetry curves at scan rate of (a) 10, (b) 25, (c) 50, (d) 100 and (e) 200 mV s^{-1} using potassium sulfate as electrolyte.

Moreover, the transformation of CV curve to an oval/ellipsoidal at higher scan rate is again attributed to increase in mass transfer resistance. Again, H_2O_2 treated MWCNTs demonstrated a good EDLC capacitive quality at scan rates of 25 and 50 mV s^{-1}. This is an indication of a

better working rate [5.55] of MWCNTs treated with H_2O_2. This is corroborated relatively to the least porosity and surface area along with slight increase in oxygen containing-groups. A reversible redox peak at ca. -0.45 V was noticed on H_2O_2 treated MWCNTs and was probably due to differences in diffusion capabilities between solvated cations and anions, saturation of electrolyte ions at the electrode surface and 'electrolyte starvation' phenomenon inside the tubes [5.52] resulting from poor ion accessibility into pores. According to the results obtained, the scan rate of 50 mV s^{-1} tends to be the optimum scan rate for H_2O_2 treated MWCNTs.

Table 5.5. Specific capacitance in F g^{-1} using potassium sulfate electrolyte.

Sample	Scan rate (mV s^{-1})				
	10	**25**	**50**	**100**	**200**
pristine	2.323	1.450	6.850	4.575	1.011
HNO_3	0.103	0.645	1.180	2.075	2.038
HCl	0.132	0.245	0.067	0.203	0.168
H_2O_2	4.200	21.600	23.550	8.675	12.950
HNO_3/HCl	29.000	33.600	32.200	23.875	7.875

Pristine MWCNTs as well as samples treated by HNO_3 and HCl performed dismally in terms of both EDLC quality and quantity of charge storage at all scan rates in K_2SO_4 electrolyte (Figure 5.9 and Table 5.4). This indicates that the increase in cationic size of the electrolyte from Na^+ to K^+ reduced charge/discharge ability of these treated samples [5.15]. The corresponding performance order was HCl/HNO_3 (C_s of 31.600 F g^{-1}), H_2O_2 (C_s of 23.550 F g^{-1}), pristine (C_s of 6.850 F g^{-1}), HNO_3 (C_s of 2.075 F g^{-1}), and HCl (C_s of 0.245 F g^{-1}). A comparison of this order with Table 5.1 infers that capacitive performance increase with increase in the oxygen-containing functionalities (HCl, pristine, H_2O_2 and HNO_3/HCl), reach a threshold with HNO_3/HCl and thereafter decreased with excess oxygen moieties content (HNO_3).

A scrutiny of CV curves and the aforementioned possibilities from all electrolytes suggest that the cation size difference down the group one metal is also crucial to the outcomes. In addition, the disappearance of humps with respective to each electrolyte at higher scan rate can be attributed to large ionic resistance [5.52]. In short, they were noted differences when MWCNTs with different oxygen-containing groups when electrochemically characterised using different cationic radius of group one sulfate electrolyte systems. This corroborates with earlier studies that concluded that electrolyte transport characteristics change with local electric

fields [5.56]. An ideal EDLC character is one which is classically associated with fast reversible reactions, i.e. rectangular CV. Unlike at higher scan rates, a steep slope on current changes at switching potentials indicate minimal storage mass-transfer resistance when the scan rate was 10 and 25 mV s^{-1} for all electrolytes.

The HCl treated samples had comparable quantities of oxygen-containing groups with pristine MWCNTs. Generally, the best performances for pristine and HCl treated MWCNTs (with lowest oxygen-containing groups) was obtained using Na_2SO_4 electrolyte (Table 5.3-5.5 and Figure 5.S2 in supplementary information), for H_2O_2 (lowest surface area) and HNO_3 (highest oxygen-containing groups) treatment it was with Na_2SO_4 whilst K_2SO_4 worked best for HNO_3/HCl treatment (highest pore volume).

The differences noted on other treated samples were because ultrasound treatment introduced new surface functionalities which influence physicochemical properties such as different ion affinities [5.33] and hence, cation adsorption capacity was altered from that of pristine MWCNTs. Also, since functionalization alters the wettability of MWCNTs [5.1,5.38], charge storage capabilities changes with respect to electrolyte. The shapes of the CVs for HNO_3 and HNO_3/HCl in this study, with high oxygen-containing groups and pore volume, concurred with the views by An *et al.* [5.57] in that increase in oxygen-containing groups provide better electrochemical performances in ECs. This is due to synergistic effects of pseudo-capacitance and improved wettability. Hence, ion transport is enhanced.

From the textural characteristics (Table 5.2), it is apparent that pristine MWCNTs had the largest BET surface area, but they generally performed poorer than the treated MWCNTs. Also from Figure 5.2f, it is clear that pristine MWCNTs had the largest ratios of tubes with thicker diameters. This means there was some contribution from spaces between MWCNT bundles to surface area, which was highest in pristine MWCNTs. However, such spaces did not effectively participate in the formation of a double layer. In addition, pores available for N_2 sorption are not necessarily available to the electrolyte and there is a possibility of MWCNTs agglomeration during device fabrication [5.46].

Cycle stability tests were done in Na_2SO_4 at a scan rate of 50 mV s^{-1} (Figure 5.S3 in supplementary work) and cycles of 10, 50 and 100 were compared. From Figure 5.S3a (supplementary information) it was seen that capacitance decreases with increase in number of cycles. Upon modification of tube walls with oxygen moieties, EDLC character was seen to change with increase in cycle numbers relative to pristine MWCNTs (Figure 5.S3b). With the

HNO_3 treatment, both current response and capacitance decreased but EDLC behaviour increased when cycles were increased from 10 to 50. However, capacitance slightly increased on the 100th cycle relative to cycle number 50. For the MWCNTs treated with HCl, both capacitance and EDLC quality increased when cycle number was raised from 10 to 50 (Figure 5.S3c) but slightly decreased on the 100th cycle. A similar trend was observed with H_2O_2 treatment but capacitance drastically deteriorates on the 100th cycle (Figure 5.S3d). The HCl/HNO_3 treatment had poorest cycle stability (Figure 5.S3e).

5.3.6.4. Electrochemical impedance analysis

Even though the highest C_s was obtained by treating MWCNTs with HNO_3 (in Li_2SO_4 and Na_2SO_4) and HCl/HNO_3 (in K_2SO_4), this was not clearly noticeable from EIS (Figure 5.10). The two treatments displayed the highest ratio of smaller OD tubes and the highest oxygen-containing moieties. Hence, a possible explanation is associated with the main contribution of pseudo capacitive character to the overall capacitance. Oxygen-containing moieties are naturally acidic and therefore they introduce electron acceptor features to the MWCNTs [5.9]. A possible mechanism involves an interaction between group one cation and species such as COO^- and O^-anions (conjugate ions of COOH and OH moieties) on the tube walls (equations 2-4). Additionally, surface functionalities enhance surface wettability, and this positively enhances charge storage, hence better charge storage functionality than pristine.

From Figure 5.10, a slight semi-circle observed for rest of the samples, except with HCl treatment using Li_2SO_4 and K_2SO_4 electrolytes, in the high frequency region was attributed to some minimal charge transfer resistance [5.58] and this corroborates with the oval/ellipsoidal observed in the respective CV curves. In Li_2SO_4, the order of charge transfer resistance deduced was HNO_3 > pristine > HCl/HNO_3 > H_2O_2 (insert in Figure 5.10a). With Na_2SO_4, the order was HCl > HCl/HNO_3 > HNO_3 > pristine > H_2O_2 (insert in Figure 5.10b). Whilst in K_2SO_4 electrolyte the order was HNO_3 > HCl/HNO_3 > H_2O_2 > pristine (insert in Figure 5.10c). The data shows that HCl treatment of MWCNTs enhances charge transfer resistance substantially in Na_2SO_4 than the rest of the samples. A possible explanation is the increase in pore accessibility for the group one sulfate electrolytes due to abundance of oxygen groups and the attack of HCl on MWCNT walls interferes with charge transfer pathways in the MWCNT material.

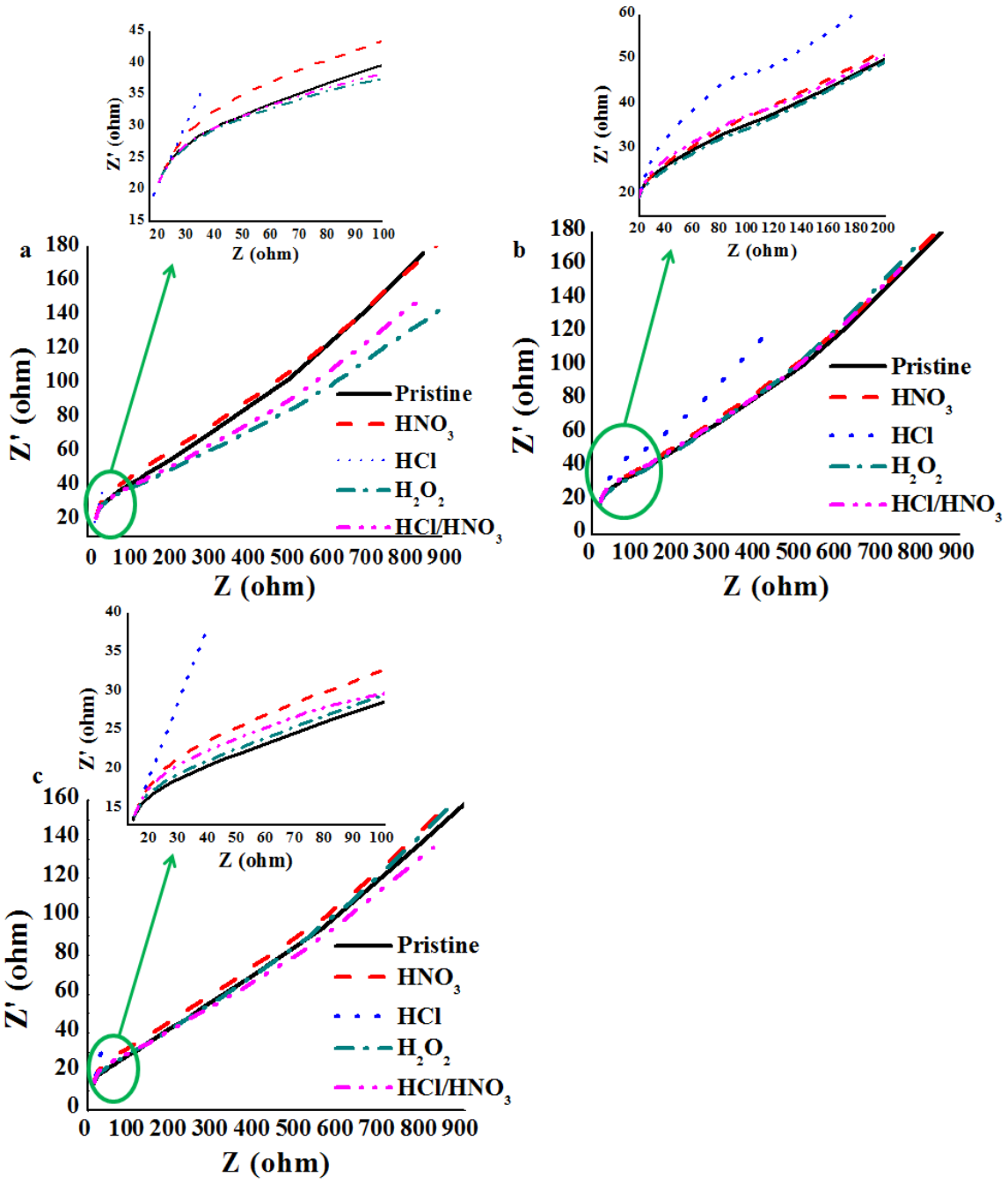

Figure 5.10. The EIS for pristine and the treated MWCNTs using (a) Li_2SO_4, (b) Na_2SO_4 and K_2SO_4 electrolytes.

Additionally, the results show that oxygen-containing moieties from the various treatments alter the surface properties of MWCNTs [5.59]. The results corroborates the findings by Liu *et al*., [5.60] on activated carbon. Short slope of about 45° in the intermediate frequency was

the evidence of the frequency dependence of the electrolyte ion diffusion from the group one sulfate electrolyte to oxygen functionalized MWCNT-based electrode, known as Warbug resistance [5.58,5.59]. The steepest slope was from HNO_3 treatment in all electrolytes and this could suggest that the electrode efficiently permitted ion diffusion [5.61]. The slanted line in the low frequency region suggests less dominance of EDLC of all samples in all electrolytes [5.60].

The most probable explanation is the contribution of oxygen-containing moieties to pseudo Faradaic reactions as proposed earlier in CV analysis (Section 3.6.1-3). The oxygen moieties attached to MWCNTs enabled their enhanced functionality in group one sulfate electrolytes [5.60]. A closer analysis of Figure 5.10a indicates that HCl had best EDLC character whilst HNO_3 and pristine treatments had comparable higher EDLC character in Li_2SO_4 but H_2O_2 showed the poorest behaviour. With reference to Table 5.1, HCl could have best EDLCs because it had the lowest oxygen-containing groups, but the minimal pseudo gave it an overall low C_s (Section 3.6.1-3). Again, in this regard, the major contribution from pseudo electrochemical charge storage in HNO_3 treated than in pristine MWCNTs could have also gave the former an overall higher C_s (Section 3.6.1-3). In Figure 5.10b all samples, except HCl treated MWCNTs, had similar EDLC behaviour but H_2O_2 treated MWCNTs displayed the best eccentric in Na_2SO_4 with pristine being the poorest.

A possible explanation is their minimal variations in terms of textural characteristics (Table 5.2). Whereas in K_2SO_4, H_2O_2 and HNO_3 treated MWCNTs exhibited the best EDLC behaviour than the rest (Figure 5.10c). Again, the EIS could not corroborate the overall C_s values (Section 3.6.1-3) because it did not account for the pseudo electrochemical processes to charge storage.

The proposed main mechanism for the current work, that corroborates with the work reported by Wang *et al.,* [5.46] and Frackowiaka *et al.*,[5.62] involves reversible oxidation of oxygen-containing groups as shown by the following equations:

$$C - OH \leftrightarrow C = O + H^+ + e^- \quad (1)$$

$$C = O + e^- \leftrightarrow C - O^- \quad (2)$$

$$COOH \leftrightarrow COO + H^+ + e^- \quad (3)$$

5.3.7. Conclusions

From this study, ultra-sound water bath treatment of MWCNTs with oxidising agents was able to introduce surface functionalities that can alter physicochemical properties either negatively or positively with respect to charge storage mechanism. HNO_3 treatment introduced the highest carboxylic, lactonic and phenolic moieties on MWCNT walls as well as highest ratio of smaller OD (outer diameter) tubes. The treatment in HCl/HNO_3 solution reduced defect intensity of MWCNTs but with comparable lactonic and carboxylic acid group content relative to HNO_3 treated samples. The findings of the study support the view that the acidic nature of oxygen-containing groups modify electron-donor characteristics of MWCNTs and thus induce electron acceptor character. On comparing the best C_s of treated MWCNTs, relative to C_s of pristine for each electrolyte, a 77, 2.5 and 4.9 times enhancement was noted for Li_2SO_4, Na_2SO_4 and K_2SO_4, respectively. Considering both rectangular shaped cyclic voltammograms and high C_s values over a wider range of scan rates, it is imperative to conclude that Na_2SO_4 electrolyte displayed the best performance as an electrochemical double layer device with the oxygen-modified MWCNTs under study. The variations in cationic radius down the group one elements electrolytes influence capacitive performances of MWCNTs.

According to this study, oxygen-containing functionalities increased charge storage capabilities of MWCNTs in terms of C_s. Addition of oxygen functionalities on MWCNT surfaces introduces pseudo characteristics, in addition to intrinsic EDLC mechanism. The work fundamentally indicates that acid treatments often done to remove residual metal catalyst and as preliminary steps in modification of MWCNTs influence the overall electrochemical properties by introducing various functionalities and physicochemical properties. Treatment transformed both qualitative and quantitative functionality of MWCNT in electrochemical capacitors.

Acknowledgements

The authors wish to thank the University of KwaZulu-Natal (UKZN) for the access to facilities used in this work and UKZN Nanotechnology Platform. This research did not receive any specific grant from funding agencies in the public, commercial, or not-for-profit sectors.

References

5.1. Motchelaho MAM, Xiong H, Moyo M, Jewell LL, Coville NJ. Effect of acid treatment on the surface of multiwalled carbon nanotubes prepared from Fe-Co supported on $CaCO_3$: Correlation with Fischer–Tropsch catalyst activity. *Journal of Molecular Catalysis A: Chemical* 2011; **335**:189-198.

5.2. Zhang S, Peng C, Ng KC, Chen GZ. Nanocomposites of manganese oxides and carbon nanotubes for aqueous supercapacitor stacks. *Electrochimica Acta* 2010; **55**:7447-7453.

5.3. Chartarrayawadee W, Moulton SE, Too CO, Kim BC, Yepuri R, Romeo T, Wallace GG. Facile synthesis of reduced graphene oxide/MWNTs nanocomposite supercapacitor materials tested as electrophoretically deposited films on glassy carbon electrodes. *Journal of Applied Electrochemistry* 2013; **43***:*865-877.

5.4. Mombeshora ET, Simoyi R, Nyamori VO, Ndungu PG. Multiwalled carbon nanotube-titania nanocomposites: Understanding nano-structural parameters and functionality in dye-sensitized solar cells. *South African Journal of Chemistry* 2015; **68**:153-164.

5.5. Lawal AT. Synthesis and utilization of carbon nanotubes for fabrication of electrochemical biosensors. *Materials Research Bulletin* 2016; **73**:308-350.

5.6. Wu MS, Zheng YR, Lin GW. Three-dimensional carbon nanotube networks with a supported nickel oxide nanonet for high-performance supercapacitors. *Chemical Communications (Cambridge)* 2014; **50**:8246-8248.

5.7. Zhang LL, Xiong Z, Zhao XS. A composite electrode consisting of nickel hydroxide, carbon nanotubes, and reduced graphene oxide with an ultrahigh electrocapacitance. *Journal of Power Sources* 2013; **222**:326-332.

5.8. Zhu X, Dai H, Hu J, Ding L, Jiang L. Reduced graphene oxide-nickel oxide composite as high performance electrode materials for supercapacitors. *Journal of Power Sources* 2012; **203**:243-249.

5.9. Mombeshora ET, Nyamori VO. A review on the use of carbon nanostructured materials in electrochemical capacitors. *International Journal of Energy Research* 2015; **39**:1955-1988.

5.10. Chen X, Tang X-Z, Liang YN, Cheah JW, Hu P, Hu X. Controlled thermal functionalization for dispersion enhancement of multi-wall carbon nanotube in organic solvents. *Journal of Material of Science* 2016; **51**:5625-5634.

5.11. Yun YS, Lee S, Kim NR, Kang M, Leal C, Park K-Y, Kang K, Jin H-J. High and rapid alkali cation storage in ultramicroporous carbonaceous materials. *Journal of Power Sources* 2016; **313:**142-151.

5.12. Wen ZB, Yu F, You T, Zhu L, Zhang L, Wu YP. A core-shell structured nanocomposite of NiO with carbon nanotubes as positive electrode material of high capacitance for supercapacitors. *Materials Research Bulletin* 2016; **74**:241-247.

5.13. Su L, Gong L, Wang X, Pan H. Improved low-temperature performance of novel asymmetric supercapacitor with capacitor/battery-capacitor construction. *International Journal of Energy Research* 2016; **40**:763-769.

5.14. Shimamoto K, Tadanaga K, Tatsumisago M. All-solid-state electrochemical capacitors using MnO_2/carbon nanotube composite electrode. *Electrochimica Acta* 2013; **109**:651-655.

5.15. Lin C-C, Kuo C-L. Effects of carbon nanotubes acid treated or annealed and manganese nitrate thermally decomposed on capacitive characteristics of electrochemical capacitors. *Journal of Nanomaterials* 2013; **2013**:1-8.

5.16. Al-zubaidi A, Inoue T, Matsushita T, Ishii Y, Hashimoto T, Kawasaki S. Cyclic voltammogram profile of single-walled carbon nanotube electric double-layer capacitor electrode reveals dumbbell shape. *Journal of Physical Chemistry C* 2012; **116**:7681−7686.

5.17. Wu JB, Guo RQ, Huang X H, Lin Y. Construction of self-supported porous TiO_2/NiO core/shell nanorod arrays for electrochemical capacitor application. *Journal of Power Sources* 2013; **243**: 317-322.

5.18. Lee S, Peng J-W. Observation of the diameter-dependent Raman dispersion effect in chemically oxidized multiwalled carbon nanotubes. *Journal of Physics and Chemistry of Solids* 2011; **72**:1133-1139.

5.19. Li Y, Hu FP, Wang X, Shen PK. Anchoring metal nanoparticles on hydrofluoric acid treated multiwalled carbon nanotubes as stable electrocatalysts. *Electrochemistry Communications* 2008; **10**:1101-1104.

5.20. Das R, Ali ME, Bee AHS, Annuar MSM, Ramakrishna S. Common wet chemical agents for purifying multiwalled carbon nanotubes. *Journal of Nanomaterials* 2014; **2014**:1-9.

5.21. Chen JH, Li WZ, Wang DZ, Yang SX, Wen JG, Ren ZF. Electrochemical characterization of carbon nanotubes as electrode in electrochemical double-layer capacitors. *Carbon* 2002; **40**:1193-1197.

5.22. Scheibe B, Borowiak-Palen E, Kalenczuk RJ. Oxidation and reduction of multiwalled carbon nanotubes-preparation and characterization. *Materials Characterization* 2010; **61**:185-191.

5.23. Kruusenberg I, Alexeyeva N, Tammeveski K, Kozlova J, Matisen L, Sammelselg V, Solla-Gullón J, Feliu JM. Effect of purification of carbon nanotubes on their electrocatalytic properties for oxygen reduction in acid solution. *Carbon* 2011; **49**:4031-4039.

5.24. Socas-Rodriguez B, Herrera-Herrera AV, Asensio-Ramos M, Hernandez-Borges J. Recent applications of carbon nanotube sorbents in analytical chemistry. *Journal of chromatography. A* 2014; **1357**:110-146.

5.25. Friedl J, Bauer CM, Rinaldi A, Stimming U. Electron transfer kinetics of the-reaction on multi-walled carbon nanotubes. *Carbon* 2013; **63**:228-239.

5.26. Mallakpour S, Behranvand V. The influence of acid-treated multi-walled carbon nanotubes on the surface morphology and thermal properties of alanine-based poly(amide–imide)/MWCNT nanocomposites system. *Colloid and Polymer Science* 2014; **293**:333-339.

5.27. Likodimos V, Steriotis TA, Papageorgiou SK, Romanos GE, Marques RRN, Rocha RP, Faria JL, Pereira MFR, Figueiredo JL, Silva AMT, Falaras P. Controlled surface functionalization of multiwall carbon nanotubes by HNO_3 hydrothermal oxidation. *Carbon* 2014; **69:**311-326.

5.28. Pumera M. Electrochemical properties of double wall carbon nanotube electrodes. *Nanoscale Research Letters* 2007; **2**:87-93.

5.29. Huang N, Kirk DW, Thorpe SJ, Liang C, Xu L, Li W, Zhang S, Sun M. Effect of carbon nanotube loadings on supercapacitor characteristics. *International Journal of Energy Research* 2015; **39**:336-343.

5.30 Wang G, Liang R, Liu L, Zhong B. Improving the specific capacitance of carbon nanotubes-based supercapacitors by combining introducing functional groups on carbon nanotubes with using redox-active electrolyte. *Electrochimica Acta* 2014; **115**:183-188.

5.31. Hua C-C, Su J-H, Wen T-C. Modification of multi-walled carbon nanotubes for electric double-layer capacitors: Tube opening and surface functionalization. *Journal of Physics and Chemistry of Solids* 2007; **68**:2353-2362.

5.32. Sivakkumar SR, Pandolfo AG. Carbon nanotubes/amorphous carbon composites as high-power negative electrodes in lithium ion capacitors. *Journal of Applied Electrochemistry* 2013; **44**:105-113.

5.33. Lu C, Chiu H. Chemical modification of multiwalled carbon nanotubes for sorption of Zn^{2+} from aqueous solution. *Chemical Engineering Journal* 2008; **139**:462-468.

5.34. Cañete-Rosales P, Ortega V, Álvarez-Lueje A, Bollo S, González M, Ansón A, Martínez MT. Influence of size and oxidative treatments of multi-walled carbon nanotubes on their electrocatalytic properties. *Electrochimica Acta* 2012; **62**:163-171.

5.35. Linga X, Wei Y, Zou L, Xua S. The effect of different order of purification treatments on the purity of multiwalled carbon nanotubes. *Applied Surface Science* 2013; **276**:159-166.

5.36. Guo H-L, Wang X-F, Qian Q-Y, Wang F-B, Xing-Hua X. A green approach to the synthesis of graphene nanosheets. *American Chemical Society* 2009; **3**:2653-2659.

5.37. Qui NV, Scholz P, Krech T, Keller TF, Pollok K, Ondruschka B. Multiwalled carbon nanotubes oxidized by UV/H_2O_2 as catalyst for oxidative dehydrogenation of ethylbenzene. *Catalysis Communications* 2011; **12**:464-469.

5.38. Lehman JH, Terrones M, Mansfield E, Hurst KE, Meunier V. Evaluating the characteristics of multiwall carbon nanotubes. *Carbon* 2011; **49**:2581-2602.

5.39. Edwards ER, Antunes EF, Botelho EC, Baldan MR, Corat EJ. Evaluation of residual iron in carbon nanotubes purified by acid treatments. *Applied Surface Science* 2011; **258**:641-648.

5.40. Pretorius E. Influence of acceleration voltage on scanning electron microscopy of human blood platelets. *Microscopy Research and Technique* 2010; **73**:225-228.

5.41. Osswald S, Havel M, Gogotsi Y. Monitoring oxidation of multiwalled carbon nanotubes by Raman spectroscopy. *Journal of Raman spectroscopy* 2007; **38**:728-736.

5.42. Carabineiro SA, Pereira MF, Pereira JN, Caparros C, Sencadas V, Lanceros-Mendez S. Effect of the carbon nanotube surface characteristics on the conductivity and dielectric constant of carbon nanotube/poly(vinylidene fluoride) composites. *Nanoscale Research Letters* 2011; **6**:1-5.

5.43. Datsyuk V, Kalyva M, Papagelis K, Parthenios J, Tasis D, Siokou A, Kallitsis I, Galiotis C. Chemical oxidation of multiwalled carbon nanotubes. *Carbon* 2008; **46**:833-840.

5.44. Chizari K, Vena A, Laurentius L, Sundararaj U. The effect of temperature on the morphology and chemical surface properties of nitrogen-doped carbon nanotubes. *Carbon* 2014; **68**:369-379.

5.45. Wang J-G, Yang Y, Huang Z-H, Kang F. Synthesis and electrochemical performance of MnO_2/CNTs-embedded carbon nanofibers nanocomposites for supercapacitors. *Electrochimica Acta* 2012; **75**:213-219.

5.46. Wang Z, Wu Z, Di Benedetto G, Zunino JL, Mitra S. Microwave synthesis of highly oxidized and defective carbon nanotubes for enhancing the performance of supercapacitors. *Carbon* 2015; **91**:103-113.

5.47. Saleem AM, Göransson G, Desmaris V, Enoksson P. CMOS compatible on-chip decoupling capacitor based on vertically aligned carbon nanofibers. *Solid-State Electronics* 2015; **107**:15-19.

5.48. Tian Y, Xue R, Zhou X, Liu Z, Huang L. Double layer capacitor based on active carbon and its improved capacitive properties using redox additive electrolyte of anthraquinonedisulphonate. *Electrochimica Acta* 2015; **152**:135-139.

5.49. Egashira M., Okada S, Korai Y, Yamaki J-I, Mochida I. Toluene-insoluble fraction of fullerene-soot as the electrode of a double-layer capacitor. *Journal of Power Sources* 2005; **148**:116-120.

5.50. Kiamahalleh MV, Zein SHS. Multiwalled carbon nanotubes based nanocomposites for supercapacitors: A review of electrode materials. *NANO: Brief Reports and Reviews* 2012; **7**:1-27.

5.51. Zhou Z, Wu X-F. High-performance porous electrodes for pseudosupercapacitors based on graphene-beaded carbon nanofibers surface-coated with nanostructured conducting polymers. *Journal of Power Sources* 2014; **262***:*44-49.

5.52. Wang H, Pilon L. Physical interpretation of cyclic voltammetry for measuring electric double layer capacitances. *Electrochimica Acta* 2012; **64**:130-139.

5.53. Brown B, Swain B, Hiltwine J, Brooks DB, Zhou Z. Carbon nanosheet buckypaper: A graphene-carbon nanotube hybrid material for enhanced supercapacitor performance. *Journal of Power Sources* 2014; **272**:979-986.

5.54. Wu M-S, Chan D-S, Lin K-H, Jow J-J. A simple route to electrophoretic deposition of transition metal-coated nickel oxide films for electrochemical capacitors. *Materials Chemistry and Physics* 2011; **130**:1239-1245.

5.55. Yan Z, Ma L, Zhu Y, Lahiri I, Hahm MG, Liu Z, Yang S, Xiang C, Lu W, Peng Z, Sun Z, Kittrell C, Lou J, Choi W, Ajayan PM, Tour JM. Three-dimensional metal graphene nanotube multifunctional hybrid materials. *American Chemical Society Nano* 2012; **7**:58-64.

5.56. d'Entremont AL, Girard HL, Wang H, Pilon L. Electrochemical transport phenomena in hybrid pseudocapacitors under galvanostatic cycling. *Journal of the Electrochemical Society* 2015; **163**:A229-A243.

5.57. An G-H, Ahn H-J. Surface modification of RuO_2 nanoparticles-carbon nanofiber composites for electrochemical capacitors. *Journal of Electroanalytical Chemistry* 2015; **744**:32-36.

5.58. Chang B, Yang B, Guo Y, Wang Y, Dong X. Preparation and enhanced supercapacitance performance of porous carbon spheres with a high degree of graphitization. *Royal Society of Chemistry Advances* 2015; **5***:*2088-2095.

5.59. Chen Y, Zhang X, Zhang D, Yu P, Ma Y. High performance supercapacitors based on reduced graphene oxide in aqueous and ionic liquid electrolytes. *Carbon* 2011; **49**:573-580.

5.60. Liu D, Zhang W, Lin H, Li Y, Lu H, Wanga Y. Hierarchical porous carbon based on the self-templating structure of rice husk for high-performance supercapacitors. *Royal Society of Chemistry Advances 2015;* **5**:19294-19300.

5.61. Farma R, Deraman M, Awitdrus IA, Talib OR, Manjunatha JG, Ishak MM, Basri NH, Dolah BNM. Physical and electrochemical properties of supercapacitor electrodes derived from CNT and biomass carbon. *International Journal of Electrochemical Science* 2013; **8**:257-273.

5.62. Frackowiaka E, Be´guin FO. Carbon materials for the electrochemical storage of energy in capacitors. *Carbon* 2001; **39**:937-950.

Appendix: Supporting information for Chapter 5

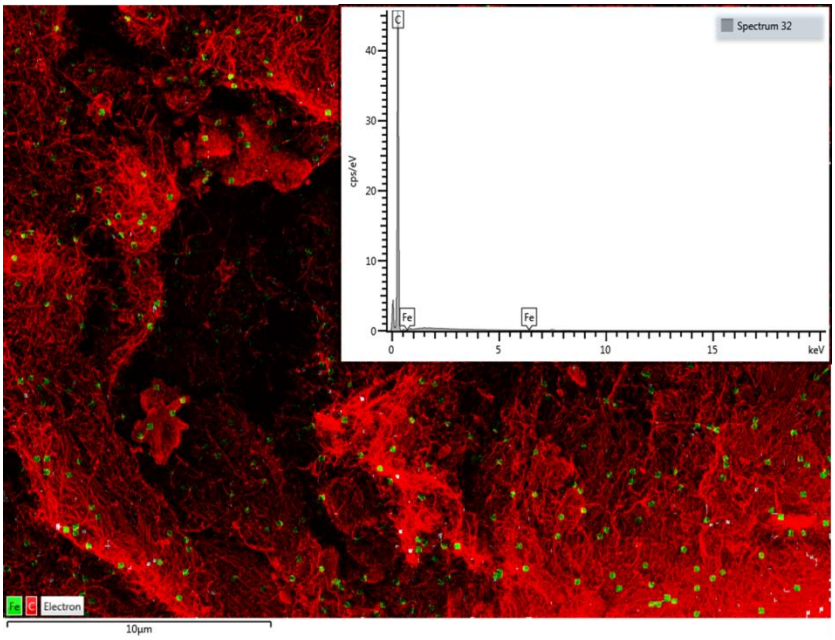

Figure 5.S1 The EDX mapping image and spectrum for pristine MWCNTs

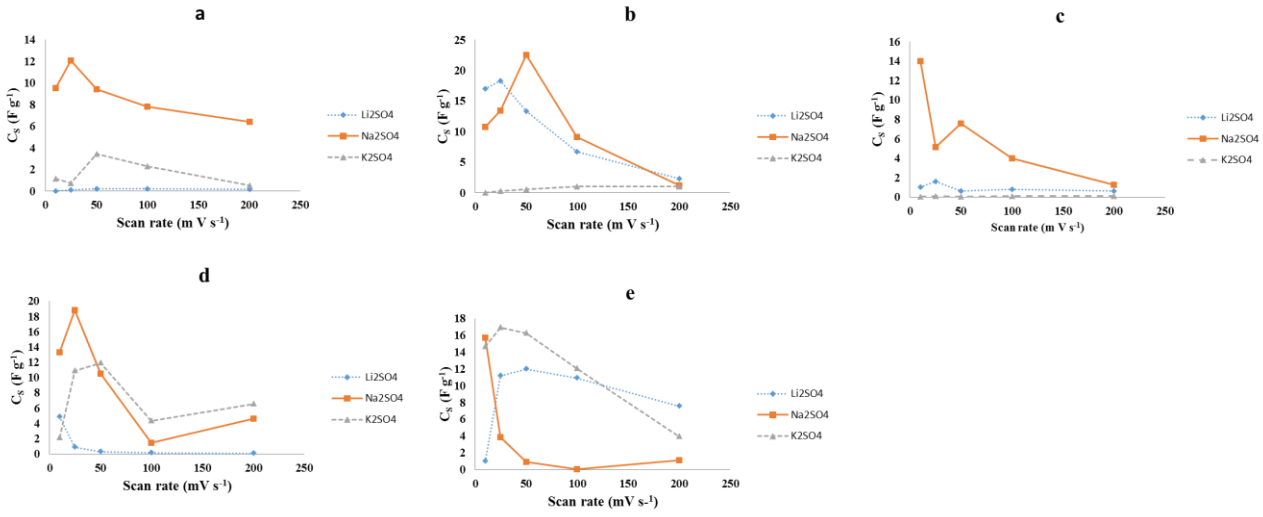

Figure 5.S2 The comparison of electrolytes for (a) pristine MWCNTs, and MWCNTs treated with (b) HNO_3 (c) HCl, (d) H_2O_2, (e) HCl/HNO_3

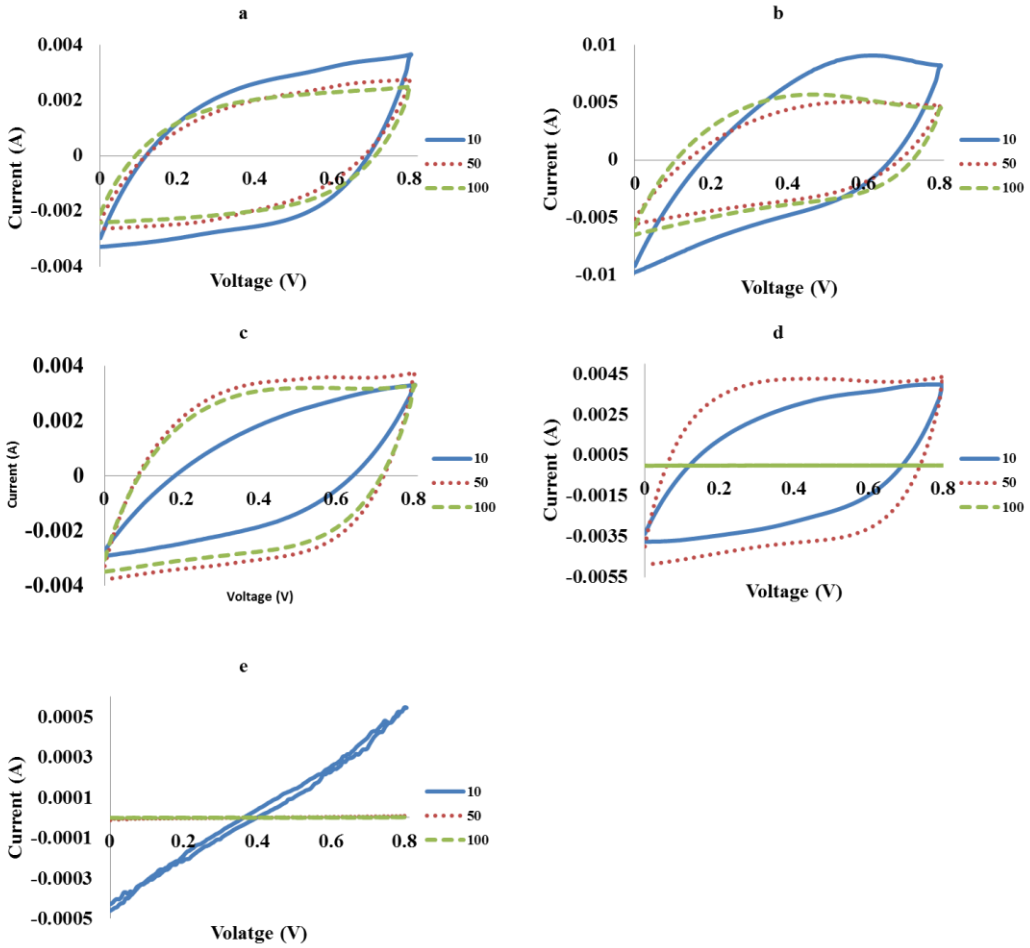

Figure 5.S3 The cycle stability test in sodium sulfate electrolyte at a scan rate of 50 mV s^{-1} for (a) pristine MWCNTs, and MWCNTs treated with (b) HNO_3 (c) HCl, (d) H_2O_2, (e) HCl/HNO_3

Table 5.S1 The integrated areas under the derivative weigh curve from TGA analysis surface

Treatment	% weight loss due to				
	water	**Oxygen-containing groups**	**Carboxylic groups**	**Lactones**	**Phenols**
HNO_3	5.84	20.21	8.94	1.44	1.02
HCl	1.27	8.51	2.31	0.63	0.60
H_2O_2	0.54	3.53	0.93	0.35	0.09
HCl/HNO_3	0.46	2.97	0.88	0.28	0.08
pristine	0.44	3.31	1.16	0.30	0.09

JOHN WILEY AND SONS LICENSE TERMS AND CONDITIONS

Nov.06, 2017

This Agreement between Mr. Edwin Mombeshora ("You") and John Wiley and Sons ("John Wiley and Sons") consists of your license details and the terms and conditions provided by John Wiley and Sons and Copyright Clearance Center.

License Number	4223050717406
License date	Nov 06, 2017
Licensed Content Publisher	John Wiley and Sons
Licensed Content Publication	International Journal of Energy Research
Licensed Content Title	Oxygen-modified multiwalled carbon nanotubes: physicochemical properties and capacitor functionality
Licensed Content Author	Edwin T. Mombeshora,Patrick G. Ndungu,A. L. Leigh Jarvis,Vincent O. Nyamori
Licensed Content Date	Jan 17, 2017
Licensed Content Pages	20
Type of use	Dissertation/Thesis
Requestor type	Author of this Wiley article
Format	Print and electronic
Portion	Full article
Will you be translating?	No
Order reference number	thesis ET Mombeshora
Title of your thesis / dissertation	Synthesis and functionality of boron-, nitrogen- and oxygen-doped shaped carbon-based nanomaterials and titania nanocomposites in electrochemical capacitors
Expected completion date	Nov 2017
Expected size (number of pages)	386
Requestor Location	Mr. Edwin Mombeshora School Of Chemistry and Physics University Of KwaZulu-Natal Westville campus, Private Bag X54001 Durban, KwaZulu-Natal 4000 South Africa Attn: Mr. Edwin Mombeshora
Publisher Tax ID	EU826007151
Billing Type	Invoice
Billing Address	Mr. Edwin Mombeshora School Of Chemistry and Physics University Of KwaZulu-Natal Westville campus, Private Bag X54001 Durban, South Africa 4000 Attn: Mr. Edwin Mombeshora

Chapter Six

The physicochemical properties and capacitive functionality of pyrrolic- and pyridinic-nitrogen, and boron-doped reduced graphene oxide

Edwin T. Mombeshora[1], Patrick G. Ndungu[1,2], and Vincent O. Nyamori*[1]

[1]School of Chemistry and Physics, University of KwaZulu-Natal, Westville Campus, Private Bag X54001, Durban, 4000, South Africa

[2]Department of Applied Chemistry, University of Johannesburg, P.O. Box 17011, Doornfontein, Johannesburg, 2028, South Africa

Vincent O. Nyamori* - nyamori@ukzn.ac.za

* Corresponding author

Graphical abstract

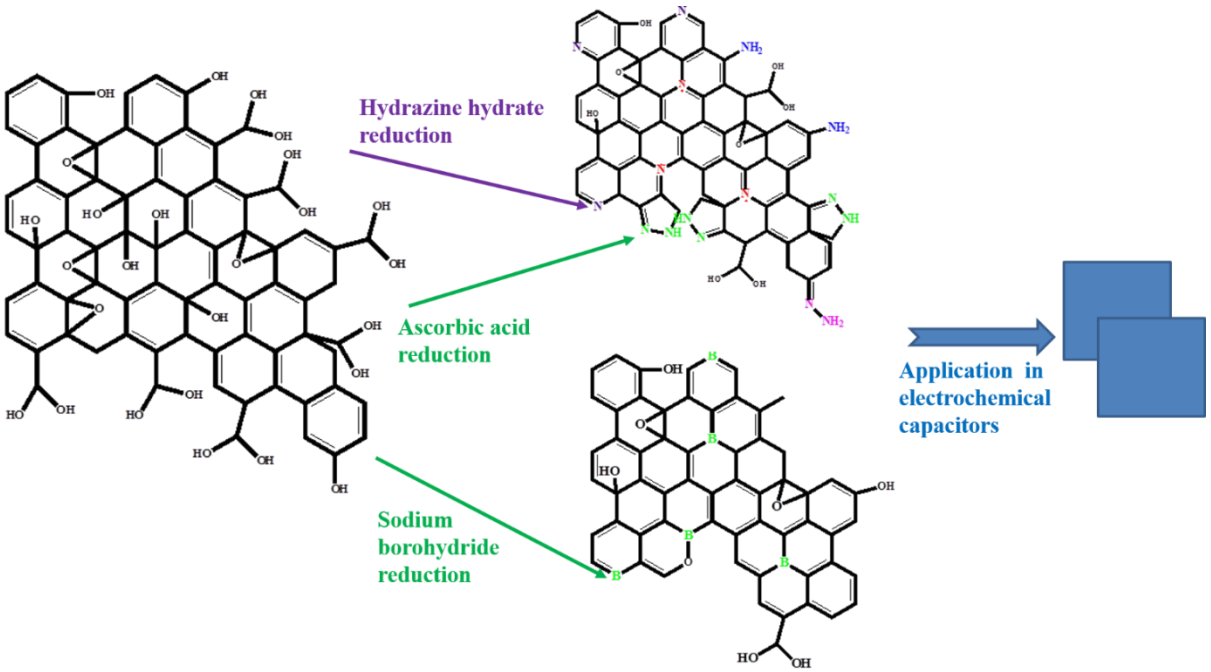

Abstract

Much focus with regards to graphene oxide (GO) reduction has been on reducing the oxygen:carbon ratio with little focus on other associated chemical transformations. The current work presents an enlightening physical and chemical transformation study of reduced graphene oxide (RGO) samples with regards to use of ascorbic acid, hydrazine hydrate and sodium borohydride as reducing agents and their associated appropriateness in electrochemical capacitors. The physical and chemical characteristics of RGO were compared by means of elemental analysis, infra-red spectroscopy, thermal gravimetric analysis, X-ray photoelectron spectroscopy, powder X-ray diffraction, textural characteristics, scanning and transmission electron microscopies, electron impedance spectroscopy and cyclic voltammetry. Hydrazine hydrate was the most effective reducing agent with the highest nitrogen at.% (4.07), surface area of 390.55 m^2 g^{-1} and was increased to 599.67 m^2 g^{-1} upon thermal treatment at 750 ˚C. The nitrogen functionalities observed in pristine-GO, ascorbic acid and hydrazine hydrate reduced GO were sp^3 N-C, pyrrolic and pyridinic, respectively. Whereas sodium borohydride RGO were B-doped with at.% of 2.49 during the reduction reaction. The N-doped RGO samples were more effective in charge storage than B-doped counterparts (76-fold better) and pyrrolic-N-doped was more effective than pyridinic- N-doped-RGO (1.35 times better).

Keywords: electrochemical capacitance, electrochemical double layer capacitor, nitrogen-doped graphene oxide, boron-doped graphene oxide

* Corresponding author*:* Vincent O. Nyamori, School of Chemistry and Physics, University of KwaZulu-Natal, Westville Campus, Private Bag X54001, Durban, 4000, South Africa

Email: nyamori@ukzn.ac.za Tel.: +27-31 2608256; Fax: +27-31 260 3091

6.1. Introduction

Electrochemical capacitors, are a promising alternative to batteries with lower energy density but higher power density, and can store energy at the electrode-electrolyte interphase 6.1,6.2]. Numerous studies have focussed on electrode materials as a way of enhancing energy density [6.3,6.4]. Carbon nano-materials such as graphene [6.1,6.5] and carbon nanotubes (CNTs) [6.6] are suitable electrochemical capacitance materials with power densities that can be altered by their physicochemical properties [6.7]. CNTs have dominated the carbon-based nanomaterial research area, but graphene is relatively cheaper [6.8]. Graphene has been known

as a building block for over 66 years, but experimental isolation was first achieved in 2004 [6.3,6.9-6.11]. Attention on graphene was mainly triggered by extraordinary surface area, thermal, mechanical and electronic properties [6.11-6.15]. The near zero bandgap of graphene [6.3,6.16] has led to current leakages in most of its applications [6.14]. Graphene-based materials are promising nanomaterials for the next generation of electrodes in energy conversion systems [6.3,6.13]. Graphene is basically synthesised by two main techniques, the bottom-up (growth from elemental carbon) and top-down approach (mechanical, electrochemical or chemical exfoliation) [6.17]. The aforementioned ways culminates in different qualities of graphene sheets and also, electronic and capacitance in graphene-based materials is layer dependant [6.7]. However, charge carrier transport, often present in ideal graphene, is absent in typical graphene oxide (GO) and in addition, reduction is often used to enhance conductivity *via* restoration of the π system [6.18]. Understanding the physical and chemical properties of a typical reduced graphene oxide (RGO) sample is still an active research area.

Chemical reduction of GO is considered an efficient, low cost and bulk scale approach to production of RGO [6.9,6.10,6.12,6.17,6.19]. Main chemical groups, located at basal planes, of GO are epoxides and hydroxyls whilst the minor components situated at the edges are carboxyl and carbonyls [6.9]. Several reducing agents have been reported such as aluminium powder in acid [6.12], hydrazine hydrate [6.20], ammonia [6.11], sodium borohydride [6.17], and ascorbic acid [6.19], amongst others. Reduction of GO with ascorbic acid is a mild and green approach when compared to the use of hydrazine hydrate [6.19], whilst sodium borohydride is relatively expensive. Concerns in reduction of GO is mainly on attainment of low oxygen content, production of defect-free sheets, selectivity of reduction agents and enhancement of dispersion stability, amongst other things [6.9,6.11,6.17]. The current work seeks to compare and ascertain the influence of chemical reduction of GO by use of ascorbic acid, hydrazine hydrate and sodium borohydride on physical and chemical properties of RGO. Additionally, the work also focuses on investigating the chemistry of the RGO samples with regards to chemical methods of choice and their associated suitability in electrochemical capacitance. To the best of our knowledge, their suitability and associated influence on capacitance has not been compared in literature. This is suitably important with regards to selection of chemical reducing agents for GO, where both the effectiveness of a reducing agent and the resulting chemical nature of the products must be critically considered.

6.2. Materials

Graphite powder (< 150 µm, 99.99%), polyethylene glycol (PEG) (99.8%) and hydrazine hydrate (50-60%) were purchased from Sigma Aldrich, South Africa. Hydrogen peroxide (30%), sodium borohydride powder (95%) and ascorbic acid (99%) were bought from Merck ltd, South Africa. Potassium permanganate (99%), sodium nitrate (99%) and absolute methanol (99.5%, AR,) were all purchased from Associated Chemical Enterprise, South Africa. Sulfuric acid (98.37%) was procured from C.C. Imelmann Ltd, South Africa. All the chemicals were used as-received with no dilutions.

6.2.1 Methods

The GO was synthesised from the modified Hummers method adapted from Mombeshora *et al.*, [6.21].

6.2.1.1 Reduction of GO

In a typical synthesis of GO, graphite and sodium nitrate were mixed with H_2SO_4 (98%, 48 mL) by stirring in an ice water bath. The mixture was further stirred for 30 minutes and thereafter, $KMnO_4$ (6 g) was slowly added to the mixture while maintaining the temperature below 10 ˚C. Afterwards, the reaction mixture was further stirred at room temperature for 12 hours and double deionised water (DI, 60 mL) was added dropwise slowly. The reaction temperature, unlike the previous report, was brought to 50 ˚C and maintained at this temperature for 5 hours. Thereafter, H_2O_2 (30%, 200 mL) was added to the mixture prior to several cycles of washing using DI until the filtrate was at neutral pH.

The GO was then reduced by three different reagents, namely; ascorbic acid, hydrazine hydrate and sodium borohydride. In a typical synthesis, accurately weighed GO (3 g) was dispersed in DI (50 mL) by an ultrasonic treatment in a water bath for 10 minutes. Hydrazine hydrate (2 mL) was added under stirring. The mixture was heated up to 90 ˚C by means of an oil bath and kept constant for one hour. Secondly, ascorbic acid (6 g) stabilised in 1% PEG was added to GO (3 g) initially dispersed in 50 mL DI under stirring followed by a temperature ramp to 90 ˚C and kept constant for one hour. The PEG was added to enhance the GO/ascorbic acid interaction, facilitate the reduction process and also acted as a stabiliser (lessens

agglomeration). Similarly, sodium borohydride (6 g) was initially dissolved in DI (20 mL) then followed by addition of the solution to GO (3 g) dispersed in DI (20 mL) and reaction temperature ramped up and kept constant as in the above-mentioned steps. The reducing agent/GO mass ratios in the synthesis were five times higher for both ascorbic acid and sodium borohydride than that of hydrazine hydrate. This was because the latter was more effective than the former two, hence, a higher mass ratio was used as an attempt to boost their reducing effect. The products were then washed five times with DI followed by washing four times with methanol under gravitational filtration. The RGO samples were dried in an oven at 50 ˚C for at least 48 hours and thereafter kept in a desiccator. The samples were named with respect to reduction reagent, i.e. pristine-GO, RGO_{AA}, RGO_{HH} and RGO_{SB} for as-synthesised GO and that reduced by means of ascorbic acid, hydrazine hydrate and sodium borohydride, respectively.

Thermal reduction effect on textural characteristics and capacitance was further investigated with RGO_{HH}. The thermal reduction was carried out at 500, 750 and 1000 ˚C using a ramp rate of 2 ˚C/ minute using a tube furnace and 10% hydrogen in argon.

6.2.1.2 Characterization techniques

The samples were analysed by means of attenuated total reflectance - Fourier transform infrared spectroscopy (Perkin Elmer spectrometer- Perkin Elmer spectrum 100 series with universal ATR accessory), thermal gravimetric analysis (TA Instruments Q series^{TM} Thermal Analyzer DSC/TGA, Q600), powder X-ray diffraction (X-ray diffractometer, Rigaku MiniFlex 60), textural characteristics (Micromeritics TRI STAR 3020V1.03 ,V1.03), transmission electron microscopy (JEOL TEM 1010 transmission electron microscope), scanning electron microscopy (JEOL JSM 6100 microscope), Raman spectroscopy analysis (100 mW Delta Nu Advantage 532^{TM} spectrometer of 10 cm^{-1} resolution with a 2D CCD detector and grating lines were 1800 mm^{-1} with a laser source (Nd:YAG) at wavelength of 532 nm, four probe electron conductivity meter (model-DMV-001, ISO-9001-2000 certified with a PID oven controlled model-2000 and a low current source model-LC-02), elemental analysis (LECO CHNS-932 elemental analyzer standardized with acetanilide) and X-ray photoelectron spectroscopy (XPS, with a Kratos Axis ultra DLD using an Al (monochromatic) anode equipped with a charge neutraliser and operating pressure was kept below 5×10^{-9} Torr). The XPS parameters used

were an emission current of 10 mA, anode voltage (HT) 15 kV, resolution to acquire scan was 160 eV using hybrid lens in the slot mode.

The working electrode was prepared by casting the sample mixed with nafion onto a 3 mm diameter glassy carbon electrode. The deposited sample, on the electrode, was thereafter dried at room temperature. The electrochemical characterisations were done by means of cyclic voltammetry (797 VA Computrace Metrohm CT798 application model with a 57970110-dosing processor) and electrochemical impedance spectroscopy (CHI 600E work station, CHI Instruments, frequency range was 10000 - 1 Hz and AC voltage used was 0.005 V). All the measurements were done using a three-electrode system in 0.5 M $NaSO_4$ electrolyte. The counter and reference electrodes were Pt and Ag/AgCl system, respectively.

6.3. Results and Discussion

The physical and chemical characterisation data is elucidated in the sections that follows.

6.3.1 Chemical composition analysis

The C1s peaks at 284.2 and 285.2 eV were assigned to C-C (C1) and C-OH (C3), respectively (Fig. 6.1 a) [6.17]. The unusually low BE for C1s in RGO_{SB} was attributed to the presence of both Na and B in the sample. This infers a transformed chemical environment due to a possible increase in valence charge on C from either B or Na. Hence, the C-B interaction as dopant in the graphene framework is most likely due to similar sizes of the atoms. The XPS spectra shows that the major component of oxygen-containing groups in the as-synthesised GO was C3 and substantially decreased upon reduction with the various agents (Fig. 6.1a). This corroborates with elemental analysis, FTIR studies and TGA (Table 6.S1 in supplementary information, Fig. 6.3 and Table 6.1).

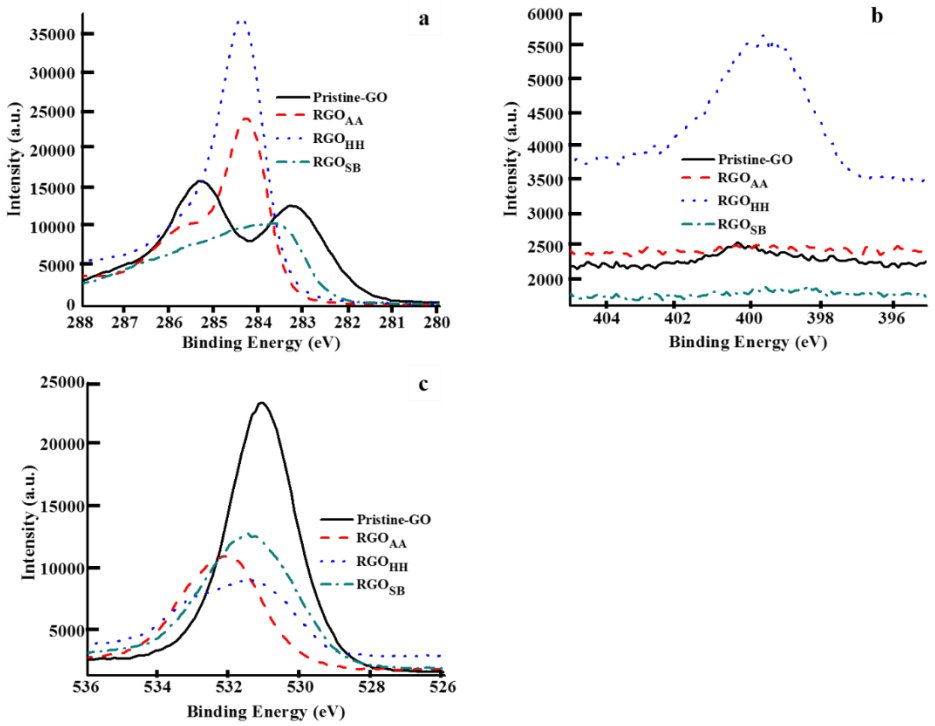

Fig. 6.1. XPS spectra for RGO samples (a) C1s, (b) N1s and (c) O1s.

The TGA weight loss, under N_2 atmosphere, in the temperature ranges 150-400 ˚C, 400-500 ˚C and 650-700 ˚C was assigned to loss from –COOH, lactones and -OH moieties [6.22,6.23], respectively. The trend, obtained by means of both TGA and elemental analysis, in terms of decreasing content of oxygen-containing groups, was pristine-GO > RGO_{SB} > RGO_{AA} > RGO_{HH} (Table 6.S1 in supplementary information and Table 6.1). The TGA data also infers that reductants used in the current work had minimum influence on quantities of both lactones and phenols (Table 6.1). In addition, sodium borohydride was the strongest –COOH reductant, followed by hydrazine hydrate but overall the latter was the most effective.

Table 6.1: Quantification of oxygen-containing groups from TGA in nitrogen gas atmosphere

Sample	% weight loss due to				
	Adsorbed water	Oxygen containing-groups	Carboxylic acid groups	Lactones	Phenols
Pristine-GO	22	44	28	4	3
RGO_{AA}	2	36	22	4	1
RGO_{HH}	7	20	15	3	2
RGO_{SB}	3	28	11	4	2

The weight loss at ca 100 ˚C, due to water loss, correlated with the pronounced decrease in the FTIR peak at ca 3400 cm^{-1}. This FTIR peak was assigned to hydroxyl stretching vibrations either in adsorbed water molecules or phenol and hydroxyl groups due to presence of carboxylic functionalities [6.11,6.19,6.24] and decrease in hydrogen-containing groups (Fig. 6.3, Table 6.S1 and Table 6.1). The RGO only displayed weight loss due to more stable oxygen moieties, i.e. weight loss between 100 and 900 ˚C (Fig. 6.2 and Table 6.1). The weight loss differences below 200 ˚C, due to different functional groups on RGO [6.11,6.25], were also observed between RGO_{AA} and RGO_{HH} with different nitrogen functionalities.

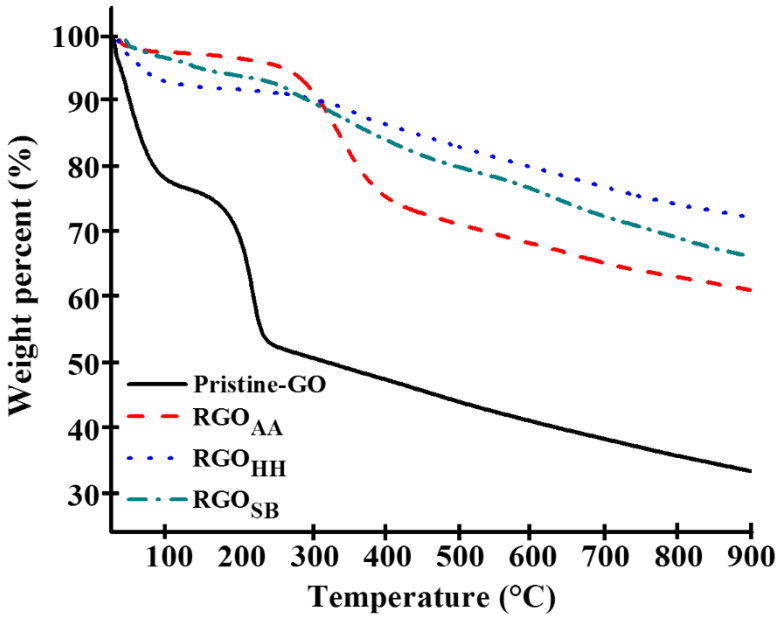

Fig. 6.2. TGA of pristine-GO and RGO samples in nitrogen (Condition: under nitrogen atmosphere, heating rate of 10 ˚C min^{-1} from room temperature to 900 ˚C).

The pristine-GO had the highest amount of oxygen at.% (Fig. 6.1c), respectively. Additionally, oxygen:carbon (O:C) ratio for all the samples, calculated from XPS data analysis (Table 6.2), were 0.32, 0.31, 0.17 and 0.10 for pristine-GO, RGO_{SB}, RGO_{AA}, and RGO_{HH} samples, respectively. This trend corroborated with the absence of the broad peak at 3400 cm^{-1} (Fig. 6.3) of RGO samples, data obtained from TGA and elemental analysis. The O:C ratio calculated from elemental analysis is not a reliable method to conclusively determine the oxygen content in GO because it is almost impossible to completely dehydrate it [6.26]. However, in the current work it was used because the samples were dried and stored under the same conditions. Hence, relative differences between samples can be identified. From the data, the number of hydrogen-containing groups was an indication of the OH moieties existence and likely hydrophilicity effects due to the chemical nature of the RGO.

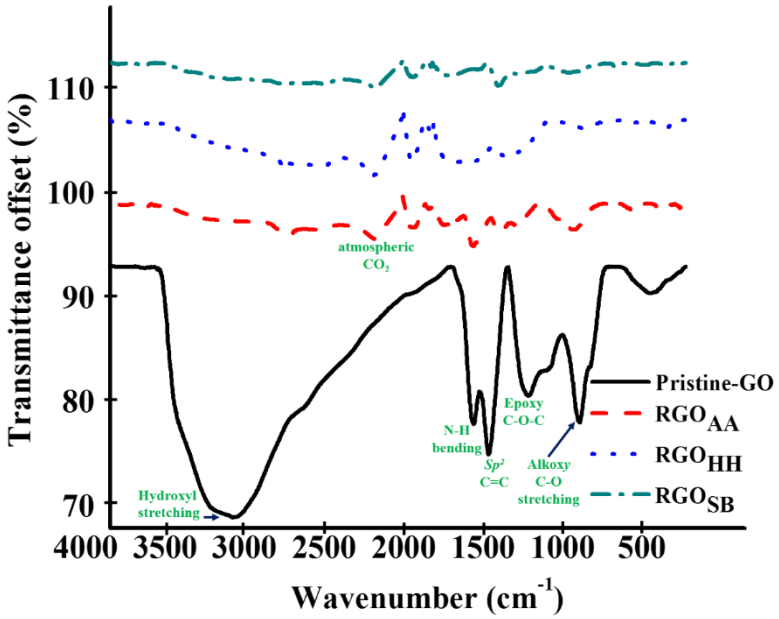

Fig. 6.3. ATR spectra of pristine-GO and RGO samples (reduced by means of ascorbic acid, hydrazine hydrate and sodium borohydride, respectively) restacked to avoid spectral overlap.

Table 6.2: Summary of XPS for pristine-GO and RGO samples

Sample	Element	Atomic concentration	Binding energy (eV)
pristine-GO	C1s	75.33	285.2
	O1s	24.22	530
	N1s	0.45	399
RGO_{AA}	C1s	84.85	284.2
	O1s	14.70	531
	N1s	0.45	403
RGO_{HH}	C1s	87.19	284.2
	O1s	8.73	531
	N1s	4.07	398
RGO_{SB}	C1s	73.44	283.5
	O1s	22.40	531
	N1s	-	-
	B1s	2.49	190
	Na1s	1.67	1070

The XPS oxygen atomic concentration (at.%) were lower than those determined by both elemental analysis and TGA although the data followed the same O:C ratio trend. This infers, with caution, that elemental analysis in conjunction with TGA (under nitrogen atmosphere) are a suitable method for determining, or at least an indication of, the effectiveness of reducing reagents on pristine-GO but maybe less accurate than XPS.

Additionally, the reduction by means of sodium borohydride is most likely to occur *via* a hydride transfer from borohydride anion to form an oxyanion and an electron deficient BH_3 molecule [6.14]. This was a possible reason for the least amount of carboxylic acid groups in RGO_{SB} (Table 6.1). The elemental analysis and XPS data infers that this mechanism is less efficient and was associated with no observable N1s peak, but a B1s, in the samples (Table 6.S1 and 6.2). A possible reason for disappearance of N is that B, due to a smaller atomic radius and the electron deficient BH_3 molecule form, was preferentially incorporated instead of N in the RGO. Also, the reduction of pristine-GO with sodium borohydride is governed by the type of carbonyl [6.14]. The current results infer its high and low efficiency in -COOH and -OH moieties reduction, respectively.

The N1s peak at binding energy (BE) of 399 in pristine-GO was assigned to sp^3 N-C [6.28]. A plausible rationale is that N is incorporated in the carbon structure (however not in the backbone of the graphitic framework) but exists as dangling bonds and this agrees with the observed FTIR N-H bending vibration (Fig. 6.3). The most probable source of N in pristine-GO is sodium nitrate used in the GO synthesis. The XPS data (Table 6.2) shows that pristine-GO and RGO_{AA} had equal N1s at.% but in different forms. In RGO_{AA}, the N1s peak at BE of 403 eV was ascribed to pyrrole-N-doping. This suggests that ascorbic acid reduction facilitated a transformation of sp^3 N-C to a pyrrolic nature. In addition, N1s peak at BE of 398 eV was attributed to either pyridinic or carbonitrile species [6.28], and the atomic concentration of N1s was highest in the RGO_{HH} sample (Table 6.2). This shows that hydrazine hydrate can result in N-doping of RGO samples. Whilst the presence of N moieties can infer presence of hydrazides and hydrazones from hydrazine reaction with lactones, anhydrides and quinones on pristine-GO [6.17], there was no noticeable functional group to support their presence in the FTIR spectra (Fig. 6.3).

A possible mechanism, reported by Pumera et al. [6.14] and Gao et al. [6.29], for the formation of typical N functionalities, in the current work, is through an attack of the epoxide moieties on pristine-GO. This mechanism is further supported by the decrease of the epoxy C-O-C and alkoxy C-O stretching vibrations peak intensities from FTIR analysis (Fig. 6.3). Additionally, the decrease in FTIR peak intensity at ca. 1500, 1600, 1250 and 980 cm^{-1}, attributed to aromatic sp^2 C=C bonds, N-H bending, epoxy C-O-C and alkoxy C-O stretching vibrations [6.19,6.24,6.27,6.28], respectively (Fig. 6.3) concurs with this mechanism. The absence of a C-N peak, particularly in the RGO_{AA} and RGO_{HH}, due to aliphatic amine stretching at ca 1074 cm^{-1} [6.11] suggest inclusion of N in the graphitic structure. In short, current results, show that pyrrolic- and pyridinic-N-doping of RGO can be facilitated by means of ascorbic acid and hydrazine hydrate GO reduction, respectively.

Hence, the current work, shows that the chemical method used for GO reduction is a manipulative means of tuning oxygen moieties content and other elemental compositions such as B, N and the N functional groups. These are phenomena often ignored in the reduction of GO in which most works focus on the reduction of O at.%.

6.3.2 Physical properties: defects, surface area, porosity and morphology

The powder X-ray diffraction peak at 2θ of 10° is a suitable qualitative indicator for the structure of GO [6.28]. Hence, the pronounced decrease in both the peak intensity and width is an indication of an effective reduction of GO indirectly through structural transformation (Fig. 6.S6, supplementary information). This decrease in peak intensity is an indication of destruction of regular stacking of pristine-GO during reduction [6.29]. The Raman peaks were fitted using a Lorenztian function.

The Raman D-band, often located at 1350 cm^{-1} (Fig. 6.S5, supplementary information), is an indicator of disruptions of the symmetrical hexagonal graphene lattice due to edge defects, internal structural defects and dangling bonds [6.29]. Typically, the more wrinkled appearance on RGO (Fig. 6.S7, supplementary information) is an indication of defects [6.13,6.16,6.30]. This suggests, from the RGO TEM images which were more transparent than pristine-GO, that exfoliation was further facilitated in the RGO samples (Fig. 6.4).

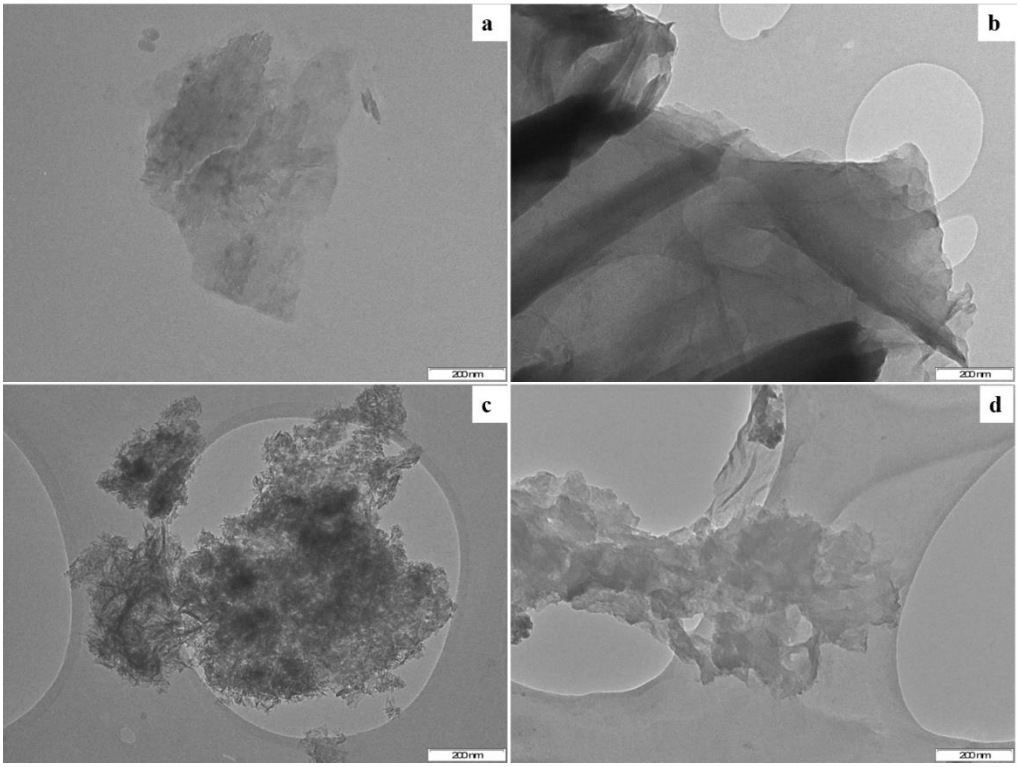

Fig. 6.4. TEM images for (a) pristine-GO, (b) RGO_{AA}, (c) RGO_{HH} and (d) RGO_{SB}.

Whereas the G-band located at 1550 cm^{-1} (Fig. 6.S5, supplementary information) is due to in-plane sp^2 carbon-carbon stretching vibrations. The I_D/I_G ratio, as defect density indicator, was determined by dividing the area under the D-band by that of G-band. The defect density of RGO_{AA} and RGO_{SB} were higher than that of pristine-GO (Fig. 6.S6b, supplementary information) due to associated reduction processes. However, the lowest defect density of RGO_{HH} is possibly due to both the lowest amount of oxygen-containing moieties and high fragmentation of sp^2-dormain [6.31]. The TGA thermogram indicates that all the RGO samples were more thermally stable than GO. A possible reason, which concurs with the work reported by Sandoval et al. [6.15] is the decrease in defects, that can be oxidised, upon RGO doping. Additionally, least possibility of electrostatic interactions, facilitated by the above-mentioned reasons, between RGO_{HH} sheets can be associated with minimum chances of agglomeration. Hence, it is associated with the largest surface area. The highest surface area of RGO_{HH} can also be attributed to highest N-doping [6.32]. Hence, from the current work, it can be ascertained that only reduction with hydrazine hydrate enhanced surface area (Table 6.3).

Table 6.3: Textural characteristics for pristine-GO and RGO samples

Treatment	Surface area (m^2/g)	Pore volume (cm^3/g)	Pore size (nm)
Pristine-GO	185.43	0.26	6.36
RGO_{AA}	17.85	0.05	10.32
RGO_{HH}	390.55	0.26	3.45
RGO_{SB}	4.22	0.01	4.71

Since RGO_{SB} and RGO_{AA} were both more agglomerated and randomly oriented than RGO_{HH} (Fig. 6.S7, supplementary information and Table 6.3), a possible rationale for the reduced surface areas of RGO_{AA} and RGO_{SB} is that chemically reduced GO is associated with π-π stacking between RGO sheets and this led to formation of agglomerates [6.19]. Agglomeration is enhanced by Van der Waals forces from the π-π interactions between RGO sheets [6.3]. Additionally, porosity in GO sheets is derived from the spaces between sheets [6.3], the decrease in pore volume in RGO_{AA} and RGO_{SB} (Table 6.3) is a further indication of agglomeration. In pristine-GO, the oxygen containing groups on the sheet surface introduces repulsive forces that may aide in separating the graphene layers, hence, any spaces between the

layers contributes to surface area and porosity [6.21]. Upon reduction (RGO_{AA} and RGO_{SB} samples), some of the processes removed or altered some of the oxygen moieties on the surfaces and this induced agglomeration and blocked or removed some spaces between RGO sheets.

The highest pore size (Table 6.3) and defect intensity (Fig. 6.S6b, supplementary information) in RGO_{AA} can conceivably suggest that ascorbic acid reduction of GO increases pore sizes. This possibly culminated on the highest compressive strain of the graphene framework. This was deduced from the highest blue shift of both the Raman spectroscopy G- and 2D-band (Table 6.S2, supplementary information). It is interesting to note that the surface area of pristine-GO was almost five times (185.43 $m^2\ g^{-1}$) more than the usual experimental values between 30-40 $m^2\ g^{-1}$ but less than theoretical values of approximately 2600 $m^2\ g^{-1}$ [6.33]. The lower experimental values are due to strong hydrogen bonding [6.33] that cause agglomeration of sheets and therefore reduce contribution of the spaces between sheets and the individual layers. In short, the textural characteristics data (Table 6.3 and Fig. 6.S6, supplementary information) infers that use of different chemical reagents during reduction of pristine-GO is a possible route of tailoring physical properties.

6.3.3 Electrochemical characterization

A small intercept in the real axis of the Nyquist plot (Fig. 6.5) hints at an associated small internal resistance (R_i). The ascending order of R_i was RGO_{AA}, RGO_{HH}, pristine-GO then RGO_{SB} (Fig. 6.5). This infers that pyrrolic-N-doping of RGO, in the current work, has lower R_i than pyridinic and they are both better than pristine-GO (Table 6.2 and Fig. 6.5). Also, B-doping increased R_i from that of pristine-GO and low R_i is significant in energy storage devices because it minimises energy wastage *via* production of unwanted heat during charging and discharging [6.34]. Pristine-GO had the largest Faradaic charge transfer resistance (R_{ct}) but, as deduced from the absence of a semi-circle, the rest of the samples had no clear resistance to charge flow (Fig. 6.5). A suitable reason for poorer electrochemical characteristics for pristine-GO is linked to high oxygen-containing groups [6.7].

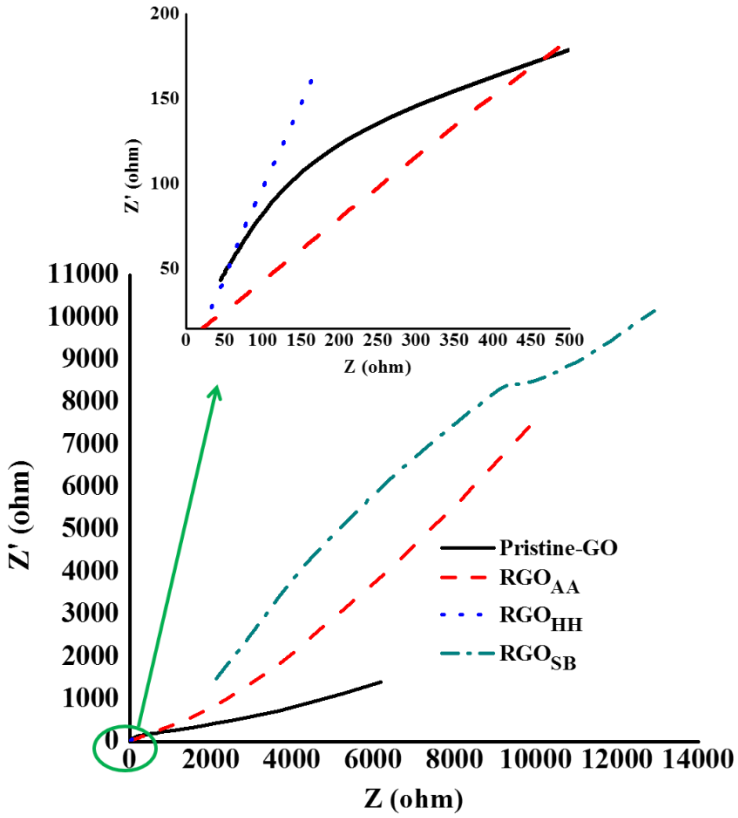

Fig. 6.5. Nyquist plot in the frequency range of 10000 - 1 Hz for pristine-GO and RGO synthesised from different reducing agents.

In the intermediate frequency, the negligible Warburg curve of RGO_{HH} (100-50 Hz, Fig. 6.5) was an indication of short ion diffusion path [6.35] and this suggested excellent electrolyte ion penetration [6.36,6.37]. This infers that pyridinic-N-doping positively facilitated sodium sulfate electrolyte ion penetration. RGO_{SB} displayed the longest diffusion path (9000-2000 Hz) and this means B-doping enhanced the diffusion path length. A larger slope associated with RGO_{HH}, i.e. almost vertical line, graph in the low frequency region was an indication of ideal EDLC behaviour [6.7,6.32,6.38].

The poor conductivity of pristine-GO is due to the disruption of the extended π-system but the reduction process restores it (Fig. 6.6) [6.30]. The pristine-GO conductivity behaviour was typical of a metal but reduction of GO render it semi-conducting [6.39]. This could be because the energy gap in pristine-GO depends on the level of oxidation, species of oxygen-containing groups and level of exfoliation [6.16,6.40], hence, a variation *via* reduction transforms the conductivity in typical materials. This concurs with blue and red shifting of the Raman G- and

2D-band peaks (Table 6.S2, supplementary information), associated with n- and p-type conducting [6.16,6.32,6.41] in the N- and B-doped-RGO, respectively. Additionally, doping of GO distorts the π electron cloud and this hinders in-plane electron movement [6.1], hence, doping was associated with lower conductivity.

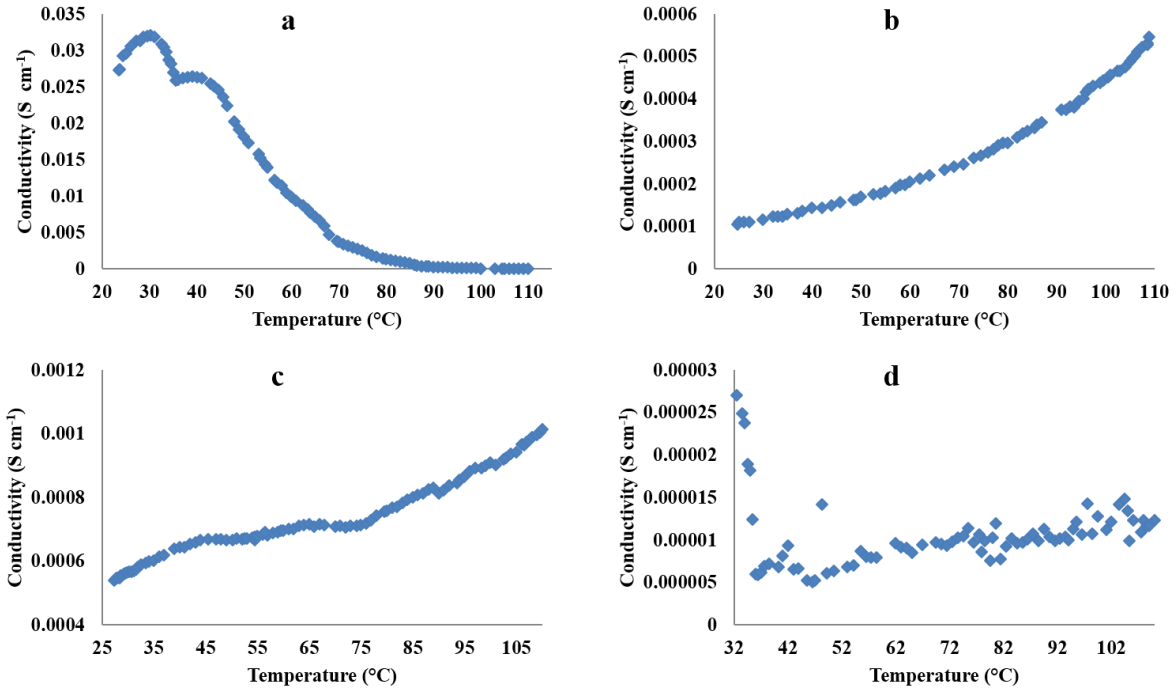

Fig. 6.6. Conductivity of (a) pristine-GO, (b) RGO_{AA}, (c) RGO_{HH} and (d) RGO_{SB}.

It can be deduced that RGO_{SB} still retained the intrinsic pristine-GO metallic conducting characteristics at lower temperatures. This can be attributed to high residual oxygen functionalities (Table 6.1) [6.14] and absence of N in the carbon framework as well as the presence of Na and B (Table 6.3). Two important remarks deduced from this data, firstly, pristine-GO was a better conductor at ambient temperatures than all RGO samples (Fig. 6.5). Secondly, there is a possibility that defects created during reduction process act as charge traps. The lower conductivity of RGO relative to pristine GO, unlike the expected improvement on conductivity upon reduction, was also attributed to the poor contact in the RGO sheets prepared for conductivity measurements in the four-probe method. This culminated from enhanced hydrophobic nature upon reduction and hence, poor contact sheets were produced. RGO_{HH} was the best semi-conductor in the current work and this was attributed to highest N content,

pyridinic-N-doping and the least defective nature. In brief, the differences in RGO conductivity was influenced by the addition of heteroatoms, N and B during reduction [6.12].

Electrochemical reduction of pristine-GO is a possibility during the cyclic voltammetry experiments, where a quinone/hydroquinone redox occurs at ca 0.5 V [6.13], but was absent in the current work (Fig. 6.7 a-b). RGO_{AA} and RGO_{HH} samples displayed good current responses at both scan rates of 5 and 100 mV s^{-1} (Fig. 6.7 a-b), and this can be attributed to their pyrrolic- and pyridinic-N functionalities, respectively, which enhanced semi-conducting character (Fig. 6.6). Also, even if RGO_{HH} was the most reduced followed by RGO_{AA} (Tables 6.1-6.2), they both displayed more pseudo characteristics, with narrower and more oblique CV curves, than pristine-GO and RGO_{SB} (Fig. 6.7a). This infers that N-doping in RGO introduced some pseudo characteristics and poor rate capabilities with regards to EDLC behaviour [6.34]. The distorted rectangular CV curves can also be attributed to the ion sieving effect within the electrode pores [6.37]. All the samples exhibited better rate capabilities and low internal resistance at higher scan rates (Fig. 6.7b).

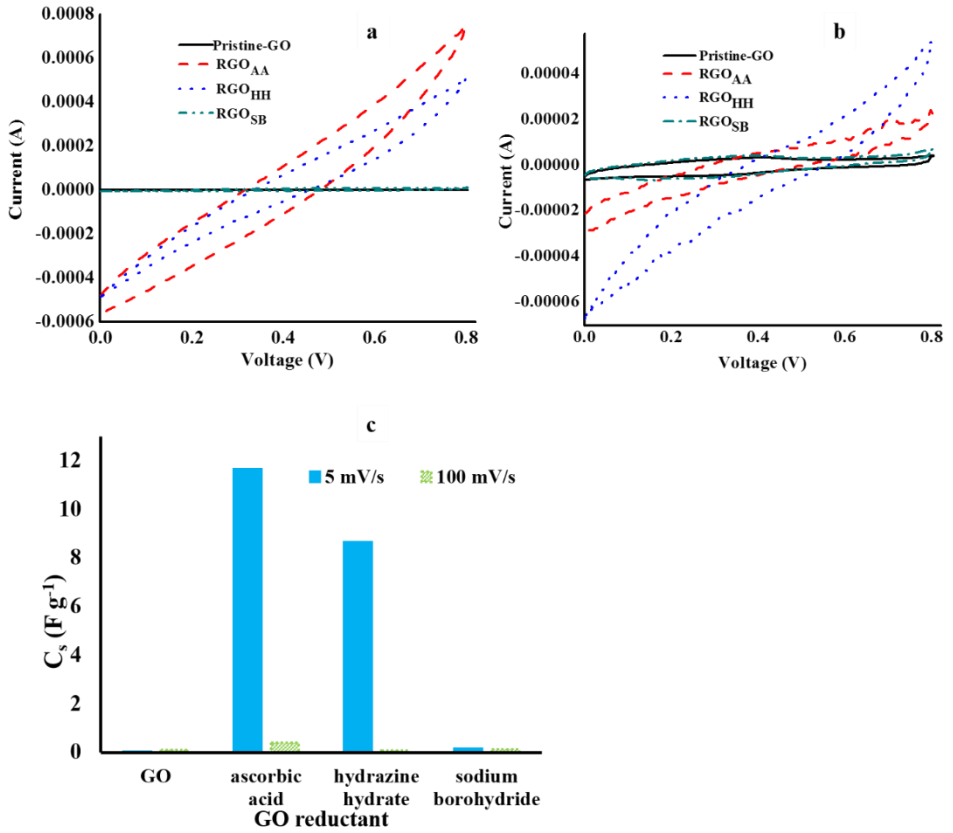

Fig. 6.7. CV curves for pristine-GO and chemically reduced GO at scan rate of (a) 5 mV s^{-1}, (b) 100 mV s^{-1} and (c) specific capacitance (C_s).

The GO reduction improved C_s significantly (Fig. 6.7c) and this can be credited to the structural and morphological modifications, smaller quantities -OH functional groups and O:C ratios, R_i decrease and the semi-conducting character, amongst other factors. The most probable explanation for higher C_s of RGO_{AA} than RGO_{HH} is that pyrrolic N-doped-RGO has lower R_i than pyridinic counterparts (Fig. 6.5 and Table 6.3). The overall higher C_s of N-doped-RGO despite the poor EDLC behaviour, relative to pristine-GO and RGO_{SB}, is because N-doped-RGO has charge storage contributions from both EDLC and pseudo mechanisms. Also, RGO_{SB}, without N, had smaller C_s but higher than that of pristine-GO. This agreed with earlier reports in that heteroatoms and other functional groups increase wettability of carbon-based electrodes and ultimately enhance C_s [6.11,6.34,6.37]. The current results are a basis of the following deductions:

i. Reduction of GO and N-doping of RGO both enhances C_s.
ii. The influence of O:C ratio on C_s. in the current samples is outweighed by N-doping.
iii. Pyrrolic N-doping moieties on RGO are better than pyridinic in terms of C_s.
iv. The surface areas and porosity, determined by nitrogen sorption analysis, were not necessarily available for electrochemical processes.

A possible rationale of these deductions is that pyridinic and pyrrolic N-doping are located near carbon vacancy with two carbon atom neighbours. This facilitates two σ bonds with neighbours, one electron in the p_z orbital for π-bonding and two lone pairs. In this way, electrochemical processes were altered from that of pristine-GO.

6.3.4 Thermal reduction studies

RGO_{HH} was thermally treated at temperatures of 500, 750 and 1000 ˚C to further investigate the influence of textural properties on RGO capacitance. Thermal reduction, except at 1000 ˚C, of RGO_{HH} enhanced both surface area and pore volume (Table 6.4). The sites where oxygen was removed during thermal treatment are the probable influence of the observed larger surface areas and pore volumes. A possible reason for the slight drop in surface area, after thermal treatment at 1000 ˚C, was that even though it restores the graphitic structure, thermal treatment enhanced agglomeration [6.42]. The defect intensity increased (Table 6.4) upon thermal treatment, a possible account of this unusual observation, is that defects such as

dangling bonds are created in the regions where oxygen and nitrogen moieties originally occupied in RGO.

Table 6.4: Textural characteristics and the I_D/I_G ratios determined from Raman spectroscopy of thermally reduced graphene oxide

Reducing temperature	Surface area (m^2/g)	Pore volume (cm^3/g)	Pore size (nm)	I_D/I_G
RGO_{HH}	390.55	0.26	3.45	0.83
500	569.39	0.39	3.43	1.52
750	599.67	0.41	3.49	1.37
1000	584.95	0.47	3.76	1.42

The CV curves at both 5 and 100 mV s^{-1} showed pseudo rectangular shapes. The EDLC quality slightly deteriorated upon thermal treatment at 500 ˚C and scan rate of 5 mV s^{-1} but thereafter improved with temperature raise. The most probable reason is that surface area and pore volume available for N_2 sorption is not necessarily available for the Na_2SO_4 electrolyte [6.3]. Additionally, it has been reported that surface area is not the only influence on C_s [6.1]. Thermal treatment of RGO lessen both N and O at.% [6.11,6.16,6.32], hence, it could be responsible for the observed traits. Additionally, at 100 mV s^{-1}, thermal treatment improved EDLC quality and this can be attributed to enhanced textural properties and hence, temperature of reduction was able to tailor the C_s of RGO. Additionally, the samples reduced at 1000 ˚C was better than RGO_{HH} (Fig. 6.8 c). Whereas, at 100 mV s^{-1}, thermal reduction culminated in enhanced C_s. For thermal reduced RGO, C_s increased with temperature raise (Fig. 6.8c). This means the heat treatment boosts the rate capability of RGO_{HH}.

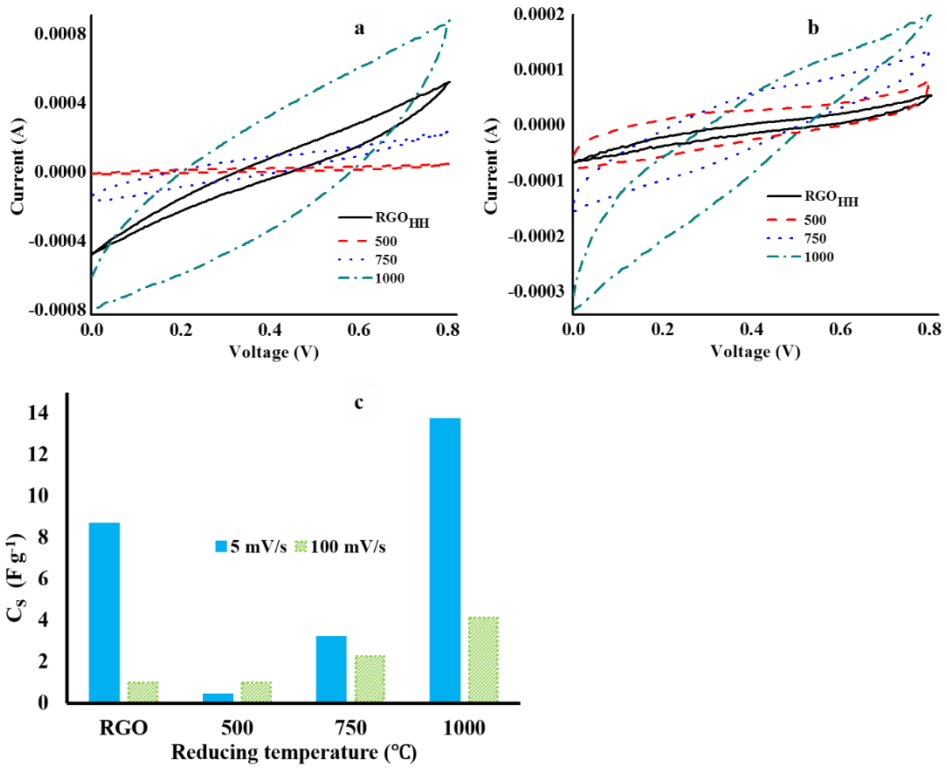

Fig. 6.8. CV curve for thermally reduced GO scan rate of (a) 5 mV s^{-1}, (b) 100 mV s^{-1} and (c) specific capacitance (C_s).

6.4. Conclusions

The major oxygen-containing moieties in the as-synthesised graphene oxide (GO) was C-OH moieties. GO was successfully reduced and the reductants transformed physical and chemical properties. The descending order of oxygen:carbon ratio was pristine-GO, RGO_{SB} (sodium borohydride reduced), RGO_{AA} (ascorbic acid), and RGO_{HH} (hydrazine hydrate reduced) samples. The N functionalities were sp^3 N-C (0.45%), pyrrolic (0.45%) and pyridinic (4.07%) for pristine-GO, RGO_{AA} and RGO_{HH}, respectively. RGO_{SB} B-doped at.% content was of 2.49. Surface area of pristine-GO was improved from 185.43 m^2 g^{-1} to 390.55 m^2 g^{-1} and 599.67 m^2 g^{-1} upon reduction with hydrazine hydrate and subsequent thermal treatment, respectively. Additionally, RGO samples were more thermally stable than pristine-GO and pyridinic-N-RGO was the least defective. Reduction and N-doping transformed metallic conductivity behaviour of pristine-GO to semi-conducting in RGO. RGO_{SB} still retained the intrinsic pristine-GO metallic conducting characteristics at lower temperatures. N-doped-RGO had lower internal resistance, shorter diffusion path lengths and better charge storage performances

than B-doped. On the other hand, pyrrolic-N-doped RGO had lower internal resistance and was more effective in charge storage than pyridinic. The data indicates that thermally treated RGO_{HH} was superior than untreated RGO_{HH}. RGO was tailored to have several attributes such as enhanced N content, semiconducting character, electrochemical behaviour and electrochemical double layer capacitor characteristics.

Acknowledgements

The authors are grateful to the University of KwaZulu-Natal (UKZN) for the infrastructure used in the current study. This research did not receive any specific grant from funding agencies in the public, commercial, or not-for-profit sectors. However, Edwin Tonderai Mombeshora is grateful to the UKZN Nanotechnology Platform for partial study bursary.

Conflicts of interest: none.

References

[6.1] K.P. Singh, D. Bhattacharjya, F. Razmjooei, J.S. Yu, Effect of pristine graphene incorporation on charge storage mechanism of three-dimensional graphene oxide: superior energy and power density retention, Scientific Reports-Nature, 6 (2016) 31555.

[6.2] J.S. Sagu, K.G.U. Wijayantha, A.A. Tahir, The pseudocapacitive nature of $CoFe_2O_4$ thin films, Electrochimica Acta, 246 (2017) 870-878.

[6.3] E.T. Mombeshora, V.O. Nyamori, A review on the use of carbon nanostructured materials in electrochemical capacitors, International Journal of Energy Research, 39 (2015) 1955-1980.

[6.4] R. Mohtadi, F. Mizuno, Magnesium batteries: Current state of the art, issues and future perspectives, Beilstein Journal of Nanotechnology, 5 (2014) 1291-1311.

[6.5] C. Schiattarella, S. Vollebregt, T. Polichetti, B. Alfano, E. Massera, M.L. Miglietta, G. Di Francia, P.M. Sarro, CVD transfer-free graphene for sensing applications, Beilstein Journal of Nanotechnology, 8 (2017) 1015-1022.

[6.6] Y. Bai, M. Du, J. Chang, J. Sun, L. Gao, Supercapacitors with high capacitance based on reduced graphene oxide/carbon nanotubes/NiO composite electrodes, Journal of Materials Chemistry A, 2 (2014) 3834-3840.

[6.7] J. Yang, S. Gunasekaran, Electrochemically reduced graphene oxide sheets for use in high performance supercapacitors, Carbon, 51 (2013) 36-44.

[6.8] C.-J. Kim, W. Khan, D.-H. Kim, K.-S. Cho, S.-Y. Park, Graphene oxide/cellulose composite using NMMO monohydrate, Carbohydrate Polymers, 86 (2011) 903-909.

[6.9] X. Gao, J. Jang, S. Nagase, Hydrazine and thermal reduction of graphene oxide: reaction mechanisms, product structures, and reaction design, Journal of Physical Chemistry C, 114 (2010) 832–842.

[6.10] A. Jana, E. Scheer, S. Polarz, Synthesis of graphene-transition metal oxide hybrid nanoparticles and their application in various fields, Beilstein Journal of Nanotechnology, 8 (2017) 688-714.

[6.11] S. Sandoval, N. Kumar, J. Oro-Solé, A. Sundaresan, C.N.R. Rao, A. Fuertes, G. Tobias, Tuning the nature of nitrogen atoms in N-containing reduced graphene oxide, Carbon, 96 (2016) 594-602.

[6.12] Z. Fan, K. Wang, T. Wei, J. Yan, L. Song, B. Shao, An environmentally friendly and efficient route for the reduction of graphene oxide by aluminum powder, Carbon, 48 (2010) 1686-1689.

[6.13] Y. Shao, J. Wang, M. Engelhard, C. Wang, Y. Lin, Facile and controllable electrochemical reduction of graphene oxide and its applications, Journal of Materials Chemistry 20 (2010) 743-748.

[6.14] Z. Wei, D. Wang, S. Kim, S.Y. Kim, Y. Hu, M.K. Yakes, A.R. Laracuente, Z. Dai, S.R. Marder, C. Berger, W.P. King, W.A. de Heer, P.E. Sheehan, E. Riedo, Nanoscale tunable reduction of graphene oxide for graphene electronics, Science, 328 (2010) 1373-1376.

[6.15] S. Sandoval, N. Kumar, A. Sundaresan, C.N. Rao, A. Fuertes, G. Tobias, Enhanced thermal oxidation stability of reduced graphene oxide by nitrogen doping, Chemistry, 20 (2014) 11999-12003.

[6.16] C.N.R. Rao, K. Gopalakrishnan, A. Govindaraj, Synthesis, properties and applications of graphene doped with boron, nitrogen and other elements, Nano Today, 9 (2014) 324-343.

[6.17] C.K. Chua, M. Pumera, Chemical reduction of graphene oxide: a synthetic chemistry viewpoint, Chemical Society Reviews, 43 (2014) 291-312.

[6.18] L. Valentini, M. Cardinali, E. Fortunati, L. Torre, J.M. Kenny, A novel method to prepare conductive nanocrystalline cellulose/graphene oxide composite films, Materials Letters, 105 (2013) 4-7.

[6.19] J. Zhang, H. Yang, G. Shen, P. Cheng, J. Zhang, S. Guo, Reduction of graphene oxide via L-ascorbic acid, Chemical Communications (Cambridge), 46 (2010) 1112-1114.

[6.20] W.S. Ma, J.W. Zhou, X.D. Lin, X-ray photoelectron spectroscopy study on reduction of graphene oxide with hydrazine hydrate, Advanced Materials Research, 287-290 (2011) 539-543.

[6.21] E.T. Mombeshora, P.G. Ndungu, V.O. Nyamori, Effect of graphite/sodium nitrate ratio and reaction time on the physicochemical properties of graphene oxide, New Carbon Materials, 32 (2017) 174-187.

[6.22] E.T. Mombeshora, P.G. Ndungu, A.L.L. Jarvis, V.O. Nyamori, Oxygen-modified multiwalled carbon nanotubes: physicochemical properties and capacitor functionality, International Journal of Energy Research, (2017).

[6.23] J.I. Paredes, S. Villar-Rodil, P. Solis-Fernandez, A. Martinez-Alonso, J.M. Tascon, Atomic force and scanning tunneling microscopy imaging of graphene nanosheets derived from graphite oxide, Langmuir, 25 (2009) 5957-5968.

[6.24] D.C. Marcano, D.V. Kosynkin, J.M. Berlin, A. Sinitskii, Z. Sun, A. Slesarev, L.B. Alemany, W. Lu, J.M. Tour, Improved synthesis of graphene oxide, ACS Nano, 4 (2010) 4806-4814.

[6.25] V. Dua, S.P. Surwade, S. Ammu, S.R. Agnihotra, S. Jain, K.E. Roberts, S. Park, R.S. Ruoff, S.K. Manohar, All-organic vapor sensor using inkjet-printed reduced graphene oxide, Angewandte Chemie International Edition in English, 49 (2010) 2154-2157.

[6.26] D.C. Marcano, D.V. Kosynkin, J.M. Berlin, A. Sinitskii, Z. Sun, A. Slesarev, L.B. Alemany, W. Lu, J.M. Tour, Improved synthesis of graphene oxide, ACS Nano, 4 (2013) 4806-4814.

[6.27] M. Xu, Q. Huang, X. Wang, R. Sun, Highly tough cellulose/graphene composite hydrogels prepared from ionic liquids, Industrial Crops and Products, 70 (2015) 56-63.

[6.28] W.-S. Hung, C.-H. Tsou, M. De Guzman, Q.-F. An, Y.-L. Liu, Y.-M. Zhang, C.-C. Hu, K.-R. Lee, J.-Y. Lai, Cross-linking with diamine monomers to prepare composite graphene oxide-framework membranes with varyingd-spacing, Chemistry of Materials, 26 (2014) 2983-2990.

[6.29] L.-L. Tan, W.-J. Ong, S.-P. Chai, A.R. Mohamed, Reduced graphene oxide-TiO_2 nanocomposite as a promising visible-light-active photocatalyst for the conversion of carbon dioxide, Nanoscale Research Letters, 8 (2013) 1-9.

[6.30] T. Rath, P.P. Kundu, Reduced graphene oxide paper based nanocomposite materials for flexible supercapacitors, RSC Advances, 5 (2015) 26666-26674.

[6.31] S.D. Perera, R.G. Mariano, K. Vu, N. Nour, O. Seitz, Y. Chabal, K.J. Balkus, Hydrothermal synthesis of graphene-TiO_2 nanotube composites with enhanced photocatalytic activity, ACS Catalysis, 2 (2012) 949-956.

[6.32] K. Gopalakrishnan, K. Moses, A. Govindaraj, C.N.R. Rao, Supercapacitors based on nitrogen-doped reduced graphene oxide and borocarbonitrides, Solid State Communications, 175-176 (2013) 43-50.

[6.33] T.N. Lambert, C.A. Chavez, B. Hernandez-Sanchez, P. Lu, N.S. Bell, A. Ambrosini, T. Friedman, T.J. Boyle, D.R. Wheeler, a.D.L. Huber, Synthesis and characterization of titania-graphene nanocomposites, Journal of Physical Chemistry C 113 (2009) 19812-19823.

[6.34] L. Zhang, G. Shi, Preparation of highly conductive graphene hydrogels for fabricating supercapacitors with high rate capability, The Journal of Physical Chemistry C, 115 (2011) 17206-17212.

[6.35] A.N. Fouda, M.K.A. Assy, G. El Enany, N. Yousf, Enhanced capacitance of thermally reduced hexagonal graphene oxide for high performance supercapacitor, Fullerenes, Nanotubes and Carbon Nanostructures, 23 (2014) 618-622.

[6.36] Z. Weng, Y. Su, D.-W. Wang, F. Li, J. Du, H.-M. Cheng, Graphene-cellulose paper flexible supercapacitors, Advanced Energy Materials, 1 (2011) 917-922.

[6.37] J. Segalini, B. Daffos, P.L. Taberna, Y. Gogotsi, P. Simon, Qualitative electrochemical impedance spectroscopy study of ion transport into sub-nanometer carbon pores in electrochemical double layer capacitor electrodes, Electrochimica Acta, 55 (2010) 7489-7494.

[6.38] K. Gopalakrishnan, A. Govindaraj, C.N.R. Rao, Extraordinary supercapacitor performance of heavily nitrogenated graphene oxide obtained by microwave synthesis, Journal of Materials Chemistry A, 1 (2013) 7563.

[6.39] W.P. Wright, V.D. Marsicano, J.M. Keartland, R.M. Erasmus, S.M.A. Dube, N.J. Coville, The electrical transport properties of nitrogen doped carbon microspheres, Materials Chemistry and Physics, 147 (2014) 908-914.

[6.40] C. Chen, W. Cai, M. Long, B. Zhou, Y. Wu, D. Wu, Y. Feng, Synthesis of visible-light responsive graphene oxide/TiO_2 composites with p/n heterojunction, ACS Nano, 4 (2010) 6425–6432.

[6.41] L.-W. Ji, T.-H. Fang, T.-H. Meen, Effects of strain on the characteristics of InGaN–GaN multiple quantum-dot blue light emitting diodes, Physics Letters A, 355 (2006) 118-121.

[6.42] Y. Wang, Z. Shi, Y. Huang, Y. Ma, C. Wang, M. Chen, a.Y. Chen, Supercapacitor devices based on graphene materials, Journal of Physical Chemistry C 113 (2009) 13103–13107.

Appendix: Supporting information for Chapter 6

Table 6.S1: Elemental analysis of pristine and reduced graphene samples

Sample	C	H	N	O	O:C ratio
Pristine-GO	44.65	2.17	0.39	30.84	0.69
RGO_{AA}	72.99	1.76	0.25	14.92	0.20
RGO_{HH}	72.55	0.67	5.96	9.76	0.13
RGO_{SB}	48.73	0.74	-	19.70	0.40

Table 6.S2: The Raman peak position analysis determined by fitting the spectra into the Lorentzian function

Sample	G-band (cm^{-1})	2D-band (cm^{-1})
Pristine-GO	1595	2330
RGO_{AA}	1599	2331
RGO_{HH}	1597	2334
RGO_{SB}	1593	2329

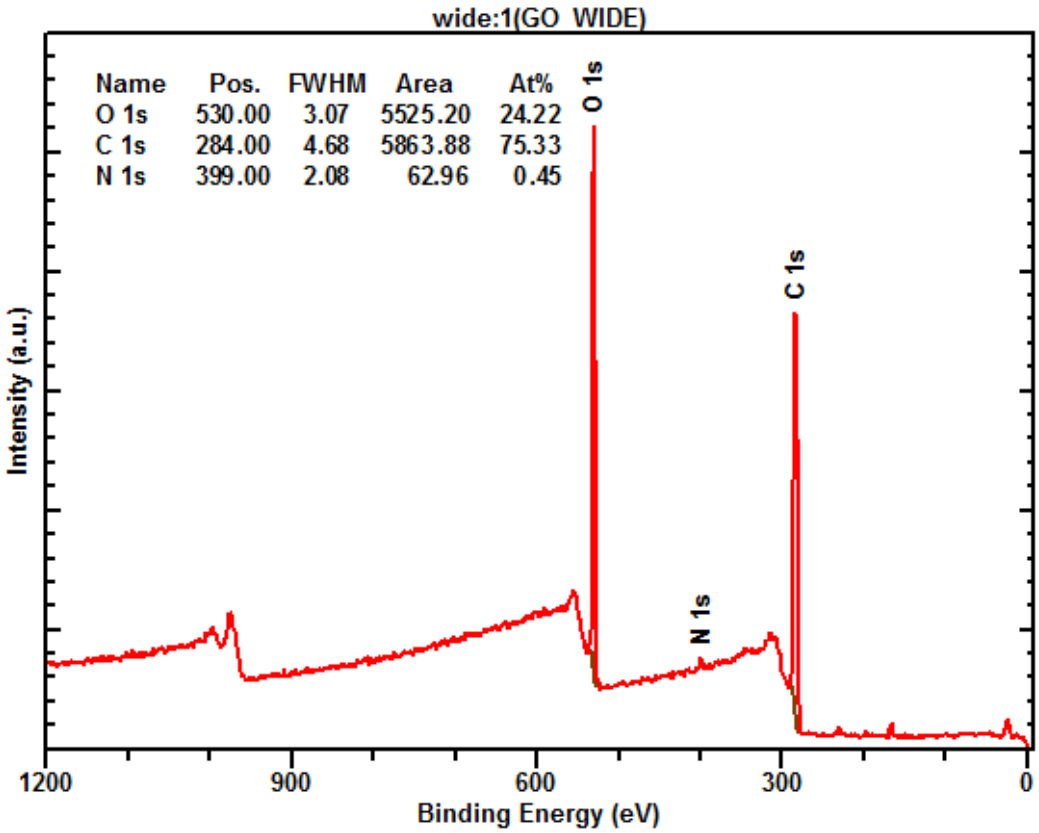

Fig. 6.S1. Representative XPS spectra for as-synthesised GO.

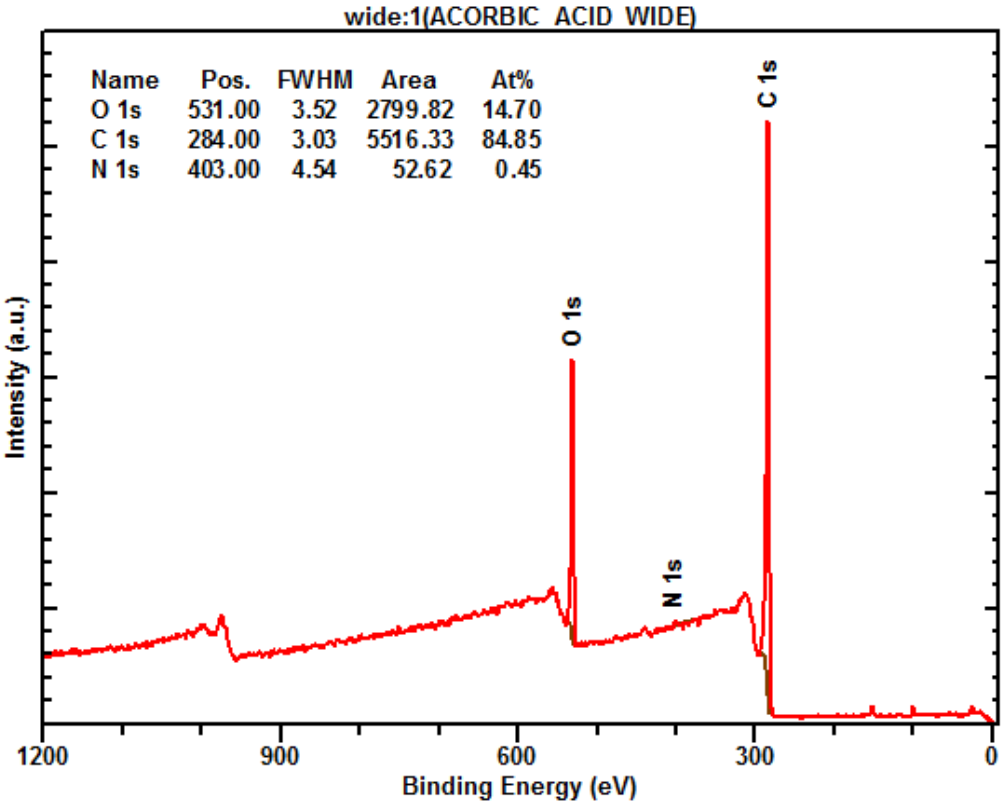

Fig. 6.S2. Representative XPS spectra for RGO reduced by ascorbic acid.

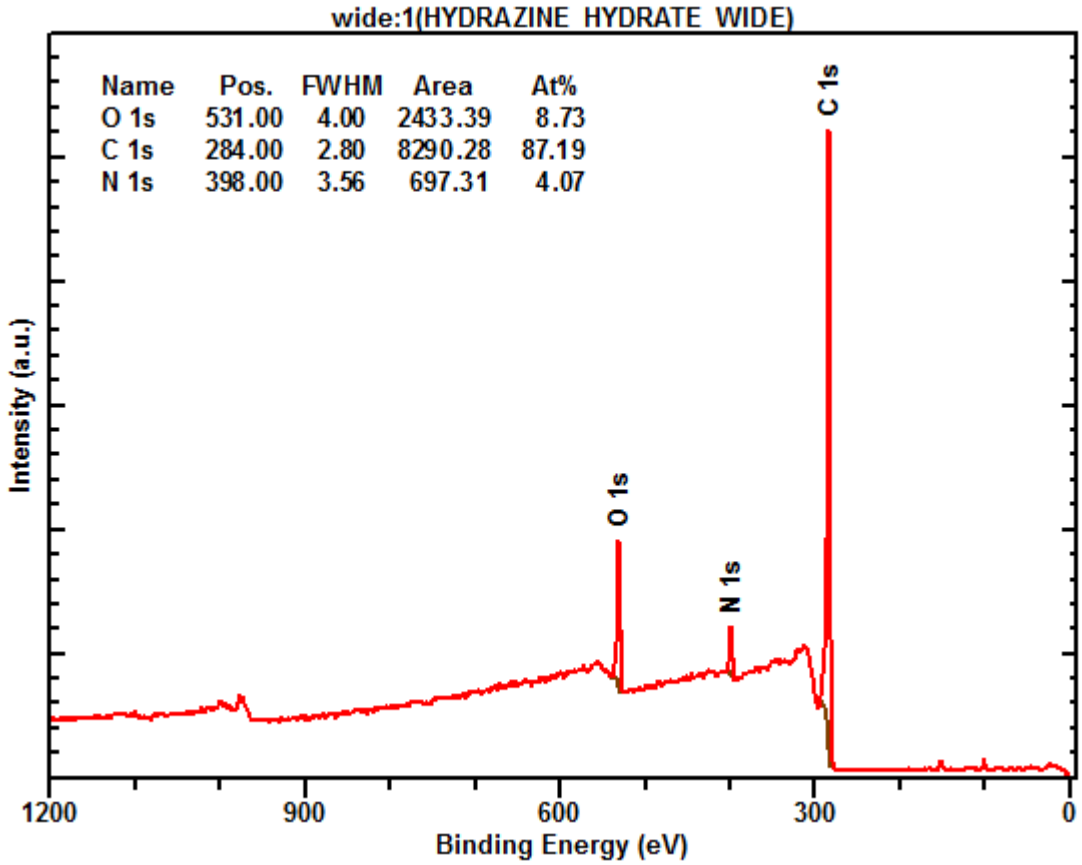

Fig. 6.S3. Representative XPS spectra for RGO reduced by hydrazine hydrate.

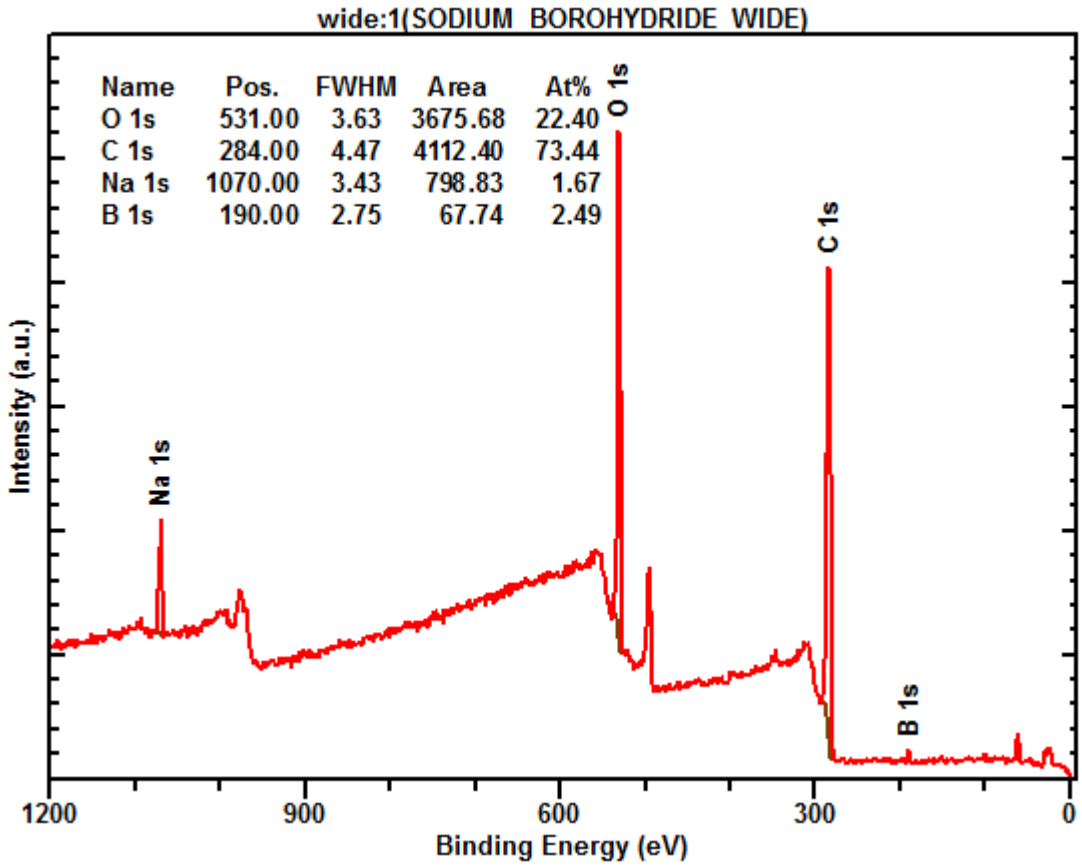

Fig. 6.S4. Representative XPS spectra for RGO reduced by sodium borohydride.

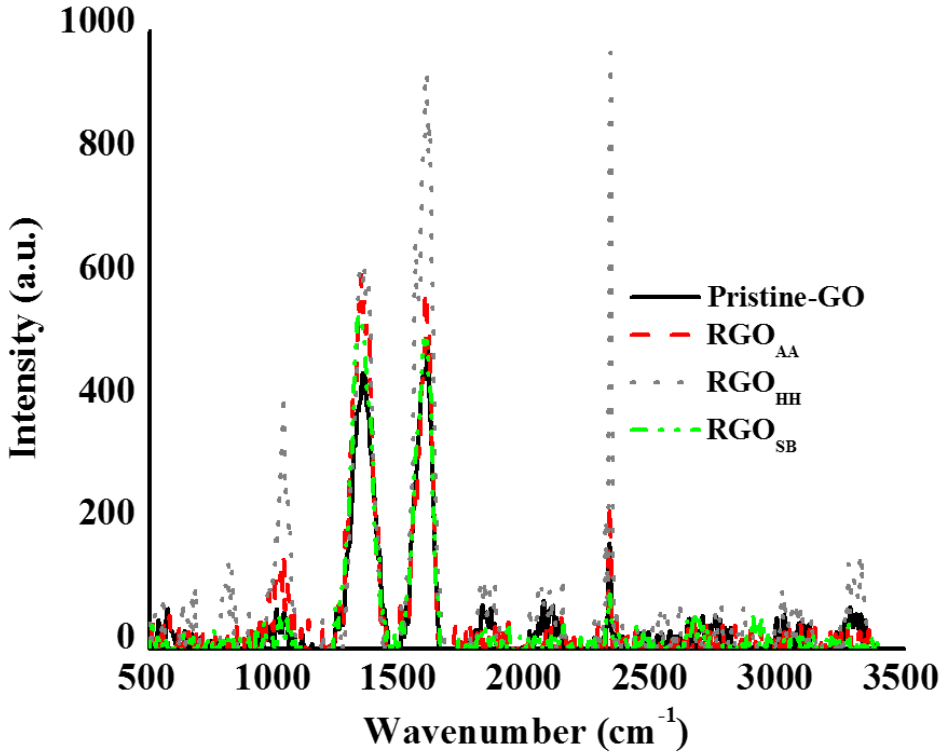

Fig. 6.S5. The Raman spectra for pristine GO and GO reduced with ascorbic acid, hydrazine hydrate and sodium borohydride.

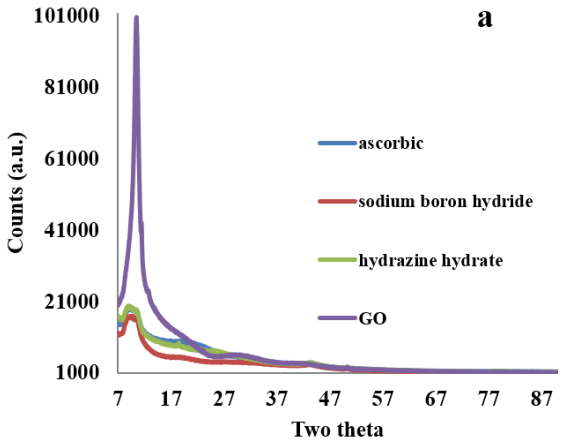

b

Sample	I_D/I_G
pristine-GO	1.27
RGO_{AA}	1.68
RGO_{HH}	0.83
RGO_{SB}	1.42

Fig. 6.S6. (a) Powder XRD spectrum and (b) Raman spectroscopy I_D/I_G ratios for pristine-GO and the RGO samples from different reagents.

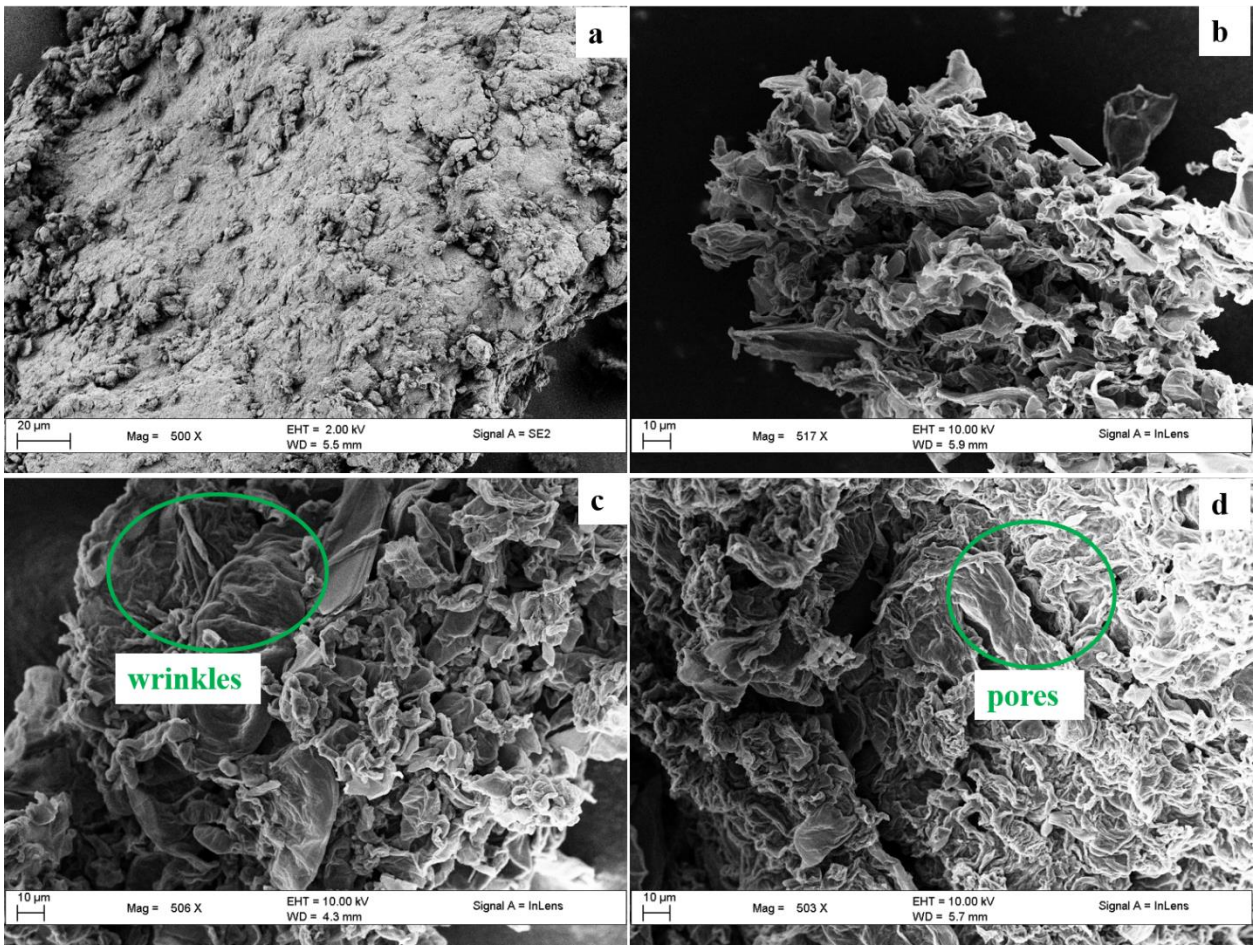

Fig. 6.S7. Scanning electron microscopy images of (a) pristine-GO, (b) RGO_{AA}, (c) RGO_{HH} and (d) RGO_{SB}.

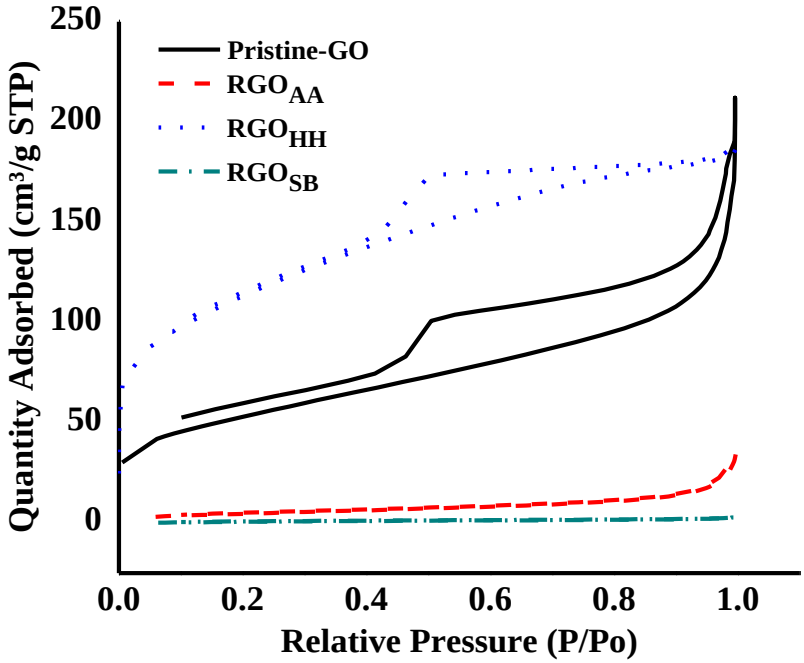

Fig. 6.S8. Textural characteristics for RGO.

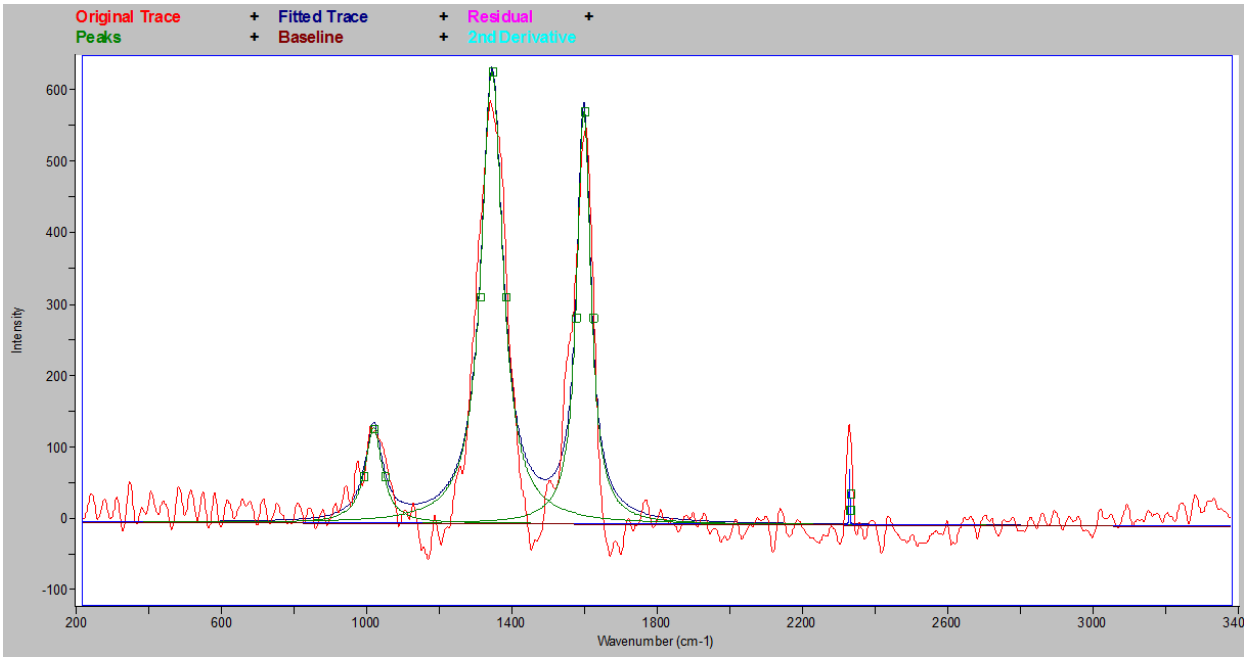

Fig. 6.S9. The representative Raman spectra peak fitting using the Lorentzian function.

Chapter Seven

Physicochemical characterisation of graphene oxide and reduced graphene oxide composites for electrochemical capacitors

Edwin T. Mombeshora and Vincent O. Nyamori*

School of Chemistry and Physics, University of KwaZulu-Natal, Westville Campus, Private Bag X54001, Durban, 4000, South Africa

J Mater Sci: Mater Electron
DOI 10.1007/s10854-017-7821-6

Physicochemical characterisation of graphene oxide and reduced graphene oxide composites for electrochemical capacitors

Edwin T. Mombeshora[1] · Vincent O. Nyamori[1]

Received: 29 May 2017 / Accepted: 29 August 2017

Abstract The aim was to prepare mesoporous composites of graphene oxide (GO) and titania with improved physicochemical properties for use as electrodes in electrochemical double layer capacitors (EDLCs). This was done by using a known amount of titania (5, 10, 20 and 40 wt%) to synthesise graphene oxide-titania (GOTi), reduced graphene oxide-titania (RGOTi) and nanocrystalline cellulose (NCC) reduced graphene oxide-titania (CRGTi) composites by sol–gel method. Titania positively impacted the exfoliation of GO sheets but excess amounts culminated in large titania agglomerates in the composites. The carbon-oxygen-titanium interactions, facilitated by oxygen moieties, were strongest in the GOTi composites. The reduction of GOTi, to form RGOTi, enhanced the surface area from 136.89 to 434.24 $m^2 g^{-1}$ for the 5 wt% titania composites. The RGOTi composites were more defective than the GOTi ones with an I_D/I_G ratio of 1.13 and 0.88, respectively, at 40 wt% titania. Inclusion of NCC in the synthesis of RGOTi composites enhanced the surface areas relative to those of both GOTi and RGOTi at 10–40 wt% titania. The 5 wt% titania RGOTi composite displayed the best EDLC quality with the highest specific capacitance of 45 F g^{-1} in sodium sulfate electrolyte.

1 Introduction

Graphene has been reported as a promising material for the next generation of electrochemical capacitor electrodes, particularly, if the electro-active area is modified and enhanced, amongst other manipulations. For instance, electrolyte ions can be tuned to diffuse easily into mesoporous structures and this lowers equivalent series resistance [1]. However, it is difficult to produce porous materials from graphene because layers easily stack on top of each other [1, 2]. Composite formation is a suitable way to counter that setback and current efforts are devoted to combining separate components to enhance electrochemical performance via synergistic effects [3, 4].

In particular, composites of carbon nanomaterials with titania have the advantage of chemical inertness and stability [3]. Additionally, incorporation of electron-accepting carbon nanomaterials, such carbon nanotubes [5, 6] and graphene [7, 8], enhance titania functionality by reducing electron/hole recombination in electronic devices. On the other hand, semiconductor materials such as titania in graphene-based materials enhance the optoelectronic, electronic, electro-catalytic and photocatalytic properties of GO [9, 10]. Additionally, titania is suitable for electrochemical reactions because

Graphical abstract

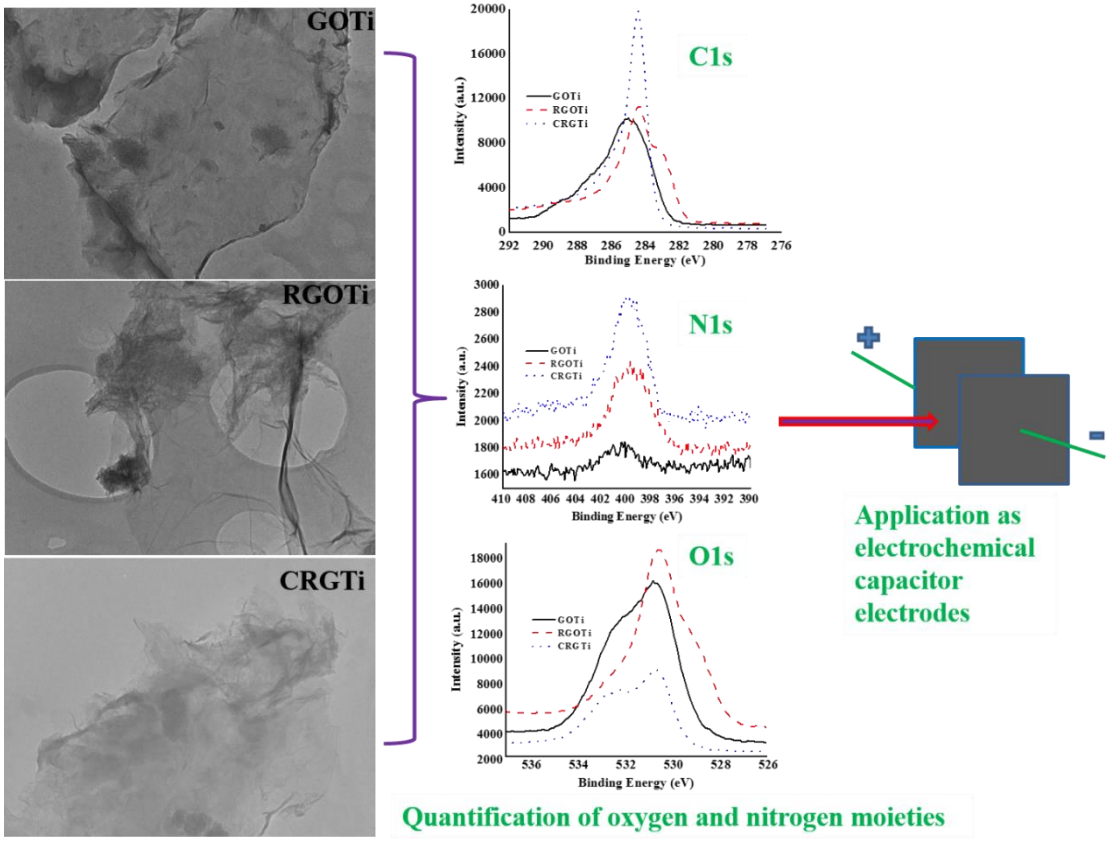

Abstract

The aim was to prepare mesoporous composites of graphene oxide (GO) and titania with improved physicochemical properties for use as electrodes in electrochemical double layer capacitors (EDLCs). This was done by using a known amount of titania (5, 10, 20 and 40 wt.%) to synthesise graphene oxide-titania (GOTi), reduced graphene oxide-titania (RGOTi) and nanocrystalline cellulose (NCC) reduced graphene oxide-titania (CRGTi) composites by sol-gel method. Titania positively impacted the exfoliation of GO sheets but excess amounts culminated in large titania agglomerates in the composites. The carbon-oxygen-titanium interactions, facilitated by oxygen moieties, were strongest in the GOTi composites. The reduction of GOTi, to form RGOTi, enhanced the surface area from 136.89 to 434.24 m^2 g^{-1} for the 5 wt.% titania composites. The RGOTi composites were more defective than the GOTi ones with an I_D/I_G ratio of 1.13 and 0.88, respectively, at 40 wt.% titania. Inclusion of NCC in the synthesis of RGOTi composites enhanced the surface areas relative to those of both GOTi and RGOTi at 10-40 wt.% titania. The 5 wt.% titania RGOTi composite displayed the best EDLC quality with the highest specific capacitance of 45 F g^{-1} in sodium sulfate electrolyte.

Keywords: reduced graphene oxide, graphene oxide, capacitance, titania, cellulose, composites

* Corresponding author*:* Vincent Nyamori, School of Chemistry and Physics, University of KwaZulu-Natal, Westville Campus, Private Bag X54001, Durban, 4000, South Africa

Email: nyamori@ukzn.ac.za Tel.: +27-31 2608256; Fax: +27-31 260309; tamoc88@gmail.com

7.1 Introduction

Graphene has been reported as a promising material for the next generation of electrochemical capacitor electrodes, particularly, if the electro-active area is modified and enhanced, amongst other manipulations. For instance, electrolyte ions can be tuned to diffuse easily into mesoporous structures and this lowers equivalent series resistance [7.1]. However, it is difficult to produce porous materials from graphene because layers easily stack on top of each other [7.1,7.2]. Composite formation is a suitable way to counter that setback and current

efforts are devoted to combining separate components to enhance electrochemical performance *via* synergistic effects [7.3,7.4].

In particular, composites of carbon nanomaterials with titania have the advantage of chemical inertness and stability [7.3]. Additionally, incorporation of electron-accepting carbon nanomaterials, such carbon nanotubes [7.5,7.6] and graphene [7.7,7.8], enhance titania functionality by reducing electron/hole recombination in electronic devices. On the other hand, semiconductor materials such as titania in graphene-based materials enhance the optoelectronic, electronic, electro-catalytic and photocatalytic properties of GO [7.9,7.10]. Additionally, titania is suitable for electrochemical reactions because of its stability against photo- and electrochemical corrosion [7.11,7.9]. Also, the varied oxidation states of transition metals enable easier charge transfer [7.3]. Thus, the inclusion of titania in carbon nanomaterial composites afford many benefits.

Graphene oxide (GO) doped with titania has been widely used in photo-catalysis since GO is known to reduce the band gap of titania [7.11-7.13]. However, GO is not appropriate as a material for electrochemical capacitors (ECs) due to poor conductivity [7.14]. The current work investigates the modification of GO with titania as a strategy to enhance its suitability for use in ECs. A typical more intimate interaction between the components is preferred for easy electron transfer from titania to GO in ECs [7.9,7.15]. Hence, the focus in this regard has been on designing 3D nanostructures that reduce the ion diffusion path length and enhance the surface area available for improved electrochemical processes [7.3,7.14].

ECs are of interest since they are known to be associated with low maintenance costs and longer cycle lives than batteries [7.6]. Additionally, graphene-based materials are ideal for ECs particularly because of their theoretically larger specific surface areas, greater mechanical strength and higher electrical conductivities, amongst other factors. Hence, in this study, reduced graphene oxide (RGO) was used to modify the electrochemical properties of GO, titania and nanocrystalline cellulose (NCC).

Fabrication of graphene based composites requires high quality graphene and effective incorporation into various matrices [7.16]. Two possible approaches are, namely, mixing of the two previously prepared components in solution, and in-situ growth of titania in the presence of a GO solution [7.12]. Several methodologies have been applied in the synthesis of graphene oxide-titania (GOTi) and reduced graphene-titania (RGOTi) composites by using different titania precursors. For example, synthesis of the aforementioned composites has been

conducted from titanium(IV) tetrafluoride by means of hydrolysis [7.12] and liquid phase deposition [7.17], UV-irradiation of GO to obtain RGOTi from titanium(IV) tetrachloride [7.16], titanium(IV) fluoride by a solvothermal approach [7.18] and hydrothermal synthesis from titanium(IV) butoxide [7.9]. In the current work, composites were synthesised by the sol-gel method. Chemical reduction is more suitable for the synthesis of RGO-inorganic composites because of the associated low cost and the provision of several routes for functionalization [7.12]. Previous reports have investigated the influence of the GO wt.% in GOTi composites [7.9], hence, herein, the effects of the TiO_2 wt.% in GOTi, RGOTi and CRGTi synthesised by the sol-gel method from titanium(IV) isopropoxide (TIP) were studied. Additionally, RGO (a closer resemblance to the newest member of the carbon family, graphene), is not well explored in terms of RGOTi composites for electrochemical applications [7.15] such as electrochemical double layer capacitance (EDLC).

Additionally, the current work seeks to investigate the influence of NCC on the GOTi and RGOTi composites. Cellulose is renewable, biodegradable and the most abundant natural polysaccharide. It is regarded as a green, inexpensive and sustainable material [7.19-7.22]. Carbon materials for electrochemical double layer capacitance have been synthesised from cellulose [7.23]. NCC, synthesised by dissolving the amorphous regions by hydrolysis, consists of rod-like NCC whiskers of about 5-70 nm in diameter and lengths of over a hundred nm [7.23,7.24]. Size variations are dependent on the origin of the NCC, and the preparation method and conditions. NCC has abundant hydroxyl groups and is held together by several inter- and intra-molecular hydrogen bonds [7.20]. Blending NCC with other materials is a lucrative direction towards the development of functional composites [7.22].

7.2 Materials

Graphite powder (< 150 µm, 99.99%) and hydrazine hydrate (50-60%) were purchased from Sigma Aldrich. Hydrogen peroxide (30%) from Merck ltd, South Africa. Titanium (IV) isopropoxide (TIP, 97%) was obtained from Alfa Aesar, whilst potassium permanganate (99%), sodium nitrate (99%) and absolute methanol (99.5%, AR,) were all purchased from Associated Chemical Enterprise, South Africa. Sulfuric acid (98.37%) was procured from C.C. Immelmann Ltd, South Africa and was used as-received without dilution.

7.2.1 Experimental methodology

GO was synthesised by a modified Hummer's method as reported earlier [7.25]. In a typical synthesis procedure, graphite powder was mixed in a ratio 1:1 with sodium nitrate. It was thereafter oxidised by use sulfuric acid, potassium permanganate and hydrogen peroxide. NCC synthesis was *via* dissolving pulp attained from a hard wood source, through a hydrolysis treatment with sulfuric acid (65% w/w). To dissolve pulp, 100 mL of sulfuric acid solution was added, and the mixture was stirred vigorously at 60 °C for 1 hour. The mixture was diluted 10-fold with double deionized water to terminate the hydrolysis reaction. The composite synthesis was in several stages as elaborated below.

7.2.2 Synthesis of composites

The targeted titania wt.% values were 5, 10, 20 and 40% on GO for all the composites. In the case of the graphene oxide-titania (GOTi) composites, GO was dispersed in 10 mL of double-deionised water (DI) by ultrasonication for 5 minutes and thereafter predetermined volumes of TIP were added with a micropipette whilst stirring. The mixture was stirred for a further 30 minutes and thereafter sonicated for 10 minutes. The mixture was left under ambient conditions for at least 48 hours and this was followed by drying at 90 °C overnight. Likewise, reduced graphene oxide-titania (RGOTi) composites were synthesised, with the addition of the same amounts of TIP to obtain the same titania to GO ratios as for the GOTi synthesis. The additional steps, after the addition of TIP, involved the addition of hydrazine hydrate (2 mL) followed by raising the temperature to 90 °C and holding it there for one hour before finally vacuum filtering and washing the product several times with DI. A control sample, RTi, was also prepared by adding hydrazine hydrate to TIP in the same manner as in RGOTi composite synthesis. The NCC-reduced graphene oxide-titania (CRGTi) composites were synthesised, similarly to RGOTi, by dispersing GO in DI (10 mL) by means of an ultrasonic water bath for 10 minutes followed by the addition of a predetermined constant volume of NCC (to provide a 1:1 NCC to GO ratio) and the other steps were conducted in the same way as for RGOTi. The composites were named as per the reagent composition, i.e. the intended titania wt.% on GO in the initial mixture.

.

7.2.3 Characterisation techniques

The samples were characterised by means of transmission electron microscopy (JEOL TEM 1010 transmission electron microscope), scanning electron microscopy (JEOL JSM 6100 microscope), attenuated total reflectance Fourier transform infrared spectroscopy (PerkinElmer spectrum 100 series infrared spectrometer with a universal ATR accessory), textural characteristics (Micrometrics TRI STAR 3020 surface area and porosity analyser), powder X-ray diffraction (Rigaku MiniFlex 60), Raman spectroscopy (100 mW Delta Nu Advantage 532^{TM} spectrometer of 10 cm^{-1} resolution with a 2D CCD detector and grating lines of 1800 mm^{-1} with a laser source (Nd:YAG) at a wavelength of 532 nm), X-ray photoelectron spectroscopy (Kratos Axis ultra DLD with an Al monochromatic anode equipped with a charge neutraliser and operating pressure was kept below 5×10^{-9} Torr, emission current of 10 mA, anode voltage (HT) 15 kV, resolution to acquire scan was 160 eV using hybrid lens in the slot mode), cyclic voltammetry (797 VA Computrace Metrohm CT798 application model with a 57970110 dosing processor, using a glassy carbon electrode coated with the composite material, platinum wire counter electrode, Ag/AgCl reference electrode and 0.5 M sodium sulfate electrolyte) and electron impedance spectroscopy (CHI 600E work station, CHI Instruments).

7.3 Results and discussion

The materials in the current study were classified as graphene oxide-titania (GOTi), reduced graphene oxide-titania (RGOTi) and NCC reduced graphene oxide-titania (CRGTi) composites. Their physicochemical and electrochemical properties are compared and discussed in the subsequent sub-sections.

7.3.1 Physicochemical characterisation

The GOTi composites synthesised from a reagent composition of 5, 10, 20 and 40 wt.% titania on GO are discussed first under each subheading. The RGOTi composites, synthesised *via* in-situ reduction of graphene oxide in the presence of titania at 5, 10, 20 and 40 wt.% titania in a similar manner to GOTi composites, are presented second under all the subheadings. Also, the

CRGTi composites, similarly synthesised *via* the in-situ reduction of graphene oxide in the presence of a fixed amount of 50 wt.% NCC and with various titania wt.% of 5, 10, 20 and 40 with respect to RGO are presented last. The wt.% of both titania and NCC were determined with respect to GO in the initial reagent mixture.

7.3.1.1 Textural characteristics

The GO sheets in the synthesised composites displayed increased transparency and were thinner as the amount of titania increased from 5-40 wt.% (Fig. 7.1 a-d). This trend suggests improved exfoliation with increase in titania wt.%. Thus, the TEM images show that addition of titania enhances exfoliation of the GO sheets. The functional groups on GO facilitate its dispersion and hence allow easier absorption in polar matrices, and this enables the formation of GO intercalated exfoliated composites [7.22]. In addition, the ratio of surface area covered with titania to size and/or the number GO sheets covered increased with increase in titania wt.%. Titania was seen to deposit preferentially on the edges and wrinkles. Wrinkles and oxygen functionalities are forms of defects which strain the graphitic structure in the sheets [7.26,7.27]. This is possibly because Ti^{4+} is a hard Lewis acid and functional groups on edges and wrinkles of GO, such as epoxides and hydroxyls, act as a template for nucleation [7.11,7.12].

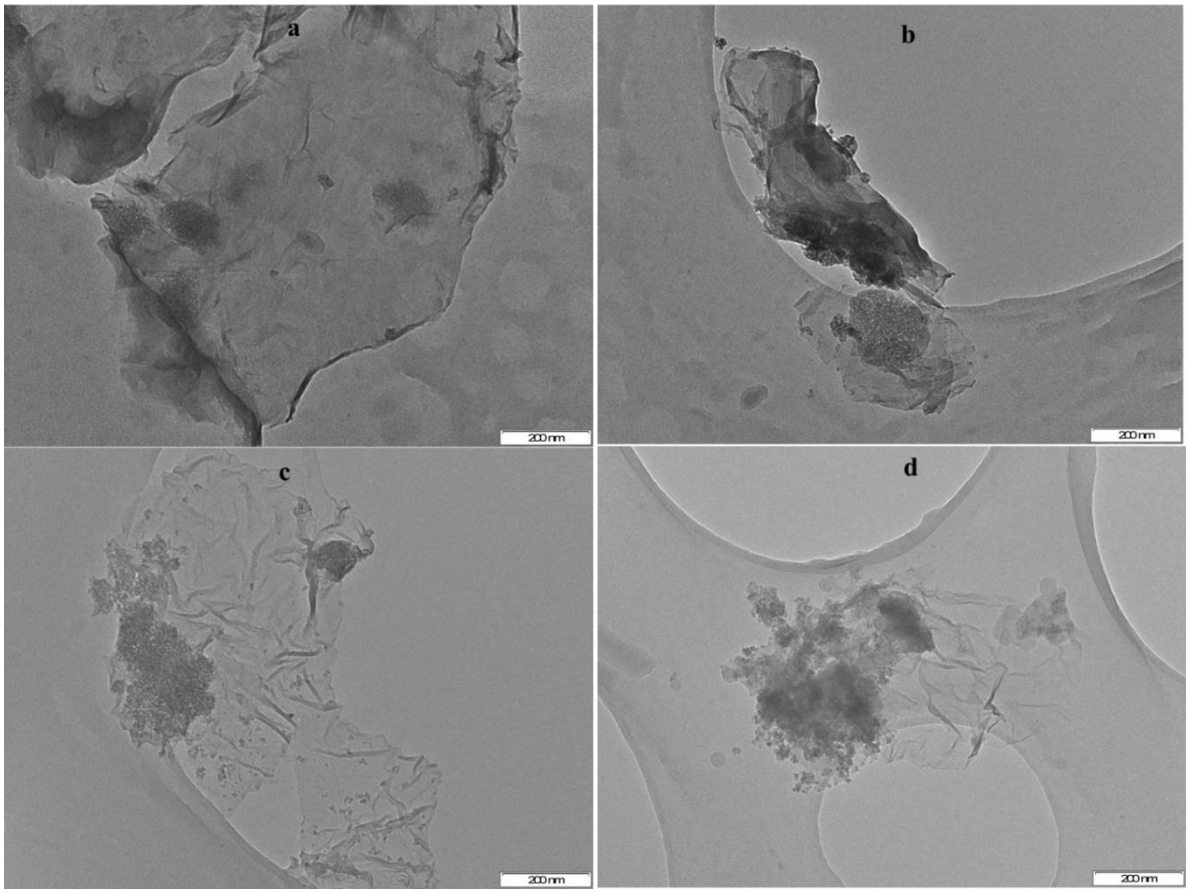

Fig. 7.1 TEM images of GOTi composites for (a) 5%, (b) 10%, (c) 20% and (d) 40% wt.% titania

For the RGOTi composites, hetero-structures with a similar sheet coating to that observed in GOTi (Fig. 7.2 a-d) were produced. The image shown in Fig. 7.2e was a 100% titania control sample made under a similar reducing environment. The traits observed in the composites, that is of increased titania coated sheets with increase in titania wt.%, corroborated with earlier studies that used dissimilar experimental conditions and precursors [7.17,7.11]. This means that the oxygen functionalities in RGOTi, like in GOTi, help to control the composite morphology by regulating the nucleation of titania crystallites against growth.

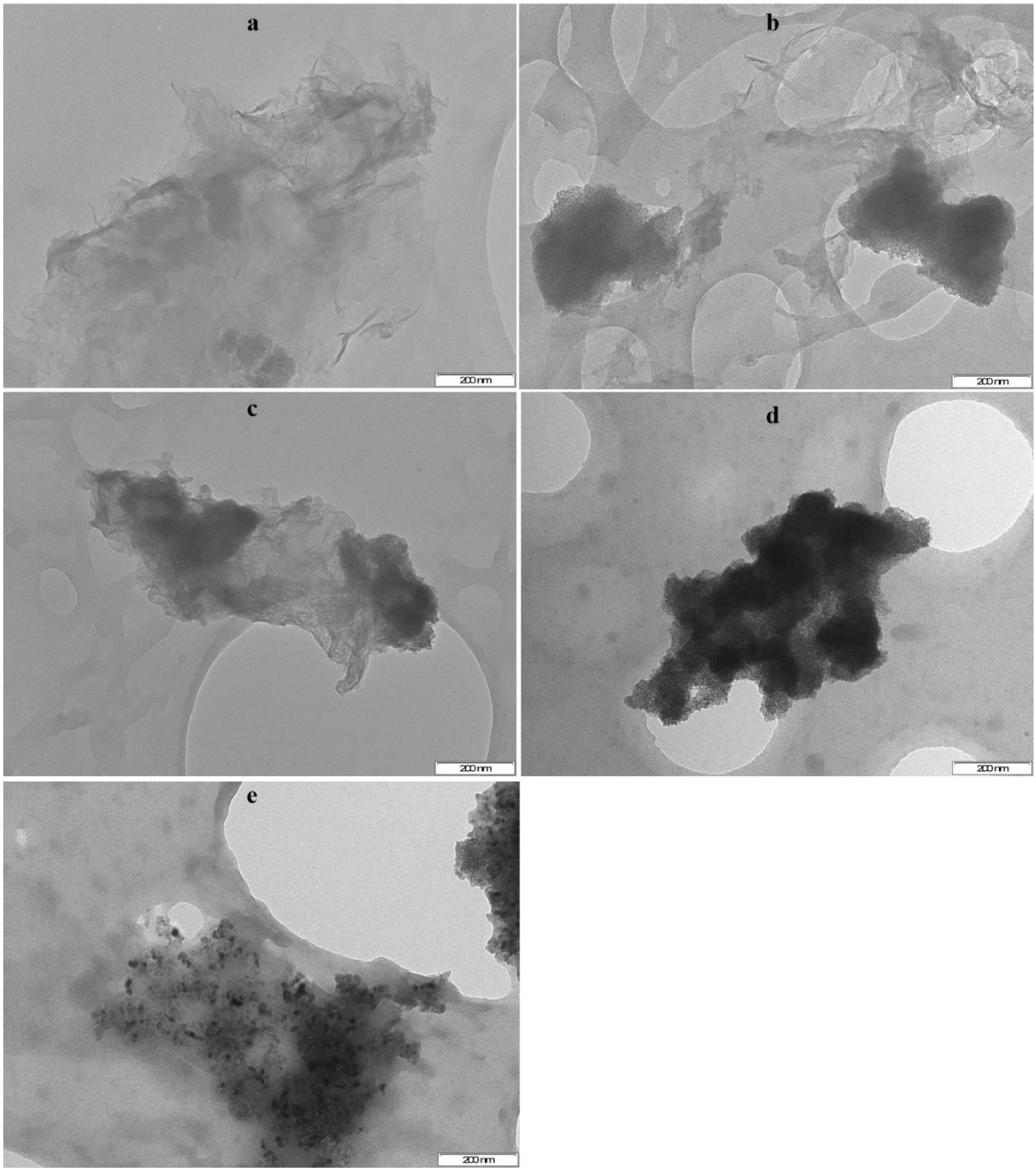

Fig. 7.2 TEM images of RGOTi composites for (a) 5%, (b) 10%, (c) 20%, (d) 40% and (e) 100% titania.

Thin transparent films of CRGTi composites with opaque regions were obtained when NCC was added to the RGOTi composites (Fig. 7.3). This indicates successful exfoliation of RGO sheets followed by coating with titania. The coating intensity in CRGTi was seen to increase with increase in titania wt.%, from 5 to 40 wt.% titania (Fig. 7.3). Also, it cannot be clearly

established where the NCC sits in the composites. This suggest a more intimate interaction with RGO and minimal agglomeration of both components. Furthermore, the intensity of titania coverage was similar to that in the RGOTi and GOTi composites which was influenced by the wt.% of titania.

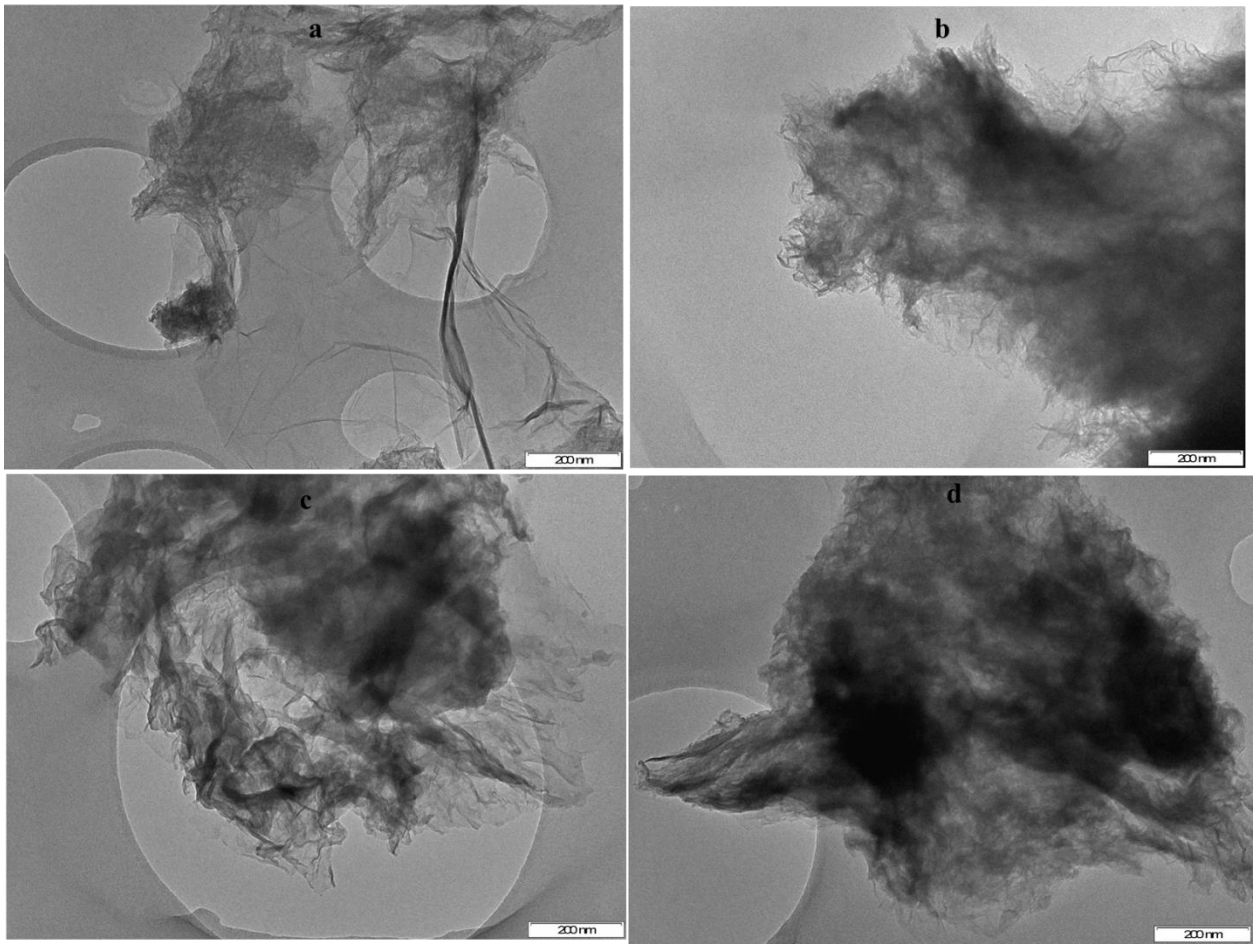

Fig. 7.3 TEM images of CRGTi composites for (a) 5%, (b) 10%, (c) 20% and (d) 40% titania

7.3.1.2 Surface morphology

Many difficulties were encountered during SEM analysis due to the high sample conductivity. The sizes of agglomerates increased with increase in the titania wt.% added during the GOTi composite syntheses (Fig. 7.4a-d). This is due to the high rate of nucleation at higher TIP concentrations. Lambert et al. [7.12] reported similar observations but theirs were seed-like agglomerates at high titania ratios. Additionally, the GO surface was a suitable matrix for titania nucleation and the number of separate crystallites increased with titania wt.%. This is a clear indication that varying the titania wt.% is a suitable approach for modifying the

morphology of typical composites with the possibility of altering other physical properties such as textural characteristics and Raman vibrations.

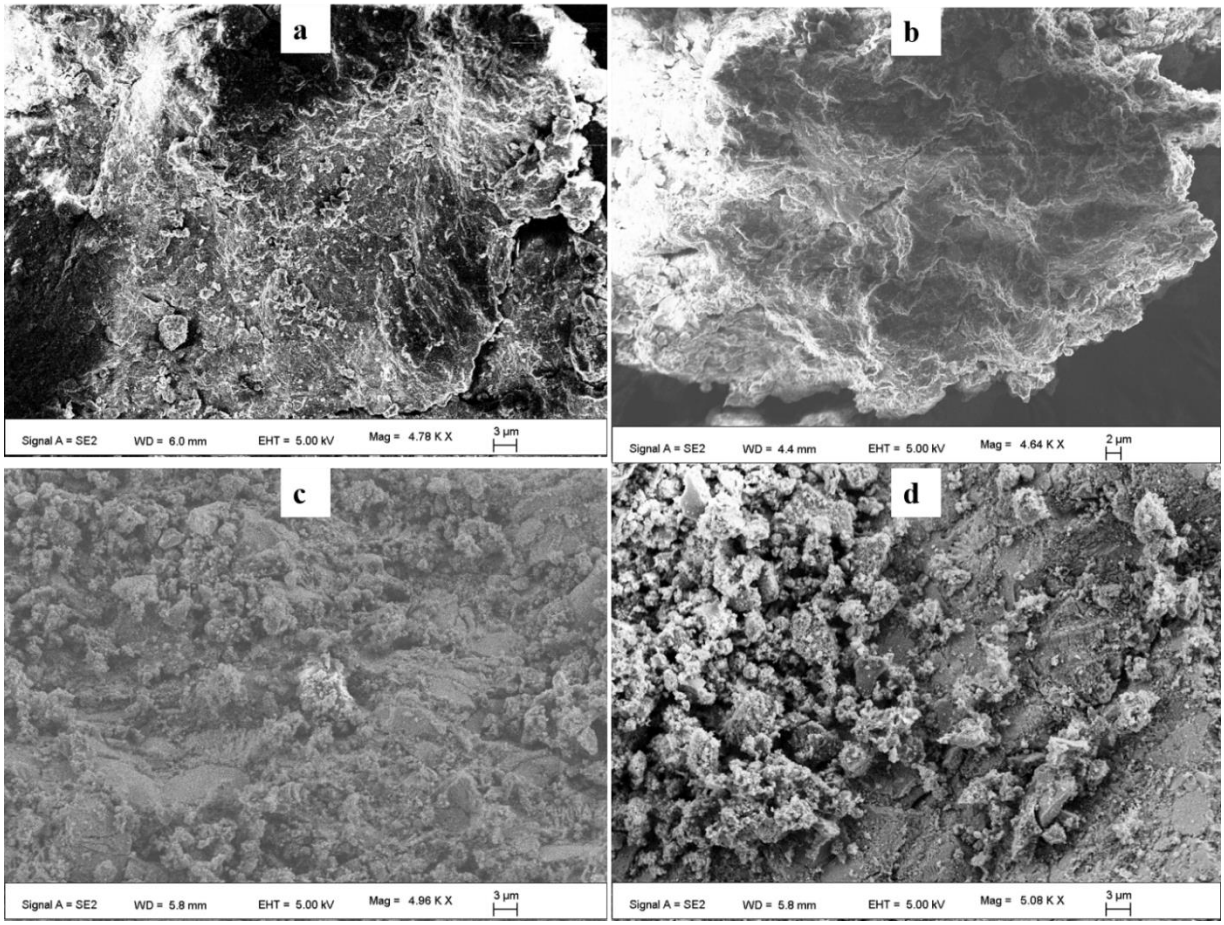

Fig. 7.4 SEM images of GOTi composites at titania wt.% of (a) 5%, (b) 10%, (c) 20% and (d) 40%

Similarly, the agglomerate sizes of titania also increased with increase in wt.% on RGO composites (Fig. 7.5a-d) and this corroborated with the TEM observations. A possible cause of this effect is the residual oxygen-containing groups on the RGO sheets that directed the particulate growth. Hence, despite the titania agglomeration, an increase in the number of titania particles tends to effect a more open RGO sheet morphology (Fig. 7.5a-d). On the other hand, a comparison of Fig 7.5 a-d with Fig. 7.5e clearly shows that RGO acted as a substrate that reduced titania agglomeration.

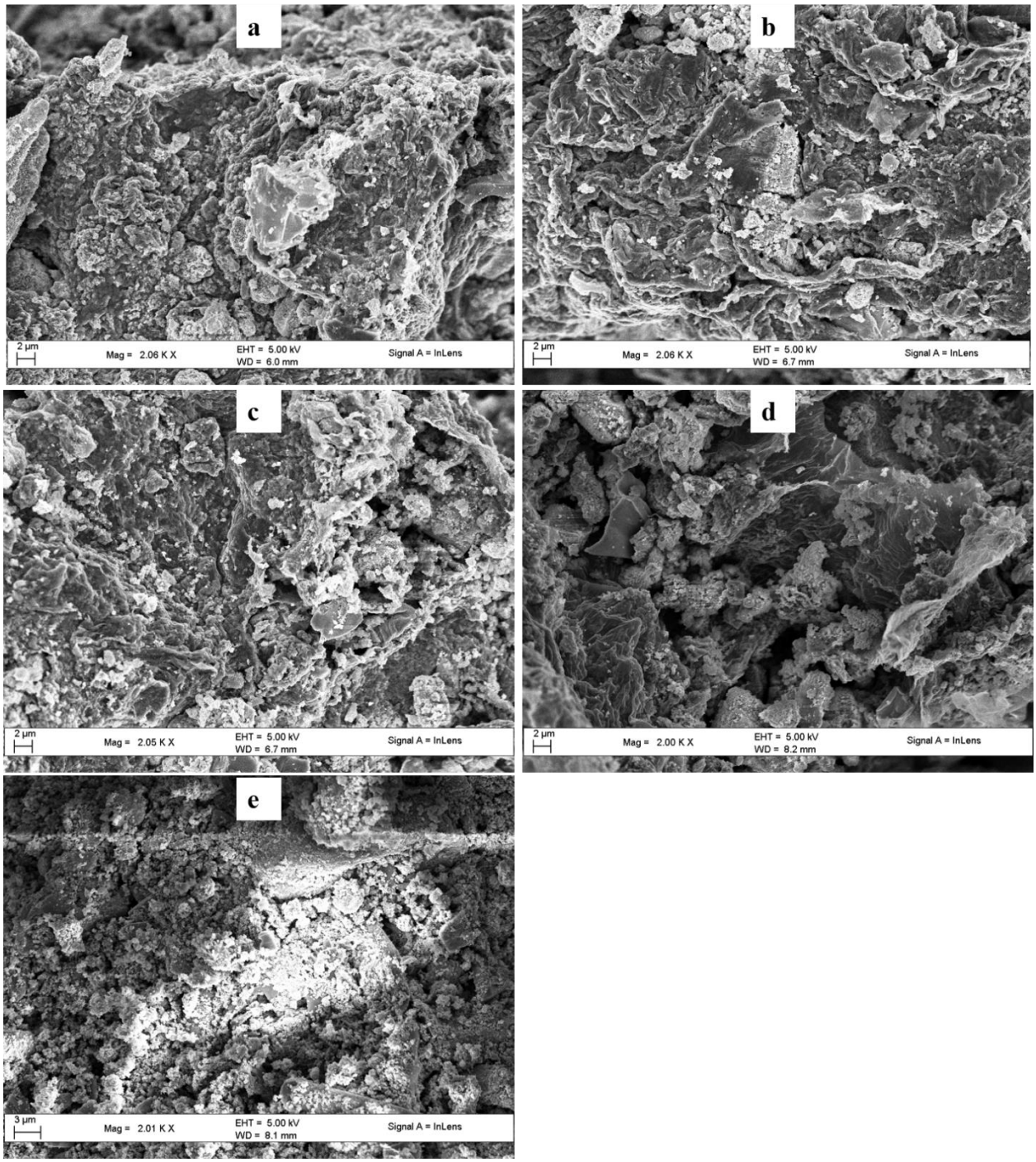

Fig. 7.5 SEM images of RGOTi composites of (a) 5%, (b) 10%, (c) 20%, (d) 40% and (e) 100% titania

With regards to the CRGTi composites, the SEM images exhibited rippled titania-coated reduced graphene oxide sheets (Fig. 7.6) with notable agglomerates. The sizes of the titania agglomerates in the RGOTi samples increased with titania wt.%. Again, NCC could not be clearly identified in the CRGTi samples.

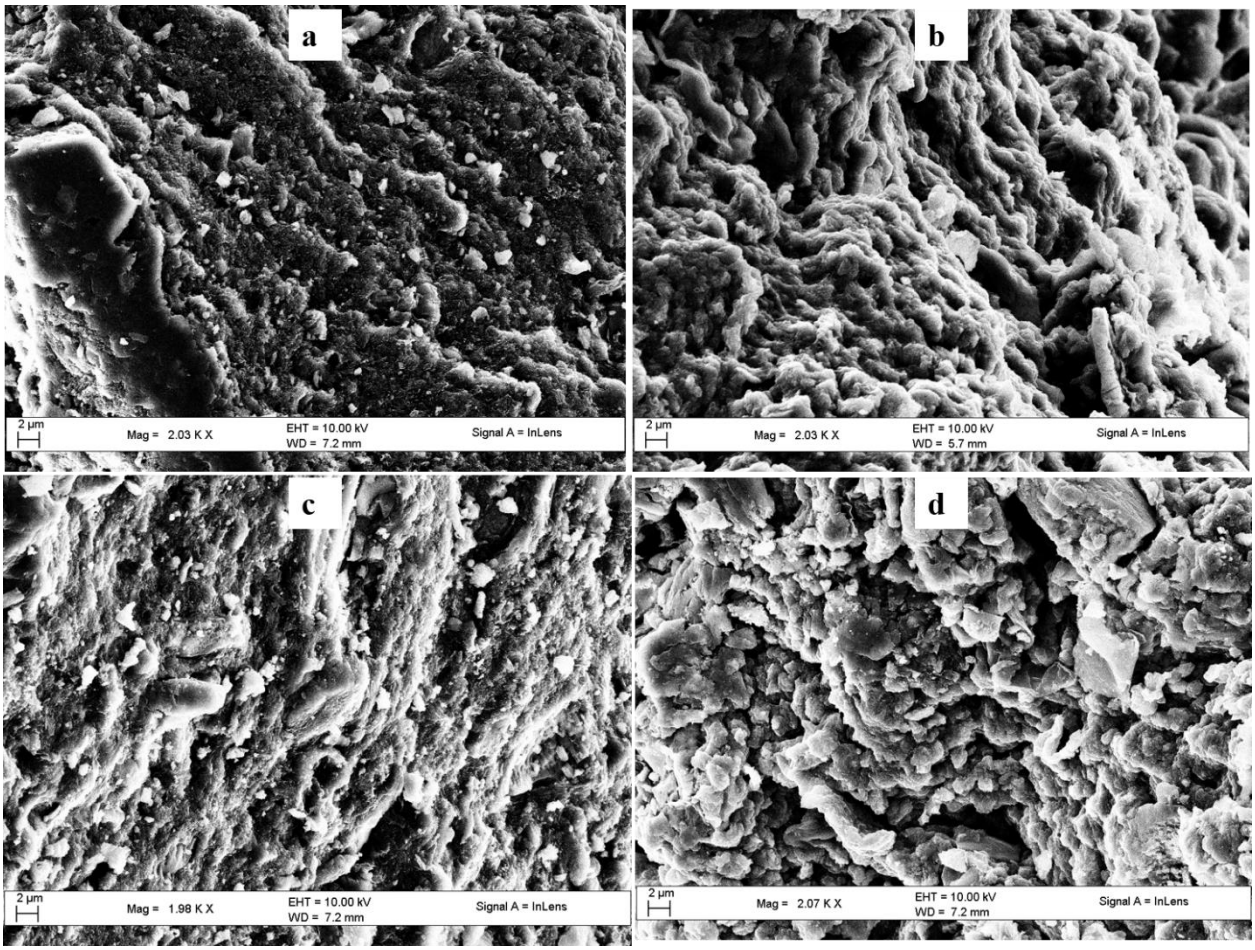

Fig. 7.6 SEM images of CRGTi composites at (a) 5%, (b) 10%, (c) 20% and (d) 40% titania

7.3.1.3 Surface functional groups

The FTIR peaks at ca. 3400, 1600 and 800 cm^{-1} due to O-H stretching vibrations, aromatic sp^2 C=C bonds and Ti-O-C bonding vibrations [7.28-7.31], respectively (Fig. 7.7a), were more intense in the 10 wt.% titania GOTi. Additionally, the peaks at ca. 1250 and 1400 cm^{-1}, attributed to epoxy C-O and carboxy C-O vibrations [7.28,7.32], decreased with increase in titania content (Fig. 7.7a). A large number of oxygen-containing moieties on graphitic frameworks are often associated with a higher defect intensity [7.25,7.33,7.27]. A possible explanation is that oxygen-containing functionalities act as anchoring sites for titania, hence, titania can be viewed as sitting on defects. This corroborates with the TEM images that showed titania preferring edges and wrinkles of GO for nucleation. This means that introduction of titania is associated with some chemical interactions which culminates in an intimate interfacial contact [7.18,7.11] and this is expected to impact the electrochemical processes on the surface.

Also, only the 5 wt.% titania GOTi composite displayed a peak at ca. 2300 cm^{-1} and this peak is due to carbon dioxide captured from the atmosphere [7.34].

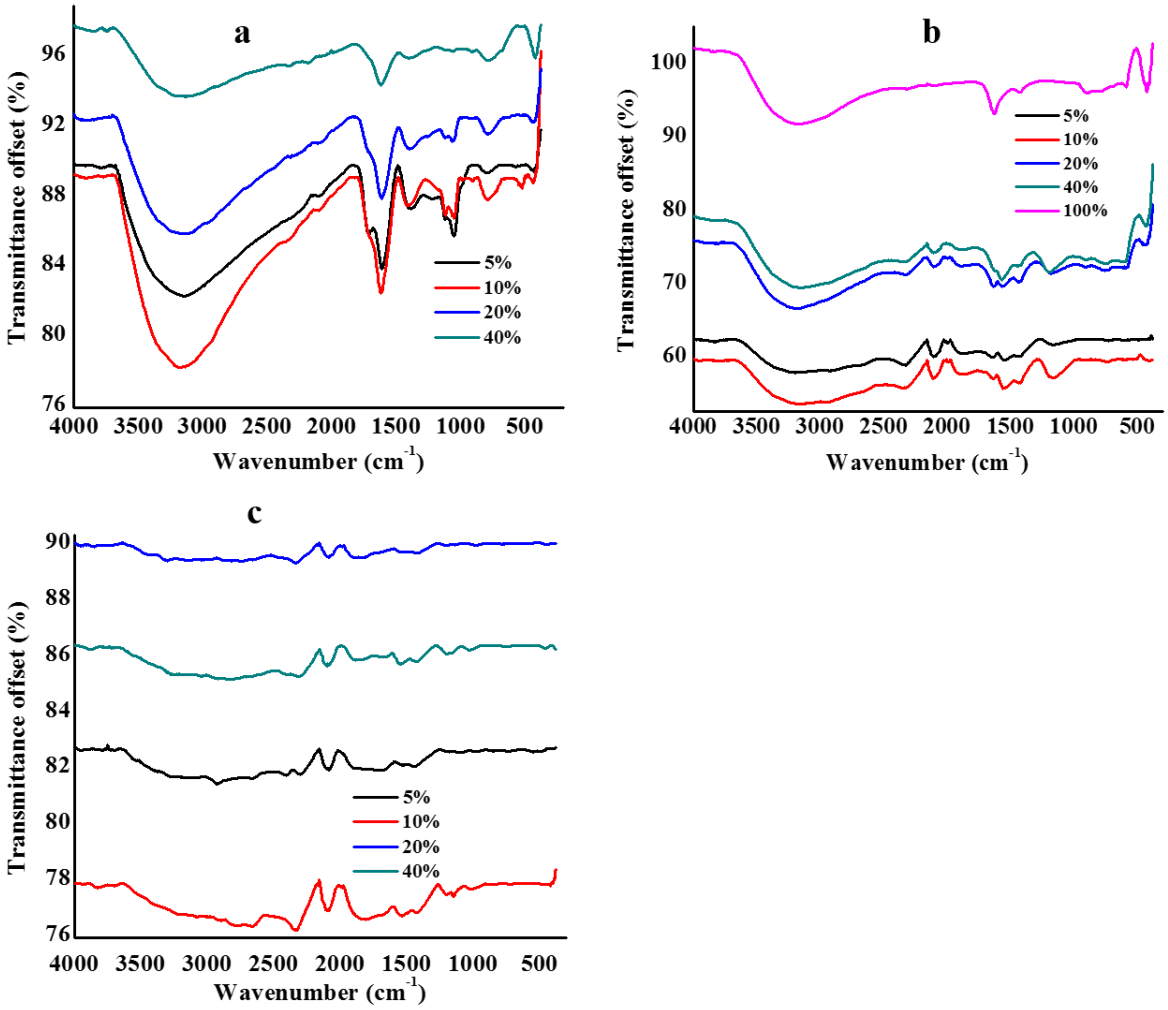

Fig. 7.7 The ATR-FTIR spectra of (a) GOTi, (b) RTi and RGOTi and (c) CRGTi composites at various titania wt.%

For the RGOTi composites, the peaks at 3400 and 1700 cm^{-1}, representing OH and C=O, respectively, were present in all samples including RTi (100% Ti, Fig. 7.7b). This means the RGOTi composites and RTi were hydrophilic and contained some carboxy C=O bonds from the precursor TIP. Similar observations, from P25-graphene composites synthesised by the hydrothermal method, were reported by Zhang et al. [7.30]. The peak at 2300 cm^{-1}, assigned to carbon dioxide captured from the atmosphere [7.34], had the highest intensity in the 5 wt.% titania RGOTi sample and decreased with increase in titania wt.% (Fig. 7.7b). Additionally,

the peak was absent from RTi. Also, the peak at ca. 1250 cm^{-1} due to C-O-C vibrations was absent in pure titania, RTi, and this infers that its source can only be unreduced C-O-C moieties from GO. The small peaks at 500 cm^{-1} were absent in 5 and 10 wt.% titania RGOTi samples (Fig. 7.7b) and this peak can be ascribed to the Ti-O-Ti vibrations of titania [7.30,7.35].

The IR spectral peaks in the CRGTi composite were generally weaker than those of the RGOTi samples (Fig. 7.7b-c) and a possible reason for this is the occurrence of a chemical transformation between the constituents of the composites upon inclusion of NCC. The broad and low intensity peak at 3400 cm^{-1} is due to O-H stretching vibrations from water. This may suggest that NCC interferes with the hydrogen bonded water molecules between RGO sheets [7.36], and displaces them. No clear trend in terms of the peak intensity at 2200 cm^{-1} in relation to the titania wt.% is evident. This peak is assigned to carbon dioxide captured from the atmosphere [7.34]. Variations due to the presence of NCC were not expected since it was present in a constant amount in all the RGOTi composites. All samples had broad peaks at ca. 1740 and 1600 cm^{-1} (Fig. 7.7c), and this was assigned to the carboxyl C=O group from either carbonyl or carboxylic groups and C=C, respectively [7.28,7.32]. A possible reason for the peak broadening is the existence of an intramolecular hydrogen bond due to the presence of NCC in the composites [7.21]. This is highly likely as a result of the more intimate interaction deduced from the morphological studies (Fig. 7.3). The epoxy C-O-C vibration peak at 1200 cm^{-1} was more pronounced in 10 and 20 wt.% titania whilst it was absent in the other CRGTi composites. The absence of this peak at both extreme loadings is probably due to obscuring of the vibrations by more titania in the composites.

7.3.1.4 Surface area and porosity

For the determination of textural properties, the composites were preheated under vacuum to a temperature of 200 °C. This was done to remove any contaminants adsorbed onto the surface [7.37]. Adsorption isotherms were then deduced from the quantity of nitrogen adsorbed at 77 K and the various gas pressures. As pressure is increased, an adsorption monolayer forms and a further increase in the gas concentration culminates in the formation of multiple layers [7.37,7.38]. A further pressure increase facilitates capillary condensation in the pores. At saturation, all pores are filled with liquid nitrogen and hence, the total pore volume can be determined [7.37]. A decrease in pressure will cause a desorption process. The desorption and adsorption branches of isotherms give useful information on porosity and surface area. This is

mostly calculated by use of the Brunauer-Emmett-Teller (BET) theory which gives the total surface area available for nitrogen sorption [7.37,7.39,7.40].

The textural characteristics in the current report clearly show, as did the work reported by Xiang et al. [7.9], a corresponding increase of both BET surface area and porosity (Table 7.1) with increase in titania wt.% in the GOTi composites. The present results can be attributed to enhanced titania coated surfaces as well as anchored crystallites on the GO sheets, and morphological variations such as numerous separate crystallites and an increase in exfoliation levels (Fig. 7.1 and 7.4). Increased exfoliation facilitates the creation of spaces between sheets by reducing agglomeration whilst nitrogen sorption by the titania particles also increasingly contributed to both the BET surface area and pore volume. Despite the aforementioned traits, there was no clear relationship between the titania wt.% and the pore sizes of the GOTi composites in the current study. This means the observed increase in pore volume was not influenced by pore sizes.

Table 7.1 Textural characteristics of GOTi, RGOTi and CRGTi composites

Composite	% Ti	Surface area (m^2/g)	Pore volume (cm^3/g)	Pore size (nm)
GOTi	0	118.40	0.04	3.17
	5	136.89	0.16	4.41
	10	164.11	0.19	4.15
	20	171.05	0.24	4.98
	40	201.60	0.29	4.88
RGOTi	0	390.55	0.26	3.45
	5	434.24	0.41	3.94
	10	377.01	0.43	4.26
	20	255.99	0.46	6.74
	40	210.95	0.46	7.47
RTi	100	117.89	0.37	9.56
CRGTi	5	394.24	0.30	3.43
	10	409.96	0.30	3.43
	20	401.26	0.31	3.48
	40	330.29	0.28	3.62

It is a common phenomenon to have a decrease in surface area upon reduction of GO to RGO due to restacking which is facilitated by intensive π-π interactions [7.6]. It is interesting to note a reverse circumstance in the current study (Table 7.1). This observation was attributed to both the presence of titania and residual oxygen in the composites. A loading of 5 wt.% titania enhanced the surface area of RGO (Table 7.1) which was also higher than that of RTi. A possible account for this observation is the existence of a chemical interaction between titania and the RGO sheets that inhibits agglomeration. The higher surface areas at lower titania wt.% are attributed to the corresponding smaller pore sizes (Table 7.1) and the smaller titania crystallite sizes (Fig. 7.5). From 10-40 wt.% titania, the surface areas of the RGOTi composites decreased with increased titania content and the values were in-between those of RGO and RTi (Table 7.1). This may suggest that beyond 5 wt.% titania, additional titania just sits or is deposited on the RGO sheets without necessarily being involved in a chemical interaction. This highlights the effects of the titania wt.% in the RGOTi composites on the textural characteristics. Similar composites prepared hydrothermally from TIP and reduction by NaOH recorded lower surface areas of 235 [7.12], 83 [7.9] and 22 $m^2\ g^{-1}$ [7.41] , respectively.

Unlike the RGOTi composites, for the CRGTi composites the surface area increased between 5 and 10 wt.% titania, and thereafter decreased with increase in titania content (Table 7.1).

Also, the variation in terms of pore sizes was negligible, hence, unlike in the RGOTi composites, the variation in surface area was not influenced by pore sizes. It was particularly interesting to note that the introduction of NCC blocks the ability to positively tailor the pore volumes and sizes by varying the titania wt.%. Pore sizes increased slightly between 10 and 40 wt.% titania, relative to those of RGO, in the CRGTi composites. The surface areas of the CRGTi composites at 10-40 wt.% titania were higher than for the corresponding composites for both GOTi and RGOTi (Table 7.1). This is attributed to morphological properties (Fig. 7.3 and 7.6).

In addition, the amount of sorbed nitrogen which clearly increased with increasing titania wt.%, for all GOTi composites showed clear hysteresis loops with H3-type isotherms (Fig. 7.8a). This means an increase in titania wt.% enhanced the mesoporosity in the GOTi samples. Additionally, Fig. 7.8a shows that increasing the titania wt.% leads to reduced participation of small pores in nitrogen sorption (region indicated by circle) and this can be attributed to titania blocking the smaller pores first.

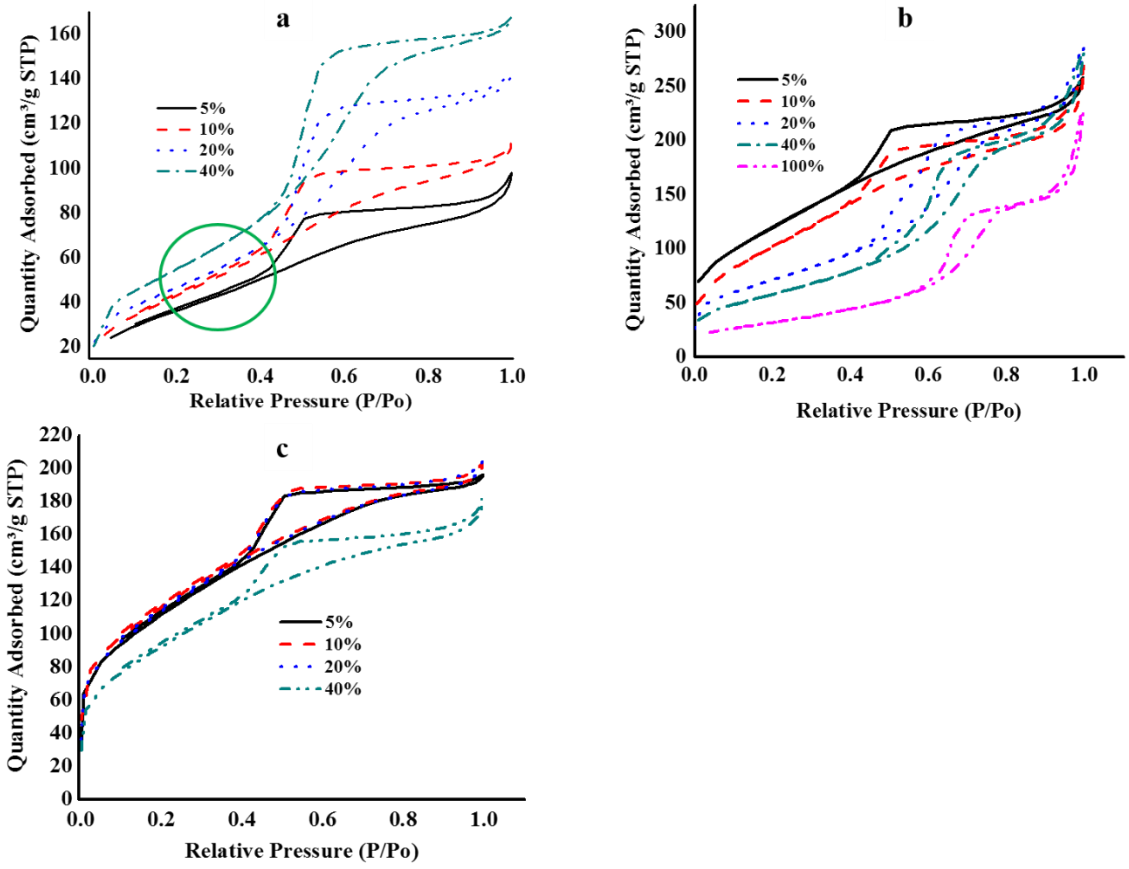

Fig. 7.8 N_2 adsorption isotherms for (a) GOTi, (b) RGOTi and (c) CRGTi composites

The RGOTi composites had higher pore volumes than both RGO and RTi. This can be rationalised by the presence of both a chemical interaction between the titania and RGO sheets, that culminated in enhancement, and the excess titania physically sitting on the RGO sheets. Pore sizes and volumes increased with an increase in titania content, and this means that the porosity in typical RGOTi samples can be positively tailored by varying the titania wt.% (Table 7.1 and Fig. 7.8b). The ability to tailor pore sizes with titania wt.% was a distinguishable feature observed with GOTi composites. Also, all the pore sizes fell in the range 3-10 nm and this means the material was mesoporous. This corroborated with the type IV isotherms with H3-type hysteresis displayed for all RGOTi composites (Fig. 7.8b). A noticeable feature was that RTi exhibited a type V isotherm with an H-3 hysteresis. This suggests a transformation of the weak titania/nitrogen interaction to stronger RGOTi/nitrogen interactions in composites.

However, relative to RGOTi, addition of NCC reduced the porosity in the composites (Table 7.1). All titania wt.% loadings showed a typical H3-hysterisis and a type IV isotherm (Fig. 7.8c). All the composites showed similar mesoporosity characteristics irrespective of the titania wt.%.

7.3.1.5 Phase composition

In the PXRD diffractograms, the peak intensity at ca. 10° 2θ, assigned to the 002 reflection of GO sheets [7.18], was almost the same for all GOTi composites (Fig. 7.9a). This is expected from a non-reducing reaction. The slight decrease in intensity of this peak with increase in titania wt.% is most likely to be due to the obscuring of GO sheets upon increased titania coverage, as well as disruption of the sheet arrangements caused by the anchored titania, and this corroborates with TEM observations (Fig. 7.9a). This infers less disruption of the GO layered stacking in the composites [7.12] and that titania had no reduction effect on GO. Additionally, the appearance of peaks at 2θ of 25°, 38°, 48° and 55° was assigned to the 100, 004, 200 and 105 reflection of the anatase phase of titania, respectively [7.17,7.8,7.5,7.42].

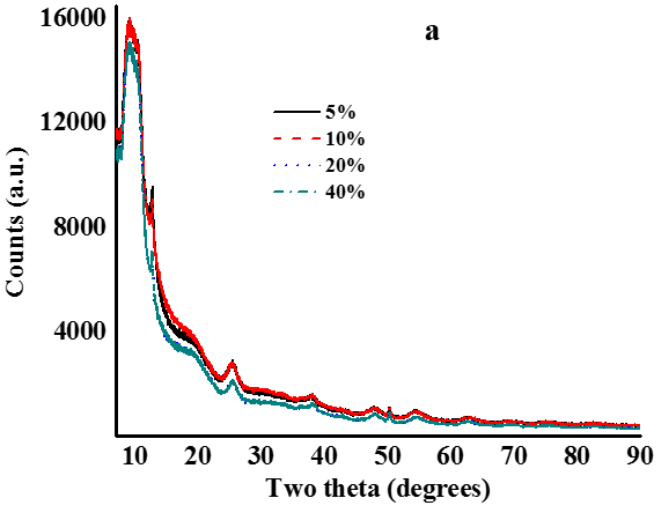

b

wt.%	I_D/I_G
5	-
10	0.79
20	0.78
40	0.88

Fig. 7.9 (a) PXRD diffractograms and (b) Raman spectroscopy I_D/I_G ratios calculated from the peak areas of the D- and G-bands of GOTi at various titania wt.%

All the RGOTi samples still showed the peak typical of GO at 2θ of 10° (Fig. 7.10a). Also, a small peak was observed at 2θ of 48° that can be assigned to the 200 reflection of the anatase phase of titania [7.8,7.17]. The observed peak broadening (Fig. 7.10a) in the nanocomposites was ascribed to surface pressure or surface confinement effects [7.31].

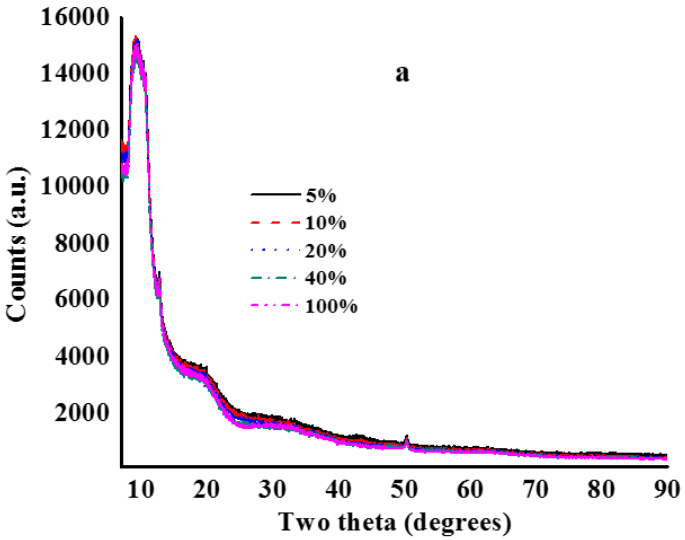

b

wt.%	I_D/I_G
5	-
10	-
20	1.04
40	1.13

Fig. 7.10 (a) PXRD diffractograms and (b) Raman spectroscopy I_D/I_G ratios of RGOTi composites

All the CRGTi samples exhibitted the peak at 2θ of 10º, typical of GO (Fig. 7.11). Furthermore, peak broadening at ca. 2θ of 18º was present in the PXRD diffractogram. Peak broadening can be associated with short-range order in RGO sheets [7.19]. The peak at 2θ of 45º, assigned to the 200 anatase reflection of the phase of titania [7.17], was slightly blue shifted in CRGTi composites and this can be attributed to the change in chemical composition. In addition, this peak decreased with increase in titania wt.% in the CRGTi samples (Fig. 7.11). The peak observed at 2θ of 51º in the CRGTi composites was similarly assigned to the blue-shifted peak of the 105 reflection of the anatase phase of titania.

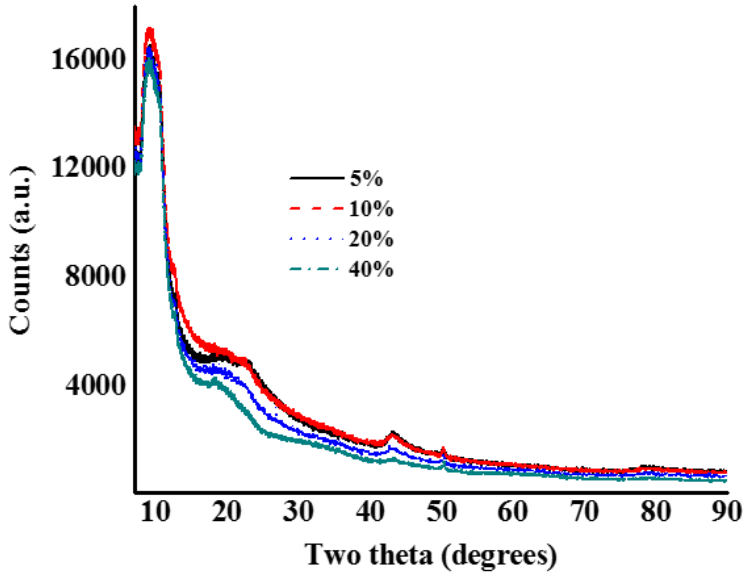

Fig. 7.11 PXRD diffractograms of CRGTi composites

7.3.1.6 Defects on graphene structures

The Raman spectral peaks were fitted to Lorentzian functions as shown in Fig. 7.S1-7.S4 of the Supplementary Data. The peaks at 1350 and 1550 cm^{-1} were assigned to the D- and G-bands [7.43-7.46]. The G-band is due to in-plane sp^2-hybridised carbon vibrations in the graphitic structure whilst the D-band is associated with defects on the graphitic structure. No detectable D-band intensities were notable for the 5 wt.% titania GOTi composite and a suitable reason is that titania sits on the graphitic defects and hence suppresses the D-band. This corroborates with the deduction of a Ti-GO chemical linkage *via* oxygen functionalities which

are usually detected as defects on graphitic materials. Additionally, the deposition of titania at the oxygen functionalised edges and on the sheet wrinkles, which are both forms of defects [7.47,7.26,7.48] (Fig. 7.1-7.2), supports this view. The I_D/I_G ratio was calculated by dividing the peak area, obtained from spectra fitted into the Lorentzian function, under the D-band with that under the G-band. The I_D/I_G ratio is an indicator of defect intensity on the graphitic structure [7.31]. The defect intensities of the 10 and 20 wt.% titania GOTi composites were similar but increased for the 40 wt.% titania composites (Fig. 7.9b). This infers that higher titania wt.% introduces more strain on the graphitic sheets whilst a lower titania wt.% eliminates it.

For the RGOTi composites, the peaks were similarly assigned as in the GOTi composites. Peaks at ca. 274, 400, 514 and 636 cm^{-1} were assigned to the E_{1g}, B_{1g}, A_{1g} and E_g vibrations of the anatase phase of titania [7.44,7.5,7.31,7.49], respectively, for the 20 and 40 wt.% titania materials (Fig. 7.S2-3, in Supplementary Data). A possible reason why these peaks were detectable for the RGOTi composites was the enhanced number of separate crystallites (Fig. 7.5). Additionally, the peaks for the control sample (RTi, 100%), at 278, 397, 516 and 638 cm^{-1}, were similarly assigned. Also, similarly to the 5 wt.% titania material in the GOTi composites, there was no detectable D-band intensity at 5-10 wt.% titania RGOTi and this can be explained by titania sitting on defects. In addition, the reduction process eliminates defects associated with oxygen functionalities on the graphitic structure of RGO. However, between 20-40 wt.% titania, the defect intensity increased. A possible rationale was that greater strain occurred in the RGO sheets at higher titania wt.% since there were less defects from oxygen functionalities, for the titania to sit on. This is a conceivable reason for the higher defect intensity on RGOTi composites relative to GOTi composites.

For a CRGTi composites, except that at 5 wt.% titania, no detectable D-band intensity was observed. However, the D-band was also not observed for the 5 wt.% titania samples of both the GOTi and RGOTi composites. A most probable reason is that NCC obscured the defects on the RGO sheets. The I_D/I_G ratio for the 5 wt.% titania CRGTi composite was found to be 1.14.

7.3.1.7 Chemical state and composition

The GOTi composites showed a slight peak at ca. 290 eV and was assigned to C1s in the C-O-Ti interaction but was not clearly observable in the RGOTi and CRGTi composites (Fig. 7.12a)

[7.50]. Additionally, a shoulder peak at 287 eV, ascribed to C1s in C-O and C=O, was more observable on the GOTi composites. This was because reduction of GO minimised oxygen functionalities and this is a probable reason for the non-observable Ti bonding to C *via* oxygen moieties in the RGOTi and CRGTi composites. Additionally, C1s on the graphitic framework at 285 eV slightly shifted to 284 eV for both the RGOTi and CRGTi composites. A possible reason is weaker Ti-C interactions. Also, this peak was sharper on CRGTi whilst a shoulder was observed at 282 eV in the RGOTi composites. The shoulder was assigned to O(C-O-Ti) or C-Ti but the chemical interaction was weaker than that observed in GOTi composites.

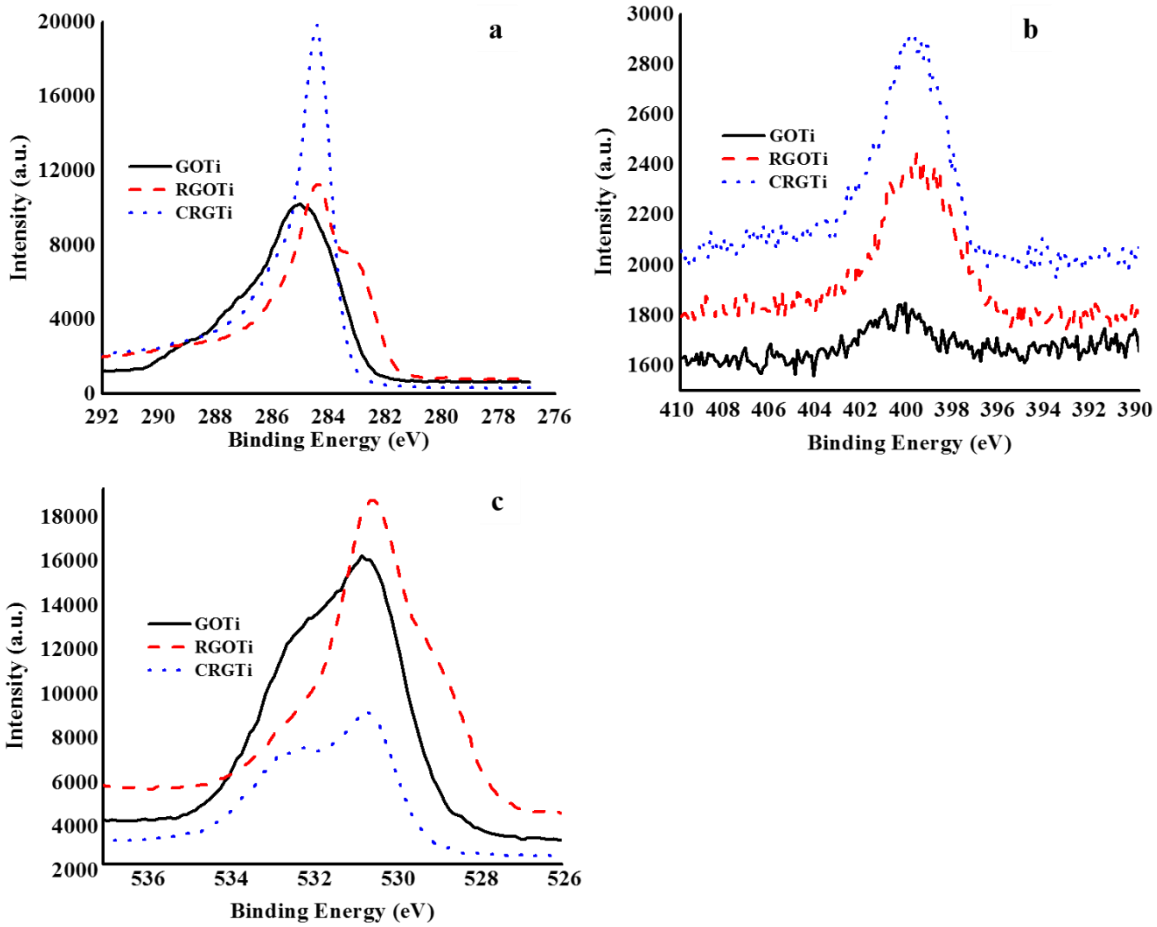

Fig. 7.12 Representative XPS spectra for GOTi, RGOTi and CRGTi composites for the peaks of (a) C1s, (b) N1s and (c) O1s

The peak at ca. 400 eV was assigned to N1s and its intensity increased in both RGOTi and CRGTi. The use of hydrazine hydrate, as a reducing agent in the preparation of RGO from GO, was the source of additional nitrogen (Fig. 7.12b and Table 7.2) whilst the source of the

small amount present in GOTi composites was impurities in the GO synthesis reagents. This means the RGO utilised in this work was nitrogen-doped. The O1s peak, assigned to surface oxygen, at 533 Ev, was notably higher in GOTi, whilst the peak at ca. 530.6 eV ascribed to lattice/bulky oxygen moieties was highest in RGOTi composites (Fig. 7.12c) [7.50,7.51]. The $Ti2p_{3/2}$ at 459 eV was observed in all composites and this was a qualitative indicator of titania. The atomic concentration (at.%) was determined by use of the CasaXPS software. The at.% of oxygen was slightly smaller in RGOTi and the decrease was greater in CRGTi, whereas the at.% of nitrogen was raised in both types of composites for the aforementioned reasons (Table 7.2). The at.% of nitrogen, 3%, was comparable because the only difference between the composites was the inclusion of NCC. The smallest value of at.% of oxygen in CRGTi was attributed to the reducing effect of NCC. This corroborates with the work reported by Dong et al. [7.52] on reducing effect of NCC on silver particles .

Table 7.2 Summary of the representative XPS data for GOTi, RGOTi and CRGTi composites

Sample	Element	Atomic concentration	Binding energy (eV)
GOTi	C1s	67.35	284
	O1s	26.72	530
	N1s	0.43	400
	Ti2p	5.50	459
RGOTi	C1s	64.26	283
	O1s	25.12	529
	N1s	2.61	399
	Ti2p	8.02	458
CRGTi	C1s	81.80	284
	O1s	12.92	530
	N1s	2.92	399
	Ti2p	2.36	458

7.3.2 Electrochemical characterisation

The section describes the suitability of the materials for electrochemical processes, in particular, for use in EC electrodes.

7.3.2.1 Cyclic voltammetry

The specific capacitance, C_s, was determined from cyclic voltammetry and was calculated by using a method we reported earlier [7.43]. At all scan rates, in the current work, for 5 wt.% titania, the order of C_s was GOTi < CRGTi < RGOTi (Fig 7.13a-c). This same order was observed at 20 and 40 wt.%. However, titania unlike at 10 wt.% titania the order was GOTi < RGOTi < CRGTi. Additionally, 5 wt.% titania RGOTi displayed the overall highest C_s of 45 F g^{-1} at a scan rate of 5 mV s^{-1}. The second highest C_s was, 30 F g^{-1}, obtained at the same scan rate, for the 10 wt.% titania CRGTi composite. The C_s values obtained in this work are an improvement on those recently reported for titania nanotube/RGO composites [7.14]. Key deductions from the current data include:

- The reduction process on GO improved C_s and this could be attributed to an enhanced BET surface area (Table 7.1) and, hence, the contribution *via* the electrochemical double layer capacitance (EDLC) increased.
- The nitrogen doping of RGO in the RGOTi and CRGTi composites (Table 7.2) is also a conceivable reason for generally higher C_s values for both RGOTi and CRGTi composites than GOTi composites.
- NCC addition in the composites had a negative effect with regards to C_s in all CRGTi composites except that for 10 wt.% titania. This means that even though NCC generally boosts the BET surface area (Table 7.1), it reduces the charge storage capabilities of the composites. The unusually high C_s of CRGTi at 10 wt.% titania can be attributed to a more uniform titania coating of the graphitic sheets (Fig. 7.3) than on either GOTi or RGOTi (Fig. 7.1 and Fig. 7.2, respectively). This will influence critical parameters such as shortening of the diffusion pathlength for the electrolyte ions. Additionally, another possible reason is the high surface area of the 10 wt.% titania CRGTi composite (Table 7.1). The combination of both uniform sheet coating and high surface area, amongst other physicochemical properties, facilitated enhanced formation of a double layer and other positive redox activities.
- The lowest scan rate, 5 mV s^{-1}, displayed the highest C_s and it decreased with increase in scan rate, hence, this indicates high contributions from the EDLC mechanism. This corroborates with the cyclic voltammogram rectangular shapes at this scan rate, especially for RGOTi (Fig. 7.14).

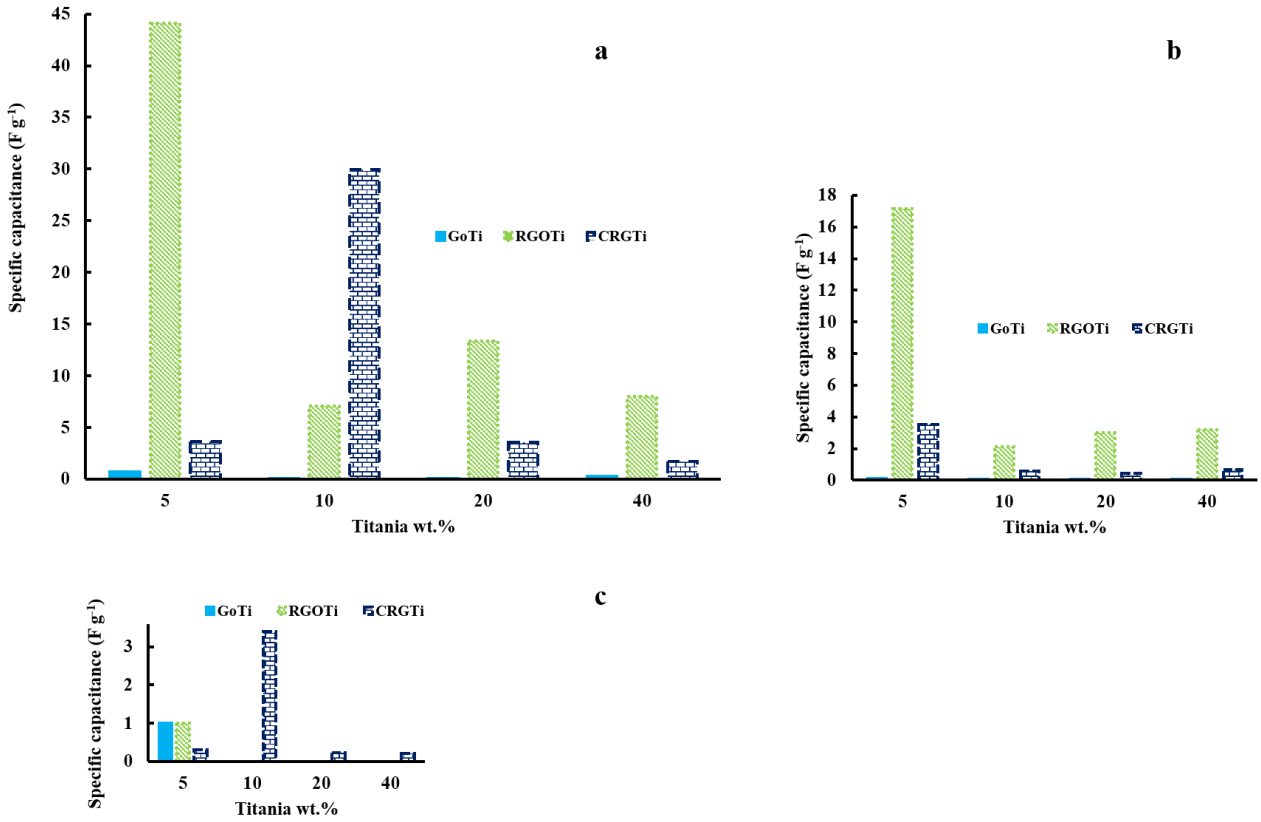

Fig. 7.13 Specific capacitance of GOTi, RGOTi and CRGTi composites at scan rates of (a) 5, (b) 20 and (c) 100 mV s^{-1}

Similar trends as obtained for increasing amounts of titania, were obtained when the best series of composites, i.e. the RGOTi, were fabricated into ECs by making pellets and measuring the capacitance with a capacitor meter (Fig. 7.S10 in Supplementary Data). However, the C_s values were much lower than those obtained by the CV method (Fig. 7.13) and this was attributed to a more compact packing of the composites when made into pellets culminating in poor ion penetration in the electrode. Also, the C_s values were stable over the period of 2 hours (Fig. 7.S10 in Supplementary Data) but the measurements were not done beyond that because of the electrolyte drying effect.

The electrochemical double layer quality for the GOTi, RGOTi and CRGTi composites for 5 wt.% titania generally showed a deviation from the rectangular shape with increase in scan rate (Fig. 7.14a-c). Additionally, the 5 wt.% titania RGOTi composite displayed the best EDLC behaviour (Fig. 7.14b). This change in performance with increase in scan rate corroborates with earlier reports [7.43,7.53-7.55] in that the best EDLC quality is displayed at lower scan rates.

This may infer slow current response, high ion mass transfer resistance and poor double layer capacitance at higher scan rates. Therefore, since the double layer formation is the main charge storage mechanism, the specific capacitance decreased with increase in scan rate.

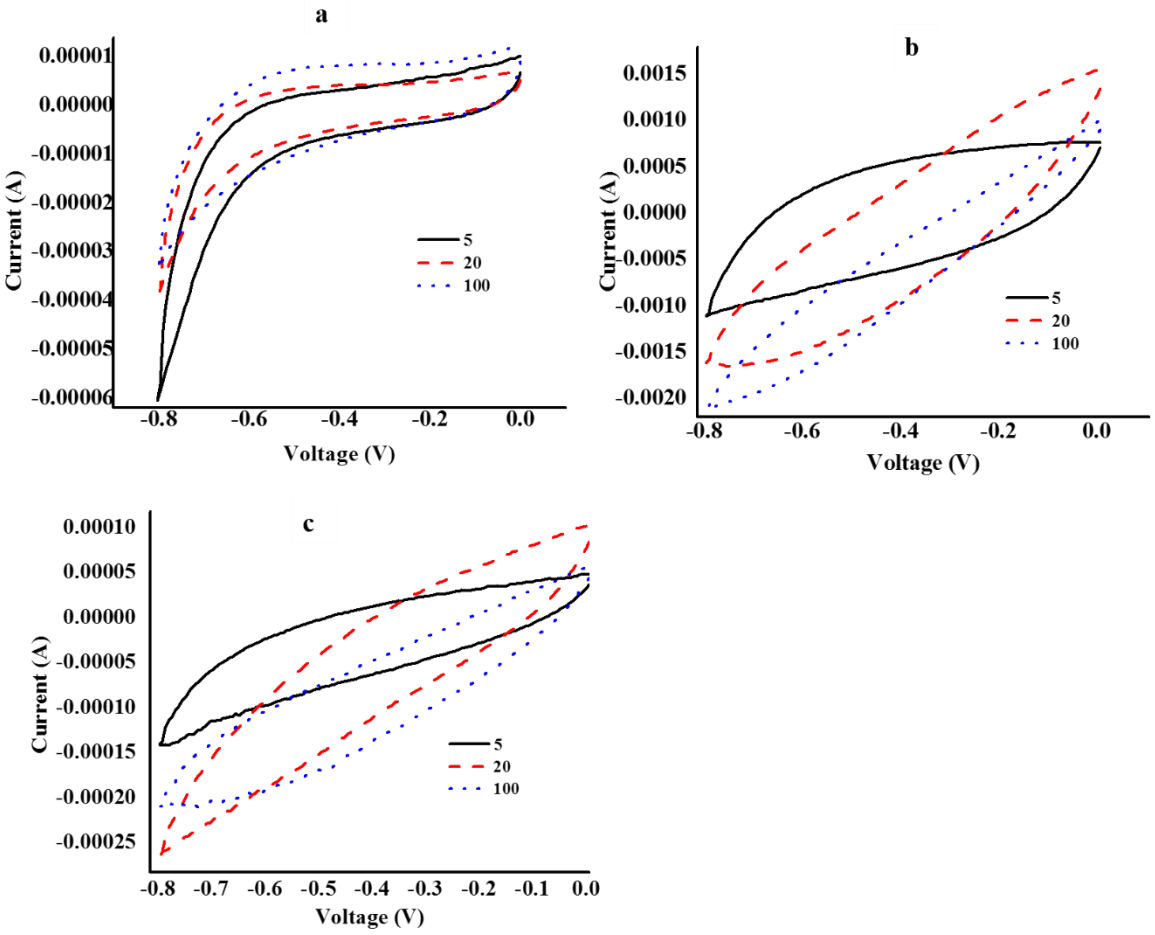

Fig. 7.14 The cyclic voltammograms for 5 wt.% titania composites of (a) GOTi, (b) RGOTi and (c) CRGTi at scan speeds of 5, 20 and 100 mV s^{-1}

There were no clear indications of a pseudo charge storage mechanism except for the GOTi composites (Fig. 7.15a-c). Possible reasons are that either the GO reduction process renders titania an inactive component for charge storage or titania is inhibited in typical composites. These pseudo characteristics in the GOTi composites (Fig. 7.15a) can be largely ascribed to the presence of oxygen functionalities from GO in the composites. Also, the control (100 wt.% titania) showed poor capacitance capabilities but RGOTi composites exhibited more rectangular CV curve shapes (Fig. 7.15b). This is a manifestation of high contribution of

graphitic structures in the obtained EDLC character. The high C_s calculated for 5 and 10 wt.% titania in RGOTi and CRGTi, respectively, can be easily visualised by the large areas under the CV curves (Fig. 7.15b-c). Additionally, the highest current responses were observed with RGOTi composites. A possible reason is improved conductivity of the GO sheet and components, upon reduction.

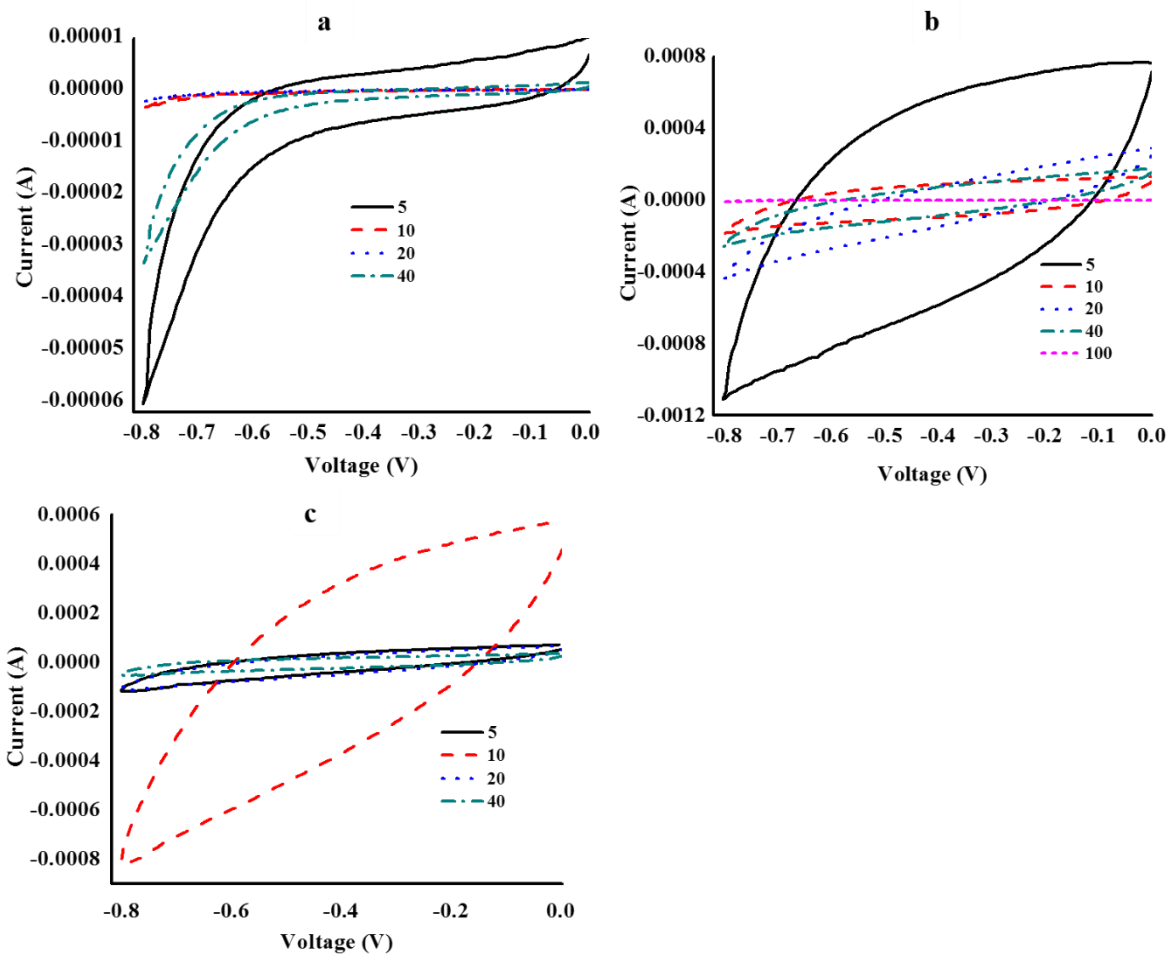

Fig. 7.15 The cyclic voltammograms recorded at a scan speed of at 5 mV s^{-1} for (a) GOTi, (b) RGOTi and (c) CRGTi composites of 5, 10, 20 and 40 wt.% titania

7.3.2.2 Electrochemical impedance spectroscopy

There was no clear semi-circle, in the high frequency region of the Nyquist plot, for all the GOTi composites and, therefore, there was no evidence of charge transfer resistance (R_{ct}, Fig. 7.16a insert). A possible reason is that GO displayed excellent charge transfer kinetics and titania did not introduce charge transfer inhibition. The Warburg length tended to increase with

titania wt.% and the composite with 40 wt.% titania showed a very large diffusion path for the electrolyte (Fig. 7.16a insert). This observation can be attributed to the increase in titania agglomerate sizes in the samples (Fig. 7.1 and 7.4) and this reduced the electrolyte ion penetration into the electrode. These are the possible reasons for a decrease in C_s as the titania wt.% increased (Fig 7.13a-c). Additionally, the 5 and 10 wt.% titania GOTi composites, with the highest slope in the low frequency region of the Nyquist plot had similar charge storage properties but this dropped with increase in titania wt.% in the 20-40 wt.% titania range (Fig. 7.16a). This means higher amount of titania reduce the ion diffusion rate and this was caused by an increase in titania agglomeration at higher titania concentrations. Also, less wt.% of GO, in the composites, means lower numbers of tunnels for effective ion transport. In short, the current EIS, SEM and TEM studies, show that larger amounts of titania enhanced the size of titania agglomerates which in turn reduces both the conductivity and electro-activity [7.3].

With regards to the reduced GO composites (Fig. 7.16b), the negligible R_{ct} means that the synthesis of the composites retained the charge transfers kinetics. The 5 wt.% titania RGOTi composites had the smallest electrolyte diffusion path length and it increases thereafter for the other composites. The 10 wt.% titania presented a negligible Warburg curve and the rest of the samples exhibited a corresponding increase with titania wt.% (Fig. 7.16b). RTi displayed the smallest slope in the low frequency region of the Nyquist plot (Fig. 7.16b) and this suggests a strong hindrance to ion diffusion. Additionally, the almost vertical line observed with 10 and 20 wt.% titania in the intermediate frequency implies a fast electron transfer into the electrolyte and adsorption on the electrode surface. This means addition of RGO in the RGOTi composites enhanced the charge transfer and capacitive character of titania. This is attributed to enhanced electron transfer pathways introduced by RGO and the associated lower agglomeration level of the titania. From the data, it can be deduced that the 10 wt.% titania RGOTi composite had the best capacitive character, even though it had an overall lower C_s value due to the lower surface area (Table 7.1) than the 5 wt.% titania composite.

Absence of a semi-circle in the high frequency region of the Nyquist plot (Fig. 7.16c) is an indication of better accessibility of electrolyte ions into the composites. The Warburg curve was small and steeper in the CRGTi composites with higher titania wt.%. In terms of capacitive behaviour, 10 wt.% titania CRGTi was better than the analogous 5 wt.% titania composite and this suggest that the enhanced surface area (Table 7.1) available for double layer formation, from the addition of NCC, was a plausible reason. This means 10 wt.% titania was the optimum for the RGOTi composites but the lower surface area gave it a disadvantage relative to the 5

wt.% composite. Hence, addition of NCC was advantageous and culminated in a higher surface area and better capacitance. The 20 and 40 wt.% titania composites were almost similar but better than that containing 10 wt.% titania (Fig. 7.16c). The high charge storage capabilities at 10 wt.% titania CRGTi corroborated with deductions from the CV data (Fig. 7.16 and Fig. 7.15c). This was a thought-provoking transformation in that a higher titania wt.% in composites performed better than lower loadings upon introduction of NCC. A possible explanation is that, at 10 wt.% titania, the NCC effectively disrupted the restacking of the RGO sheets and it increased the surface available for growth of titania. Hence, NCC reduced agglomeration of both titania and RGO, and this positively influenced ion diffusion in the composites.

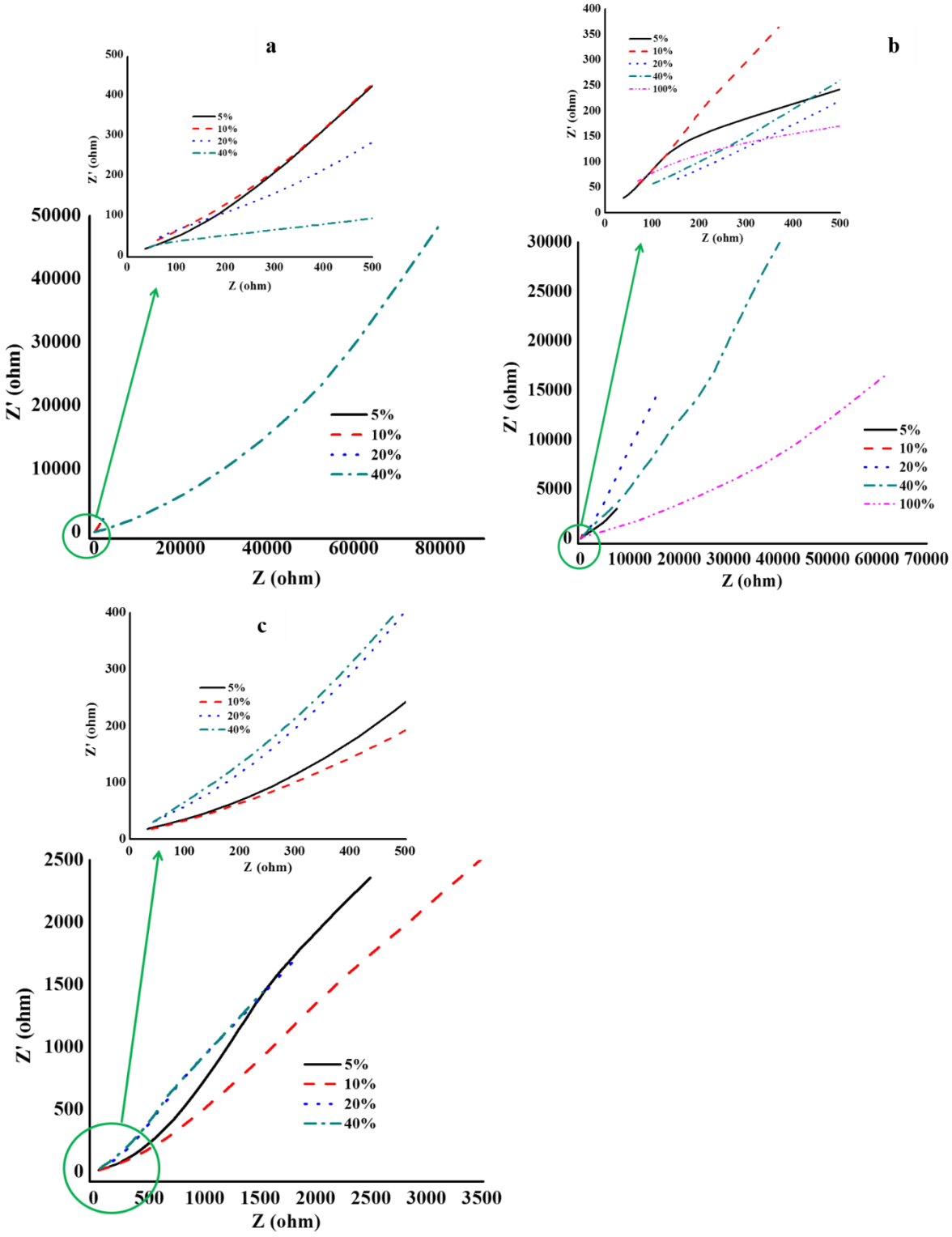

Fig. 7.16 The Nyquist plots of (a) GOTi, (b) RGOTi and (c) CRGTi composites

7.4 Conclusions

Titania facilitated exfoliation of the graphene oxide sheets and the large crystallite sizes at higher titania wt.% supressed the carbon-based defects. All composites in the current work were mesoporous. The Ti atoms were chemically linked to graphitic carbon atoms *via* oxygen-containing functionalities and this interaction was strongest in the GOTi composites. The surface area and porosity of the GOTi composites was tailored by changing the titania wt.%. The RGOTi composites were more defective than the GOTi composites. The presence of the titanium cation on the sheet surface of GOTi reduced the EDLC performance of GO. The surface area and specific capacitance of the GOTi composites was suitably improved by reduction with hydrazine hydrate. Also, NCC amplified the surface area of the RGOTi composites and the specific capacitance of the 10 wt.% titania composite increased from 7 to 30 F g^{-1} at a scan rate of 5 mV s^{-1} upon the addition of NCC. High amount of titania in the GOTi composites reduced the charge storage capabilities through an increased path length for ion diffusion and a reduced diffusion rate. The optimum titania wt.% for the best EDLC quality and highest specific capacitance, of 45 F g^{-1}, was 5% in the RGOTi composite. The capacitance decreased with increase in titania wt.% in the RGOTi composites. The best scan speed was 5 mV s^{-1} and the main charge storage mechanism was the electrochemical double layer. It appeared that the capacitor functionality of titania and GO can be improved by nitrogen doping of GO and synthesising suitable composites with appropriate distribution of components. It would thus be worthy to deliberately dope GO and RGO with nitrogen and observe the charge storage properties.

Acknowledgements

The authors would like to thank Mr Vashen Moodley and Prof Werner van Zyl for their generous donation of NCC used for the synthesis of CRGTi composites. We thank Prof Martincigh for proofreading the manuscript. The authors are also grateful to the University of KwaZulu-Natal (UKZN) and UKZN Nanotechnology Platform for the facilities used in this work and a partial study bursary for Mr ETM, respectively.

Conflict of Interest: The authors declare that they have no conflict of interest.

References

7.1. Kiamahalleh MV, Zein SHS (2012) Multiwalled carbon nanotubes based nanocomposites for supercapacitors: A review of electrode materials. NANO: Brief Reports and Reviews 7 (2):1-27

7.2. Chung DDL (2015) A review of exfoliated graphite. Journal of Materials Science 51 (1):554-568. doi:10.1007/s10853-015-9284-6

7.3. Chen T, Fan Y, Wang G, Zhang J, Chuo H, Yang R (2016) Rationally designed carbon fiber@NiCo2O4@polypyrrole core–shell nanowire array for high-performance supercapacitor electrodes. Nano 11 (02):1650015. doi:10.1142/s1793292016500156

7.4. Lee J, Lee K, Park SS (2015) Environmentally friendly preparation of nanoparticle-decorated carbon nanotube or graphene hybrid structures and their potential applications. Journal of Materials Science 51 (6):2761-2770. doi:10.1007/s10853-015-9581-0

7.5. Mombeshora ET, Simoyi R, Nyamori VO, Ndungu PG (2015) Multiwalled carbon nanotube-titania nanocomposites: Understanding nano-structural parameters and functionality in dye-sensitized solar cells. South African Journal of Chemistry 68:153–164. doi:10.17159/0379-4350/2015/v68a22

7.6. Bai Y, Du M, Chang J, Sun J, Gao L (2014) Supercapacitors with high capacitance based on reduced graphene oxide/carbon nanotubes/NiO composite electrodes. Journal of Materials Chemistry A 2 (11):3834-3840. doi:10.1039/c3ta15004f

7.7. Durantini J, Boix PP, Gervaldo M, Morales GM, Otero L, Bisquert J, Barea EM (2012) Photocurrent enhancement in dye-sensitized photovoltaic devices with titania–graphene composite electrodes. Journal of Electroanalytical Chemistry 683:43-46. doi:10.1016/j.jelechem.2012.07.032

7.8. Du J, Lai X, Yang N, Zhai J, Kisailus D, Su F, Wang D, Jiang L (2011) Hierarchically ordered macro mesoporous TiO2 graphene composite films: improved mass transfer, reduced charge recombination, and their enhanced photocatalytic activities. American Chemical Society Nano 5 (1):590-596

7.9. Xiang Q, Yu J, Jaroniec M (2011) Enhanced photocatalytic H(2)-production activity of graphene-modified titania nanosheets. Nanoscale 3 (9):3670-3678. doi:10.1039/c1nr10610d

7.10. Gualdrón-Reyes AF, Meléndez AM, Niño-Gómez ME, Rodríguez-González V, Carreño-Lizcano MI (2015) Photoanodes modified with reduced graphene oxide to enhance photoelectrocatalytic performance of B-TiO_2 under visible light. Revista de la Academia Colombiana de Ciencias Exactas, Físicas y Naturales 39 (0):77. doi:10.18257/raccefyn.252

7.11. Geng W, Liu H, Yao X (2013) Enhanced photocatalytic properties of titania-graphene nanocomposites: a density functional theory study. Physical Chemistry Chemical Physics 15 (16):6025-6033. doi:10.1039/c3cp43720e

7.12. Lambert TN, Chavez CA, Hernandez-Sanchez B, Lu P, Bell NS, Ambrosini A, Friedman T, Boyle TJ, Wheeler DR, Huber ADL (2009) Synthesis and characterization of titania-graphene nanocomposites. Journal of Physical Chemistry C 113:19812-19823

7.13. Qu L-L, Wang N, Li Y-Y, Bao D-D, Yang G-H, Li H-T (2017) Novel titanium dioxide–graphene–activated carbon ternary nanocomposites with enhanced photocatalytic performance in rhodamine B and tetracycline hydrochloride degradation. Journal of Materials Science 52 (13):8311-8320. doi:10.1007/s10853-017-1047-0

7.14. Anitha VC, Hamnabard N, Banerjee AN, Dillip GR, Joo SW (2016) Enhanced electrochemical performance of morphology-controlled titania-reduced graphene oxide nanostructures fabricated via a combined anodization-hydrothermal process. RSC Advances 6 (15):12571-12583. doi:10.1039/c5ra23722j

7.15. Bell NJ, Ng YH, Du A, Coster H, Smith SC, Amal R (2011) Understanding the enhancement in photoelectrochemical properties of photocatalytically prepared tio_2-reduced graphene oxide composite. The Journal of Physical Chemistry C 115 (13):6004-6009. doi:10.1021/jp1113575

7.16. Akhavan O, Ghaderi E (2009) Photocatalytic reduction of graphene oxide nanosheets on TiO_2 thin film for photoinactivation of bacteria in solar light irradiation. Journal of Physical Chemistry C 113:20214–20220

7.17. Zhang H, Xu P, Du G, Chen Z, Oh K, Pan D, Jiao Z (2010) A facile one-step synthesis of TiO_2/graphene composites for photodegradation of methyl orange. Nano Research 4 (3):274-283. doi:10.1007/s12274-010-0079-4

7.18. Sun J, Zhang H, Guo LH, Zhao L (2013) Two-dimensional interface engineering of a titania-graphene nanosheet composite for improved photocatalytic activity. ACS Applied Materials Interfaces 5 (24):13035-13041. doi:10.1021/am403937y

7.19. Rath T, Kundu PP (2015) Reduced graphene oxide paper based nanocomposite materials for flexible supercapacitors. RSC Advances 5 (34):26666-26674. doi:10.1039/c5ra00563a

7.20. Kim C-J, Khan W, Kim D-H, Cho K-S, Park S-Y (2011) Graphene oxide/cellulose composite using NMMO monohydrate. Carbohydrate Polymers 86 (2):903-909. doi:10.1016/j.carbpol.2011.05.041

7.21. Valentini L, Cardinali M, Fortunati E, Torre L, Kenny JM (2013) A novel method to prepare conductive nanocrystalline cellulose/graphene oxide composite films. Materials Letters 105:4-7. doi:10.1016/j.matlet.2013.04.034

7.22. Han D, Yan L, Chen W, Li W, Bangal PR (2011) Cellulose/graphite oxide composite films with improved mechanical properties over a wide range of temperature. Carbohydrate Polymers 83 (2):966-972. doi:10.1016/j.carbpol.2010.09.006

7.23. Liu Y, Wang H, Yu G, Yu Q, Li B, Mu X (2014) A novel approach for the preparation of nanocrystalline cellulose by using phosphotungstic acid. Carbohydrate Polymer 110:415-422. doi:10.1016/j.carbpol.2014.04.040

7.24. Montes S, Carrasco PM, Ruiz V, Cabañero G, Grande HJ, Labidi J, Odriozola I (2015) Synergistic reinforcement of poly(vinyl alcohol) nanocomposites with cellulose nanocrystal-stabilized graphene. Composites Science and Technology 117:26-31. doi:10.1016/j.compscitech.2015.05.018

7.25. Mombeshora ET, Ndungu PG, Nyamori VO (2017) Effect of graphite/sodium nitrate ratio and reaction time on the physicochemical properties of graphene oxide. New Carbon Materials 32 (1):174-187

7.26. Wahab HS, Ali SH, Hussein AMA (2015) Synthesis and characterization of graphene by Raman spectroscopy. Journal of Materials Sciences and Applications 1 (3):130-135

7.27. Kostiuk D, Bodik M, Siffalovic P, Jergel M, Halahovets Y, Hodas M, Pelletta M, Pelach M, Hulman M, Spitalsky Z, Omastova M, Majkova E (2016) Reliable determination of the few-layer graphene oxide thickness using Raman spectroscopy. Journal of Raman Spectroscopy 47 (4):391-394. doi:10.1002/jrs.4843

7.28. Marcano DC, Kosynkin DV, Berlin JM, Sinitskii A, Sun Z, Slesarev A, Alemany LB, Lu W, Tour JM (2010) Improved synthesis of graphene oxide. ACS Nano 4 (8):4806-4814. doi:10.1021/nn1006368

7.29. Xu M, Huang Q, Wang X, Sun R (2015) Highly tough cellulose/graphene composite hydrogels prepared from ionic liquids. Industrial Crops and Products 70:56-63. doi:10.1016/j.indcrop.2015.03.004

7.30. Zhang H, Lv X, Li Y, Wang Y, Li J (2010) P25-Graphene composite as a high performance photocatalyst. American Chemical Society 4 (1):380-386

7.31. Perera SD, Mariano RG, Vu K, Nour N, Seitz O, Chabal Y, Balkus KJ (2012) Hydrothermal synthesis of graphene-TiO_2 nanotube composites with enhanced photocatalytic activity. ACS Catalysis 2 (6):949-956. doi:10.1021/cs200621c

7.32. Hung W-S, Tsou C-H, De Guzman M, An Q-F, Liu Y-L, Zhang Y-M, Hu C-C, Lee K-R, Lai J-Y (2014) Cross-linking with diamine monomers to prepare composite graphene oxide-framework membranes with varyingd-spacing. Chemistry of Materials 26 (9):2983-2990. doi:10.1021/cm5007873

7.33. King AA, Davies BR, Noorbehesht N, Newman P, Church TL, Harris AT, Razal JM, Minett AI (2016) A New Raman metric for the characterisation of graphene oxide and its derivatives. Sci Rep 6:19491. doi:10.1038/srep19491

7.34. Atchudan R, Pandurangan A, Joo J (2013) Synthesis of multilayer graphene balls on mesoporous Co-MCM-41 molecular sieves by chemical vapour deposition method. Microporous and Mesoporous Materials 175:161–169

7.35. Tan L-L, Ong W-J, Chai S-P, Mohamed AR (2013) Reduced graphene oxide-TiO_2 nanocomposite as a promising visible-light-active photocatalyst for the conversion of carbon dioxide. Nanoscale Research Letters 8 (465):1-9

7.36. Dreyer DR, Park S, Bielawski CW, Ruoff RS (2010) The chemistry of graphene oxide. Chemical Society Reviews 39 (1):228-240. doi:10.1039/b917103g

7.37. Sing K (2001) The use of nitrogen adsorption for the characterisation of porous materials. Colloids and Surfaces A: Physicochemical and Engineering Aspects 187–188:3–9

7.38. Tan YH, Davis JA, Fujikawa K, Ganesh NV, Demchenko AV, Stine KJ (2012) Surface area and pore size characteristics of nanoporous gold subjected to thermal, mechanical,

or surface modification studied using gas adsorption isotherms, cyclic voltammetry, thermogravimetric analysis, and scanning electron microscopy. Journal of Material Chemistry 22 (14):6733-6745. doi:10.1039/C2JM16633J

7.39. Mombeshora ET, Nyamori VO (2015) A review on the use of carbon nanostructured materials in electrochemical capacitors. International Journal of Energy Research 39 (15):1955-1980. doi:10.1002/er.3423

7.40. Barrett EP, Joyner EG, Halenda PP (1951) The determination of pore volume and area distributions in porous substances. I. Computations from nitrogen isotherms. The volume and area distributioins in porous substances 73:373-380

7.41. He D, Li Y, Wang J, Yang Y, An Q (2016) Tunable nanostructure of tio$_2$/reduced graphene oxide composite for high photocatalysis. Applied Microscopy 46 (1):37-44. doi:10.9729/am.2016.46.1.37

7.42. Luan X, Gutierrez Wing MT, Wang Y (2015) Enhanced photocatalytic activity of graphene oxide/titania nanosheets composites for methylene blue degradation. Materials Science in Semiconductor Processing 30:592-598. doi:10.1016/j.mssp.2014.10.032

7.43. Mombeshora ET, Ndungu PG, Jarvis ALL, Nyamori VO (2017) Oxygen-modified multiwalled carbon nanotubes: physicochemical properties and capacitor functionality. International Journal of Energy Research. doi:10.1002/er.3702

7.44. Wang Y, Liu M, Liu Y, Luo J, Lu X, Sun J (2017) A novel mica-titania@graphene core-shell structured antistatic composite pearlescent pigment. Dyes and Pigments 136:197-204

7.45. Wang J, Kondrat SA, Wang Y, Brett GL, Giles C, Bartley JK, Lu L, Liu Q, Kiely CJ, Hutchings GJ (2015) Au–Pd nanoparticles dispersed on composite titania/graphene oxide-supports as a highly active oxidation catalyst. ACS Catalysis 5 (6):3575-3587. doi:10.1021/acscatal.5b00480

7.46. Mugadza K, Nyamori VO, Mola GT, Simoyi RH, Ndungu PG (2017) Low temperature synthesis of multiwalled carbon nanotubes and incorporation into an organic solar cell. Journal of Experimental Nanoscience:1-21. doi:10.1080/17458080.2017.1357842

7.47. Mohan VB, Brown R, Jayaraman K, Bhattacharyya D (2015) Characterisation of reduced graphene oxide: Effects of reduction variables on electrical conductivity. Materials Science and Engineering: B 193:49-60. doi:10.1016/j.mseb.2014.11.002

7.48. Beams R, Gustavo Cancado L, Novotny L (2015) Raman characterization of defects and dopants in graphene. Journal of Physics: Condensed Matter 27 (8):083002. doi:10.1088/0953-8984/27/8/083002

7.49. Maruthamani D, Divakar D, Harshavardhan M, Kumaravel M (2016) Evaluation of bactericidal activity of reduced graphene oxide supported titania nanoparticles under visible light irradiation. Journal of Chemical and Pharmaceutical Research 8 (1):236-244

7.50. Georgios P, Wolfgang SM (2010) X-ray photoelectron spectroscopy of anatase-TiO_2 coated carbon nanotubes. Solid State Phenomena 162:163-177

7.51. Ruzicka J-Y, Bakar FA, Thomsen L, Cowie BC, McNicoll C, Kemmitt T, Brand HEA, Ingham B, Anderssonf GG, Golovko VB (2014) XPS and NEXAFS study of fluorine modified TiO_2 nano-ovoids reveals dependence of Ti^{3+} surface population on the modifying agent. RSC Advances 4:20649-20658

7.52. Dong Y-Y, Liu S, Liu Y-J, Meng L-Y, Ma M-G (2017) Ag@Fe_3O_4@cellulose nanocrystals nanocomposites: microwave-assisted hydrothermal synthesis, antimicrobial properties, and good adsorption of dye solution. Journal of Materials Science 52 (13):8219-8230. doi:10.1007/s10853-017-1038-1

7.53. Wang J-G, Yang Y, Huang Z-H, Kang F (2012) Synthesis and electrochemical performance of MnO_2/CNTs–embedded carbon nanofibers nanocomposites for supercapacitors. Electrochimica Acta 75:213-219. doi:10.1016/j.electacta.2012.04.088

7.54. Zhou Z, Wu X-F (2014) High-performance porous electrodes for pseudosupercapacitors based on graphene-beaded carbon nanofibers surface-coated with nanostructured conducting polymers. Journal of Power Sources 262 44-49

7.55. Yun YS, Lee S, Kim NR, Kang M, Leal C, Park K-Y, Kang K, Jin H-J (2016) High and rapid alkali cation storage in ultramicroporous carbonaceous materials. Journal of Power Sources 313:142-151. doi:10.1016/j.jpowsour.2016.02.068

Appendix: Supporting information for Chapter 7

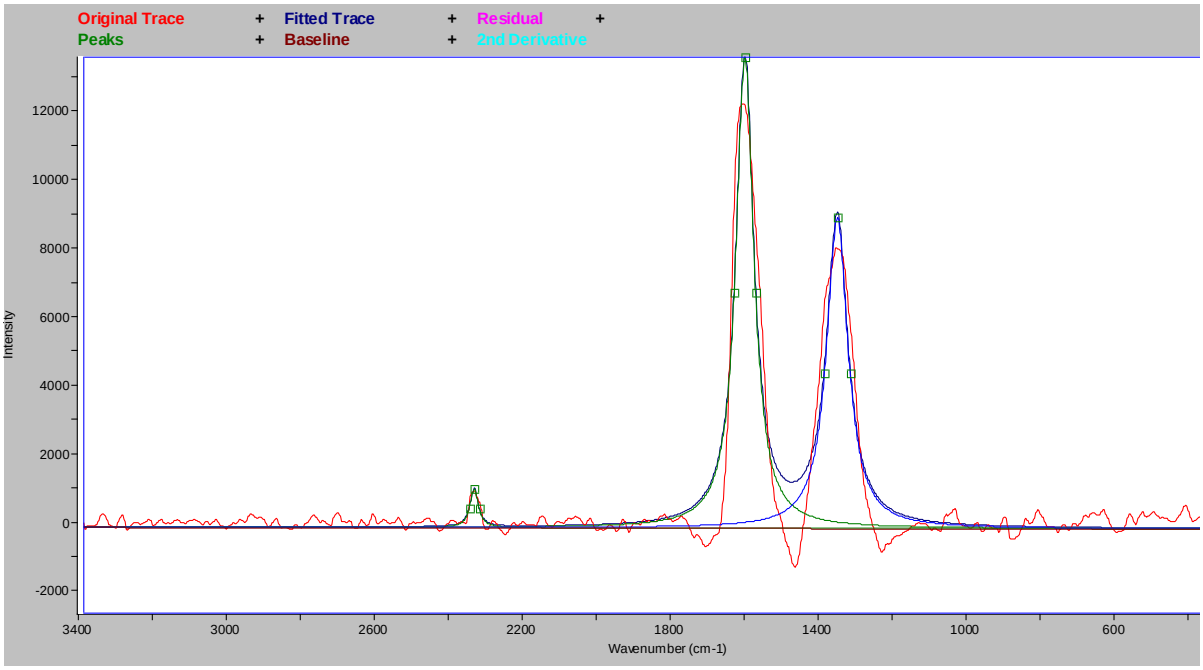

Fig. 7.S1 Raman spectra of 20 titania wt.% GOTi

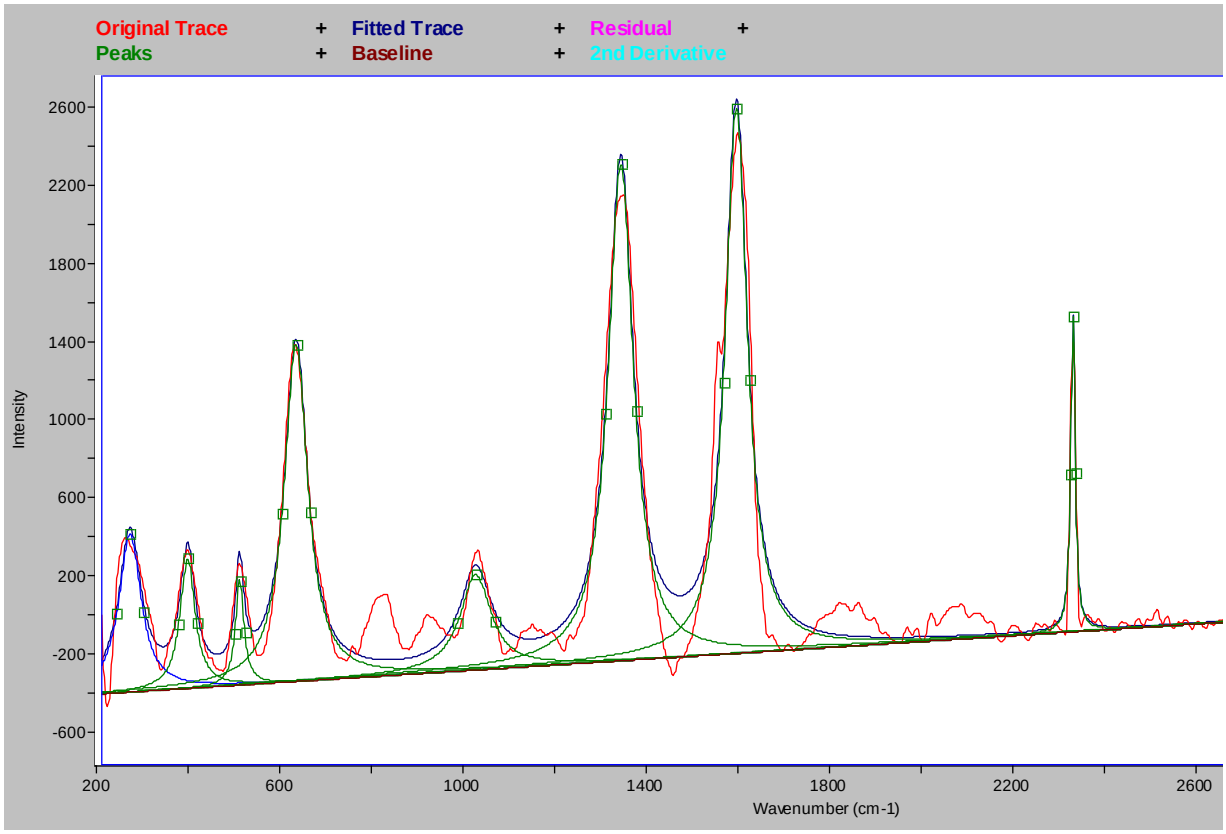

Fig. 7.S2 Raman spectra of 20 titania wt.% RGOTi composite

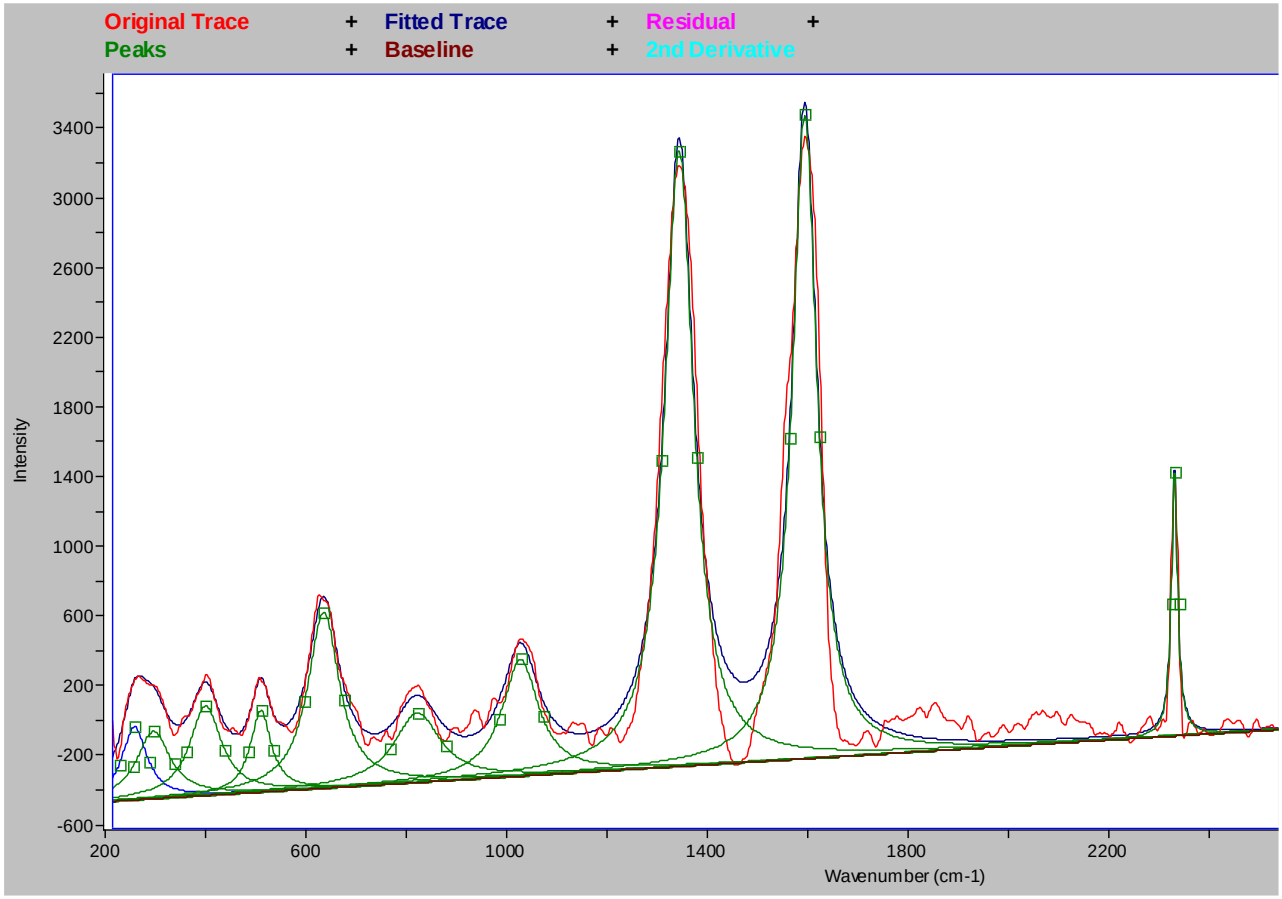

Fig. 7.S3 Raman spectra of 40 titania wt.% RGOTi composite

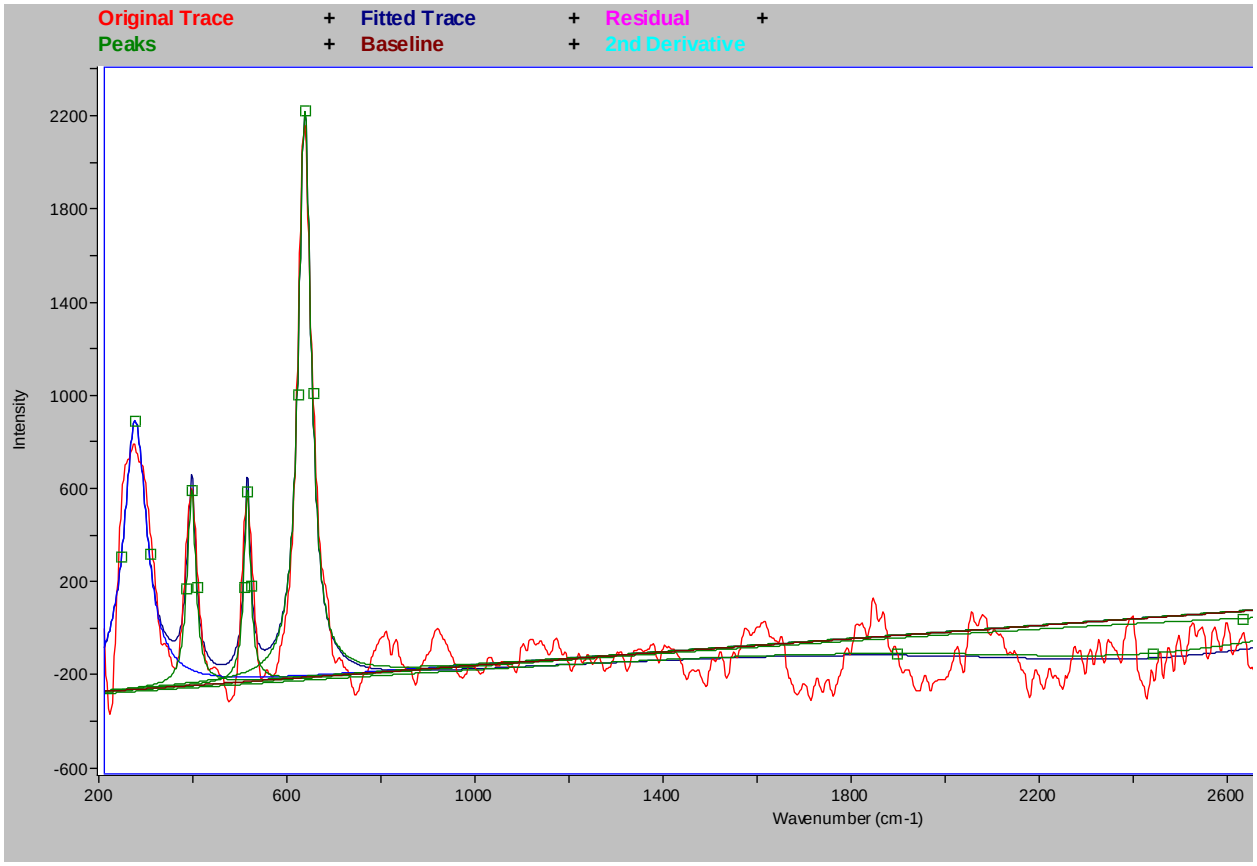

Fig. 7.S4 Raman spectra of 100 titania wt.% RTi

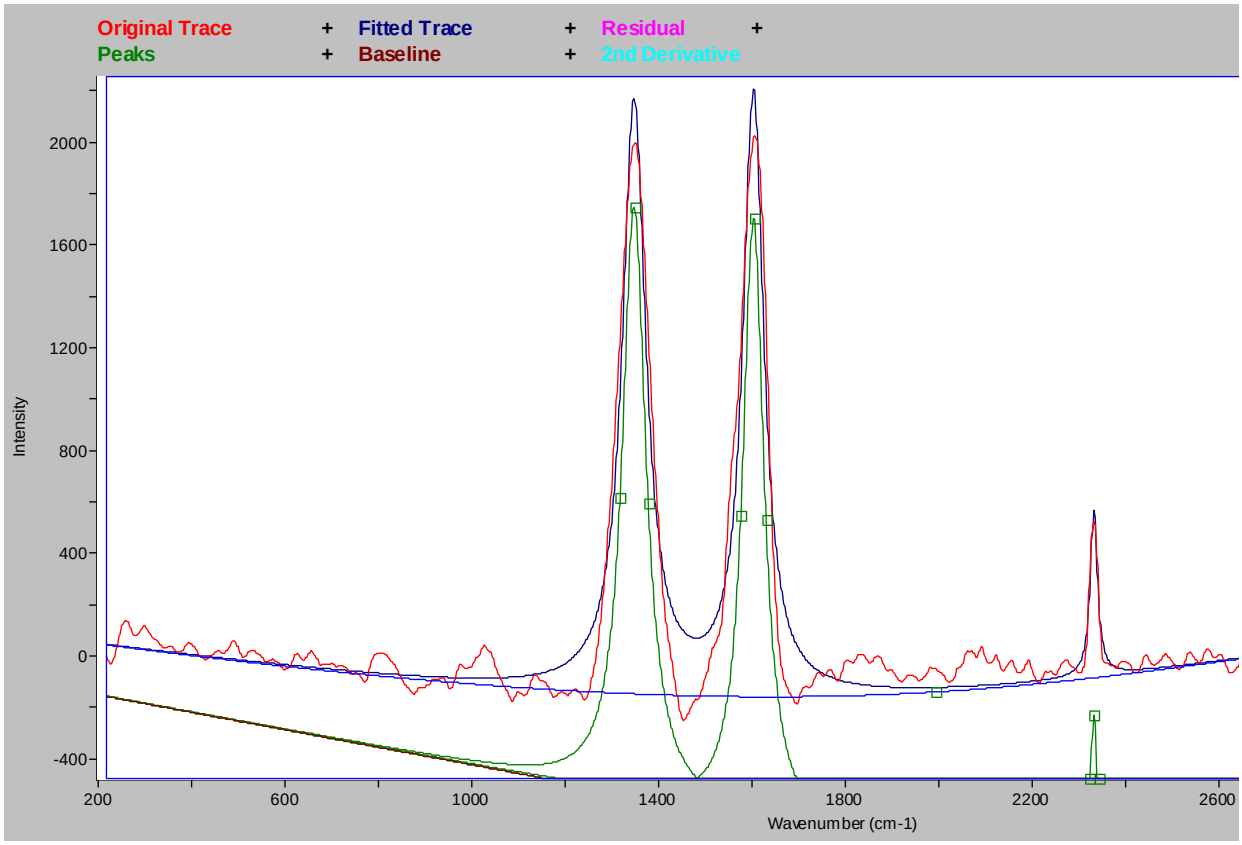

Fig. 7.S5 Raman spectra of 5 titania wt.% CRGTi

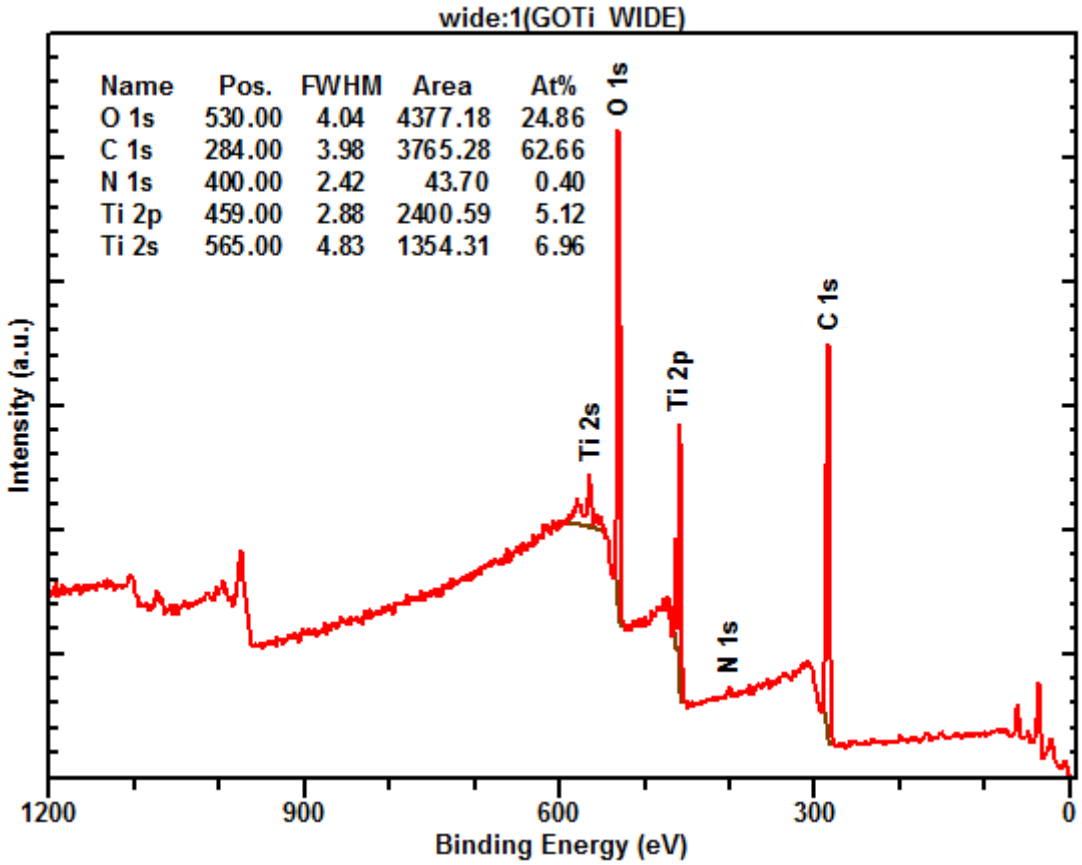

Fig. 7. S6 Representative XPS spectra for GOTi composites at 10 titania wt.%

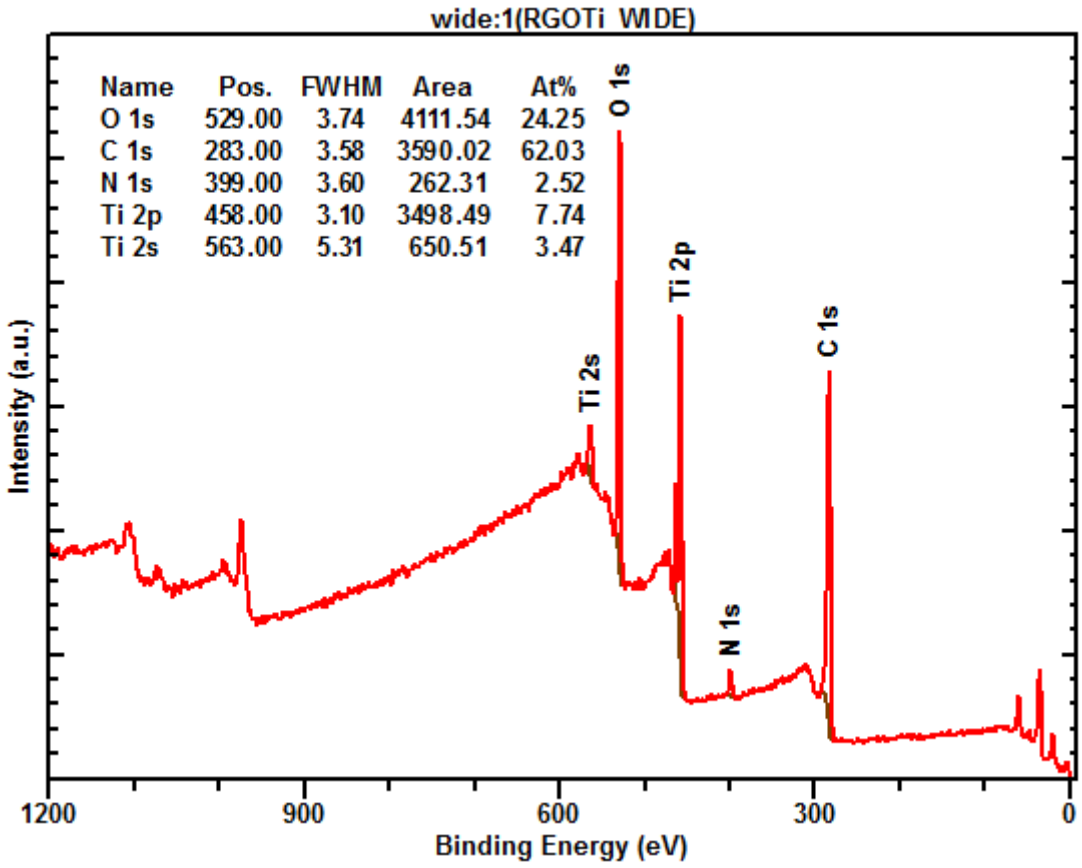

Fig. 7.S7 Representative XPS spectra for RGOTi composites at 10 titania wt.%

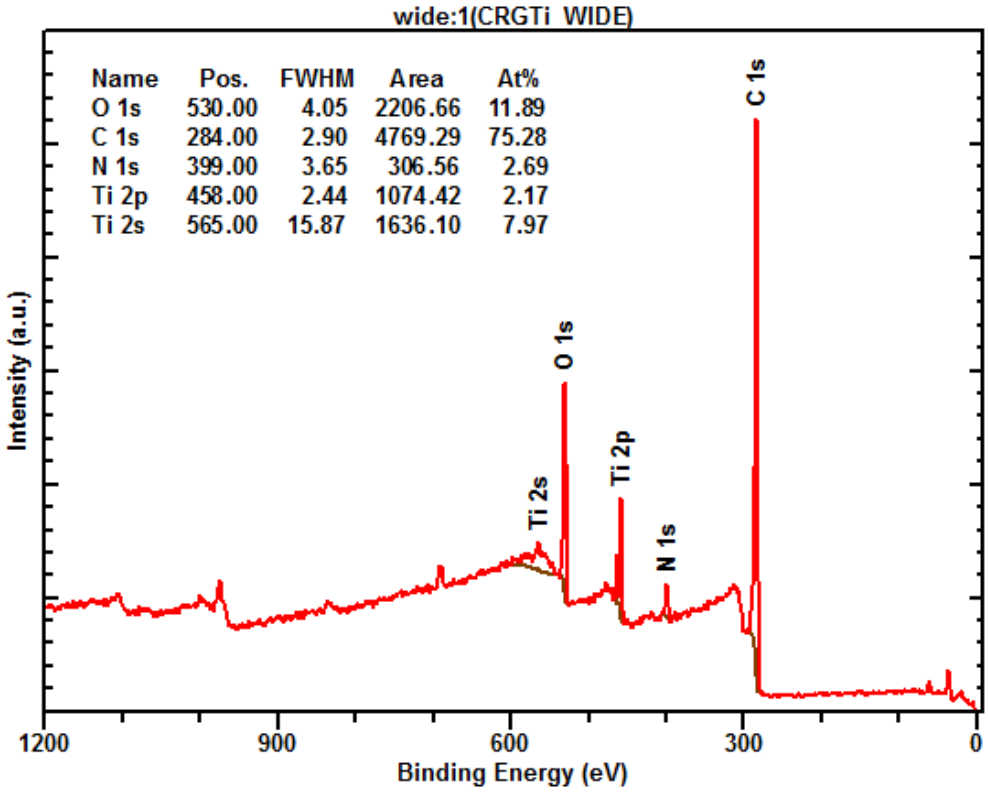

Fig. 7.S8 Representative XPS spectra for CRGTi composites at 10 titania wt.%

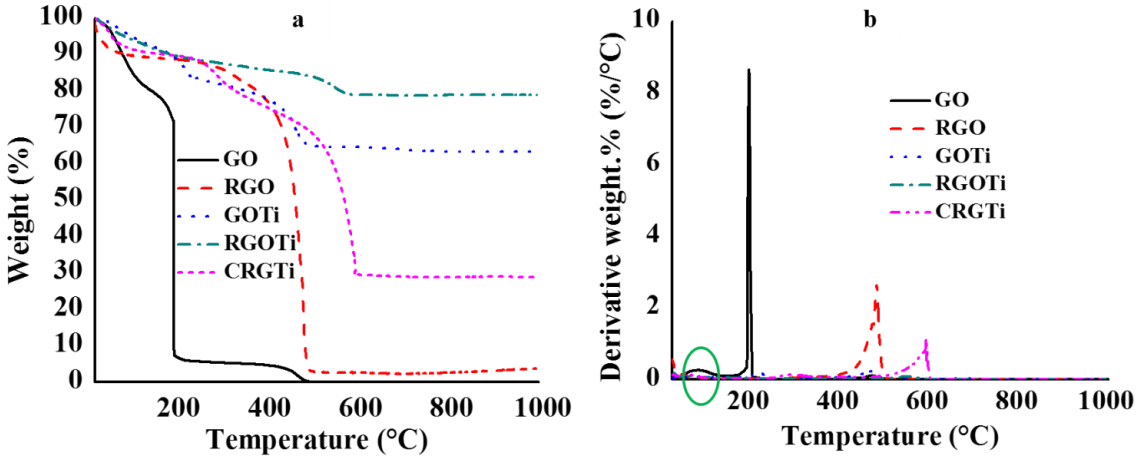

Fig. 7.S9 Representative thermal stability comparison (a) wt.% thermogram and (b) derivative weight curve

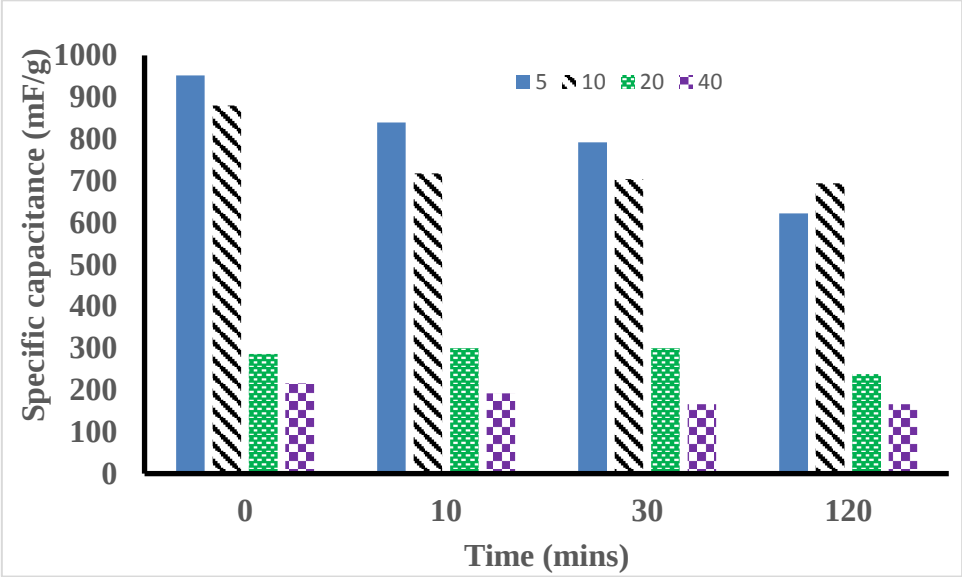

Fig. 7.S10 Representative specific capacitance values from the devices fabricated by making two pellets as electrodes, and using sodium sulfate and filter paper as electrolyte and electrode separator, respectively

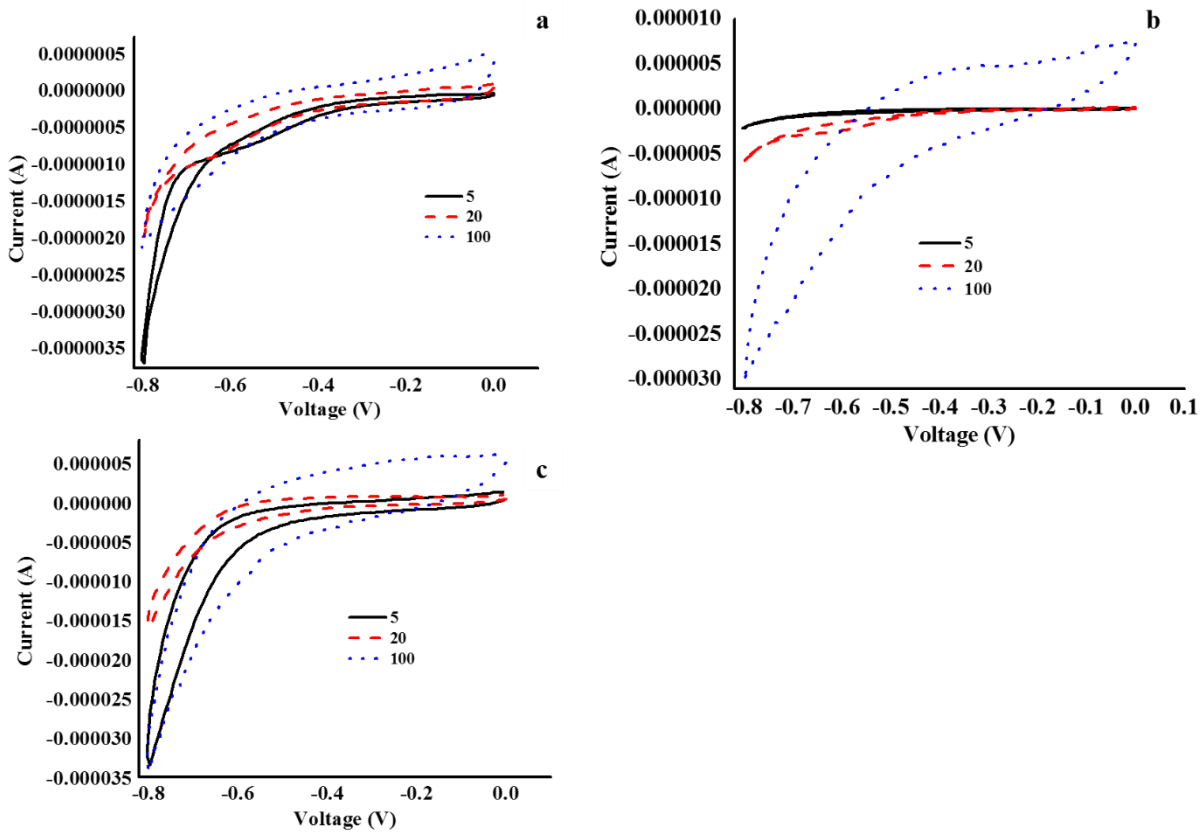

Fig. 7.S11 CV curves for GOTi composites at (a) 10, (b) 20 and (c) 40 wt.% Ti

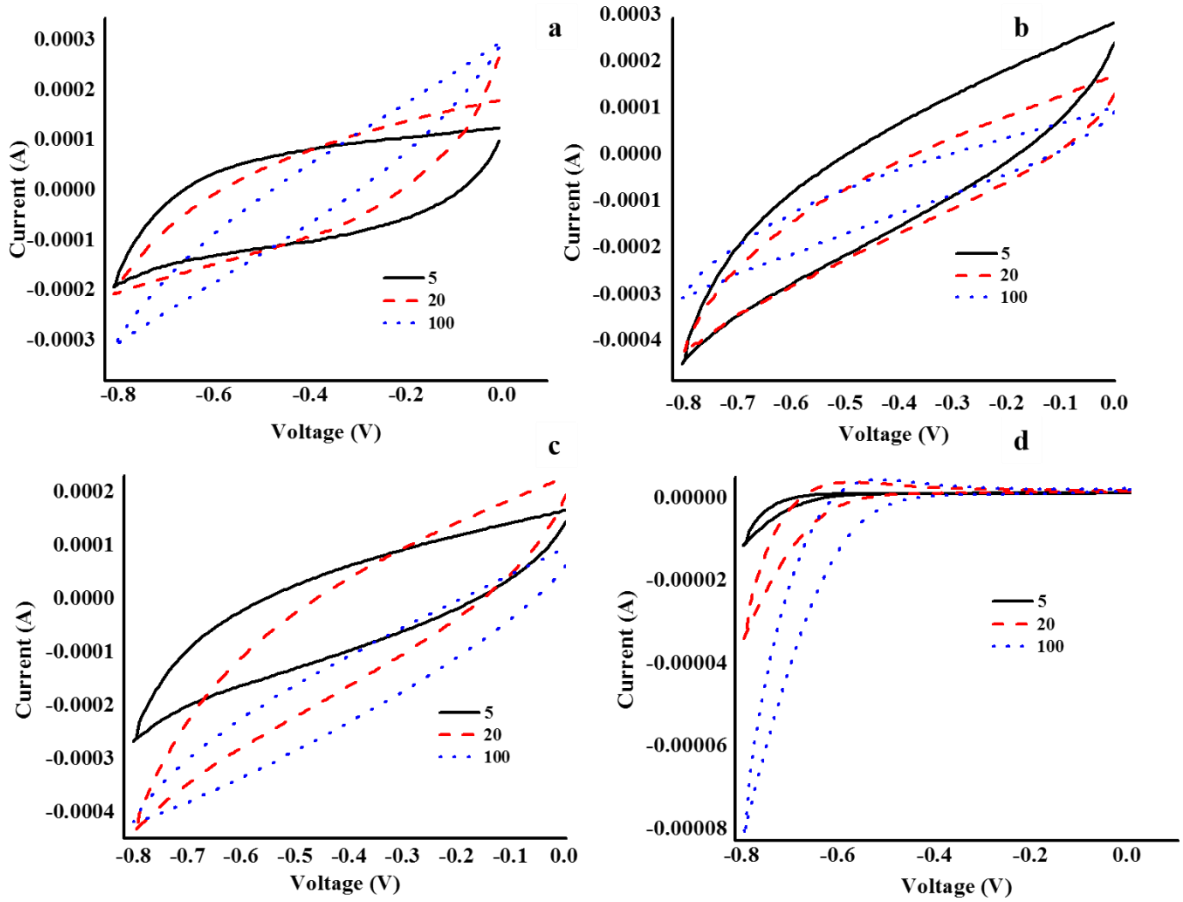

Fig. 7.S12 CV curves for RGOTi composites at (a) 10, (b) 20, (c) 40 and (d) 100 wt.% Ti

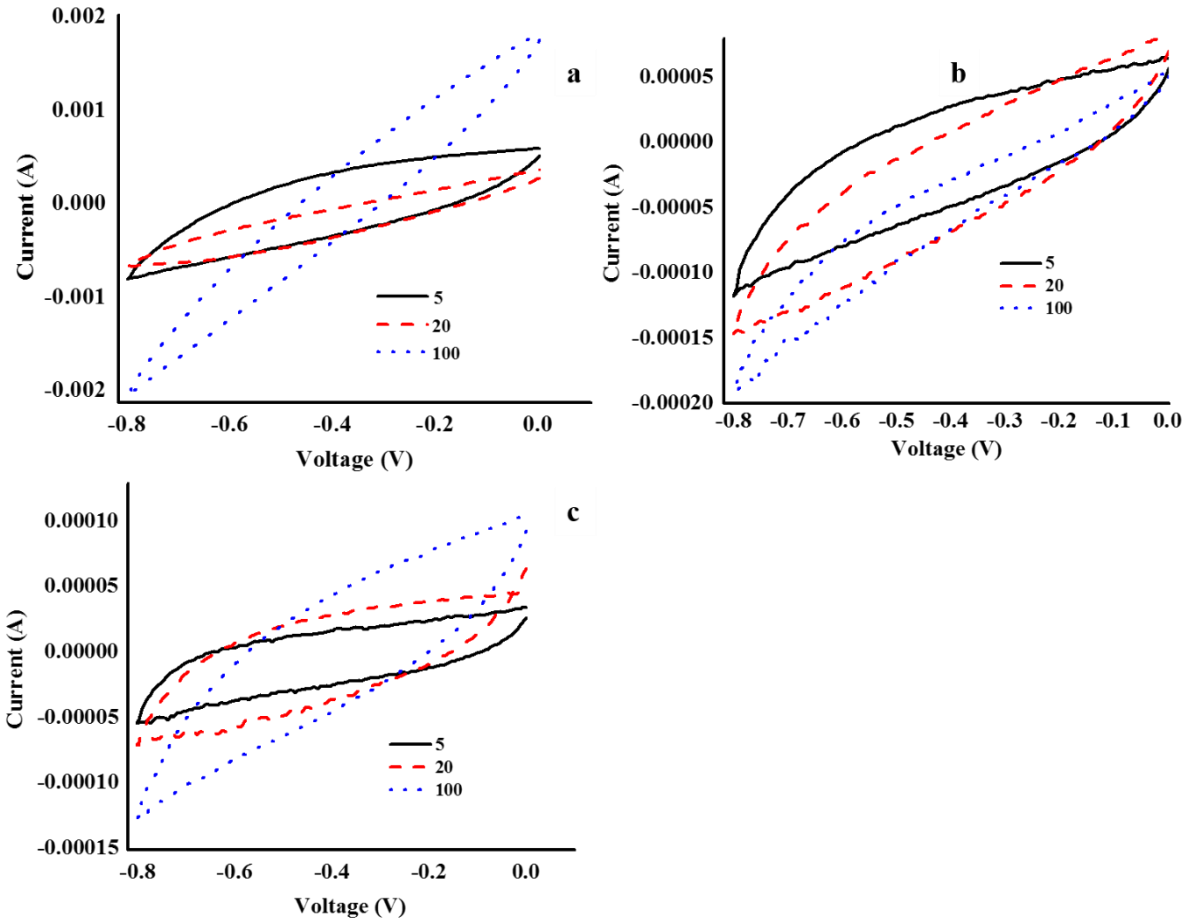

Fig. 7.S13 CV curves for CRGTi composites at (a) 10, (b) 20 and (c) 40 wt.% Ti

SPRINGER LICENSE
TERMS AND CONDITIONS

Nov 06, 2017

This Agreement between Mr. Edwin Mombeshora ("You") and Springer ("Springer") consists of your license details and the terms and conditions provided by Springer and Copyright Clearance Center.

License Number	4223070220758
License date	Nov 06, 2017
Licensed Content Publisher	Springer
Licensed Content Publication	Journal of Materials Science: Materials in Electronics
Licensed Content Title	Physicochemical characterisation of graphene oxide and reduced graphene oxide composites for electrochemical capacitors
Licensed Content Author	Edwin T. Mombeshora, Vincent O. Nyamori
Licensed Content Date	Jan 1, 2017
Type of Use	Thesis/Dissertation
Portion	Full text
Number of copies	1
Author of this Springer article	Yes and you are the sole author of the new work
Order reference number	ET Mombeshora thesis
Title of your thesis / dissertation	Synthesis and functionality of boron-, nitrogen- and oxygen-doped shaped carbon-based nanomaterials and titania nanocomposites in electrochemical capacitors
Expected completion date	Nov 2017
Estimated size(pages)	386
Requestor Location	Mr. Edwin Mombeshora School Of Chemistry and Physics University Of KwaZulu-Natal Westville campus, Private Bag X54001 Durban, KwaZulu-Natal 4000 South Africa Attn: Mr. Edwin Mombeshora
Billing Type	Invoice
Billing Address	Mr. Edwin Mombeshora School Of Chemistry and Physics University Of KwaZulu-Natal Westville campus, Private Bag X54001 Durban, South Africa 4000 Attn: Mr. Edwin Mombeshora

Chapter Eight

Nitrogen-doped carbon nanotube- and reduced graphene oxide-titania nanocomposites: Synthesis and application in charge storage

Edwin T. Mombeshora,[a] Patrick G. Ndungu,[c] A. L. Leigh Jarvis[b] and Vincent O. Nyamori[a] *

[a]School of Chemistry and Physics, University of KwaZulu-Natal, Westville Campus, Private Bag X54001, Durban, 4000, South Africa

[b]School of Electrical, Electronic and Computer Engineering, University of KwaZulu-Natal, King George V Avenue, Durban, 4014, South Africa

[c]Department of Applied Chemistry, University of Johannesburg, P.O. Box 17011, Doornfontein, Johannesburg, 2028, South Africa

Graphical abstract

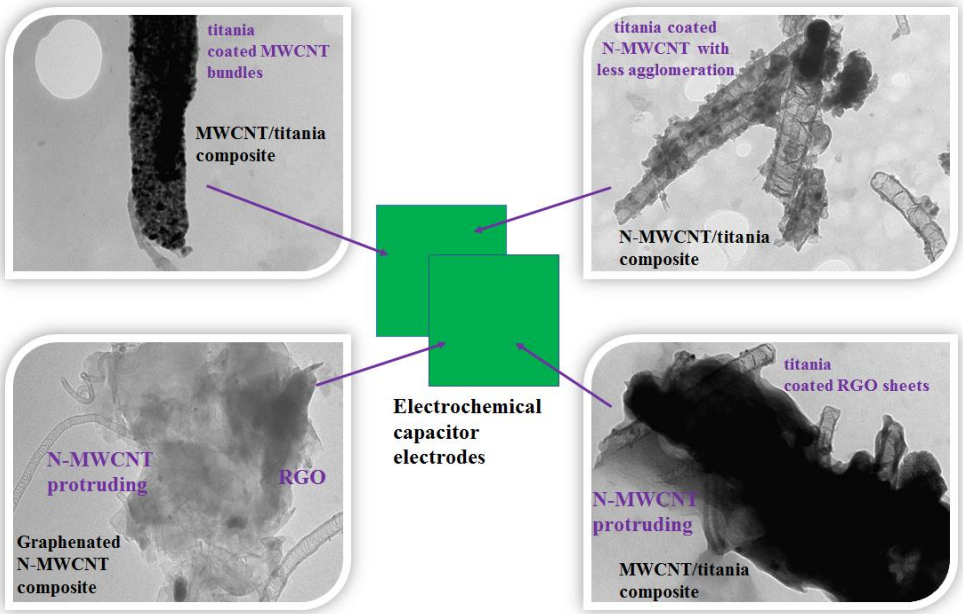

Abstract

The study was aimed at understanding and tuning the electrochemical properties as well as other associated physicochemical properties of nitrogen-doped multiwalled carbon nanotubes (N- MWCNTs) for application in electrochemical double layer capacitors (EDLC). This was done by synthesising composites of N-MWCNTs with both reduced graphene oxide (RGO) and titania. The current study also investigated the suitability of composites from either sol-gel or chemical vapour deposition (CVD) method in EDLC applications. The physicochemical properties of the composites were investigated by means of transmission electron microscopy and scanning electron microscopy, thermogravimetric analysis, X-ray photoelectron spectroscopy, Raman spectroscopy, cyclic voltammetry and electrochemical impedance spectroscopy. The study showed a deterioration of EDLC quality with increase in pyrrolic % composition of nitrogen moieties in N-MWCNTs from 35, 45 and to 60%. The sol-gel was more appropriate for composite synthesis method than CVD since it provides both favourable physicochemical properties and specific capacitance (C_s). The Warbug length was successfully reduced *via* synthesis of composites and this enhanced C_s of N-MWCNTs. RGO/N-MWCNTs composite exhibited the shortest diffusion path length and highest C_s of 30 F g^{-1}. Composite synthesis with RGO was a suitable way to positively tune the EDLC functionality of pyrrolic N-MWCNTs.

Keywords: pyrrolic nitrogen, capacitance, composites, reduced graphene oxide, electrochemical properties

* Corresponding author*:* Vincent O. Nyamori, School of Chemistry and Physics, University of KwaZulu-Natal, Westville Campus, Private Bag X54001, Durban, 4000, South Africa

Email: nyamori@ukzn.ac.za Tel.: +27-31 2608256; Fax: +27-31 260 3091

8.1. Introduction

Reduced graphene-based materials are suitable materials for electrochemical capacitor (EC) applications and recent focus on them was prompted by their excellent mechanical strength, high electron mobility and surface area [8.1,8.2]. The KOH activation on microwave exfoliated

and thermally reduced graphene oxide (RGO) are some of the typical ways of enhancing surface areas [8.1,8.3] and ultimately better EC performances. Graphene is the basic component of multiwalled carbon nanotube (MWCNT) sheets, each ring comprises of graphene sheets [8.4,8.5]. Both graphene and MWCNTs have interesting thermal, mechanical and electrical properties [8.4,8.6]. Hence, there is much interest is studying them towards energy conversion and storage devices, amongst others. Graphene oxide (GO) is an inexpensive precursor of RGO [8.4]. Common drawbacks in both RGO and MWCNTs include high agglomeration and this has negatively impacted on the fabrication of energy devices *via* solution processing strategies [8.4]. In addition, use of surfactants and polymeric dispersants often decrease their maximum potential due to insulating effects.

Composite synthesis, using two components of similar physical properties is a suitable way to generate useful synergistic and minimal adverse effects. Also, nanocomposites benefit more from the synergy between inorganic and organic components and this plays a crucial role in the development of advanced materials [8.7-8.9]. Hence, the current work combines *2-D* RGO and *1-D* MWCNTs to possibly form *3-D* scaffolds of RGO/MWCNT composites. The graphene (G)/MWCNT composite is known to have high surface area and edge charge density which are favourable properties for EC applications [8.10,8.11]. MWCNTs are suitable components of bridging the defects between sheets and consequently can facilitate electron transfer [8.7,8.12], thus, can act as electrical conductivity networks. The co-deposition of both MWCNTs and GO in anhydrous hydrazine has been reported by Qiu et al. [8.4]. In their report, MWCNTs with oxygen-containing groups were found to disperse easily in polar hydrazine. The current work reports on MWCNTs and nitrogen-doped multiwalled carbon nanotubes (N-MWCNTs) treated with HCl to purify them without adding oxygen-containing groups. Also, the study aimed at understanding the influence of the different nitrogen species and their distribution. For example, increasing compositional % of pyrrolic nitrogen moieties in EC quality of N-MWCNTs, amongst other physicochemical properties. Additionally, enhancement of electrochemical double layer capacitance (EDLC) *via* synthesis of *3-D* graphenated MWCNTs with variable foliate density has been reported [8.13,8.12]. However, the current work focus was on investigating the suitability of RGO/N-MWCNT, RGO/MWCNT/Ti and RGO/N-MWCNT/Ti composites in ECs. Also, the current work investigates and eliminates the effect of titania precursors since the composites synthesised were from the same precursor, titanium (iv) isopropoxide (TIP) when sol-gel and CVD methods were compared.

8.2. Experimental

The composites were synthesised as explained in the following subsection.

8.2.1 Materials and methods

MWCNTs (8 - 15 nm OD, length 10 - 50 μ m, Ash >1.5 wt %, SSA > 233 m^2/g, EC > 10^{-2} S/ cm, SKU number 030102) were bought from Cheaptubes.com (USA). For the dispersion of the materials, an ultrasonic water bath (UD150SH-6L model at 40 Hz, Shalom laboratories) was used.

In brief, GO was synthesised by a modified Hummer method as described in our previous article [8.14]. The GO was typically synthesised by mixing 1 g of graphite (< 150 µm, 99.99%, Sigma Aldrich), 1 g of Na_2SO_4 (99%, Associated Chemical Enterprise) and 48 mL of H_2SO_4 (98%, C.C. Imelmann Ltd) and stirring in an ice water bath. The reaction was kept in an ice bath for 30 minutes and thereafter $KMnO_4$ (99%, Associated Chemical Enterprise) was slowly added to the mixture. Afterwards, the reaction mixture was further stirred at room temperature for 12 hours and then double distilled water was added slowly. The reaction temperature was then ramped to 50 °C and maintained for at least 5 hours. H_2O_2 (30%, Merck ltd) was then added slowly and then the products were washed in several cycles using double distilled water till the filtrate was neutral in pH.

Additionally, the N-MWCNTs were also synthesised as described in our previous submission [8.15]. In brief, N-MWCNTs were synthesised at 900 ℃ from *N*,*N*'-dimethylformamide (99.8, Sigma Aldrich) mixed with acetonitrile (99.9%, Sigma Aldrich) in a ratio of 1:3, respectively, as nitrogen and carbon sources. The catalyst was ferrocene carboxaldehyde (98%, Sigma Aldrich). The as synthesised N-MWCNTs were purified by refluxing in HCl (32%, Merck ltd) for 24 hours at 90 ℃. The N-MWCNTs were washed with double distilled water several times and vacuum filtered till the filtrate was neutral in pH. The N-MWCNTs were thereafter dried at 120 ℃ and stored in a dessicator.

The first set of composites were synthesised with titania and either MWCNTs or N-MWCNTs using the sol-gel method. This method was adapted from Mombeshora et al. [8.16] and in short,

either MWCNTs or N-MWCNTs (0.2g) were dispersed by use of an ultra-sonic waterbath in absolute ethanol (10 mL), for 10 minutes. This was followed by addition of 274.5 µL of TIP (97%, Alfa Aesar) under stirring condition and then stirred further for another 30 minutes. Thereafter, the reaction mixture was left under ambient conditions in a fume hood until the sample had dried. The sol-gel samples were then calcined at 400 ℃ for 30 minutes in a tube furnace under open air. On the other hand, chemical vapor deposition method (CVD) was similarly used to make corresponding composites. The only variation here was that, after drying at ambient temperature, the CVD composites were then loaded into a reactor. The reactor was evacuated for several hours before the temperature was ramped to 100 ℃ and kept constant for 30 minutes. This was followed by further ramping temperature up to 400 ℃ and held constant for 30 minutes.

The third set of composites, RGO/N-MWCNT, RGO/MWCNT/Ti and RGO/N-MWCNT/Ti, were synthesised by using a similar sol-gel method. The ratio of RGO to MWCNTs that gave the highest BET surface area was initially optimised. In a typical synthesis, 22.2 g of GO (2% GO in double distilled water) were dispersed in 20 mL of double distilled water by means of an ultra-sonic water bath for 10 minutes. Also, 0.15 g of MWCNTs were dispersed in 20 mL double distilled water. The dispersed MWCNTs were then stirred and thereafter, the dispersed GO was added dropwise under stirring. After, 696 µL of TIP was added to the mixture under stirring and this was followed by a further stirring for 10 minutes, then treatment by an ultrasonic water bath. Thereafter, 2 mL, of hydrazine hydrate (50-60%, Sigma Aldrich) was added to the mixture and then the temperature was ramped up to 90 ℃ and maintained for one hour. The synthesized RGO/MWCNT/Ti was washed several times with DI, vacuum filtered and dried at 90 ℃. N-MWCNTs was similarly used to make RGO/N-MWCNT (without addition of TIP) and RGO/N-MWCNT/Ti.

Characterisation of composites were done by means of thermal gravimetric analyser (TA Instruments Q series^{TM} Thermal Analyzer DSC/TGA, Q600), gas sorption analysis (Micromeritics TRI STAR 3020V1.03 ,V1.03), transmission electron microscopy (JEOL TEM 1010 transmission electron microscope), scanning electron microscopy (JEOL JSM 6100 microscope), Raman spectroscopy analysis (100 mW Delta Nu Advantage 532TM spectrometer at resolution of 10 cm^{-1} and wavelength of 532 nm with a 2D CCD detector and grating lines of 1800 mm^{-1} with a laser source (Nd:YAG) and X-ray photoelectron spectroscopy (SPECS PHOIBOS 150 analyser and a monochromatic Al source (1487.1 eV), total experimental resolution was approximately 0.7 eV).

The electrochemical analyses were done with cyclic voltammetry (797 VA Computrace Metrohm CT798 application model with a 57970110 dosing processor) and electrochemical impedance spectroscopy (CHI 600E work station, CHI Instruments). The working electrode was prepared by casting the composite mixed with nafion onto a glassy carbon electrode (3 mm diameter). The deposited composite, on the electrode, was dried under room temperature conditions. Electrolyte, typically 1 M Na_2SO_4 (97%, Merck), was degassed with nitrogen for 5 minutes prior to analysis. The electrodes for electrochemical impedance spectroscopy were similarly prepared. All the electrochemical measurements were done using a three-electrode system. The counter and reference electrodes were Pt and Ag/AgCl system, respectively.

8.3. Results and discussion

The composites were characterised by several techniques as mentioned in the synthesis and materials section and the data is presented and discussed in the following sub-sections.

8.3.1 N-CNTs/Ti nanocomposites

The sol-gel products, MWCNT/Ti composites (Fig. 8.1a and c) were less agglomerated than the CVD products (Fig. 8.1b and d). This is similar to our earlier report in that the ultra-sonic water bath treatment in sol-gel method de-bundles the tubes [8.16]. Hence, both the MWCNTs and N-MWCNTs were coated as bundles in the CVD approach. The N-MWCNTs, in the CVD approach (Fig. 8.1d), were coated as random entities unlike in the case of MWCNTs (Fig. 8.1b). This infers less agglomeration in the N-MWCNTs than MWCNTs. In short, this means sol-gel method was a better facilitator for coating of individual or small collections of both MWCNTs and N-MWCNTs than the CVD method. Also, the N-MWCNTs typically displayed bamboo compartments which are characteristic of their N-doping.

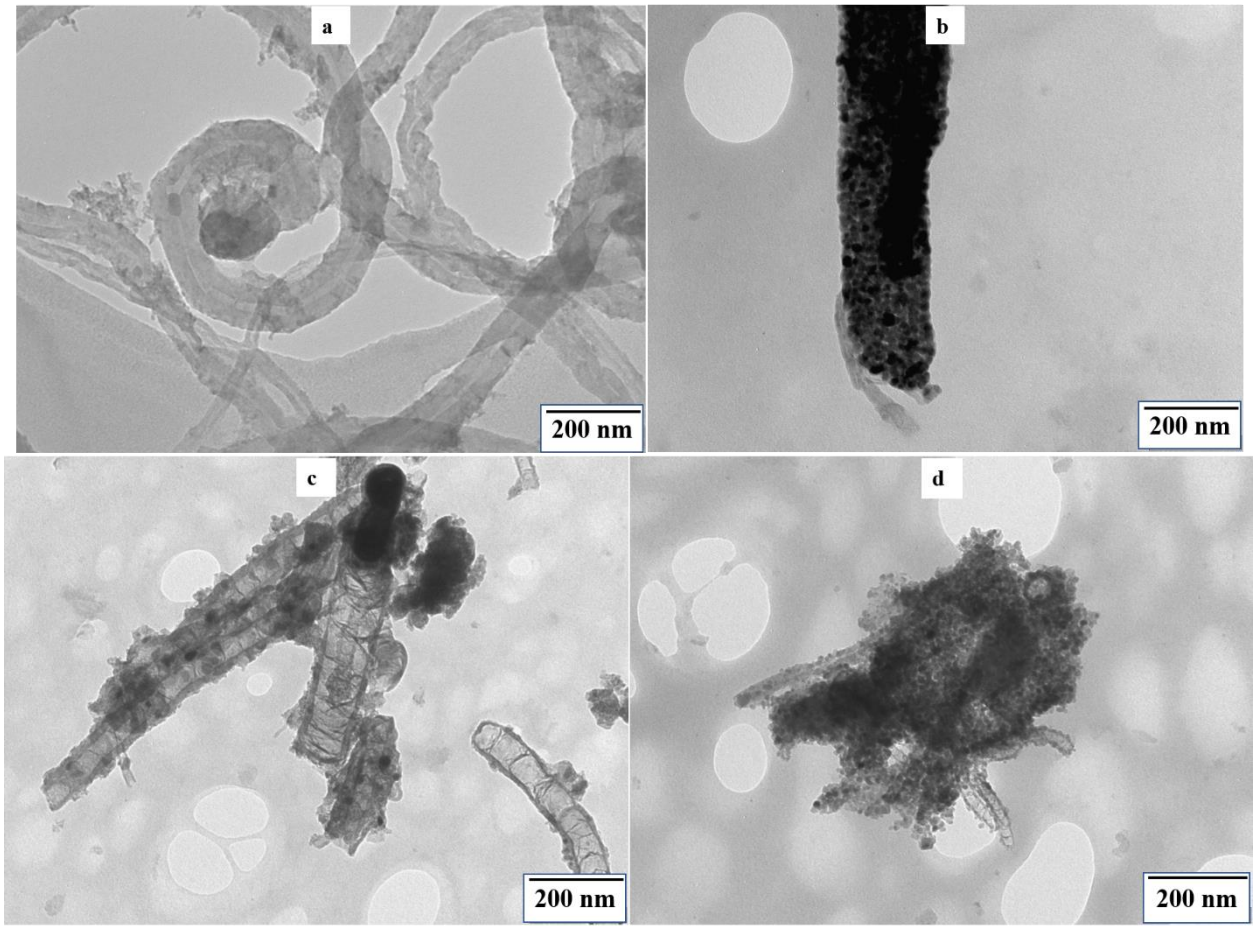

Fig. 8.1 TEM images of (a) MC/Ti sol, (b) MC/Ti cvd, (c) N-MC/Ti sol (d) N-MC/Ti cvd

The SEM images corroborated the TEM analysis; specifically, the CVD composites were more agglomerated with some noticeable tube bundling (Fig. 8.2a - d). The titania agglomerates were also larger on CVD composites than sol-gel. This was because ultrasonic treatment, in the sol-gel approach, facilitates de-bundling of the CNTs and this provides more nucleation sites for the growth of TiO_2. Additionally, the same amount of titania nucleating on a greater amount of nucleation sites, should result in smaller agglomerates.

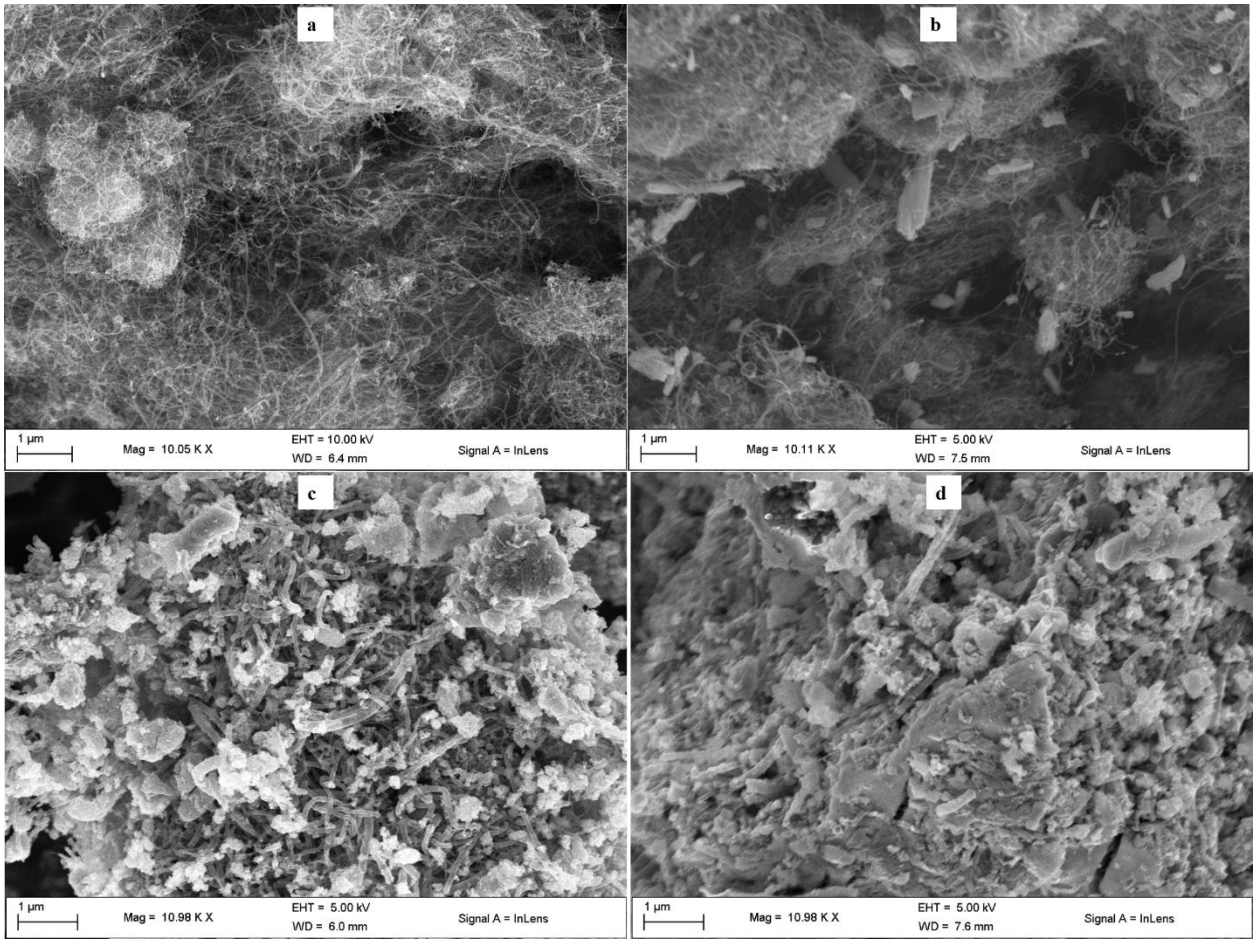

Fig. 8.2 SEM images of (a) MWCNT/Ti sol, (b) MWCNT/Ti cvd, (c) N- MWCNT/Ti sol (d) N- MWCNT/Ti cvd

Raman spectroscopy investigates vibrational and physical properties of carbon structures [8.17]. The Raman peaks were fitted using a Lorentzian function. The G-band, at 1550 cm^{-1}, is associated with longitudinal optical phonon mode whilst the D-band, at 1350 cm^{-1}, is due to special edge shapes, stacking disorder between layers and atomic defects within [8.17,8.18]. The I_D/I_G ratio was calculated by dividing the area under the D-band with that under the G-band (Fig. 8.3). The I_D/I_G is an indicator of degree of graphitization or defect density within carbon materials. The data clearly shows that the composites synthesised by means of sol-gel method were associated with fewer defects than those from CVD. Also, the inclusion of nitrogen as a dopant in MWCNTs increased the defect intensity of the respective composites. The increase in defect density due to N-doping is similar to several reports in the literature [8.19-8.22]. This is because the N-C bond length is shorter than the normal C-C bond, hence the former strains the graphitic framework.

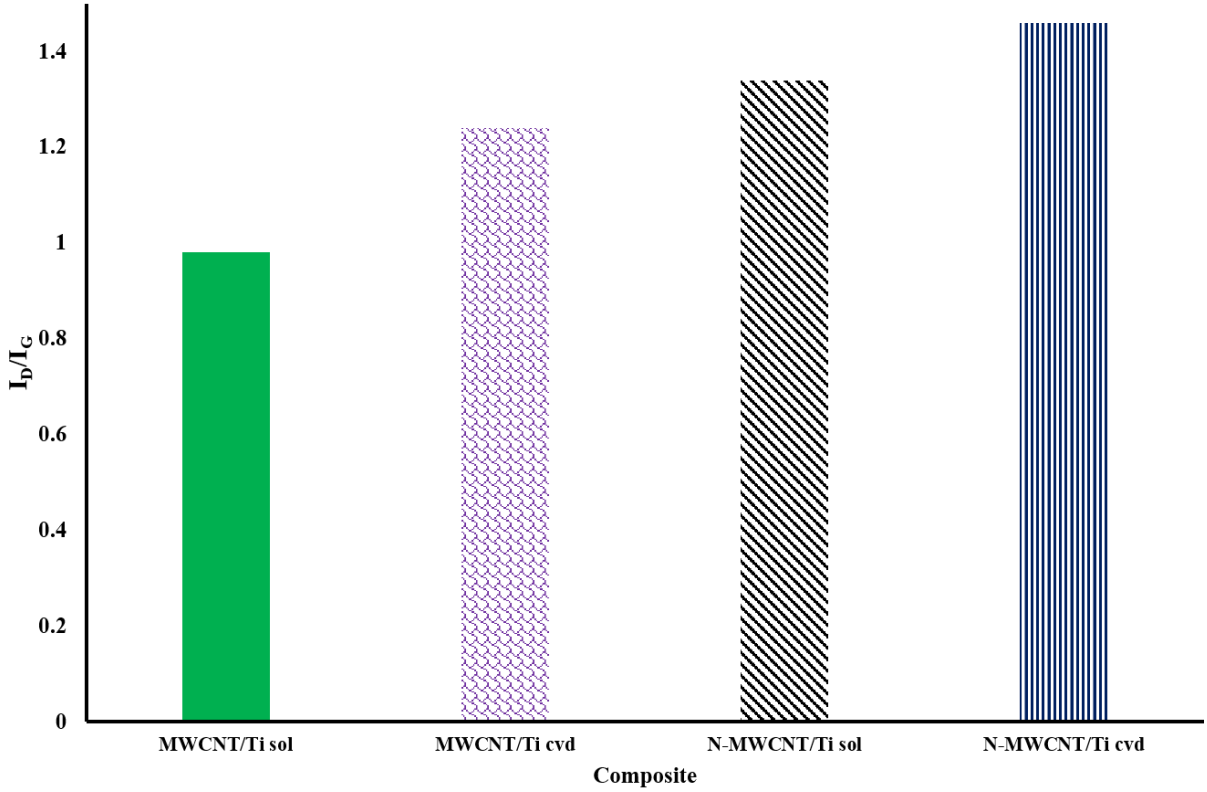

Fig. 8.3 Comparison of the Raman spectroscopy I_D/I_G ratios calculated by dividing the integrated peak area under the D- and G-band, respectively

Thermogravimetric analysis was done in oxygen from room temperature to 1000 ℃. The weight loss at c.a. 100 ℃ was ascribed to water loss and the current data suggest that the sol-gel composites were more hygroscopic than CVD for both N-MWCNT/Ti and MWCNT/Ti samples. The TGA thermogram suggest that the sol-gel approach was a better loading method for titania and this is seen by values closer to the targeted wt.% of 20. The source of higher residual metal in N-MWCNT/Ti is possibly attributed to encapsulated Fe metal inside the tubes. All the composites, except MWCNT/Ti by sol-gel, displayed similar thermal stability properties despite their associated defect density (Fig. 8.4). A possible reason for higher thermal stability of MWCNT/Ti CVD was that tubes were coated with larger titania agglomerates as bundles (Fig 8.1-8.2), hence, was associated with least exposure of MWCNTs during thermal decomposition. Their counterparts, N-MWCNT/Ti had similar random oriented morphologies with less agglomeration, hence, were associated with negligible thermal stability differences. This suggest that the defect density effects on thermal stability were outweighed by morphological variations.

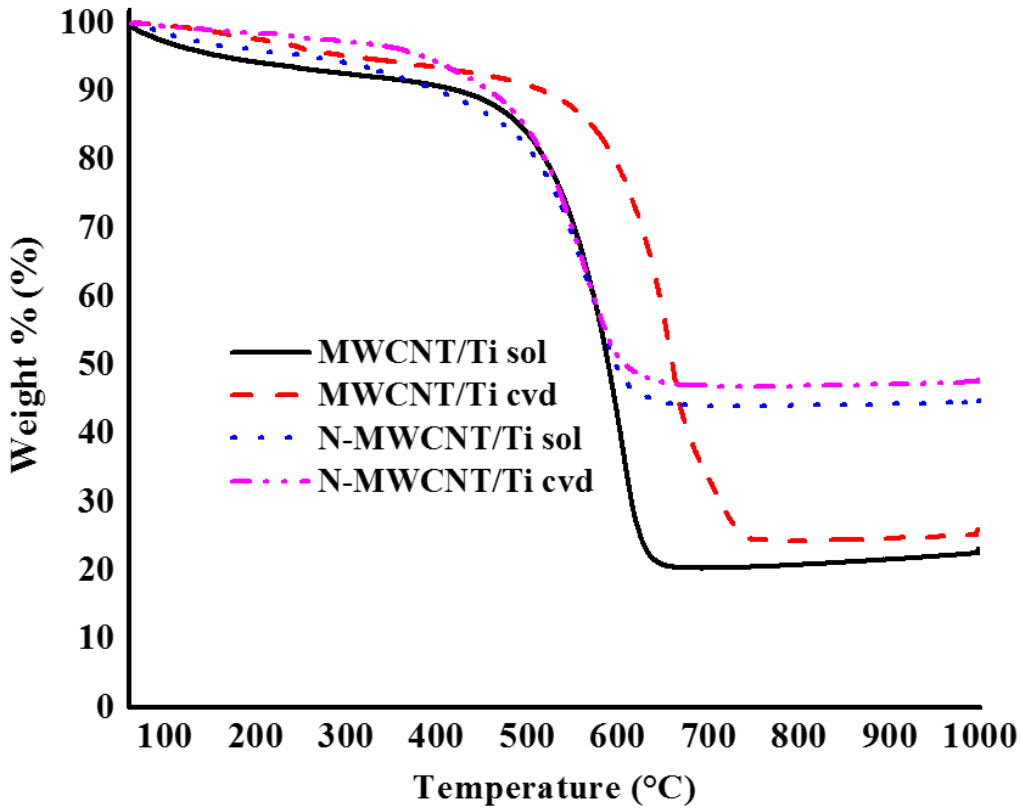

Fig. 8.4 The thermal analysis of MWCNT/Ti and N-MWCNT/Ti composites

The synthesis of composites culminated in a decrease in the surface area of pristine MWCNTs (Fig. 8.5a). The increase in particulate size, i.e. increase in the overall size due to titania coating, is a possible reason for the decrease in BET surface area. In addition, the effect was more on the CVD composites than sol-gel. In general, the composites by means of the sol-gel method had higher BET surface area than those from CVD technique. This agreed with our earlier explanation on the influence of the ultra-sonic treatment. This is due to the agglomerated morphology observed on both TEM and SEM images (Fig. 8.1-2). The N-MWCNT/Ti composites and N-MWCNTs had lower surface area than MWCNT/Ti and MWCNTs, respectively (Fig. 8.5a-b). A possible rationale is linked to the intrinsic properties of both MWCNTs and N-MWCNTs. On the contrary to MWCNTs and MWCNT/Ti case, composites synthesis with N-MWCNTs, in N-MWCNT/Ti, enhanced BET surface area. Both composites, of MWCNTs and N-MWCNTs, were meso-porous with and H3-type hysteresis loop (Fig. 8.S1 in the supplementary information).

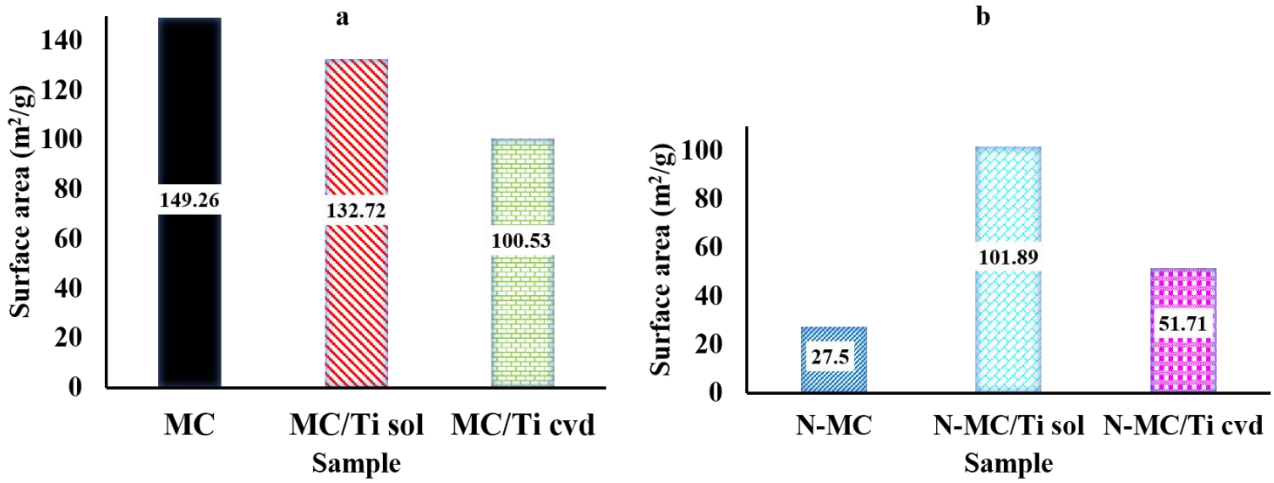

Fig. 8.5 Textural characteristics of (a) MWCNT/Ti and (b) N- MWCNT/Ti composites

Also, the determination of the nitrogen functionalities in the synthesised N-MWCNTs was determined by X-ray photoelectron spectroscopy and was reported in our earlier report [8.15]. The suitability of N-MWCNTs with a varied composition of 35, 45 and 60% pyrrolic moieties in charge storage was studied (Fig. 8.6). The CV data presented, with the aid of the inset, shows that enhancing the percent composition of pyrrolic functionalities in N-MWCNTs led to severe deterioration in EDLC quality and current response. The poor capacitance is possibly associated with the resulting poor conductivity with increase in pyrrolic nitrogen composition [8.21]. Hence, an investigation using titania and the N-MWCNTs to make composites was conducted, as an approach towards enhancing the capacitance of the parent material. The opted N-MWCNTs used to make the composites in the current work had a 45% pyrrolic nitrogen function. The rationale behind the choice was that it had the highest overall at.% nitrogen i.e. overall highest nitrogen content. The poor EDLC quality associated with use of N-MWCNTs alone provide a better reference point, for the current study, on the effect of composites synthesis.

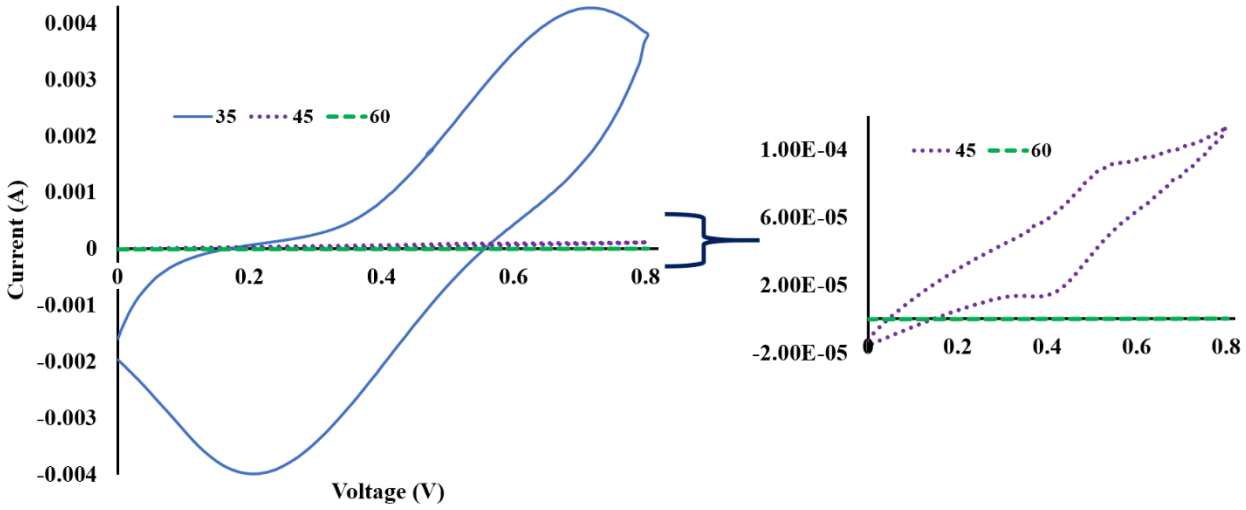

Fig. 8.6 The electrochemical study of the percentage composition of pyrrolic nitrogen functionalities effect on N-MWCNTs in 1 M sodium sulfate electrolyte and at scan rate of 50 mV s^{-1}.

The composites were then specifically tested for their suitability in electrochemical capacitance (EC) applications. The MWCNT/Ti composites generally displayed better EDLC quality than N-MWCNT/Ti (Fig. 8.7a -b). The slight redox activities in the MWCNT-based composites were attributed to the oxygen groups on titiana (Fig. 8.7a). Hence, the redox activities were more pronounced in MWCNT/Ti composites by sol-gel method, with more sites for titania nucleation resulting in smaller titania agglomerates. Additionally, the MWCNT/Ti composites synthesised by sol-gel method were better, in terms of both quality and specific capacitance (C_s), than those from the CVD approach (Fig. 8.7a and c) but it was vice-versa in the case of N-MWCNT/Ti composites (Fig. 8.7b-c). This observed trait from CV data, highlights that the method of synthesis is an important parameter which is subjective to the materials under study. Also, the C_s at 10 mV s^{-1} was higher than that at 100 mV s^{-1}. The observed better capacity functionality in MWCNT/Ti composites and the performance difference between sol-gel and CVD methods was attributed to higher surface area. In the current work, this means, the surface area determined by use of the BET equation, could be indicative of the active surface area available for the double layer formation. Also, the lower C_s values for N-MWCNT/Ti is possibly due to the above-mentioned reasons. The higher C_s value for the N-MWCNT/Ti CVD composites than sol-gel (Fig. 8.7b) can possibly be attributed to the morphological influence in which random orientation of coated tubes was favourable (Fig. 8.2).

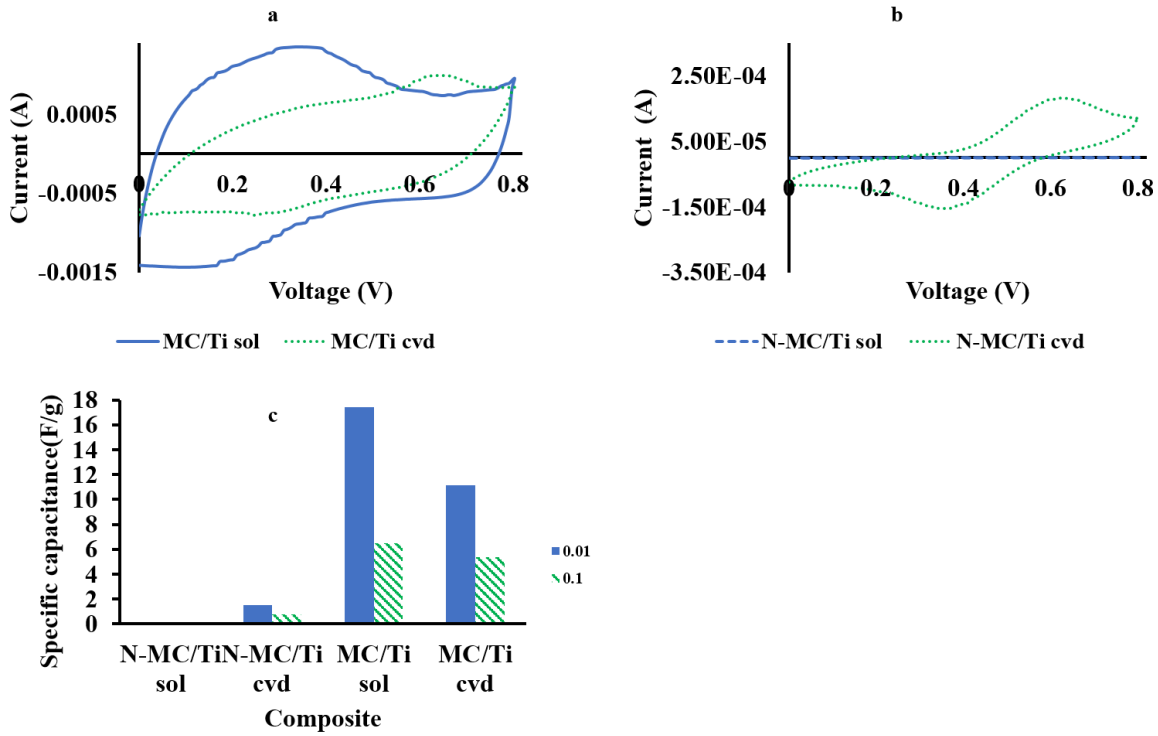

Fig. 8.7 CV curves of (a) MWCNT/titania composites and (b) N-MWCNT/titania in 1 M sodium sulfate electrolyte and at scan speed of 10 mV s^{-1}. (c) Specific capacitance of various composites

The electrochemical properties, with regards to EC functionality, of composites were further studied with electrochemical impedance spectroscopy (EIS). The Nyquist plot for MWCNT/Ti by both CVD and sol-gel methods displayed a semi-circle of almost the same size in the high frequency region (Fig. 8.8). This infers that the methods of synthesis had no effect on charge transfer resistance (R_{ct}) [8.2,8.8] with respect to MWCNT/Ti composites. On the other hand, the N- MWCNT/Ti cvd composites exhibited high R_{ct} values than MWCNT/Ti sol composites. This could be attributed to the dynamics linked to the intrinsic electrical conductivity of the pyrrolic nitrogen moieties in the N-CNTs. The higher R_{ct} in N-MWCNT/Ti composites is a possible reason for poorer EDLC quality and lower C_s values than MWCNT/Ti composites (Fig 8.7a-b). Additionally, the R_{ct} for N-MWCNT/Ti sol was lower than the N-MWCNT/Ti cvd. This infers that morphological variations such as bundling of tubes and larger titania agglomerates (Fig. 8.1-8.2) effected by CVD synthesis method, influenced charge transfer

kinetics in N-MWCNT/Ti, unlike in MWCNT/Ti composites. The higher R_{ct} values of N-MWCNT/Ti was a suitable reason for the perceived poorer EDLC functionality (Fig. 8.7).

The Warburg path-length, except for N-MWCNT/Ti sol was similar in all composites (Fig. 8.8, intermediate frequency). This means the electrolyte diffusion path-length was unusually higher for N-MWCNT/Ti sol. This was a conceivable reason for the lowest C_s value and poorest EDLC quality associated N-MWCNT/Ti sol composite (Fig. 8.7c). The effect of titania agglomerate sizes was minimal because the wt.% in the current work was small and same amount was added during synthesis. Another distinctive feature noticeable with the current composites was that the associated ascending order of Nyquist plot length, MWCNT/Ti sol < MWCNT/Ti cvd < N- MWCNT/Ti cvd < N-MWCNT/Ti sol (Fig. 8.8), substantiated the decreasing order of both C_s and EDLC quality (Fig. 8.7a-c CV).

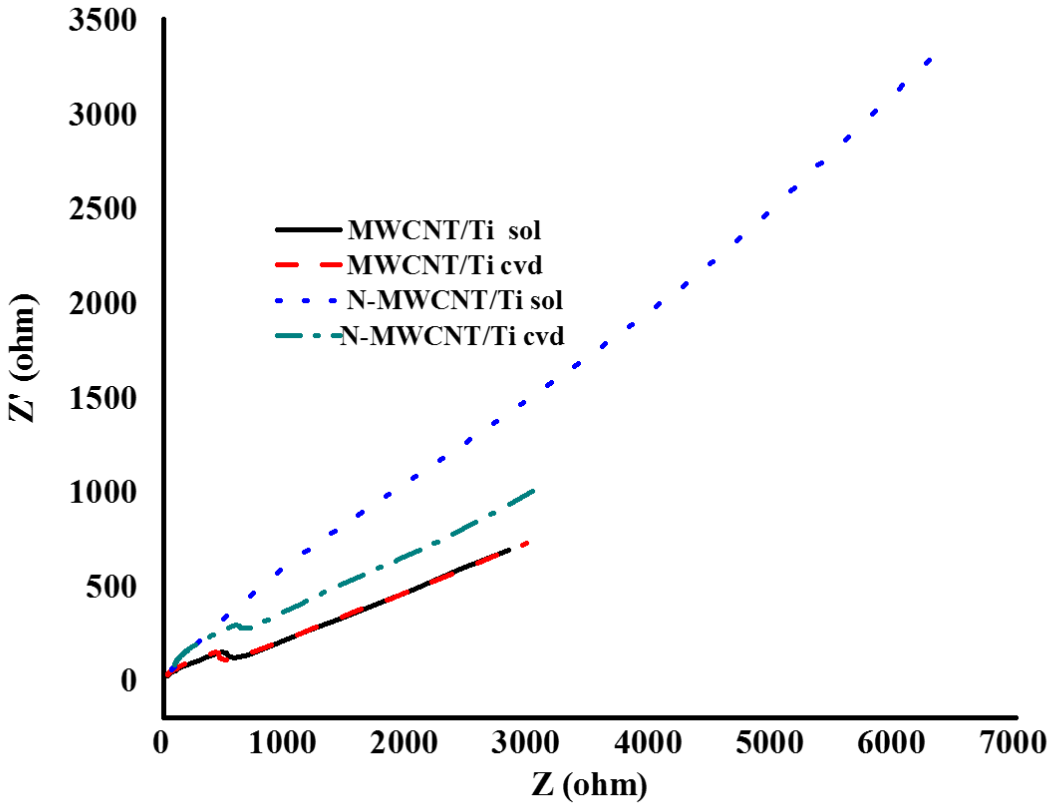

Fig. 8.8 Nyquist plot of MWCNT- and N- MWCNT-titania composites in 1 M sodium sulfate electrolyte

8.3.2 RGO/N-MWCNT/Ti nanocomposites

Before the RGO/N-MWCNT/Ti nanocomposites were synthesised, the optimal ratio between RGO and MWCNTs was determined by textural characterisation, surface area was particularly determined by means of the BET equation (Table 8.1). The synthesis of composites successfully tuned-up the surface area from that of both RGO and MWCNTs. The BET surface area increased with increase in RGO wt.% in the sample and reached a plateau with RGO:MWCNT ratio of 3:1 and thereafter decreased with further increase (Table 8.1). This surface area enhancement suggests the occurrence of chemical transformation in the composites. Possible interactions between the two components include non-covalent interactions facilitated by π-π stacking between MWCNTs and RGO [8.12]. The porosity decreased with increase in RGO proportions in the composites.

Table 8.1: Tuning of textural characteristics by varying RGO to MWCNTs ratio

RGO:MWCNT ratio	Surface area (m^2/g)	Pore volume (cm^3/g)	Pore size (nm)
0:1	135.36	0.64	19.26
1:2	218.83	0.91	20.62
1:1	253.86	0.78	16.01
2:1	355.15	0.68	10.29
3:1	417.46	0.48	4.95
4:1	333.98	0.48	4.97
1:0	390.55	0.26	3.45

Hence, in the work reported herein, RGO/MWCNT/Ti, RGO/N-MWCNT and RGO/N-MWCNT/Ti composites were synthesised using either RGO:MWCNT or RGO:N-MWCNT ratio of 3:1. The TEM images showed the typical N-MWCNTs (Fig. 8.9a), with bamboo compartments, protruding from the transparent RGO sheets in the RGO/N-MWCNT composites (Fig. 8.9b). Also, the titania coated MWCNTs instead of RGO sheets, i.e. the RGO was more transparent in RGO/MWCNT/Ti than in RGO/N-MWCNT/Ti (Fig. 8.9c-d). This was further supported by a comparison between Fig. 8.9b and 9d, which shows that the composites were more transparent in RGO/N-MWCNT than in RGO/N-MWCNT/Ti.

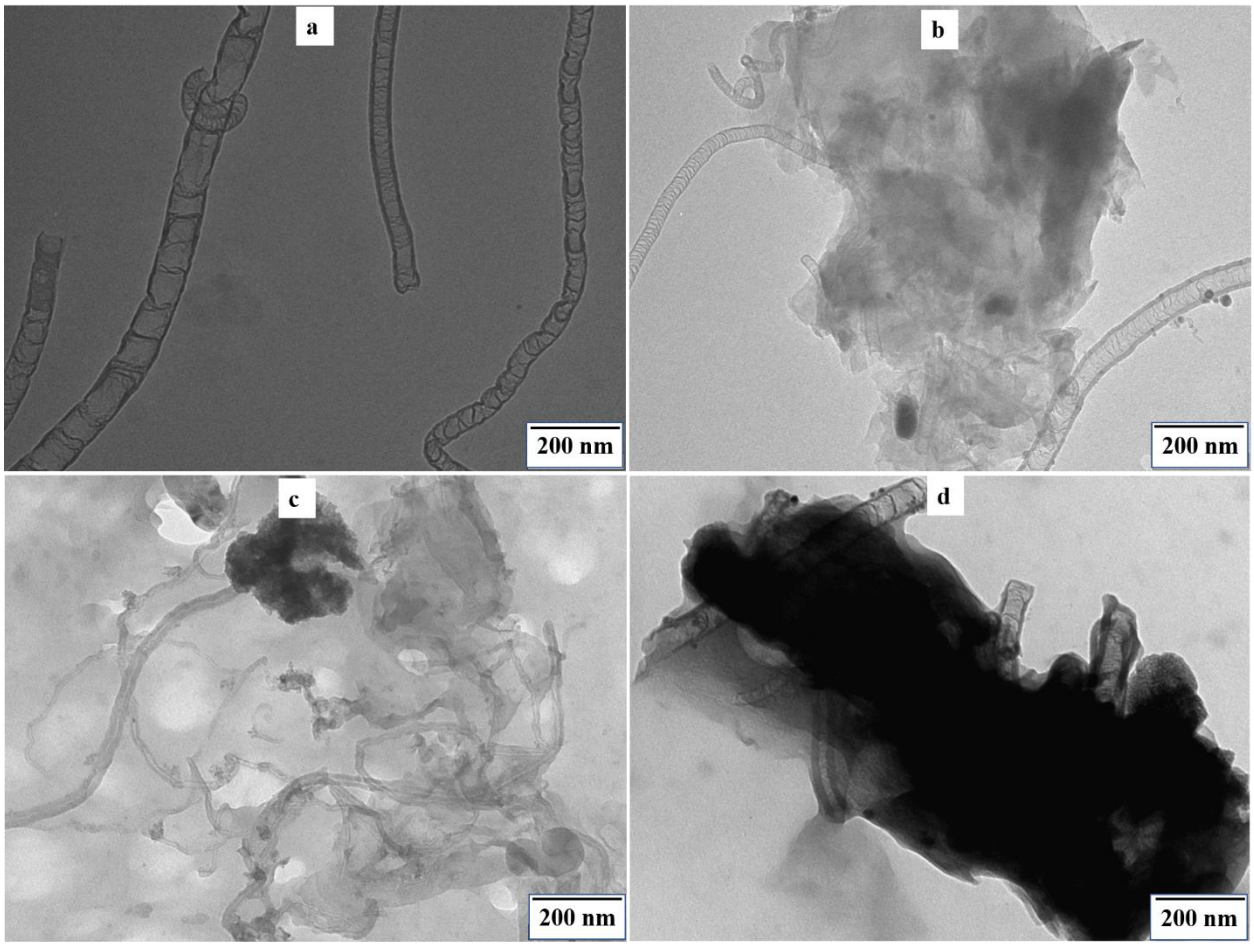

Fig. 8.9 TEM images of of (a) N-MWCNTs, (b) RGO/N-MWCNT (c) RGO/MWCNT/Ti and (d) RGO/N-MWCNT/Ti

The RGO/N-MWCNT composites were homogeneous with no distinguishable agglomerates of N-MWCNTs (Fig. 8.10a-b). This was attributed to the ultra-sonic treatment in the sol-gel method and this facilitated the dispersion process by reducing agglomeration of tubes and hence, in terms of solution processing this was a better approach. Also, the high aspect ratio of RGO to N-MWCNTs enabled the formation of a continuous network between the components [8.4]. Additionally, the lone pair of electrons on N-MWCNTs can also form a delocalised *pi*-system with RGO [8.23,8.6]. Similar observations were observed with RGO/MWCNT/Ti and the smaller MWCNT sizes are the possible reasons for the indistinguishable blend in the RGO/MWCNT/Ti composites (Fig. 8.10c). With regards to the RGO/N-MWCNT/Ti composites, large titania agglomerates were noticed. Additionally, titania coated both N-MWCNTs and RGO sheets (Fig. 8.10d). This means there were two sites competing for titania nucleation.

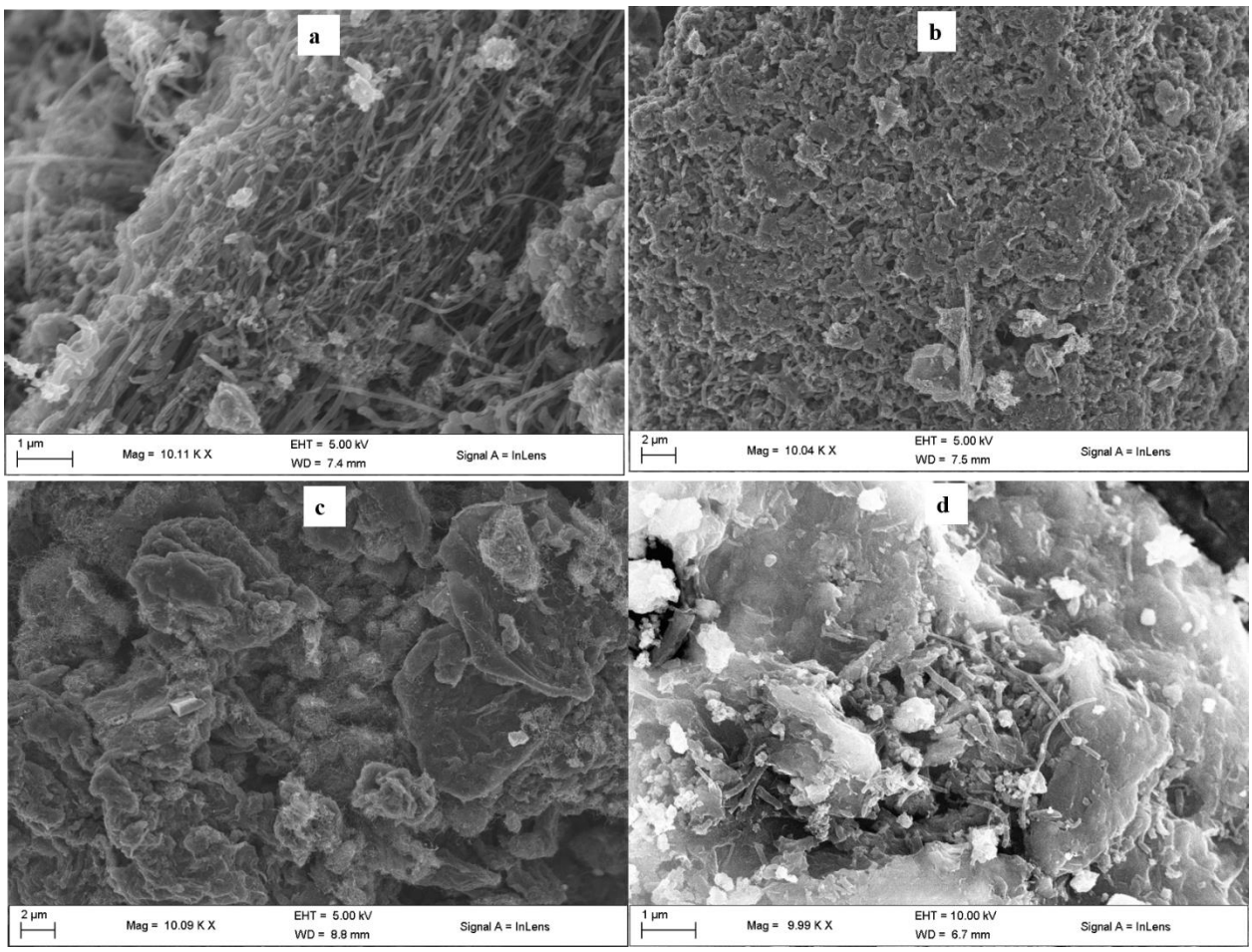

Fig. 8.10 The scanning electron microscopy images of (a) N-MWCNTs, (b) RGO/N-MWCNT (c) RGO/MWCNT/Ti and (d) RGO/N-MWCNT/Ti

Herein, the Raman spectroscopy data infers that synthesis of composites was an appropriate way to reduce defect intensity on N-MWCNT walls. The three composites, RGO/N- MWCNT, RGO/MWCNT/Ti and RGO/N-MWCNT/Ti were typically tuned to have an almost equal defect intensity (Fig. 8.11). This suggest negligible, if any, influence of defects with respect to EDLC functionality. A probable reason for minimal variation in defect intensity is the high RGO ratio in composites which obscures the influence of defective N-MWCNTs. The slight decrease in defect intensity in RGO/N-MWCNT/Ti, relative to RGO/N-MWCNT (Fig. 8.11), can be explicated by titania sitting on the graphitic defects. This was a similar case, when N-

MWCNTs defect intensity was compared to N-MWCNT/Ti composites synthesized by both sol-gel and CVD techniques.

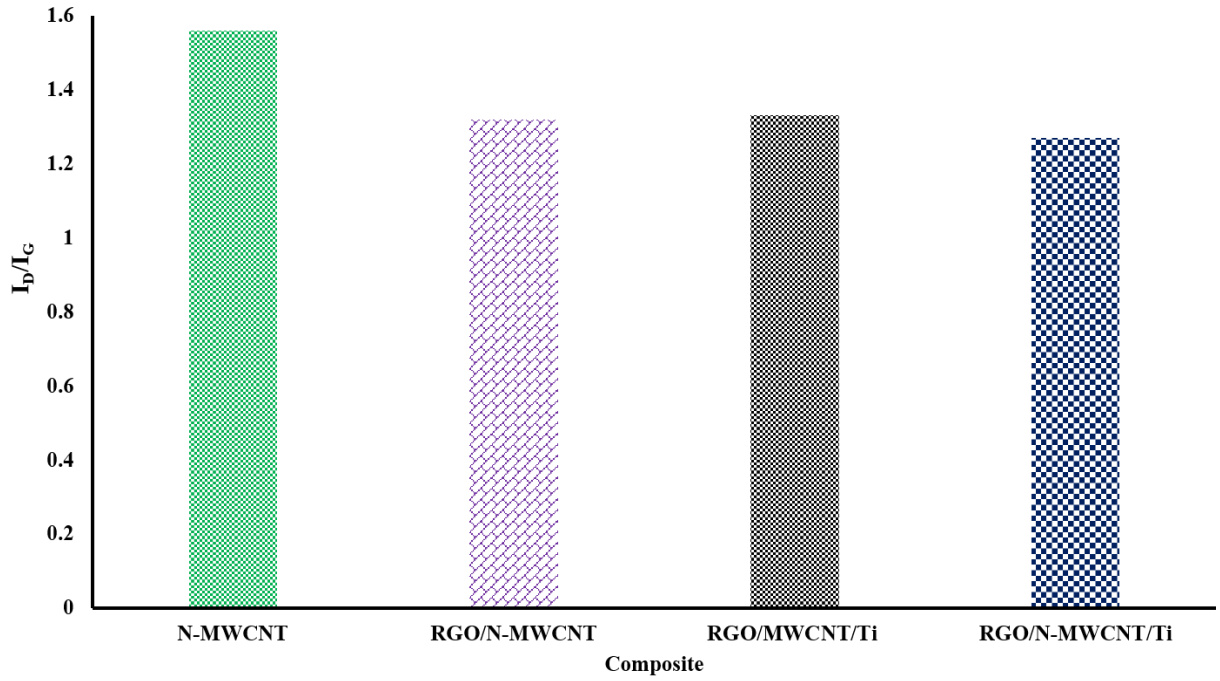

Fig. 8.11 Comparison of the Raman spectroscopy I_D/I_G ratios calculated by dividing the peak area under the D- and G-band, respectively

The N-MWCNTs had the least metal residue, i.e. almost zero, and this conjectures that HCl purification was successful (Fig. 8.12). The N-MWCNTs was also the most thermally stable with a steeper thermogram and this is an indication of a high sample homogeneity. The RGO/N- MWCNT/Ti was the second most thermally stable but with the highest residual metal. Also, RGO/N-MWCNT/Ti was the least thermally stable with the second lowest metal residual. This means RGO had some metal residual associated with it despite the dialysis purification process. Another deduction with respect to RGO amalgams was that the titania inclusion enhanced thermal stability of the RGO/N-MWCNTs (Fig. 8.12). This can be similarly explained by the limited exposure of graphitic structures to oxygen, *via* surface coverage, during thermal decomposition. However, the defect intensity (Fig. 8.11) could not account for the difference in thermal stability, regarding N-MWCNTs, and this is because N-MWCNTs proportion in composites was small (1: 3 wt.% ratio of RGO).

The composites had weight loss at 100 ℃ and between 200 - 400 ℃. These losses were ascribed to adsorbed water from RGO as well as from titania components of the composites, i.e., amorphous carbon and other oxygen-containing moieties on RGO sheets, respectively. In addition, the thermogram of both RGO/N-MWCNT and RGO/N-MWCNT/Ti show decomposition of sp^2-hybridised carbons in two different structures, i.e. RGO and N-MWCNTs at temperatures of c.a. 400 and 500 ℃, respectively (Fig. 8.12).

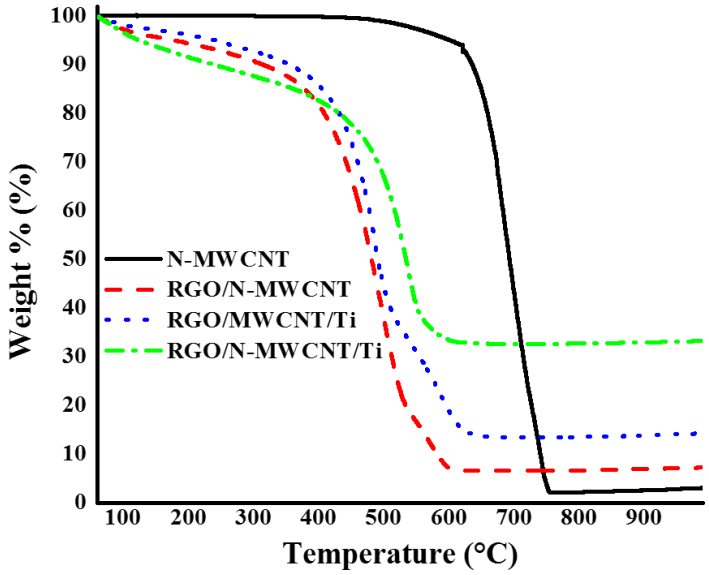

Fig. 8.12 Thermal analysis of N-MWCNTs, RGO/N-MWCNTs, RGO/MWCNT/Ti and RGO/N- MWCNT/Ti composites

Composites synthesised with RGO showed enhanced surface area relatively to pristine N-MWCNTs. Additionally, associated surface area was comparable to the RGO/MWCNT/Ti even though RGO/N- MWCNT/Ti was slightly lower than both. The conjectures here was that composite synthesis, *via* inclusion of RGO, was a fruitful solution processing strategy of both N-MWCNTs and MWCNTs in the current work. The important deduction from Fig. 8.5 and Fig. 8.13 was that inclusion of RGO transforms surface areas of N-MWCNT/Ti and N-MWCNTs to be comparable to that of MWCNT/Ti. The surface area enhancement, of both MWCNT/Ti and N-MWCNT/Ti composites, *via* inclusion of RGO concurs with the work on MWCNT/NiO reported by Bai et al. [8.8] Additionally, the surface area and I_D/I_G ratio trend corresponded, i.e. RGO/MWCNT/Ti > RGO/N-MWCNT > RGO/N-MWCNT/Ti, (Fig. 8.13 and Fig. 8.11). This also agrees with the report by Lin et al. [8.18] in that higher defect intensity

of MWCNT/Graphene was associated with higher surface areas. The larger titania agglomerates in RGO/N-MWCNT/Ti composites (Fig. 8.10) are a suitable explanation for the decrease in surface area.

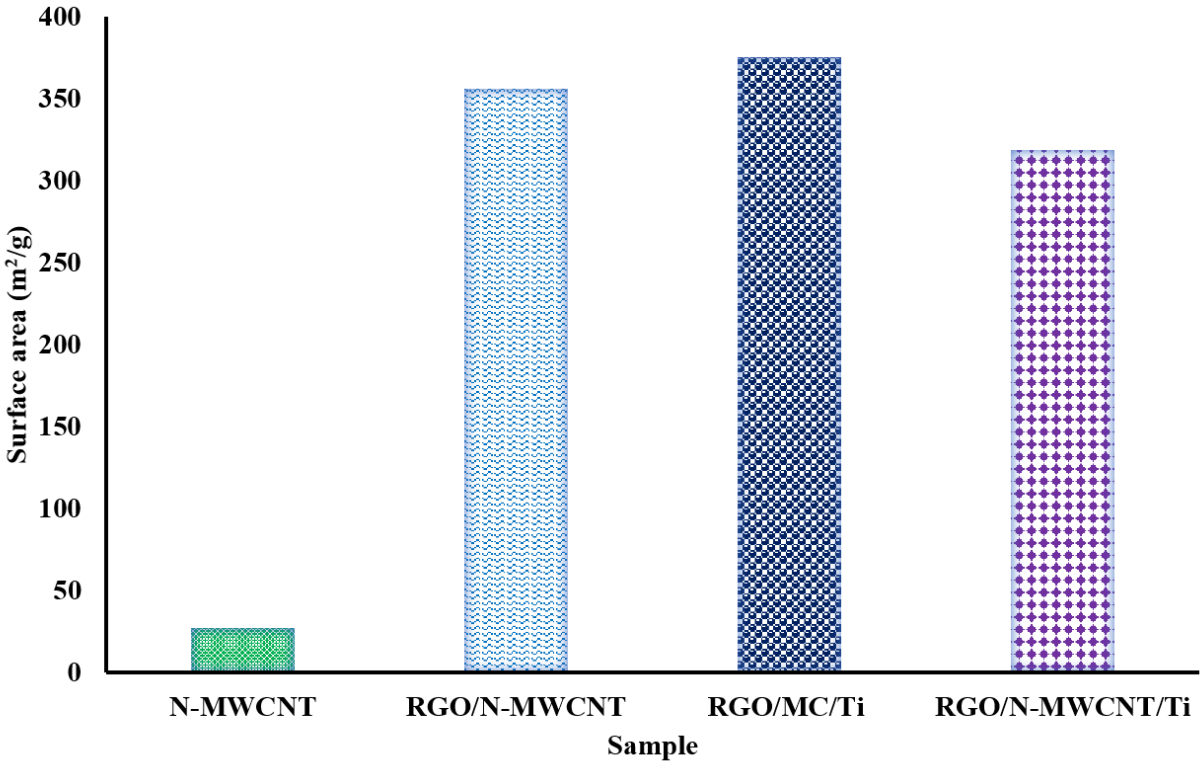

Fig. 8.13 Textural characteristics of RGO/MWCNT/Ti and RGO/N-MWCNT/Ti composites

The CV analysis data infers that RGO/N-MWCNT and RGO/MWCNT/Ti exhibited the best and second-best EC quality and C_s (Fig. 8.14). The observations were both attributed to their higher surface areas. This means there was minimum restacking of RGO sheets in the composites, hence, improved electrolyte penetration [8.4]. The inclusion of titania in the synthesis of RGO/N-MWCNT/Ti indicates that there was no improvement to N-MWCNTs capacitance. Also, C_s was highest at 10 mV s^{-1} than at 100 mV s^{-1} and this infers a domination of double layer charge storage mechanism.

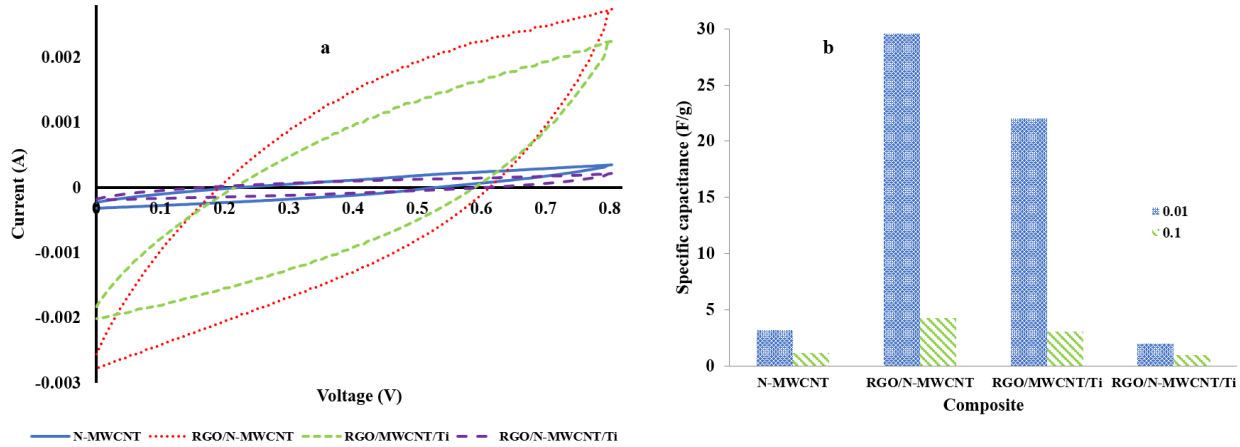

Fig. 8.14 (a) CV curves of RGO/MWCNT/titania and RGO/N-MWCNT/titania composites at scan speed of 10 mV s^{-1} in 1 M sodium sulfate electrolyte and (b) specific capacitance

The N-MWCNTs, alone, was associated with detectable R_{ct} but composite synthesis improved charge transfer (Fig. 8.15). This was deduced from the presence and absence of a semi-circle in the high frequency region of N-MWCNTs and composites, respectively [8.2]. Additionally, composite synthesis with both RGO and titania severely reduced the Warbug curve and an almost straight line, parallel to the R_{im} axis was exhibited (Fig. 8.15) on the Nyquist plot of both RGO/N-MWCNT and RGO/MWCNT/Ti composites. This was an indication of a more ideal capacitive character in the above-mentioned composites [8.2,8.24]. This means composite synthesis positively transformed the electrochemical properties. Also, scrutiny of Fig. 8.15, with the aid of insert, shows that the ascending order of diffusion path-length was RGO/N-MWCNT < RGO/MWCNT/Ti < RGO/N-MWCNT/Ti < N-MWCNTs. This agreed with decrease in C_s and EDLC quality. Additionally, the Nyquist plot in the low frequency region hints on the improvement of EDLC performance in the composite synthesised, predominantly with RGO (Fig. 8.15). Also, the high R_{ct} in N-MWCNTs was a possible reason for poor EDLC quality and C_s (Fig. 8.14).

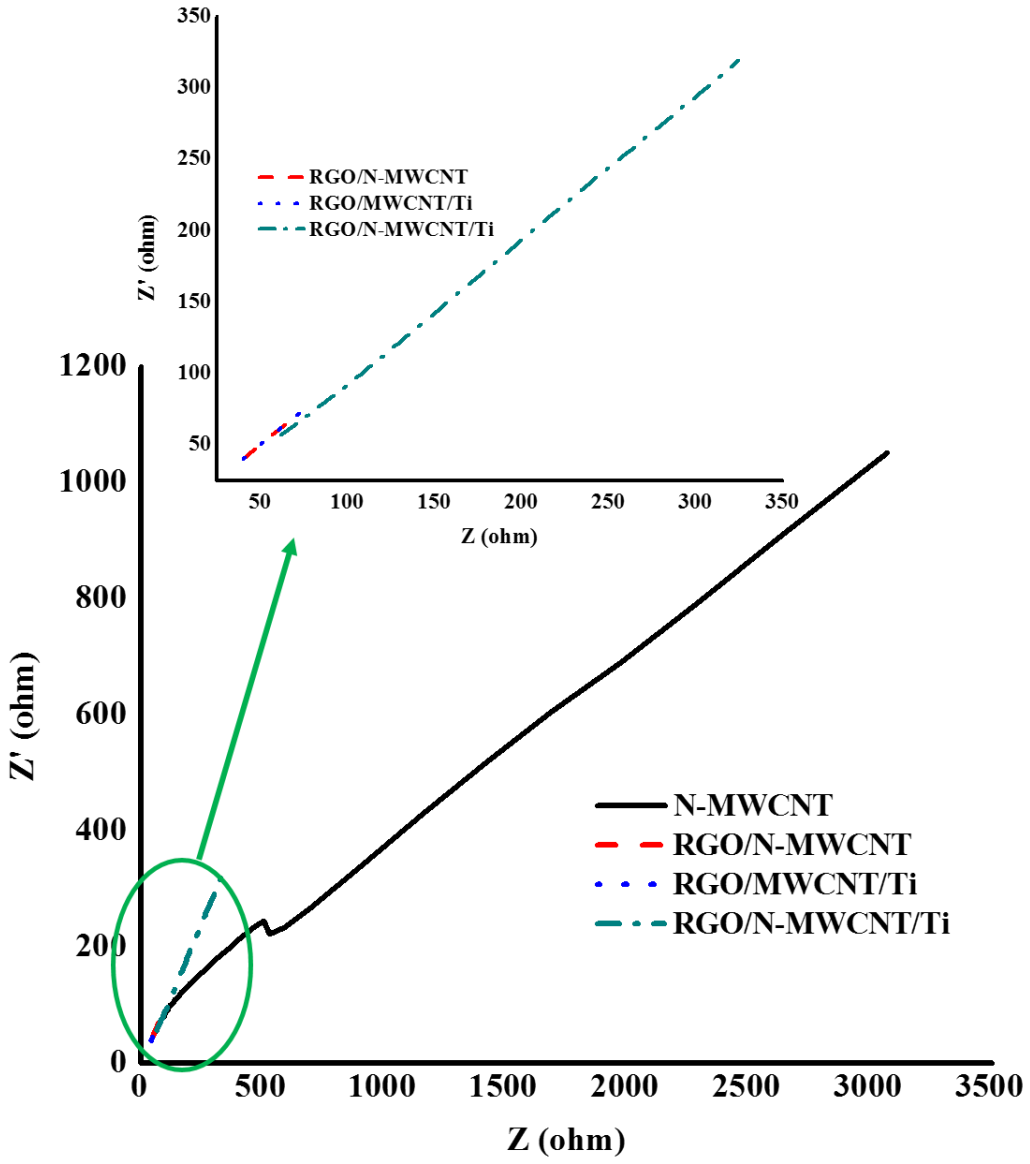

Fig. 8.15 The Nyquist plot for graphenated MWCNTs and N-MWCNTs composites with titania

8.4. Conclusions

The titania agglomerates were smaller and more uniformly distributed in the sol-gel method. Also, the chemical vapor deposition (CVD) technique was associated with more tube bundling than the sol-gel method. Tube bundling in multiwalled carbon nanotube/titania (MWCNT/Ti) composites synthesised *via* the CVD approach rendered them more thermally stable than sol-gel counterparts. CVD approach decreased the hydrophilic nature of both MWCNTs and nitrogen-doped multiwalled carbon nanotubes (N-MWCNTs) in their respective composites. Titania inclusion enhanced surface area in composites involving N-MWCNTs while an opposite effect was noticed in those made with MWCNTs. In general, sol-gel had higher surface area than CVD composites. Higher surface area was associated with better capacitor functionality. According to the data presented in this work, the method of composite synthesis is an important parameter which must be cautiously optimised with respect to material functionality in electrochemical double layer capacitors (EDLCs). MWCNT/Ti, *via* sol-gel method, had the best EDLC quality and highest specific capacitance (C_s) of 18 F g^{-1}. The longest Warbug length in N-MWCNT/Ti composites was associated with the poorest C_s values and EDLC quality.

Then optimal RGO:MWCNT ratio, with respect to the highest BET surface area of 417.46 m^2 g^{-1}, was 3:1. The RGO/N-MWCNT was homogeneous and hence, the sol-gel method was an appropriate solution processing technique in the current work. The N-MWCNTs was successfully purified with HCl reflux process. Titania coverage of both graphitic structures, MWCNT/Ti and N-MWCNT/Ti, raised the thermal stability. Further, synthesis of composites with the inclusion of RGO, is a suitable way to enhance textural characteristics of N-MWCNTs. RGO/N-MWCNT had the highest C_s of 30 F g^{-1} and the shortest diffusion path length. The diffusion path length was inversely proportional to C_s. The work showed that composite synthesis is a suitable strategy to enhance the capacitance and other physicochemical properties of N-MWCNTs.

Acknowledgements

The authors acknowledge the support from the University of KwaZulu-Natal and National Research Fund (NRF) for access to relevant infrastructure utilised in the research work. The author also thanks Dr Bryan Doyle and Dr Emanuela Carleschi for X-ray photoelectron spectroscopy analysis. ETM is grateful to UKZN Nanotechnology Platform for funding this work.

References

8.1. Zhu Y, Murali S, Stoller MD, Ganesh KJ, Cai W, Ferreira PJ, Pirkle A, Wallace RM, Cychosz KA, Thommes M, Su D, Stach EA, Ruoff RS (2011) Carbon-based supercapacitors produced by activation of graphene. Science 332:1537-1541

8.2. Dang Y-Q, Ren S-Z, Liu G, Cai J, Zhang Y, Qiu J (2016) Electrochemical and Capacitive Properties of Carbon Dots/Reduced Graphene Oxide Supercapacitors. Nanomaterials 6 (11):1-12. doi:10.3390/nano6110212

8.3. Mombeshora ET, Nyamori VO (2015) A review on the use of carbon nanostructured materials in electrochemical capacitors. International Journal of Energy Research 39 (15):1955-1980. doi:10.1002/er.3423

8.4. Qiu L, Yang X, Gou X, Yang W, Ma ZF, Wallace GG, Li D (2010) Dispersing carbon nanotubes with graphene oxide in water and synergistic effects between graphene derivatives. Chemistry 16 (35):10653-10658. doi:10.1002/chem.201001771

8.5. Zhao J-g, Xing B-y, Yang H, Pan Q-l, Li Z-p, Liu Z-j (2016) Growth of carbon nanotubes on graphene by chemical vapor deposition. New Carbon Materials 31 (1):31-36. doi:10.1016/s1872-5805(16)60002-1

8.6. Zhu X, Ning G, Fan Z, Gao J, Xu C, Qian W, Wei F (2012) One-step synthesis of a graphene-carbon nanotube hybrid decorated by magnetic nanoparticles. Carbon 50:2764-2771

8.7. Nardecchia S, Carriazo D, Ferrer ML, Gutierrez MC, del Monte F (2013) Three dimensional macroporous architectures and aerogels built of carbon nanotubes and/or graphene: synthesis and applications. Chem Soc Rev 42 (2):794-830. doi:10.1039/c2cs35353a

8.8. Bai Y, Du M, Chang J, Sun J, Gao L (2014) Supercapacitors with high capacitance based on reduced graphene oxide/carbon nanotubes/NiO composite electrodes. Journal of Materials Chemistry A 2 (11):3834-3840. doi:10.1039/c3ta15004f

8.9. S B, T T-T, C V, A M (2015) Graphene hybrids :Synthesis strategies and applications in sensors and sensitized solar cells. Frontiers in Chemistry 3 (38):1-19. doi:10.3389/fchem.2015.00038

8.10. Stoner BR, Raut AS, Brown B, Parker CB, Glass JT (2011) Graphenated carbon nanotubes for enhanced electrochemical double layer capacitor performance. Applied Physics Letters 99 (18):183104. doi:10.1063/1.3657514

8.11. Parker CB, Raut AS, Brown B, Stoner BR, Glass JT (2012) Three-dimensional arrays of graphenated carbon nanotubes. Journal of Materials Research 27 (07):1046-1053. doi:10.1557/jmr.2012.43

8.12. Jiang J, Li Y, Gao C, Kim ND, Fan X, Wang G, Peng Z, Hauge RH, Tour JM (2016) Growing carbon nanotubes from both sides of graphene. ACS Applied Materials & Interfaces 8 (11):7356-7362. doi:10.1021/acsami.5b12254

8.13. Parker CB, Raut AS, Brown B (2012) Three-dimensional arrays of graphenated carbon nanotubes. Materials Research Society 27 (7):1046-1053

8.14. Mombeshora ET, Ndungu PG, Nyamori VO (2017) Effect of graphite/sodium nitrate ratio and reaction time on the physicochemical properties of graphene oxide. New Carbon Materials 32 (1):174-187

8.15. Mombeshora ET, Jarvis ALL, Ndungu PG, Doyle BP, Carleschi E, Nyamori VO (2017) Some perspectives on nitrogen-doped carbon nanotube synthesis from acetonitrile and *N*,*N*′-dimethylformamide mixtures. Materials Chemistry and Physics 199:435-453. doi:10.1016/j.matchemphys.2017.07.044

8.16. Mombeshora ET, Simoyi R, Nyamori VO, Ndungu PG (2015) Multiwalled carbon nanotube-titania nanocomposites: Understanding nano-structural parameters and functionality in dye-sensitized solar cells. South African Journal of Chemistry 68:153–164. doi:10.17159/0379-4350/2015/v68a22

8.17. Dresselhaus MS, Jorio A, Saito R (2010) Characterizing graphene, graphite, and carbon nanotubes by Raman spectroscopy. Annual Review of Condensed Matter Physics 1 (1):89-108. doi:10.1146/annurev-conmatphys-070909-103919

8.18. Lin C-C, Lin Y-W (2015) Synthesis of carbon nanotube/graphene composites by one-step chemical vapor deposition for electrodes of electrochemical capacitors. Journal of Nanomaterials 2015:1-8. doi:10.1155/2015/741928

8.19. Lin YG, Hsu YK, Wu CT, Chen SY, Chen KH, Chen LC (2009) Effects of nitrogen-doping on the microstructure, bonding and electrochemical activity of carbon

nanotubes. Diamond and Related Materials 18 (2-3):433-437. doi:10.1016/j.diamond.2008.09.009

8.20. Lou F, Buan MEM, Muthuswamy N, Walmsley JC, Rønning M, Chen D (2016) One-step electrochemical synthesis of tunable nitrogen-doped graphene. J Mater Chem A 4 (4):1233-1243. doi:10.1039/c5ta08038j

8.21. Suboch AN, Cherepanova SV, Kibis LS, Svintsitskiy DA, Stonkus OA, Boronin AI, Chesnokov VV, Romanenko AI, Ismagilov ZR, Podyacheva OY (2016) Observation of the superstructural diffraction peak in the nitrogen doped carbon nanotubes: Simulation of the structure. Fullerenes, Nanotubes and Carbon Nanostructures 24 (8):520-530. doi:10.1080/1536383x.2016.1198331

8.22. Capasso A, Dikonimos T, Sarto F, Tamburrano A, De Bellis G, Sarto MS, Faggio G, Malara A, Messina G, Lisi N (2015) Nitrogen-doped graphene films from chemical vapor deposition of pyridine: influence of process parameters on the electrical and optical properties. Beilstein J Nanotechnol 6:2028-2038. doi:10.3762/bjnano.6.206

8.23. Wei Q, Tong X, Zhang G, Qiao J, Gong Q, Sun S (2015) Nitrogen-doped carbon nanotube and graphene materials for oxygen reduction reactions. Catalysts 5 (3):1574-1602. doi:10.3390/catal5031574

8.24. Wang G, Zhang J, Kuang S, Zhou J, Xing W, Zhuo S (2015) Nitrogen-doped hierarchical porous carbon as an efficient electrode material for supercapacitors. Electrochimica Acta 153:273-279. doi:10.1016/j.electacta.2014.12.006

Appendix: Supporting information for Chapter 8

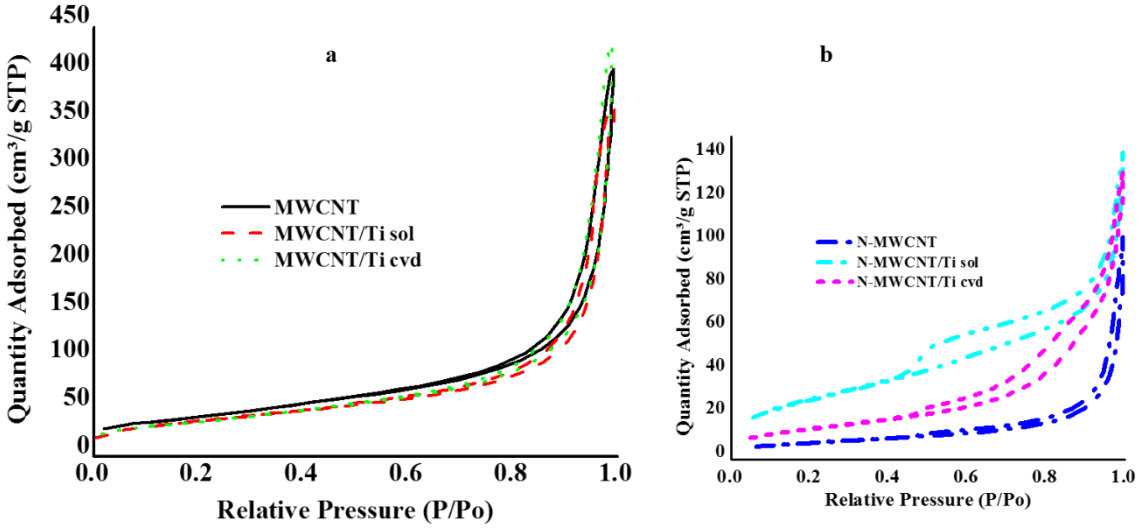

Fig. 8.S1 Textural characteristics isotherms of (a) MWCNT/Ti and (b) N-MWCNT/Ti composites

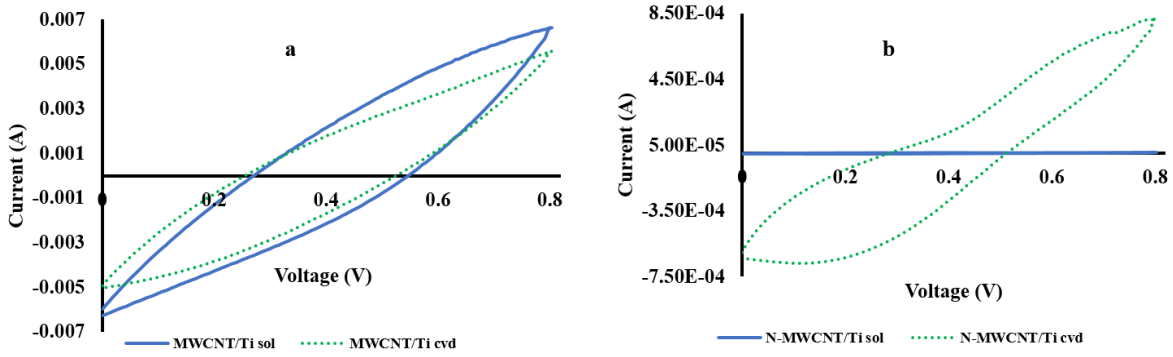

Fig. 8.S2 CV curves of (a) MWCNT/Ti and (b) N-MWCNT/Ti composites at scan speed of 100 mV s^{-1}

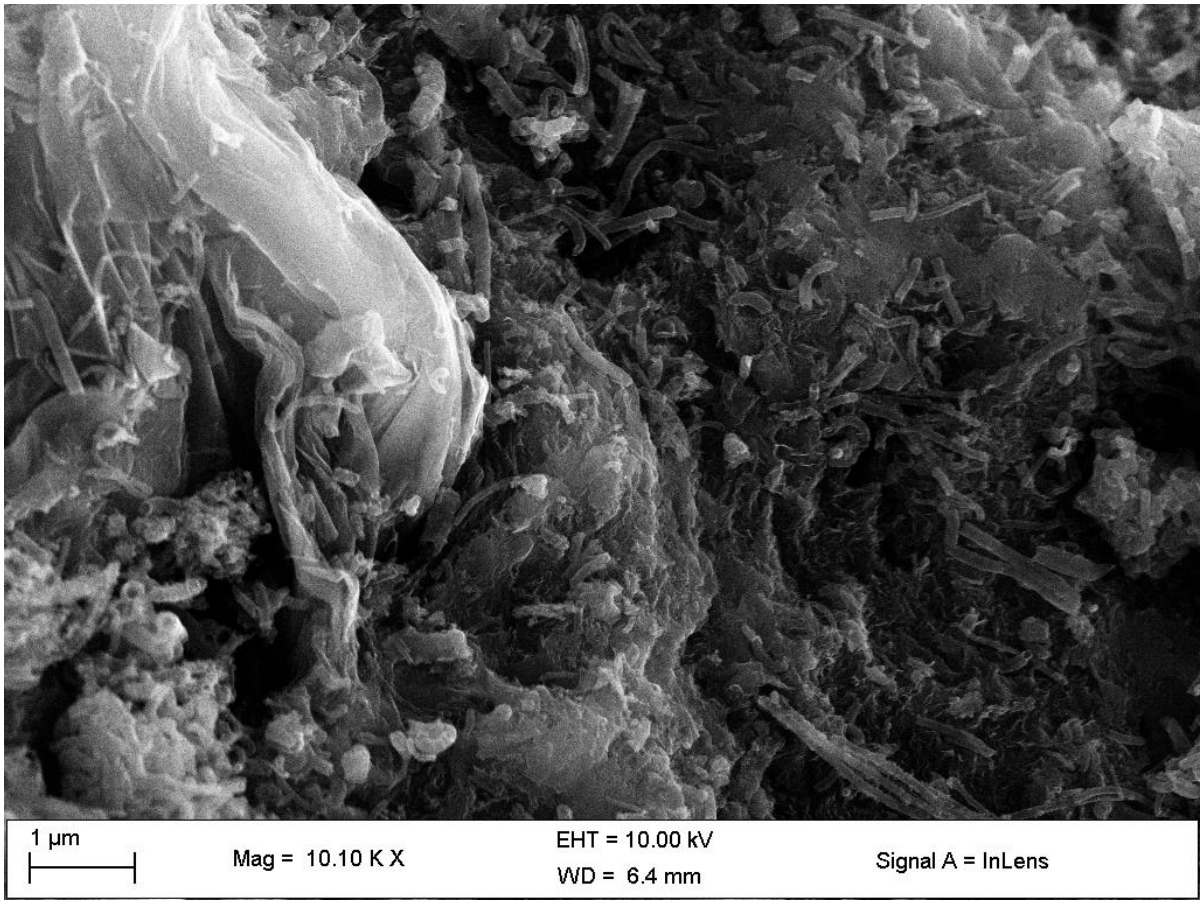

Fig. 8.S4 The representative SEM image of RGO/MWCNT

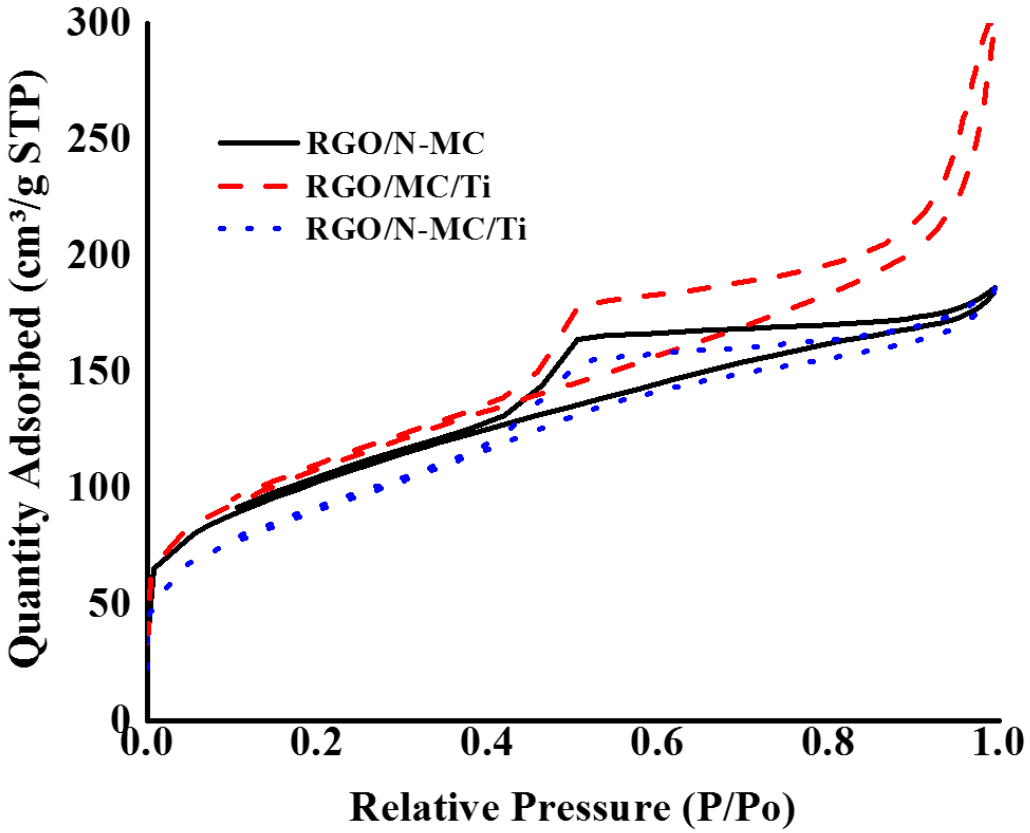

Fig. 8.S5 Textural isotherms for RGO/MWCNT/Ti and RGO/N-MWCNT/Ti composites

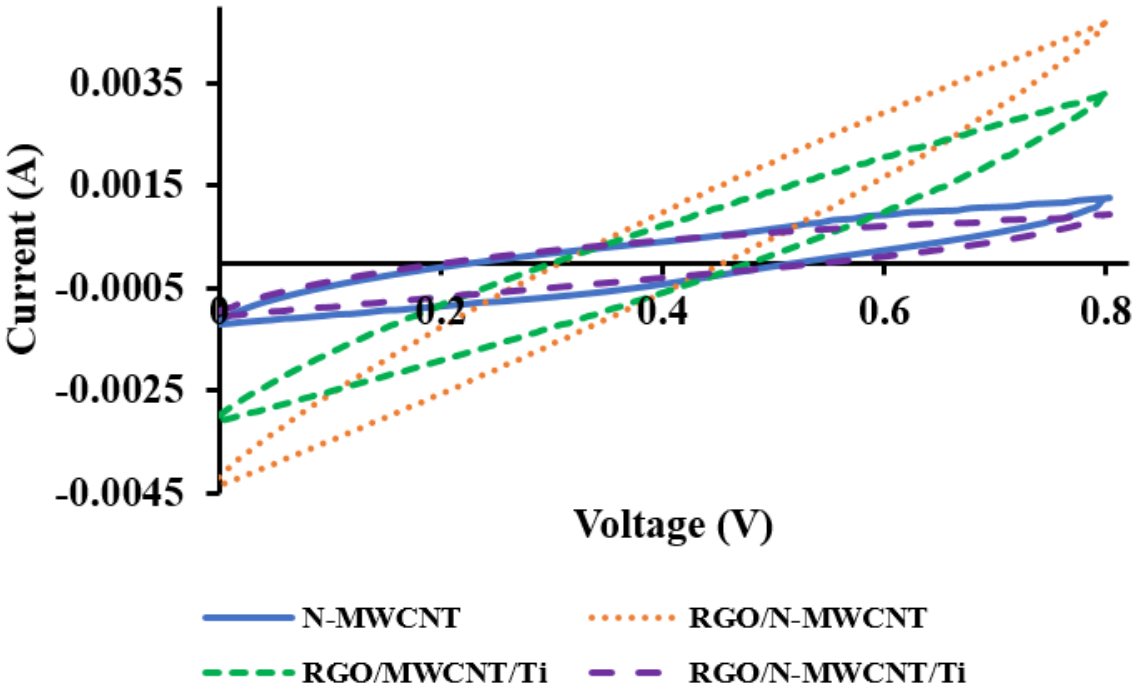

Fig. 8.S6 CV curves of RGO/MWCNT and RGO/N-MWCNT titania composites at scan speed of 100 mV s^{-1}

Chapter Nine

Summary, conclusions and future work

This chapter presented the overall summary, conclusions and future recommendations from the presented thesis.

9.1. Project summary

The current drive towards usage of renewable energy resources and the obligation to develop cheaper energy alternatives, to the existing sources, has spearheaded the advancement of energy storage systems to be a requirement. Cheap carbon-based nanomaterials are promising electrode materials for the development of electrochemical capacitors. The work reported herein investigated usage of nanostructured materials, namely, multiwalled carbon nanotubes (MWCNTs) and reduced graphene oxide (RGO) in electrochemical double layer capacitors (EDLCs). This study included a thorough review of carbon nanomaterial applications in EDLC. The main goal was to explore physicochemical properties and pursue feasible strategies of enhancing the EDLC functionality by use of carbon-based nanomaterials. This encompassed tailoring physicochemical properties towards better EDLC performance by controlling synthesis parameters namely, reagent mixing ratios, reaction temperature and time. Functional materials synthesised, in the current study, include nitrogen-doped multiwalled carbon nanotubes (N-MWCNTs), graphene oxide (GO) and RGO. The influence of both content and functional groups of nitrogen present in N-MWCNTs and RGO towards better EDLC performance was successfully studied. The physicochemical traits associated with oxygen-modified MWCNTs and GO, both containing oxygen-containing groups, were also positively investigated and EDLC functionality was accordingly elucidated on this basis.

Another physicochemical tuning approach studied was composite synthesis and the various components used in this regard were GO, RGO, MWCNTs, N-MWCNTs, titania and cellulose. The effect of different combinations and wt.% ratios on both physicochemical and EDLC characteristics were studied. The suitability of group one sulfates, namely; lithium sulfate, sodium sulfate and potassium sulfate, were compared as electrolytes for EDLC testing and the best electrolyte was used in all the materials studied in this thesis.

9.2. Conclusions

Energy storage devices still require a focused study to boost energy resources for viable economic growth and stability. One of the key ways towards achieving this is development of electrode materials with functional shaped carbon nanostructured material (SCNM). N-MWCNTs were effectively synthesised from small molecules, as both carbon and nitrogen sources using the floating catalyst chemical vapor deposition method. The sp^3-hybridised nitrogen, in reagents, had better doping effect (5.87%) than *sp*-hybridised source (3.49%). The synthesis temperature was a critical parameter which needed thorough optimization with respect to yield composition and wt.% of nitrogen in the N-MWCNTs. Also, by changing the synthesis temperature, it was possible to tune the number of concentric shells of N-MWCNTs from sp^3 sources. On the other hand, within the reagent used, the ratio at which the sp^3: *sp* nitrogen sources are mixed, influenced physicochemical properties of the N-MWCNTs. The current work also showed that associated physicochemical properties of typical N-MWCNTs, such as porosity, nitrogen functional groups, metallicity, outer and inner diameters, can successfully be manipulated through changing of sp^3: *sp* ratio of nitrogen sources in the reagent. The 1:3 ratio of sp^3: *sp*-hybridised nitrogen sources, had the highest N-doping of 9.38%, hence it enhanced the doping effect of both sp^3- and *sp*-hybridised sources. The products consisted mostly of pyrrolic-nitrogen moieties and to less extent, some pyridinic- and quaternary-nitrogen as well as nitrogen oxides.

With regards to graphene oxide (GO) synthesis, the graphite: sodium nitrate ratios, as modified Hummer's method reagents, were practically optimised. Higher sodium nitrate proportion in the reagents was used to increase the oxygen-containing moieties, surface area, porosity, amongst other physicochemical properties. Increasing oxygen-containing moieties on graphitic sheets amplified their defect intensity and was associated with overall decrease in thermal stability. The 1:1 ratio, of graphite: sodium nitrate, produced GO with the least roughened sheet surfaces, highest exfoliation extent and with no detectable residual graphite in the products (reaction completion). Hence, 1:1 ratio, of graphite: sodium nitrate, was optimised as the best reagent mixing ratio utilised for all the synthesis and applications that involved GO in the current thesis. Additionally, the use of sodium nitrate, in the modified Hummer's method, introduces nitrogen functionalities on GO sheets. Furthermore, according to the current study, the intensity of defects, such as wrinkling and paper-like morphologies, can be

tuned-down by increasing reaction time. In short, it is imperative to state that graphite to sodium nitrate ratio, in reagents of the modified Hummer's method, affect the sheet roughness, exfoliation extent, overall defect intensity, oxygen concentration on the carbon framework, thermal stabilities and textural characteristics of the produced GO, amongst other physicochemical characteristics.

A study to investigate the influence of oxygen-containing groups on SCNMs functionality in electrochemical capacitors (ECs) by use of group one sulfates; namely, Li_2SO_4, Na_2SO_4 and K_2SO_4, was done with oxygen-modified MWCNTs. One of the key objective herein was to determine the best electrolyte for use with rest of the materials in this thesis. The electrolyte with best overall EDLC quality and higher charge storage performances was Na_2SO_4. The study could highlight that the cationic sizes of electrolytes must critically be considered when materials are tested for EDLC performances. A bad electrolyte choice might give a wrong impression of the materials being examined. In addition, oxygen modification on MWCNTs enhanced their EC functionality and the charge storage mechanism was deduced to be *via* both pseudo and EDLC. This was an interesting transformation since the carbon materials are popularly known to store charge *via* the EDLC mechanism. The data, presented in this thesis, infers that the ultrasonic treatment can suitably be utilised in introducing oxygen-containing groups on the tube walls and this modifies their physicochemical properties. In summary, this deduction highlights the importance of critically considering the choice of reagents for purification of MWCNTs, particularly those for electronic applications. This is often ignored as much focus is usually on the most effective purification method, with the least residual metal. Also, attaching oxygen-containing moieties on MWCNTs was a fruitful approach of tailoring their physicochemical properties and positively tuned-up their charge storage performances.

The elemental analysis, thermogravimetric analysis under nitrogen atmosphere and X-ray photoelectron spectroscopy, corroborated and, are all suitable techniques to evaluate the effectiveness of GO reductants towards graphene synthesis. Hydrazine hydrate was the most effective reductant when compared to sodium borohydride and ascorbic acid since it produced RGO with the highest surface area and nitrogen content. Viable manipulation of nitrogen moieties in RGO was achieved by varying the reductants. Nitrogen moieties in GO existed as dangling bonds but reduction with ascorbic acid and hydrazine hydrate facilitated N-doping within graphitic structures as pyrrolic and pyridinic, respectively. Additionally, sodium borohydride reduction doped RGO with boron and eliminated nitrogen moieties. The study

also showed that N-doped RGO facilitated better performances in charge storage than B-doped. B-doped RGO lowered electrolyte ion penetration but pyridinic-nitrogen moieties positively transformed it in this regard. N-doping decreased the intrinsic resistance, and this was a positive attribute since it minimises energy wastage as heat in charge storage devices. Also, charge storage characteristics increased with raise in temperature of thermal treatment of hydrazine hydrate reduced GO. To sum up, in the quest for effective reductants of GO, the choice must be scrutinised with regards to associated physicochemical transformations and intended applications. Conductivity of RGO was tailored positively by increasing N-doping, changing nitrogen functional groups and controlling defect intensity by use of an appropriate reductant. For ECs, N-doping positively tuned charge storage performances of RGO and typical materials stored charge by both pseudo and EDLC mechanism. In terms of capacitance, the pyrrolic-N-doped RGO had better performances than pyridinic-counterparts.

In the titania composites investigated, varying wt.% of titania was used as a strategy to alter morphology of RGO and GO sheets. Increasing wt.% of titania aptly boosted the textural characteristics of graphene oxide/titania (GOTi) composites. Higher oxygen-containing groups facilitated chemical bonding between GO and titania. Reduction of GOTi was an efficacious approach of improving their charge storage performance whilst cellulose was a suitable way of improving their surface area, however, it caused detrimental effects to charge storage processes. In summary, from the current investigation, higher titania wt.% deteriorated capacitance of the composites since it culminated in increasing diffusion path-length. Also, a more compact packing of electrode materials negatively affected ion penetration. The main charge storage mechanism of the reduced composites was EDLC and composite synthesis enhanced charge storage performances of titania.

The N-MWCNTs were investigated and appropriately tuned as electrode materials of ECs. Their pyrrolic-nitrogen composition was practically tailored upwards by increasing the portion of sp^3-hybridised nitrogen source in the reagent mixture which contained both *sp* and sp^3 nitrogen sources in solution. In the current thesis, evaluation of the allied EC characteristics, showed a decrease with increase in pyrrolic-nitrogen content in N-MWCNTs. The sol-gel method was suitable for producing de-bundled N-MWCNTs/titania composites with fewer agglomerates and low defect intensity, and higher surface areas than CVD approach. In short, method utilised for composite synthesis is a feasible strategy to tune physicochemical properties but affected MWCNTs and N-MWCNTs in a different way. The ratio of RGO and MWCNTs in composites was effectively exploited to control the associated surface areas and

enhanced the characteristics from that of individual components. In addition, N-doping of MWCNTs improved metal adhesion on their walls with ultimate enhanced surface areas. The path-length associated with the N-MWCNTs was magnificently decreased *via* composite synthesis with RGO and this improved capacitance. From the current work, it is important to highlight that the control of defect intensity, *via* variation of component compositions in N-MWCNT/RGO/Ti and MWCNT/RGO/Ti composites, yield positive alterations of surface area and the main charge storage mechanism was EDLC. The inclusion of RGO enabled a positive transformation in the above-mentioned composites by decreasing the diffusion path-length with an associated better-quality EDLC character. In summary, the composite synthesis of N-MWCNTs was an effective route that shortened the diffusion path-length for the electrolyte ion and this increased charge storage performances.

From the data presented in this work, one of the fundamental deductions was that high oxygen content of MWCNTs enhanced capacitance whilst low content in RGO was associated with high capacitance. This highlighted morphological influence on electrochemical capacitance of the typical materials, amongst other physicochemical properties. The physicochemical properties of GO, RGO, MWCNTs and N-MWCNTs were successfully tuned *via* control of oxygen and nitrogen content, manipulation of associated functional groups and composite synthesis. The associated nano-structural parameters were successfully studied and linked to charge storage characteristics.

9.3. Future work

1. Although the effect of pyrrolic-nitrogen composition on capacitance was studied in the current work, a future focused study on the influence of at.% of N-doping, particularly on pyridinic-nitrogen and quaternary-nitrogen moieties with respect to capacitance of graphitic structures is recommended.
2. The influence of reagent ratios, namely sodium nitrate and graphite, in the initial step of the modified Hummer's method were studied in this work. The effect of the concentration of both sulfuric acid and hydrogen peroxide, and ratios of the sulfuric acid, hydrogen peroxide and potassium permanganate to graphite in the subsequent steps can be similarly studied.
3. The work also opens new avenues for dedicated studies focusing on the influence of pore sizes of the materials in current study, and solvated ion sizes of various

electrolytes. This can be approached by tuning pore sizes over a wider range and investigating the optimum pore sizes for the three group one sulfates investigated. Another interesting study would be the optimisation of group one sulfate electrolyte concentration with the deduced ideal pore sizes and the best group one sulfate electrolyte. Other electrolytes such as ionic liquids and sulfuric acid can also be investigated with materials studied in the current work.

4. Industrial test of the materials in the form of current commercial capacitors can be explored *via* fabrication of devices in the same form as industrial devices with the current materials pressed onto current collectors. The charge/discharge experiments can be done at known currents with a galvanostat as a further characterisation technique.
5. The work also opened new arenas for theoretical investigations through computational studies focusing on the influence of various oxygen functional groups of the oxygen-modified MWCNTs and graphene oxide, and the formation of an electrochemical double layer.